CRANFIELD INSTITUTE OF TECHNOLOGY

COLLEGE OF AERONAUTICS

Ph.D. Thesis

J.M. SHANKS

STATIC AND DYNAMIC ANALYSIS OF MARINE PIPELINES AND RISERS

Supervisor: Dr. C.L. Kirk

March 1985

SUMMARY

This thesis investigates two slender body problems, namely the static and dynamic analysis of submarine pipeline spans and the dynamic analysis of marine risers. In view of structural and environmental similarities, these problems are closely related and where possible common analysis procedures have been developed.

For the problem of pipe spanning, attention is focused on the possibility of vortex induced vibration and the associated question of span assessment. This situation arises when following the discovery of a span, an assessment is required to determine if any remedial repair work is required. To assist in this assessment, and also to provide a more fundamental understanding of span behaviour, a number of mathematical models are developed.

First linear beam-column theory is used to determine the span natural frequencies and buckling load for a single span supported continuously on either side by an elastic foundation. The effects of internal/external pressures and product temperature are included and the results presented in terms of two independent nondimensional parameters.

Next the effects of pipe/soil friction and change in geometry are considered utilising a nonlinear Finite Element model. Theories are developed for a nonlinear pipe element with axial/bending coupling and a nonlinear nonconservative pipe/soil friction element. The effects of initial seabed geometry and finite amplitude vibration are included and it is shown that span frequencies are sensitive to both end friction constraints and seabed geometry.

For marine riser dynamics, an attempt is made to synthesise the best parts from the many and varied analysis methods developed to date, into a simple but flexible

design-orientated program. The riser is represented using a Finite Element model similar to that employed for the pipeline spans, and a reduced set of equations obtained using a component mode synthesis method. Several riser/ articulated column designs are considered and the results found to agree with published data.

CONTENTS

LIST OF FIGURES

NOTATION

The notation used in this thesis is as defined in the main text.

ACKNOWLEDGEMENTS

The author would like to thank the following people for the assistance they have given him over the last three years:-

Dr.C.L.Kirk, under whose supervision this work was carried out.

The Aircraft Design staff and research students who have made working in the department an interesting and enjoyable experience.

The Science and Engineering Research Council for providing the funds for this study.

Frances Creckendon for her patient and accurate typing of this thesis.

My wife, Marie, for her encouragement and constant support.

CHAPTER 1

INTRODUCTION TO PIPELINES

1.0 Introduction to North Sea Operations

The rapid growth in World energy demands over the last 20 years together with a steady increase in the price of oil has resulted in oil exploration and production moving offshore, often into hostile environments. In the North Sea this development has been spectacularly fast with some 1700 exploration wells plus another 500 appraisal wells drilled during the last two decades. This concentrated activity has resulted in significant discoveries with total proven plus probable offshore reserves in the UK sector currently estimated at some 25 billion barrels (oil equivalent). The production of hydrocarbons from these reserves has required the construction and installation of some 35 major deepwater production platforms in the central and Northern UK sector of the North Sea plus a large number of mainly small gas facilities in the Southern basin. As a result UK oil and gas production is currently some 3 million barrels/day (oil equivalent) placing Britain fifth in the league table of oil producers and second amongst world offshore producers. In the Norwegian sector development has been more moderate, mainly because Norway was essentially self sufficient in energy without the oil and had a reasonably healthy economy when oil was discovered. Nevertheless some 25 major platforms have been installed with current production standing at 1.1 million barrels/day (oil equivalent). Future development also looks assured with the UK offshore operators association recently forecasting the development of as many as 80 new fields before the end of the century. According to the report this could involve drilling 1500 wells, building 100 production platforms and laying more than 3,000 miles of pipeline with a total estimated

capital investment of £44 billion. The emphasis during this "second phase" of development will be from conventional offshore technologies to potentially cost reducing techniques capable of exploiting the increasing number of smaller marginal fields. In addition if current deep water drilling north of 62^{o}N and west of the Shetland Islands results in significant finds, increased emphasis will be focussed on floating production and subsea systems.

The offshore production of oil and gas in the volumes indicated above leads to the requirement for a safe and efficient means of transporting such production to land based refinery and processing facilities. For oil production this requirement may be satisfied utilising

a) Offshore loading involving some form of single point mooring plus shuttle tanker(s)
b) Submarine Pipeline

During the early years of North Sea development the favoured option was offshore loading particularly in the Norwegian sector. At that time the main factors influencing this decision were

a) Low capital cost together with favourable cash flow resulting from early production,
b) Technical difficulty and high cost of installing a purpose built pipeline. This factor was particularly significant in the Norwegian sector in view of the deep waters encountered in the Norwegian trench.

The main disadvantage of such facilities is the down time associated with poor weather conditions, a difficulty minimised by providing storage capacity on either the production platform(s) or the single point mooring. A typical example of such an arrangement is the Norwegian

Statfjord development where three concrete gravity platforms with a total storage capacity of over 6 million barrels offload via three articulated loading towers. For some early developments, offshore loading was installed in advance of a planned pipeline with the single point mooring either removed once the pipeline was installed or retained as a backup during pipeline inspection and maintenance operations. A similar switch to pipelines has also been made in a number of fields where extreme operating difficulties have been experienced with the single point mooring.

The alternative approach to oil and gas export via a submarine pipeline is highly reliable, insensitive to weather conditions and offers the advantage of low operating costs. At the present time some 6,000 km of pipeline has been installed in the North Sea ranging from small diameter flow lines to the major oil and gas trunk lines indicated in table 1.1. With the possible exception of north of $62^{o}N$ these trunk lines provide a comprehensive drainage system for the major fields in the North Sea and are likely to dictate any further growth to the network. The availability of this system means that new fields brought on stream may often be tied into the existing network via a relatively short feeder line.

1.1 History of Pipeline Development in the North Sea

The first North Sea offshore pipeline was 68km of 16in diameter gas line from BP's West Sole field to Easington on the Yorkshire coast, figure 1.1. This line was laid in 1966 and was followed by a further 500km of 16in, 28in but mostly 30in line all from or within the Southern gas basin of the UK sector. Ten such lines were laid up to 1975 with only one exceeding the 100km length and all in relatively shallow water. Meanwhile by 1972 seven major oil and gas fields had been discovered at Ekofisk, Montrose, Forties,

ROUTE	OIL/GAS	LENGTH km	D inches	INSTALLATION date
EKOFISK-TEESSIDE	OIL	355	34	73/74
FORTIES-CRUDEN BAY	OIL	180	32	73/74
PIPER-FLOTTA	OIL	210	30	74/75
EKOFISK-EMDEN	GAS	440	36	74/75
FRIGG-ST.FERGUS 1	GAS	175	32	74/75
FRIGG-ST.FERGUS 2	GAS	185	32	75/76
CORMORANT-SULLOM VOE	OIL	175	36	75/76
NINIAN-SULLOM VOE	OIL	170	36	75/76
BRENT-ST.FERGUS	GAS	450	36	77/78
RP1-KARSTO	GAS	225	28	83
STATFJORD-KARSTO	GAS	310	30	83/84
HEIMDAL-EKOFISK	GAS	345	36	83/84
FULMER-ST.FERGUS	GAS	290	20	84

TABLE 1.1 Major North Sea Trunk Lines

Auk, Frigg, Brent and Argyl, figure 1.1. Significantly, these and subsequent discoveries were further away from land, further north and in deeper more hostile waters. As a consequence the industry was initially reluctant to test the calibre of the pipelaying contractors and of the first seven fields on stream only Forties opted for a pipeline from the start. This significant decision followed Mediterranean trials in 1972 during which the Italian pipelaying contractor Saipem were able to convince BP that its Castoro Due laybarge would be able to handle the large 32in pipe and 130m water depth required for the Forties line. During the following 1973/74 seasons the first oil trunk lines, Ekofisk to Teesside and Forties to Cruden Bay, were laid so ushering in a 5 year period of concentrated activity. Subsequent developments quickly followed with the Piper-Flotta, Ekofisk-Emden and Frigg-St. Fergus 1 lines installed during the 1974/75 seasons and the Frigg-St. Fergus 2, Cormorant-Sullom Voe and Ninian-Sullom Voe lines completed in 1975/76. An important development during this period was the arrival of third generation lay barges in the form of the semi-submersible Viking-Piper and ship type ETPM1601. These vessels were developing the double jointing concept, welding two 12m lengths in advance so halving the number of field joints needed to be made on board. As well as increasing laying rates these vessels were working in over 150m of water while at the same time significantly widening the weather window. Other vessels built at this time and destined to have a significant impact on pipelaying technology were Saipem's Castoro Sei and Brown and Root's Bar 420 (formerly Semac I), both semi-submersible type vessels. This initial period of sustained activity ended in 1978 when the laybarge Semac I finished work on the Brent-St. Fergus FLAGS (Far North Liquids and Associated Gases System) line, figure 1.2. Involving 450km of 36in diameter X60 steel pipe this project was at the time the largest to date and introduced a number of significant new developments including

a) Elimination of trenching in deepwater by developing a high strength pipe coating capable of tolerating repeated contact by heavy fishing gear. This was achieved by increasing the steel reinforcement in the coat to 0.9% of the cross sectional area and utilising high strength concrete rated at 6,000 psi at 28 days. Before this the strongest coating specification had been on BP's Forties line where 4,600psi concrete and 0.57% steel was used. This development enabled more than 70% of the FLAGS line to be left untrenched.

b) Introduction of semi-automatic welding system with specially developed preweld induction heating at 730^{o}C for 30 seconds. In addition to decreasing weld times this method proved highly reliable with only 4% of the total welds requiring repair.

c) Development of water based gels which picked up 35t of debris within the pipe prior to dewatering.

With the notable exception of any lines to Norway the major trunk lines were now installed and further development consisted of small intrafield and interfield flow lines. Interesting developments associated with this work included

a) First North Sea use of reel ship technology when Santa Fe's Apache laid four 4in flowlines of 1700m length plus two umbilical control lines connecting BP's Buchan template with two remote wellheads, figure 1.3. This vessel was also used to lay the 16km Ninian Spur on the FLAGS system where its high accuracy and use of full dynamic positioning involving no anchors, offered minimal danger to the large number of lines already installed in the area.

b) First North Sea use of towing methods when in 1976 three 32in feeder lines were bottom towed for about 5 miles and tied into the Frigg-St. Fergus intermediate booster platform. This platform houses compression equipment and is located approximately

midway between the Frigg field and St. Fergus in 100m of water. In the following year R.J.Brown and associates undertook a 400km bottom tow of a 2.1km length of 36in line from its Norwegian fabrication site to the Statfjord field where it linked up the main platform with its loading tower. This tow involved crossing the Norwegian Trench at a maximum depth of 385m. In 1980 Conoco refined this technique when it used its buoyant off-bottom tow method to install three lengths of 12.75in flowline bundles at its Murchison field. These bundles incorporated two 3.5in flowlines and four hydraulic control lines with the shortest string over 750m in length and the longest about 1,900m.

c) First hyperbaric tie-in completed on the Frigg-St. Fergus line in 1975. Subsequent research, including tests by the diving support vessel Uncle John as part of deep water research for the Statpipe project, has shown that this method may be used in 300m of water or more.

d) Introduction of first subsea plough on the Statfjord bottom tow project in 1977. At the time this method was considered quicker and less costly than the traditional jetting methods of burial in view of the hard consolidated clays encountered at Statfjord. Subsequent work has tended to concentrate on trenching machines with most emphasis on deepwater applications for the Norwegian Trench and Mediterr-anean.

Further development of the major trunk line system started again in 1983 when McDermott's LB200 (formerly Viking Piper) working on the Statpipe project made the first crossing of the Norwegian trench from Karsto to Riser Platform 1, figure 1.4. During the same season LB200 also started the Statfjord-Karsto line in preparation for a second crossing of the trench the following season.

Significant developments associated with this work include

a) Installation of 30in diameter pipe in 300m of water across the flat bottom of the Norwegian Trench. In addition high seabed slopes were involved especially on the steep eastern side of the trench close in to shore.

b) Design for bottom stability without trenching using thick concrete coatings (up to 125mm) and two densities of concrete (2.2t/m^3 and 2.9t/m^3). Heaviest coating was used generally in the areas of high current (up to 1.5m/s) with concrete thickness otherwise falling within the more nominal 50-75mm range.

c) Installation of six 6m wide concrete units to form a 760m long shore approach tunnel. This structure runs down to the 40m water depth mark over the uneven and steep rocky seabed so providing essential protection for the pipeline from wave action, figure 1.5. After prefabrication the units were floated to site and stressed together. They are designed to remain in place as gravity structures resting on prefabricated concrete supports grouted in place on level areas blasted on the bedrock.

Another major difficulty which had to be overcome on this section of line was to pick a route among the large pockmarks which occur in the trench particularly on the gradual western slope. These structures, which can be several hundred metres in diameter by 5m or more deep, are believed to be caused by ancient methane eruptions. Similar problems arise with large seafloor gullies caused by past ice ages which in view of their predominant North-South orientation are difficult to avoid. In cases where such irregularities could not be avoided special prefabricated pipeline supports and seabed infilling were used to avoid excessively large spans. Meanwhile further work

on the project continued with the ship type ETPM1601 laying the shallower section of Statpipe from Ekofisk to Heimdal via Riser Platform 1 (RP1). This operation provided an opportunity to test the contingency hyperbaric welding repair methods when working north towards Heimdal ETPM1601 was forced to stop operations in 7-8m waves and prepare for a temporary abandonment of the line. While preparations were being made to weld an end plug the line suffered a low cycle fatigue failure near to the end of the stinger and dropped in 80m of water so flooding the line back to RP1. This situation was rectified by continuing the operation southwards from Heimdal and joining the two sections of pipe by hyperbaric weld supported from the semi-submersible Uncle John. On start up in January 1986 (possibly to be brought forward to Autumn 1985) the Statpipe system will bring wet gas ashore from the Statfjord field for separation at the Karsto terminal. With the ngl fractions removed the dry gas will be pumped out to sea again to RP1 where together with gas from Heimdal it will be pumped via Ekofisk to Emden on the West German coast. Besides the obvious commercial benefits the system will prevent damage to the Ekofisk oil field caused by continued gas re-injection after 1986.

Finally another major project recently completed is Shell Expro's Fulmar-St. Fergus line installed during the 1984 season by Saipem's layharge Castoro Sei. Placed in a maximum water depth of 119m this 20in dia line is planned to form the backbone of an important gas gathering scheme with initial export from Fulmar and nearby Clyde (Britoil). Three "T" assemblies have been included in the line in order to receive later supplies from Gannet, Kittiwake and another as yet unnamed deep gas discovery along the route. These prospective tie-ins are one reason why the line makes a northerly deviation through Shell/Esso blocks on its way to St. Fergus while another important

factor is the need to avoid the highly prized Turbot Bank fishing grounds. The crossing of the BP Forties line was achieved relatively simply using conventional pipeline mattressing techniques after an inspection had shown the Forties line to be deeply embedded some 1.5m below the surface.

1.2 Pipeline Installation Methods

The North Sea pipelaying operations described above have utilised several different installation procedures including lay barge, reel barge and towing. Some of these methods are more suited for a particular application, for instance accurate laying of small diameter pipe, while others are more suited to (say) deepwater installations. Since the installation method selected also has a direct influence on the pipeline design and materials specification a brief outline of the various methods is presented in this section.

The most common method of pipelaying is the lay-barge method, figure 1.6, involving either a ship shape or semisubmersible type vessel. Semisubmersibles are more expensive to build but in view of their more favourable response motions have a better weather window. For example modern semisubmersible vessels can continue operations in significant wave heights H_S up to 4-5m from any direction while ship vessels can operate for H_S up to 3-4m for the case of head seas. During pipelaying single or double length joints are transferred from storage to an automatic rack for feeding to the line up table. Here the new section of pipe is aligned using an internal clamp prior to passing through the various welding and radiographic/ultrasonic testing stations. After inspection and any required repair the field joint is completed by applying corrosion prevention and infill coatings before the pipe passes over the stinger on its

way to the seabed. During this operation the pipeline takes up an S-curve configuration, figure 1.6, consisting of an overbend and sagbend region. Since deflections over the stinger may be controlled relatively large strains, sometimes in excess of yielding, are permissible. In other sections of the pipe, and especially the sag bend, pipe curvatures are controlled by means of large tensioning devices on the lay barge. Associated vessels required for the operation include supply boats, anchor handling tugs and diving support vessels.

An alternative method of installation, suitable for pipe up to 16in dia without concrete weight coating, is the reel method as used by Santa Fe's reel barge Apache, figure 1.7. Here pipe is prewelded under factory conditions into stalks of 1,000 ft or more. All welds are X-rayed and coated and the assembled pipe stored on racks ready for spooling onto the vessel's 2000t capacity main reel. During spooling the reel is rotated to pull the pipe up the adjustable stern ramp and coil it around the reel's 54ft diameter hub. As each 1000ft stalk reaches the final welding station spooling operations are halted while another length is welded to the string. By this means some 25km of 10in pipe can be taken aboard. Once on site the pipeline is unwound from the main reel and the permanent curvature induced by reeling removed using a pipe straightening system mounted at the top of the stern ramp. By adjusting the angle of this ramp between 18^{o} and 60^{o} from horizontal a wide range of S-curve and J-curve configurations can be obtained in the suspended section of pipe. This geometry, together with accurate control over line tension using tensioners mounted at the bottom of the stern ramp, enables a wide range of water depths to be handled.

Tow methods of pipeline installation, like the reel barge method, offer the advantage of pipe assembly on shore. Also towing requires relatively small vessels for trans-

porting the pipe string to its intended site. The basic methods for undertaking the tow are

a) Surface tow
b) Below surface tow
c) Off bottom tow
d) Bottom tow

During a surface tow flotation devices and spar buoys are used to support the pipeline at the surface or, in the case of a below surface tow, below significant wave action, figure 1.8. In addition to the main tow vessel a hold back vessel is required in order to maintain sufficient tension and to assist in controlling the line. The main advantage of this method is the relatively low towing power required while disadvantages include exposure to wave action and marine traffic plus the requirement for specific procedures to lower the pipe to the seabed. Once on site lowering of the pipe may be achieved by regulating buoyancy in the flotation devices, implementing a pull-down procedure using sheaves anchored to the seabed, or a combination of these methods. An additional procedure is the so called RAT method developed by Elf-Aquitaine and Total for deepwater. Here pipe strings are surface or below surface towed to a special lay barge, figure 1.9. Since only a small number of field welds are required a single weld station can be used without significantly reducing the laying rate. This arrangement is also advantageous if high strength steel pipe, requiring special weld or heat treatment procedures, is being used. By using special variable buoyancy floats it is also possible to eliminate the need for a stinger and considerably reduce top tension requirements.

For an off-bottom tow the buoyancy tanks attached to the pipeline carry suspended lengths of chain, figure 1.10. During tow the weight of chain lifted off the seabed

balances the buoyancy force so that the pipe is suspended at a predetermined height above the seafloor. If the tow route includes areas where lateral currents might affect the stability of the pipe, the length of chain pulled on the seabed can be designed to provide a stabilising force. Should the route cross existing pipelines or other obstructions the hold back tug can increase tension in the line causing the height of pipeline above seabed to increase. Advantages of this method include relatively low tow power and minimal exposure to marine traffic and adverse weather conditions. The main disadvantage is the design and economics of the buoyancy system both for normal tow operations and for final release and retrieval. In addition for deepwater applications the buoyancy tanks may require partial pressurisation or filling and/or design to pressure vessel codes in order to avoid collapse.

In marked contrast to the above methods the majority of the pipeline during a bottom tow is in contact with the seabed, figure 1.11. As a result the tow route is a basic design criteria influencing choice of coating, stability during tow, tow vessel size and optimum string length. The main advantages of this method are minimal exposure to weather conditions, absence of buoyancy system, safe and fast abandonment of tow during adverse weather, and long term stability of the pipe string resting in its own tow track. Disadvantages include high power requirement, risk of damage to pipe coating and potential for mechanical damage to pipe caused by seabed obstructions.

Finally for deepwater applications considerable research has been undertaken into the J-curve method of pipelaying in which the pipe leaves the lay barge in a near vertical manner, figure 1.12. With this geometry, access is possible to only one joint at a time so potentially reducing laying rates. To overcome this an extremely rapid welding technique is required in order to make the J-curve

competitive with conventional S-curve pipelaying where, since the line leaves the barge near horizontal, access is possible simultaneously to a number of joints along the deck length. Methods developed to do this include Total's electron welding machine and Norske Shell's radial friction welding method. Using this method of installation, Total estimate that pipes up to 36in dia may be installed with water depth, depending on size, up to 3,000m.

1.3 Pipeline Elements

The basic component used in constructing a pipeline consists of a single pipe joint, figure 1.13, typically 12m in length. For reel and towing methods of installation these joints are prefabricated into a complete line prior to transportation to site. Alternatively if a lay barge is used the joints are transported to site using one or more supply vessels and joined on the barge during installation, using field welds. The basic elements of a pipe joint are

a) High strength steel pipe normally specified in the range API grade X52 (minimum yield strength 358N/mm^2) to API grade X65 (minimum yield strength 448N/mm^2). In some cases grades as high as X70 may be used but in addition to the extra cost these steels require preheating facilities for the field welds. In addition to strength the steel must also possess good weldability and, in view of the environmental conditions, have a low transition temperature (normally below -40^{o}C). In general for modern line pipe steels these properties are obtained using low carbon equivalent chemistries together with such techniques as controlled thermomechanical rolling to obtain a refined grain size. Small diameter pipe is normally seamless while larger pipe is fabricated from a single plate by pressing into a cylindrical shape and joining the two

edges using a longitudinal weld.

b) Pipe external coating of corrosion prevention material. Common types include asphaltic bitumen coatings, fusion bonded epoxy powder coatings and various elastomers such as neoprene and hypalon. As well as preventing corrosion these coatings must also resist mechanical effects due to pipe bending during installation (especially reel barge method) and radial expansion during hydrostatic pressure testing. For pipelines without concrete weight coating additional resistance is also required against severe installation impacts and abrasions experienced by the line as it passes through the tensioner and stinger. Alternatively if the pipeline has a concrete weight coating this protects the corrosion coating but may cause problems due to

i) Mechanical damage to corrosion coating under the impact of the concrete aggregates during weight coat application.

ii) risk of damage due to concrete slippage on smooth corrosion coating.

These problems may be overcome by specifying an intermediate polymer cement coating as used by Marathon on their Brae-Forties line. Internal corrosion protection in the form of an inner plastic coating may also be required for some products, particularly sour gas. In extremely harsh conditions, as encountered on some flowlines transporting untreated products at high temperatures, stainless steel pipe may be specified.

c) Concrete weight coating, used in order to make the pipe sufficiently heavy to be stable on the bottom during installation and operation, but not so heavy that construction is unduly difficult. In addition to providing the correct specific gravity this coating also serves to protect the pipe and its anti-corrosion coating against mechanical damage due to anchors and fishing gear. It is noted that if a reel barge is

used the concrete weight coating is unable to tolerate the high reeling strains involved (up to ε = .02) and instead additional weight must be obtained using increased wall thickness in the steel pipe.

In addition to the above coatings it may also be necessary to insulate the line if loss of product temperature has to be avoided in order, for example, to prevent the formation of hydrates. In such cases a polyurethane foam coating may be included as used by Brown and Root on a 11km line linking the Danish Skjold field to the central processing platform at Gorm. Here a 60mm thick polyurethane coating was formed underneath a high density polyethylene sleeve around the 6.6in line previously coated with fusion bonded epoxy resin. As a result of the increased buoyancy, the concrete density was increased from the usual 2.2t/m^3 to 3.0t/m^3.

The various pipe coatings described above terminate some 300mm from each end of the pipe joint in order to facilitate the field welds, figure 1.13. As a result special field coatings must be applied in order to protect the exposed sections of pipe once the field weld is complete. The most common method consists of a cold applied anti-corrosion tape comprising a rubber/bitumen compound bonded to a PVC backing and applied by spiral or cigarette wrap with a specified percentage overlap. Alternative anti-corrosion coatings in use are

a) Heat shrink sleeves comprising an inner lining of anti-corrosion adhesive attached to an outer sheath of heat shrinkable plastic.
b) Fusion bonded epoxy powder as used on the line pipe itself.

This coating is then covered by a hot pour Mastic infill formed within a steel mould designed to present a flush pipeline external surface. To reduce time requirements for

this operation mouldless infill systems using epoxy concrete, polymer concrete or polyurethan foam are also being developed. With these systems the infill material reaches its ultimate or sufficient strength on the barge and can pass over the stinger without the protection of a steel mould. An alternative development under consideration is to cold form a mastic infill using applied pressure rather than a remelt process.

Other basic elements included in the installed pipeline system include

a) Sacrifical anodes attached to the pipeline at regular intervals in order to provide an effective cathodic protection system, figure 1.14. These anodes are normally attached to the pipe via steel bands with electrical connection made by welding an electrical pigtail either directly to the pipe or indirectly via a pre-installed welding pad.

b) Buckle arrestors installed every 100-300m along the pipeline in order to inhibit the propagation of any local buckles initiated in the pipe. The most common design is the free-ring type consisting of a steel sleeve slipped over the pipe joint and grouted into position, figure 1.15. Other types include the heavy-walled cylinder or integral arrestor and the welded-ring arrestor, figure 1.16.

c) Valves, diverters and "T" assemblies in order to ensure safe and efficient operation of the pipeline and to accomodate any future tie-ins.

d) Pipe supports, anchors, mattresses and weights used to ensure the pipe is stable on the seabed and does not suffer any excessive free spans due to uneven bottom conditions or other obstructions.

1.4 Basic Pipeline Design Considerations

In this section a brief overview is presented of some of the fundamental considerations involved in the design of a submarine pipeline. The basic requirements of this design may be summarised as (Jinsi, 1982)

a) The internal diameter of the pipe must be sufficient to transmit the maximum specified throughput under conditions of either single-phase or two-phase flow. Factors which influence the calculation of pipe size are overall length of line, inlet and outlet pressures and the anticipated limitations in pumping power. Economic considerations also influence the calculation since an increase in diameter increases construction and installation costs but reduces power requirements for pumping.

b) The line must be strong enough to withstand the various axial, bending and impact stresses induced during installation and operation.

c) The negative buoyancy of the pipe must be sufficient to resist movements both horizontally and vertically under environmental forces during installation and operation.

Once the pipe internal diameter D_i has been decided as in (a) above the steel pipe wall thickness t is calculated so that the circumferential hoop stress

$$\sigma_\theta = \frac{p D_i}{t} \qquad (1.1)$$

due to the maximum internal operating pressure p does not exceed the permissible stress as specified by the relevant design code or government regulations. The permissible stress σ_p is

$$\sigma_p = k\,\sigma_y \qquad (1.2)$$

where k is the design factor and σ_y the minimum yield stress for the steel pipe. For oil and gas pipelines respectively design factors of 0.72 and 0.57 are normally used reducing to 0.5 in the approach to a platform. Temperature derating factors may also be required if the product temperature exceeds 120°C. Economic considerations again influence the final selection since higher steel grades lead to thinner wall thickness and reduced steel tonnage but the unit cost of the steel will be higher. For example calculated wall thickness for a 36in pipe using steel grades ranging from API grade B (minimum yield strength 248N/mm^2) to API grade X70 (minimum yield strength 483N/mm^2) are shown in figure 1.17 for the various design factors given above. Where different designs are used along the pipeline route it is preferable to maintain a constant internal diameter in order to avoid potential problems with pigging. In addition to the computed thickness it is common practice to allow a further 4-6mm against the corrosive and erosive effects of the product medium during the planned lifetime of the pipeline.

The selected combination of steel grade and wall thickness described above must also be adequate to withstand the installation loads arising from pipe weight, barge motion, external pressure and hydrodynamic forces due to wave and current actions. If the pipe is not strong enough these loads may cause a local buckle to form as indicated in figure 1.18. The extent of damage caused by this buckle depends on the magnitude of the external pressure to the initiation and propagation pressures. If the external pressure is less than the initiation pressure a local buckle, caused by say overbending, will in theory be limited to a small inward dent on the compressive side of the pipe

wall. If on the other hand the external pressure is greater than the initiation pressure the bending buckle changes its configuration into a longitudinal buckle and may propagate along the pipe. Once initiated buckle propagation can continue into parts of the pipe that are not bent as long as the net external pressure remains higher than the propagation pressure, figure 1.19. With a properly designed pipeline and carefully controlled installation procedure the likelihood of buckle initiation and propation is small but nevertheless does occur especially during abandonment and recovery of the line. As a consequence buckle arrestors are included in order to minimise damage as described in section 1.3.

Once installed the various forces per length affecting pipe horizontal stability on the seabed are pipe submerged weight W , vertical reaction R , horizontal shear force μR , hydrodynamic drag and inertia forces F_D and F_I and lift force F_L , figure 1.20. Resolving these forces horizontally and vertically gives

$$\mu R = F_D + F_I \qquad (1.3a)$$

$$W = F_L + R \qquad (1.3b)$$

Thus for stability the submerged weight of the pipeline must satisfy

$$W > F_L + \frac{1}{\mu}(F_D + F_I) \qquad (1.4)$$

For an unburied pipeline this check is performed both for an empty pipe immediately after installation using a wave with a return period of typically one year and also for a pipe full of oil (or gas) using a wave with a return period of typically 50-100 years. In both cases the hydrodynamic

loads are calculated using fluid velocities and accelerations occurring at the top of the pipe and using the wave phase angle giving the worst combination of loads. Particle velocities near the seabed are often computed by first using a suitable wave theory to evaluate the fluid velocity $u_1(t)$ occurring 1m above the seabed. The 1/7th power law

$$u(z,t) = u_1(t)\, z^{1/7} \qquad (1.5)$$

is then used to calculate fluid velocities in the seabed boundary layer where z is the vertical elevation from the seabed. Pipe weight may be adjusted by varying the density and/or thickness of the concrete weight coating or increasing thickness in the steel pipe.

Vertical stability of the pipe must also be checked by ensuring that the pipeline does not have a tendency to sink or float during storm conditions when soil strength may become reduced, figure 1.21. This is achieved by requiring

$$\gamma_{SOIL} - R_{SOIL} < \gamma < \gamma_{SOIL} + R_{SOIL} \qquad (1.6)$$

where γ_{SOIL} and γ are weight densities of soil and pipe respectively and R_{SOIL} is the total soil resistance to pipe movement per unit volume of pipe. This later quantity may be estimated using (Mousselli, 1981)

$$R_{SOIL} = \frac{2C}{D} \qquad (1.7)$$

where C is the remoulded cohesive shear strength of the soil and D is the pipe external diameter. Normally equation (1.6) is divided by the weight density of water γ_w to give the upper and lower limits of the pipe specific

gravity SG as

$$SG_1 < SG < SG_2 \qquad (1.8a)$$

where

$$SG_{1,2} = SG_{soil} \mp 2c/\gamma_w D \qquad (1.8b)$$

Other design considerations include effects of soil movements, burial requirements, design of connections, tie-ins and safety valves and effects of thermal loads. The effect of pipe free spanning and vortex induced oscillations are described in the following section.

1.5 Pipeline Spanning and Vortex Induced Vibrations

Unsupported pipeline spans may occur along the pipeline route as a result of

a) Uneven or rocky seabed conditions or natural obstructions such as boulders, pockmarks or seafloor gullies. Under such conditions the pipeline is unable to follow the rapidly varying seabed geometry with the result that non-contact lengths or spans naturally form. Since such spans are a direct consequence of the selected route and normally exist for the complete lifetime of the pipeline they are referred to as design spans.

b) Scour around the pipeline resulting from current and/or wave action on granular or cohesiveless soils. For a pipe initially in full contact with the seabed but subjected to strong currents the overburden may gradually erode leading to a complicated situation where the length and form of the span may be continuously changing. In shallow waters storm waves can also produce appreciable fluid velocities near the seabed disturbing the equilibrium of granular sediments and causing soil movement. The effect of the pipe itself on fluid flow may also initiate scour or in some cases

cause additional local scour. As the storm develops an initially buried pipeline may be completely exposed while during subsidence the pipe may be either left exposed on top of the trench or reburied.

Once formed such spans induce additional static stresses into the pipeline and in addition are susceptible to dynamic response resulting from hydrodynamic forces. Since wave Spectra contain no significant energy near the natural frequency of a typical exposed length of pipeline direct wave forces are unlikely to produce significant dynamic response. However when a steady current flows past a bluff body such as a pipeline alternate vortices are shed from the pipe resulting in unsteady hydrodynamic forces on the body. Under certain conditions these forces can lead to a resonant situation in which considerable transverse and in-line response can occur leading to possible pipeline damage. Reported occurrences of such vortex induced vibrations includes an incident in 1975 when part of the Cormorant-Sullom Voe line, figure 1.1, floated to the surface following the loss of 60% of its concrete weight coating over some 1500m of pipeline. The incident occurred about 5km from landfall in Yell Sound off the Shetlands where high currents up to 3.6m/s can be experienced during tidal changes. Other incidents involving pipeline free spanning in the North Sea are reported by Strating (1981). In view of the importance of vortex induced vibrations to the safety of such free spans a brief description of the phenomena is now presented.

Considering first uniform flow past a fixed smooth cylinder Lienhard (1966) has shown that the various flow regimes experienced depend on Reynolds number

$$R_e = \frac{UD}{\nu} \qquad (1.9)$$

where V is the free stream velocity, D the cylinder diameter and ν the kinematic viscosity of the fluid. At low Re (< 5) the flow does not separate being essentially equivalent to that predicted using inviscid potential theory, figure 1.22a. Increasing Re gives rise to the separation of the laminar boundary layer and the formation of two standing vortices immediately behind the cylinder, figure 1.22b. As Re is further increased these vortices elongate until at about Re = 40 one of them breaks away resulting in a laminar periodic wake and staggered vortex street, figure 1.22c. This flow remains laminar up to $Re \simeq 150$ and then enters a transition range to turbulent flow for $150 < Re < 300$, figure 1.22d. The range $300 < Re \lesssim 3 \times 10^5$, termed the subcritical regime, is characterised by a fully turbulent vortex street and a well defined shedding frequency f_s and remains virtually unchanged as long as the boundary layer on the cylinder remains laminar, figure 1.22d. At a transition Re of approximately 3×10^5, depending on free stream turbulence and surface roughness (Roshko, 1961), the boundary layer just after separation becomes turbulent with subsequent reattachment and formation of a bubble giving rise to a narrowing wake and reduced drag, figure 1.23b. This so called critical regime persists up to $Re \simeq 3.5 \times 10^6$ and is characterised by disorganised vortex shedding with a broad band of shedding frequencies, figure 1.22e. At still higher values of Re, i.e. in the supercritical regime, the boundary layer undergoes transition to turbulence before separation and a stable situation is again reached with the reappearance of regular vortex shedding, figure 1.22f.

For typical North Sea pipelines representative Reynolds numbers are calculated in figure 1.24 for approach flow velocities of 1, 2 and 3m/sec. From this data it is clear that Reynolds numbers up to about 2×10^6 may be encountered indicating flows in both the regular vortex shedding sub-critical regime as well as the irregular shedding critical

regime. From the point of view of span assessment the first of these is generally the most critical since the regular shedding of vortices may lead to a resonant situation if the shedding frequency is close to the span natural frequency. For the smooth cylinder considered above dimensional considerations indicate that the frequency at which vortex pairs are shed may be written

$$f_s = S(Re)\frac{V}{D} \quad Hz \tag{1.10}$$

where $S(Re)$ is the Strouhal number (Strouhal, 1878). Leinhard (1966) has shown that over the subcritical regime this number is largely independent of Re having a value close to 0.2, while in the critical regime the shedding frequency may be defined in terms of the dominant frequency in a broad band of shedding frequencies, figure 1.25. As each vortex is shed an associated pressure field is generated around the cylinder resulting in transverse and in-line force components on the pipe. In the case of the transverse force a vortex shed from the top of the pipe will induce pressure forces opposite in direction to those of a similar vortex shed from the bottom of the pipe. It follows that a complete cycle in the transverse force comprises the successive shedding of two complementary vortices with the result that the forcing frequency is equal to the shedding frequency of vortex pairs as defined by equation (1.10) above. On the other hand for the in-line force the pressure differential is similar irrespective of whether a given vortex is shed from the top or bottom of the cylinder. The in-line forcing frequency is therefore set by the frequency at which individual vortices (irrespective of location) are shed from the pipe, i.e. $2f_s$.

For a given set of conditions the frequency of vortex shedding along the length of a rigidly fixed cylinder can be estimated with reasonable engineering accuracy using

equation (1.10) above. However in calculating the total hydrodynamic force on such a cylinder it is necessary to also consider the 3 dimensional aspects of the flow. For such a fixed structure King (1977) describes the vortex shedding as taking place in cells where the length of each cell along the cylinder is generally less than 2-3 diameters. For a long cylinder, such as a pipeline free span, this results in the hydrodynamic force components along the cylinder being out-of-phase and so cancelling. At first sight this result suggests that for a flexible cylinder flow induced vibration will never occur even if regular vortex shedding is taking place. However, although this is true for some flow conditions, considerable response may occur in other cases as indicated schematically in figure 1.26 for the case of an elastic cylinder vibrating in water. It is noted that three modes of response, two in-line and one transverse, are observed dependent on the nondimensional reduced velocity

$$V_R = \frac{V}{f_n D} \qquad (1.11)$$

where f_n is the fundamental natural frequency of the cylinder in still water (Wootton et al 1972, King 1974). These motions are associated with the phenomena known as "lock-in" where the response of the structure synchronises the wake along the cylinder so increasing the net generalised hydrodynamic force. For the transverse mode and second in-line mode the peak response occurs at reduced velocities in the range 5.5 - 6.5 and 2.5 - 3.5 respectively with a wake structure similar to that observed in the sub-critical regime for a fixed rigid cylinder. Recalling that for this case the frequency f_L of the transverse lift force is f_S and taking $S = 0.2$ as typical, equation (1.10) gives $f_L = 0.2\,V/D$. Thus setting $f_L = f_n$ for resonance the corresponding reduced velocity may be calculated as

$$V_R = \frac{V}{f_n D} = \frac{V}{f_L D} = 5$$

In a similar manner taking the frequency f_D of the in-line non-steady drag force as $2f_s$ and setting $f_D = f_n$ gives V_R = 2.5. These estimated values are sufficiently close to the observed values to suggest that the two modes under consideration arise essentially as a result of structural resonance under the forces observed on a fixed cylinder. This interaction is two-way since the motion of the cylinder organises the wake and increases the vortex strength (Toebes 1969, Griffin and Ramberg 1972). In addition as the flow velocity V is increased across the lock-in range of either of these modes, the frequency of response remains largely constant and equal to the natural frequency of the structure in still water f_n . Thus unlike simple structural resonance the cylinder motion is seen to control both the frequency and strength of the exciting force so enabling lock-in to be maintained over a broad band of flow velocities, figure 1.26. As V is further increased this interaction eventually breaks down with the result that both spanwise wake correlation and cylinder amplitude of vibration are reduced and the shedding frequency jumps back to its nominal value, equation (1.10).

In contrast to the above the first in-line mode, centred at V_R = 1.9 - 2.1, is associated with symmetric vortex shedding, figure 1.26. This situation indicates that a more complicated fluid-structure interaction is involved in which a new (and unstable) wake structure, not previously observed for a fixed cylinder, is generated. During lock-in in this mode vortex shedding frequencies are insensitive to cylinder motions and instead continue to be governed by the normal Strouhal number relationship (King et al 1973).

Now considering the effect of such flow induced vibration on a suspended pipeline span it is noted that the maximum amplitude of vibration for transverse motion is on the order of 1-2 pipe diameters. Since this is an order of magnitude larger than the maximum in-line response it is common practice to focus attention on this mode when performing span assessment (Tsahalis 1984). The flow speeds for the onset and peak in such transverse motion depend on Reynolds number, figure 1.27, from which we may conclude that initiation will be avoided if

$$V_R < 3.5 \qquad (1.12)$$

Alternately if cross flow motion is excited a wide range of wind-tunnel and water-channel tests have indicated that within limits the amplitude of response is governed by the stability parameter

$$K_S = \frac{2m\delta}{\rho D^2} \qquad (1.13)$$

where m is the cylinder mass per length (including added mass if in water), δ is the logarithmic decrement of structural damping in air and ρ is the fluid mass density. This parameter is a combination of the non-dimensional mass ratio $m/\rho D^2$ and damping parameter δ and arises theoretically by equating the energy input from the free stream to the energy dissipated in structural damping at the resonant condition (Vickery and Watkins 1962). Using this parameter and considering figure 1.28 it is clear that significant transverse motion will be avoided provided

$$K_S > 10 \qquad (1.14)$$

Now for a typical submarine pipeline the mass ratio is in the range 2.0 - 3.0 while for a linear SDOF system with viscous damping the logarithmic decrement of structural damping is given in terms of the damping ratio β as

$$\delta = \frac{2\pi\beta}{(1-\beta^2)^{1/2}}$$

Thus taking $m/\rho D^2$ = 3.0 as typical, k_s may be evaluated in terms of β as indicated in the following table

β	δ	k_s
0.1	1.63	3.8
0.2	1.28	7.7
0.3	1.98	11.9
0.4	2.74	16.4
0.5	3.63	21.8

Table 1.2

Stability parameter k_s against damping ratio β assuming $m/\rho D^2$ = 3.0

It is seen that the low mass ratio of a typical submarine pipeline in water requires damping in excess of 30% of critical in order to satisfy equation (1.14). Since this is approximately an order of magnitude larger than accepted values for a welded steel structure it seems that in practice a pipeline span will always experience transverse vibration for reduced velocities in the synchronisation range (Griffin and Ramberg 1982).

The above discussion has primarily considered the relatively simple case of uniform flow past an isolated

smooth cylinder. For a typical pipeline span, figure 1.29, additional factors which must be considered include

a) The pipe is normally suspended 1-2 diameters above the seabed with the result that even ignoring flow separation effects the flow is no longer symmetric about the pipeline. In addition as the bed gap to pipe diameter ratio G/D decreases the flow velocity past the cylinder increases suggesting a possible increase in shedding frequency.

b) The pipe is often immersed in a thick turbulent boundary layer formed by fluid flow over the rough seabed with the result that large differences in flow velocity may occur between the top and bottom of the pipe. In addition the approach flow may be further modified if the pipeline is lying in an open trench.

c) The pipe surface is not hydraulically smooth but instead has a characteristic roughness dependent on surface coating. Boundary layer disturbances induced by such pipe roughness can significantly affect the transition from laminar to turbulent conditions in the pipe boundary layer with consequential effect on vortex shedding behaviour.

d) The nominal flow velocity will in general comprise components due to current and wave actions and will be inclined at an arbitrary angle to the pipeline.

Despite the fact that a considerable volume of literature has been addressed to individual or related aspects of the above problem a complete understanding of the hydroelastic response of a suspended pipeline span has not yet been achieved. General reviews of the literature concerning vortex incuded vibrations have been given by Parkinson (1974), Blevins (1977), Chen (1977), King (1977), McCroskey (1977), and Sarpkaya (1979, 1981) while a more specific review, concerning applications to marine tubulars and risers, is given by Griffin and Ramberg (1982). A review of literature

of specific relevance to pipeline spans is given in the following section.

1.6 Literature Survey on Vortex Induced Vibration

Considering first the effect on vortex shedding of a plane boundary placed near to the cylinder, Bearman and Zdravkovich (1978) have undertaken a series of wind tunnel tests up to a Reynolds number of 4.5×10^4. For these tests a rigid 19mm diameter cylinder with a length to diameter ratio of 32 was placed at various distances above a 10mm thick partition plate placed horizontally across the working section. A 1mm trip wire was attached near to the leading edge of this plate so that the thickness of the turbulent boundary layer at the cylinder location was 0.8D. Using spectral analysis of hot-wire signals they found that regular vortex shedding persisted at the same Strouhal number for all gap to diameter ratios G/D down to 0.3. For values of $G/D < 0.3$ strong regular vortex shedding was found to be suppressed.

In similar tests Goktun (1975) has investigated the flow around a circular rigid cylinder near to a wall at Reynolds numbers between 0.9×10^5 and 2.5×10^5. He found that the Strouhal number S increased from 0.198 in the free stream to 0.206 at $G/D = 0.5$. Although the thickness of the boundary layer was not measured the close proximity of the cylinder to the leading edge of the splitter plate indicates that the boundary layer was thin and presumably laminar. A similar increase in Strouhal number is reported by Haffen (1975) but this time at a bed gap to cylinder diameter ratio $G/D = 0.75$.

Buresti and Lanciotti (1979) have reported wind tunnel experiments to investigate vortex shedding from smooth and roughened rigid cylinders in cross flow near a plane boundary.

These tests, carried out for $Re = 0.85 \times 10^5 - 3.0 \times 10^5$, used a 117.8mm diameter cylinder suspended above a 20mm thick plate with an associated boundary layer thickness of 12mm. For a smooth isolated cylinder hot wire signals were used to demonstrate the transition from subcritical to critical flow regimes. In addition measured Strouhal numbers in the subcritical regime were found to agree adequately with published data. These flow features were reported unaltered for all $G/D > 0.4$ while for $G/D < 0.4$ regular vortex shedding disappeared. For roughened cylinders the importance of Reynolds number $Re_k = kV/\nu$, based on the typical roughness size k, was noted. In particular their results indicated the possibility of obtaining supercritical conditions for $Re_k \gtrsim 200$. As was the case for the smooth cylinder, the presence of the boundary did not alter the frequency of vortex shedding for gap ratios down to $G/D = 0.4$ provided the flow regime was subcritical, i.e. $Re_k \lesssim 150$. In the supercritical regime vortex shedding was noted at $G/D = 0.3$ for $200 \lesssim Re_k \lesssim 350$.

Similar tests to the above, but this time using a water channel, have been carried out by Angrilli et al (1982). For these experiments three different cylinders (with corresponding Re of 2860, 3820 and 7640) were placed at varying distances from a polished 1mm thick stainless steel sheet. The cylinders were located 10 diameters from the leading edge of this plate where the measured boundary layer thickness was less than 5mm. They noted that vortex shedding frequencies increase as the wall is brought closer to the cylinder with a maximum increase over the free stream value of about 10%. This result is noted to be in agreement with those obtained by Goktun (1975) but to contrast those of Bearman and Zdravkovich (1978) and Buresti and Lanciotti (1979).

Related experiments were undertaken by Kiya et al (1980) using a recirculating liquid channel to investigate vortex shedding for smooth rigid cylinders in uniform shear flow at subcritical Reynolds numbers. They concluded that Strouhal number defined by the approach velocity at the centre of the cylinder increased with increasing velocity gradient. For example at $Re = 10^3$ the Strouhal number was increased by 15% of its uniform flow value when the velocity difference across the cylinder was 25% of the centre line value. They also noted that vortex shedding was suppressed when the velocity gradient across the cylinder exceeded a critical value dependent on Reynolds number.

Grass et al(1984) present experimental results on the separate and combined effects of bed proximity and large velocity gradients on the frequency of vortex shedding from smooth rigid pipeline spans immersed in the thick boundary layers of tidal currents. These tests were performed in an open flow channel using nominal flow velocities of 80mm/s and 160mm/s over both the hydraulically smooth varnished surface of the existing channel bed and also a hydraulically rough bed produced by a single layer of sharp-edged gravel graded between 5-10mm sieve sizes. These surfaces produced a thick boundary layer of approximately 150mm or six pipe diameters. In addition, to assess the separate effects of bed proximity in the absence of velocity gradients, tests were also performed in a uniform approach flow. This flow was simulated by the free stream region outside the thin (approximately 7mm) laminar boundary layer of a 3mm thick splitter plate placed 50mm above the channel bed. For uniform approach flow they concluded that the shedding frequency increased gradually as the bed gap ratio G/D was reduced below 2, reaching a maximum of 5-10% higher than the free stream value at $G/D = 0.75$. Below $G/D = 0.3$ vortex shedding was noted to be sharply suppressed. In contrast a maximum increase

in shedding frequency of 25% was noted with the pipeline immersed in the realistically thick boundary layers produced by the smooth and rough channel surfaces. This increase was attributed to the velocity gradient across the cylinder resulting from the sheared velocity distribution in the boundary layer. By subtracting the increments in Strouhal number observed under uniform flow from similar increments obtained in the thick boundary layers, the effect of velocity gradient alone was determined. The resulting net percentage increase was then found to be approximately half the difference in approach velocity across the pipe, expressed as a percentage of the approach velocity measured at the pipe centre. Using this observation the authors suggest that when calculating the reduced velocity parameter V_R for span assessment, the velocity gradient effect is approximately accounted for by using the approach velocity at the top of the pipe.

Considering now the effect of a non-rigid cylinder Tsahalis and Jones (1981) have determined experimentally the vortex induced transverse vibrations of a flexible cylinder in close proximity to a plane boundary for bed gap to diameter ratios G/D = 1.0 - 6.0. The results are compared to those for an isolated cylinder and the following conclusions drawn. First the onset of perceptible vibration takes place at a higher reduced velocity (typically $V_R \simeq 5.0$) while the maximum response amplitude and frequency are both reduced. In addition the reduced velocities at which such maximum response occurs are also increased with significant response observed up to V_R = 12 for all gap sizes noted above. This is in marked contrast to their results for an isolated cylinder where peak response is observed at V_R = 7. In a later paper Tsahalis and Jones (1982) use these experimental results to calculate the effect of seabottom proximity on the fatigue life of a concrete coated prototype pipeline exposed to a "steady" current due to tidal fluctuations. Their analysis uses

the Palmgrem-Miner fatigue model together with an assumed simply supported beam span with sinusoidal fundamental mode shape. To illustrate the method a simplified tidal flow is assumed with a period of 12 hours and a maximum flow of 6.5ft/sec. at a point 16ft above the seabed. Flow velocities near the pipe are then calculated assuming a logarithmic velocity distribution in the turbulent boundary layer over a smooth and rough seabed. They conclude that reduced G/D leads to increased fatigue life of a suspended span or equivalently an increased safe span length for a given fatigue life. This method is extended by Tsahalis (1983) who defines a "generalised fatigue damage universally applicable to all suspended spans". He shows that the dependence of fatigue life on span length is nonmonotonic exhibiting a minimum corresponding to a critical length L_c dependent on pipeline properties and flow characteristics. For span lengths L less than L_c, fatigue life is shown to decrease rapidly with L as the pipeline frequency decreases and the span becomes more susceptible to flow induced vibrations. For L larger than L_c fatigue life increases as a result of the stress reduction associated with increased span length.

A further extension to investigate the flow induced vibration of a flexible cylinder near a plane boundary and exposed to steady and wave induced currents is made by Tsahalis (1984). These tests used an aluminium model pipeline ballasted so that its specific gravity of 2.25 was representative of product filled concrete coated pipelines. Spherical rod end bearings were used to provide simple supports for this model in both horizontal and vertical directions. In the axial direction the pipe ends were restrained and the tension adjusted so that for $G/D \neq \infty$ the natural frequency of the model in still water was 4.55Hz. Since this frequency was the same in both vertical and horizontal directions the author concludes that negligible

sag existed in the system. For these still water tests the log decrement was found to be 0.20 implying a structural log decrement in air of less than 0.10. Results are presented for both transverse and in-line response of the pipeline for gap ratios $G/D = \infty$ (i.e. isolated pipe) and 1 and for Keulegan-Carpenter numbers KC = 0 (i.e. steady current only) and 20. For the case of an isolated pipe exposed to steady current only, the response is noted to be typical of low structural damping, low specific gravity systems. In this case the in-line response frequency is twice that in the transverse direction indicating a figure-of-eight motion. On the other hand introducing a plane boundary such that G/D = 1, the maximum observed transverse response is reduced by a factor of about two while the in-line and transverse response frequencies are noted to be equal. The author notes that this indicates that the interaction patterns between the wake and the vibrating cylinder in the presence of the plane boundary are different from those of an isolated pipe and the cylinder appears to undergo an oval shape motion. Next considering an isolated cylinder exposed to combined steady and wave-induced flow such that KC = 20, it is observed that significant flow induced vibrations occur for all reduced velocity in the range $0 < V_R \leq 12$. The results of this test are compared to those of an isolated cylinder exposed to uniform flow and the following observations noted. First in the transverse direction the maximum amplitude is larger for $V_R < 6$ and smaller for $V_R > 7$ while the dominant response frequency remains unchanged. In the in-line direction the maximum amplitude is larger for all V_R while the dominant response frequency changes dramatically following closely the dominant response frequency in the transverse direction. In addition the presence of significant spectral peaks near the dominant response frequency in both in-line and transverse response spectra indicate that the pipe does not undergo simple harmonic motion. Finally introducing a plane boundary such that G/D = 1, the transverse response of the

pipe is noted to be virtually constant over the range $2 < V_R < 10$ with a maximum amplitude of 0.6D. Similar results are observed in the in-line direction where the corresponding maximum response is 0.15D. Dominant response frequencies in both these directions follow similar trends and are slightly higher than those noted for the transverse response of an isolated cylinder under uniform flow. Again the presence of secondary peaks in the response spectra indicates that the pipe does not undergo pure harmonic motion.

Bruschi et al (1982) have undertaken a series of wind tunnel tests to investigate the steady and unsteady forces acting on a rigid cylinder placed at varying distances from a plane boundary. The tests were performed on a 118mm diameter cylinder using three different boundary layers of approximate thickness 12mm, 50mm and 140mm. They note that at G/D = 0.4, the influence of the plane on the fluctuating forces is small with no significant variations observed with respect to results for an isolated cylinder. At a critical distance $G/D \simeq$ 0.3 - 0.2 regular vortex shedding was suppressed and a simultaneous reduction in the unsteady forces was noted. They also conducted full scale tests on a 20" diameter pipe placed in the Fisolo canal in the Venice Lagoon. At this site periodic tidal currents produce velocities up to 0.8m/s with a near uniform profile across the canal. Since actual support conditions of a pipeline span are difficult to assess the pipe was designed with simple supports either end of a 67m span. This length was selected so that the pipe natural frequency fell within the expected shedding frequencies produced by the above current levels. Initially the end supports also allowed the possibility of limited axial movement but after early tests, and to avoid possible damage to the supports, these were subsequently modified to increase the allowed axial movement. Tests on this full scale model were undertaken using both the smooth steel pipe surface (relative roughness 0.5 x 10^{-3})

and with the pipe wrapped in a 1.5mm thick, 10 x 10mm mesh net simulating a relative roughness of 1.5×10^{-3}. As a result of the anticiaption of flow regimes caused by such surface roughness, synchronisation for the "rough" pipe was anticipated to occur in the supercritical regime. This was confirmed during the experiments in which strong synchronised transverse oscillations of the "rough" pipe occurred at Re values associated with the supercritical regime observed on a fixed rough cylinder. These motions were observed to be sinusoidal over a wide range of current velocities and to occur at a constant frequency significantly lower than the fundamental natural frequency of the pipeline in still water. Maximum amplitudes associated with this response occurred at the centre of the span and varied from 0.8D - 2.5D, the upper values being obtained when the allowed axial displacement at the end constraints was increased. In addition a strong hysteresis behaviour was observed with oscillations under reducing velocity conditions persisting down to velocity levels lower than the corresponding initiation levels observed under increasing flow. In contrast the results presented for the "smooth" pipe show a maximum response of 0.5D and occur at a frequency close to the first natural frequency in still water. In addition no hysteresis behaviour was observed and the start and end of the oscillations for both increasing and decreasing current velocities were always rather abrupt. This is in marked contrast to the "rough" pipe results where a more gradual transition was always observed.

An extension of the above experiments to consider random wave induced flow is made by Jacobsen et al (1984) who investigate the cross-flow vibrations of a 0.1m diameter cylinder close to a rigid boundary. The study was conducted by elastically mounting a rigid cylinder on to an oscillating carriage located on rails above the 35m test section of a 3m wide current flume. The cylinder used was 0.75m long and

was provided with a sandpaper roughness with an equivalent sand roughness of 1mm. This pipe was allowed to move perpendicular to its axis (cross-flow direction only) and was located at various distances from a 6m long plate used to simulate the seabed. Tests were undertaken for

a) Steady current
b) Regular waves
c) Steady current plus regular waves
d) Irregular waves

and with gap ratios G/D = 1.0, 0.5 and 0.0. For cases (a), (b) and (c) and with G/D = 0.0 it was noted that the forcing mechanism was not related to regular vortex shedding but instead appeared to be associated with a velocity squared lift force of sufficient strength to lift the model pipeline clear of the seabed. As the pipeline moved away from its foundation, the resulting flow under the pipe devalued this lift force so causing the pipe to fall back to its equilibrium position. By this means the pipe was observed to undergo a complicated "bouncing" motion. Another interesting observation was that for G/D = 0.5 and regular wave with Keulegan-Carpenter number 90, the amplitude of pipe response followed the variation in flow velocity building up to a maximum shortly after each peak (in either direction) of the flow velocity. Further imposing a 0.2m/sec current, such that the total fluid velocity was significantly asymmetric, the pipe was noted to undergo strong oscillations in the half period when current and wave induced velocities combined, whereas vibrations ceased when the two velocity components cancelled. In contrast to these results it was noted that under random wave action the pipe experienced no significant motion for long periods of time. However coincident with the arrival of a group of large waves, large vortex induced vibrations quickly built up and then died-out in a transient manner following the

passage of the waves. The probability distribution of double amplitude response associated with such complicated time histories is compared to that computed by treating each positive zero crossing in the random fluid velocity as an isolated wave component and using the test results under harmonic flow conditions. It is noted that the probability of small amplitudes computed this way is smaller than the actual number measured while for large amplitudes the opposite is true. Despite this the overall trend of the two curves is close and the authors conclude that the computed distribution is useful for an initial assessment of span fatigue life under random wave conditions.

1.7 Literature Survey on Pipeline Spans

Since the hydroelastic response of pipelines is dependent on the structural properties of the suspended span, a complete understanding of the problem also requires an insight into the fundamental mechanics of span formation and behaviour. This may be achieved using either full scale or model tests or by developing suitable mathematical models to investigate the basic parameters which might to influence pipeline integrity. However in view of the complex conditions encountered on the seabed, the use of realistic models is extremely difficult and all of the tests reviewed in the preceding section have used simplified mechanical representations of the free span. As a consequence it is also necessary to develop mathematical models which, although based on simple assumptions, can hopefully incorporate some of the complexities omitted in the above model tests. In this thesis a number of such models, of varying complexity, are developed. Before describing this work, a review of recent literature relating to the static and dynamic analysis of suspended pipeline spans is presented.

Considering first an installed unburied pipeline Hoskins

(1982) uses multi-span small slope beam-column theory to determine the static deflections occurring in a single unsupported span resting on an inelastic seabed. As a result of pipe rotations at the end supports, pipe sections either side of the central span are caused to lift up so forming additional non-contact regions of unknown length. By using compatibility, equations governing these lengths are determined and solved iteratively. The span fundamental frequency is then estimated by applying an additional distributed load to the pipeline and equating the corresponding potential energy to the associated kinetic energy (i.e. Rayleigh's Principle). Although not stated in the paper, this method assumes that the fundamental mode shape is symmetric and appears to ignore the effect of axial end constraints arising from friction forces. Pipeline tension/compression and seabed slopes are included in the analysis and the author concludes that the effect of variable non-contact length is to reduce frequency with increased amplitude of vibration.

Hobbs (1983) uses essentially the same theory to solve pipeline lifting problems associated with tie-in and repair activities. Again the location of the pipe separation point from the rigid seabed is treated as the primary unknown and determined numerically using a Newton-Raphson algorithm. The results are presented in a compact non-dimensional form and provide information on displacements, pipe moments and stresses, lift forces and weld root gaps. In addition optimal sling arrangements are identified in order to minimise line bending moments and sling lifting forces.

In a related paper Hobbs (1980) considers the effect of soil modulus on pipeline stresses induced by such lifting operations. The conventional assumption of a rigid seabed is discarded in favour of treating that part of the pipeline which remains in contact with the seabed as a beam on an

elastic foundation. It is noted that although this theory is only approximate, it represents a reasonable model for certain soils and provides a good starting point for the analysis. Two cases of practical interest are considered, namely the lift of a continuous line by a pair of slings and the lift of a pipe end using a single sling. The effect of line tension is ignored and the results presented in a non-dimensional form. It is noted that the maximum bending moment and sling force are both insensitive to foundation flexibility while although the lifted length changes significantly as the soil modulus falls, the overall deflection shape is relatively unaffected. The author concludes that the intuitive assumption of a rigid seabed is confirmed although small scale operations may require consideration of foundation flexibility.

Similar soil properties are assumed by Hall and Healey (1980) who develop a 2 dimensional finite element analysis for the dynamic stresses induced in a suspended marine pipeline during laying operations. Harmonic or arbitrary excitations are considered at the surface and the dynamic response is assumed small about an initial static configuration which must be known beforehand. Initially a time domain model is developed including nonlinearities due to hydrodynamic drag force and ocean bottom unilateral support conditions. These later conditions are modelled using a visco-elastic bilinear support model in which pipeline nodes in contact with the seafloor are provided with a discreet reaction force dependent on displacement and velocity. The results of this nonlinear analysis are compared with those of a linearised frequency domain solution where drag force is linearsied using an equivalent work method. In addition the bottom reactions are linearised by assuming that those nodes initially in contact remain so, while those initially in the sag bend region never penetrate the seabed. The authors conclude that the linearised method

compares reasonably well with the more exact time domain solution and note that stress levels predicted in the lower sag bend region are conservative.

Returning now to the rigid foundation model Maier et al (1979) present a large displacement elastoplastic analysis to determine the equilibrium configuration of a marine pipeline unilaterally supported by a rigid, frictionless and uneven profile. Complementarity relations (i.e. the requirement that in a pair of corresponding sign-constrained variables at least one is zero) are used to provide a unified treatment to the unilateral contact and piecewise linear elastoplastic theories utilised in the analysis. Algebrization of the equations is achieved using cubic spline functions and a nonlinear programming Newton-like solution devised to determine the stress state during a typical laying operation. The pipe length considered in this analysis includes the overbend region in unilateral contact with the barge stinger, the free span, and some pipe length unilaterally supported by the uneven rigid seabed. In a second analysis the equations for an installed pipeline are linearised by assuming small displacements. This analysis reveals that over certain sections of the line the uneven nature of the seabed leads to excessive bending moments in the pipe. The authors note that this must be corrected using seabed excavations and/or the use of artificial supports inserted beneath the pipe. Since this work is expensive an optimisation scheme is developed in order to determine a nimimum cost solution to the problem of avoiding pipe overstressing.

Considering further the aspect of pipe seabed interaction Healey and Seo (1984) develop a 3 dimensional Finite Element model to investigate the dynamic stability of an exposed but fully supported section of pipeline. Hydrodynamic drag, lift and added mass terms are included

and the soil model provides for the hysteresis effects caused by pipe sliding. This is done using an elasto-plastic representation for both normal and tangential friction forces in which the friction coefficients depend linearly on soil compression until sliding occurs, after which they remain at their maximum values. The resulting equations of motion are integrated in the time domain and used to investigate the stability of a prototype flowline during the passage of an extreme wave. Their results show that under the combined influence of hydrodynamic drag and lift forces, the flowline is displaced several feet from its initial position. They conclude that conventional stability design methods are conservative and suggest the use of the presented analysis if limited movement can be tolerated.

Friction coefficients for pipes subjected to lateral and longitudinal pulling forces are determined by Anand and Agarwal (1981) using small-scale model and large-scale prototype tests. For the model tests three short lengths of 3in, 6in and 9in diameter pipe were used and the pulling force found to be proportional to the submerged pipe weight. Coefficients of friction for longitudinal pulls were 0.575 - 0.63 for fine sand, 0.54 - 0.61 for coarse sand, and 0.75 - 0.94 for silty soils. For the prototype tests, concrete pipes of 11in, 17in and 40in diameter were used with corresponding coefficients of friction 0.60 - 0.84 for fine sand, 0.54 - 0.63 for coarse sand and 0.33 - 0.53 for silty soils. In addition field studies were also undertaken on 300m lengths of 42in diameter concrete coated pipe under bottom tow conditions. It was found that the initial coefficient of frictional resistance for the concrete pipe on sand was 1.17 reducing to approximately 1.0 once the pipeline had started moving.

Returning now to some specific aspects associated with

structural modelling Konuk (1982) presents a general foundation for developing reliable and rigorous formulations for 3-D pipeline problems including the effects of twist. The treatment concentrates on two aspects of the geometrically nonlinear problem, namely the description of the deformed state using Eulerian angles and the stiffness of the resulting differential equations. It is noted that such numerical stiffness, when combined with strong nonlinearity, results in the convergence of any classical solution technique being mostly a matter of chance. To overcome this, and hence solve the problem in a numerically stable way, the original problem is replaced by a sequence of problems with pipe bending stiffness ranging from a large initial starting value down to its actual value. Each problem in this sequence is solved iteratively and the results used as the starting configurations for the next and more flexible problem. Typical results are illustrated for a pipelaying stress analysis in which the pipeline is curved in both vertical and horizontal directions. Dynamic effects are not considered and no discussion is presented concerning the treatment of the unilateral boundary conditions at the seabed and laybarge stinger.

A similar problem is considered by Odorizzi and Schrefler (1981) who present a three-dimensional geometrically nonlinear Finite Element formulation for pipelines suspended between the ocean floor and the lay barge. The approach is unusual in that continuum elements are used with the pipe represented as a thick walled shell structure. By this means the effects of ovalisation are automatically included and complex problems such as lateral buckling in the sag-bend region may be investigated. Only small strain linear elasticity is considered and the resulting equations solved using a frontal technique. Several examples are presented including the determination of the equilibrium configuration for a $10^{3}/4$in pipe using in turn a model composed of shell type elements and a model composed of a

single line of solid elements with an equivalent cross section. Despite a slight stress induced variation in cross section for the shell model, results are similar and agree with other published data.

Considering an alternative method of installation Kan and Healey (1981) develop a 2 dimensional steady state stress analysis for a long submerged pipe under subsurface tow. The resulting static configuration of the pipe is determined using a state variable beam method based on a Bernoulli-Euler beam model with large deflection. The resulting geometrically nonlinear equations are nondimensionalised and solved numerically using a transfer matrix technique with successive linearisation. It is shown that as the towing speed is increased, higher deflections and stresses are imposed on the pipeline. Therefore higher lead barge pull and more support buoys must be used to maintain safe stress levels at higher transporting velocities.

Returning now to the problem of vortex induced vibrations, Whitney et al (1981) use random vibration analysis to determine the root-mean-square (RMS) displacements and accelerations of a long ocean-mining riser pipe due to vortex shedding. The normal modes and eigenfrequencies of the pipe, determined using a Finite Element model, are used to uncouple the linear equations of motion and an empirical relationship between the RMS lift coefficient and Reynolds number established using experimental data. In addition the random nature of vortex shedding along the span is accounted for by introducing a cross spectral density function for the lift force at two stations z_1 and z_2 along the pipe. The mathematical form used for this density function is as recommended by Vickery and Clark (1972) based on an investigation of the response of tapered stacks in a sheared wind environment. The authors conclude that for the long pipes considered, excitation can occur at low crossflow velocities with the close spacing of modal

frequencies resulting in no quiescent zones.

An extension of this method is given by Whitney and Nikkel (1983) who develop a random vibration analysis for the lateral response of marine risers due to vortex shedding in a vertically sheared cross flow. An existing finite difference code and eigen-processor were initially used to calculate the generalised mass and stiffness coefficients associated with the normal modes and frequencies of the riser. In addition the method presented makes use of laboratory observations (Mair and Stansby 1975) indicating that under shear flow conditions vortices are shed in cells with shedding frequencies jumping discontinuously across cell boundaries. This situation is modelled by dividing the riser pipe into a number of regions where for each such length locked-in response in a single mode is assumed. The allocation of these regions depends on the current distribution and is such that the corresponding reduced velocity (calculated using the appropriate modal frequency) is in the synchronisation range $4.5 < V_R < 10$. The amplitude of vibration in each of the assigned modes is now determined by a balance between energy input to the system over the lock-in region and energy dissipated primarily by fluid damping over the remainder of the riser. Their calculation follows the random vibration analysis of Blevins and Burton (1976) while fluid damping is estimated by considering the drag force in the relative velocity direction and linearising assuming small riser response. The authors conclude that more than one mode can be excited by shear flows while the use of an assumed uniform cross flow tends to over-predict riser response.

In contrast to the above random methods, Nordgren (1982) develops a 3 dimensional deterministic method for the response of a marine riser excited by vortex shedding. The riser is modelled using a hybrid finite element method

with deflections and moments selected as the basic variables. The resulting equations are integrated in the time domain together with a set of vortex oscillation equations obtained using the 2 dimensional coupled wake oscillator model proposed by Iwan and Blevins (1974). The author notes that this model is only applicable to flow regimes where the vortex shedding is fully locked-in to the motion of the structure and suggests that the vortex model could be applied selectively to regions of the riser. The results presented include a 2 dimensional analysis for the transverse motion of a 152m riser under steady depth-dependent current. In-line vibrations and coupling effects are not considered although it is noted that the method may be extended to other more complicated vortex models as they become available. It is noted that steady resonant response occurs at the Strouhal critical velocities corresponding to each of the riser modes.

1.8 Pipeline Span Assessment

As noted in section 1.7 it is necessary to complement the experimental work on pipe spanning by developing realistic mathematical models of the system. By this means an additional understanding can be gained into aspects of the problem too difficult to model experimentally. In addition such mathematical models will also provide an important input into the practical question of span assessment. This problem arises when any significant span is discovered, either during a routine pipeline survey, or at any other time. Since the consequence of vortex induced oscillation in such a span is potentially serious, an assessment must be made to determine if any remedial repair work is required. However in view of the high cost associated with such offshore repair work, economic considerations dictate that any such span assessment should not be unduly conservative. On the other hand care must also be taken to avoid the poten-

tially dangerous situation where an unsafe span is left unrectified. Methods used for span assessment include the intuitively obvious approach of determining for each span the threshold flow conditions required for the initiation of significant flow induced vibration. Normally an assumed steady current is used and the span considered unsafe if the reduced velocity associated with the actual current exceeds an initiation value of 3.5, equation (1.12). A less conservative approach is to use an "acceptance" criterion in which vortex induced oscillation is tolerated and the safety of the span assessed in terms of the fatigue life of the steel pipe (Tsahalis and Jones 1981). This approach is more compicated than the simple "initiation" method since the dynamic response of the pipeline must now be determined. In addition the durability of the concrete weight coating under long term cyclic load presents a further uncertainty about which little is presently known. However this method may prove to be more realistic since under the complex and variable flow conditions encountered around the pipe, most pipeline spans may undergo some form of vortex induced vibration.

1.9 Scope of the Present Work

Although the above discussion establishes the need for suitable analytical methods it appears that relatively little work has been undertaken concerning the development of realistic mathematical models for pipeline spans formed by the process of soil erosion. As a consequence a number of such models are developed in this thesis and used to investigate several aspects of span behaviour. Specific details of this work are outlined in the following section. This is then followed by a summary of work included in this thesis concerning marine riser dynamics.

1.9.1 Pipeline Spans

The scope of the present work on pipeline spans is summarised in the following chapter by chapter account.

Chapter 2 develops a linear beam column on elastic foundation model for a single pipeline span supported on either side by an infinite elastic foundation. Since pipeline frequencies play a central role in controlling vortex induced vibrations, attention is focused on determining the span frequencies in terms of a small number of independent nondimensional parameters. In addition the linear elastic buckling load for the elastically supported pipeline is determined and the effects of coupling between adjacent spans considered.

Chapter 3 concerns a nonlinear Finite Element model in which the effect of pipe soil friction and change in geometry are considered. Theories are developed for a nonlinear pipe element with axial/bending coupling and a nonlinear nonconservative pipe/soil friction element. These elements are used to establish the pipeline configuration arising from the formation of a long span in an otherwise flat seabed. Frequencies associated with small amplitude vibration about these configurations are then determined using a tangent stiffness approach with special attention paid to the end axial constraints imposed on the span. To illustrate the theory, results are presented for typical small, medium and large diameter pipelines.

Chapter 4 extends the methods of Chapter 3 to consider the effect of initial seabed geometry on span behaviour. A simple parametric representation of the seafloor profile is first introduced and its effect on pipeline equilibrium incorporated into the model. Pipeline deflections resulting from span formation are then computed using a modified form of the incremental load path solution developed in Chapter 3.

Three basic seabed geometries are considered, namely valley, valley side and hill. Results are presented for pipeline deflection and stress as well as span frequencies. These results are found to be strongly dependent on initial geometry.

Chapter 5 further extends the theory to consider the effect of finite amplitude vibrations in the free span. In order to deal with the nonlinear and path dependent aspects of the formulation, a modified Wilson-θ scheme is devised in order to integrate the equations of motion for large free vibration of the pipeline about its static equilibrium position. This algorithm is used to investigate the pipeline response under different amplitudes of vibration and for span lengths of 25m and 50m. Results are presented showing pipe displacement and stress time histories from which span frequencies are deduced. The chapter ends with a summary of the main conclusions obtained using the elastic foundation models developed in Chapters 2 to 5.

Chapter 6 develops a nonlinear theory for a pipe/rigid foundation contact element. The element equations are developed using a Lagrangian approach in which the unknown lifted length of pipe is treated as a time variable generalised coordinate. This approach is unusual and to the author's knowledge has not been investigated in any previous work. It is demonstrated that for the static case under zero tension, this method yields the exact result. In addition an independent equilibrium check using first principles is demonstrated for the dynamic case. Some suggested applications and possible improvements to the theory are indicated but no attempt has been made to implement the method.

1.9.2 Riser Dynamics

The problems of suspended pipeline spans and marine risers are closely related and may be classified together

under the more general heading of slender body dynamics. Consequently the scope of the present work also includes riser dynamics, the aim being to synthesize the many and varied analysis methods developed for riser analysis into a simple but flexible design-orientated program. In order to increase flexibility at the modelling stage, the riser is initially represented by a Finite Element model similar to that used for the pipeline spans. A transformation is then made to a mixed set of physical plus modal coordinates using a component mode synthesis method. Finally an improved frequency domain solution is suggested and a range of riser/articulated column configurations analysed. This work, together with a brief review of riser analysis methods, is presented in Chapter 7.

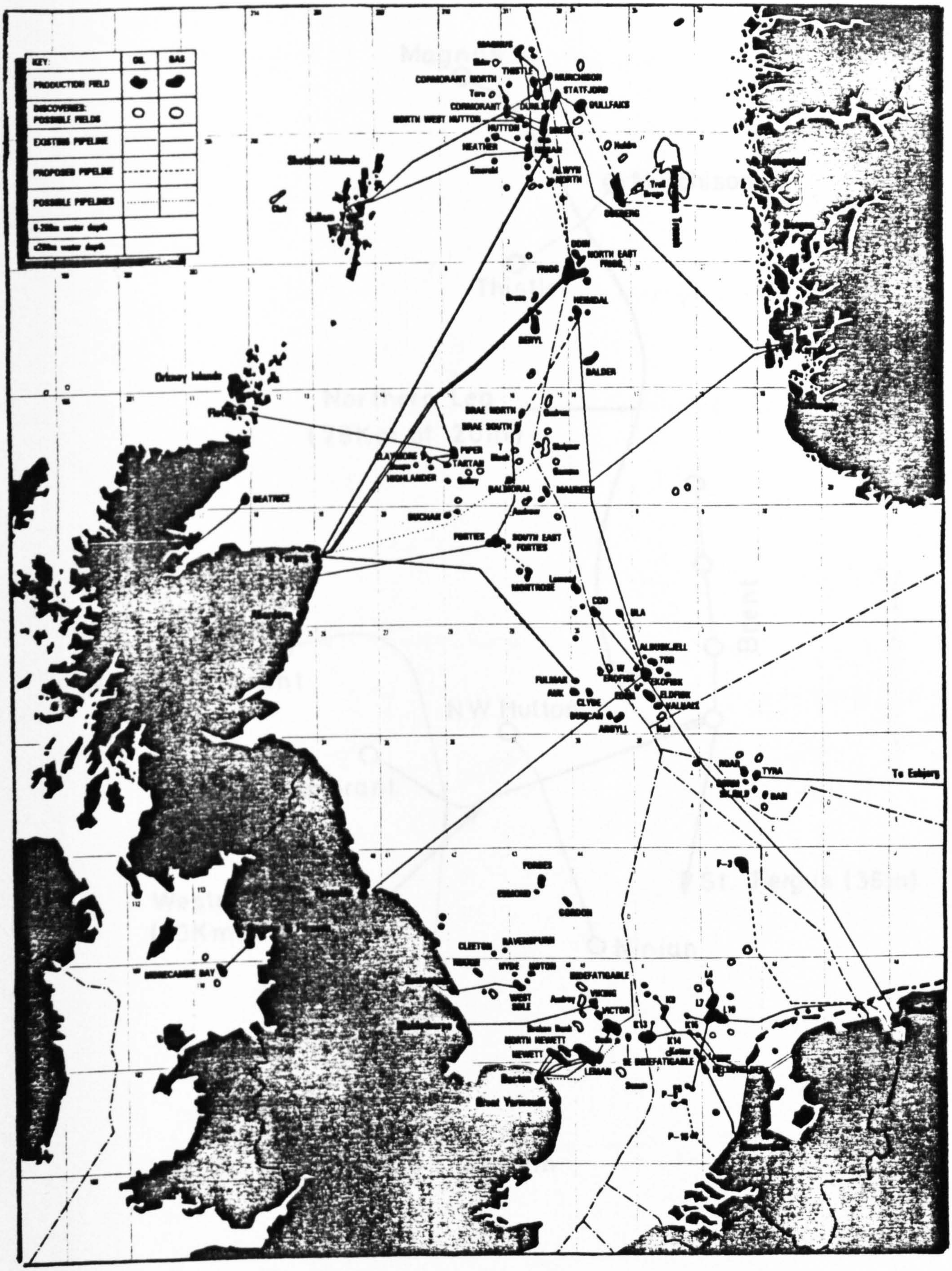

FIG 1.1 North Sea Major Pipelines

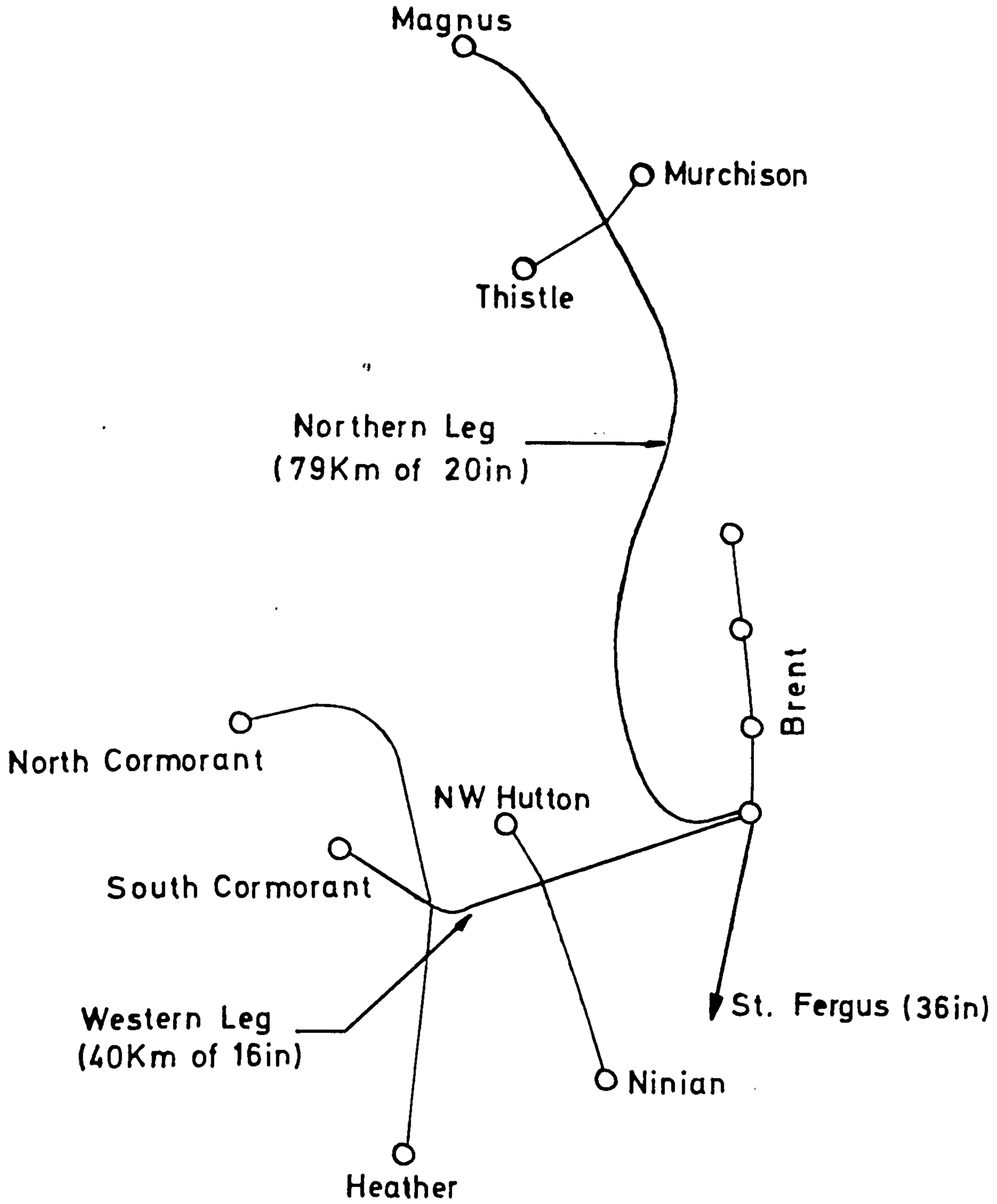

FIG 1.2 FLAGS System

a) General Arrangement
(Not to scale)

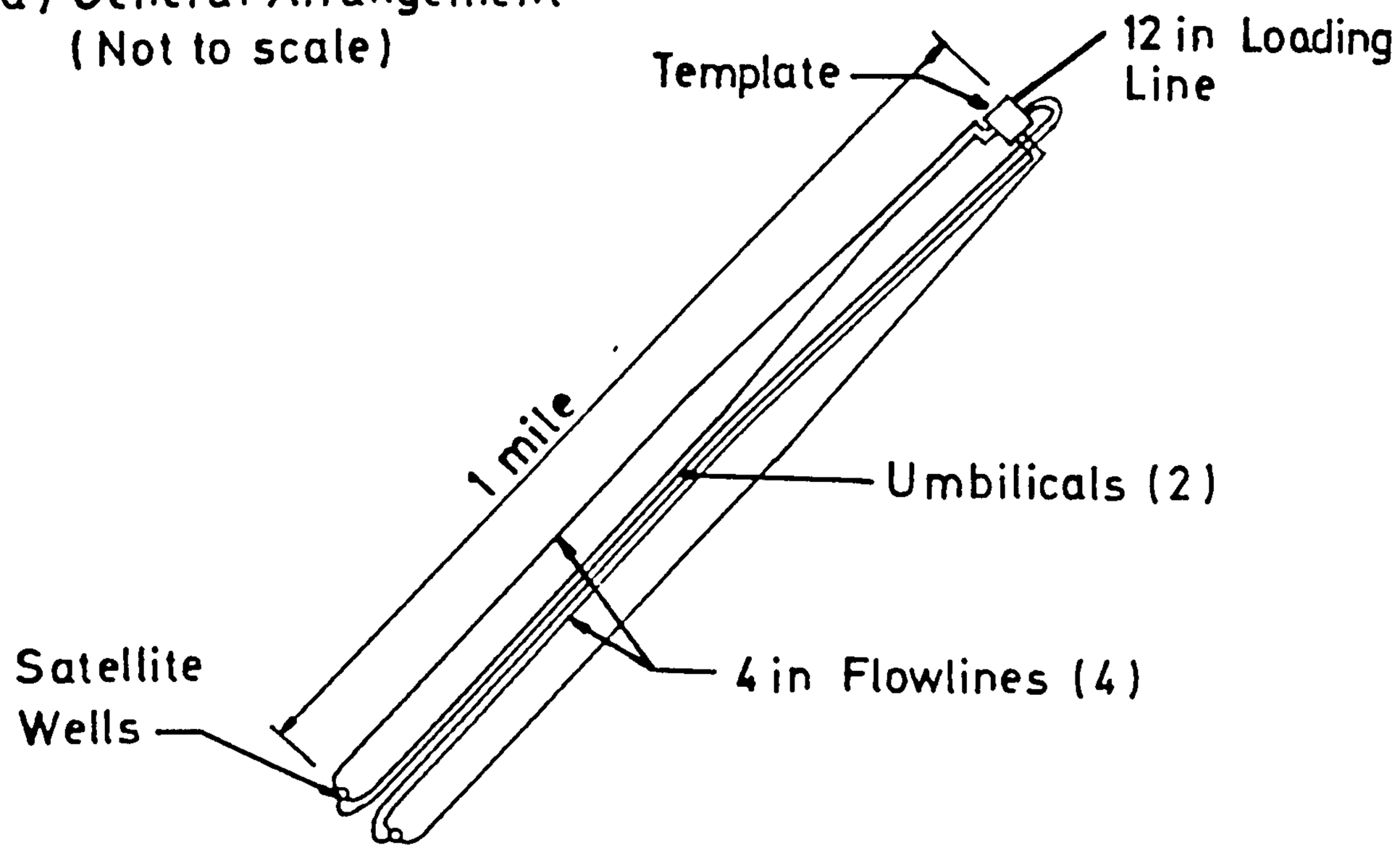

b) Satellite Well Connections

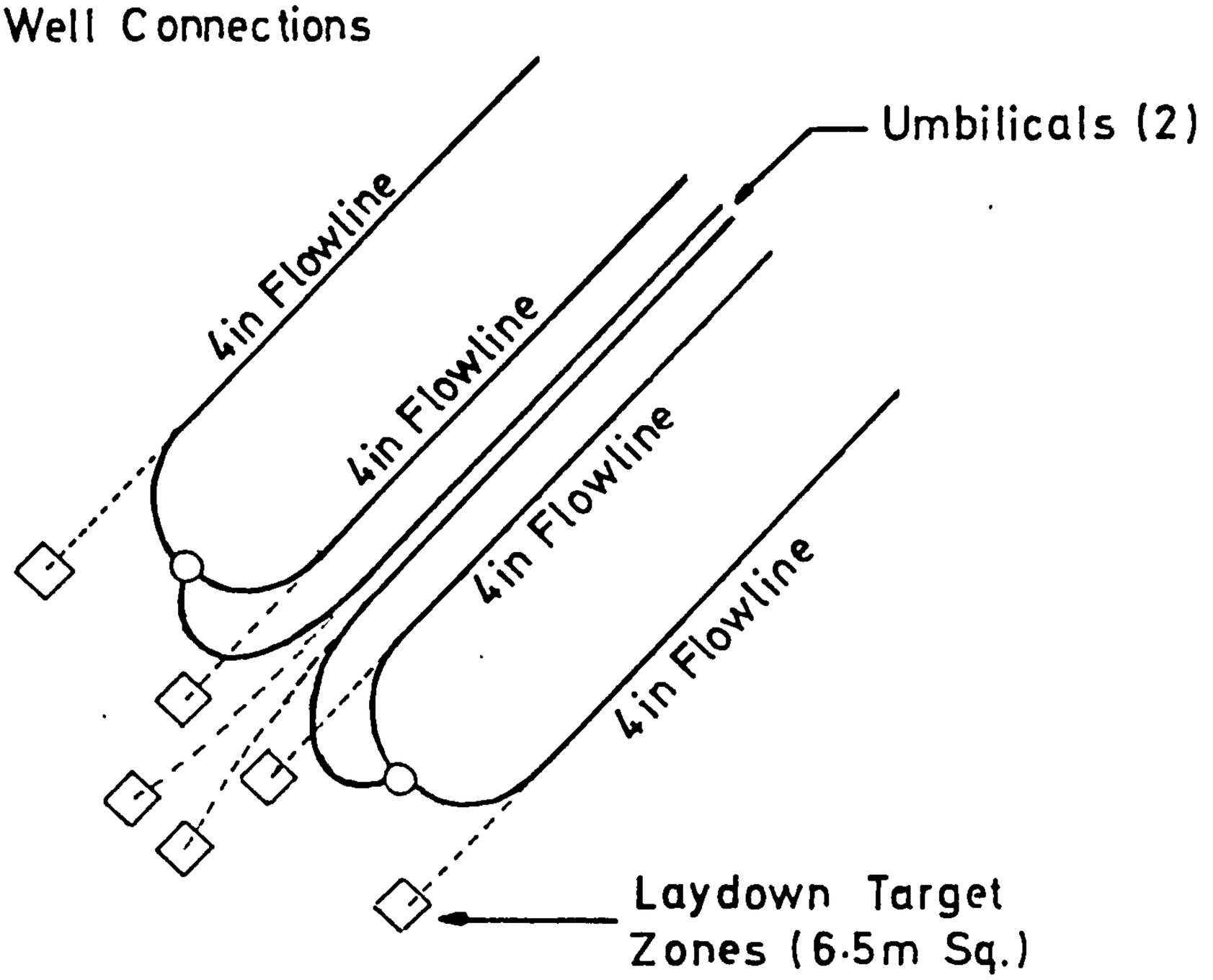

FIG 1.3 Buchan Flowline Arrangement

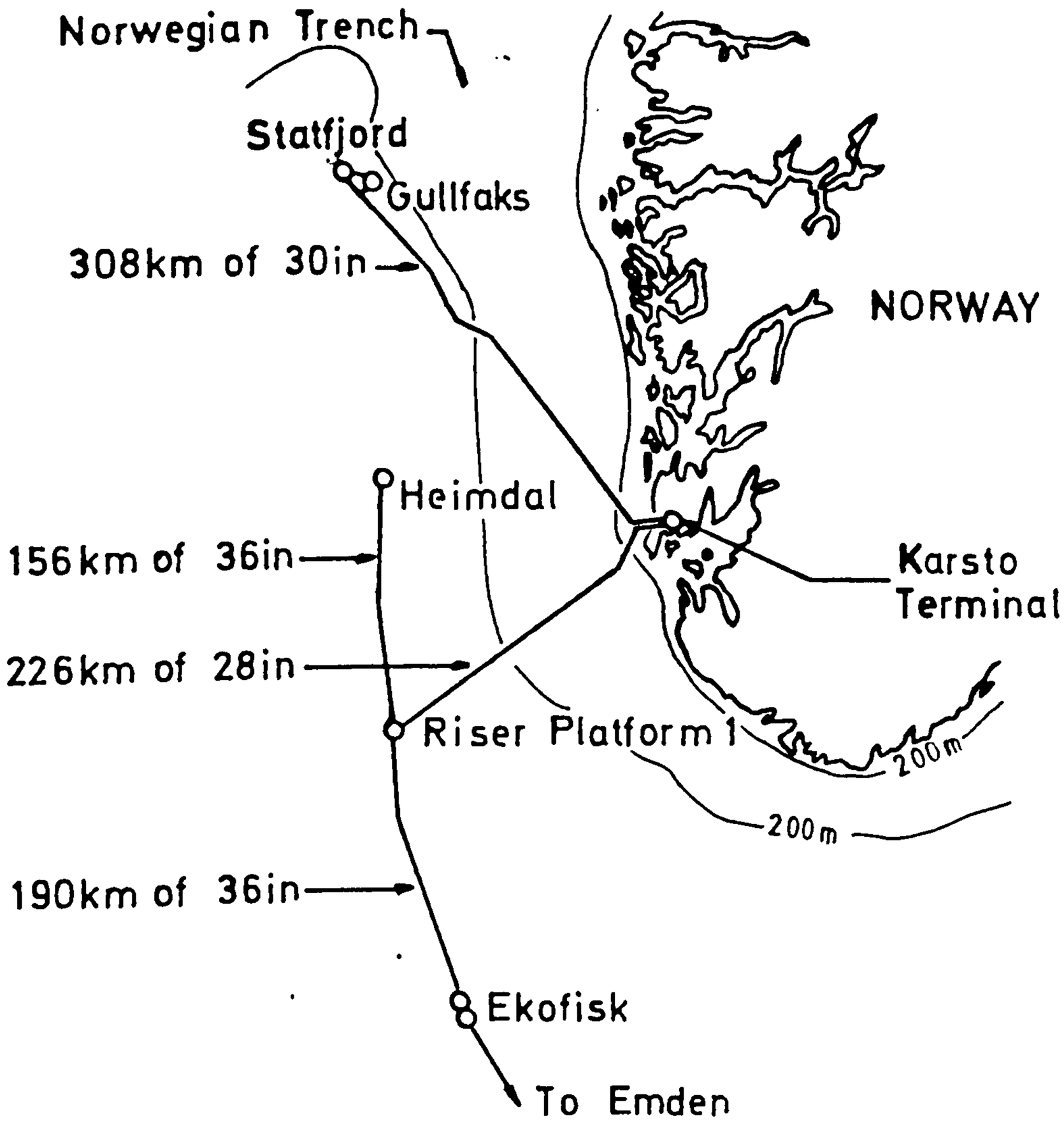

FIG 1.4 Statpipe System

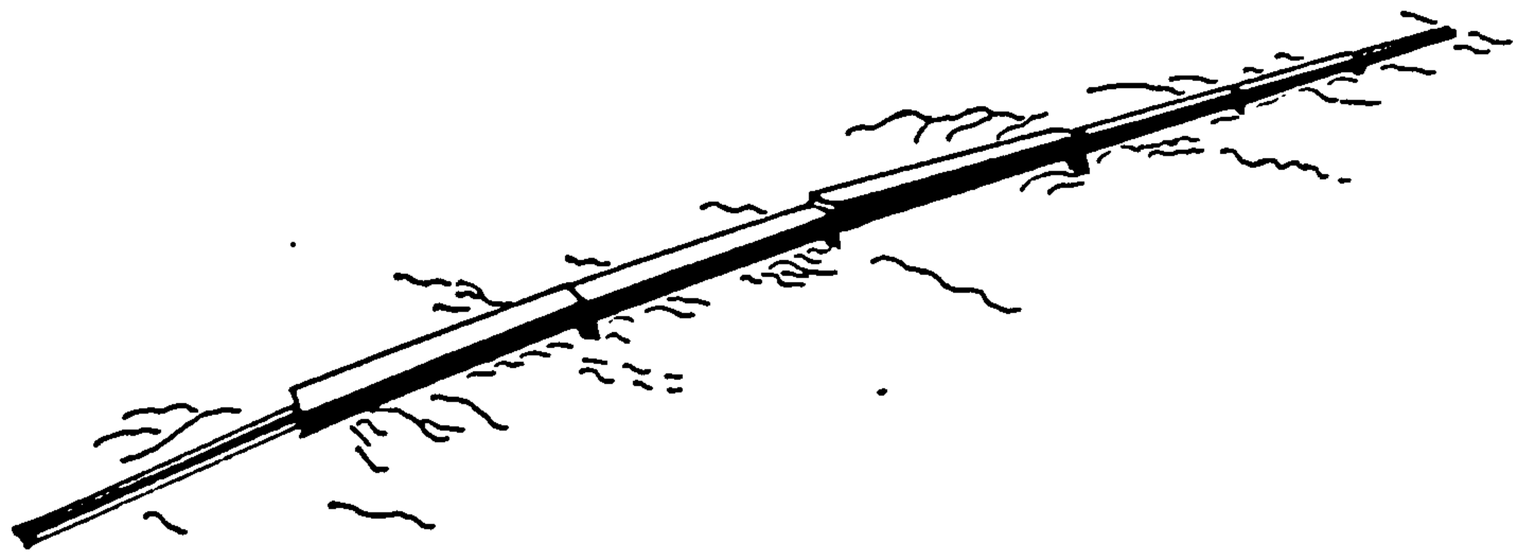

FIG 1.5 Statpipe Shore Approach Tunnel

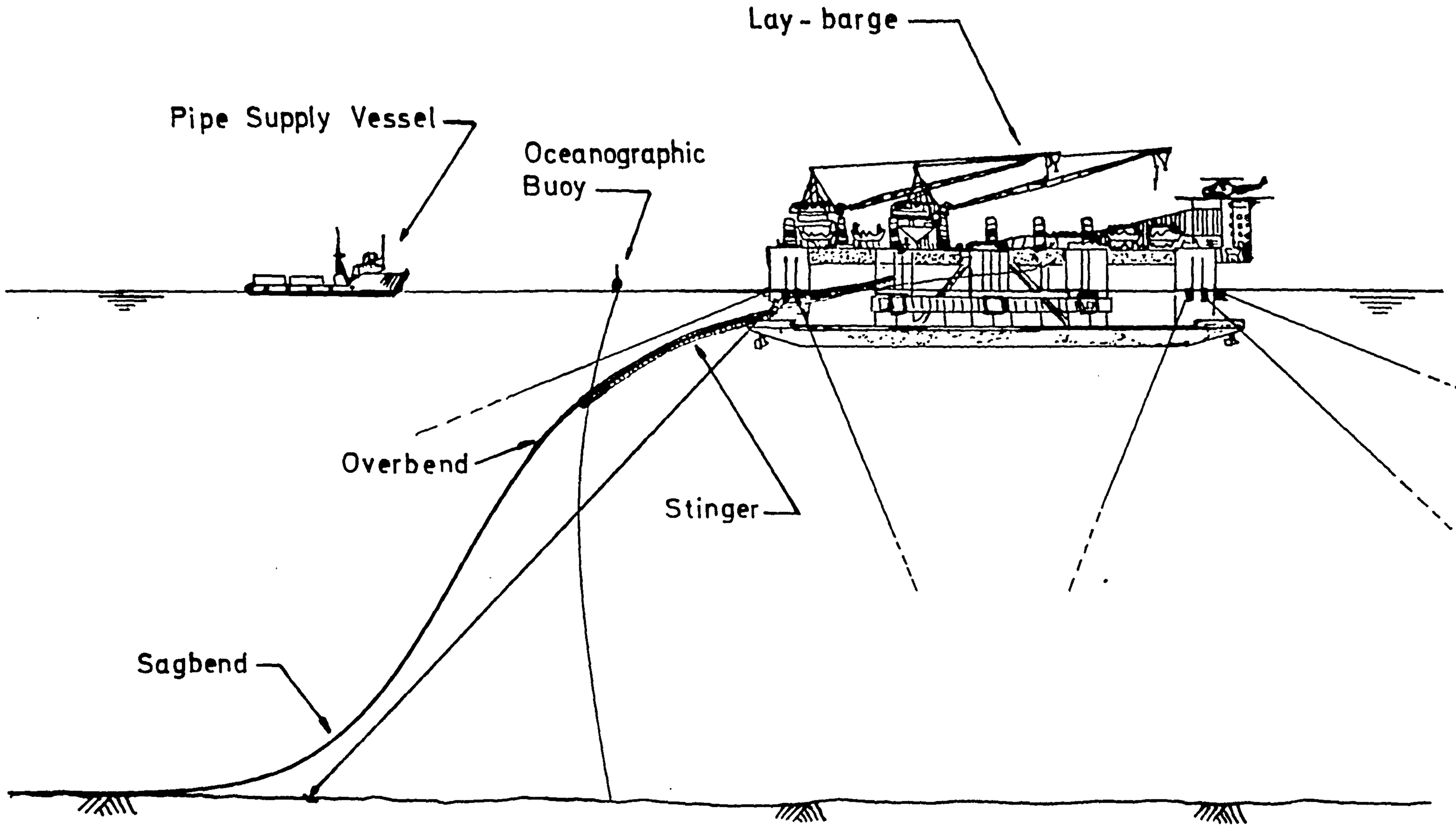

FIG 1.6 Pipe Laying Using Lay - barge

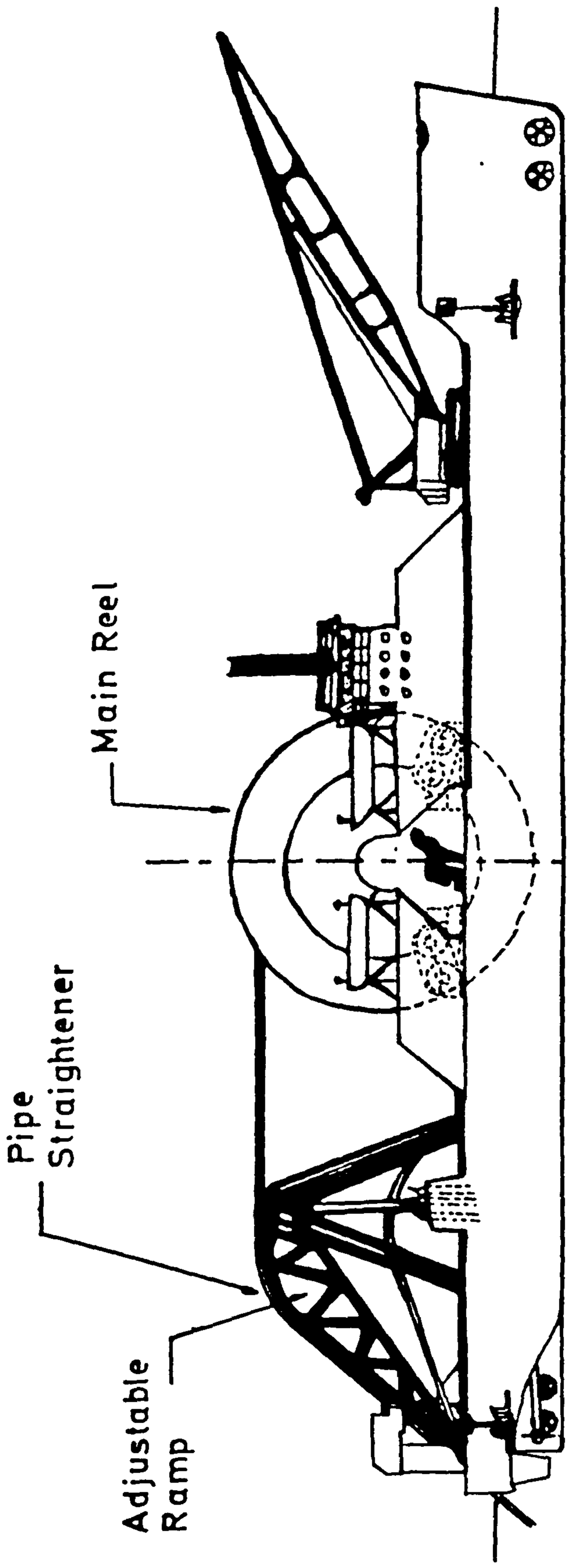

FIG 1.7

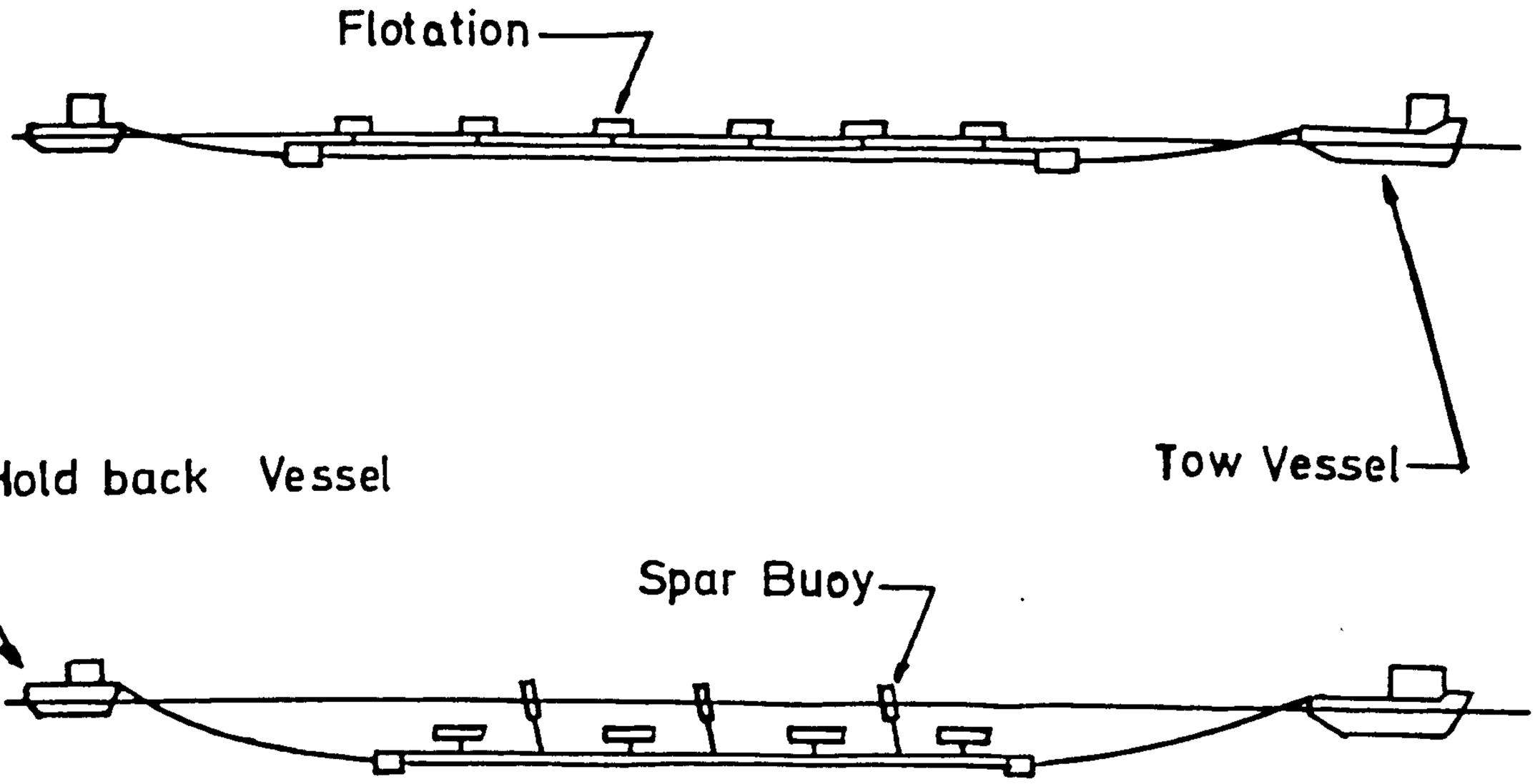

FIG 1.8 Surface and Below Surface Tow

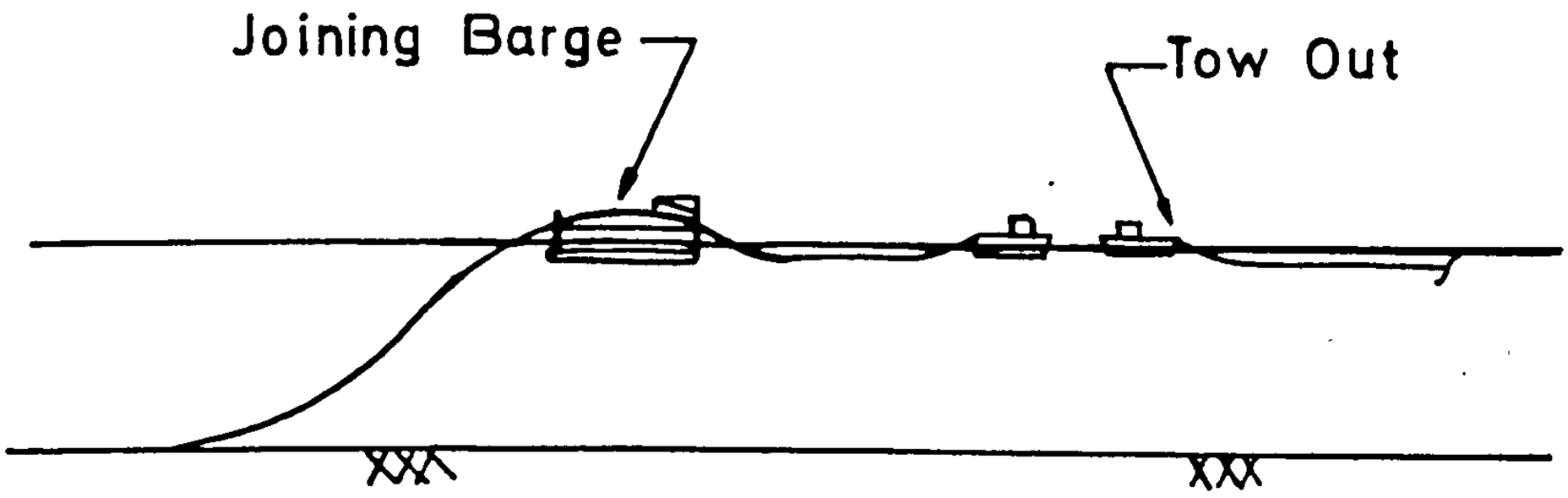

FIG 1.9 RAT Method

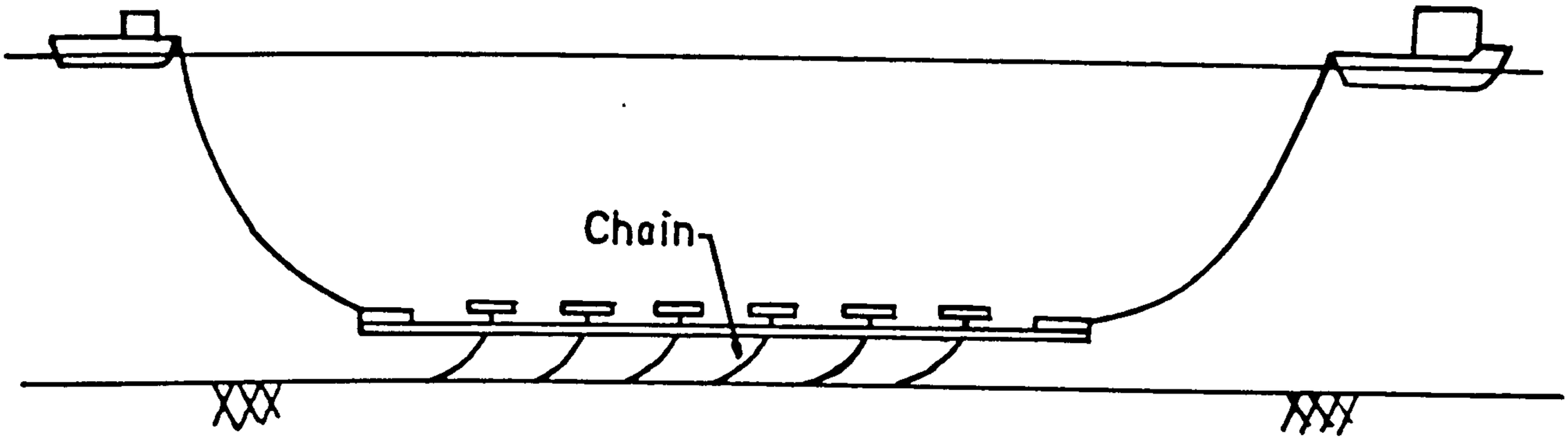

FIG 1.10 Off bottom Tow

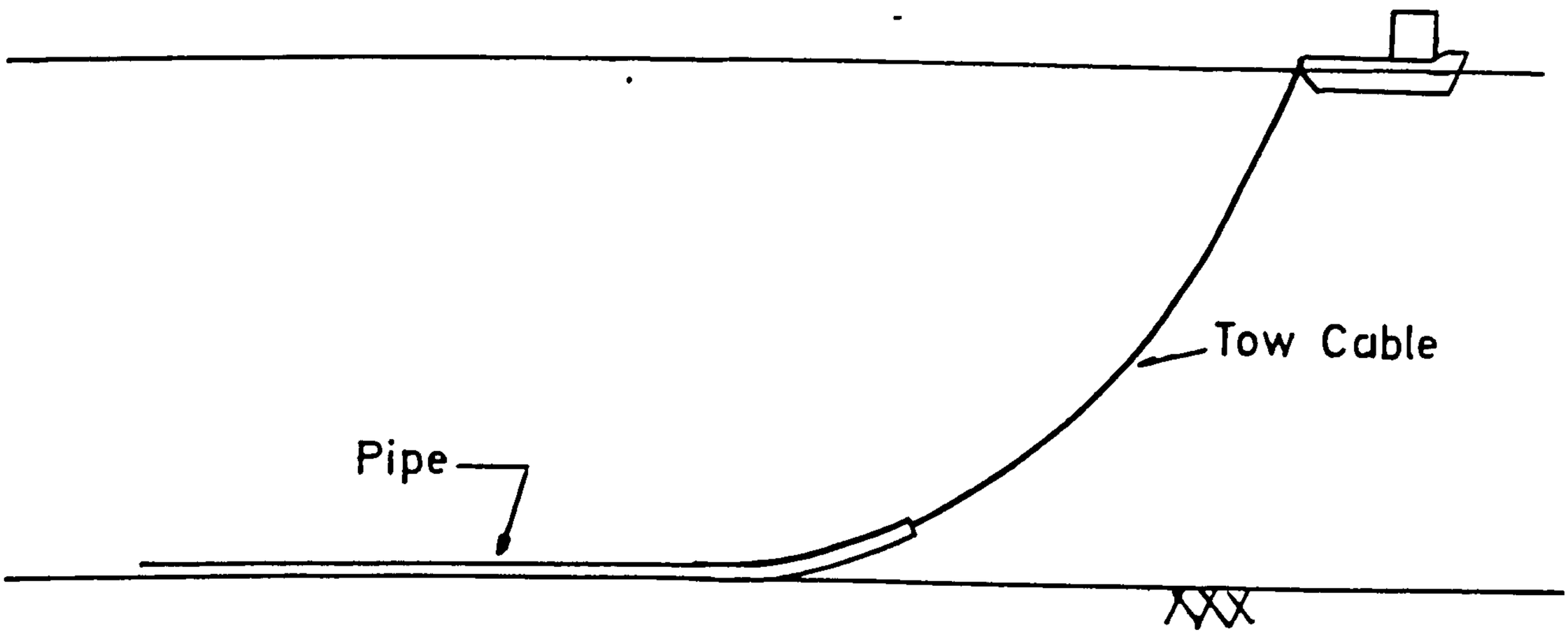

FIG 1.11 Bottom Tow

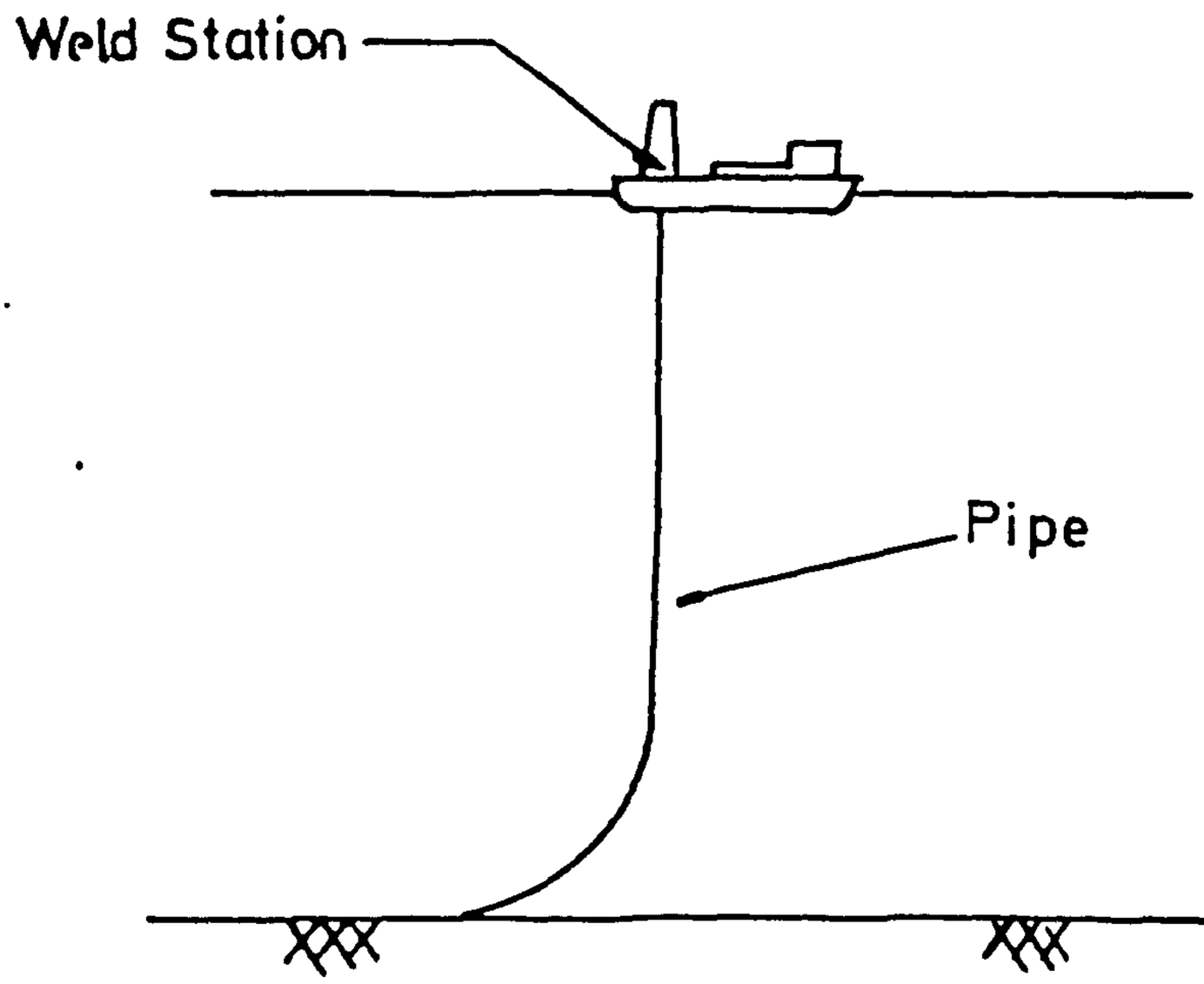

FIG 1.12 J-Curve Pipe Laying

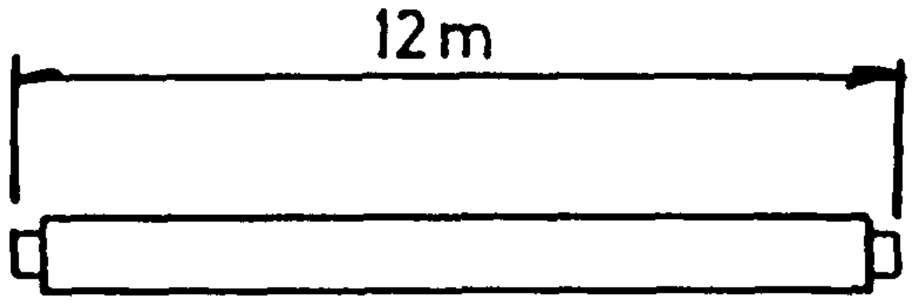

FIG 1.13 Pipe Joint

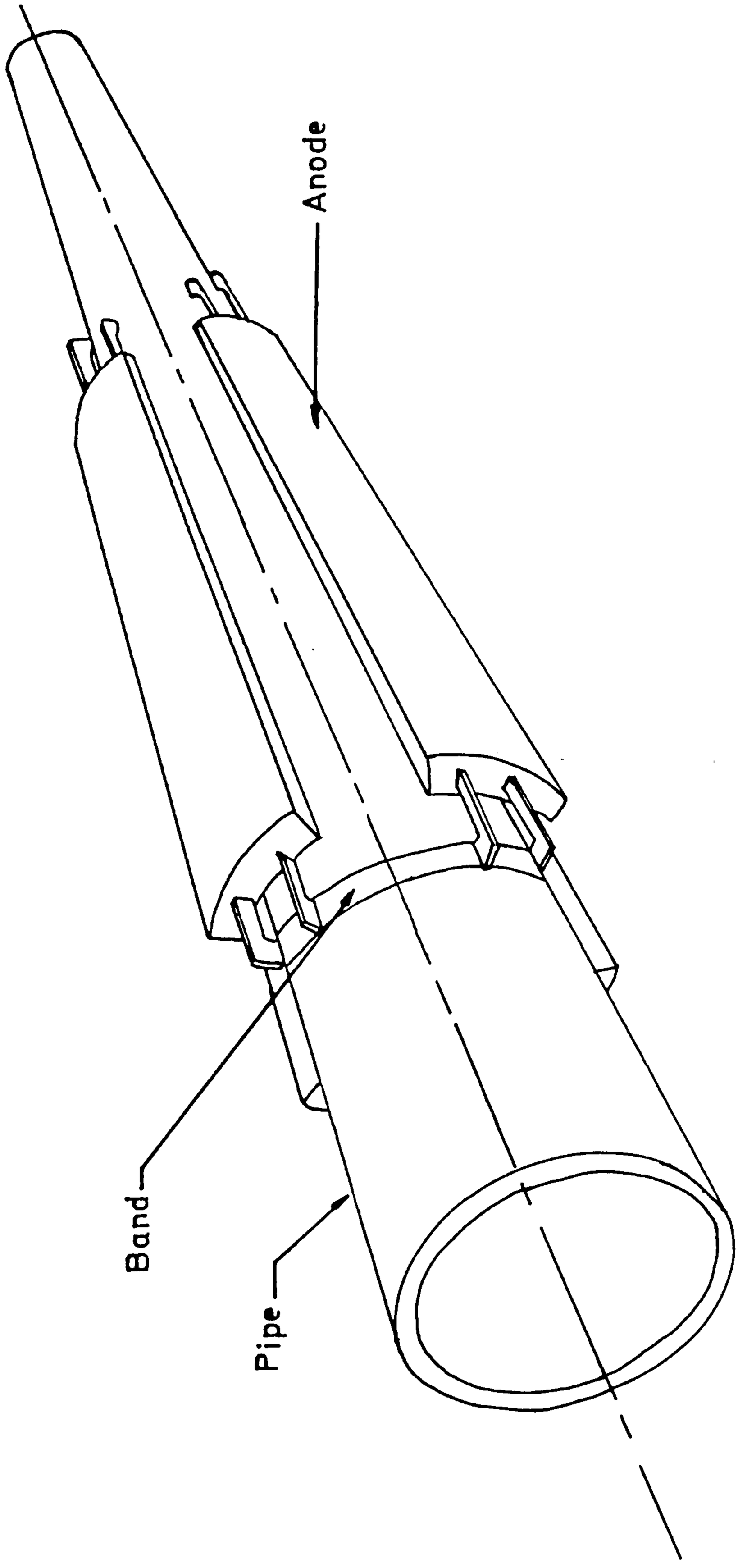

FIG 1.14 Pipeline Sacrifical Anode

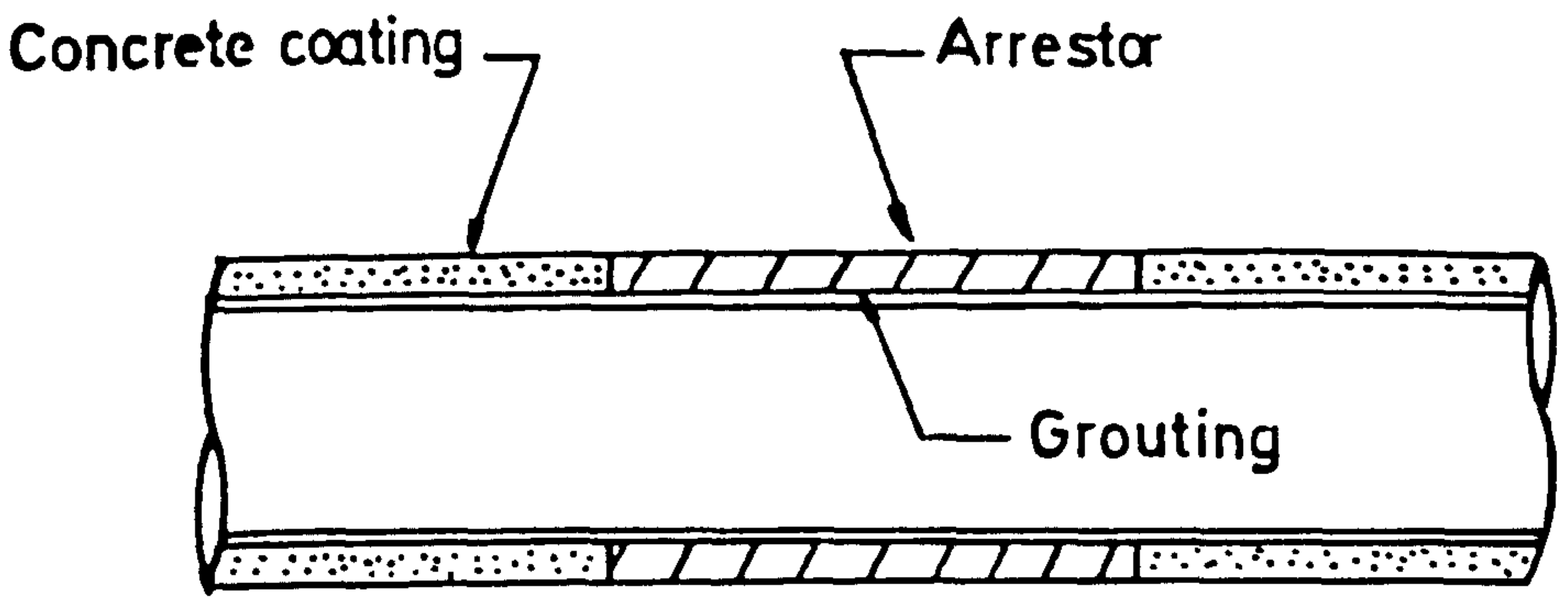

FIG 1.15 Free Ring Buckle Arrestor

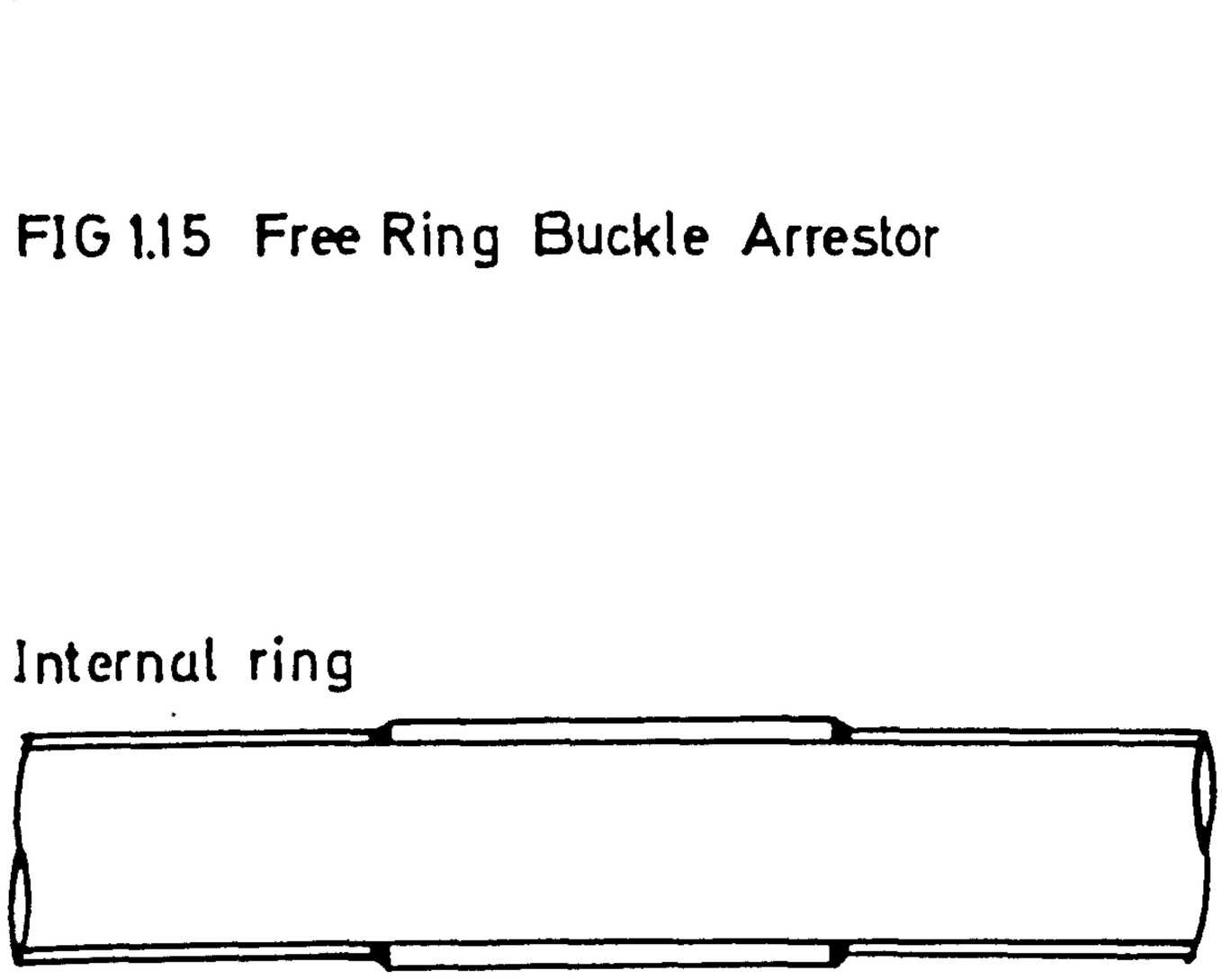

FIG 1.16 Other Buckle Arrestors

Design Data :-

Pipe Dia. = 1000 mm

Internal Pressure = 10 N/mm²

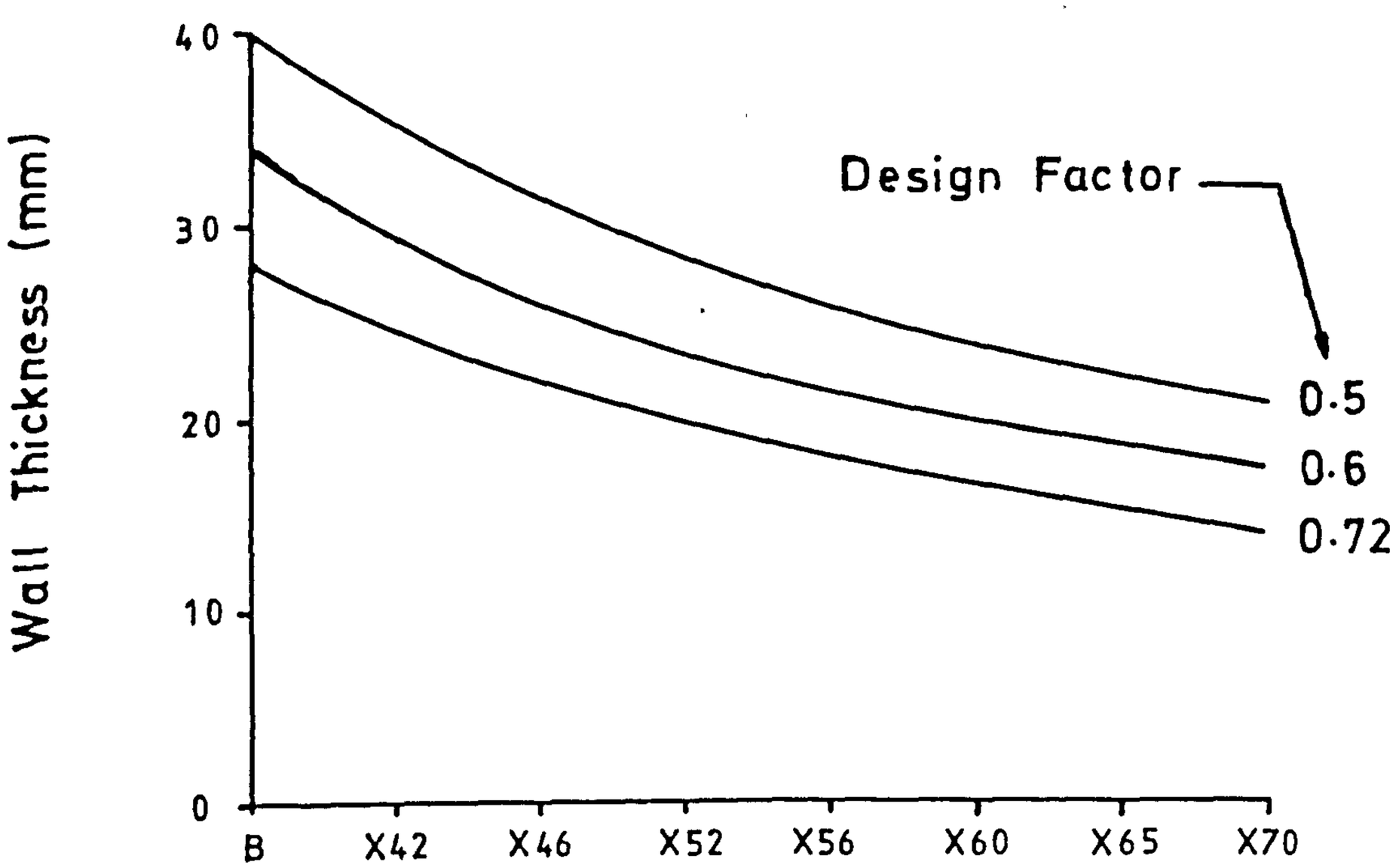

FIG 1.17 Calculated Pipe Wall Thickness

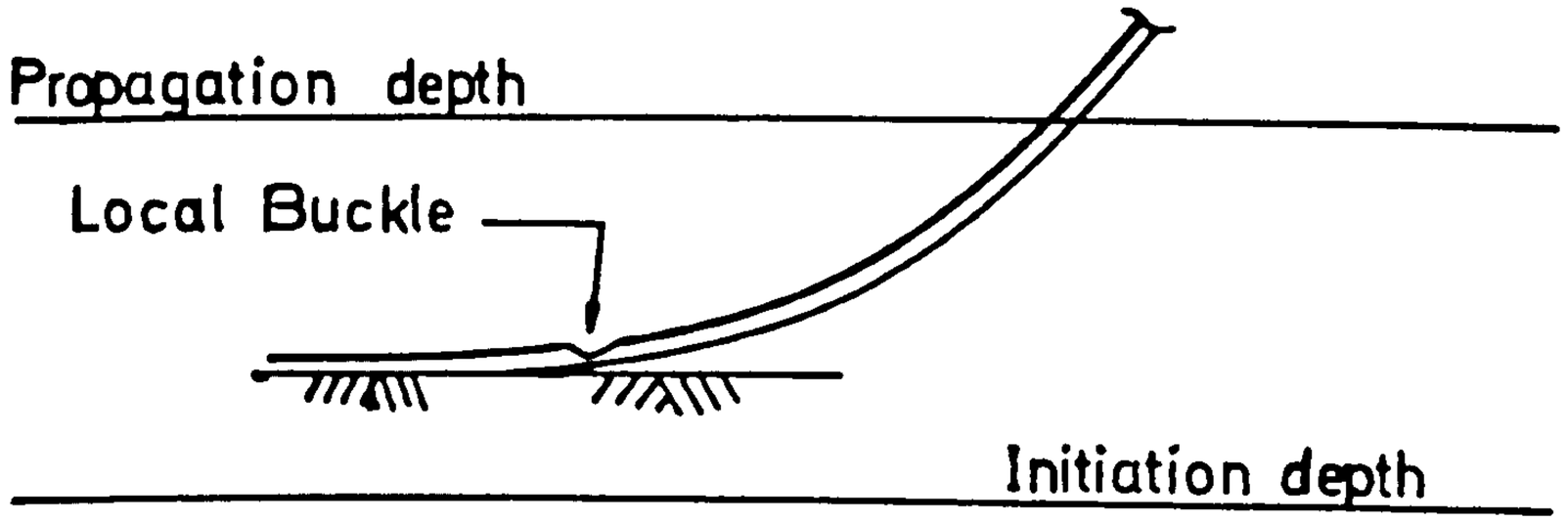

FIG 1.18 Local Buckle

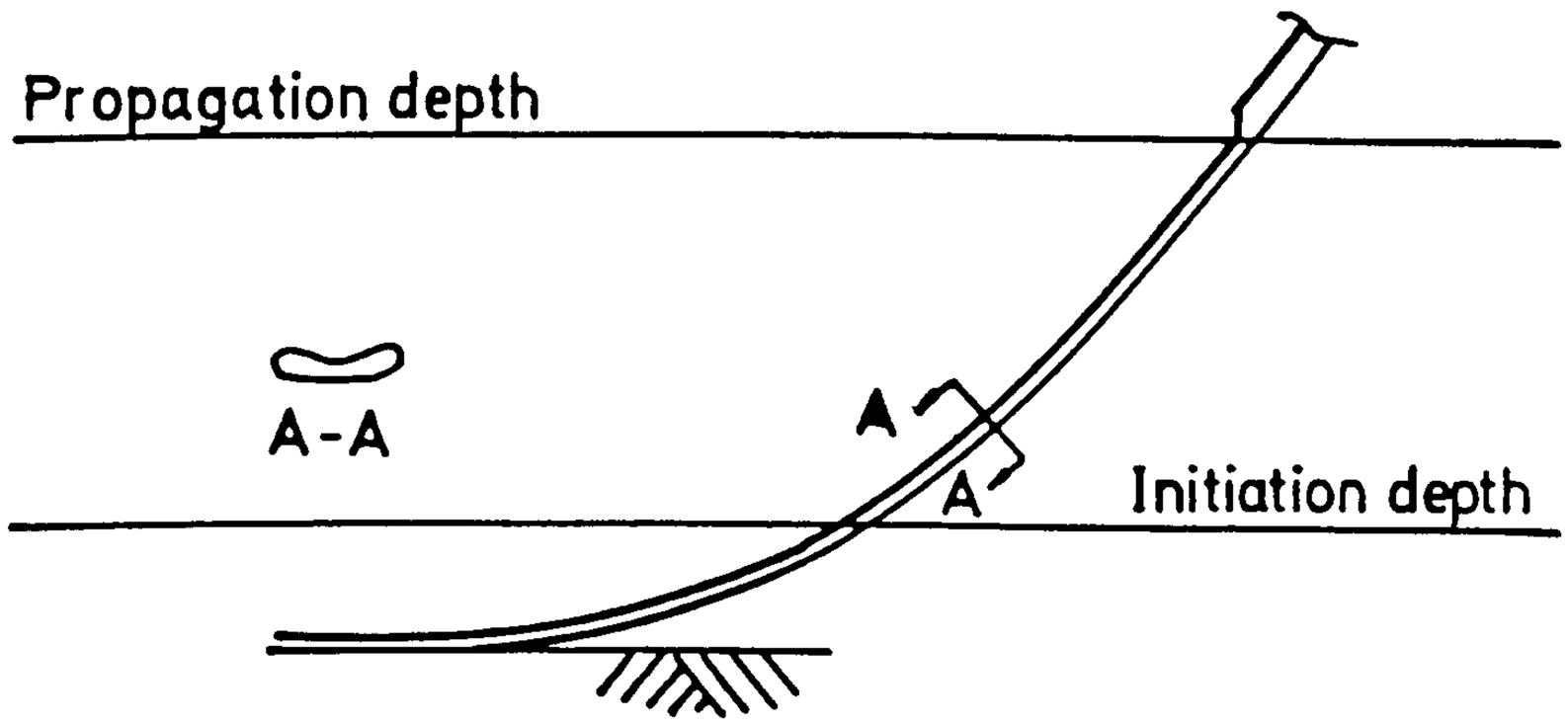

FIG 1.19 Buckle Propagation

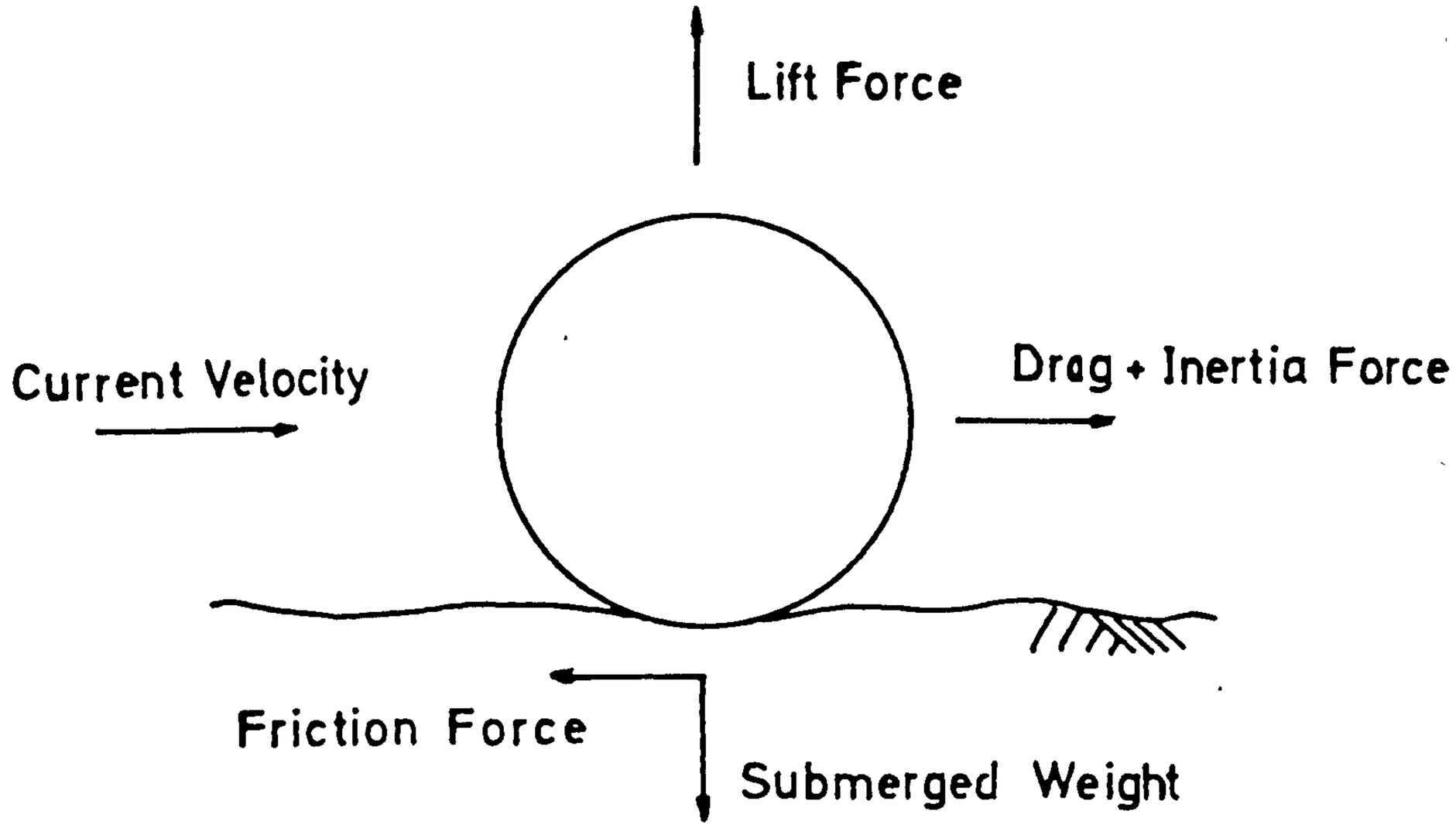

FIG 1.20 Horizontal Pipeline Stability

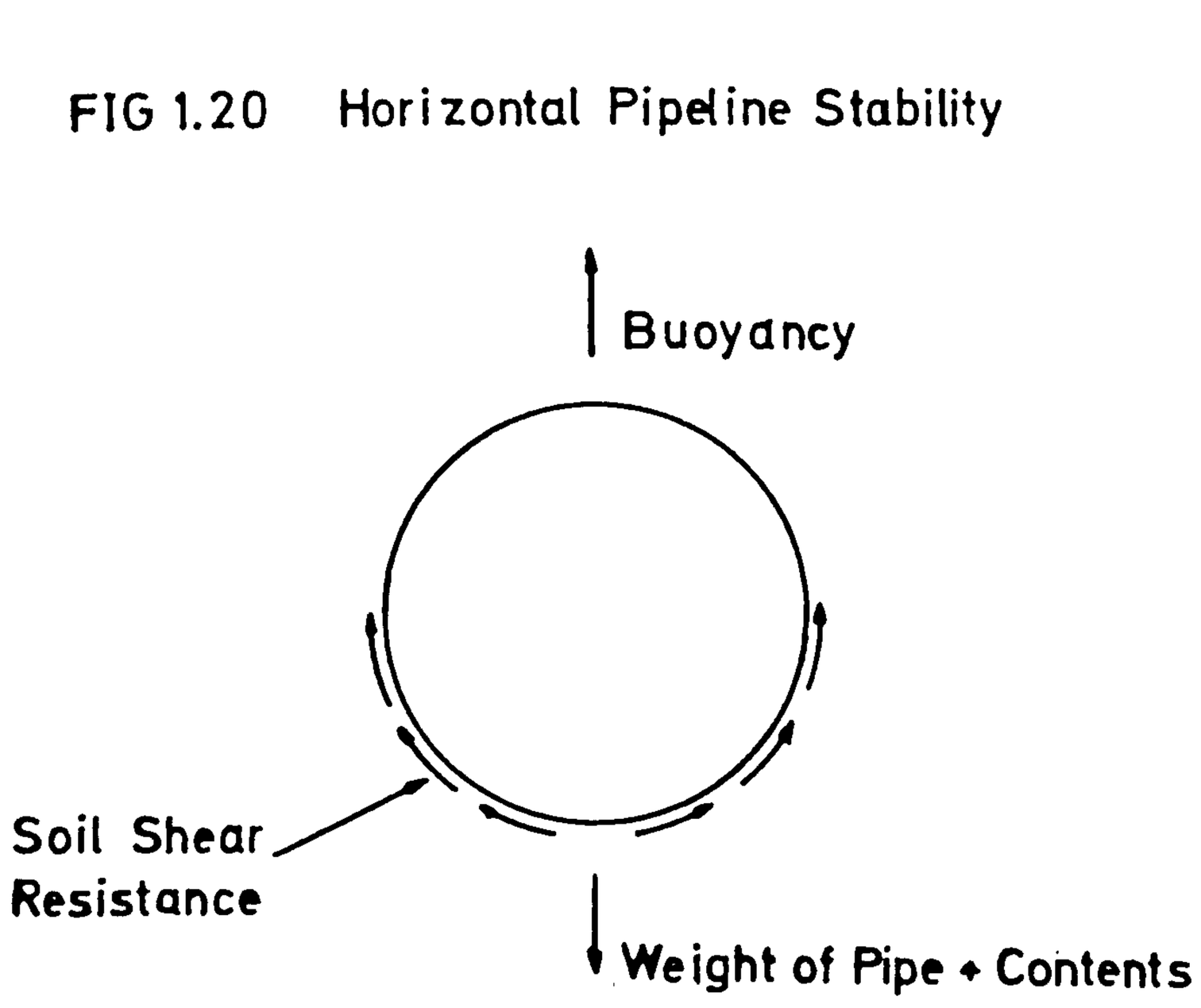

FIG 1.21 Vertical Pipeline Stability

a) 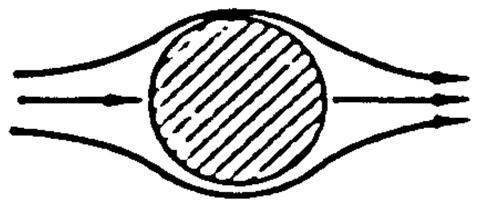

$\underline{Re < 5}$ REGIME OF UNSEPARATED FLOW

b) 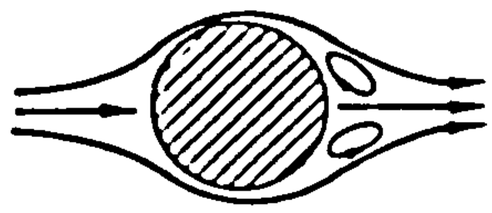

$\underline{5 \text{ TO } 15} < Re < 40$ A FIXED PAIR OF FÖPPL VORTICES IN WAKE

c) 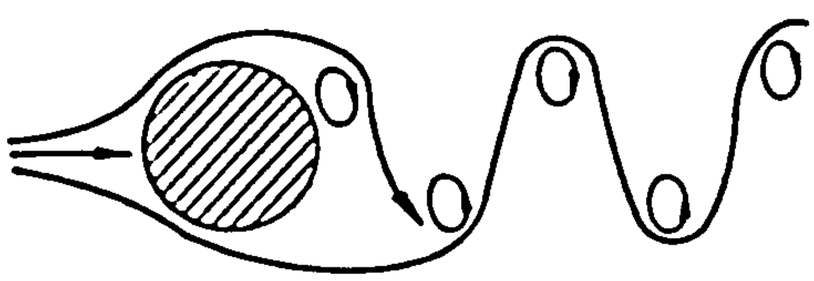

$\underline{40 \leq Re < 90 \text{ AND } 90 \leq Re < 150}$
TWO REGIMES IN WHICH VORTEX STREET IS LAMINAR

d) 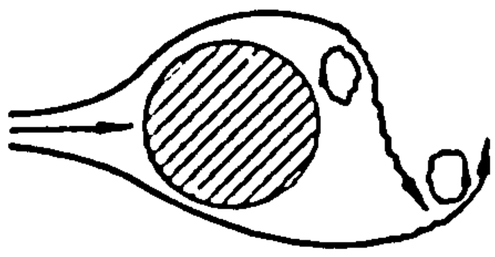

$\underline{150 \leq Re < 300}$ TRANSITION RANGE TO TURBULENCE IN VORTEX

$\underline{300 \leq Re \gtrsim 3 \times 10^5}$ VORTEX STREET IS FULLY TURBULENT

e) 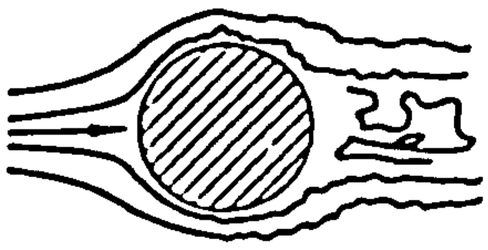

$\underline{3 \times 10^5 \gtrsim Re < 3.5 \times 10^6}$
LAMINAR BOUNDARY LAYER HAS UNDERGONE TURBULENT TRANSITION AND WAKE IS NARROWER AND DISORGANIZED

f) 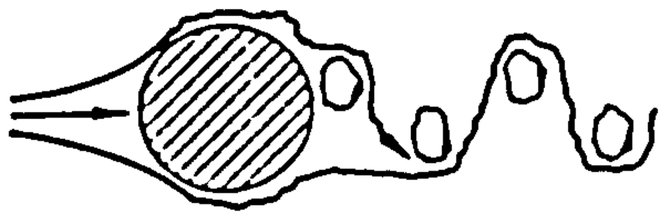

$\underline{3.5 \times 10^6 \leq Re}$
RE-ESTABLISHMENT OF TURBULENT VORTEX STREET

FIG 1.22 Flow Regimes Across a Fixed Cylinder
(Lienhard, 1966)

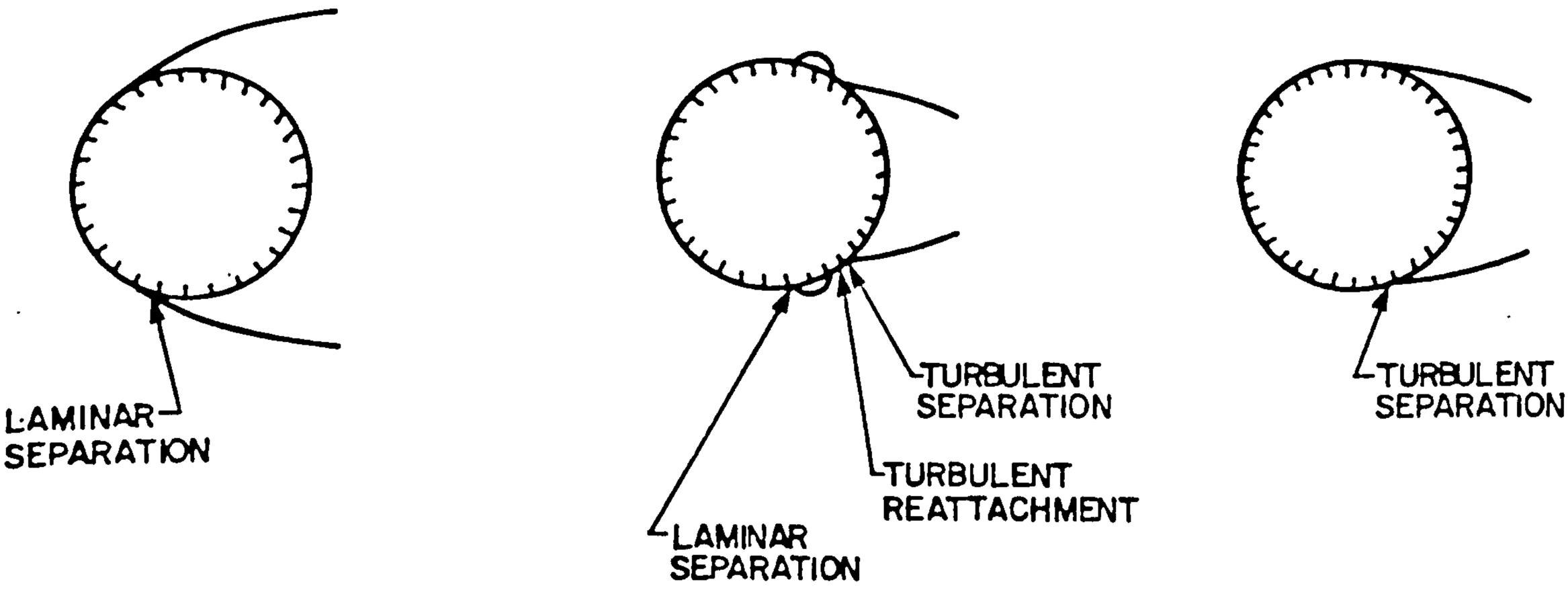

a) Subcritical b) Critical c) Supercritical

FIG 1.23 Flow Separation/Reattachment

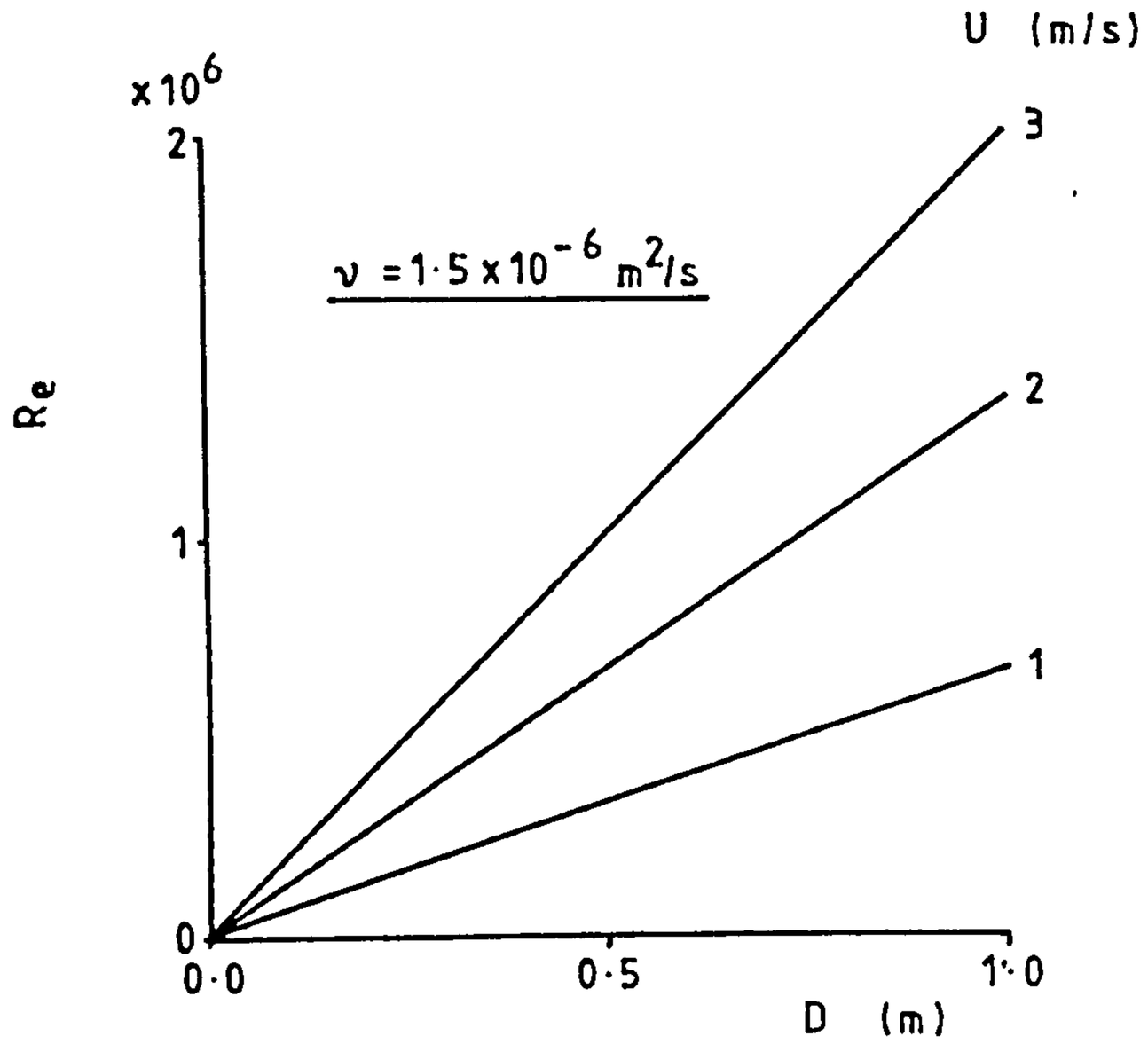

FIG 1.24 Typical Reynolds Number for Pipeline

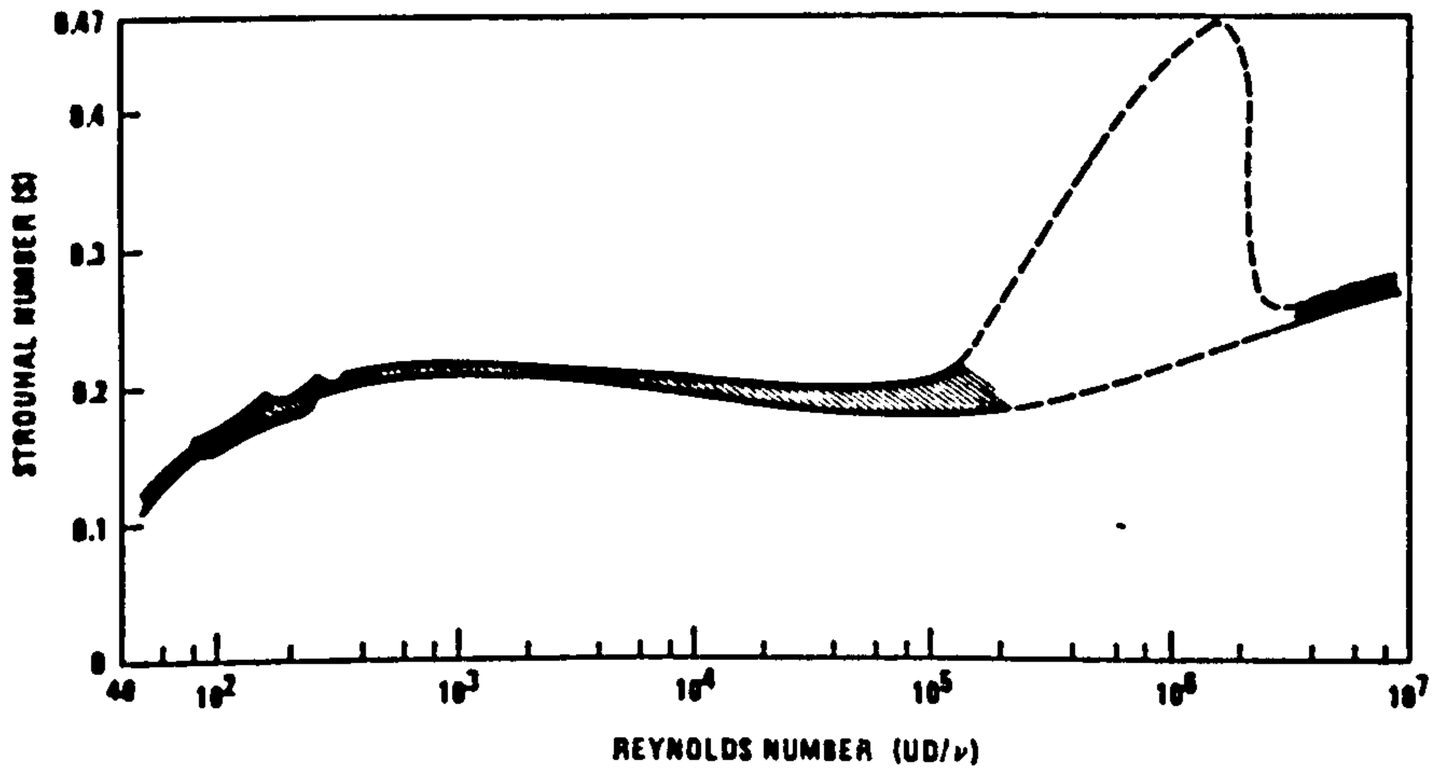

FIG 1.25 Strouhal-Reynolds Number Relationship (Lienhard, 1966)

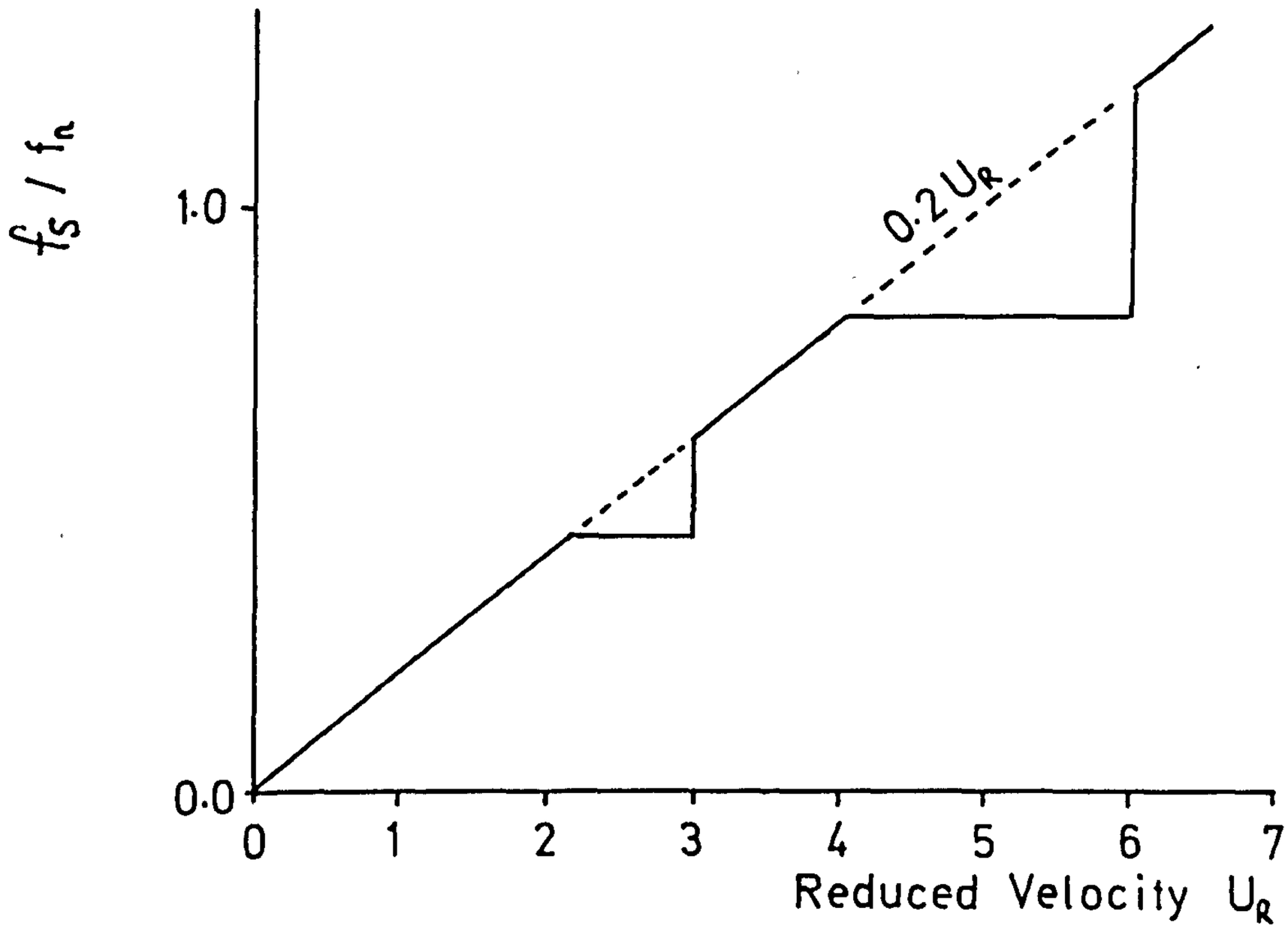

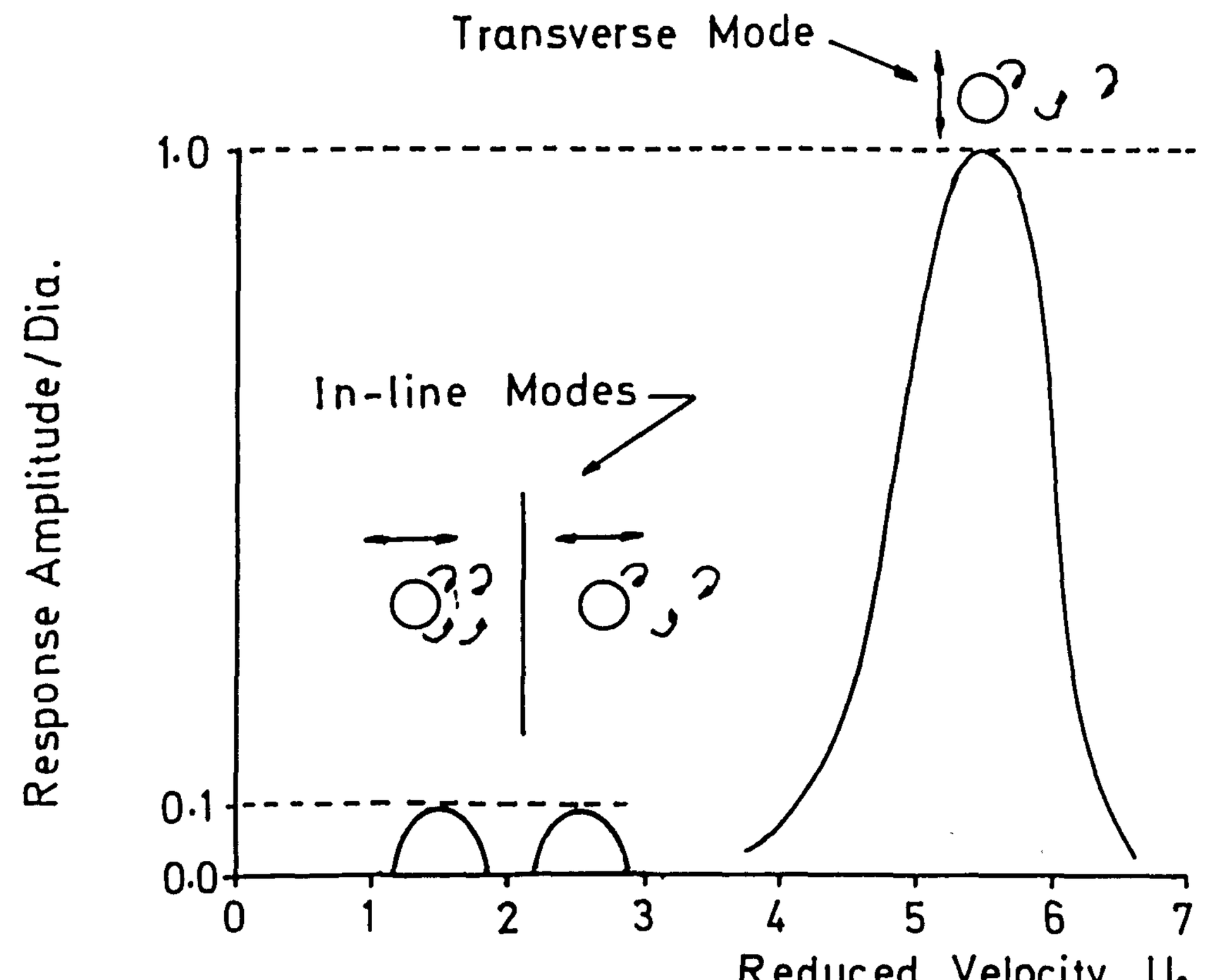

FIG 1.26 Locked-in Modes of Response - Qualative Comparison

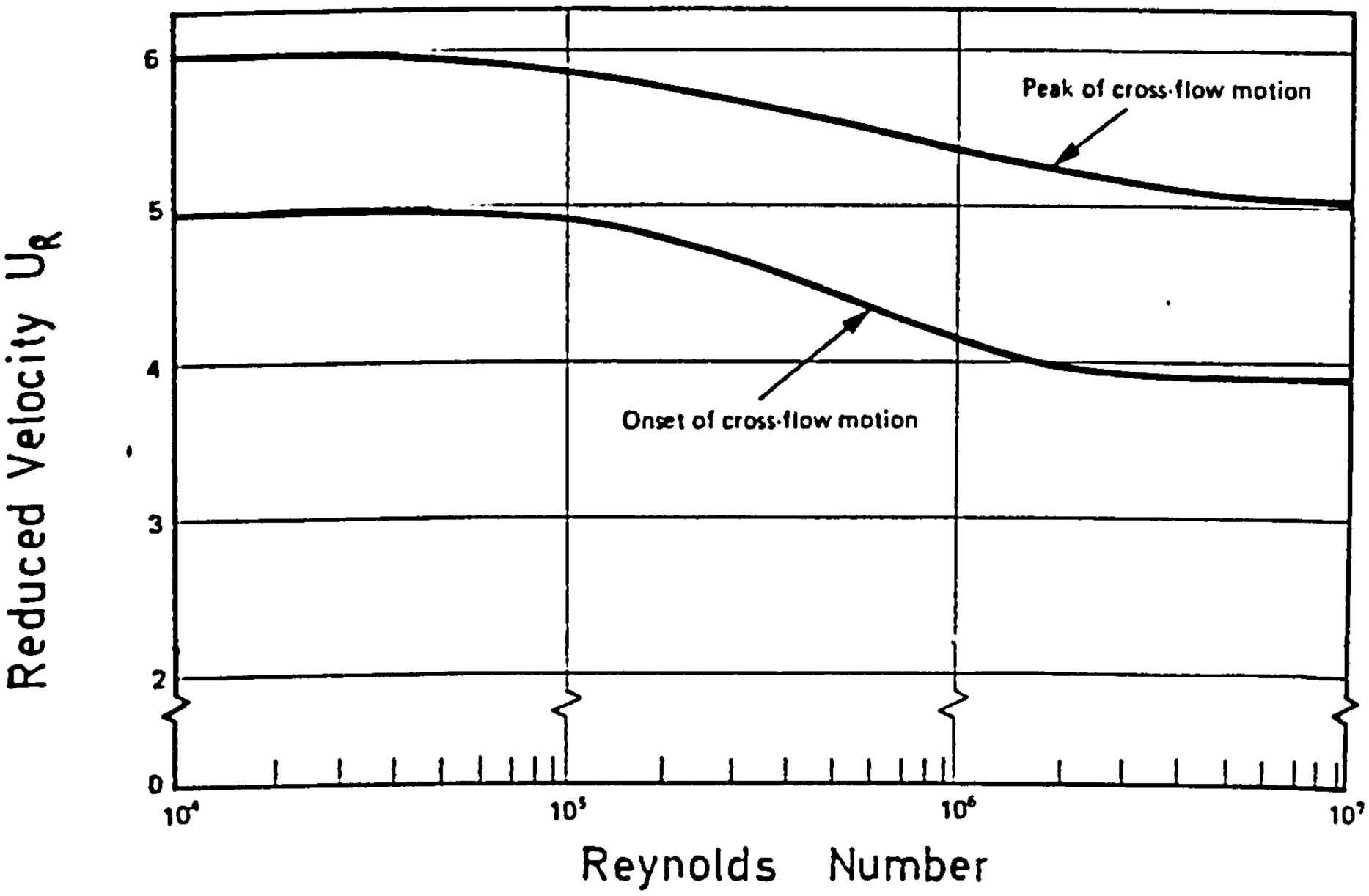

FIG 1.27 Flow Speeds for the Onset of Cross-flow Motion

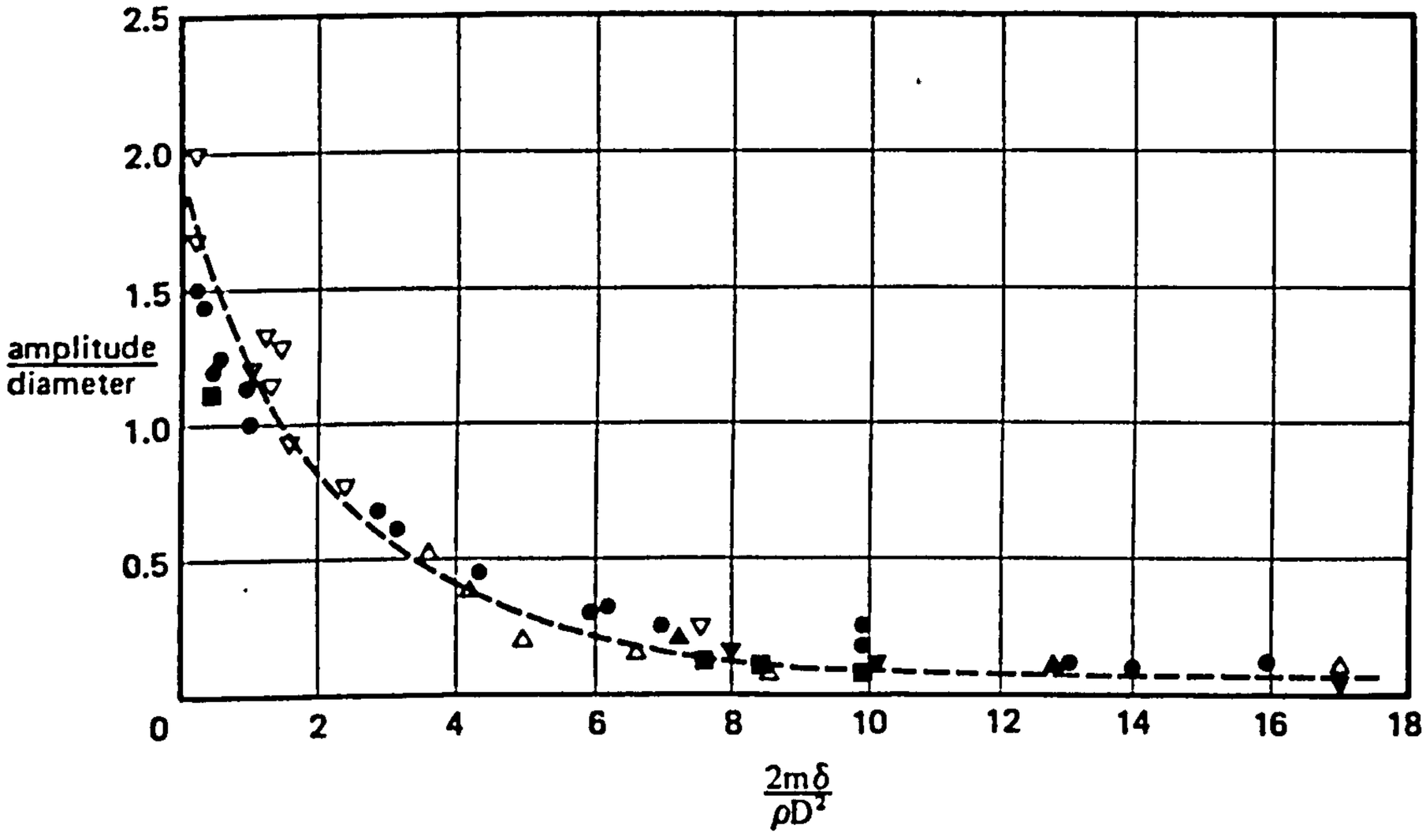

FIG 1.28 Amplitude of Cross-flow Motion versus Stability Parameter (King 1974)

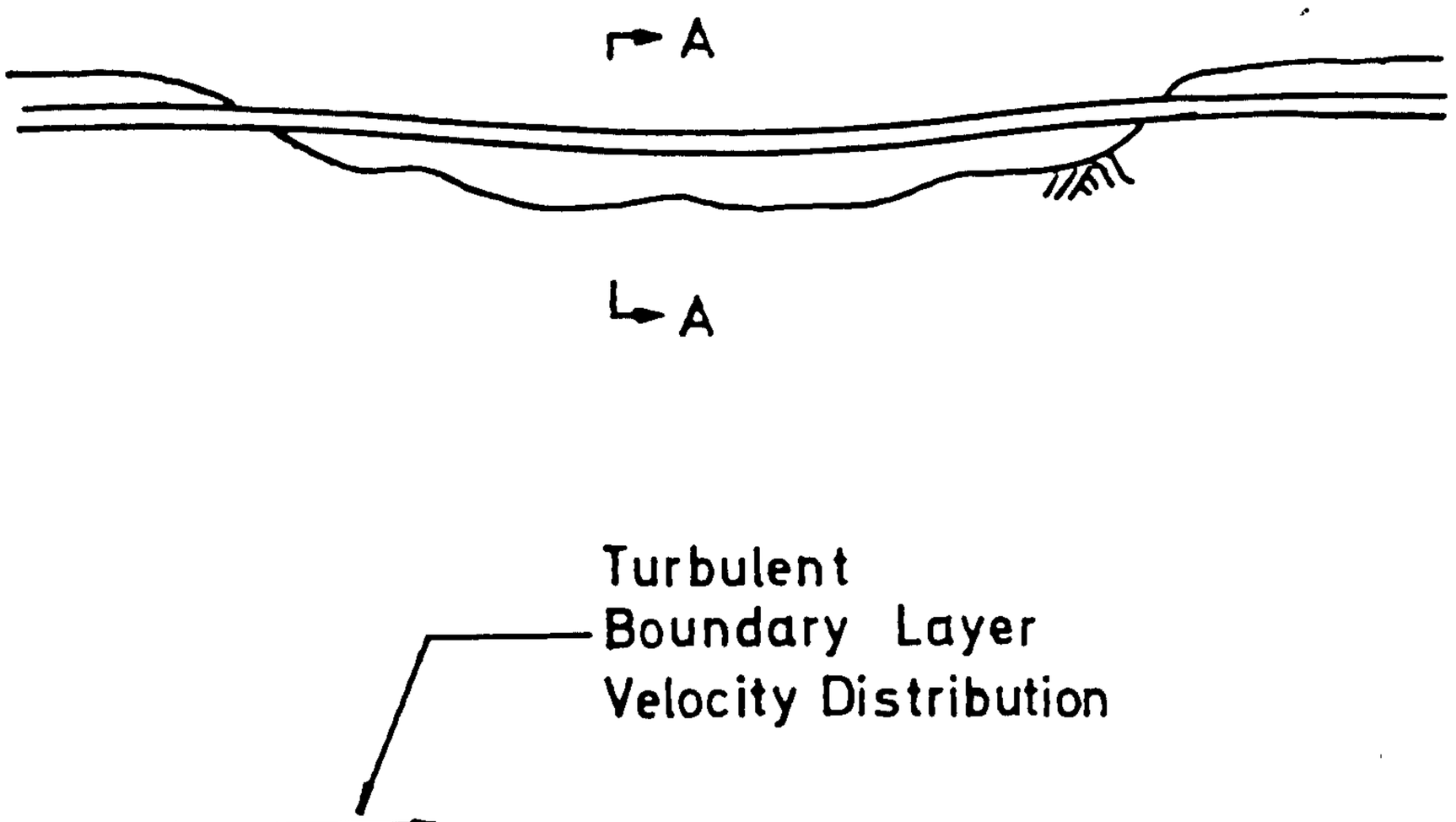

A - A

FIG 1.29 Typical Pipeline Span

CHAPTER 2

LINEAR BEAM COLUMN ON ELASTIC FOUNDATION

2.0 Introduction

As discussed in Chapter 1 the free vibration frequencies of an exposed pipeline span significantly affect the pipeline susceptibility and response to vortex induced vibrations. In turn the span frequencies depend on a large number of parameters many of which are known only within fairly broad limits. In addition, due to seabed scour or variable pipeline operating conditions, some of these parameters change with time while others vary from location to location along the pipeline route. Therefore in developing suitable analysis methods emphasis should be placed on evaluating the sensitivity of span frequencies to various parametric changes in order to assess the effect of such uncertainties and to afford a basic understanding of such a continuously evolving system.

With the above in mind a simple method is now developed for evaluating the frequencies of a pipeline span supported on either side by an infinite elastic foundation. Since an effective compression acts in many operating pipelines the model developed is also used to evaluate the linear elastic buckling load for the system.

2.0.1 Pipeline Free Span Parameters

The basic parameters affecting span behaviour may be conveniently classified into the following groups

a) Geometric parameters including span length L, end elevations δ_1 and δ_2 and nominal seabed slopes either side of the free span θ_1 and θ_2, figure 2.1.

b) Pipeline properties including steel pipe internal and external diameters D_i and D_o plus total external diameter resulting from any anti-corrosion, insulating and weight coatings, figure 2.2. Also included in this group are

Young's modules for steel	E
Poisson's ratio for steel	ν
Initial lay tension	T_L
Internal, external pressures	p_i, p_o
Temperature rise	ΔT
Pipeline effective weight	W

The pipeline effective weight per length W may be calculated using

$$W = W_s + W_p - W_w \qquad (2.1)$$

where W_s, W_p and W_w represent respectively the weights per length of steel pipe plus coatings, contained product (oil or gas) and displaced sea water.

c) Soil elastic foundation modulus k and coefficient of friction μ as described in section 2.0.2.

d) Amplitude of vibration q

Assumptions relating to these parameters are described in section 2.0.3.

2.0.2 Soil Properties

The selection of suitable parameters to represent the soil behaviour is an area of considerable complexity since in addition to any nonisotropic and nonhomogenous effects a full description of soil mechanics requires consideration of nonlinear and or viscous effects. Such complexities are considered outside the scope of this

work and instead the pipeline is assumed to rest on a continuous elastic foundation as traditionally used in beam on elastic foundation theory (Timoshenko and Gere, 1963). In this theory the lateral deflection v of any infinitesimal element of length dx along the pipe is assumed to be resisted by a reaction force

$$dF_v = kv\,dx \tag{2.2}$$

where k is the elastic foundation modulus. Clearly this assumption implies that the foundation transmits forces in the vertical direction only, a condition consistant with the assumption of zero shear strength in the soil. This assumption may be removed by using solutions in which the reaction force is no longer directly proportional to the deflection at a given location but instead is proportional to a function of the displacements near the given location. However, since the linearity of the soil is open to question, such additional complications are not considered justified here.

Considering now the evaluation of the elastic foundation modulus k the settlement under a foundation of width B resting on a semi-infinite elastic half space is (Winterkorn and Fang, 1975)

$$S = \frac{q_s B}{E_s}(1-\nu_s^2) I_s \tag{2.3}$$

where q_s is the soil contact pressure and E_s and ν_s are the elastic constants for the soil subgrade. The factor I_s represents a shape factor which for long slender structures such as a pipeline is normally taken as 2. The foundation modulus is consequently given by

$$k = \frac{E_s B}{S} = \frac{E_s}{2(1-\nu_s^2)} \qquad (2.4)$$

The following table shows some typical data as might be used in the analysis

Soil Type	E_s N/m^2	ν_s	k N/m^2
Soft Clay	0.9 x 10^6	.5	0.6 x 10^6
Sand	4.6 x 10^6	.3	2.5 x 10^6
Stiff Clay	16 x 10^6	.5	11 x 10^6
Very Stiff Clay	40 x 10^6	.5	27 x 10^6

Table 2.1 : Typical Soil Data

Considering next an axial deflection u applied to the element dx the resisting force due to friction between pipe and soil is assumed of the form

$$dF_u = \mu W dx \qquad (2.5)$$

where μ is the coefficient of friction. It should be noted that the use of W in the above is somewhat arbitrary since although it represents the nominal contact force per length for a surface resting pipe this is no longer true for the fully buried case. In this case the friction forces arise essentially from the internal pressure in the soil surrounding the pipe with the result that values of μ in excess of unity may be required in equation (2.5) above. This friction force is independent

of the deflection u and always acts so as to resist any pipe movement.

2.0.3 Basic Assumptions

Since the aim of this chapter is to develop a simple "initial look" model a number of simplifying assumptions must be made. Some, but not all, of these assumptions are relaxed in Chapter 3 by utilising a nonlinear Finite Element Model for the pipeline. For the moment however we proceed with the following assumptions

a) The pipeline section ℓ_∞ , figure 2.3, maintains full contact at all times with the elastic foundation. This assumption is clearly reasonable for a buried pipeline or surface resting pipe on soft soil. For hard clay or rocky seabeds the assumption is more difficult to justify and alternative rigid foundation models may be preferred.

b) The coefficient of friction μ between pipe and soil is taken as zero with the result that axial end deflections of the span may occur unresisted. Consequently the pipe tension is unaffected by any static or dynamic span displacements and instead remains constant.

c) The pipeline deflections are small. This assumption together with (b) above enables the differential equation of motion to be derived using elementary beam column theory. Since this theory is linear the initial displaced geometry of the pipeline span has no effect on stiffness and hence frequency. In this chapter, therefore, the end supports are taken as straight, horizontal and on the same level with the dynamic motion considered as occurring about an initial undisplaced configuration, figure 2.3. As a result of symmetry only one half of this system is modelled.

d) The pipeline mass per length ρ is constant

along all sections of the line.

e) The flexural and axial rigidities of the pipe are constant along its length and are calculated on the steel section only using

$$EI = \frac{E\pi}{64}\left(D_o^4 - D_i^4\right) \qquad (2.6a)$$

$$EA = \frac{E\pi}{4}\left(D_o^2 - D_i^2\right) \qquad (2.6b)$$

This assumption ignores the effects of concrete weight coating and field joints on pipeline strength.

It is noted that the pipeline mass per length over the free span may be calculated using

$$\rho = \rho_s + \rho_p + \rho_A \qquad (2.7)$$

where ρ_s , ρ_p and ρ_A are respectively the masses per length of steel pipe plus coatings, contained product and hydrodynamic added mass. This later quantity is given by

$$\rho_A = C_A \frac{\pi D^2}{4} \rho_w \qquad (2.8)$$

where ρ_w is the density of seawater and C_A is the added mass coefficient dependent on the bed gap to pipe diameter ratio G/D , figure 2.4. In addition over the supported sections the soil particles are required, at least in the full contact case, to follow the motion of the pipe giving rise to an added mass effect similar to equation (2.8) above. As a result of these considerations

the true mass distribution varies along the pipeline requiring the use of a representative value in the simple model of this chapter. One way of doing this is to use an effective mass per length given by

$$\rho_e = \frac{\int_0^\infty \rho(x)\,\phi^2(x)\,dx}{\int_0^\infty \phi^2(x)\,dx} \qquad (2.9)$$

where $\phi(x)$ is a mode shape and $\rho(x)$ the required non-constant mass distribution. By this means the kinetic energy of the system is correctly calculated for the selected mode although an iterative scheme is now required.

2.0.4 Effective Tension

It is noted in the previous section that the pipeline tension is assumed constant. However the appropriate tension (or compression) to use in the analysis differs from the initial lay tension T_L due to the combined effects of thermal expansion plus internal and external hydrostatic pressures. Considering first a temperature rise ΔT (assumed constant along both span and supports) the resulting axial strain for an unrestrained section of pipe is

$$\varepsilon_T = \alpha \Delta T \qquad (2.10)$$

where α is the coefficient of thermal expansion for steel pipe. Next assuming the internal pressure is zero at installation the effect of an operational internal pressure p_i is to generate an additional hoop stress in the steel pipe given by

$$\sigma_\theta = \frac{p_i D_i}{t} \qquad (2.11)$$

where $t = (D_o - D_i)/2$ equals the wall thickness. Thus ignoring any radial stress effects as small the corresponding axial strain for an unrestrained length of pipe is given by

$$\varepsilon_p = -\frac{\nu}{E}\sigma_\theta = -\frac{\nu p_i D_i}{2Et} \qquad (2.12)$$

Combining equations (2.10) and (2.12) the total axial strain due to operating conditions ΔT and p_i is

$$\varepsilon_u = \alpha \Delta T - \frac{\nu p_i D_i}{2Et} \qquad (2.13)$$

Note that the effect of external pressure is not included at this stage since it is assumed not to change between installation and normal operation. Now considering a long section of pipe, figure 2.5, it is clear that as the pipe ends move out due to the strain ε_u the motion is resisted by soil friction forces. As a result a compression force builds up until a point is reached at which no further relative displacement occurs between the pipe and its foundation. At this stage the pipe is fully constrained and the axial compression along the centre section is

$$P_c = EA\varepsilon_u = \alpha EA\Delta T - \frac{\nu A p_i D_i}{2t} \qquad (2.14)$$

In this thesis it is assumed that the free span under consideration is sufficiently removed from the end conditions to allow equation (2.14) to be used. The tension in the pipeline is therefore

$$T_R = T_L - P_e = T_L - \alpha E A \Delta T + \nu A p_i D_i / 2t \qquad (2.15)$$

Now considering the effect of the internal and external pressure forces on the curved sides of the displaced pipe, figure 2.6, the end pressure effect is

$$T_p = -\frac{\pi}{4}\left(p_i D_i^2 - p_o D_o^2\right) \qquad (2.16)$$

In evaluating pipe lateral deflections this tension force must be added into the real tension as given by equation (2.15) above. Thus combining equations (2.15) and (2.16) the effective tension is

$$T = T_R + T_p = T_L - \alpha E A \Delta T + \nu A p_i D_i / 2t - \frac{\pi}{4}\left(p_i D_i^2 - p_o D_o^2\right) \qquad (2.17)$$

Substituting for A using equation (2.6b) enables the 3rd term in the above to be written

$$\frac{\nu A p_i D_i}{2t} = \frac{\nu \pi p_i \left(D_i^2 + D_o D_i\right)}{4} \simeq \frac{\nu \pi p_i D_i^2}{2}$$

which on substituting back into equation (2.17) gives

$$T = T_L - \alpha E A \Delta T - \frac{\pi}{4}(1-2\nu)p_i D_i^2 + \frac{\pi}{4} p_o D_o^2$$

Finally taking ν = 0.3 for steel this becomes

$$T = T_L - \alpha E A \Delta T - \frac{\pi}{20}(2 p_i D_i^2 - 5 p_o D_o^2) \qquad (2.18)$$

In practice it is noted that although the pipe wall may be in tension the effect of high internal pressure often generates a net effective compression in the pipe. By reference to figure 2.6 it is noted that the addition of T_p, as given by equation (2.16), into the real tension T_R is consistant with the inclusion of W_p and W_w in the effective weight calculation given by equation (2.1).

2.1 Frequency Equations for Single Pipe Span

Using the above assumptions the differential equation of motion for undamped vibration is derived in Appendix A as

$$\rho \frac{\partial^2 v}{\partial t^2} + EI \frac{\partial^4 v}{\partial x^4} - T \frac{\partial^2 v}{\partial x^2} + kv = f(x,t) \qquad (2.19)$$

For free vibration in a single node we now set $f(x,t) = 0$ and

$$v(x,t) = \begin{cases} \phi_1(x_1) \sin \omega t, & \text{Section } AB \\ \phi_2(x_2) \sin \omega t, & \text{Section } B\infty \end{cases}$$

where $\phi_1(x_1)$ and $\phi_2(x_2)$ represent the required mode shape and ω the corresponding frequency. Thus since k is taken as zero over the free span AB the required equation of motion over sections AB and $B\infty$ are respectively

$$\frac{\partial^4\phi_1}{\partial x_1^4} - 4\gamma^2\frac{\partial^2\phi_1}{\partial x_1^2} - 4\beta_1^4\phi_1 = 0 \qquad (2.20a)$$

$$\frac{\partial^4\phi_2}{\partial x_2^4} - 4\gamma^2\frac{\partial^2\phi_2}{\partial x_2^2} + 4\beta_2^4\phi_2 = 0 \qquad (2.20b)$$

where γ^2, β_1^4 and β_2^4 are given by

$$\gamma^2 = T/4EI \qquad (2.21a)$$

$$\beta_1^4 = \rho\omega^2/4EI \qquad (2.21b)$$

$$\beta_2^4 = (k-\rho\omega^2)/4EI \qquad (2.21c)$$

The general solutions corresponding to equations (2.20) are now obtained separately in the following sections.

2.1.1 General Solution for Section AB

Considering first equation (2.20a) and substituting $\phi_1 = \exp(\beta x_1)$ we find

$$\beta^4 - 4\gamma^2\beta^2 - 4\beta_1^4 = 0 \qquad (2.22)$$

The roots to this characteristic equation are given by

$$\beta^2 = 2\gamma^2 \pm 2\left[\gamma^4 + \beta_1^4\right]^{1/2} \tag{2.23}$$

Thus since $\gamma^4 > 0$ and $\beta_1^4 > 0$ the mode shape ϕ_1 in the free span is

$$\phi_1 = \bar{A}\cosh\lambda_1 x_1 + \bar{B}\sinh\lambda_1 x_1 + \bar{C}\cos\mu_1 x_1 + \bar{D}\sin\mu_1 x_1 \tag{2.24a}$$

where $\bar{A}$, $\bar{B}$, $\bar{C}$ and $\bar{D}$ are arbitrary constants and

$$\lambda_1 = \left(2\left[\gamma^4 + \beta_1^4\right]^{1/2} + 2\gamma^2\right)^{1/2} \tag{2.24b}$$

$$\mu_1 = \left(2\left[\gamma^4 + \beta_1^4\right]^{1/2} - 2\gamma^2\right)^{1/2} \tag{2.24c}$$

For symmetric modes the boundary conditions at the span centre require zero slope and shear which in view of equation (A2)gives

$$\left.\frac{\partial \phi_1}{\partial x_1}\right|_{x_1=0} = \left.\frac{\partial^3 \phi_1}{\partial x_1^3}\right|_{x_1=0} = 0$$

Thus $\bar{B} = \bar{D} = 0$ and equation (2.5a) may be written

$$\phi_1 = A_1 \cosh\lambda_1 x_1 + B_1 \cos\mu_1 x_1 \tag{2.25}$$

For antisymmetric modes the boundary conditions are

$$\phi_1(0) = \left.\frac{\partial^2 \phi_1}{\partial x_1^2}\right|_{x_1=0} = 0$$

with corresponding general solution

$$\phi_1 = A_1 \sinh \lambda_1 x_1 + B_1 \sin \mu_1 x_1 \qquad (2.26)$$

2.1.2 General Solution for Section $\beta\infty$

Considering next equation (2.20b) the associated characteristic equation is

$$\beta^4 - 4\gamma^2\beta^2 + 4\beta_2^4 = 0 \qquad (2.27)$$

with roots given by

$$\beta^2 = 2\gamma^2 \pm 2\left[\gamma^4 - \beta_2^4\right]^{1/2} \qquad (2.28)$$

Mathematically three cases must now be considered namely $\gamma^4 < \beta_2^4$, $\gamma^4 = \beta_2^4$ and $\gamma^4 > \beta_2^4$. Each of these is now considered separately:

a) $\gamma^4 < \beta_2^4$

Using equations (2.21) this condition may be written as

$$\omega^2 < k/\ell - T^2/4EI\ell \qquad (2.29)$$

It follows that since $\omega^2 > 0$ this situation can occur only if as a necessary condition

$$T < 2\sqrt{kEI} \qquad (2.30)$$

Assuming these conditions are satisfied the roots of equation (2.27) may be written

$$\beta_1 = \lambda_2 + i\mu_2 \tag{2.31a}$$

$$\beta_2 = -\lambda_2 - i\mu_2 \tag{2.31b}$$

$$\beta_3 = \lambda_2 - i\mu_2 \tag{2.31c}$$

$$\beta_4 = -\lambda_2 + i\mu_2 \tag{2.31d}$$

where $i = \sqrt{-1}$ and the real constants λ_2 and μ_2 are given by

$$\lambda_2 = \left[\beta_2^2 + \gamma^2\right]^{1/2} \tag{2.32a}$$

$$\mu_2 = \left[\beta_2^2 - \gamma^2\right]^{1/2} \tag{2.32b}$$

Thus since we require a finite solution as x_2 tends to infinity the general solution for section $\delta\omega$ becomes

$$\phi_2 = e^{-\lambda_2 x_2}\left(A_2 \cos\mu_2 x_2 + B_2 \sin\mu_2 x_2\right) \tag{2.33}$$

where A_2 and B_2 are arbitrary constants.

b) $\underline{\gamma^4 = \beta_2^4}$

In a similar manner to the above this condition may be written

$$\omega^2 = k/\rho - T^2/4EI\rho \tag{2.34}$$

Under this rather special condition the roots of the characteristic equation (2.27) occur as repeated real roots given by

$$\beta_1 = \beta_3 = \lambda_2 \tag{2.35a}$$

$$\beta_2 = \beta_4 = -\lambda_2 \tag{2.35b}$$

where here the real constant λ_2 is given by

$$\lambda_2 = \sqrt{2}\ \gamma \tag{2.36}$$

Thus discarding the positive roots as in the above section the general solution becomes

$$\phi_2 = e^{-\lambda_2 x_2}(H_2 + \delta_2 x/L) \tag{2.37}$$

Note that the factor L^{-1} is included in the second term in order that the arbitrary constant δ_2 has dimension of length.

c) $\gamma^4 > \beta_2^4$

This final case requires

$$\omega^2 > k/\ell - T^2/4EI\ell \tag{2.38}$$

If this condition is satisfied and in addition $\beta_2^4 > 0$ the roots of equation (2.27) become

$$\beta_1 = -\beta_2 = \lambda_2 \tag{2.39a}$$

$$\beta_3 = -\beta_4 = \mu_2 \tag{2.39b}$$

where the real constants λ_2 and μ_2 are now given by

$$\lambda_2 = (2r^2 + 2[r^4 - \beta_2^4]^{1/2})^{1/2} \qquad (2.40a)$$

$$\mu_2 = (2r^2 - 2[r^4 - \beta_2^4]^{1/2})^{1/2} \qquad (2.40b)$$

Thus discarding the positive roots the general solution becomes

$$\phi_2 = A_2 e^{-\lambda_2 x_2} + B_2 e^{-\mu_2 x_2} \qquad (2.41)$$

It is noted that the assumed condition $\beta_2^4 > 0$ used in deriving this equation may using equation (2.21c) be written as

$$\omega^2 < \omega_{RB}^2 \qquad (2.42)$$

where $\omega_{RB} = \sqrt{k/\ell}$ represents the rigid body frequency for an infinite pipe on a continuous foundation. For $\omega^2 > \omega_{RB}^2$ the term μ_2 defined by equation (2.40b) above becomes imaginary and the form of the solution again changes. However since in all practical cases this limiting frequency is extremely high such cases are not considered in this thesis. Combining equations (2.38) and (2.42) the general solution given by equation (2.41) above is valid for all frequencies in the range

$$k/\ell - T^2/4EI\ell < \omega^2 < k/\ell \qquad (2.43)$$

2.1.3 Compatibility Conditions

The general solutions ϕ_1 and ϕ_2 obtained above are required to satisfy the conditions of compatibility at

the common point B. In terms of beam-column theory this requires continuity of displacement, slope, bending moment and shear force. It is shown in Appendix A that the moment and shear force are given in terms of the pipe deflections as

$$M = EI \frac{\partial^2 v}{\partial x^2} \tag{2.44a}$$

$$S = T \frac{\partial v}{\partial x} - EI \frac{\partial^3 v}{\partial x^3} \tag{2.44b}$$

It follows that since the quantities T and EI are assumed constant along the pipe the required conditions may be written as

$$\phi_1^{(n)}(x_1 = L/2) = \phi_2^{(n)}(x_2 = 0) \tag{2.45}$$

where the superscript n = 0 - 3 denotes the order of differentiation. Using equations (2.25) and (2.33) for the case of a symmetric mode with $\omega^2 < k/\ell - T^2/4EI\ell$ these conditions give

$$[F_1]\underline{A} = 0 \tag{2.46}$$

where $\underline{A}^T = (A_1\ B_1\ A_2\ B_2)$ is a vector of arbitrary constants and

$$F_1 = \begin{bmatrix} \cosh P_1 & \cos Q_1 & -1 & 0 \\ P_1 \sinh P_1 & -Q_1 \sin Q_1 & P_2 & -Q_2 \\ P_1^2 \cosh P_1 & -Q_1^2 \cos Q_1 & (Q_2^2 - P_2^2) & 2P_2Q_2 \\ P_1^3 \sinh P_1 & Q_1^3 \sin Q_1 & (P_2^3 - 3P_2Q_2^2) & (Q_2^3 - 3P_2^2Q_2) \end{bmatrix} \tag{2.47}$$

Here the nondimensional quantities P_i and Q_i are obtained using equations (2.24) and (2.32) as

$$P_1 = \lambda_1 L/2 = (2[\chi^4 + \beta_1^4]^{1/2} + 2\chi^2)^{1/2}(L/2) \qquad (2.48a)$$

$$Q_1 = \mu_1 L/2 = (2[\chi^4 + \beta_1^4]^{1/2} - 2\chi^2)^{1/2}(L/2) \qquad (2.48b)$$

$$P_2 = \lambda_2 L/2 = (\beta_1^2 + \chi^2)^{1/2}(L/2) \qquad (2.48c)$$

$$Q_2 = \mu_2 L/2 = (\beta_2^2 - \chi^2)^{1/2}(L/2) \qquad (2.48d)$$

It is clear that similar equations can be obtained by using different forms of the general solutions in sections AB and $B\infty$. This leads to six cases as summarised in the following table

CASE NO	SOLUTION FOR AB		SOLUTION FOR B∞		FREQUENCY CONSTRAINT
	FORM	EQ.NO.	FORM	EQ.NO.	
1	Sym	2.25	A	2.33	$\omega^2 < \omega_c^2$
2	Sym	2.25	B	2.37	$\omega^2 = \omega_c^2$
3	Sym	2.25	C	2.41	$\omega_c^2 < \omega^2 < \omega_{RB}^2$
4	Anti-Sym	2.26	A	2.33	$\omega^2 < \omega_c^2$
5	Anti-Sym	2.26	B	2.37	$\omega^2 = \omega_c^2$
6	Anti-Sym	2.26	C	2.41	$\omega_c^2 < \omega^2 < \omega_{RB}^2$

TABLE 2.2 : Possible Solution Cases

The quantity ω_c appearing in the above table is defined as

$$\omega_c^2 = k/\ell - T^2/4EI\ell \qquad (2.49)$$

and is noted to play a role analogous to critical damping for a SDOF mass spring dashpot system. Thus for modes such that $\omega^2 < \omega_c^2$ the mode shape over the section $\ell \infty$, equation (2.33), oscillates about zero as we move along the x_2 axis. On the other hand for $\omega^2 \gg \omega_c^2$ the mode shape, as represented by equations (2.37) and (2.41), decays to zero in a nonoscillatory manner. The matrices F_1 through F_6 corresponding to each of the cases in the above table are tabulated in Appendix B.

2.1.4 Frequency Equations

Considering again case 1 the corresponding frequency equation is obtained from the condition that for non-trivial $\underset{\sim}{A}$, equation (2.46) requires the determinant of F_1 to be zero. Thus in view of equations (2.47) and (2.48) and noting equations (2.21) we may write

$$Det(F_1) = f_1(\omega, \rho, EI, T, k, L) = 0 \qquad \omega^2 < \omega_c^2 \qquad (2.50)$$

Combining this equation with those for cases 2 and 5 (see Appendix B for details) enables the complete frequency equation for symmetric modes to be written as

$$f_s(\omega, \rho, EI, T, k, L) = 0 \qquad (2.51a)$$

where f_s is defined by

$$f_S = \begin{cases} f_1(\omega, \rho, EI, T, k, L) & , \quad \omega^2 < \omega_c^2 \\ f_2(\omega, \rho, EI, T, k, L) & , \quad \omega^2 = \omega_c^2 \\ f_3(\omega, \rho, EI, T, k, L) & , \quad \omega_c^2 < \omega^2 < \omega_{RB}^2 \end{cases} \tag{2.51b}$$

and $f_i = Def(F_i)$. Similarly for the antisymmetric modes

$$f_A(\omega, \rho, EI, T, k, L) = 0 \tag{2.52a}$$

$$f_A = \begin{cases} f_4(\omega, \rho, EI, T, k, L) & , \quad \omega^2 < \omega_c^2 \\ f_5(\omega, \rho, EI, T, k, L) & , \quad \omega^2 = \omega_c^2 \\ f_6(\omega, \rho, EI, T, k, L) & , \quad \omega_c^2 < \omega^2 < \omega_{RB}^2 \end{cases} \tag{2.52b}$$

2.2 Nondimensional Analysis

In order to decrease the number of independent parameters occurring in the above analysis it is convenient at this stage to nondimensionalise the equations. By this means it will be found possible to present the results in a compact form in terms of a small number of independent nondimensional parameters. To do this consider first the fundamental frequency of an untensioned beam of length L given by

$$\bar{\omega} = a\sqrt{EI/\rho L^4} \tag{2.53}$$

where for clamped-clamped end conditions $a = 22.37$. Using this result the mass per length ρ of the pipeline may be written as

$$\rho = \frac{a^2 EI}{\bar{\omega}^2 L^4} \tag{2.54}$$

Substituting this result into equations (2.48) and rearranging gives

$$P_1 = \tfrac{1}{2}\left(\left[a^2R^2 + \delta^2/4\right]^{1/2} + \delta/2\right)^{1/2} \tag{2.55a}$$

$$Q_1 = \tfrac{1}{2}\left(\left[a^2R^2 + \delta^2/4\right]^{1/2} - \delta/2\right)^{1/2} \tag{2.55b}$$

$$P_2 = \tfrac{1}{2}\left(\tfrac{1}{2}\left[\gamma - a^2R^2\right]^{1/2} + \delta/4\right)^{1/2} \tag{2.55c}$$

$$Q_2 = \tfrac{1}{2}\left(\tfrac{1}{2}\left[\gamma - a^2R^2\right]^{1/2} - \delta/4\right)^{1/2} \tag{2.55d}$$

where the non-dimensional frequency ratio R is given by

$$R = \frac{\omega}{\bar{\omega}} \tag{2.56a}$$

and the independent parameters γ and δ are defined as

$$\gamma = \frac{kL^4}{EI} \tag{2.56b}$$

$$\delta = \frac{TL^2}{EI} \tag{2.56c}$$

Thus in view of equations (2.55) above the frequency

equation (2.50) may be considered in the form

$$f_1(R, \gamma, \delta) = 0 \tag{2.57}$$

This equation may be solved for R subject to the condition (2.29) which using equation (2.54) above may be written as

$$R^2 < [\gamma - \delta^2/4]/a^2 \tag{2.58}$$

Repeating this process for the other 5 cases enables the non-dimensional frequency equations for symmetric and anti-symmetric modes to be written respectively as

$$f_S(R, \gamma, \delta) = 0 \tag{2.59}$$

$$f_A(R, \gamma, \delta) = 0 \tag{2.60}$$

where the functions f_S and f_A now have the form

$$f_S = \begin{cases} f_1(R, \gamma, \delta), & R^2 < R_c^2 \\ f_2(R, \delta), & R^2 = R_c^2 \\ f_3(R, \gamma, \delta), & R_c^2 < R^2 < R_{RB}^2 \end{cases} \tag{2.61}$$

$$f_A = \begin{cases} f_4(R, \gamma, \delta), & R^2 < R_c^2 \\ f_5(R, \delta), & R^2 = R_c^2 \\ f_6(R, \gamma, \delta), & R_c^2 < R^2 < R_{RB}^2 \end{cases} \tag{2.62}$$

and the non-dimensional frequencies R_c and R_{RB} are given by

$$\ell_c^2 = (\gamma - \delta^2/4)/a^2 \qquad (2.63\,a)$$

$$\ell_{RB}^2 = \gamma/a^2 \qquad (2.63b)$$

In section 2.4 these equations are solved numerically for the first four modes (two symmetric plus two antisymmetric) occurring in the pipeline span.

2.3 Effect of compression

In developing the above theory the pipeline has been assumed under a constant non-zero tension T . For the case of zero tension equation (2.19) takes the form

$$\rho\frac{\partial^2 v}{\partial t^2} + EI\frac{\partial^4 v}{\partial x^4} + kv = f(x,t) \qquad (2.64)$$

whereas for a compressive load P the equation becomes

$$\rho\frac{\partial^2 v}{\partial t^2} + EI\frac{\partial^4 v}{\partial x^4} + P\frac{\partial^2 v}{\partial x^2} + kv = f(x,t) \qquad (2.65)$$

Solving these equations as above and examining the solutions now shows that for $\ell^2 < \ell_c^2$ the new solutions may be obtained from the tension case by simply substituting $T=0$ or $T=-P$ respectively. On the other hand for $\ell^2 > \ell_c^2$ the above equations do not yield any solutions which tend to zero as $x_2 \to \infty$ and instead the calculated mode shapes extend to infinity along the supported sections of the pipeline. Since this situation is closely related to the buckling behaviour of the span the linear elastic buckling loads are calculated in the following sections.

2.3.1 Buckling Loads for Single Pipe Span

From a practical point of view the effect of increased compression in the pipeline is to lower the generalised stiffness and hence natural frequency of the free span. By this means a critical end load P_{cr} is reached under which the system has zero lateral stiffness and may consequently develop unstable lateral deflections under zero lateral load. To determine the value of this critical end load consider the static case corresponding to equation (2.65) above

$$EI\frac{\partial^4 v}{\partial x^4} + P\frac{\partial^2 v}{\partial x^2} + kv = f(x) \qquad (2.66)$$

We now seek to determine the axial load P under which a non-trivial buckled shape of equilibrium is possible for zero lateral load. Thus setting $f(x) = 0$ and noting that $k = 0$ over the free span the governing equations over sections AB and $B\infty$ are respectively

$$\frac{\partial^4 v_1}{\partial x_1^4} + 4\gamma_p^2\frac{\partial^2 v_1}{\partial x_1^2} = 0 \qquad (2.67a)$$

$$\frac{\partial^4 v_2}{\partial x_2^4} + 4\gamma_p^2\frac{\partial^2 v_2}{\partial x_2^2} + 4\beta^4 v_2 = 0 \qquad (2.67b)$$

where γ_p and β are given by

$$\gamma_p^2 = P/4EI \qquad (2.68a)$$

$$\beta^4 = k/4EI \qquad (2.68b)$$

The general solutions corresponding to these equations are now obtained separately in the following sections.

2.3.2 General Solution for Section AB

Considering first equation (2.67a) and substituting $v_1 = \exp(\beta x_1)$ we find

$$\beta^2(\beta^2 + 4\gamma_\rho^2) = 0 \qquad (2.69)$$

The corresponding general solution is thus

$$v_1 = \bar{A}\cos\lambda_1 x_1 + \bar{B}\sin\lambda_1 x_1 + \bar{C} + \bar{D}x_1 \qquad (2.70a)$$

where $\bar{A}, \bar{B}, \bar{C}$ and $\bar{D}$ are arbitrary constants and

$$\lambda_1 = 2\gamma_\rho \qquad (2.70b)$$

For a symmetric mode shape the boundary conditions $v_1'(0) = v_1'''(0) = 0$ require $\bar{B} = \bar{D} = 0$ so that equation (2.70a) may be written as

$$v_1 = A_1\cos\lambda_1 x_1 + B_1 \qquad (2.71)$$

2.3.3 General Solution for Section Bꝏ

Considering next equation (2.67b) the associated characteristic equation is

$$\beta^4 + 4\gamma_\rho^2\beta^2 + 4\beta^4 = 0 \qquad (2.72)$$

with roots given by

$$\beta^2 = -2\gamma_\rho \pm 2\left[\gamma_\rho^4 - \beta^4\right]^{1/2} \qquad (2.73)$$

As in the frequency analysis three cases are now mathematically possible namely $\gamma_\rho^4 < \beta^4$, $\gamma_\rho^4 = \beta^4$ and $\gamma_\rho^4 > \beta^4$. Using equations (2.68) the first of these conditions may

be written as

$$P < 2\sqrt{kEI} \tag{2.74}$$

Now considering the case $L = 0$, the free span AB disappears and the pipe becomes continuously supported along its complete length. In this case the critical load is given by (Timoshenko and Gere, 1963)

$$\bar{P}_{CR} = 2\sqrt{kEI} \tag{2.75}$$

Thus since for the case $L > 0$ the critical load P_{CR} is lower than $\bar{P}_{CR}$ it is clear that at $P = P_{CR}$ condition (2.74) above is satisfied. It follows that only the first of the above three cases need be considered and the roots of equation (2.72) become

$$\beta_1 = -\beta_2 = \lambda_2 + i\mu_2 \tag{2.76a}$$

$$\beta_3 = -\beta_4 = \lambda_2 - i\mu_2 \tag{2.76b}$$

where

$$\lambda_2 = (\beta^2 - \gamma_p^2)^{1/2} \tag{2.77a}$$

$$\mu_2 = (\beta^2 + \gamma_p^2)^{1/2} \tag{2.77b}$$

Thus for a finite solution as $x_2 \to \infty$ we find

$$v_2 = e^{-\lambda_2 x_2}(A_2 \cos\mu_2 x_2 + B_2 \sin\mu_2 x_2) \tag{2.78}$$

2.3.4 Compatibility Conditions

As for the frequency analysis the compatibility conditions at B require that the two solutions, together

with their derivatives up to 3rd order, are continuous. Thus using equations (2.71) and (2.78) we find

$$\left[B\right] \underset{\sim}{A} = 0 \qquad (2.79)$$

where $\underset{\sim}{A}^T = (A_1, B_1, A_2, B_2)$ and the matrix B is

$$B = \begin{bmatrix} \cos P_1 & 1 & -1 & 0 \\ -P_1 \sin P_1 & 0 & P_2 & -Q_2 \\ -P_1^2 \cos P_1 & 0 & (Q_2^2 - P_2^2) & 2P_2Q_2 \\ P_1^3 \sin P_1 & 0 & (P_2^3 - 3P_2Q_2^2) & (Q_2^3 - P_2^2Q_2) \end{bmatrix}$$

.... (2.80)

Here the nondimensional quantities P_i and Q_i are obtained using equations (2.70b) and (2.77) as

$$P_1 = \lambda_1 L/2 = \gamma_p L \qquad (2.81a)$$

$$P_2 = \lambda_2 L/2 = \frac{1}{2}(\beta^2 - \gamma_p^2)^{1/2} L \qquad (2.81b)$$

$$Q_2 = \mu_2 L/2 = \frac{1}{2}(\beta^2 + \gamma_p^2)^{1/2} L \qquad (2.81c)$$

It follows that for non-trivial $\underset{\sim}{A}$ the determinant of the matrix B must be zero. Thus in view of equations (2.80) and (2.81) and noting equations (2.68) we may write

$$Det(B) = b(P, EI, k, L) = 0 \qquad (2.82)$$

This equation may now be solved for the first positive root $p = p_{cr}$ once the other parameters have been specified. Before doing this however it is again convenient to reduce the number of independent parameters by nondimensionalising the equations. Thus substituting equations(2.68) into (2.81) we may write

$$p_1 = \tfrac{1}{2}\delta_p^{1/2} \tag{2.83a}$$

$$p_2 = \tfrac{1}{2}\left(\tfrac{1}{2}\gamma^{1/2} - \tfrac{1}{4}\delta_p\right)^{1/2} \tag{2.83b}$$

$$q_2 = \tfrac{1}{2}\left(\tfrac{1}{2}\gamma^{1/2} + \tfrac{1}{4}\delta_p\right)^{1/2} \tag{2.83c}$$

where the independent parameters δ_p and γ are

$$\delta_p = \frac{pL^2}{EI} \tag{2.84a}$$

$$\gamma = \frac{kL^4}{EI} \tag{2.84b}$$

As a consequence equation (2.82) may be considered in the simplified form

$$b(\delta_p, \gamma) = 0 \tag{2.85}$$

Solving this equation for $\delta_p = \delta_{p_{cr}}$ now enables the critical load for the pipe span to be calculated using

$$p_{cr} = \frac{EI}{L^2}\,\delta_{p_{cr}} \tag{2.86}$$

2.4 Results and Discussion

In this thesis the nondimensional frequency equations (2.59) and (2.60) together with the buckling equation (2.85) are solved numerically using a simple bisection or false position method. In practice this process proves straight forward enough for the buckling equation but requires some care in respect of the two frequency equations. Some observations obtained as a result of practical experience in solving these later equations are included in Appendix B.

Considering first linear elastic buckling the results obtained by solving equation (2.85) for a range of γ are shown in figure 2.7. It is noted that for $\gamma > 10^5$ the critical buckling load is within 10% of that for an equivalent built in beam as given by

$$P_{cr} = 4\pi^2 \frac{EI}{L^2} \qquad (2.87)$$

Now considering equation (2.56b) it is seen that such large values of γ are obtained by either or both of the following

a) Increasing the soil modulus k thereby increasing the end stiffness seen by the free span.
b) Increasing the span length L or decreasing EI thereby decreasing the span effective stiffness.

Clearly under such conditions the effective end stiffness provided by the soil foundation is large compared to the stiffness of the free span and the assumption of built in end conditions may be used. At the other extreme small values of γ are obtained as either the soil modulus and/or the span length are decreased, or the pipe rigidity EI is increased. Under these conditions the critical buckling load

assumes the same order of magnitude as that given by equation (2.75) for a zero length span.

In considering the applicability of the above results it must be re-emphasised that they apply to the idealised case of zero friction between pipe and soil. As noted in section 2.0.3 this implies zero axial restraint at the span ends resulting in the compression load P remaining constant and independent of any pipe deflections. For the more realistic case of non-zero friction it is shown in Chapter 3 that pipeline deflections in the free span induce a corresponding sag tension which acts to stabilise the system.

Next figures 2.9 to 2.15 show the nondimensional frequency ratios corresponding to each of the first four modes of the system. Considering first figure 2.9 for the fundamental frequency R_1 under tension, it is seen that the general trend of these results are similar to those observed for the buckling loads. Thus for $\gamma > 10^7$ the observed frequencies are within 10% of those for an equivalent beam with built in end conditions as shown for the zero tension case by the dotted line $R_1 = 1$. In addition considering again figure 2.7 it is seen that for such large values of γ the generalised stiffnesses due to bending and tension are approximately equal when $\delta = 4\pi^2$. This suggests that for large γ the dependency of frequency on δ may be approximated by

$$R_1 \propto (1 + \delta/40)^{1/2} \qquad (2.88)$$

For example taking $\delta = 0$ and 200 this equation indicates that the corresponding frequencies differ by a factor of $\sqrt{5}$, a figure which agrees well with the exact results shown in figure 2.8. Now from an engineering point of view the main areas of uncertainty associated with the

problem as formulated are the soil stiffness k and line tension T . As a result of the above discussion it is seen that for large γ the influence of k on frequency is small whereas in view of equation (2.88) the influence of tension is large.

Considering next the effect of decreasing γ , the frequency ratio ρ_1 decreases slowly at first but then more rapidly below $\gamma = 10^4$. At this stage the general form of the solution over the supported section $\beta\alpha$ changes from form A through form B into form C. Here solutions forms A, B and C refer to equations (2.33), (2.37) and (2.41) as indicated in table 2.2. In addition the dependency of frequency on δ becomes markedly reduced while due to the steepness of the curves the influence of γ becomes more important. The roles of these parameters are consequently reversed from those indicated in the preceding paragraph. Extending these results into negative values of δ (i.e. compression) gives the series of curves shown in figure 2.9. These results are similar to the tension case except that now only form A solutions are considered. It is noted that the fall off in ρ_1 with decreasing γ and δ now eventually leads to the condition of "infinite" modes as the span approaches its buckling load.

The curves for ρ_2 , ρ_3 and ρ_4 are shown in figures 2.10 to 2.15. These results show similar characteristics to those discussed above for the fundamental frequency ρ_1 .

2.5 Uncoupling of Adjacent Spans

The analysis so far has concentrated on a single span problem but extension to the multi-span case are readily made. Georgiou (1983) has studied the two span problem shown in figure 2.16 for the case of zero tension. In this case the frequency ratio R defined by

$$\rho = \frac{\omega}{\bar{\omega}} = \frac{\omega}{a}\sqrt{\frac{\rho L_1^4}{EI}} \qquad (2.89)$$

is evaluated in terms of the following nondimensional parameters

$$\gamma = KL_1^4/EI \qquad (2.90a)$$

$$\alpha = L_2/L_1 \qquad (2.90b)$$

$$\varepsilon = L_3/L_1 \qquad (2.90c)$$

An important question associated with such a system is under what conditions are the two spans uncoupled enabling the single span results of this chapter to be used. In this section a simple approximate criteria for answering this question is determined and found to compare well with Georgiou's results.

2.5.1 Damping Length

Consider again the single span problem, figure 2.3. Under the condition $\omega^2 < \omega_c^2$ (the normal case) the general solution over the supported section $\beta\infty$ is given by equation (2.33) as

$$\phi_2 = e^{-\lambda_2 x_2}(A_2 \cos\mu_2 x_2 + B_2 \sin\mu_2 x_2) \qquad (2.91)$$

Considering the general form of this solution we now define a damping length L_D in the supported section using

$$\lambda_2 L_D = \pi \qquad (2.92)$$

where it is noted that $e^{-\pi} \approx 0.04$. Using equations (2.21)

and (2.32) this gives

$$L_D = \frac{2\pi}{\left(2\left[\frac{k-\rho\omega^2}{EI}\right]^{1/2} + \frac{T}{EI}\right)^{1/2}} \qquad (2.93)$$

and we may conclude that

a) L_D decreases as k and/or T are increased
b) L_D increases as ρ, ω or EI are increased.

Now considering the two span problem, figure 2.16, we define a necessary condition for the two spans to be uncoupled as

$$L_2 > L_D \qquad (2.94)$$

In addition it is clear that if the two spans AB and CD are fully uncoupled a second necessary condition is that the frequency ω equals one of the frequencies for spans L_1 and L_3 calculated separately using the single span theory. Thus considering fundamental modes only we have two cases

a) $\omega = \omega_1$ (2.95a)

b) $\omega = \omega_3$ (2.95b)

where ω_1 and ω_3 represent the fundamental frequencies for spans L_1 and L_3 respectively calculated using the single span theory. Thus considering case (a) the frequency ω_1 is calculated using

$$\omega_1 = R_1(\gamma_1, \delta_1)\,\bar{\omega}_1 \qquad (2.96)$$

where the parameters for span L_1 are

$$\gamma_1 = KL_1^4/EI \tag{2.97a}$$

$$\delta_1 = TL_1^2/EI \tag{2.97b}$$

$$\bar{\omega}_1 = a\sqrt{EI/\rho L_1^4} \tag{2.97c}$$

and $R_1(\gamma_1, \delta_1)$ is evaluated using figures 2.8 and 2.9. Substituting this result into equation (2.93) gives

$$L_{D_1} = \frac{2\pi L_1}{\left(2\left[\gamma_1 - a^2 R_1^2\right]^{1/2} + \delta_1\right)^{1/2}} \tag{2.98}$$

Thus if $L_2 > L_{D_1}$ both necessary conditions (2.94) and (2.95a) are satisfied and the two spans may be considered as uncoupled for free vibrations in the fundamental mode of span L_1. In a similar manner for case (b), equation (2.95b), we have

$$L_{D_3} \qquad \frac{2\pi L_3}{\left(2\left[\gamma_3 - a^2 R_3^2\right]^{1/2} + \delta_3\right)^{1/2}} \tag{2.99}$$

so that if $L_2 > L_{D_3}$ the two spans may also be considered as uncoupled for free vibration in the fundamental mode of span L_3.

2.5.2 Example Problem

The theory outlined in this chapter is now illustrated by a typical example for which the following data applies.

External diameter of steel pipe	= 500mm
Internal diameter of steel pipe	= 475mm
Overall diameter of pipeline	= 632mm
Length of span 1	= 50m
Length of span 3	= 10m
Soil modulus	= $2.5 MN/m^2$
Internal pressure	= $15 MN/m^2$
External pressure	= $1 MN/m^2$
Temperature of oil	= $10^{o}C$
Coeff. of expansion for steel	= $12 \times 10^{-6}/^{o}C$
Lay tension	= 0.75MN
Youngs modulus for steel	= $2 \times 10^{5} MN/m^2$

Using this data equations (2.6) give the flexural and axial rigidities of the pipeline as

$$EI = \frac{E\pi}{64}(D_o^4 - D_i^4) = 114\ MN m^2$$

$$EA = \frac{E\pi}{4}(D_o^2 - D_i^2) = 3830\ MN$$

Next the pipeline effective tension is calculated using equation (2.18) as

$$T = T_L - \alpha EA\Delta T - \frac{\pi}{20}(2p_i D_i^2 - 5p_o D_o^2)$$

$$= -0.58\ MN$$

Thus γ and δ for span L_1 are evaluated as

$$\gamma_1 = RL_1^4/EI = 1.37 \times 10^5$$

$$\delta_1 = TL_1^2/EI = -12.6$$

Now using figure 2.7 we see that for this data $\delta_{\rho_{cr}} = 34$ which on comparison with the above value of δ_1 indicates that the span L_1 is well within its critical load. Now using figure 2.9 we find that $R_1 = 0.6$ which on substituting into equation (2.98) gives $L_{0_1} = 11.7$m. Thus if $L_2 > 11.7$, the fundamental frequency of span L_1 may be considered unaffected by the presence of the smaller span. Repeating this calculation for the span L_3 we find

$$\gamma_3 = RL_3^4/EI = 2.19 \times 10^2$$

$$\delta_3 = TL_3^2/EI = -0.5$$

Hence using figure 2.9 we find $R_3 = 0.29$ which on substituting into equation (2.99) gives $L_{0_3} = 12.3$m. Thus if $L_2 > 12.3$m the fundamental frequency of the span L_3 is unaffected by the longer span L_1. Assuming this to be the case the fundamental frequencies of the two spans are given by

$$f_1 = \frac{\omega_1}{2\pi} = \frac{aR_1}{2\pi}\sqrt{\frac{EI}{\rho L_1^4}} \qquad (2.100a)$$

$$f_3 = \frac{\omega_3}{2\pi} = \frac{aR_3}{2\pi}\sqrt{\frac{EI}{\rho L_3^4}} \qquad (2.100b)$$

which assuming a total mass/length ℓ = 900 kg/m and using the above values of k_1 and k_3 gives

$$f_1 = 0.305 \text{ Hz}$$

$$f_3 = 3.69 \text{ Hz}$$

The corresponding reduced velocities are consequently

$$U_{R_1} = \frac{U}{f_1 D} = 5.19\, U$$

$$U_{R_3} = \frac{U}{f_3 D} = 0.43\, U$$

indicating that the 50m span will be susceptible to transverse vortex induced vibrations for $U > 0.67$ m/sec (i.e. $U_{R_1} > 3.5$).

2.5.3 Simplified Span Coupling Assessment

Considering again equations (2.98) and (2.99) it is clear that for large γ the damping length L_D may be calculated with acceptable engineering accuracy using $R = \delta = 0$ giving

$$\frac{L_D}{L} = \frac{2\pi}{(2\gamma^{1/2})^{1/2}} \qquad (2.101)$$

For example using the above data gives L_D = 11.5m (independent of span length) which compares well with the more exact values L_{D_1} = 11.7m and L_{D_3} = 12.3m calculated above. It follows that this simplified equation may be used for assessing span coupling as indicated in figure 2.17.

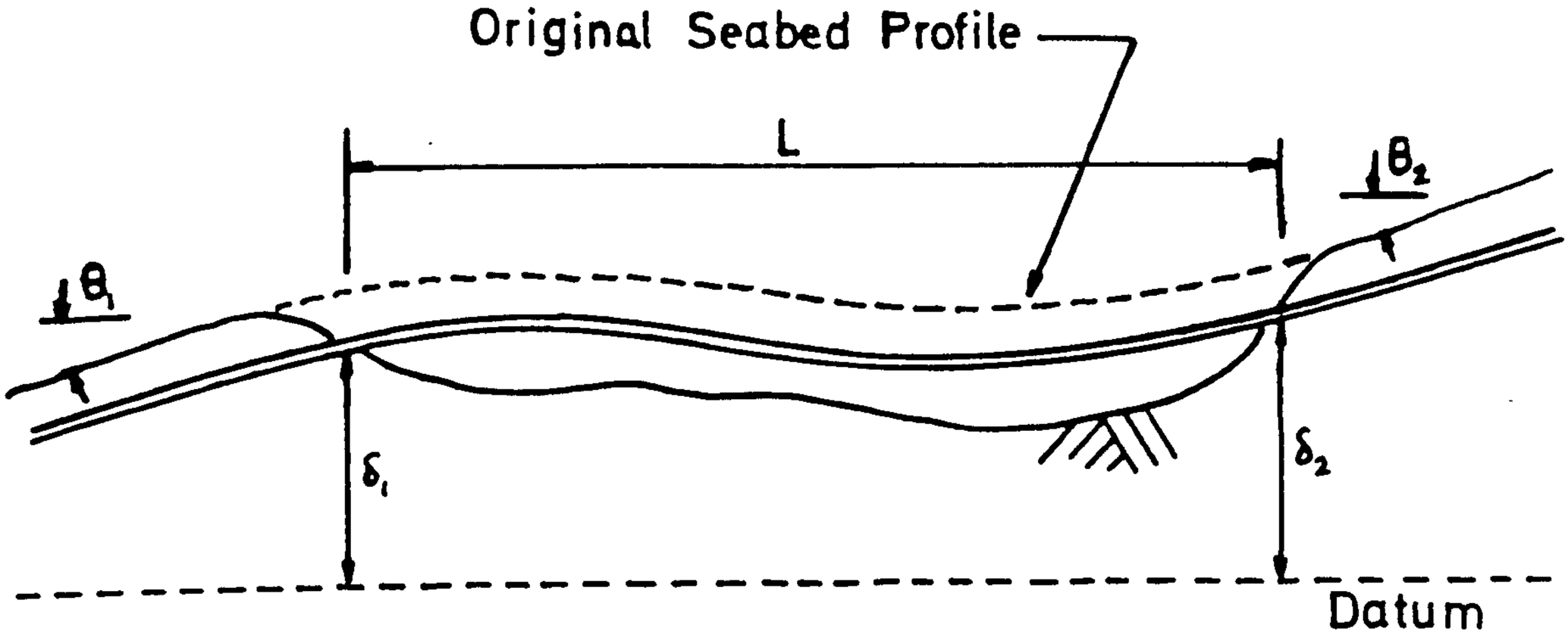

FIG 2.1 Free Span Geometry

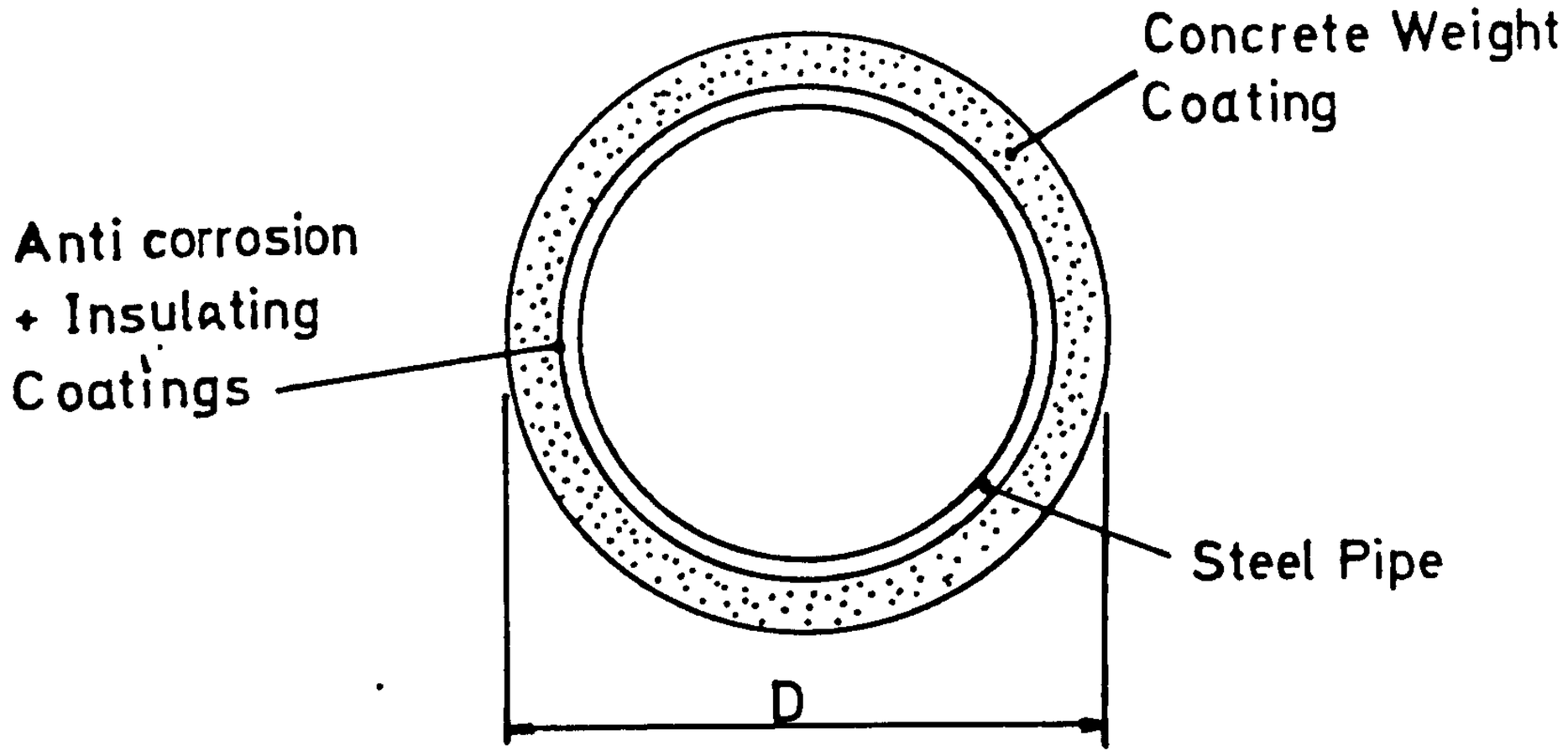

FIG 2.2 Pipe Section

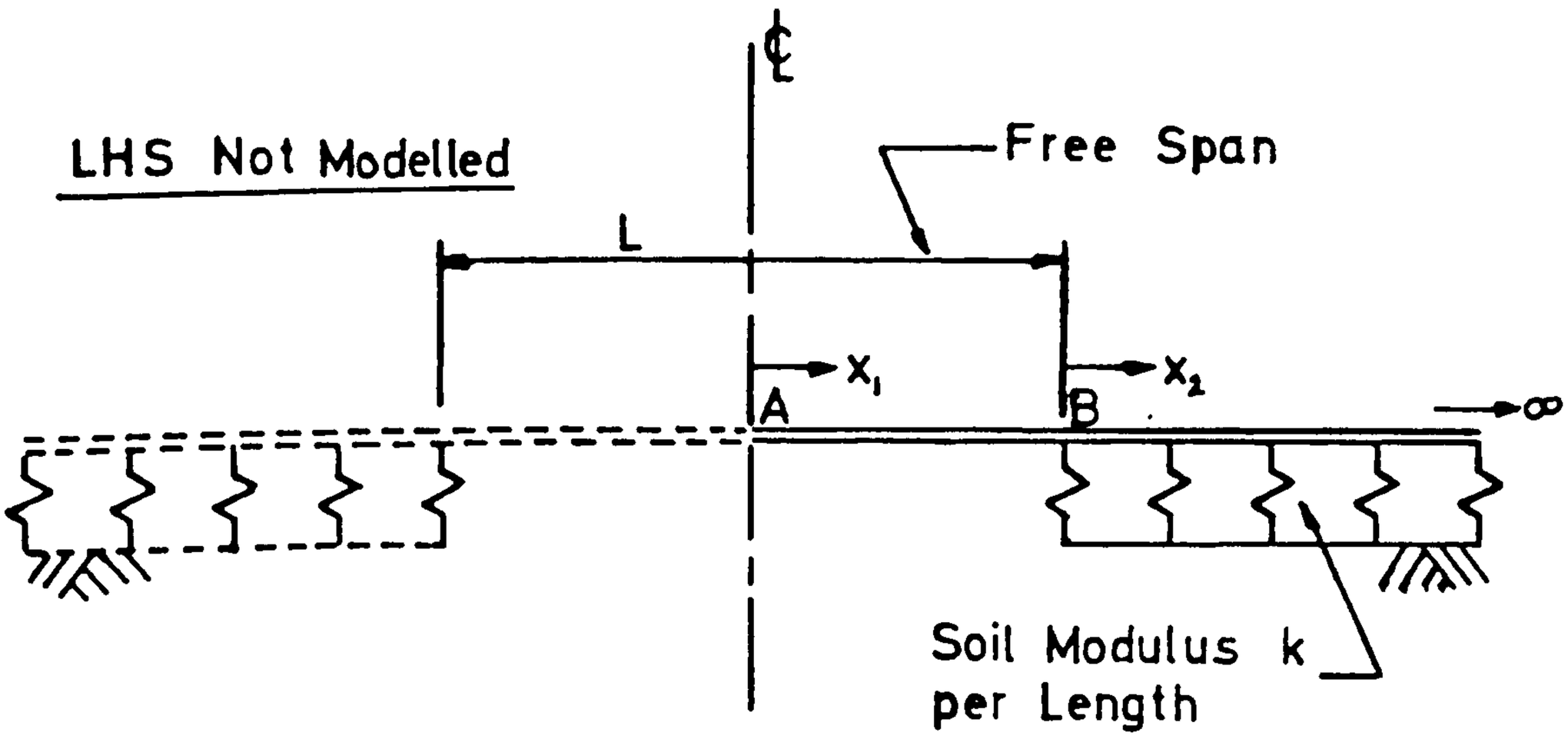

FIG 2.3 Simple Elastic Foundation Model

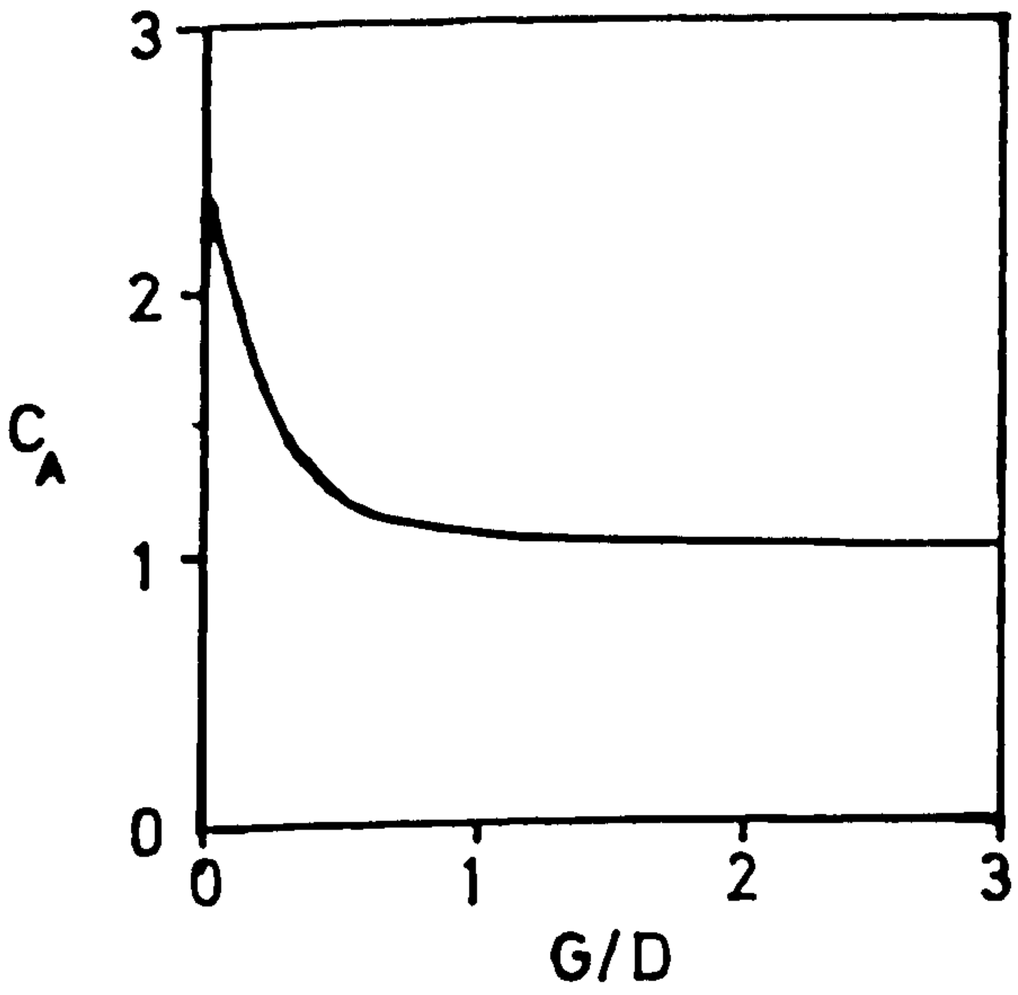

From DnV "Rules for Sub-marine Pipeline Systems" 1981.

FIG 2.4 Variation of Pipe Added Mass Coefficient With Bed Gap Ratio G/D

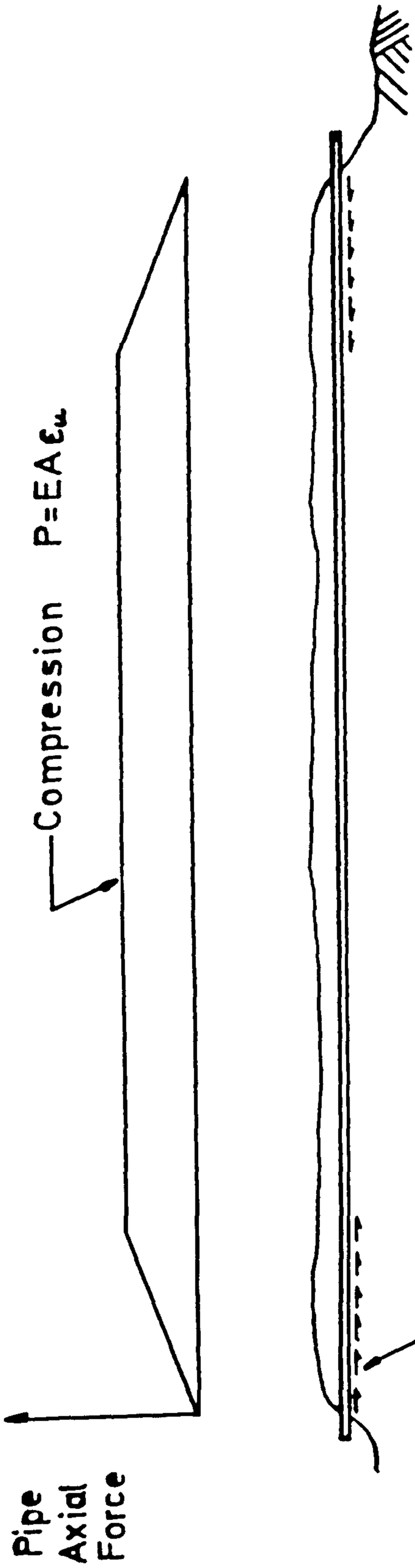

FIG 2.5 Long Pipe Subjected to Temperature Rise ΔT
Plus Internal Pressure p_i

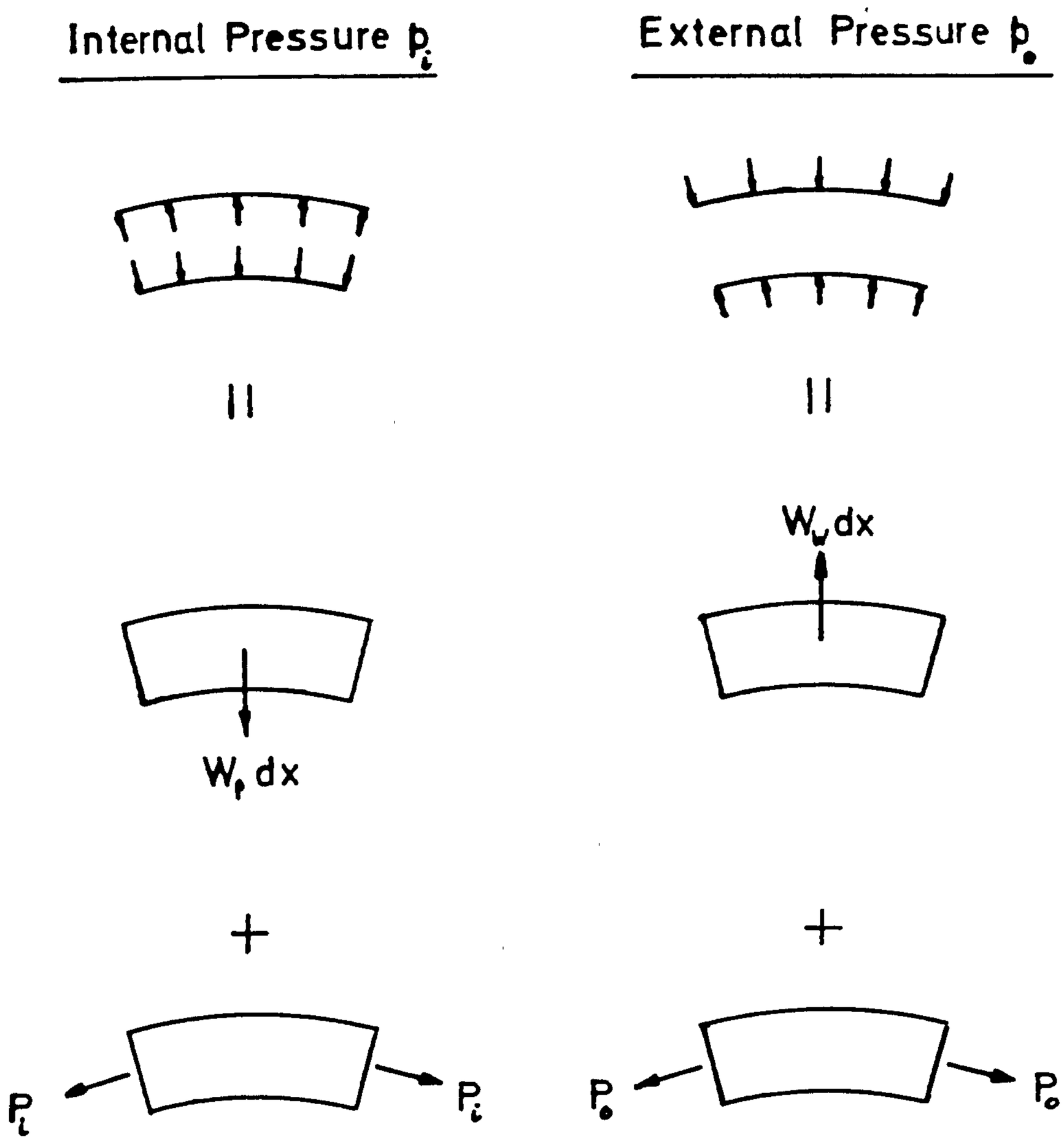

$$P_i = -\frac{\pi}{4} p_i D_i^2$$

$$P_o = +\frac{\pi}{4} p_o D_o^2$$

FIG 2.6 Effective Tension due to Internal and External Wall Pressures

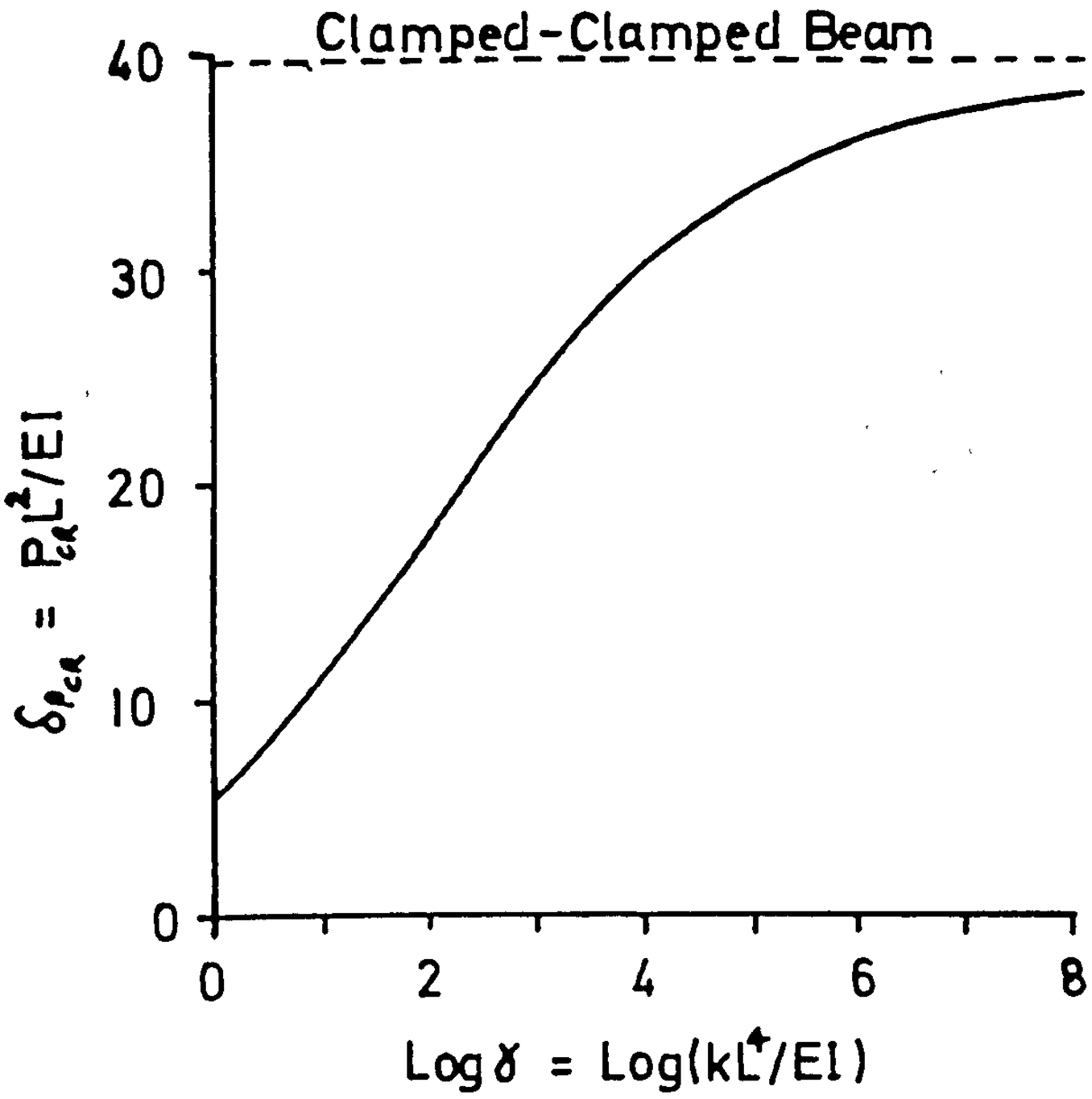

FIG 2.7 Linear Elastic Buckling Load
For Single Pipeline Span

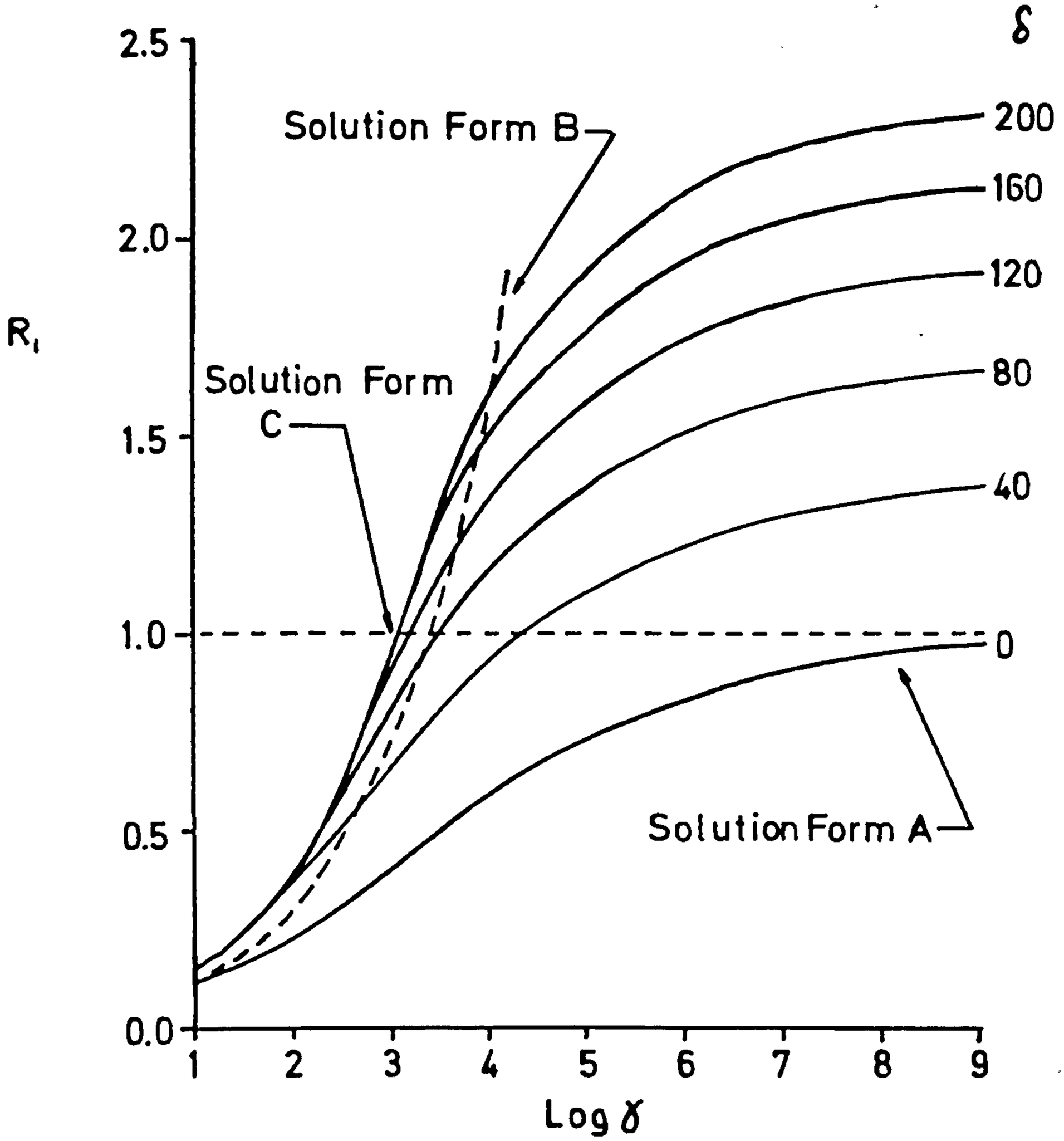

FIG 2.8 Frequency Ratio R_1 For Single Span Under Tension

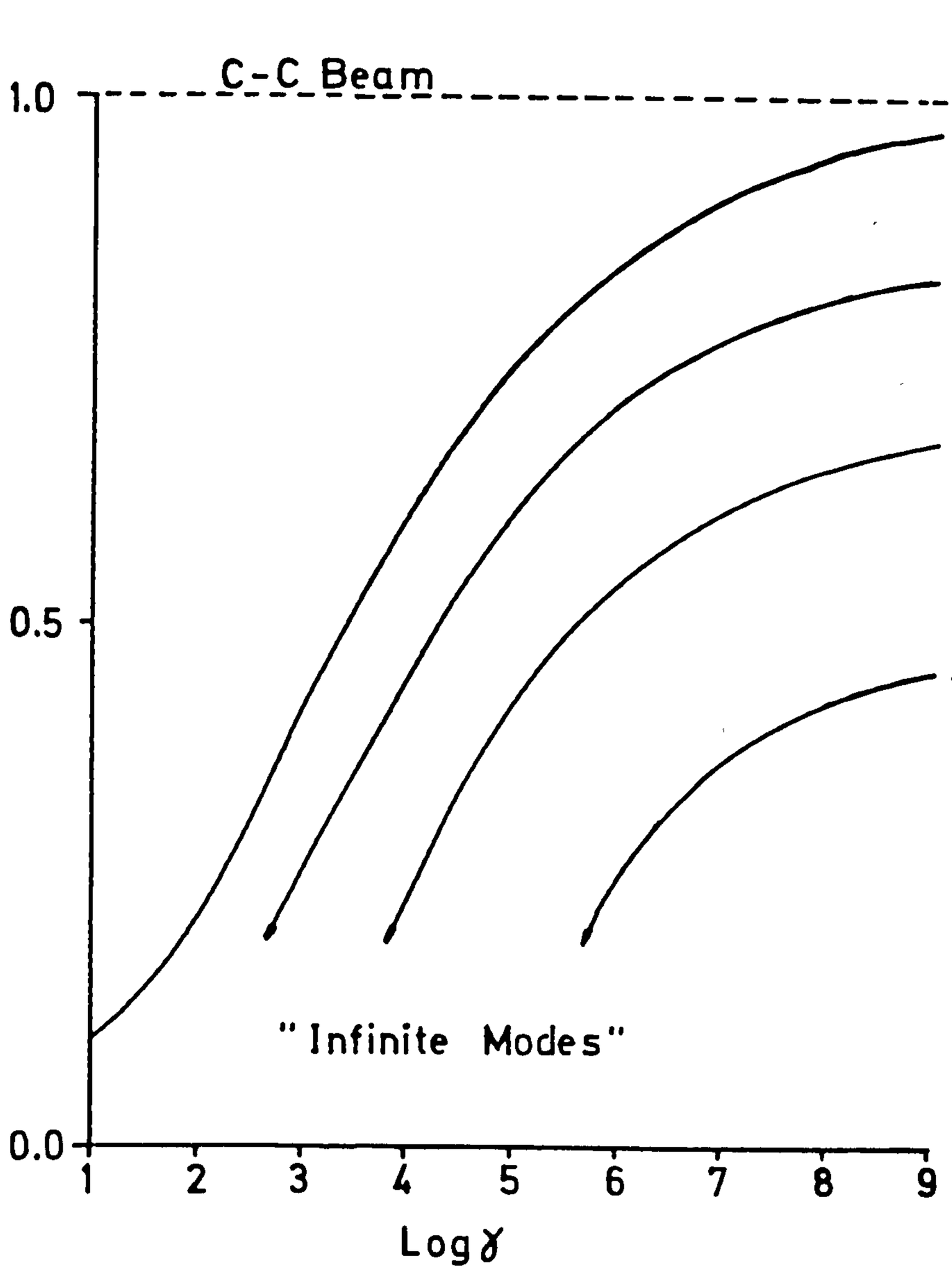

FIG 2.9 Frequency Ratio R_1 For Single Span Under Compression

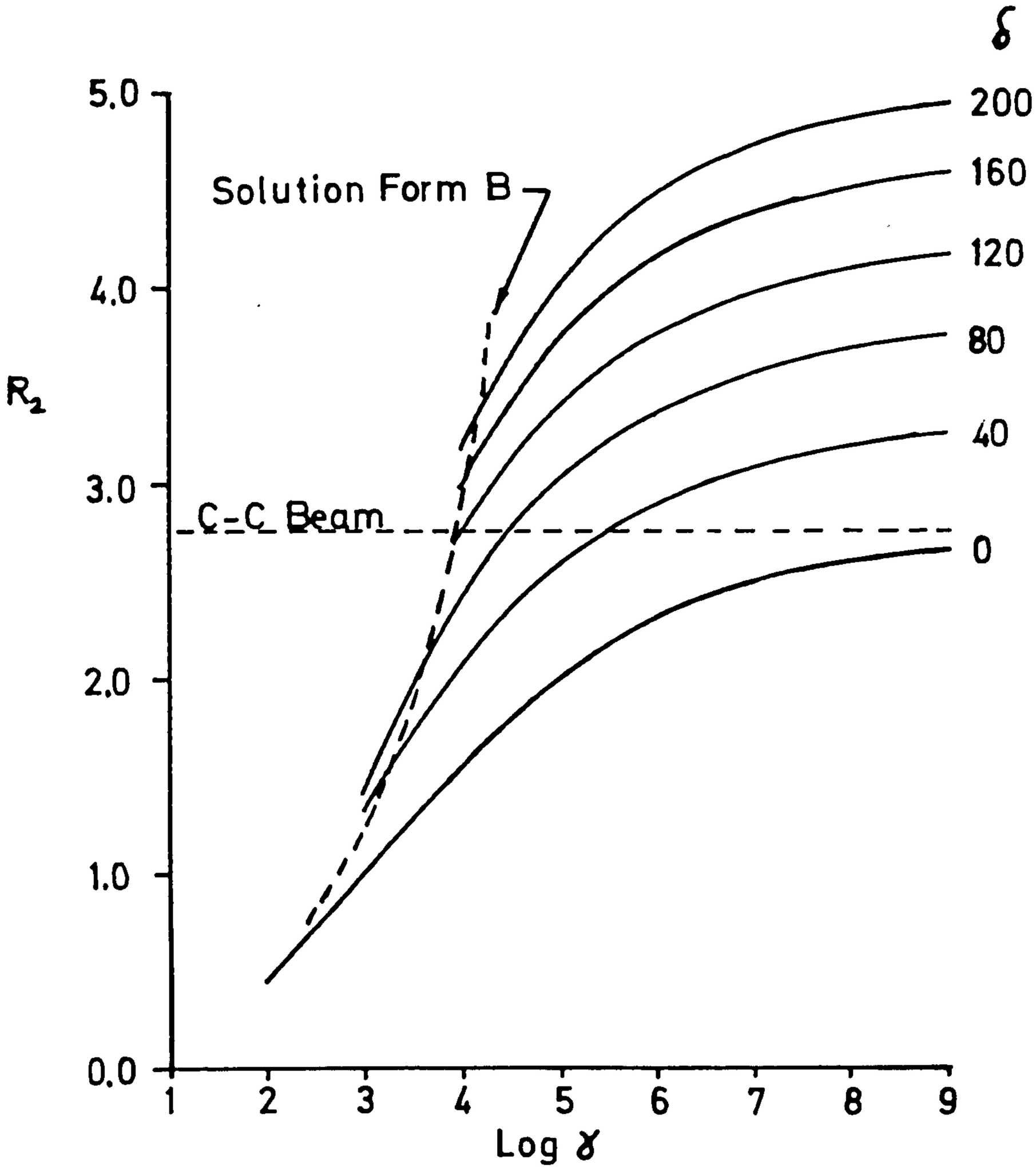

FIG 2.10 Frequency Ratio R_2 For Single Span Under Tension

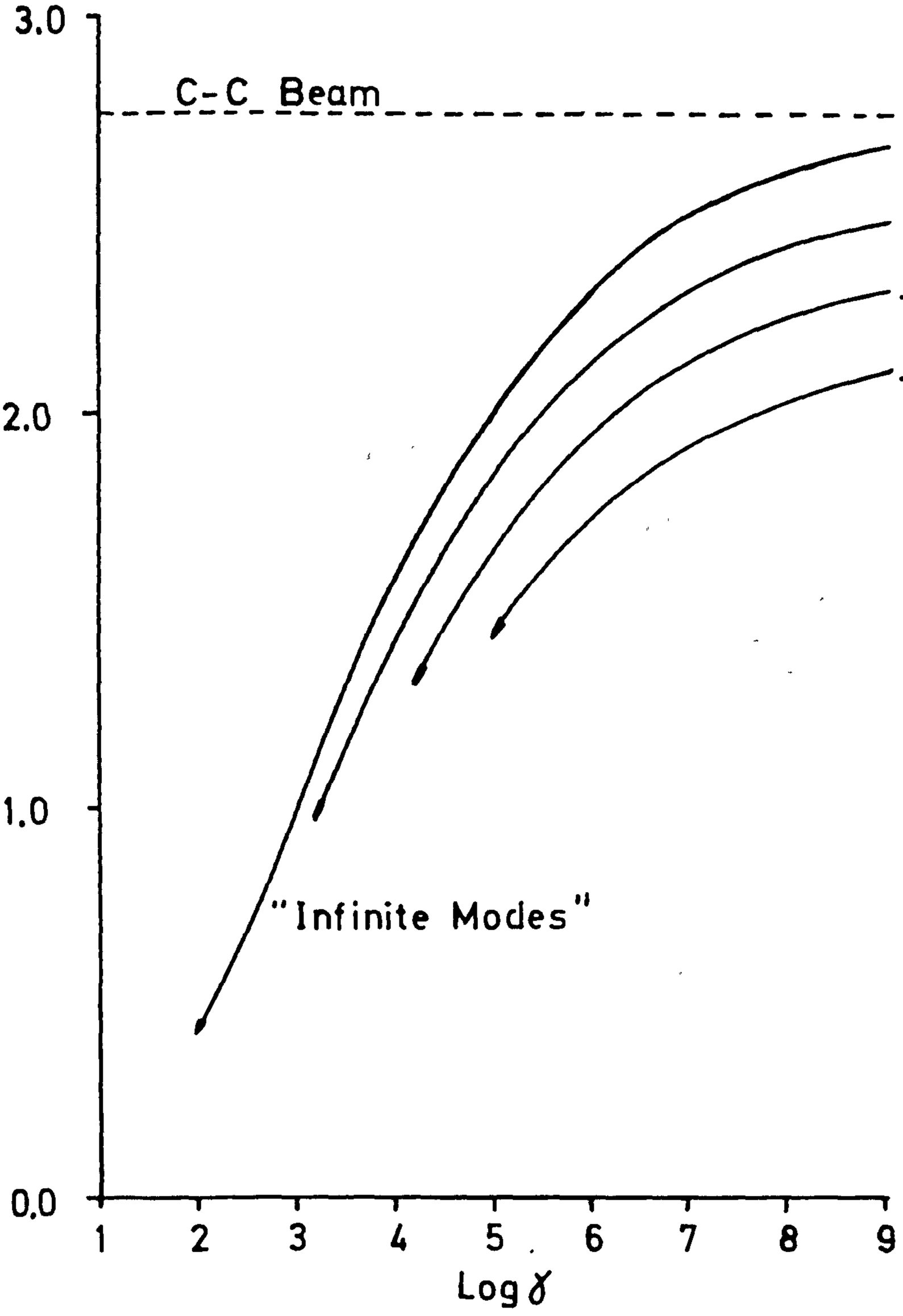

FIG 2.11 Frequency Ratio R_2 For Single Span Under Compression

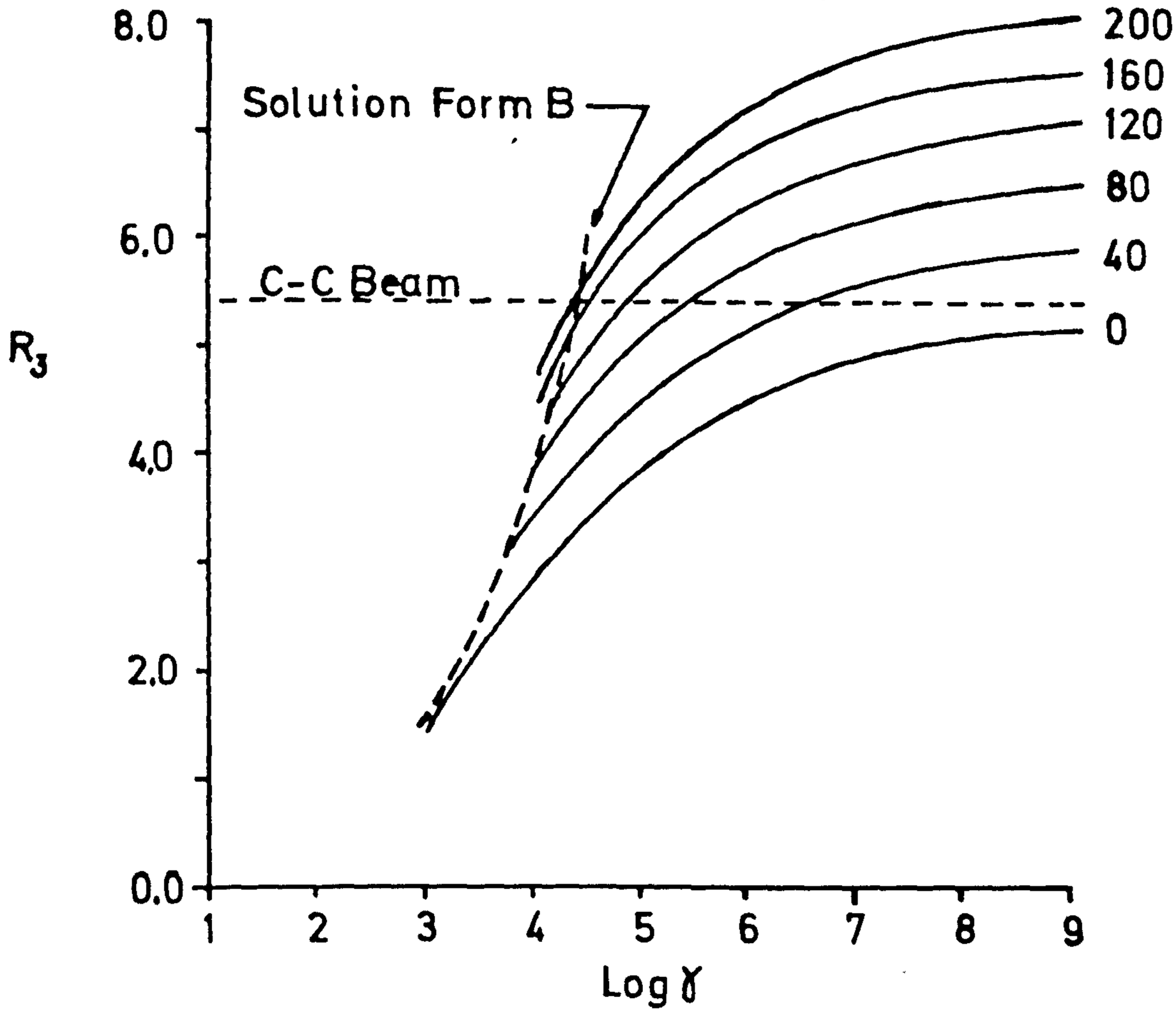

FIG 2.12 Frequency Ratio R_3 For Single Span Under Tension

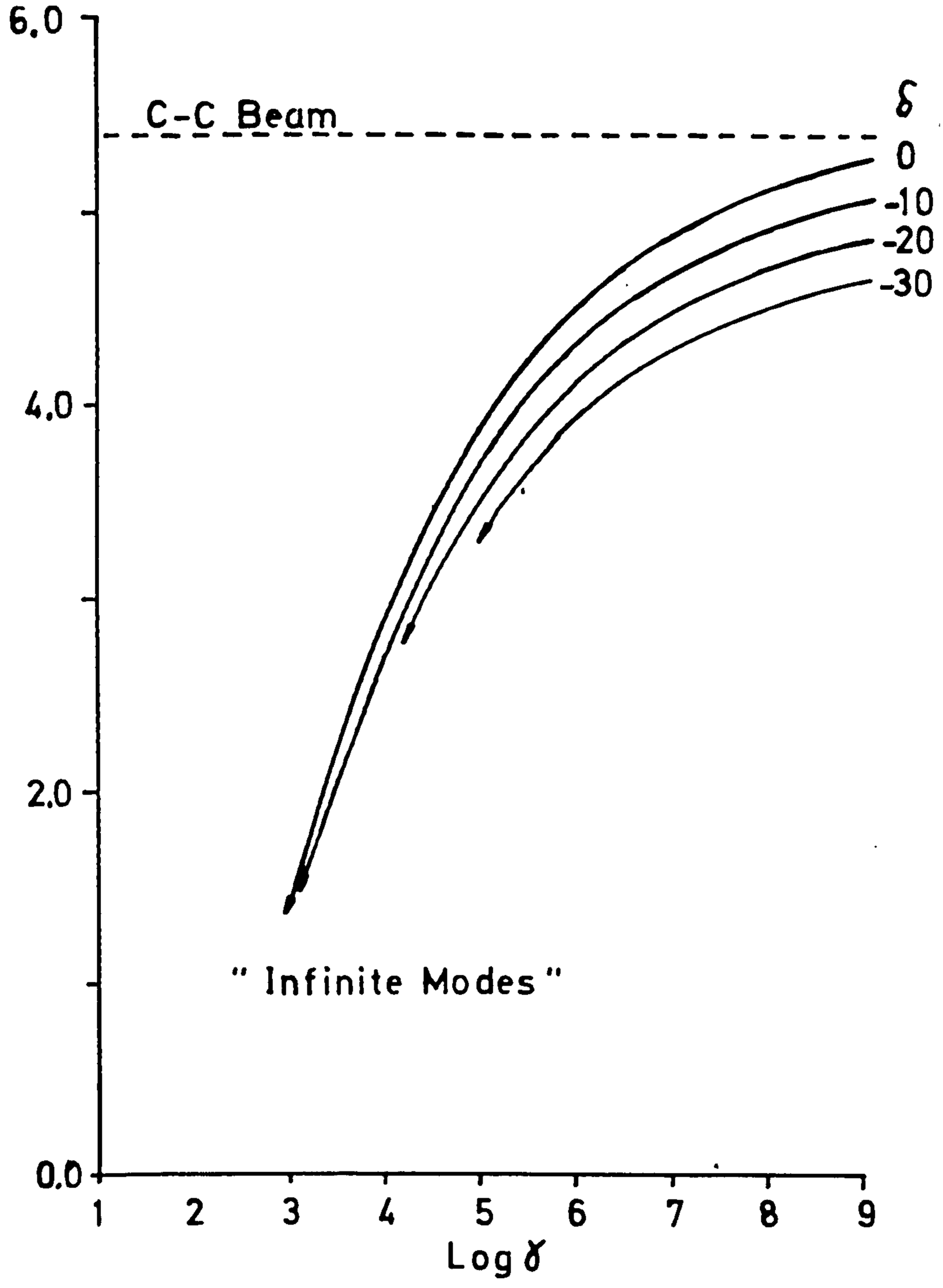

FIG 2.13 Frequency Ratio R_3 For Single Span Under Compression

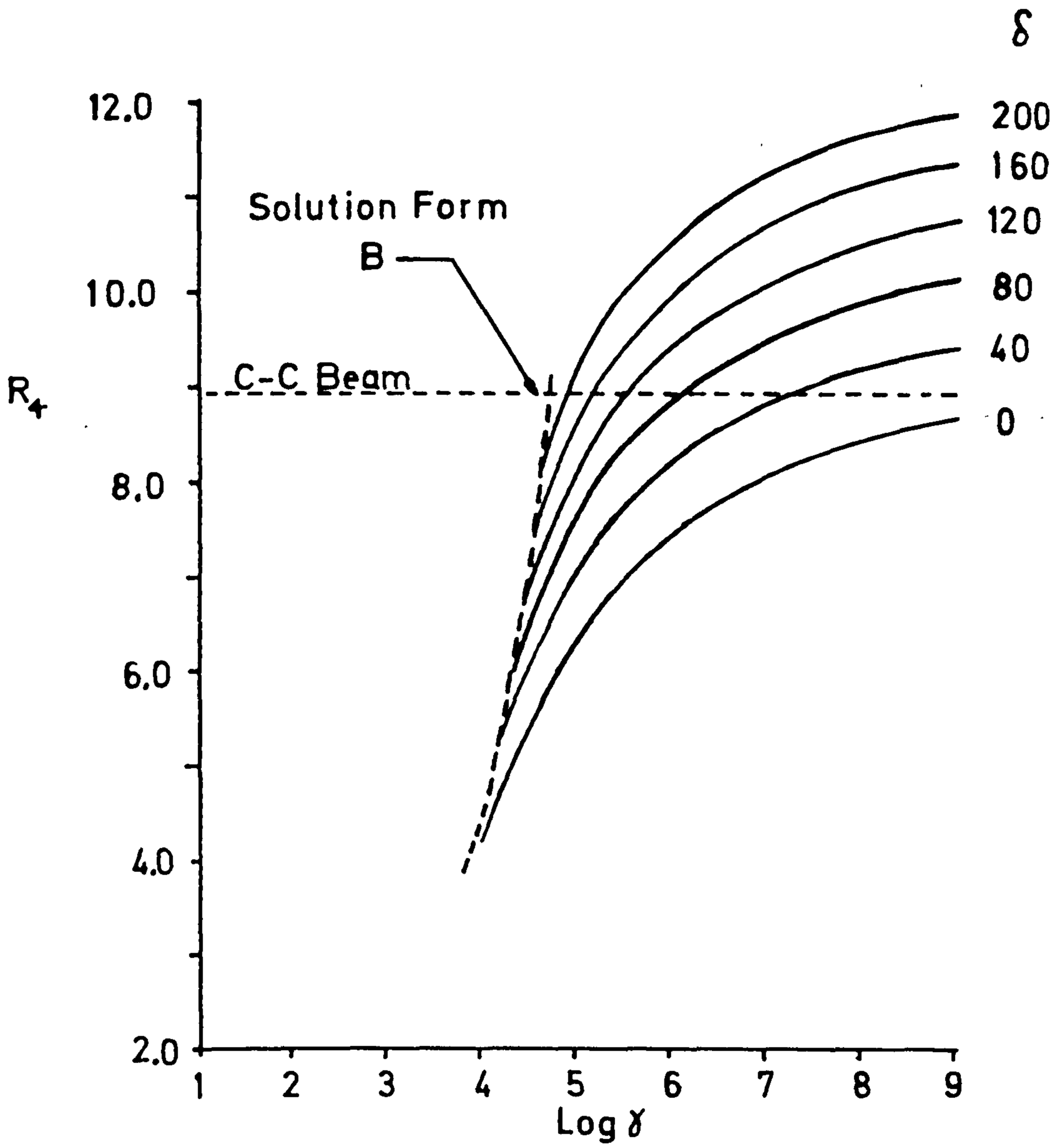

FIG 2.14 Frequency Ratio R_4 For Single Span Under Tension

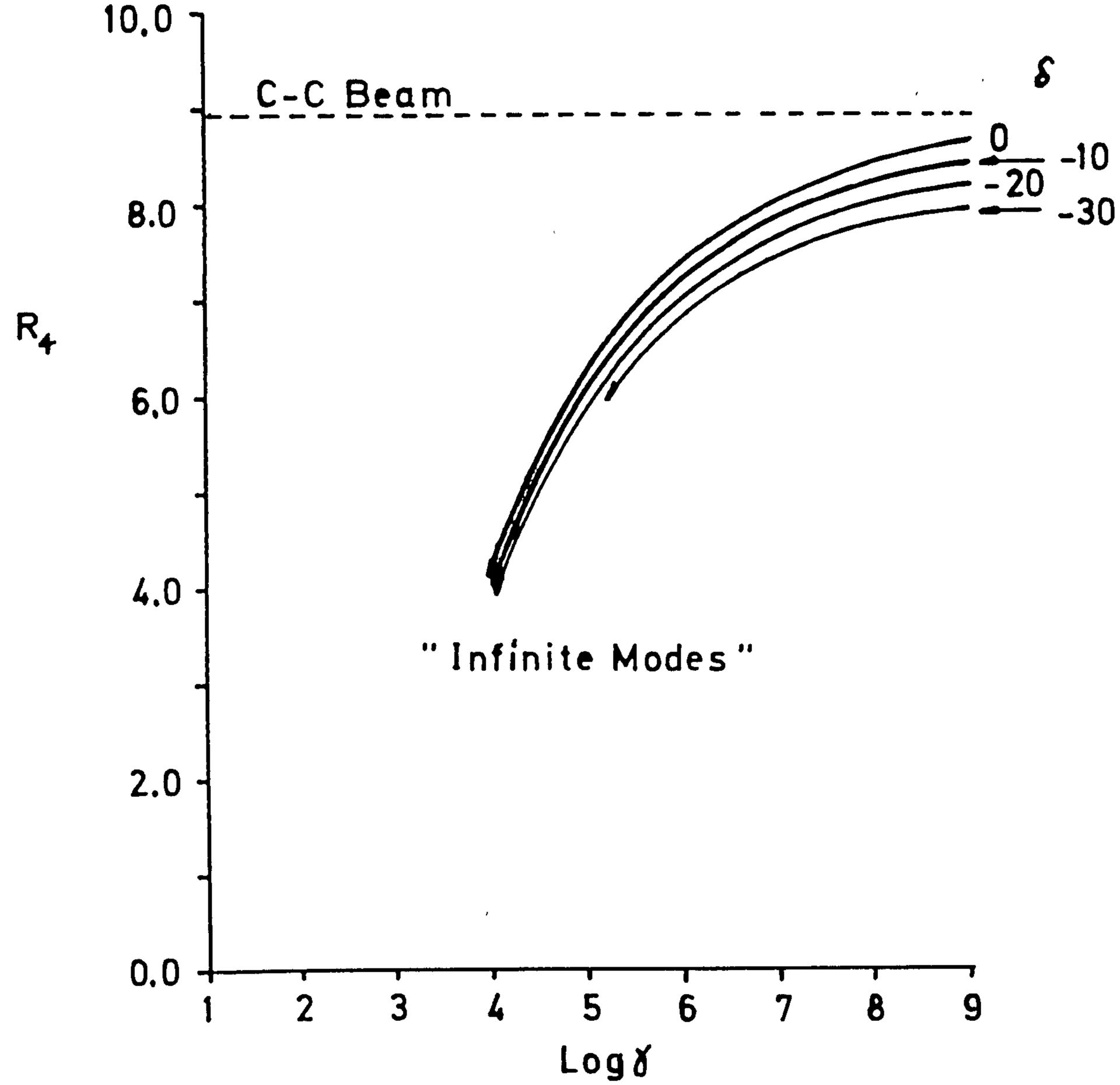

FIG 2.15 Frequency Ratio R_4 For Single Span Under Compression

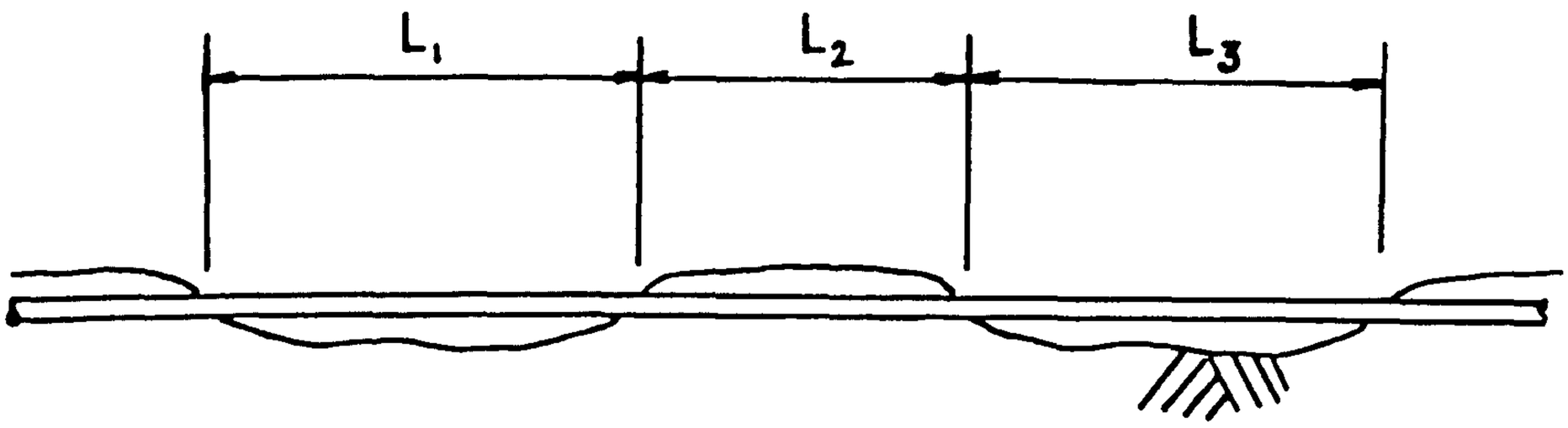

FIG 2.16 Two Span Problem

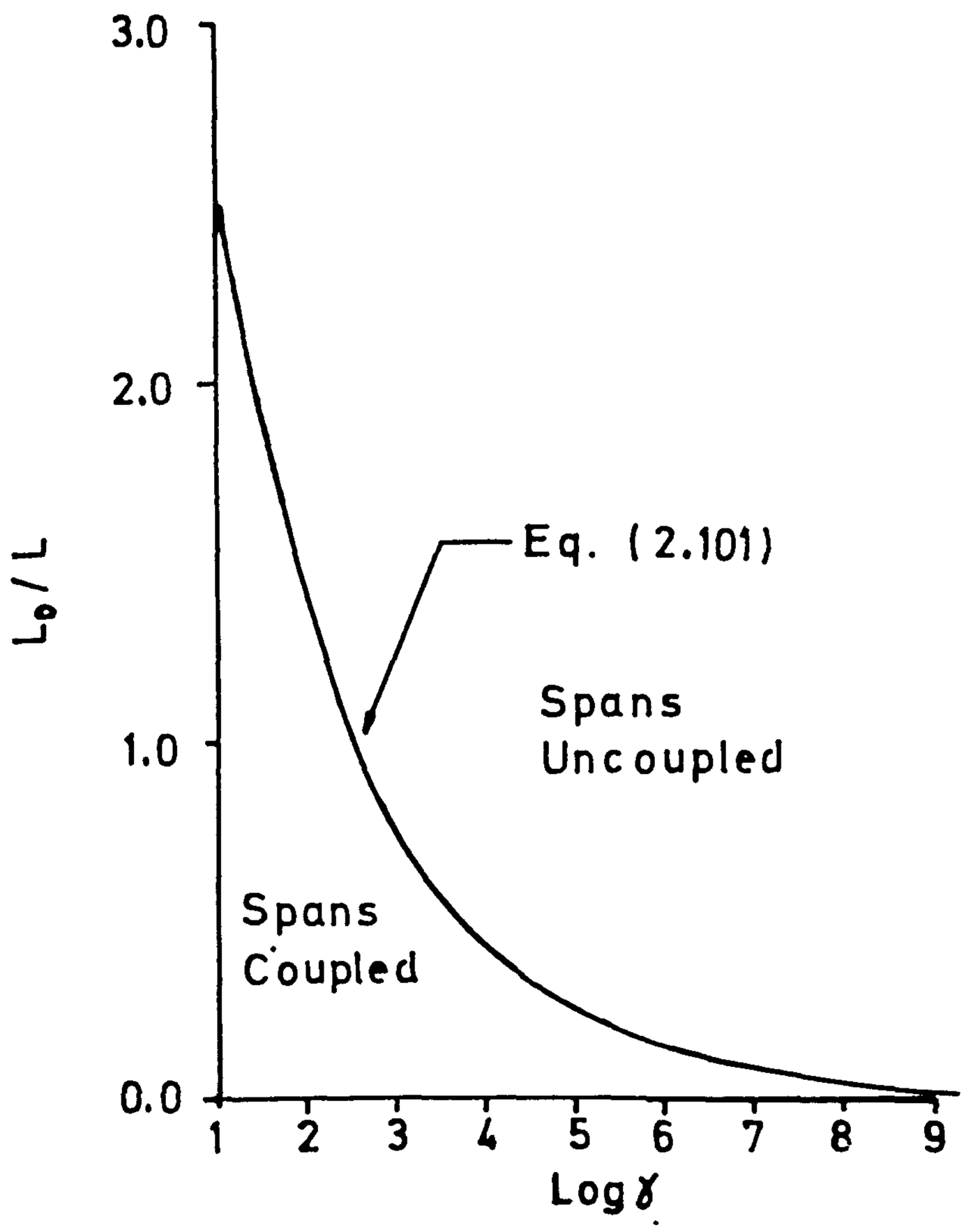

FIG 2.17 Coupling Between Spans

CHAPTER 3

FINITE ELEMENT MODEL

3.0 Introduction

The simple linear theory developed in Chapter 2, although providing much useful information, is based on the assumption that the coefficient of friction between pipe and soil is zero. This situation implies a condition of zero end restraint on the free span and consequently constant tension. In practice it is clear that as the free span forms by soil erosion the pipe deflects statically into the scoured depression, figure 3.1, resulting in end axial deflections u_B and u_C . Such end motion or "pull-in" will in turn be resisted by friction forces in the supported sections AB and CD leading to the development of a local overtension or sag tension in the pipeline. It is clear from the discussion of section 2.4 that for a long span (and consequently large γ) this increase in tension will have a considerable effect on span frequencies and hence should be included in the analysis. For this reason a numerical Finite Element Model (FEM) is developed in this chapter using assumptions similar to those outlined in section 2.0.3 but with μ no longer taken as zero. Additionally, although the theory used provides a first order correction for the change in geometry, the end deflections (δ_1 θ_1 δ_2 θ_2) are initially taken as zero as in the linear analysis of Chapter 2. The effect of such end geometry together with a consideration of the influence of finite amplitude vibrations is postponed at this stage until Chapters 4 and 5.

3.1 Overview of the model

The complete model developed herein consists of the following submodels

a) Linear Finite Element Model for the supported lengths AB and CD of the pipeline
b) Nonlinear Finite Element Model for the free span BC
c) Nonlinear nonconservative friction model for the pipe-soil interaction in sections AB and CD

Before deriving the detailed equations used in each of these submodels a brief description of each together with an indication of the way they interact with each other is presented.

Considering first figure 3.2 each supported length is divided into a number of linear beam on elastic foundation elements. The displacement freedoms associated with these elements are the lateral translations v_i and rotations θ_i at each node. These freedoms are used, together with standard cubic beam functions, to derive an infinitesimal displacement stiffness and mass matrix for each element based on its bending, tension, elastic foundation and inertia properties. It is noted that these elements do not include any axial displacement freedoms since the tension distribution in the pipeline over the supported sections is provided by the friction model.

Next over the free span the pipeline is idealised using nonlinear beam column elements utilising both (v_i, θ_i) bending displacements together with (u_i) axial freedoms. As a consequence of the theory used these degrees of freedom are coupled enabling the pull-in effects discussed above to be correctly modelled. As indicated in figure 3.3 this nonlinear model of the free span couples to the linear model used for the supported sections via the common bending freedoms (v_B θ_B v_C θ_C). In a similar manner coupling to the friction model is achieved via the inplane or axial freedoms (u_B u_C).

Axial effects in the supported spans AB and CD are

modelled using two infinite "pipe on friction foundation" elements described in terms of the end pull-in displacements u_B and u_C respectively. As shown in section 3.4 these elements are both nonlinear and nonconservative.

Considering now the overall procedural aspects, the first step is to undertake a nonlinear static analysis to determine the sag deflections and tension distribution in the pipeline. This is done using an incremental tangent stiffness approach with equilibrium iterations used at the end of each step to ensure accuracy. Once this static solution is found the final tangent stiffness matrix, together with the assembled mass matrix, is used in a standard eigenvalue calculation to determine the frequencies of free vibration about the static equilibrium position. In view of the system nonlinearities these frequencies must be considered valid for infinitesimally small amplitude vibration only.

3.2 Linear Finite Element Model

Considering a typical beam element as used to model a supported section of the pipeline, figure 3.4, the nodal displacements and generalised forces associated with the element may be written in column matrix form as

$$\underset{\sim}{a}^{B} = \begin{bmatrix} v_1 \\ \theta_1 \\ v_2 \\ \theta_2 \end{bmatrix} = \begin{bmatrix} a_1^B \\ a_2^B \\ a_3^B \\ a_4^B \end{bmatrix} \qquad (3.1a)$$

$$\underset{\sim}{f}^{\beta} = \begin{bmatrix} S_1 \\ M_1 \\ S_2 \\ M_2 \end{bmatrix} = \begin{bmatrix} f_1^{\beta} \\ f_2^{\beta} \\ f_3^{\beta} \\ f_4^{\beta} \end{bmatrix} \tag{3.1b}$$

The derivation of the various stiffness and mass matrices associated with this simple form of beam element is well documented and requires little further explanation here (Prezemiemiecki 1968). However, despite this fact, a brief outline of the development is given primarily to introduce some of the notation. Thus following standard Finite Element procedure (Zienkiewicz 1977) the lateral displacement at station x along the beam is written as

$$v(x,t) = \begin{bmatrix} N_1^{\beta} & N_2^{\beta} & N_3^{\beta} & N_4^{\beta} \end{bmatrix} \underset{\sim}{a}^{\beta}$$

$$= \left[N^{\beta} \right] \underset{\sim}{a}^{\beta} \tag{3.2}$$

where N^{β} is a row matrix of shape funcitons. These are taken as the deformations developed in a uniform untensioned beam subjected to unit end displacements as given by (Clough 1975)

$$N_1^{\beta} = (1 - 3\xi^2 + 2\xi^3) \tag{3.3a}$$

$$N_2^{\beta} = (\xi - 2\xi^2 + \xi^3) L_e \tag{3.3b}$$

$$N_3^{\beta} = (3\xi^2 - 2\xi^3) \tag{3.3c}$$

$$N_4^\beta = (\xi^3 - \xi^2) L_e \qquad (3.3d)$$

where the nondimensional coordinate $\xi = x/L_e$. The associated strain/potential energy stored in the element is

$$U^T = \frac{1}{2}\int_0^{L_e} \left(EI(v'')^2 + T^F(v')^2 + k^s v^2 \right) dx \qquad (3.4)$$

where EI is the flexural rigidity of the pipe, T^F the effective tension as calculated by the friction model, k^s the soil modulus[1] and prime denotes differentiation wrt x. Using equations (3.2) and (3.4) the coefficients of the element stiffness matrix are evaluated as

$$k_{ij} = \frac{\partial^2 U^T}{\partial a_i^\beta \partial a_j^\beta} = \int_0^{L_e} \left(EI(N_i^\beta)''(N_j^\beta)'' + T^F(N_i^\beta)'(N_j^\beta)' + k^s N_i^\beta N_j^\beta \right) dx \qquad (3.5)$$

Thus assuming EI , T^F and k^s are all constant along the length of the element we find

$$k_{ij} = EI\, k_{ij}^\beta + T^F k_{ij}^\sigma + k^s k_{ij}^s \qquad (3.6)$$

where the subscripted terms k_{ij}^β , k_{ij}^σ and k_{ij}^s are given by

. . . . . .

---

(1) The notation k for soil stiffness as used in Chapter 2 is not continued here in order to avoid confusion with the various element matrices defined in this chapter.

$$k_{ij}^{\beta} = \int_0^{Le} (N_i^{\beta})'' (N_j^{\beta})'' \, dx \qquad (3.7a)$$

$$k_{ij}^{\sigma} = \int_0^{Le} (N_i^{\beta})' (N_j^{\beta})' \, dx \qquad (3.7b)$$

$$k_{ij}^{s} = \int_0^{Le} (N_i^{\beta})(N_j^{\beta}) \, dx \qquad (3.7c)$$

Using these terms the linear element force-displacement transformation is given by

$$\underset{\sim}{f}^{\beta} = \left[EI k^{\beta} + T^F k^{\sigma} + R^s k^s \right] \underset{\sim}{q}^{\beta} \qquad (3.8)$$

where the 4 x 4 matrices k^{β}, k^{σ} and k^s contain the coefficients (3.7) above and are evaluated for reference in Appendix C. In addition assuming T^F is constant the corresponding variational form is

$$\delta \underset{\sim}{f}^{\beta} = \left[EI k^{\beta} + T^F k^{\sigma} + R^s k^s \right] \delta \underset{\sim}{q}^{\beta}$$

$$= \left[k_T^{\beta} \right] \delta \underset{\sim}{q}^{\beta} \qquad (3.9)$$

where k_T^{β} represents the 4 x 4 element tangent stiffness matrix. Strictly speaking this later equation is only approximate since, as outlined in section 3.4.8, the tension force T^F occurring in the supported sections is calculated by the friction elements and so depends on the span end displacements u_B and u_C. As a result additional terms in δu_B and δu_C appear in equation (3.9) leading in general to a loss of symmetry in the assembled tangent matrix. However, since in practice the element stiffness

due to tension is small in the supported sections, these additional terms are small and may be neglected. In any case it should be noted that the use of the approximate tangent stiffness matrix defined by equation (3.9) in no way affects the final solution so long as the exact force expression equation (3.8) is used in evaluating equilibrium.

3.2.1 Element Mass Matrix

In a similar manner to the above the element kinetic energy associated with the displacement $v(x,t)$ is

$$T_{KE} = \frac{1}{2}\int_0^{Le} \rho \dot{v}^2 dx \qquad (3.10)$$

where as described in section 2.0.3 ρ represents the mass per length of pipe plus product plus added mass. Thus following standard Finite Element methods the 4 x 4 mass matrix may be written as

$$\rho M^{\beta} = \rho \left[m_{ij}^{\beta} \right] \qquad (3.11)$$

where the coefficients m_{ij}^{β} are given by

$$m_{ij}^{\beta} = \int_0^{Le} (N_i^{\beta})(N_j^{\beta}) dx = R_{ij}^{s} \qquad (3.12)$$

3.2.2 Element Load Vector

Finally considering the pipe weight W as given by equation (2.1) the potential associated with $v(x,t)$ is

$$U^e = \int_0^{Le} W v \, dx \qquad (3.13)$$

which again following standard theory gives the element load vector as

$$\underset{\sim}{p}^{\beta} = \left\{ p_i^{\beta} \right\} \tag{3.14}$$

Here the coefficients p_i^{β} are given by

$$p_i^{\beta} = -W \int_0^{Le} N_i^{\beta} \, dx \tag{3.15}$$

and are evaluated for reference in Appendix C.

3.3 Nonlinear Finite Element Model

In developing a suitable element for the free span the main requirement is that the bending and axial effects are coupled thereby giving a realistic modelling for the pull-in effects. To do this it is necessary to remove the assumption of infinitesimally small displacements since this leads to the standard linear theory in which bending and axial effects are uncoupled. In this linear theory the axial strain occurring in the element is taken as

$$\varepsilon_x = \frac{\partial u}{\partial x} + y \frac{\partial^2 v}{\partial x^2} \tag{3.16}$$

where the axial and lateral displacements u and v are assumed small and y is measured from the neutral axis, figure 3.5. If the assumption of small displacements is no longer valid then (3.16) must be replaced by the corresponding Green's strain defined as (Fung 1965)

$$\varepsilon_x = \frac{\partial u}{\partial x} + \frac{1}{2}\left[\left(\frac{\partial u}{\partial x}\right)^2 + \left(\frac{\partial v}{\partial x}\right)^2 \right] + y \frac{\partial^2 v}{\partial x^2} \tag{3.17}$$

In practice since the axial stiffness of the beam is generally large the term $(\partial u/\partial x)^2$ is small compared to $\partial u/\partial x$ and is neglected. In this case the axial strain becomes

$$\varepsilon_x = \frac{\partial u}{\partial x} + \frac{1}{2}\left(\frac{\partial v}{\partial x}\right)^2 + y\frac{\partial^2 v}{\partial x^2} \qquad (3.18)$$

Using this definition of strain a candidate element may be formulated using established Finite Element procedures (Zienkiewicz 1977). However it has been shown recently (Wen 1983) that this process leads to an excessively high non-linear stiffness for the element. As a result it has been suggested that the non-linear term in equation (3.18) be replaced by its average over the length of the element so that the axial strain is redefined as

$$\varepsilon_x = \frac{\partial u}{\partial x} + \frac{1}{2Le}\int_0^{Le}\left(\frac{\partial v}{\partial x}\right)^2 dx + y\frac{\partial^2 v}{\partial x^2} \qquad (3.19)$$

Thus the variation in strain along the element due to the nonlinear term is reduced to order zero, a process closely resembling the use of reduced integration in certain continuum elements (Bathe 1982). Now considering an unrestrained element subjected to a lateral deflection the relative displacement σ_b between the two ends due to the bending or bowing action is given for small slopes as

$$\sigma_b = \frac{1}{2}\int_0^{Le}\left(\frac{\partial v}{\partial x}\right)^2 dx \qquad (3.20)$$

Thus comparing this with equation (3.19) we may write

$$\varepsilon_x = \frac{\partial u}{\partial x} + \frac{\sigma_b}{Le} + y\frac{\partial^2 v}{\partial x^2} \qquad (3.21)$$

where the nonlinear term may now be interpreted as a simple change in length over original length form. In the following section this direct interpretation of the axial strain, suitably modified to account for any pressure and temperature effects, is used directly to derive the required element equations. It should be noted that the resulting formulation, although nonlinear, is restricted to problems in which the displacements while no longer small are not excessively large. Gross deformations may be included in the theory by the use of updated coordinates (Oran 1976) in which the element displacements and forces are measured relative to a local coordinate system which follows the rigid body motions of the element. However for the purpose of pipe span assessment such additional refinements are considered unnecessary at this stage.

3.3.1 Internal Strain Energy

Considering figure 3.5 the nodal displacements associated with the nonlinear beam element are written in matrix form as

$$\underset{\sim}{a} = \begin{bmatrix} \underset{\sim}{a}^{\rho} \\ \underset{\sim}{a}^{\beta} \end{bmatrix} \tag{3.22}$$

Here the column matrix $\underset{\sim}{a}^{\beta}$ is as defined by equation (3.1a) while the inplane displacements are given by

$$\underset{\sim}{a}^{\rho} = \begin{bmatrix} a_1^{\rho} \\ a_2^{\rho} \end{bmatrix} \tag{3.23}$$

The associated generalised forces are written as

$$\underset{\sim}{f} = \begin{bmatrix} \underset{\sim}{f}^{\rho} \\ \underset{\sim}{f}^{\beta} \end{bmatrix} \tag{3.24}$$

where $\underset{\sim}{f}^{\beta}$ is given by equation (3.1b) and the inplane forces are

$$\underset{\sim}{f}^{\rho} = \begin{bmatrix} f_1^{\rho} \\ f_2^{\rho} \end{bmatrix} \tag{3.25}$$

The axial and lateral displacements at station x along the pipe are now given by

$$\underset{\sim}{u} = \begin{bmatrix} u(x,t) \\ v(x,t) \end{bmatrix} = \begin{bmatrix} N_1^{\rho} & N_2^{\rho} & 0 & 0 & 0 & 0 \\ 0 & 0 & N_1^{\beta} & N_2^{\beta} & N_3^{\beta} & N_4^{\beta} \end{bmatrix} \underset{\sim}{a}$$

$$= [N]\,\underset{\sim}{a} \tag{3.26}$$

Here the bending functions N_i^{β} are taken identical to those used for the linear element, equations (3.3), while the inplane functions are taken as

$$N_1^{\rho} = 1 - \xi \tag{3.27a}$$

$$N_2^{\rho} = \xi \tag{3.27b}$$

The deflections defined by equation (3.26) are taken relative to an initial configuration in which the pipe element is straight and subjected to a tension T_L plus external pressure p_o as shown in figure 3.6. This initial configuration is selected since it corresponds closely to the environmental conditions acting on the pipeline shortly after installation. If the pipe is now subjected to a temperature rise ΔT plus internal pressure p_i the decrease in length of the element, assuming the tension T_L is held constant, is obtained using equation (2.13) as

$$\sigma_o = -L_e \varepsilon_u = \frac{\nu L_e p_i D_i}{2Et} - \alpha L_e \Delta T \qquad (3.28)$$

If in addition the pipe is allowed to bend the resulting bowing action leads to a further relative displacement given by equations (3.7b), (3.20) and (3.26) as

$$\sigma_b = \frac{1}{2} k^{\sigma}_{ij} a^b_i a^b_j \qquad (3.29)$$

where here and subsequently the repeated subscripts on the bending displacements imply summation from 1 to 4. Thus as shown in figure 3.6 the total relative displacement during the constant tension stage of the element deformation is

$$\sigma = \sigma_o + \sigma_b = \sigma_o + \frac{1}{2} k^{\sigma}_{ij} a^b_i a^b_j \qquad (3.30)$$

Next since the actual relative displacement is $(a^p_2 - a^p_1)$ an elastic elongation occurs, figure 3.6, and the axial force increases to

$$T^{\nu}_R = T_L + \frac{EA}{L_e}(a^p_2 - a^p_1 + \sigma) \qquad (3.31)$$

as indicated by the load deflection curve, figure 3.7a. Here it is convenient to introduce the effect of the internal and external pressures p_i and p_o on the lateral stability by transforming from real to effective tension. As discussed in section 2.0.4 this is achieved by adding to the real tension the end pressure term given by

$$T_p = -\frac{\pi}{4}(p_i D_i^2 - p_o D_o^2) \tag{3.32}$$

Thus combining equations (3.31) and (3.32) the variable effective tension acting on the deformed element is

$$T^v = T_L + T_p + \frac{EA}{Le}(a_2^p - a_1^p + \sigma) \tag{3.33}$$

Using equation (3.30) this may be written in the convenient form

$$T^v = T + \frac{EA}{Le}(a_2^p - a_1^p + \frac{1}{2}k_{ij}^{\sigma} a_i^g a_j^g) \tag{3.34}$$

where T represents the initial effective tension as used in the linear analysis of Chapter 2, equation (2.18), repeated here for convenience as

$$T = T_L - \alpha EA\Delta T - \frac{\pi}{20}(2p_i D_i^2 - 5p_o D_o^2) \tag{3.35}$$

The associated effective axial strain energy is now given by the area under the effective tension curve, figure 3.7b, as

$$V^p = (T_t + T_p)(a_2^p - a_1^p + \sigma) + \frac{EA}{2L_e}(a_2^p - a_1^p + \sigma)^2 \qquad (3.36)$$

In addition to this the lateral deflection $v(x,t)$ results in strain energy due to bending plus any elastic foundation of(1)

$$V^b = \frac{1}{2}\int_0^{L_e} (EI(v'')^2 + k^s v^2)\,dx \qquad (3.37)$$

which using the assumed displacements equation (3.26) becomes

$$V^b = \frac{1}{2}(EIk_{ij}^b + k^s k_{ij}^s)a_i^b a_j^b \qquad (3.38)$$

Finally combining equations (3.36) and (3.38) the total internal strain energy for the deformed element is

$$V^T = V^p + V^b \qquad (3.39)$$

---

(1) The inclusion of the elastic foundation term here arises from the need to temporarily support sections of the free span during the nonlinear static solution as outlined in section 3.5.

3.3.2 Element Force-Displacement Transformation

The inplane generalised forces f_1^ρ and f_2^ρ shown in figure 3.5 are obtained from the internal energy equation (3.39) as

$$f_1^\rho = \frac{\partial V^T}{\partial a_1^\rho} = -T^v \tag{3.40a}$$

$$f_2^\rho = \frac{\partial V^T}{\partial a_2^\rho} = +T^v \tag{3.40b}$$

where T^v is the variable effective tension equation (3.33) or (3.34). In a similar manner for the i^{th} bending freedom

$$f_i^\beta = \frac{\partial V^T}{\partial a_i^\beta} = (EIk_{ij}^\beta + T^v k_{ij}^\sigma + R^s k_{ij}^s) a_j^\beta \tag{3.41}$$

In view of these equations the element force-displacement transformation is seen to be nonlinear with the inplane and bending actions coupled. This follows since the variable effective tension, T^v, appearing in both equations (3.40) and (3.41), depends linearly on the inplane displacements a_i^ρ and quadratically on the bending displacements a_i^β. A significant exception to the above general cases occurs when dealing with the classical beam-column problem, figure 3.8. In this case since the end axial restraint on the beam is zero the real tension T_L in the beam becomes statically determinant. Thus setting the effective tension $T^v = T_L + T_\rho$ equation (3.41) may be written as

$$\underset{\sim}{f}^\beta = \left[EIk^\beta + (T_L + T_\rho)k^\sigma + R^s k^s\right]\underset{\sim}{a}^\beta \tag{3.42}$$

which since ($T_L + T_P$) is now constant is identical in form to that derived for the linear element equation (3.8). In addition setting either $f_1^P = -(T_L + T_P)$ in equation (3.40a) or $f_2^P = (T_L + T_P)$ in equation (3.40b) gives, in view of equation (3.33), that

$$a_2^P - a_1^P + \sigma = 0 \tag{3.43}$$

This simply states that the axial shortening in the constant tension case is given by σ and may be calculated as a second step once the linear bending problem has been solved. It is clear that this constant tension case corresponds to the linear analysis developed in Chapter 2.

3.3.3 Tangent Stiffness Matrix

Merging the inplane and bending forces as given by equations (3.40) and (3.41) into the single element force vector $\underset{\sim}{f}$, equation (3.24), enables the first variation in element forces to be written compactly as

$$\delta f_i = \frac{\partial f_i}{\partial a_m^P}\, \delta a_m^P + \frac{\partial f_i}{\partial a_n^\beta}\, \delta a_n^\beta \quad , \quad i = 1-6 \tag{3.44}$$

where the summation on m is from 1 to 2 and that on n from 1 to 4. Carrying out the differentiations we find

$$\delta \underset{\sim}{f} = \left[k_o + k_\sigma + k_L \right] \delta \underset{\sim}{a} = k_T\, \delta \underset{\sim}{a} \tag{3.45}$$

where following established notation (Zienkiewicz 1977) k_o represents the small displacement elastic stiffness matrix, k_σ is the initial stress or geometric matrix and k_L is the initial displacement or large displacement matrix. Following the partitioning scheme used in section 3.3.1 these matrices are obtained here as

$$k_b = \left[\begin{array}{c|c} EA\,R^{\beta} & 0 \\ \hline 0 & EI\,k^{\beta} + R^{s}k^{s} \end{array}\right] \qquad (3.46a)$$

$$k_\sigma = \left[\begin{array}{c|c} 0 & 0 \\ \hline 0 & T^{r}R^{\sigma} \end{array}\right] \qquad (3.46b)$$

$$k_L = \left[\begin{array}{c|c} 0 & EA\,R_L^{c} \\ \hline Sym & EA\,R_L^{\beta} \end{array}\right] \qquad (3.46c)$$

where the 4 x 4 matrix partitions k^{β}, k^{s} and k^{σ} are as given in section 3.2 for the linear element and

$$k^{\rho} = \frac{1}{Le}\begin{bmatrix} 1 & -1 \\ -1 & 1 \end{bmatrix} \qquad (3.47a)$$

$$k_L^{\beta} = \frac{1}{Le}\begin{bmatrix} b_1 b_1 & b_1 b_2 & b_1 b_3 & b_1 b_4 \\ & b_2 b_2 & b_2 b_3 & b_2 b_4 \\ & & b_3 b_3 & b_3 b_4 \\ Sym & & & b_4 b_4 \end{bmatrix} \qquad (3.47b)$$

$$k_L^c = \frac{1}{Le}\begin{bmatrix} -b_1 & -b_2 & -b_3 & -b_4 \\ b_1 & b_2 & b_3 & b_4 \end{bmatrix} \qquad (3.47c)$$

$$b_i = k_{ij}^{\sigma} a_j^{\beta} \qquad (3.47d)$$

Note that the repeated subscript on the bending displacements in equation (3.47d) implies summation from 1 to 4 and that the 6 x 6 symmetric tangent stiffness matrix k_T defined by equation (3.45) is displacement dependent.

3.3.4 Element Mass Matrix

The mass matrix for the nonlinear beam element is evaluated in a similar manner to that used for the linear element, equation (3.11). Thus the total kinetic energy of the element is

$$T_{KE} = \frac{1}{2}\int_0^{Le} (\rho_s \dot{u}^2 + \rho \dot{v}^2)\, dx \qquad (3.48)$$

where ρ_s and ρ represent respectively mass per length of steel pipe (plus coatings) and mass per length of pipe plus product plus added mass. Using this expression the required mass matrix becomes

$$\left[\begin{array}{c|c} \rho_s m^{\rho} & 0 \\ \hline 0 & \rho m^{\beta} \end{array}\right] \qquad (3.49)$$

where the elements of the 4 x 4 bending partition m^{β} are

as evaluated for the linear beam element, equation (3.12), while the 2 x 2 inplane partition m^{ρ} is given by

$$m_{ij}^{\rho} = \int_{0}^{Le} N_i^{\rho} N_j^{\rho} \, dx \tag{3.50}$$

This matrix is evaluated for reference in Appendix C.

3.3.5 Element Load Vector

Finally assuming that no external axial forces are applied to the free span the element load vector is

$$\underset{\sim}{f} = \begin{bmatrix} \underset{\sim}{f}^{\rho} \\ \underset{\sim}{f}^{B} \end{bmatrix} = \begin{bmatrix} 0 \\ f^{B} \end{bmatrix} \tag{3.51}$$

where the bending partition f^{B} is as evaluated for the linear element, equation (3.15).

3.4 Friction Model

The final section of the complete mathematical model shown in figure 3.2 consists of the two friction elements used to represent the pipe foundation interaction arising from horizontal movement of the pipeline. Considering first figure 3.9a, section AB consists of an infinite pipe on friction foundation subjected to an initial lay tension T_L plus external hydrostatic pressure p_0. As in section 3.3.1 this configuration is used since it represents the pipeline condition shortly after installation. In the following sections the static displacement at the pipe end caused by a change in these initial conditions is calculated using simple static principles. This approach uses only the axial properties of the pipeline which, since

the deflections occurring in the supported lengths may be assumed small, are taken as uncoupled from any transverse bending effects.

3.4.1 Initial Loading Phase

Considering a temperature rise ΔT plus internal pressure p_i the compression force generated in a fully constrained section of pipeline is given by equation (2.14) as

$$P_c = \alpha E A \Delta T - \frac{\nu A p_i D_i}{2t} \tag{3.52}$$

Using this result the condition that the pipe end undergoes zero deflection requires a reduced end load T_R given by equation (2.15) as

$$T_R = T_L - P_c \tag{3.53}$$

Now if the end load is given by $T_R + \Delta T_1$, where ΔT_1 represents the increased tension measured relative to T_R, the end deflection will undergo some nonzero increment Δa_1 as indicated in figure 3.9b. In turn this motion is resisted by friction forces which act over all sections of the pipe which move in a like manner. As in section 2.0.2 these forces are assumed to be of constant intensity μw per length with the result that the tension in the pipeline decreases linearly with distance x from the free end until there is no further relative movement between the pipe and its foundation. At this point the pipe is fully constrained and the axial tension in the system is given by (3.53) above. Now denoting the length over which these friction forces act as L_1 the tension (again measured relative to T_R) in the pipeline section $x \leq L_1$ is given by

$$\Delta T_1(x) = \Delta T_1 - \mu w x \tag{3.54}$$

In addition from equilibrium

$$\Delta T_1 = \mu W L_1 \tag{3.55}$$

so that the end displacement increment Δa_1 is given by

$$\Delta a_1 = \int_0^{L_1} \frac{\Delta T_1(x)}{EA}\, dx = \frac{(\Delta T_1)^2}{2\mu W E A} \tag{3.56}$$

In the above we have tacitly assumed $\Delta T_1 > 0$ [1]. By considering the case $\Delta T_1 < 0$ it is easy to show that the specific result (3.56) above may be replaced by the more general case

$$\Delta a_1 = \frac{\Delta T_1 \,|\Delta T_1|}{2\mu W E A} \tag{3.57}$$

Solving for ΔT_1 gives

$$\Delta T_1 = \operatorname{sgn}(\Delta a_1)\, k_1 \,|\Delta a_1|^{1/2} \tag{3.58}$$

where $\operatorname{sgn}(\Delta a_1)$ indicates the sign of Δa_1 and the constant k_1 is given by

$$k_1 = (2\mu W E A)^{1/2} \tag{3.59}$$

Using these equations and defining initial conditions $a_0^\rho = T_0^\rho = 0$ the total end displacement and corresponding overtension during the initial loading phase may be written respectively as

---

(1) If $\Delta T_1 < 0$ equation (3.55) gives L_1 negative.

$$a^{\rho} = a_0^{\rho} + \Delta a_1 \qquad (3.60a)$$

$$T^{\rho} = T_0^{\rho} + \Delta T_1 \qquad (3.60b)$$

In view of the above it is seen that during this initial loading phase the friction element behaves as a nonlinear softening spring. In addition it is shown in Appendix D that one half of the total work done by the overtension is stored as recoverable strain energy in the pipeline while the other half is lost overcoming the friction forces. As a result the system is also nonconservative and it is anticipated that during unloading a different load-deflection curve to that obtained above will apply. This unloading curve is obtained in the following section.

3.4.2 Unloading and Re-loading Cycles

Consider now the situation where following an initial load increment $\Delta T_1 > 0$ a load reversal $\Delta T_2 < 0$ is applied, figure 3.10. It follows that the pipe end now moves from right to left (i.e. negative increment), a motion resisted by friction forces acting over all sections of the pipe moving in a like manner. As a result the pipeline tension increases with distance x from the free end until a point is reached at which there is no further movement during the current unloading phase 2. At this point, labelled C in figure 3.10, the new "front" generated during the current unloading phase meets the original "front" generated during the initial loading phase and there is consequently no change in tension in the pipeline. As indicated in figure 3.10 the new front moves down through the diagram as the unloading progresses with the result that the length L_2 steadily increases. Equilibrium now gives

$$\Delta T_2 = -2\mu W L_2 \qquad (3.61)$$

The corresponding displacement increment is obtained by integrating the strain increment over L_2 as

$$\Delta a_2 = \int_0^{L_2} \frac{(\Delta T_2 + 2\mu W x)}{EA}\, dx = -\frac{(\Delta T_2)^2}{4\mu W E A} \qquad (3.62)$$

In the above we have assumed $\Delta T_1 > 0$ and $\Delta T_2 < 0$. By considering the alternative case $\Delta T_1 < 0$ and $\Delta T_2 > 0$ it is easy to show that equation (3.62) above may be replaced by the more general result

$$\Delta a_2 = \frac{\Delta T_2 \left| \Delta T_2 \right|}{4\mu W E A} \qquad (3.63)$$

or solving for ΔT_2

$$\Delta T_2 = \mathrm{sgn}(\Delta a_2)\, k_2 \left| \Delta a_2 \right|^{1/2} \qquad (3.64a)$$

$$k_2 = (4\mu W E A)^{1/2} \qquad (3.64b)$$

The total end displacement a^ρ and overtension T^ρ are now given by

$$a^\rho = a_1^\rho + \Delta a_2 \qquad (3.65a)$$

$$T^\rho = T_1^\rho + \Delta T_2 \qquad (3.65b)$$

where a_1^ρ and T_1^ρ represent the corresponding total values at the end of the initial loading phase 1. It is noted that the presence of these terms indicates the system has memory, a feature characteristic of its nonconservative property.

In a similar manner to the above a second load reversal results in total end displacement and overtension given by

$$a^{\rho} = a_2^{\rho} + \Delta a_3 \qquad (3.66a)$$

$$T^{\rho} = T_2^{\rho} + \Delta T_3 \qquad (3.66b)$$

$$\Delta T_3 = \mathrm{sgn}(\Delta a_3) k_2 \left| \Delta a_3 \right|^{1/2} \qquad (3.66c)$$

where a_2^{ρ} and T_2^{ρ} represent the total values at the end of the unloading phase 2. In this case, figure 3.11, a third tension front is generated which as indicated moves up through the diagram as the load is gradually re-applied. It is clear that if during this reloading phase 3 the end load T^{ρ} reaches its previous maxima T_1^{ρ}, the 3rd and 1st fronts coalesce while the 2nd front disappears. At this stage the whole of the 1st front again becomes active and further increase in load follows the load deflection curve for the original loading phase 1 as represented by equations (3.58) to (3.60).

3.4.3 Example Problem

To illustrate the above analysis consider the typical pipeline example used in section 2.5.2 for which the following data applies

Axial Rigidity	EA	= 383OMN
Weight per length	w	= 2.5KNm^{-1}
Coefficient of friction	μ	= 0.6

Using this data the constants k_1 and k_2 given by equations (3.59) and (3.64b) respectively are evaluated as

$$k_1 = 3.390 \text{ MNm}^{-\frac{1}{2}}$$
$$k_2 = 4.794 \text{ MNm}^{-\frac{1}{2}}$$

The pipe is initially subjected to an end load T_R so that the overtension T_0^P and end displacement a_0^P are both zero. An end displacement of 20mm is now applied and then subsequently cycled between 10mm and 20mm. The resulting overtensions are computed in table 3.1 and the results plotted in figure 3.12.

Loading Phase	Δa_i (mm)	ΔT_i (KN)	a^P (mm)	T^P (KN)
1	0	0	0	0
	5	239.7	5	239.7
	10	339.0	10	339.0
	15	415.2	15	415.2
	20	479.4	20	479.4
2	-0	0	20	479.4
	-5	-339.0	15	140.4
	-10	-479.4	10	0
3	0	0	10	0
	5	339.0	15	339.0
	10	479.4	20	479.4

TABLE 3.1

Considering figure 3.12 it is seen that during the initial loading phase 1 the element stiffness is initially infinite but quickly decreases with increased deflection. This basic characteristic of the system is repeated at each load reversal.

3.4.4 Effective Tension

The force-displacement transformations obtained in the above sections have been calculated in terms of the over-tension measured relative to the real tension T_R required for zero end displacement. However it is recalled that both Finite Element models outlined in the preceding sections were formulated in terms of effective tension so that for compatibility a similar transformation is required here. Thus recalling that the overtension T^p is measured relative to the nominal real tension T_R the total effective end tension is given by

$$f^p = T_R + T_p + T^p = T + T^p \qquad (3.67)$$

where T_p represents the hydrostatic pressure term equation (3.32) and T represents as normal the nominal effective tension in the pipeline. Now combining equations (3.58), (3.60), (3.64) and (3.65) the transformed force-displacement equations for loading phase $i \geq 1$ may be written compactly as

$$a^p = a^p_{i-1} + \Delta a_i \qquad (3.68a)$$

$$f^p = f^p_{i-1} + \mathrm{sgn}(\Delta a_i) k_i |\Delta a_i| \qquad (3.68b)$$

$$k_i = \begin{cases} (2\mu W E A)^{1/2}, & i = 1 \\ (4\mu W E A)^{1/2}, & i \geq 2 \end{cases} \qquad (3.68c)$$

where a^p_{i-1} and f^p_{i-1} represent respectively the values of a^p and f^p at the end of load phase $i-1$ and the initial conditions are $a^p_0 = 0$, $f^p_0 = T$. As outlined in section 3.5 these force-displacement transformations are

used, together with those for the linear and nonlinear beam elements, to assemble a set of nonlinear system equilibrium equations.

3.4.5 Tangent Stiffness

Differentiating equations (3.68) enables the first variation in element forces to be written as

$$\delta f^{\rho} = \frac{\partial f^{\rho}}{\partial a^{\rho}} \delta a^{\rho} = k_T^{\rho}(\Delta a_i)\, \delta a^{\rho} \qquad (3.69)$$

where the tangent stiffness term k_T^{ρ} is given by

$$k_T^{\rho}(\Delta a_i) = \frac{k_i}{2\left|\Delta a_i\right|^{1/2}} \qquad (3.70)$$

During the solution stage this term is calculated for each friction element and assembled into the global tangent stiffness matrix at the appropriate diagonal location. One problem encountered with this procedure, however, occurs at the start of each new element loading phase when the displacement increment Δa_i is zero. In this case the tangent stiffness calculated by equation (3.70) becomes infinite and so for numerical reasons must be replaced with a large but finite value(1). This is done here by specifying to the program a minimum value Δa_{min} (typically 10^{-6}m) to use in equation (3.70) above. Using this value the corresponding effective tension during the current element loading phase is given by equation (3.68b) as

---

(1) An alternative is to fix the displacement to zero when solving the assembled equations but in this case the pipe end never moves.

$$f^{\rho} = f_{i-1}^{\rho} + k_i \Delta a_{min}^{1/2} \qquad (3.71)$$

Now for $|\Delta a_i| < \Delta a_{min}$ the force-displacement curve, figure 3.13, is approximated by the straight line segment shown so that the tangent stiffness term (3.70) is replaced by

$$k_T^{\rho} = \frac{k_i}{\Delta a_{min}^{1/2}} \qquad (3.72)$$

Typically this expression is used on the first iteration of each new element loading phase after which the displacement increment Δa_i is sufficiently large to enable equation (3.70) to be used.

3.4.6 Inertia Forces

In the preceding sections the friction element force-displacement transformations have been derived using simple static considerations. In the dynamic case axial inertia forces will also occur in the pipeline due to its horizontal accelerations. In this thesis such inertia forces are assumed small in comparison to the friction forces and are consequently neglected. As a result the above transformations may be considered valid in both static and dynamic cases with the element mass matrix in the later case being taken as null.

3.4.7 Transformation from Local to Global Coordinates

As a consequence of the simple model geometry, figure 3.2, the alignment between local element directions and the corresponding global coordinate directions has, for all elements considered so far, been exact. As a consequence no transformations are required to convert local element quantities into the global coordinate directions prior to

assembly. One exception to this situation occurs with the friction element CD , figure 3.14a, where the element displacement a^ρ as used above is in the opposite direction to the corresponding global freedom u_c . However since friction element behaviour in compression is identical to its behaviour in tension the element quantities for this element may be reversed, figure 3.14b, provided the initial conditions are taken as

$$a_o^\rho = 0 \qquad (3.73a)$$

$$f_o^\rho = -T \qquad (3.73b)$$

By this means all elements in the model may be considered with local element directions aligned with global.

3.4.8 Calculation of Tension for Supported Sections

As noted in the model overview section 3.1 the friction elements are used to calculate the effective tension force T^F for use in the linear element equations (3.8) and (3.9). Strictly speaking this value should be calculated by consideration of the various tension distribution diagrams, figures 3.9 to 3.11. However in deciding a practical modelling procedure to adopt here the following points are noted

a) The programming logic of the above "exact" procedure is complicated

b) The effect of tension on the stiffness of supported sections of pipe is small

c) The lengths l_1 , l_2 etc. over which the friction forces act are usually large, on the order of 100m. In contrast (see section 3.8) the length of supported sections AB and CD used in the Finite Element model is 30m. It follows that the variation in tension over these sections is relatively small.

With these points in mind it seems reasonable to take a constant tension distribution in each of the supported sections and set

$$T^F = \begin{cases} f_B^p & \text{Element in section AB .} \\ -f_C^p & \text{Element in section CD} \end{cases}$$

where f_B^p and f_C^p represent respectively the generalised element forces in the friction elements AB and CD. It is noted that the minus sign arises for section CD since as previously described in section 3.4.7 the local element direction has been reversed for this element.

3.5 Nonlinear Static Analysis

Referring to figure 3.2 the assembled displacement vector for the complete model is written as

$$\underset{\sim}{\alpha}^T = \{\alpha_i\}^T = \{v_A\ \theta_A \cdots u_B\ v_B\ \theta_B \cdots u_C\ v_C\ \theta_C \cdots \cdots v_D\ \theta_D\} \qquad (3.74)$$

The corresponding external load vector may be written symbolically as

$$\underset{\sim}{P} = \{P_i\} = \sum_{e_L} \underset{\sim}{P}^B + \sum_{e_N} \underset{\sim}{P} \qquad (3.75)$$

where the summations are over the linear elements e_L and nonlinear elements e_N respectively and P^B and P represent the linear and nonlinear element external load vectors. In addition the difference in vector lengths is accounted for via the standard assembly procedure of

relating each element freedom to its corresponding location in the assembled displacement vector $\underset{\sim}{\alpha}$. In a similar manner the internal element forces may be assembled as

$$\underset{\sim}{F}(\underset{\sim}{\alpha}) = \{F_i\} = \sum_{e_F}^{1} f^{\rho} + \sum_{e_L}^{1} \underset{\sim}{f}^{\beta} + \sum_{e_N}^{1} \underset{\sim}{f} \qquad (3.76)$$

where e_F represents the friction elements and f^{ρ} , $\underset{\sim}{f}^{\beta}$ and $\underset{\sim}{f}$ represent the element internal force vectors derived in the above sections. Equilibrium now requires

$$\underset{\sim}{\Psi}(\underset{\sim}{\alpha}) = \underset{\sim}{F}(\underset{\sim}{\alpha}) - \underset{\sim}{P} = 0 \qquad (3.77)$$

To solve this equation using the iterative Newton-Raphson method consider the following Taylor series expansion about $\underset{\sim}{\alpha}$

$$\underset{\sim}{\Psi}(\underset{\sim}{\alpha}+\delta\underset{\sim}{\alpha}) = \underset{\sim}{\Psi}(\underset{\sim}{\alpha}) + \left[K_T(\underset{\sim}{\alpha})\right]\delta\underset{\sim}{\alpha} \qquad (3.78)$$

where the global tangent matrix is given by

$$K_{T_{ij}}(\underset{\sim}{\alpha}) = \left.\frac{\partial \Psi_i}{\partial \alpha_j}\right|_{\underset{\sim}{\alpha}} \qquad (3.79)$$

Thus taking $\underset{\sim}{\alpha}+\delta\underset{\sim}{\alpha}$ as an improved solution from some initial trial value $\underset{\sim}{\alpha}$ we may write

$$\delta\underset{\sim}{\Psi} = \left[K_T(\underset{\sim}{\alpha})\right]\delta\underset{\sim}{\alpha} = -\underset{\sim}{\Psi}(\underset{\sim}{\alpha}) = \underset{\sim}{P} - \underset{\sim}{F}(\underset{\sim}{\alpha}) \qquad (3.80)$$

and so solve for the required displacement increment $\delta\underset{\sim}{\alpha}$. To do this it is first necessary to assemble the global tangent stiffness matrix $K_T(\underset{\sim}{\alpha})$. Thus using equations (3.76) and (3.77) and noting that $\underset{\sim}{P}$ is constant we may

write the first variation of $\underset{\sim}{\Psi}$ as

$$\delta\underset{\sim}{\Psi} = \delta\underset{\sim}{F} = \sum_{e_F}^{I} \delta f^{\rho} + \sum_{e_L}^{I} \delta\underset{\sim}{f}^{\beta} + \sum_{e_N}^{I} \delta\underset{\sim}{f} \qquad (3.81)$$

Using the element incremental force-displacement equations (3.9), (3.45) and (3.69) this becomes

$$\delta\Psi = \sum_{e_F}^{I} k_T^{\rho} \delta a^{\rho} + \sum_{e_L}^{I} k_T^{\beta} \delta\underset{\sim}{a}^{\beta} + \sum_{e_N}^{I} k_T \delta\underset{\sim}{a}$$

$$= \left(\sum_{e_F}^{I} k_T^{\rho} + \sum_{e_L}^{I} k_T^{\beta} + \sum_{e_N}^{I} k_T \right) \delta\underset{\sim}{\alpha} \qquad (3.82)$$

Thus comparing equations (3.80) and (3.82) the assembled tangent stiffness matrix may be written symbolically as

$$K_T(\underset{\sim}{\alpha}) = \sum_{e_F}^{I} k_T^{\rho} + \sum_{e_L}^{I} k_T^{\beta} + \sum_{e_N}^{I} k_T \qquad (3.83)$$

Here note that as above the difference in size between the various matrices is accounted for by relating each pair of element freedoms to the corresponding freedoms in the assembled displacement vector $\underset{\sim}{\alpha}$. Using this matrix in equation (3.80) leads to an improved solution $\underset{\sim}{\alpha} + \delta\underset{\sim}{\alpha}$ and the whole process may be repeated, figure 3.15a, until convergence is achieved. A variation on this basic iterative approach is to employ a modified Newton method, figure 3.15b, in which the tangent matrix is only updated on specific iterations. In practice both these methods can lead to extremely accurate solutions provided the load step is not too large so as to cause convergence problems. In this case an alternative incremental approach, figure 3.16a,

may be used with the load applied gradually in a series of small steps. This method effectively follows the load path on the structure and has the advantage of providing a solution to virtually any problem. However as indicated in the figure the computed solution tends to slowly drift away from the true solution leading to the possibility of large errors. To overcome this problem the two methods outlined above may be combined in an incremental with equilibrium iterations procedure, figure 3.16b. Here the load is applied incrementally with the Newton-Raphson iterative procedure, equation (3.80), used at the end of each load step to ensure accuracy. In all of these schemes it is necessary at the start of the solution to assemble the tangent stiffness, equation (3.83), about some initial configuration usually taken as $\underset{\sim}{\alpha} = 0$. However for the pipe span problem under consideration here this leads in many cases to a singular matrix since the initial effective tension T is less than the linear elastic buckling load $-P_{cr}$ as derived in section 2.3. To overcome this difficulty a modified incremental procedure is used here in which for the first "load" step the free span is initially supported along its complete length, figure 3.17. As a consequence this initial step models the pipeline prior to the span formation with a constant vertical displacement along all sections of the pipeline given by

$$v = -W/R^s \tag{3.84}$$

It is noted that this displacement produces no corresponding axial or horizontal motion with the result that the effective tension in the pipeline remains constant and equal to T. Subsequent "load" steps are now invoked by removing the elastic foundation support from successive elements adjacent to the span centre, figure 3.17. By this means the load path of the structure is followed not by incrementing the external load W (this load is applied in full on the first

load step) but instead by increasing the free span length ℓ. During this process the following points apply

a) During each load step accuracy is ensured by applying a series of equilibrium iterations until

$$\frac{\| \delta \underset{\sim}{\alpha} \|}{\| \underset{\sim}{\alpha} \|} < \varepsilon \qquad (3.85)$$

where $\| \quad \|$ indicates the Euclidian Norm and ε is a small number taken here as 10^{-12}.

b) As the span length ℓ increases the overtension T^p generated in each of the friction elements increases monotonically so that only element loading phase 1 is involved at this stage.

c) Strictly speaking the friction elements should be moved back at each load step in line with the span formation, figure 3.17. In practice this situation is ignored and instead the friction elements are located for all load steps at the final span end points B and C. This approach ignores the friction forces between pipe section BC and its foundation prior to the process of soil erosion. However since by definition such forces are absent in the final configuration the only effect is to produce a slightly modified load path but with identical final configuration.

A flow chart of the above solution process is given for reference in figure 3.18.

3.6 Eigenvalue Analysis

Once the nonlinear static analysis has converged to some value say $\underset{\sim}{\alpha}_s$ the equations of motion for small amplitude dynamic vibration about the static equilibrium position may be written as

$$[M]\,\delta\ddot{\underset{\sim}{\alpha}} + \delta\underset{\sim}{F} = 0 \qquad (3.86)$$

where $[M]$ represents the assembled mass matrix and $\delta\underset{\sim}{F}$ is the increment in internal forces corresponding to $\delta\underset{\sim}{\alpha}$. Here $[M]$ is obtained by the same assembly procedure as used for the tangent stiffness written symbolically as

$$[M] = \sum_{e_L} m^b + \sum_{e_N} m \qquad (3.87)$$

with m^b and m representing the appropriate element mass matrices. Now substituting equation (3.81) into equation (3.86) above

$$[M]\,\delta\ddot{\underset{\sim}{\alpha}} + [K_T(\underset{\sim}{\alpha}_s)]\,\delta\underset{\sim}{\alpha} = 0 \qquad (3.88)$$

which on setting $\delta\underset{\sim}{\alpha} = \underset{\sim}{\phi}\sin\omega t$ for free vibration in a single mode becomes

$$[-\omega^2 M + K_T(\underset{\sim}{\alpha}_s)]\,\underset{\sim}{\phi} = 0 \qquad (3.89)$$

This equation is now in standard form and may be solved for the eigenpairs (ω_i, $\underset{\sim}{\phi}_i$). It is noted that the assembled tangent stiffness used in equation (3.89) is identical to that used in the last iteration of the static analysis and consequently contains stiffness terms for the two friction

elements in the diagonal locations corresponding to the freedoms u_B and u_C . At this stage both these elements are in their initial loading phase since as discussed in section 3.5 above the simple loading considered here leads to a monotonic increase in the overtension T^P . Under these conditions the eigenvalue results obtained are described in this thesis as having "constant end stiffness". However as discussed in section 3.4.2 the friction elements follow a hysterisis loading path under cyclic load with the conclusion that it appears more reasonable to consider the freedoms u_B and u_C as fixed during any small amplitude dynamic motion. In this case equation (3.88) becomes

$$\left[M^c\right]\delta\underset{\sim}{\alpha}^c + \left[k_T^c(\underset{\sim}{\alpha}_s)\right]\delta\underset{\sim}{\alpha}^c = 0 \qquad (3.90)$$

where following standard Finite element procedures the constrained quantities M^c , k_T^c and $\delta\underset{\sim}{\alpha}^c$ are obtained from the corresponding unconstrained quantities by deleting all rows and columns pertaining to the constrained displacements u_B and u_C . Now setting $\delta\underset{\sim}{\alpha}^c = \underset{\sim}{\phi}^c \sin\omega t$ the modified eigenproblem becomes

$$\left[-\omega^2 M^c + k_T^c(\underset{\sim}{\alpha}_s)\right]\underset{\sim}{\phi}^c = 0 \qquad (3.91)$$

As discussed in section 3.9 the effect of these constraints is to cause a significant shift in frequencies for the symmetric modes of vibration.

3.7 Parametric Study

At this stage it is useful to review the basic parameters used in the FEM developed above. Thus with reference to equation (2.50) these include the following variables as used in the linear analysis of Chapter 2.

Span frequency	ω
Pipeline mass per length	ρ
Flexural rigidity	EI
Nominal effective tension	T
Soil stiffness	R^S
Span length	L

In addition as a result of the friction effects included in this chapter we also have

Coefficient of friction	μ
Axial rigidity	EA
Pipe effective weight per length	W

It is now possible to nondimensionalise the Finite Element equations developed in this chapter by using the original nondimensional parameters

$$\gamma = \frac{R^S L^4}{EI}$$

$$\delta = \frac{TL^2}{EI}$$

$$R = \omega/\bar{\omega}$$

together with the additional parameters

$$\eta = \frac{WL^3}{EI}$$

$$\lambda = \frac{EAL^2}{EI}$$

These 5 parameters together with the (nondimensional) coefficient of friction μ now comprise a reduced set of 6 independent nondimensional parameters. However from a

practical point of view such a reduction is of little help since a full parametric study in terms of 6 independent parameters still presents many difficulties not least of which involves the presentation of results. For this reason, and considering also the increased abstraction associated with the use of nondimensional parameters, it is considered here that the above nondimensional scheme offers little advantage and the Finite Element equations are consequently left in their original form.

With the above points in mind the model developed in this chapter is applied to three different pipe designs as tabulated in table 3.2. These designs are selected here since they are considered to cover most of the common pipe sizes currently in use

PIPE NO	D_o mm	D_i mm	t_A mm	t_c mm	D mm	T_L KN
1	150	130	6	40	242	100
2	500	465	6	60	632	750
3	1000	950	6	90	1192	1000

Steel Pipe External Daimater D_o
Steel Pipe Internal Diameter D_i
Asphaltic coating (thickness) t_A
Concrete coating (thickness) t_c
Overall pipe Diameter D
Lay tension (real) T_L

Table 3.2 Pipeline Designs

For each of these basic designs the operating conditions are taken as

Temperature rise ΔT = 10°C
Internal pressure p_i = 15 MN/m^2
External pressure p_o = 1 MN/mm^2

In addition other basic parameters, applicable to all three designs, are taken as

Young's Modulus for steel E = 2 x 10^{11} N/m^2
Coeff of expansion for steel α = 12 x 10^{-6} /°C
Density of steel ρ_{ST} = 7840 kg/m^3
Density of Asphalt ρ_A = 1300 kg/m^3
Density of concrete ρ_C = 2500 kg/m^3
Density of oil ρ_O = 800 kg/m^3
Density of seawater ρ_W = 1024 kg/m^3
Added mass coefficient C_A = 1.0
Soil stiffness k^s = 2.5 MN/m^2

Using this data the derived parameters for each pipeline are as tabulated in table 3.3

PIPE	EA MN	EI MNm^2	T KN	W KN/m	ρ kg/m
1	0.88 x 10^3	2.17	-68	0.65	160
2	5.31 x 10^3	155	-710	3.0	950
3	15.3 x 10^3	1.82 x 10^3	-4.3 x 10^3	8.1	3110

Table 3.3 : Derived Parameters

In the following sections the static deflection and frequencies occurring in each of these pipelines is investigated in terms of the span length L and coefficient of friction μ . Thus the important aspects of system behaviour resulting from increased span length L are established under differing degrees of nonlinearity as measured by μ .

3.8 Design and verification of FEM

Considering again the Finite Element model, figure 3.2, it is necessary to select a reasonable length for the supported sections AB and CD of the pipeline. Thus using equation (2.101)the damping length may be approximated by

$$L_D = \frac{2\pi L}{(2\gamma^{1/2})^{1/2}} \qquad (3.92)$$

where using the notation of this chapter

$$\gamma = \frac{\rho^S L^4}{EI} \qquad (3.93)$$

Substituting equation (3.93) into (3.92) gives

$$L_D = \pi \left(\frac{4EI}{\rho^S}\right)^{1/4} \qquad (3.94)$$

which taking EI = 1820 MNm^2 for pipe 3 and ρ^S = 2.5 MN/m^2 gives L_D = 23m. With this result in mind the supported sections AB and CD are taken of length 30m.

Considering next the number of elements to use figure 3.19 shows pipe 2 frequencies for a 60m span against the number of elements used in each of the three sections AB, BC and CD. In this test μ = 0 and the end freedoms u_B and u_C are taken as unconstrained as in equation (3.89). As discussed in section 3.3.2 these conditions lead to the linear results of Chapter 2 as indicated by the dotted lines in the figure. For each of the first four modes considered it is noted that the FEM results converge rapidly with increasing elements to a value slightly lower than the exact result. This situation is unusual since in most FEM applications the discretisation process leads

to increased stiffness and, particularly for the higher modes, higher frequencies. In this case the loss of stiffness (i.e. frequency) is associated with the truncated support sections AB and CD, a condition which appears to cancel the normal discretisation errors.

Next figure 3.20 shows results for the same span with μ = 1.0 and the end freedoms u_B and u_C constrained for the eigenvalue analysis. It is seen that the convergence rates are similar to those for the linear case above with acceptable results being obtained with 10 elements per section. In this case the complete model, figure 3.2, contains a total of 73 dof and may be conveniently run in time sharing on the CIT VAX 782 computer. For this reason the value of 10 elements per section is considered to provide a reasonable balance between accuracy and economy and all results presented in the following section are based on this level of discretisation.

3.9 Results and Discussion

In this section the three typical pipeline designs described above are tested for a range of span lengths up to 100m and under the following levels of friction

Case No	Coeff. of Friction μ
1	0.0
2	0.1
3	0.3
4	1.0
5	3.0
6	10.0

These values are selected since they enable a comparison to be made between the linear (i.e. μ = 0.0) results and the nonlinear case with μ varied by an order of magnitude

either side of unity.

3.9.1 Pipe 1 Results

Pipe 1 centre deflection is shown in figure 3.21 for the various friction levels tabulated above. It is seen that for μ = 0.0 the centre deflection increases without limit as the span length L approaches some critical value L_{CR} defined using equation (2.86) as

$$L_{CR} = \left(\delta_{P_{CR}} \frac{EI}{P_{CR}} \right)^{1/2} \tag{3.95}$$

Thus setting $P_{CR} = -T$ =68KN (see table 3.3) and using a simple iterative scheme on figure 2.7 we find L_{CR} = 34m as indicated by the dotted line in figure 3.21. It follows that for the linear case μ = 0 span lengths in excess of 30m are prohibited since the excessive static deflections result in the pipe touching down along the bottom of the depression. On the other hand for $\mu > 0$ this unlimited increase in deflection after L = 30m no longer occurs and instead the centre deflection increases more or less linearly with span length L with an overall stiffness dependent on μ . For example with μ = 1.0 the centre deflection for a 100m span is limited to approximately 3m with the conclusion that in practice such long spans may readily occur. The physical effect causing this reduced deflection is the rapid increase in sag tension as shown in figure 3.22. For example with μ = 1.0 the variable effective tension T^V is positive for $L >$ 25m and at L = 100m has increased to some 250KN. The corresponding value of the nondimensional tension parameter is thus

$$\delta^V = \frac{T^V L^2}{EI} = \frac{250 \times 10^3 \times 100^2}{2.17 \times 10^6} = 1150 \tag{3.96}$$

which, following the discussion of section 2.4, indicates a generalised stiffness due to tension some 30 times that due to bending[1]. The length L_1 along each support section over which this sag tension acts is shown in figure 3.23. It is seen that the results now show a large dependency on μ and indicate that tension coupling may occur between spans separated by several hundreds of metres. It is noted in retrospect that the coupling of spans discussed in section 2.5 is due to bending action only and, due to the short damping lengths involved, will be of secondary importance to the tension coupling under consideration here.

Next considering span frequencies, figure 3.24 shows the first four modal frequencies corresponding to the case $\mu = 0.0$. Apart from the small modelling errors discussed in section 3.8 these results are identical to those given by the linear theory of Chapter 2 and show a rapid decrease in frequency as the span length approaches the critical value $L_{CR} = 34m$. The frequencies shown on this and other figures may be compared to the frequency of vortex shedding from a fixed cylinder given by equation (1.10) as

$$f_s = \frac{S V}{D} \qquad (3.97)$$

Now setting $f_s = f_n$ for resonance, $S = 0.2$ as typical, and solving for the free stream velocity V we find

---

(1) This stiffness factor is approximate since the linear analysis of Chapter 2 does not include stiffening effects due to initial geometry. Such effects are included in the present FEM via the initial displacement matrix, k_L, equation (3.46c).

$$V = 5Df_n \tag{3.98}$$

This expression may be used to rescale the frequency axis as shown on the right hand side of figure 3.24. By this means a useful indicator for the stability of the span at any given current level is obtained and, in addition, the rescaled axis provides a convenient means of comparing results between different pipe designs.

The effect of introducing a modest level of friction, μ = 0.1, into the system is shown in figure 3.25a. It is seen that the rapid decrease in frequency occurring in the μ = 0 case is now arrested as the sag tension builds up in the free span. In addition the normally wide spacing of modal frequencies becomes much reduced for L > 60m leading to the possibility of complicated mixed mode response. The corresponding vertical and horizontal displacements for each of these four modes are shown in figure 3.26a for the case L = 100m.

Considering the vertical component these modes may be classified as first symmetric, first antisymmetric, second symmetric and second antisymmetric. Note that the end vertical displacement for these curves is slightly different from zero due to the presence of the elastic foundation (not shown) on either side of the free span.

Next considering the horizontal components the symmetric nodes are seen to exhibit zero motion at mid span with the first of these requiring a large cyclic end motion. Such motion is allowed to occur at this stage since the axial stiffness seen by each end of the span is equal to the friction element tangent stiffness referred to the static equilibrium configuration. On the other hand for the antisymmetric modes the centre section of the

span rocks from left to right with little or no end pull in motion.

The effect on pipe span frequencies of constraining the end axial displacements u_B and u_C is shown in figure 3.25b. In this case the antisymmetric modes are virtually unaffected while each of the symmetric modes now passes through a cross over point at approximately L = 22m and L = 33m. This rapid change in frequency is associated with increased static deflection or sag and is well documented in flat-sag suspended cable theory (Irvine 1981, Rega 1984). The corresponding mode shapes for the case L = 100m are shown in figure 3.26b while the change in form of the first symmetric mode as it passes through its cross over point is illustrated in figure 3.27.

Figure 3.28b shows the effect on frequency of increasing the level of friction to μ = 0.3. In this case the reduced centre deflection causes the cross over point for the second symmetric mode to be delayed until L = 60m while the cross over point for the first symmetric mode appears little affected. Further increase in friction, as illustrated by figures 3.29 to 3.31, now slowly delays the cross over point for the first symmetric mode while the cross over point for the second symmetric mode occurs, if at all, for span lengths in excess of 100m.

3.9.2 Pipe 2 and 3 Results

The results for pipes 2 and 3 are given in figures 3.32 to 3.41 and 3.42 to 3.51 respectively and show similar characteristics to those outlined above for pipe 1. To aid comparison table 3.4 summarises some of the main results for the cases μ = 1.0 with L = 50, 100m. It is seen that for L = 100m the value of δ^V for pipe 2 is 51 indicating a rough balance between bending and tension stiffness. In contrast the corresponding value for pipe 3 is δ^V = -5 indicating a slight loss of stiffness due to

the residual compression remaining in the system. However despite these differences the deformed geometry, as measured by the centre deflection $v_{1/2}$ and overtension length L_1 , is remarkably similar for all three pipe designs. This fact is probably associated with the occurrence of the effective weight per length W in the friction element stiffness terms derived in section 3.4. This close similarity also applies to the minimum frequency f_{min} (u_B , u_C constrained) occurring in the deformed span. However rescaling these frequencies using equation (3.98) indicates that as a result of increased pipe diameters the larger pipes are considerably more stable against vortex induced oscillations.

PARAMETER	L = 50m			L = 100m		
	PIPE 1	PIPE 2	PIPE 3	PIPE 1	PIPE 2	PIPE 3
D_{mm}	242	632	1192			
T kN	-68	-710	-4300			
L_{cr} m	34	87	122			
T^v kN	122	-250	-3940	252	790	-900
L_1 m	290	150	45	500	500	420
δ^v	140	-4.0	-5.4	1160	51	-4.9
$v_{1/2}$ m	1.3	0.66	0.27	3.0	2.8	2.4
f_{min} Hz	0.70	0.69	0.59	0.42	0.44	0.49
V m/sec	0.85	2.2	3.5	0.51	1.4	2.9

Table 3.4

Comparison of main results for μ = 1.0 and L = 50, 100 m

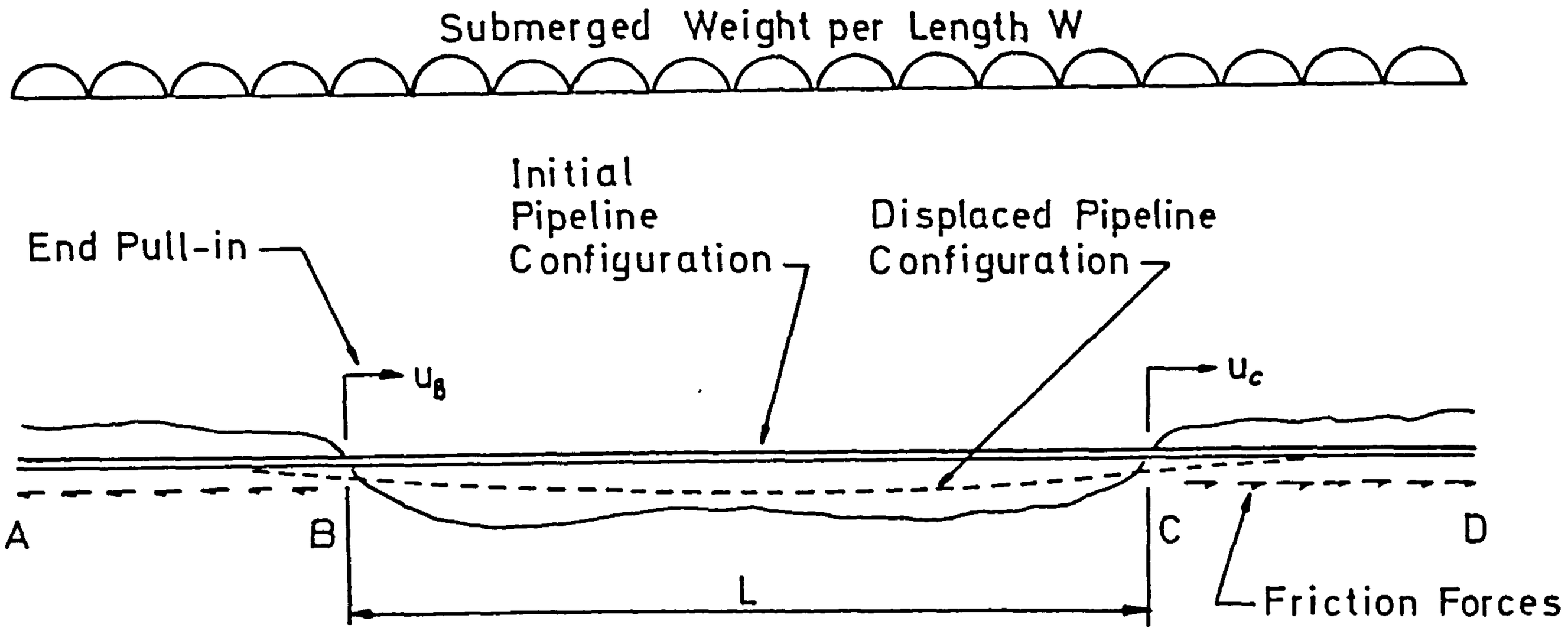

FIG 3.1 Pipe Span Static Deflections

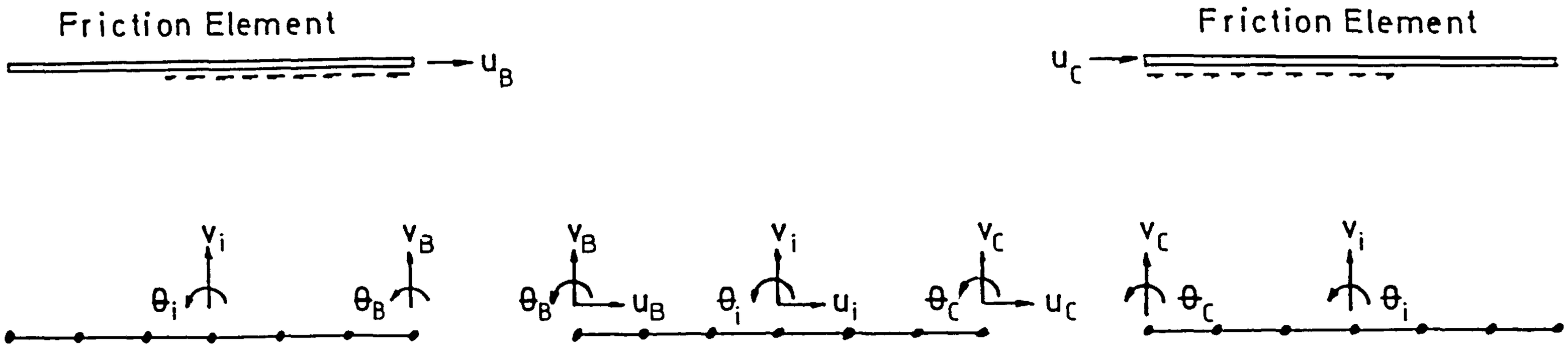

FIG 3.2 Finite Element Model

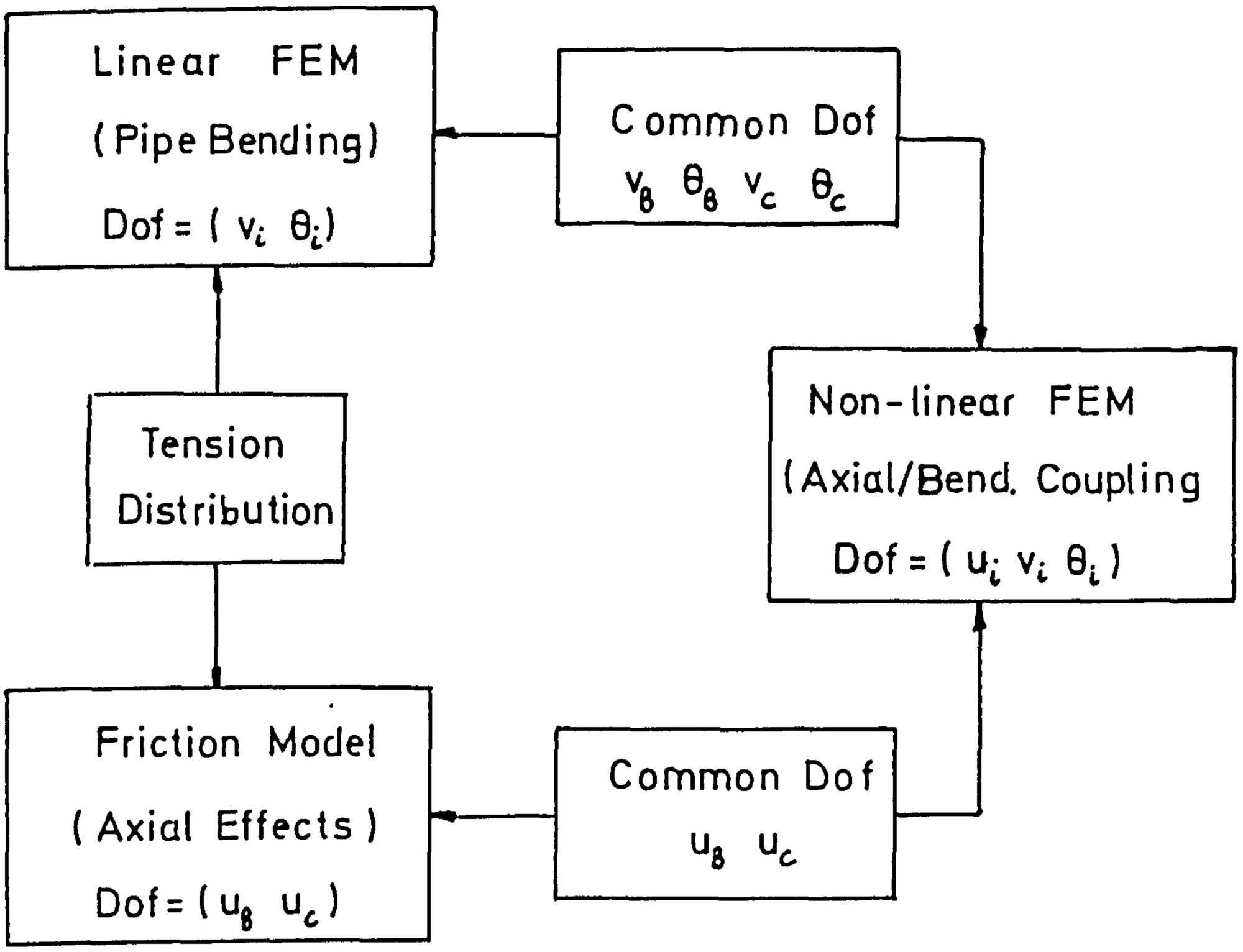

FIG 3.3 Coupling Between Sub-models

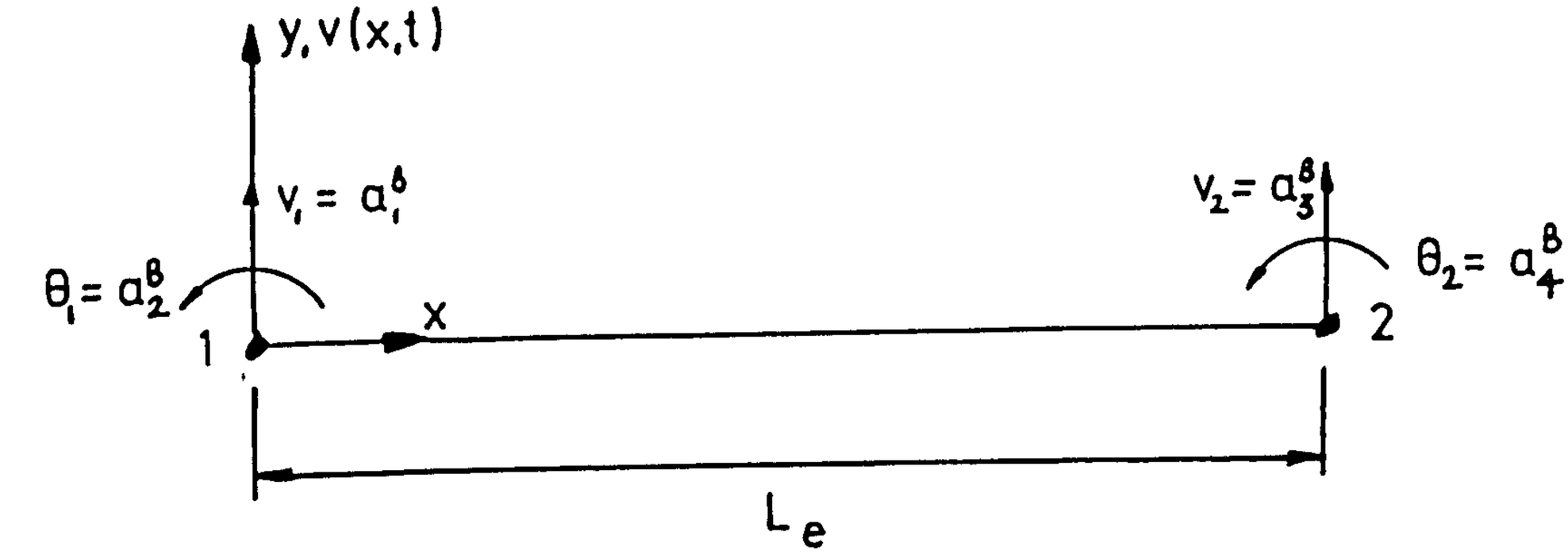

a) Element Displacements

b) Element Forces

FIG 3.4 Linear Beam Element

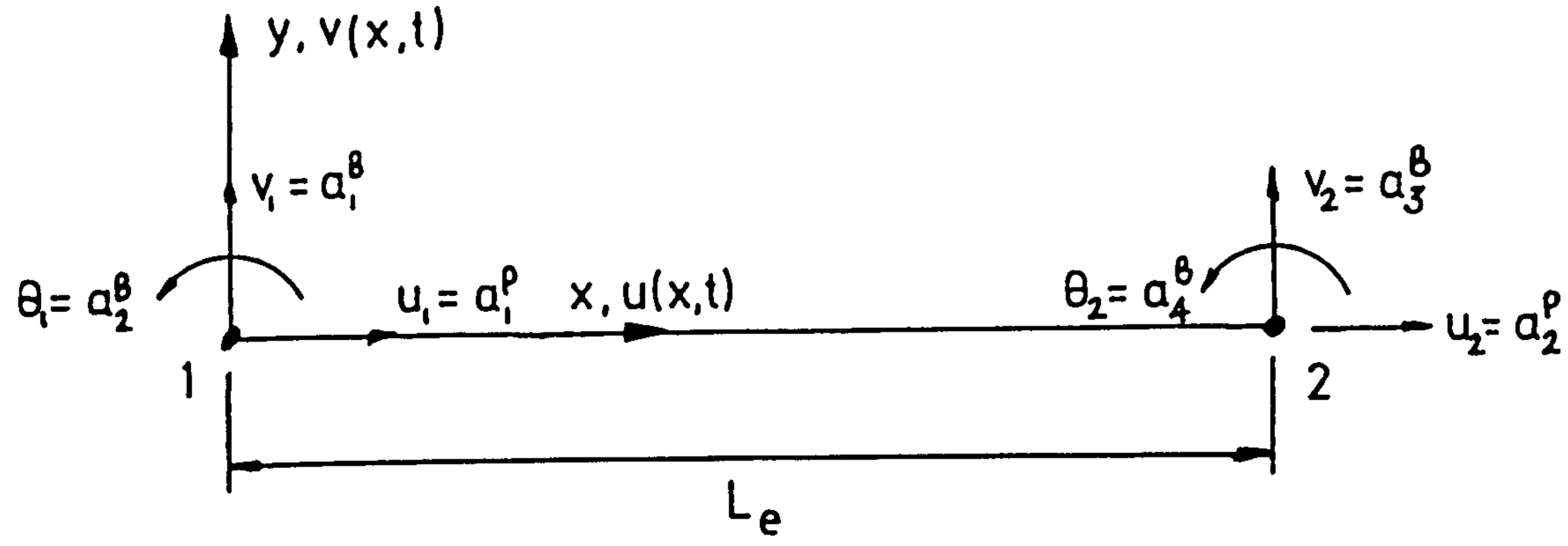

a) Element Displacements

b) Element Forces

FIG 3.5 Non-linear Beam Element

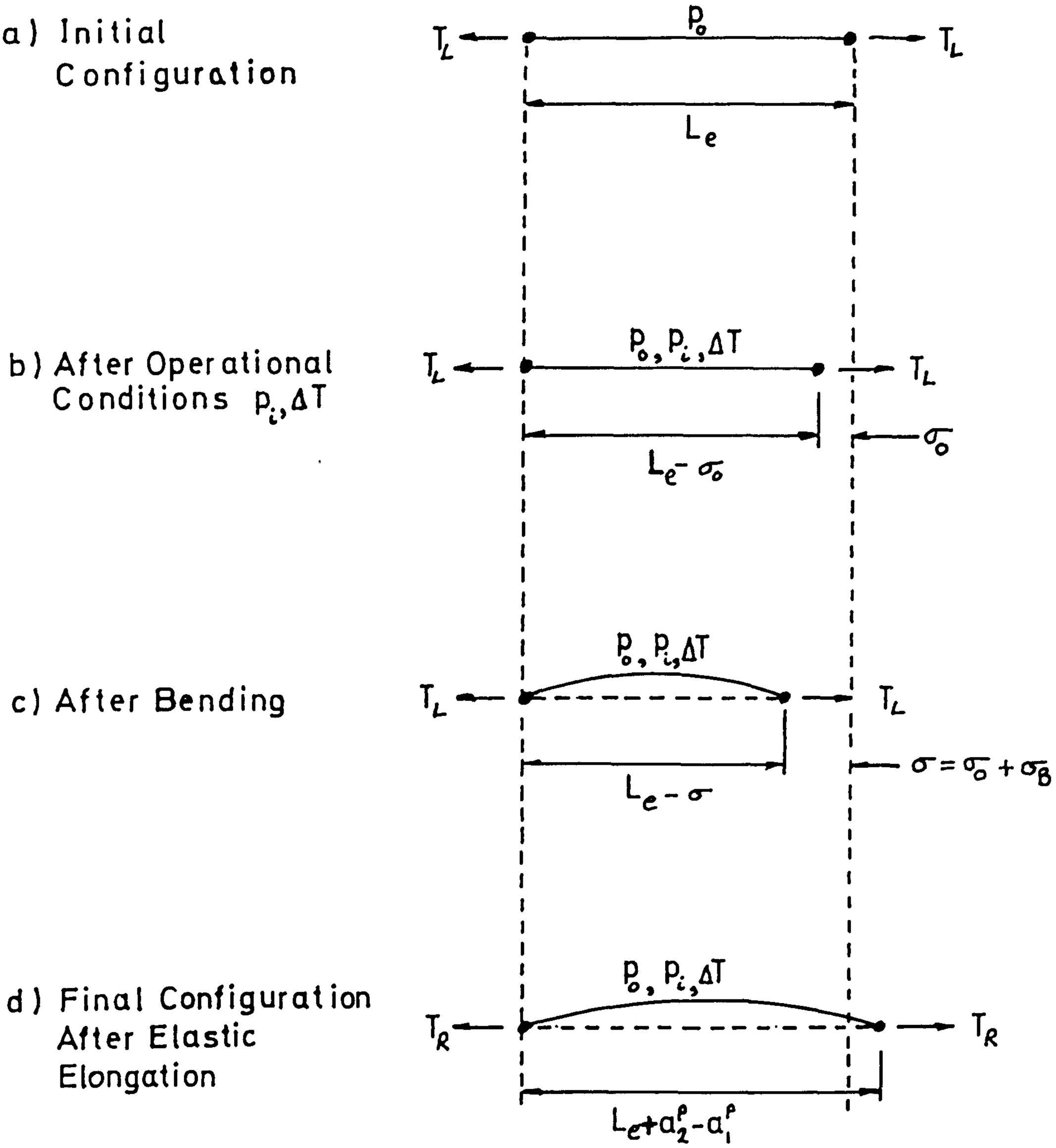

FIG 3.6 Non-linear Beam Element Deformations

a) Real Tension

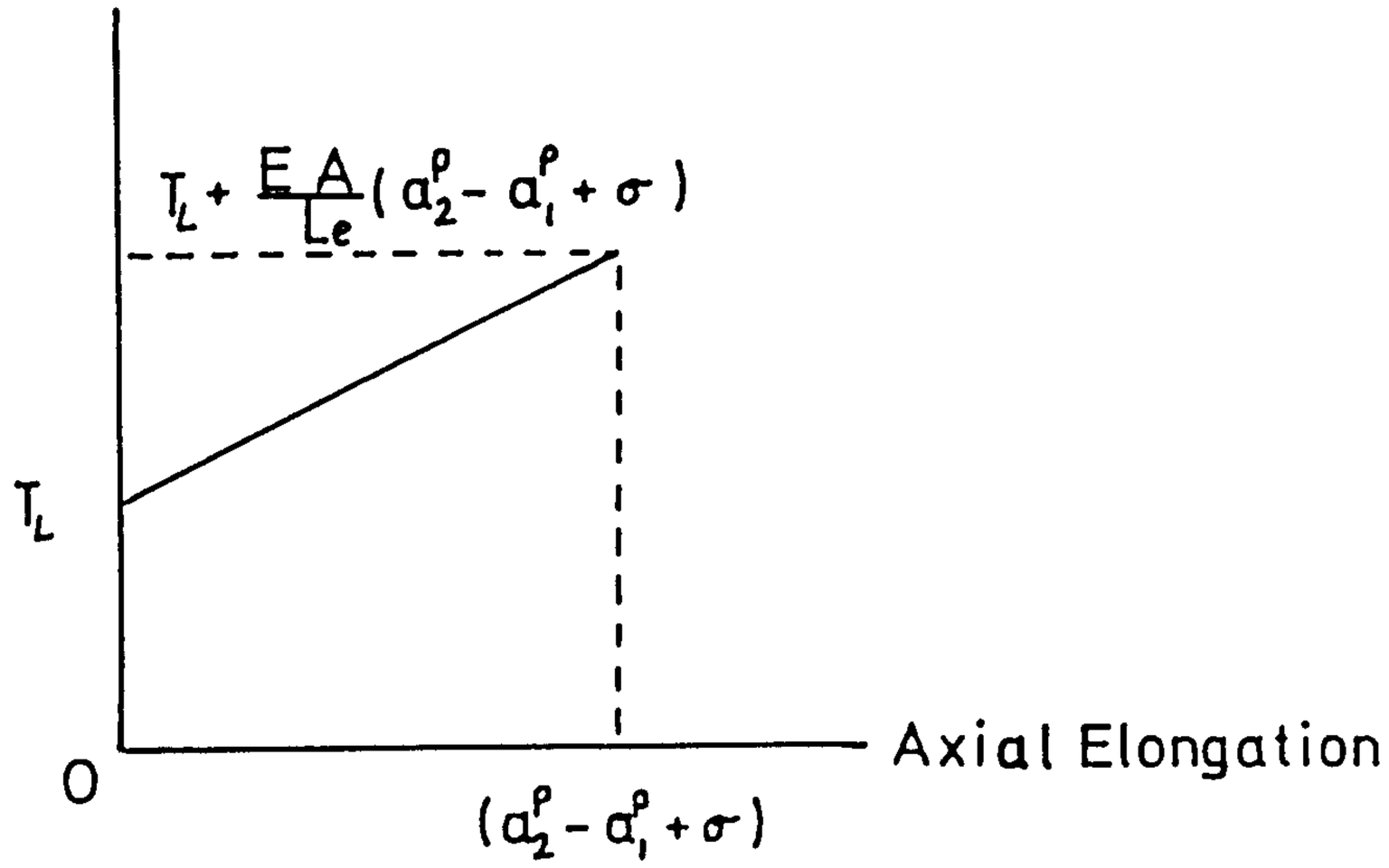

b) Effective Tension

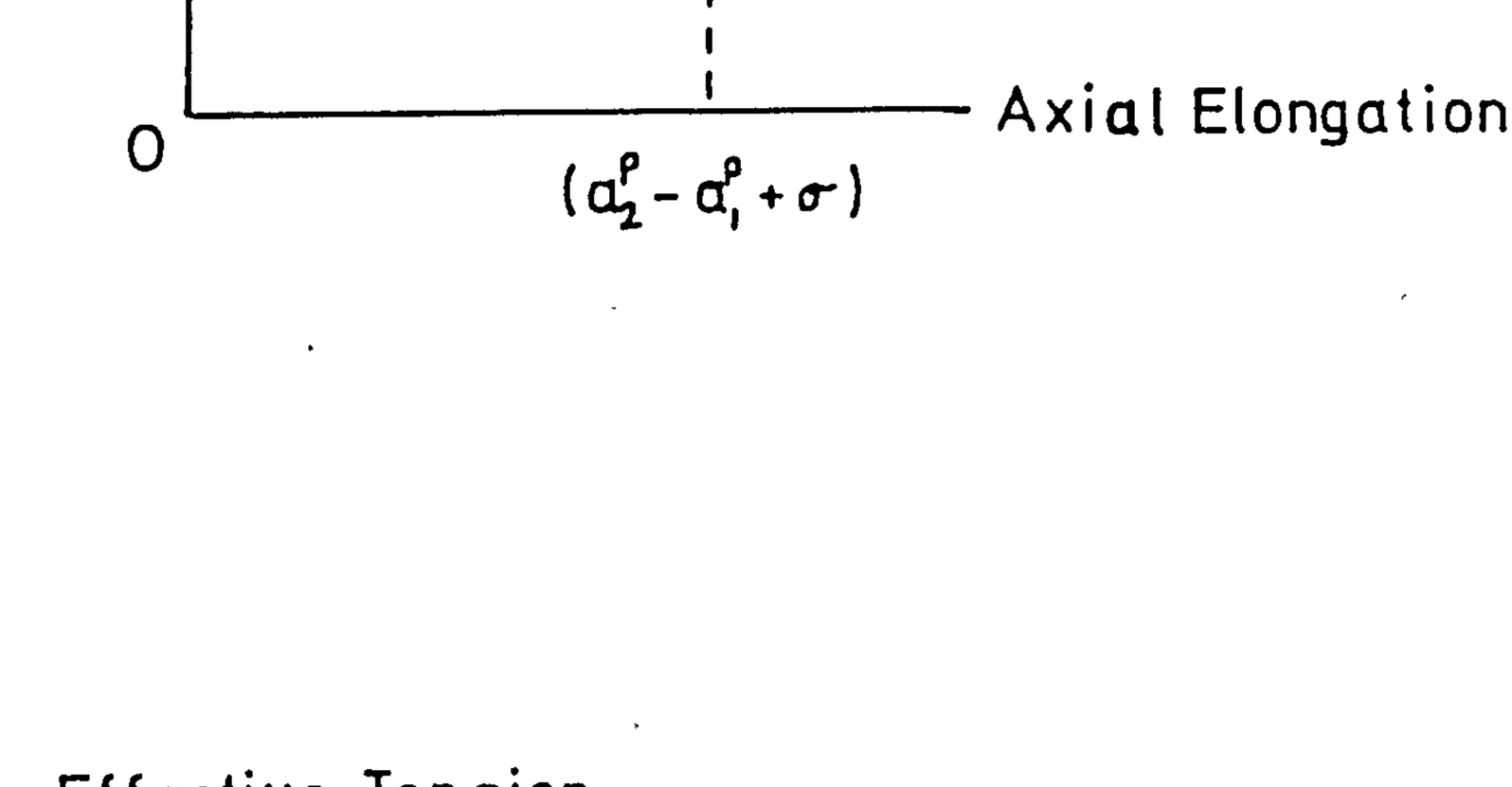

FIG 3.7 Real and Effective Tensions Against Axial Extension

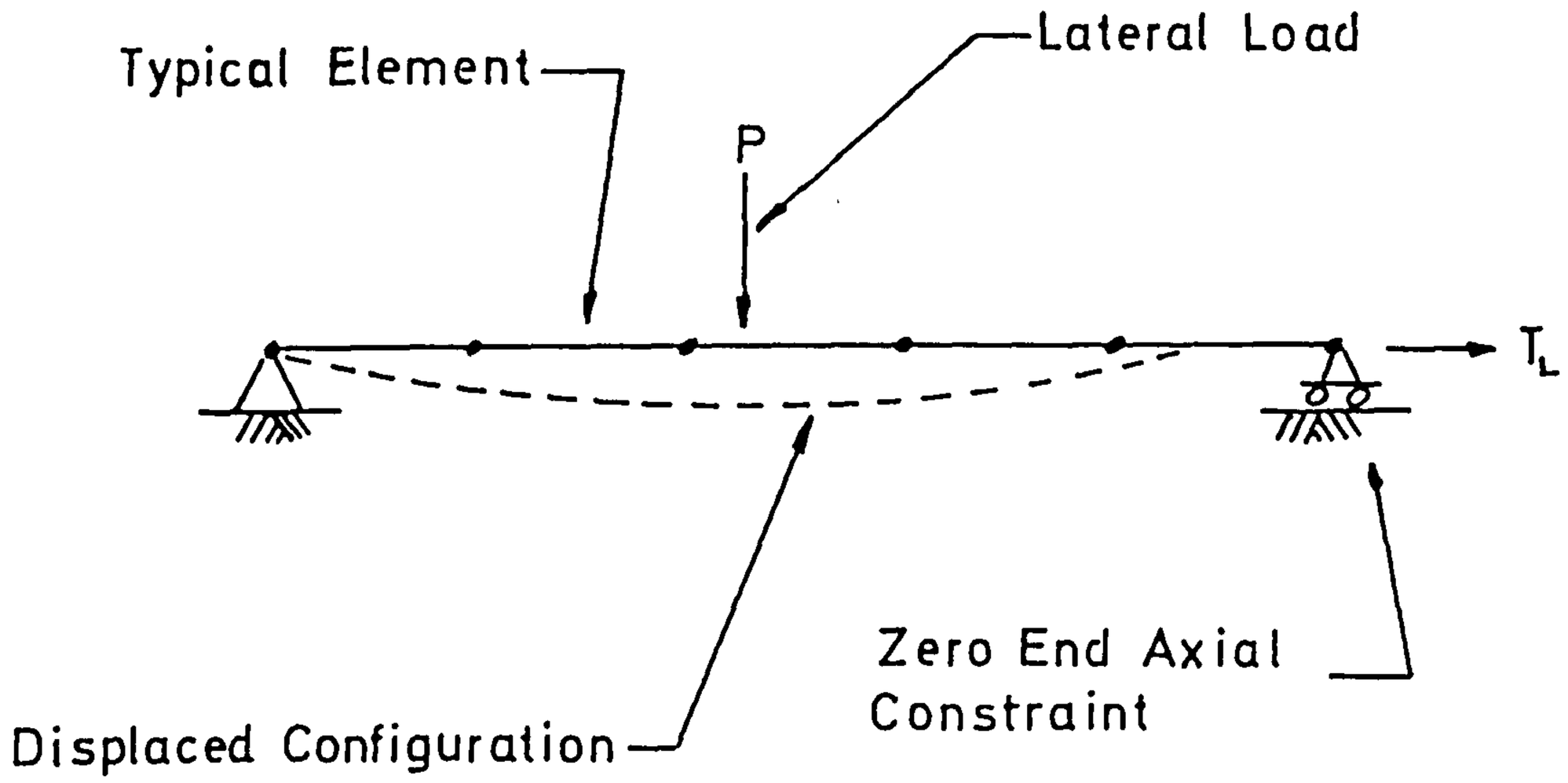

FIG 3.8 Classical Beam-column Problem

a) Initial Conditions

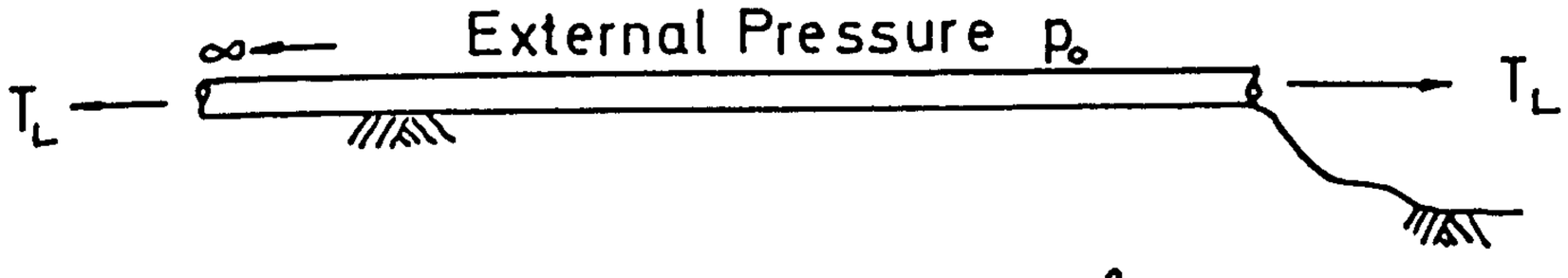

End Deflection $a_o^p = 0$
End Overtension $T_o^p = 0$

b) After Operating Conditions Plus End Displacement Increment Δa_1

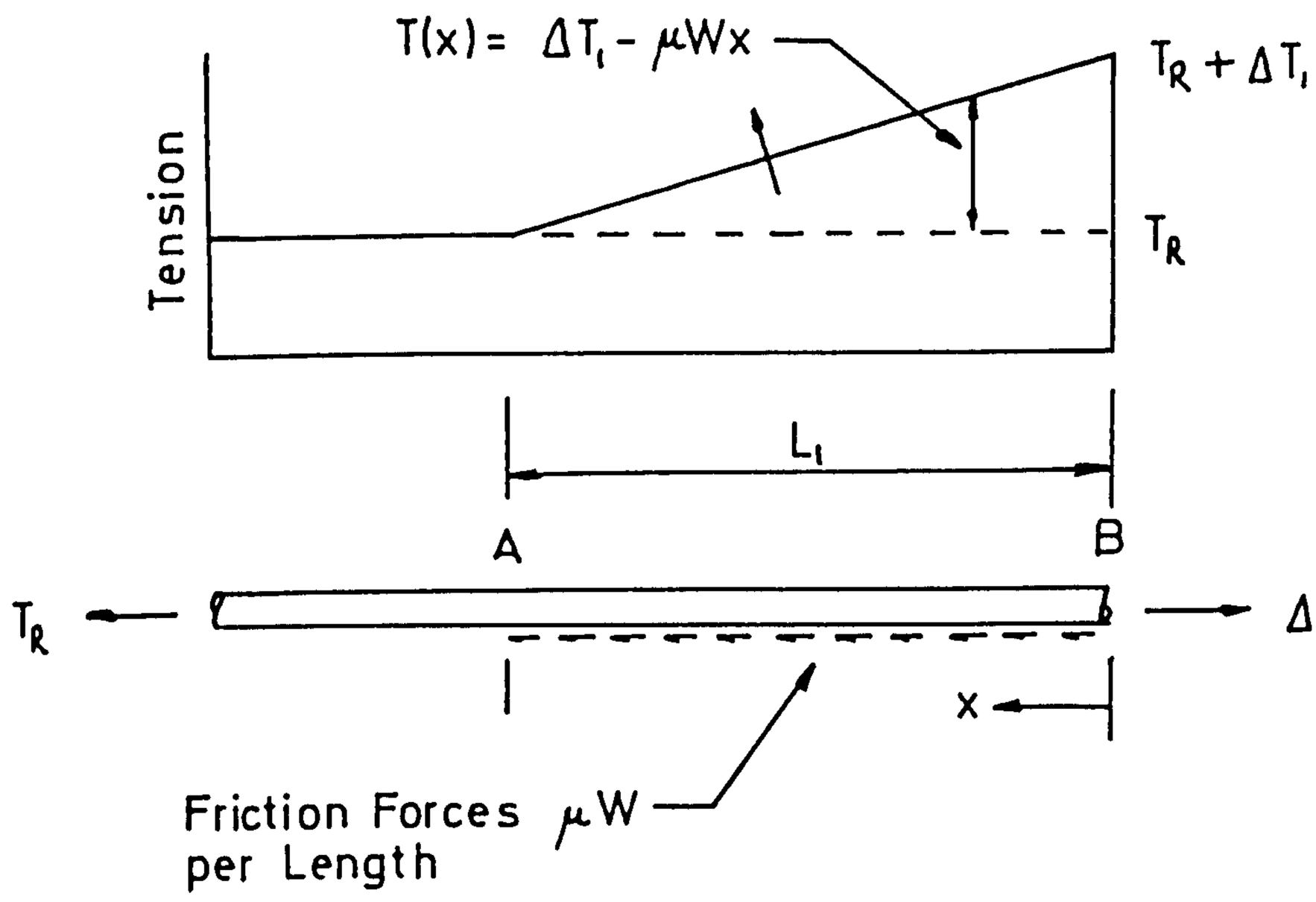

FIG 3.9 Tension Distribution in Friction Element During Initial Loading Phase 1

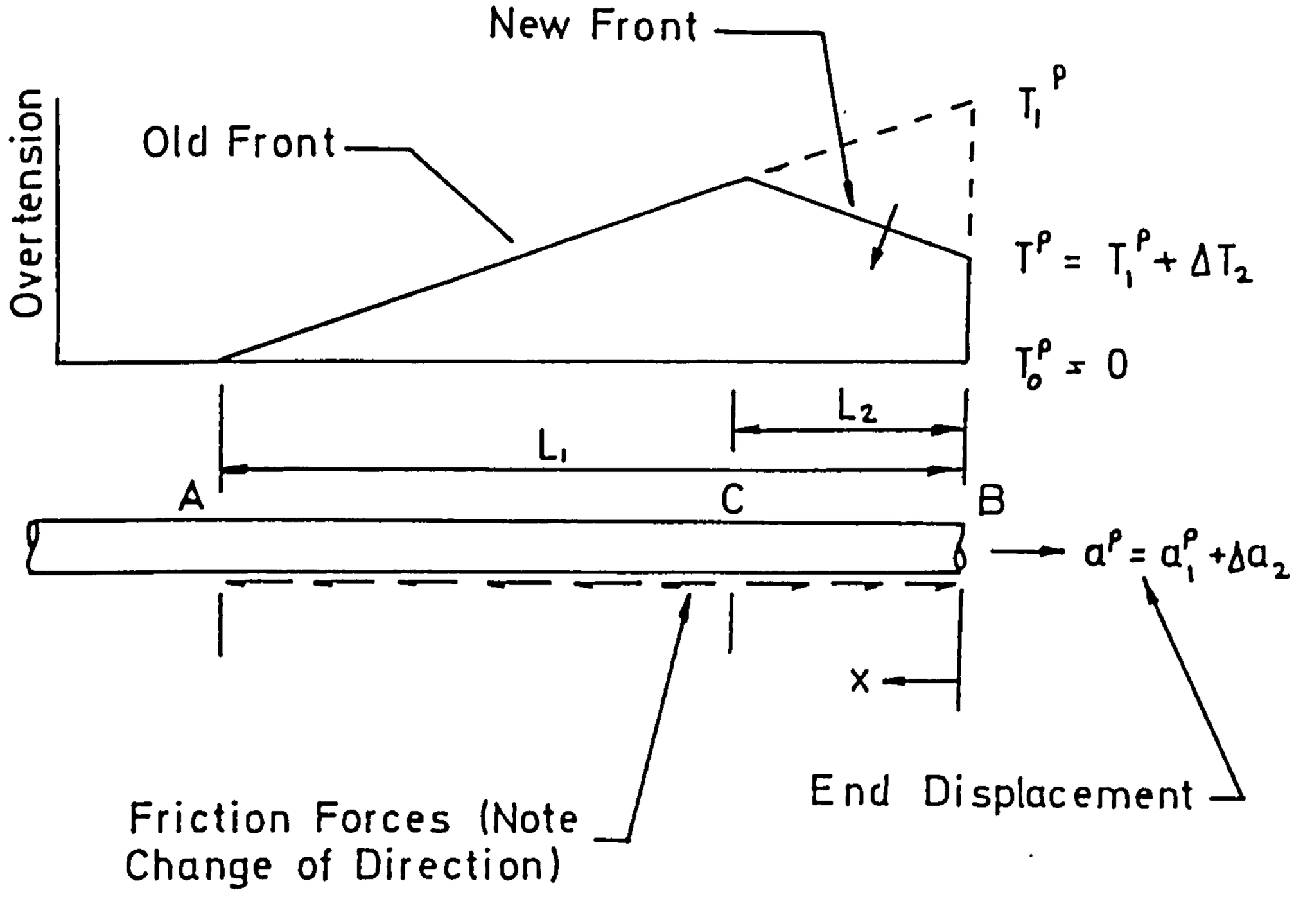

Total Displacement at end of Load Phase 1 = a_1^p

Total Overtension at end of Load Phase 1 = T_1^p

FIG 3.10 Tension Distribution in Friction Element During Unloading Phase 2

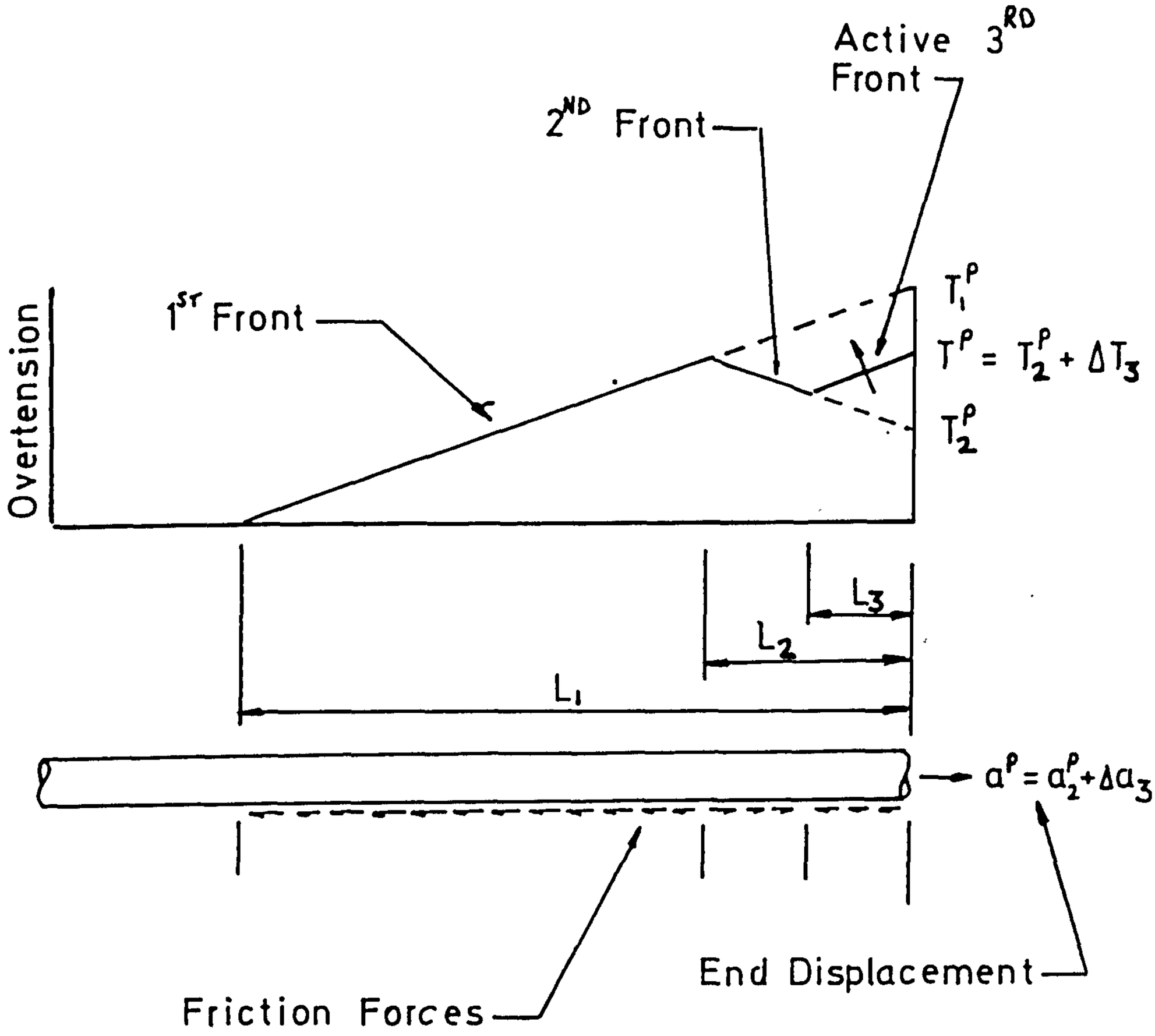

Total Displacement at end of Load Phase 2 = a_2^ρ
Total Overtension at end of Load Phase 2 = T_2^ρ

FIG 3.11 Tension Distribution in Friction Element During Re-loading Phase 3

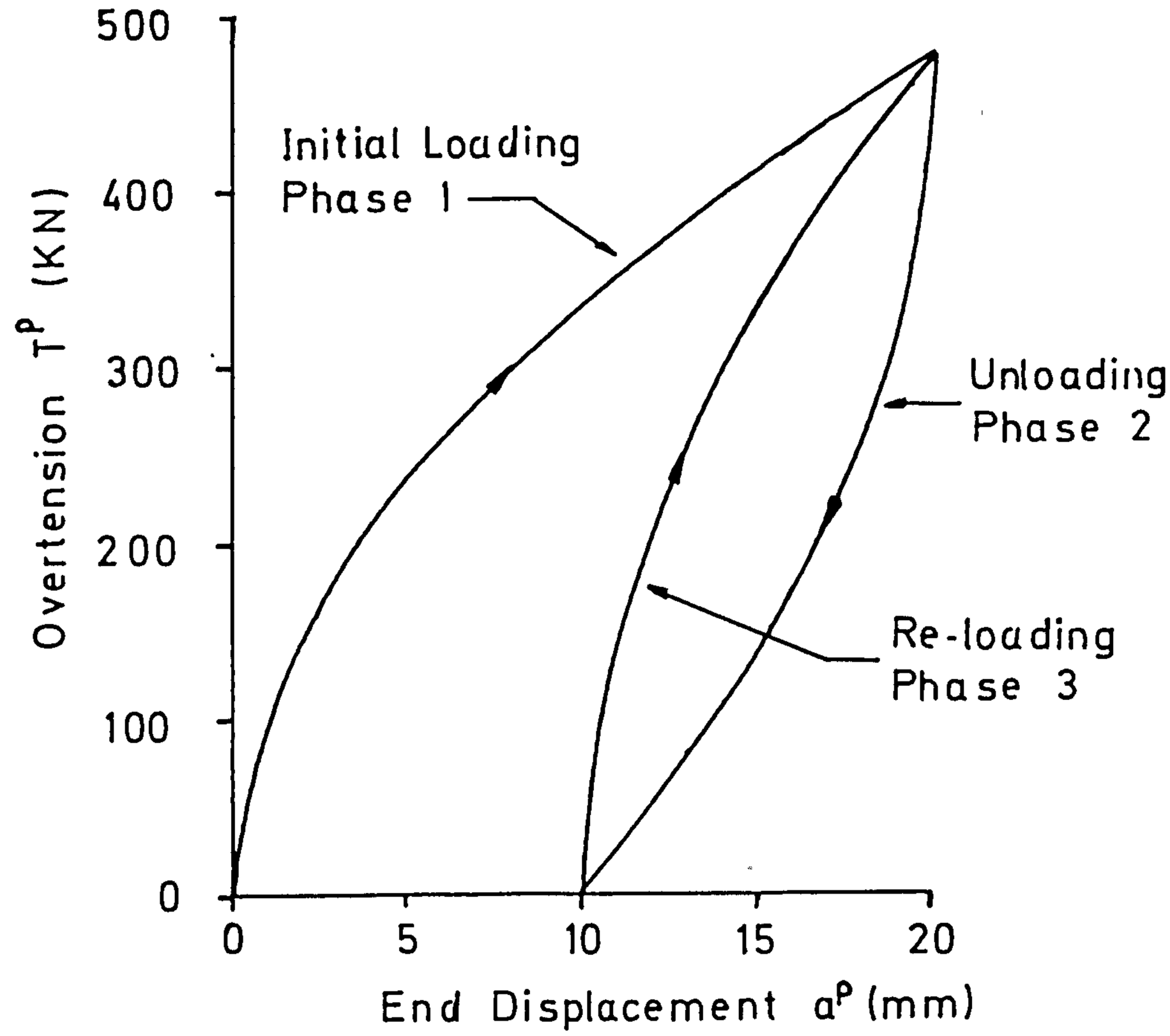

FIG 3.12 Typical Friction Element Load Deflection Curve

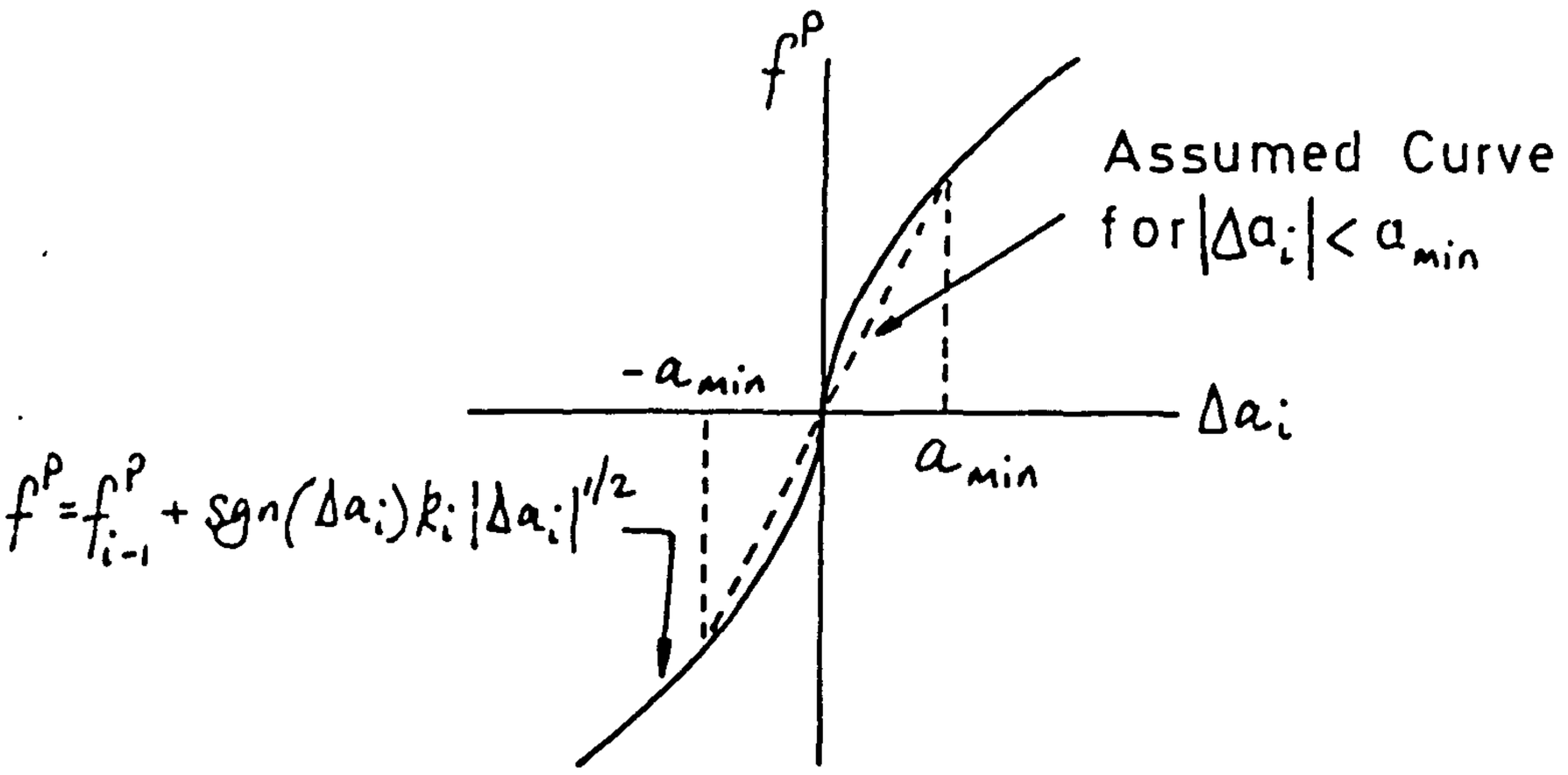

FIG 3.13 Approximate Friction Element Tangent Stiffness for Small Δa_i

a) Initial Conditions $a^\rho_o = o$, $f^\rho_o = T$

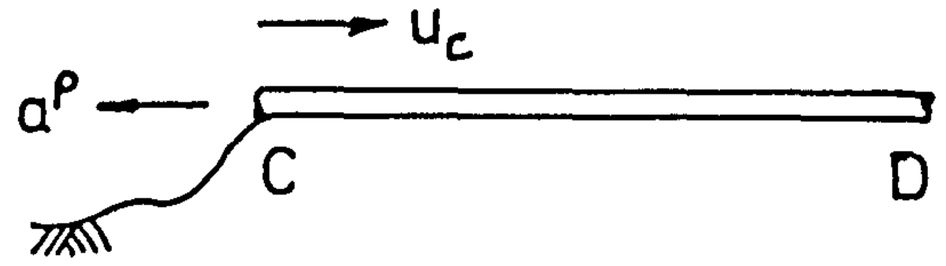

b) Initial Conditions $a^\rho_o = o$, $f^\rho_o = -T$

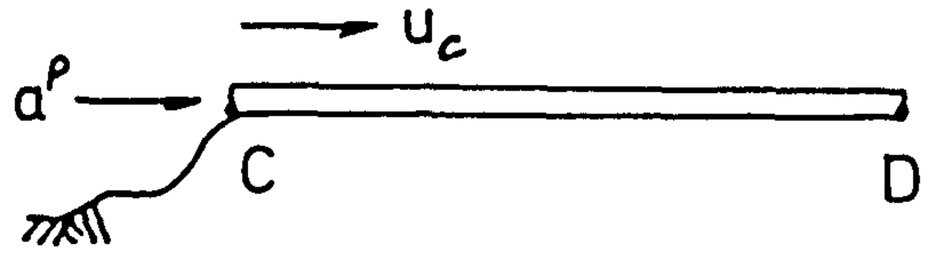

FIG 3.14 Local and Global Directions for Friction Element CD

a) Standard Method

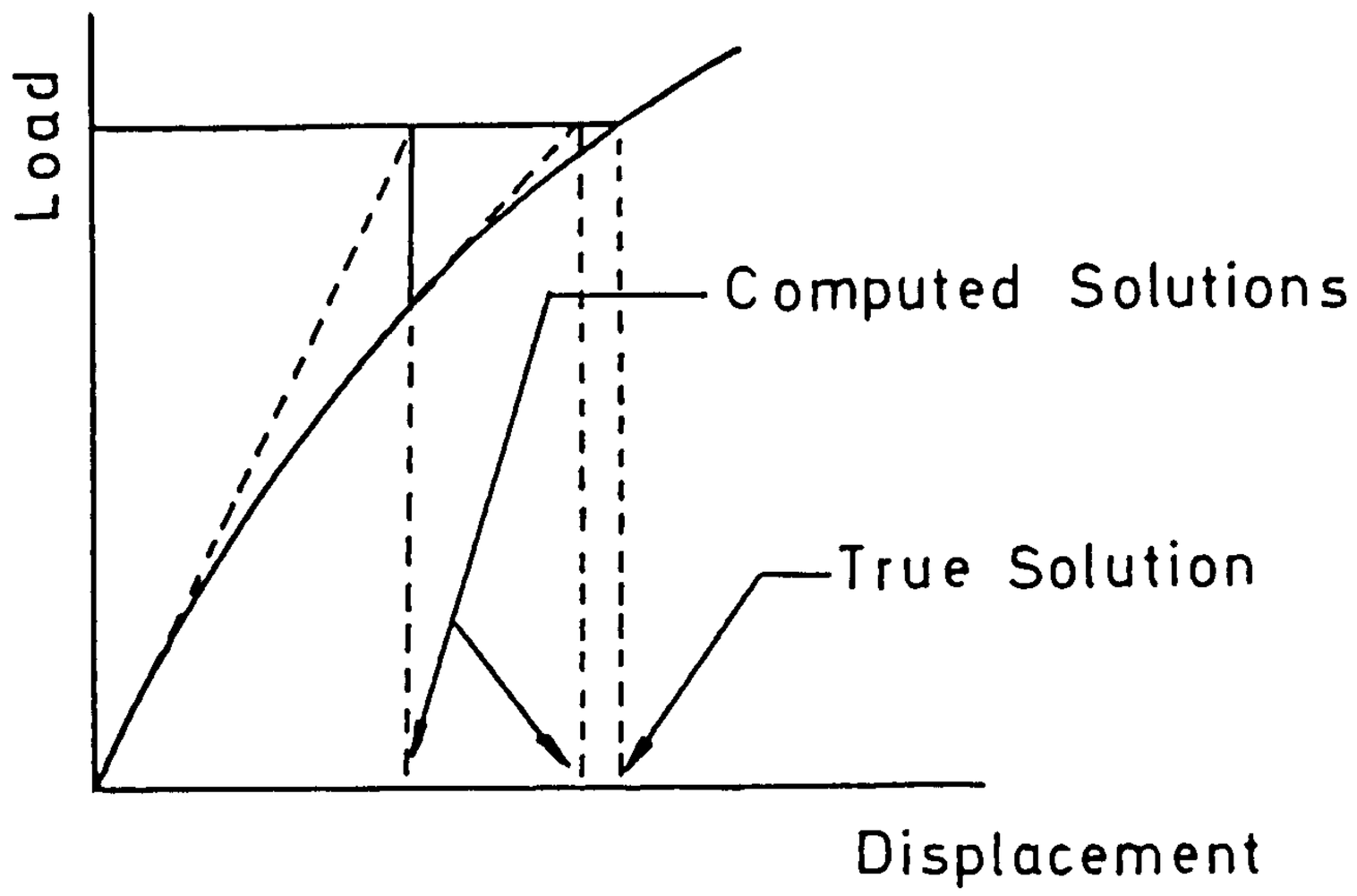

b) Modified Method

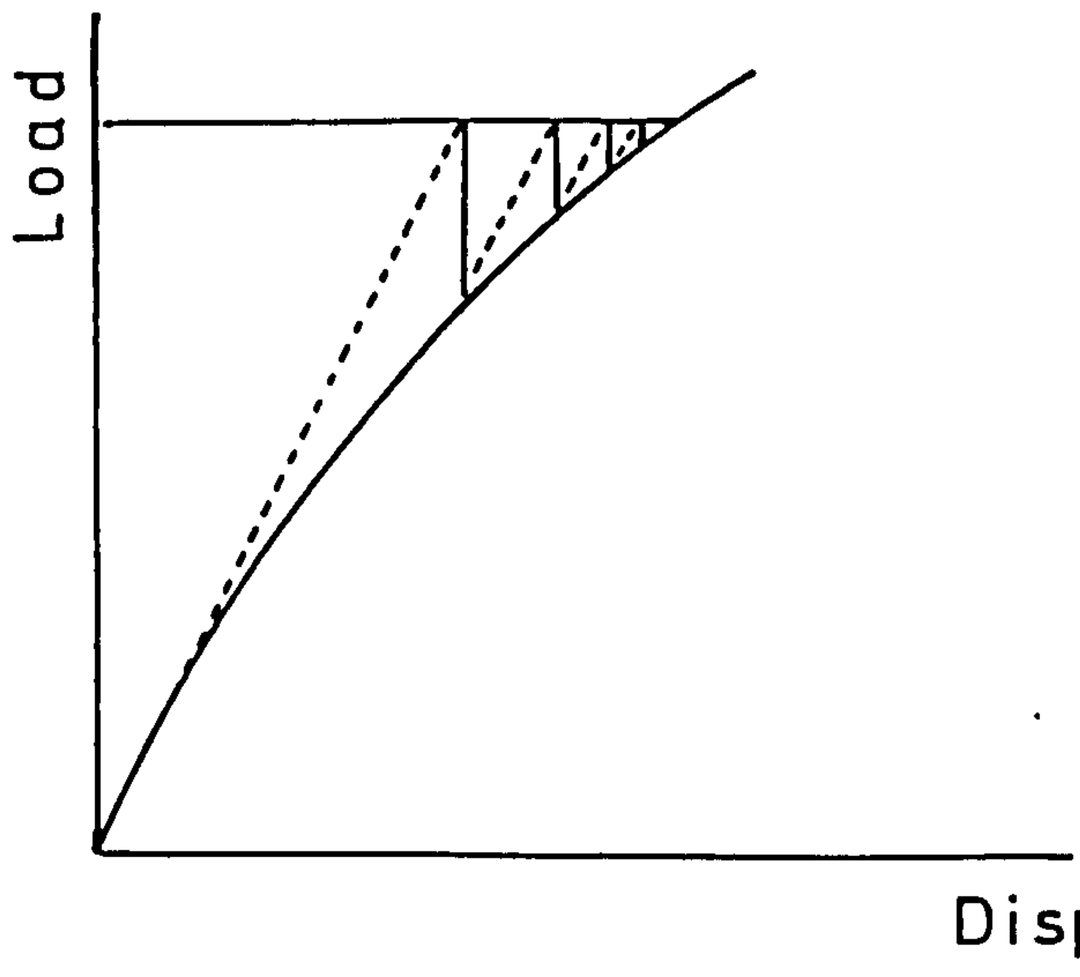

FIG 3.15 Newton - Raphson Iterative Solution for SDOF System

a) Incremental Method

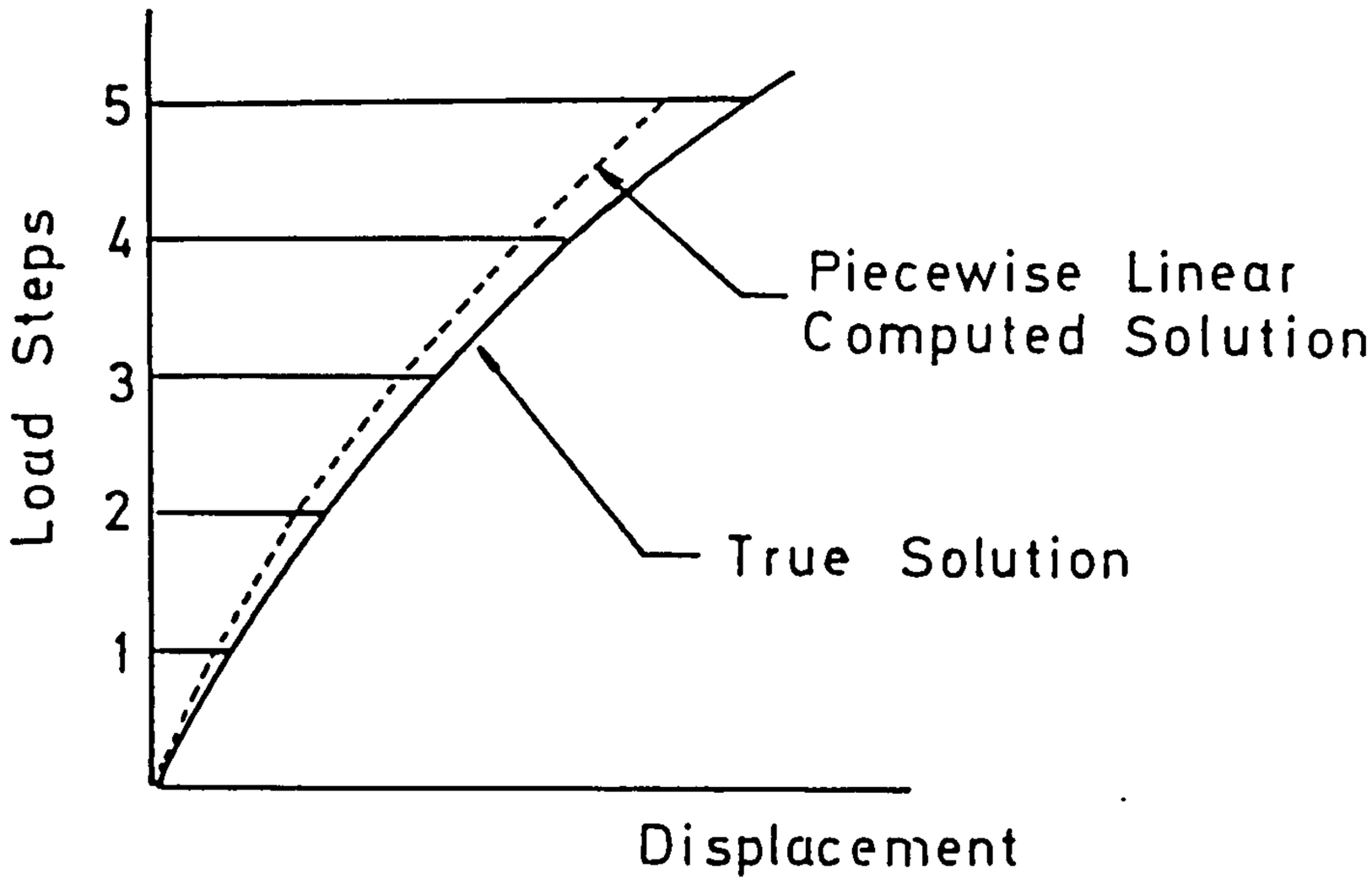

b) Incremental with Equilibrium Iterations

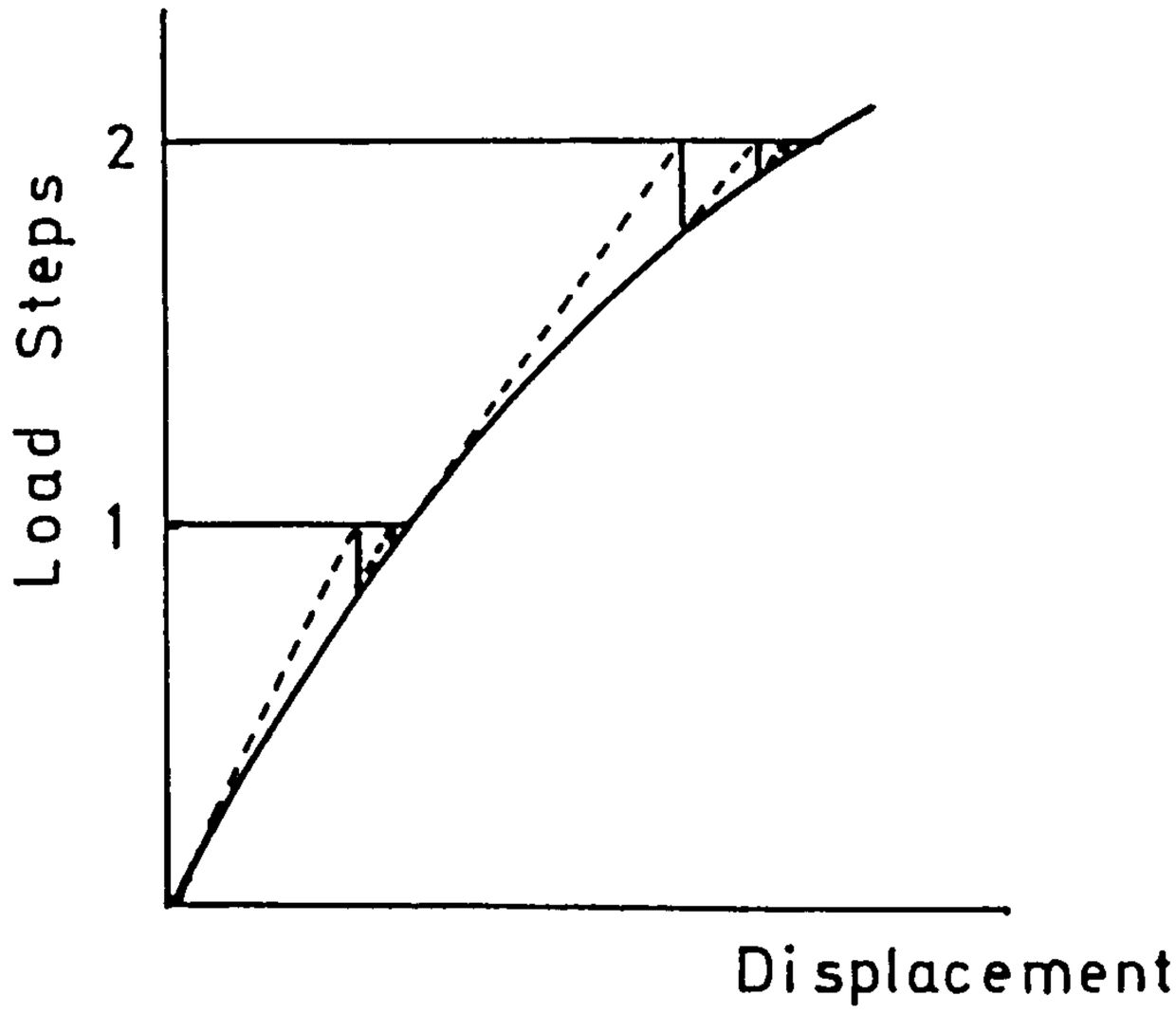

FIG 3.16 Incremental and Incremental/Iterative Solution Methods

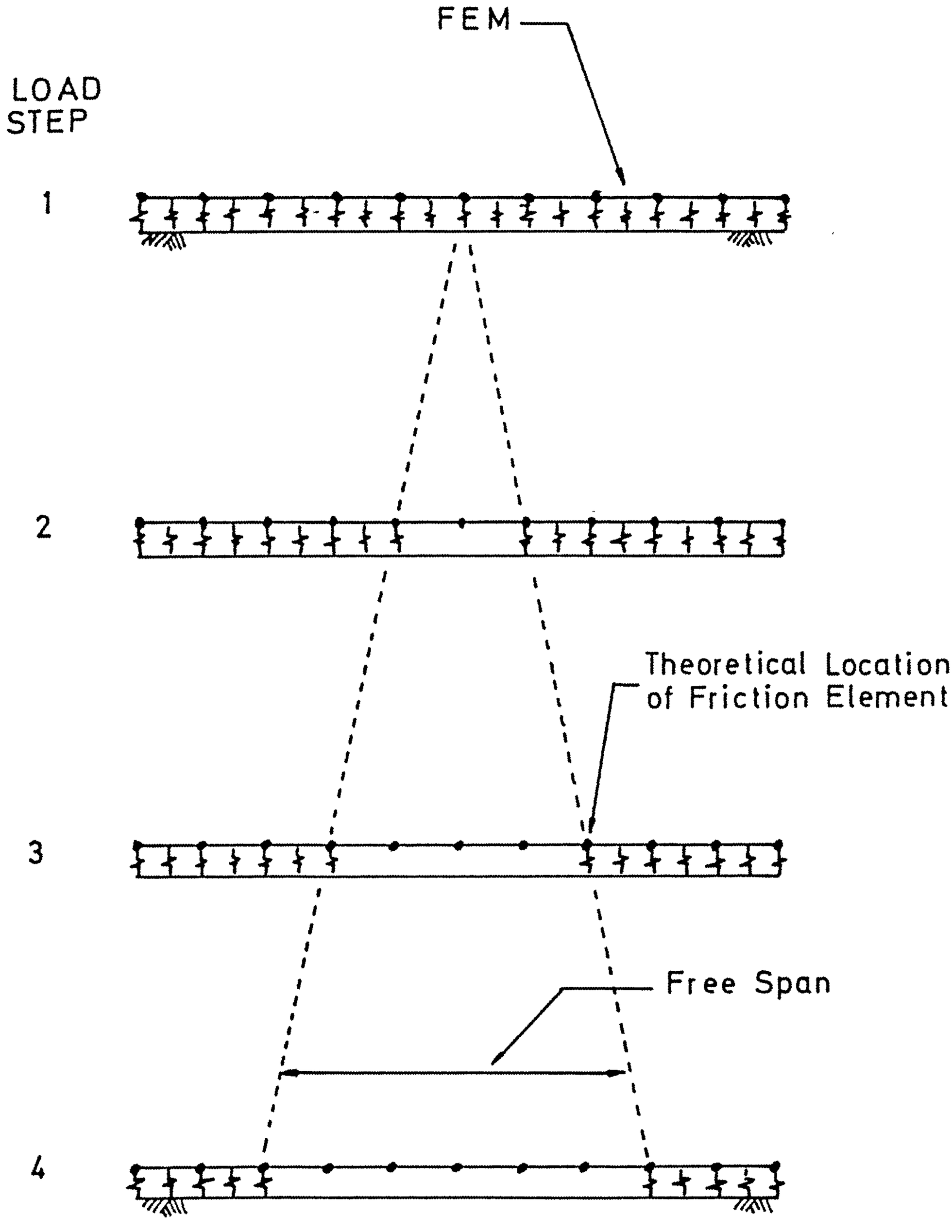

FIG 3.17 Incremental Formation of Free Span

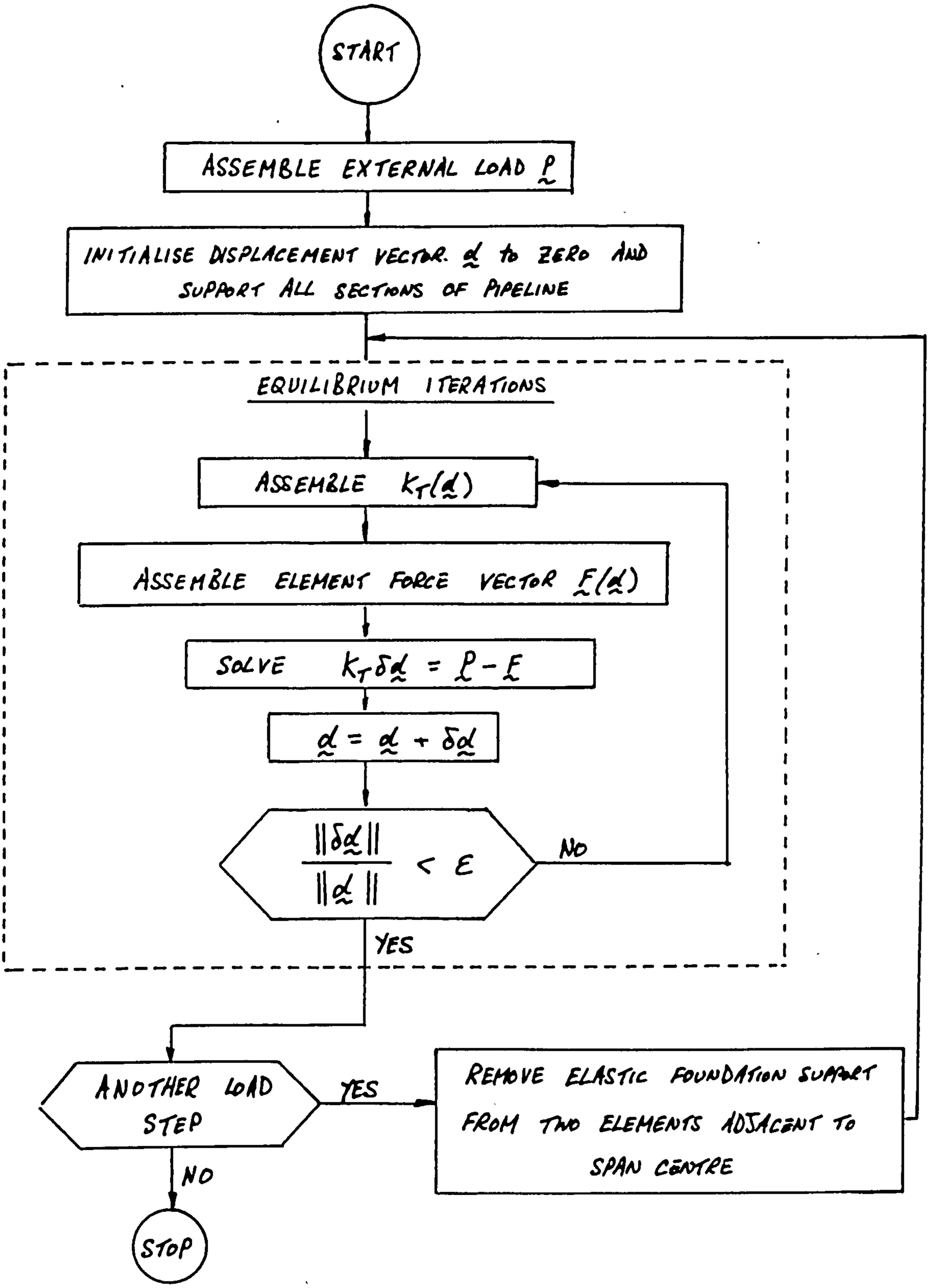

FIG 3.18 Flow Chart for Solution Process

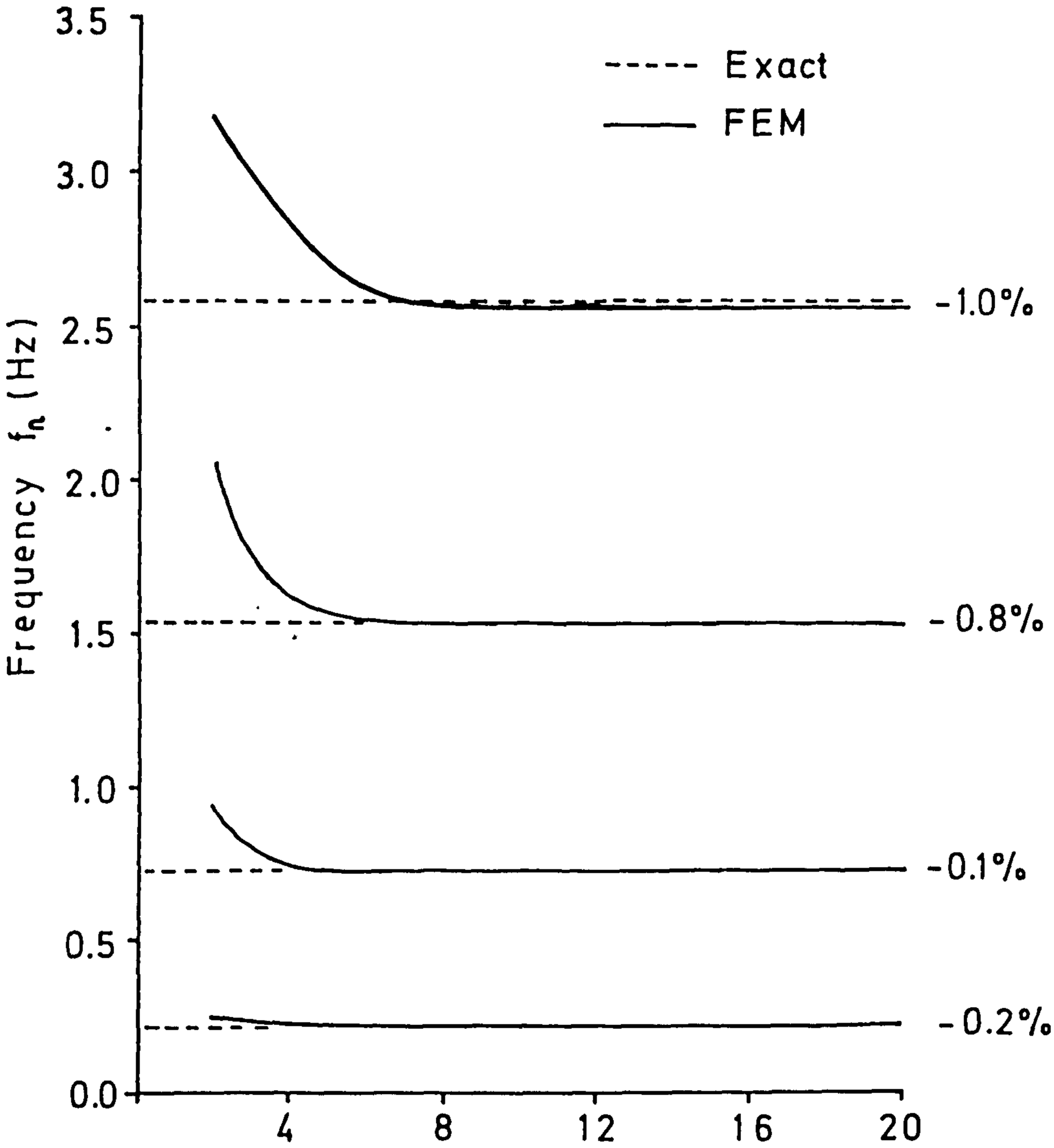

FIG 3.19 Pipe 2 Convergence Test, $\mu = 0.0$

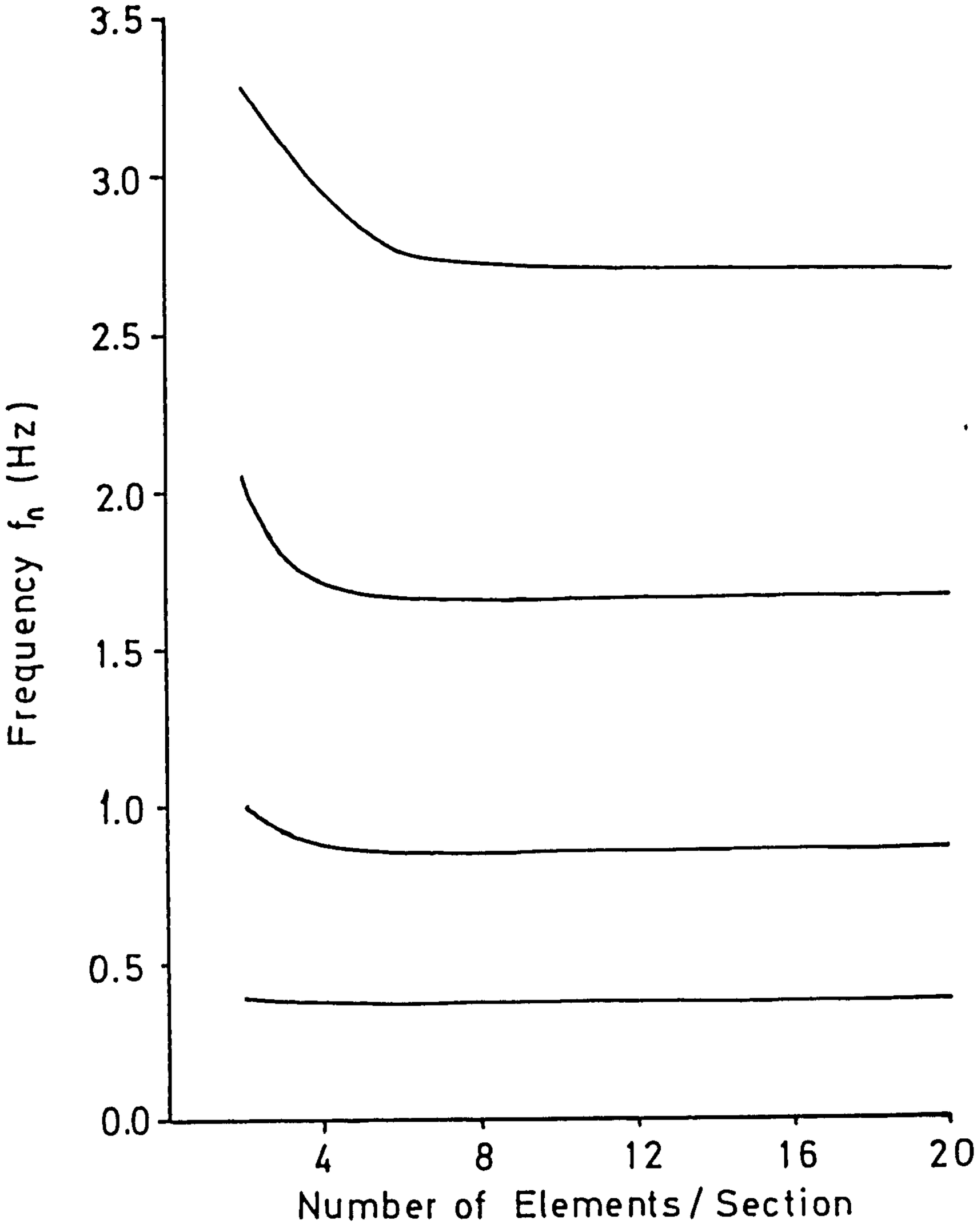

FIG 3.20 Pipe 2 Convergence Test, $\mu = 1.0$, u_B, u_C Constrained

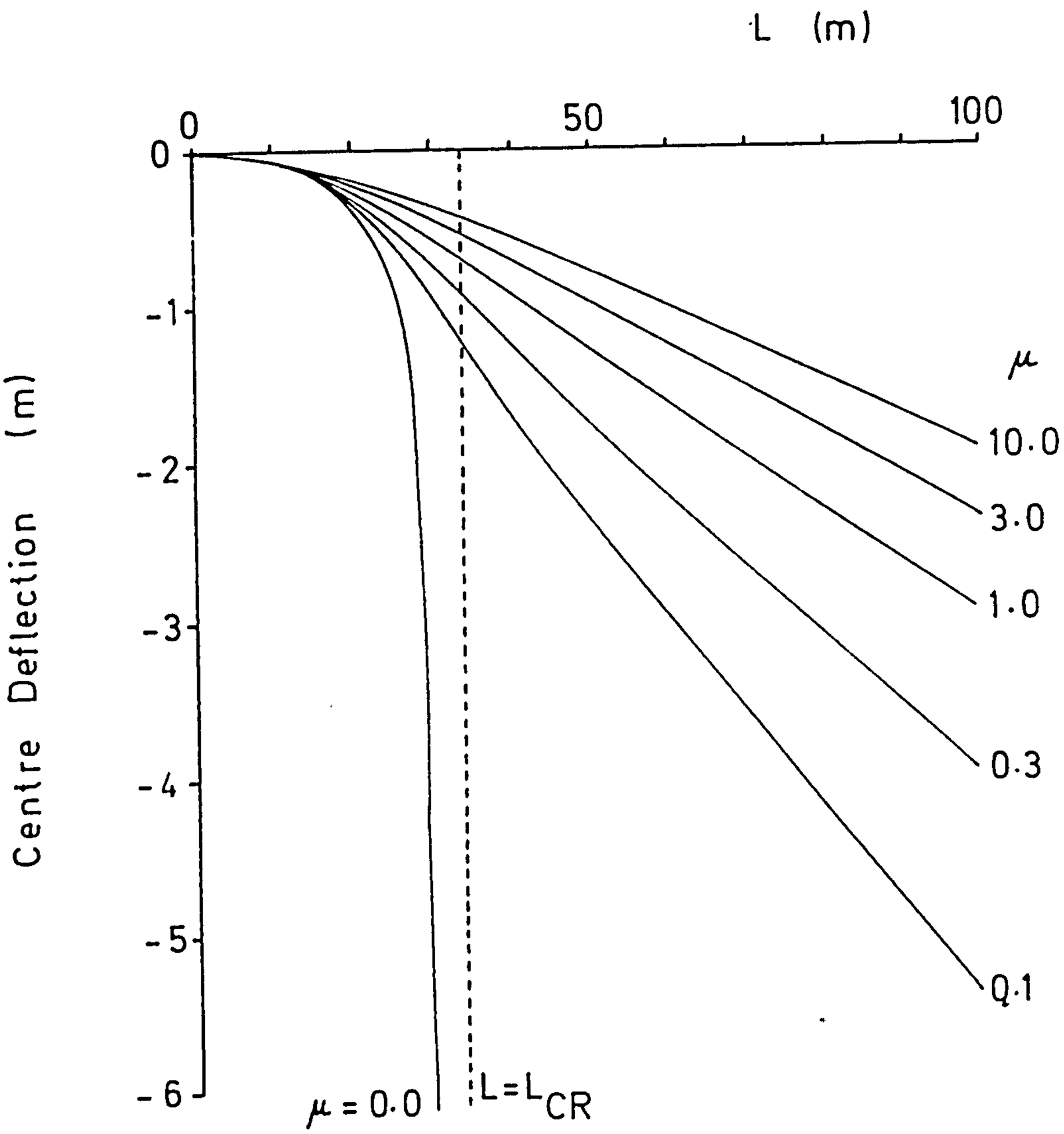

FIG 3.21 Pipe 1 Centre Deflection

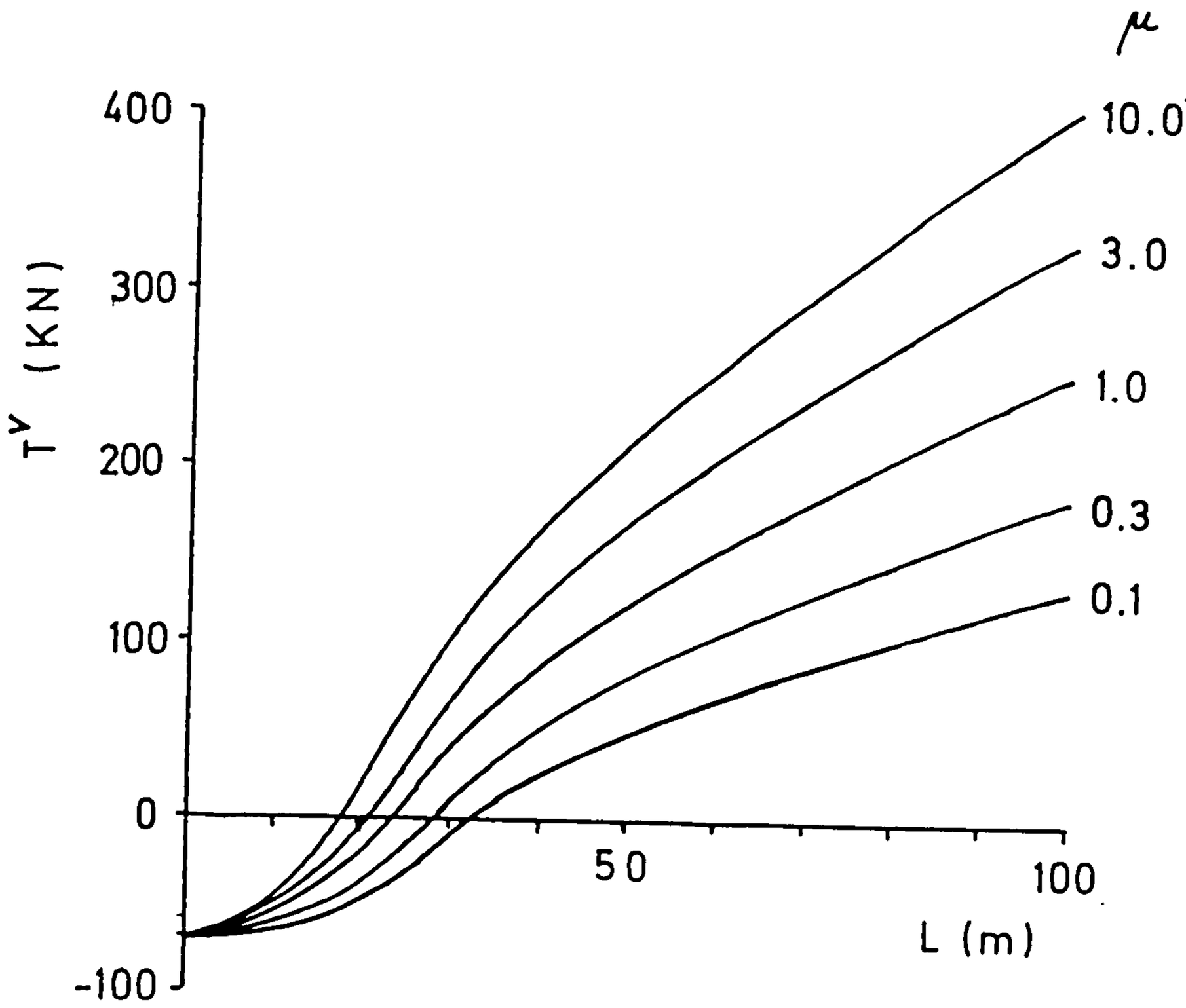

FIG 3.22 Pipe 1 Variable Effective Tension T^V

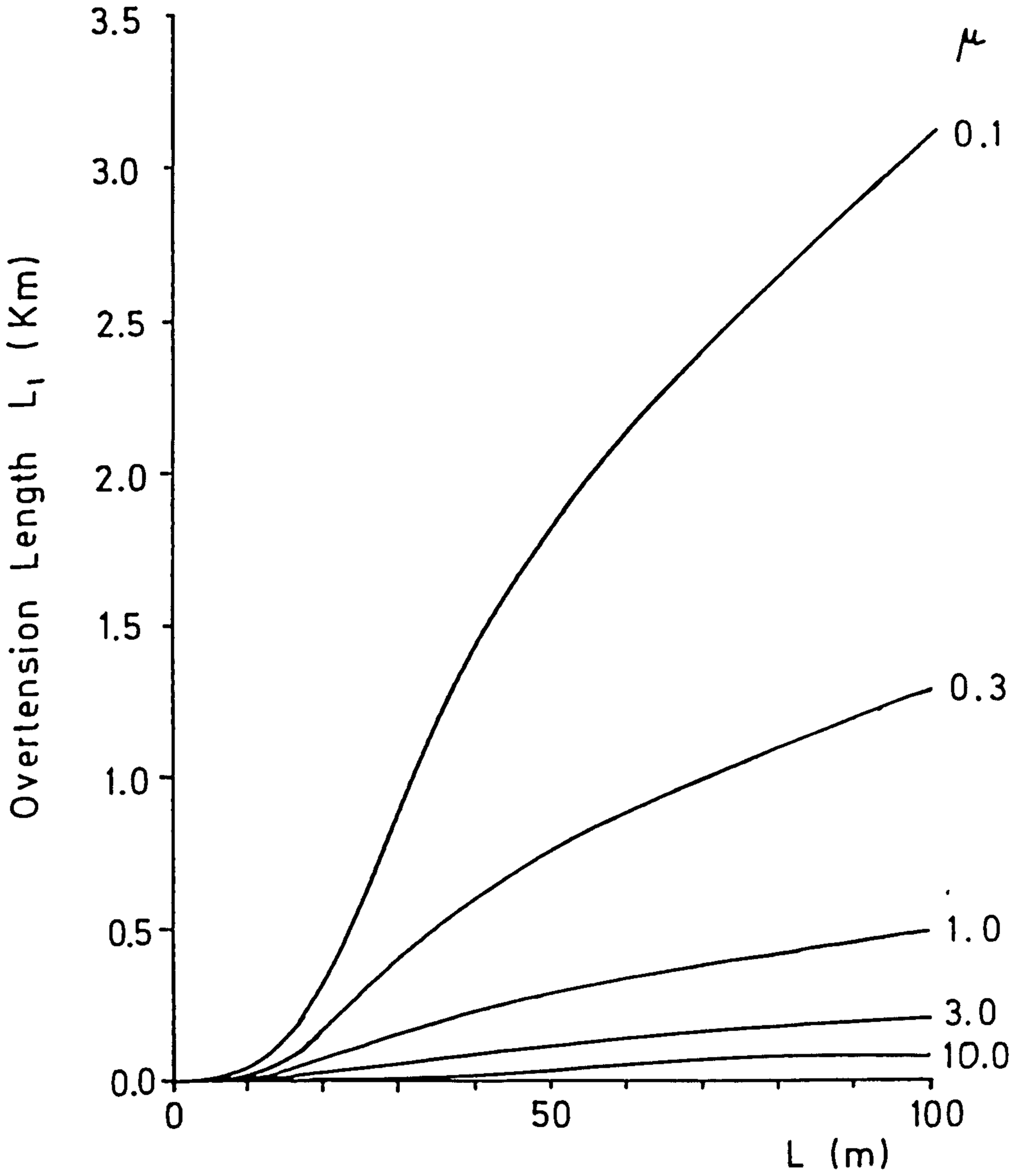

FIG 3.23 Pipe 1 Overtension Length L_1
(See Fig 3.9)

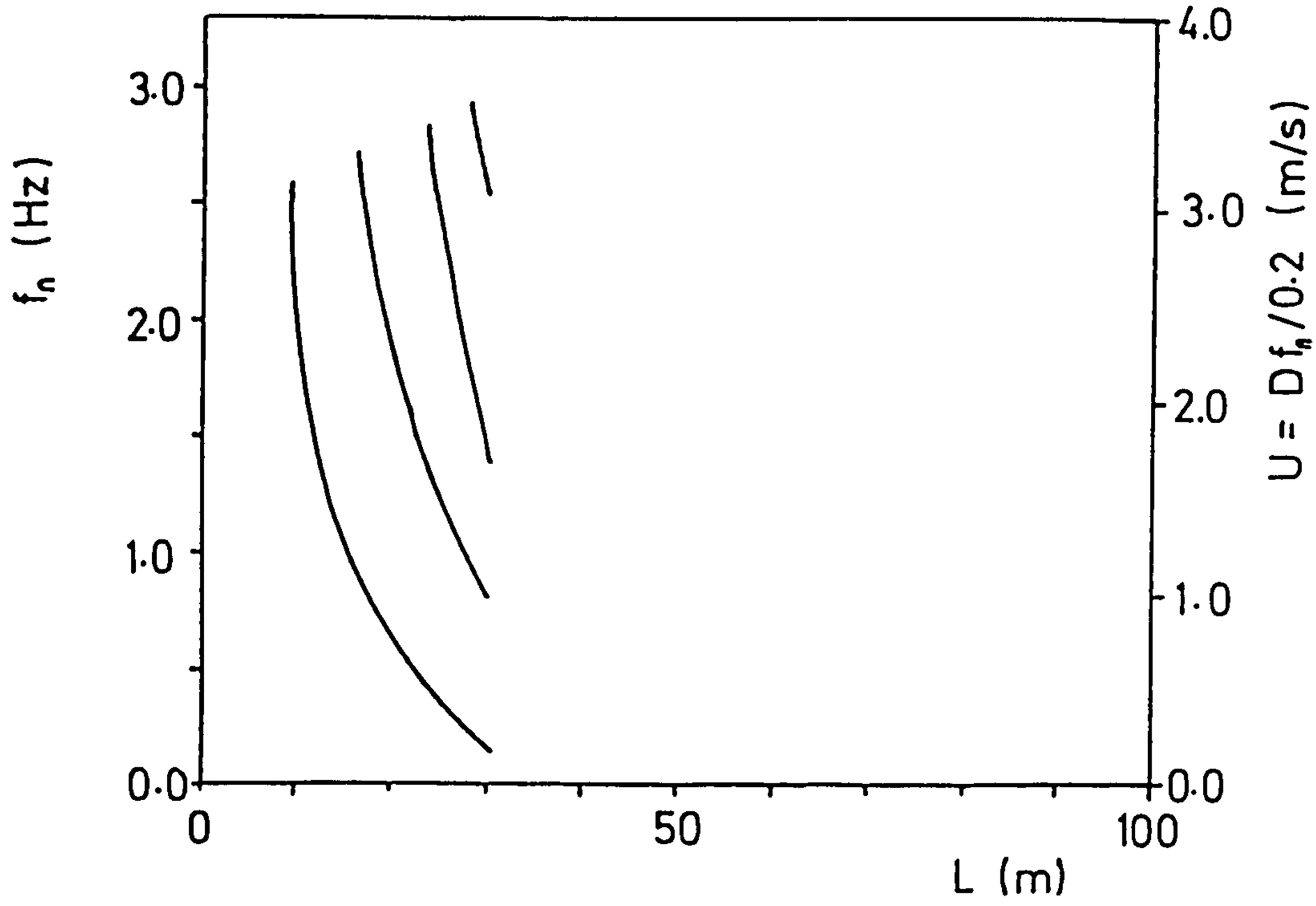

FIG 3.24 Pipe 1 Frequencies, $\mu = 0.0$

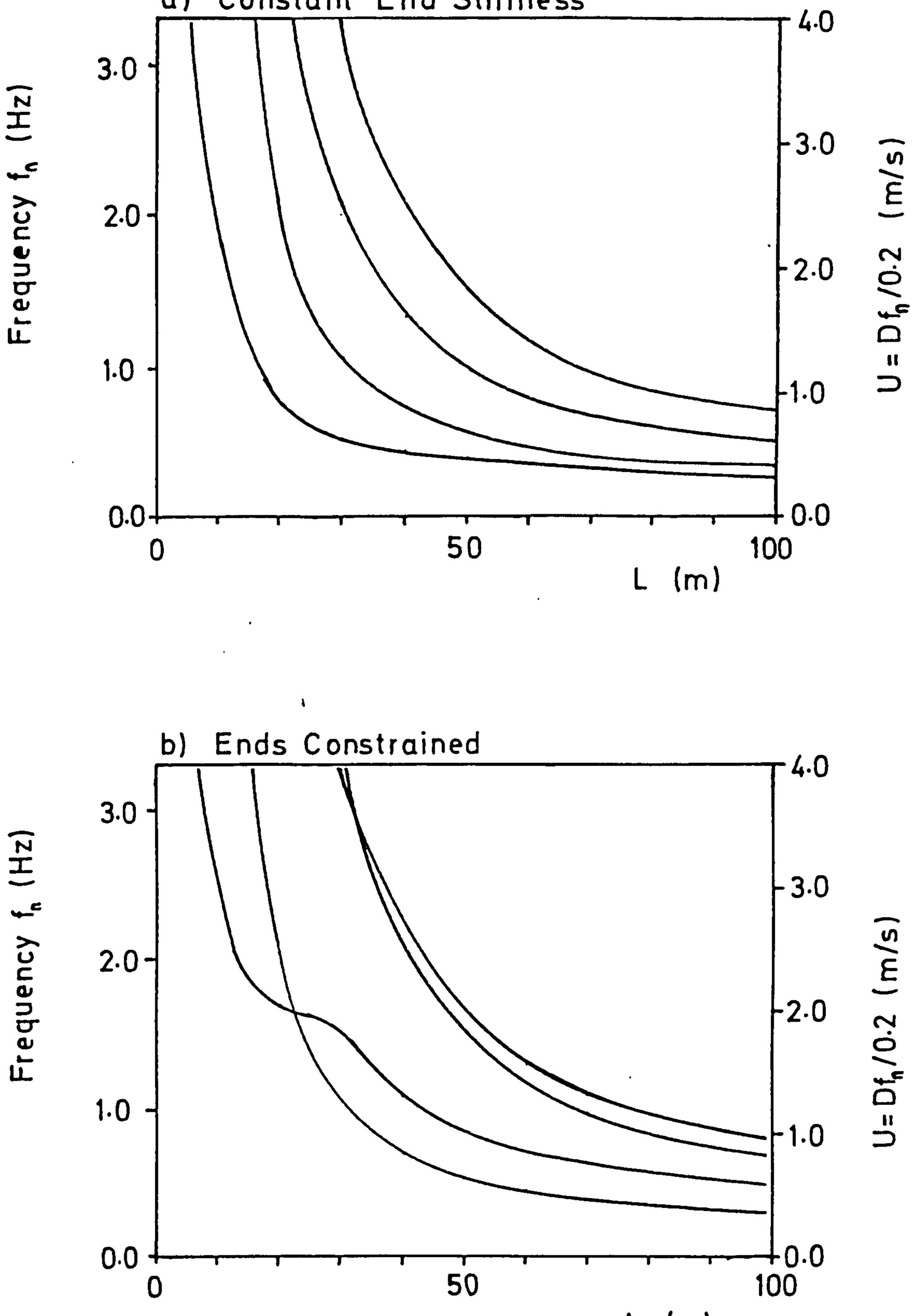

FIG 3.25 Pipe 1 Frequencies, $\mu = 0.1$

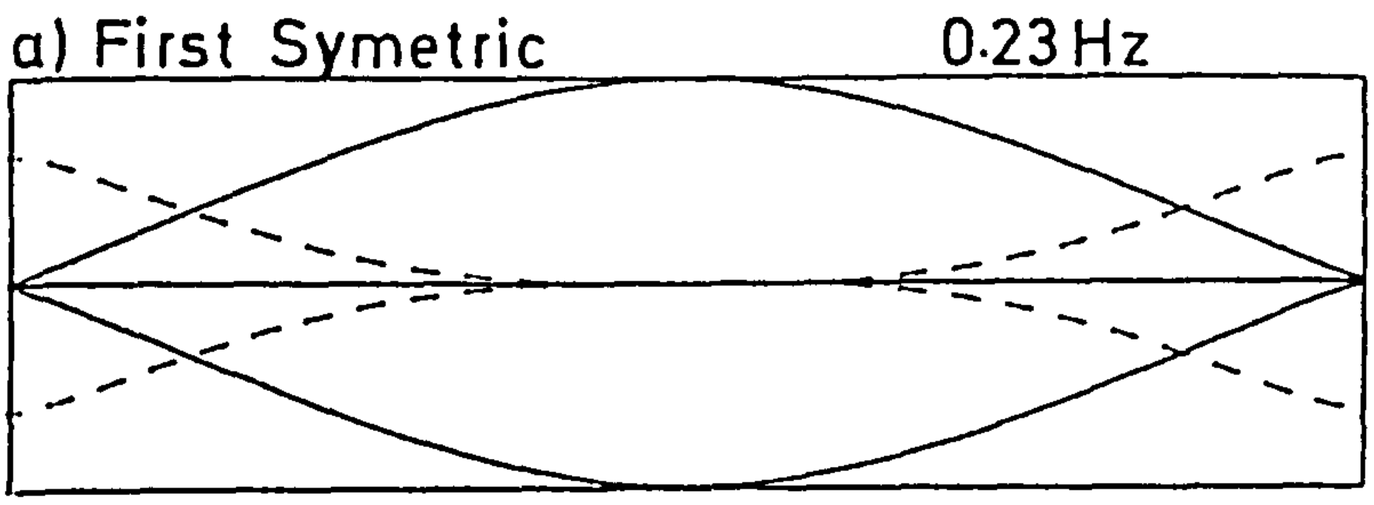

FIG 3.26 a Pipe 1 Mode Shapes, L = 100 m, μ = 0·1, Constant End Stiffness

a) First Antisymmetric 0.31 Hz

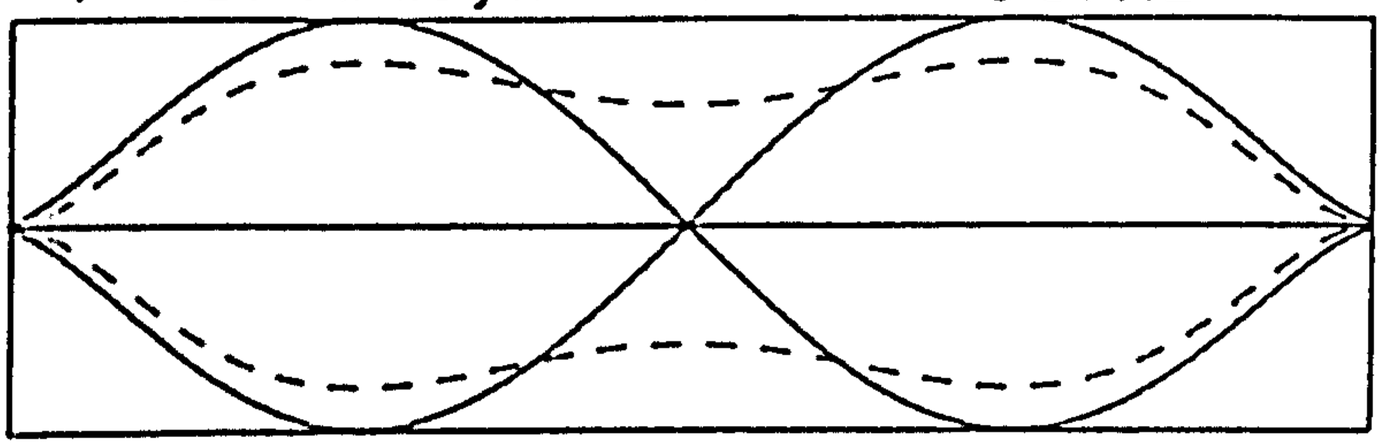

b) First Symmetric 0.48 Hz

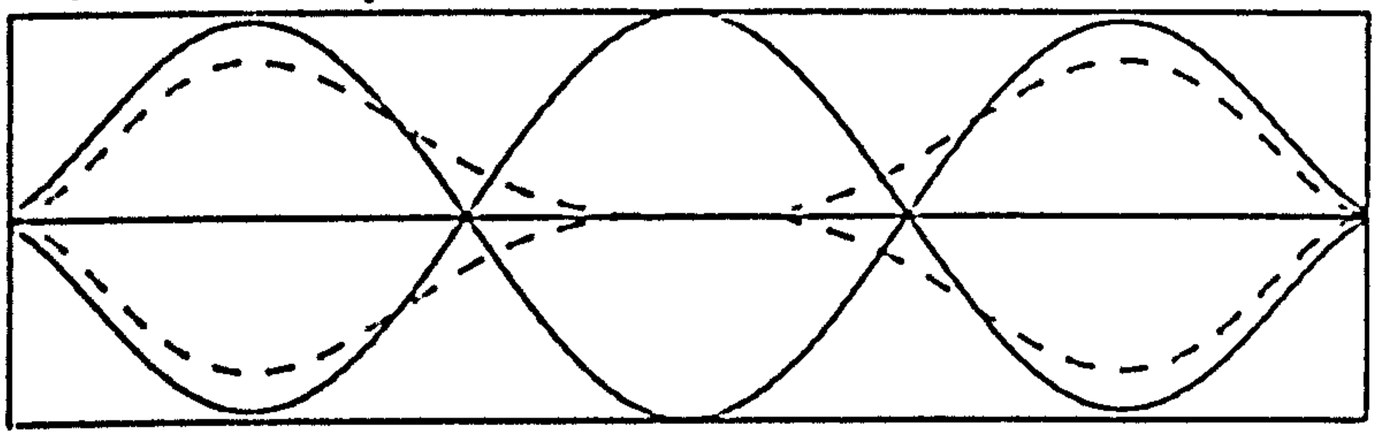

c) Second Antisymmetric 0.68 Hz

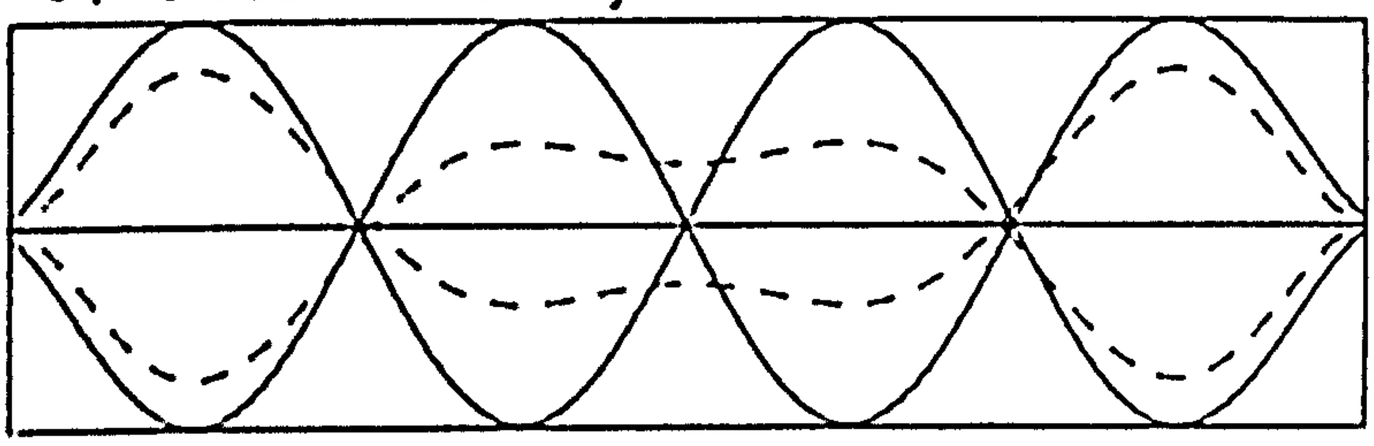

d) Second Symmetric 0.81 Hz

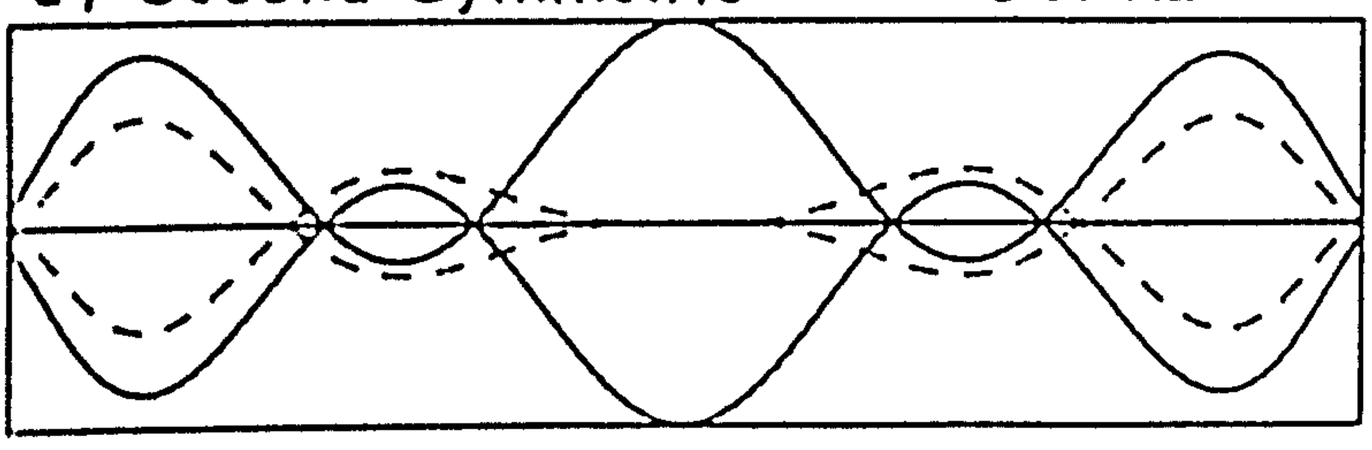

——— Vertical Disp.

------- Horizontal Disp. (x5)

FIG 3.26b Pipe 1 Mode Shapes, L=100m, μ=0.1, Ends Constrained

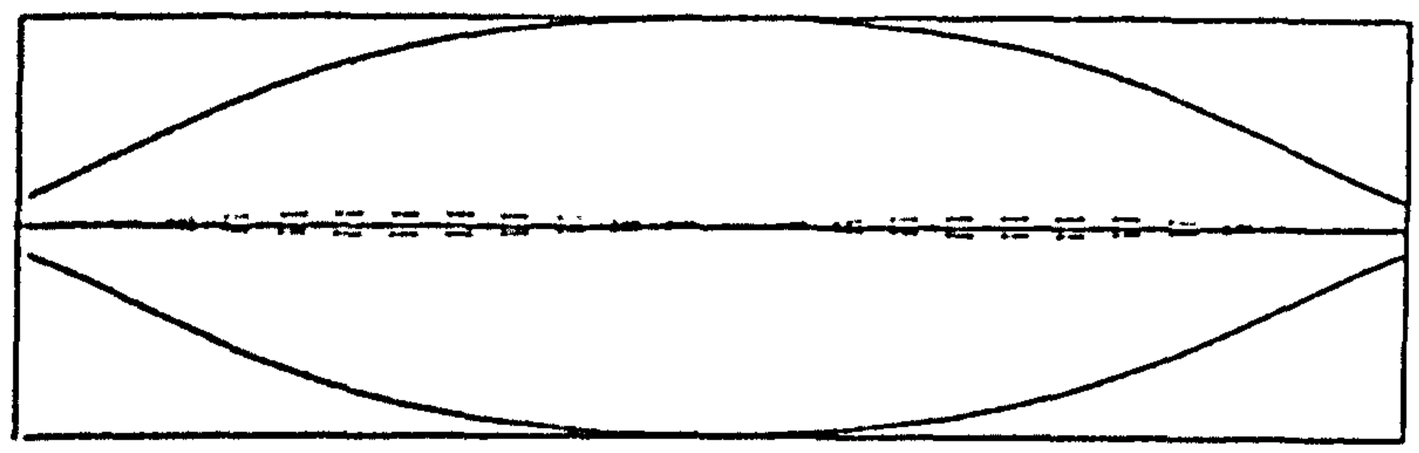

FIG 3.27 Pipe 1 First Symmetric Mode, $\mu = 0.1$
Ends Constrained

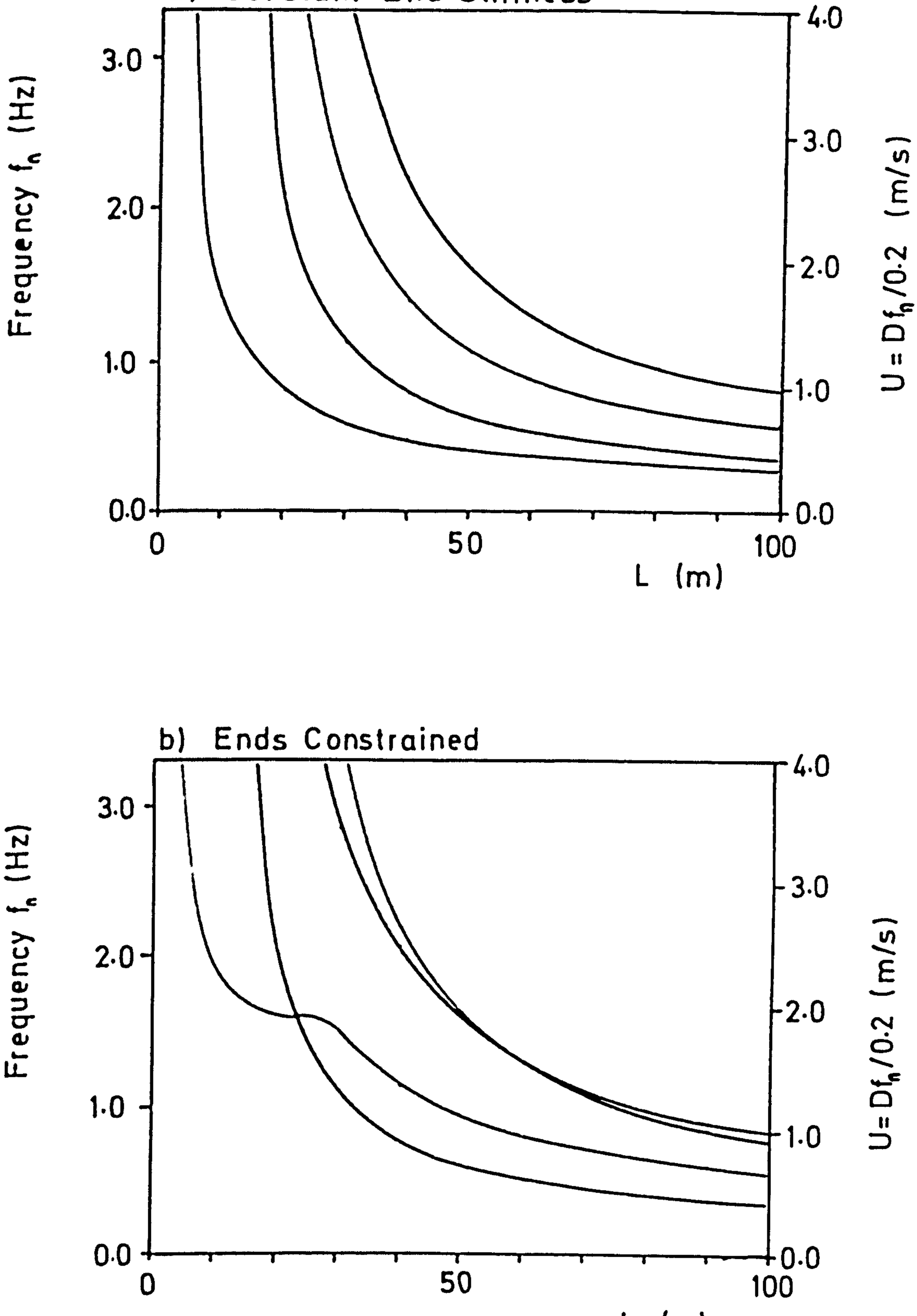

FIG 3.28 Pipe 1 Frequencies, $\mu = 0.3$

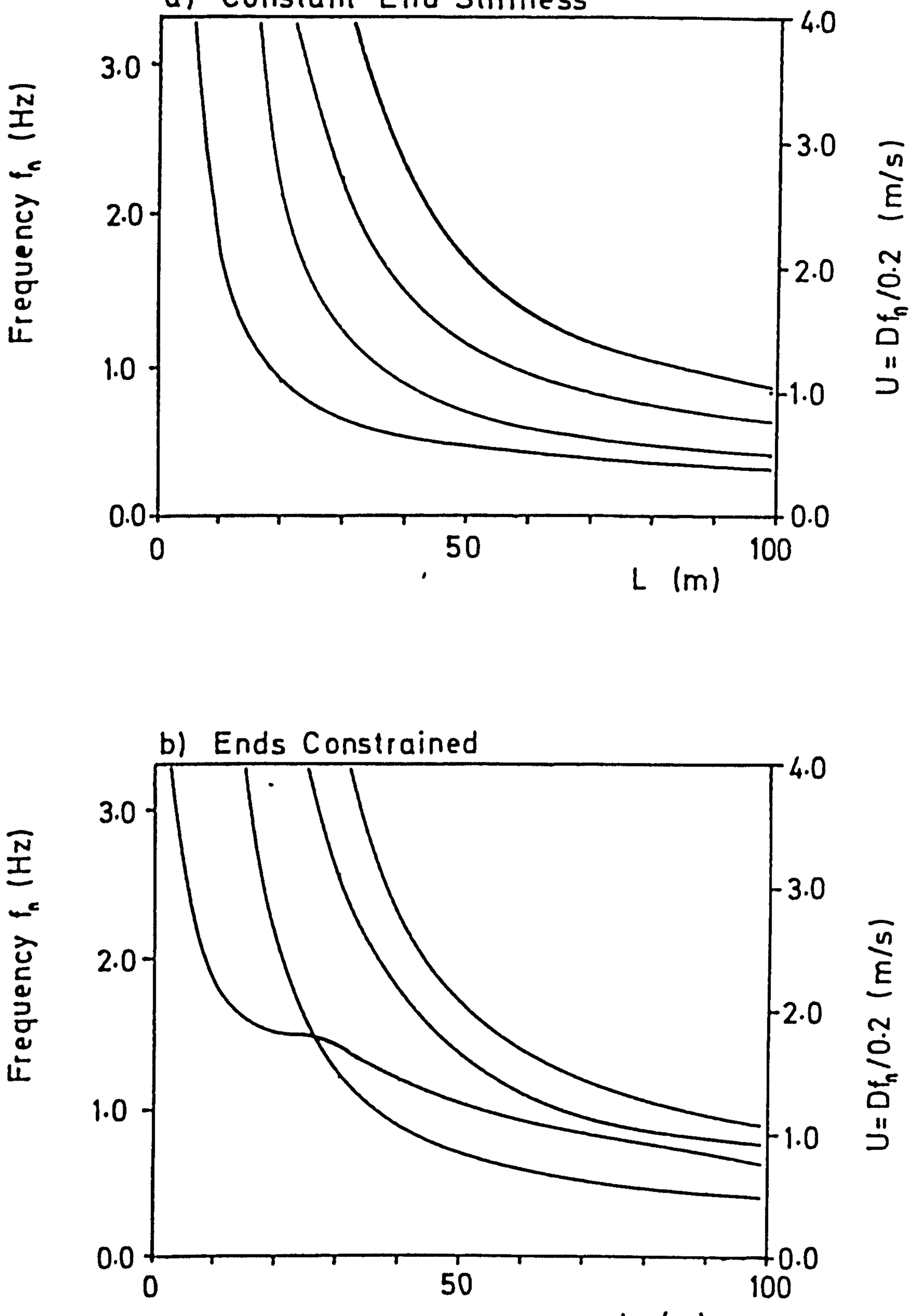

FIG 3.29 Pipe 1 Frequencies, $\mu = 1.0$

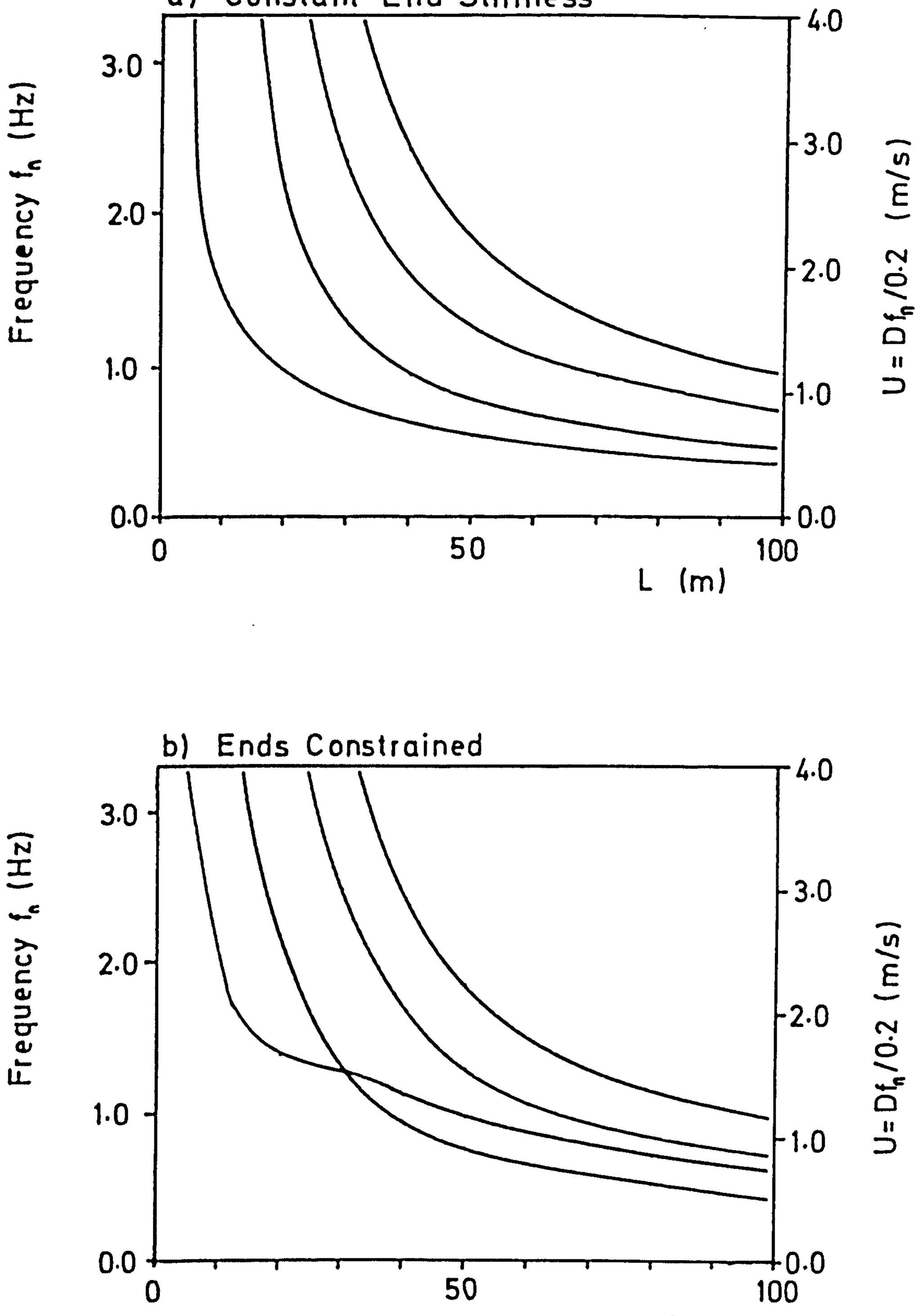

FIG 3.30 Pipe 1 Frequencies, $\mu = 3.0$

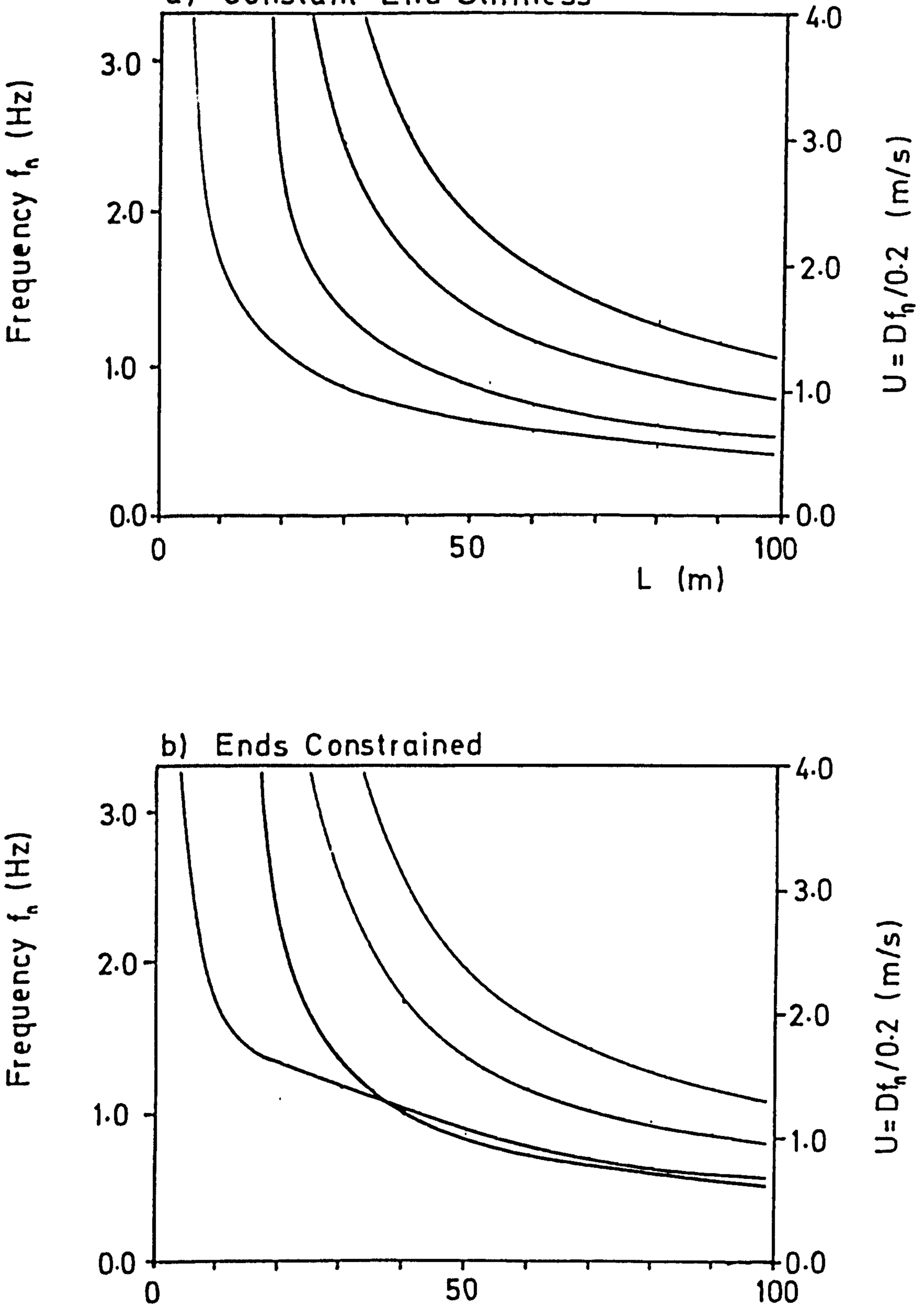

FIG 3.31 Pipe 1 Frequencies, $\mu = 10.0$

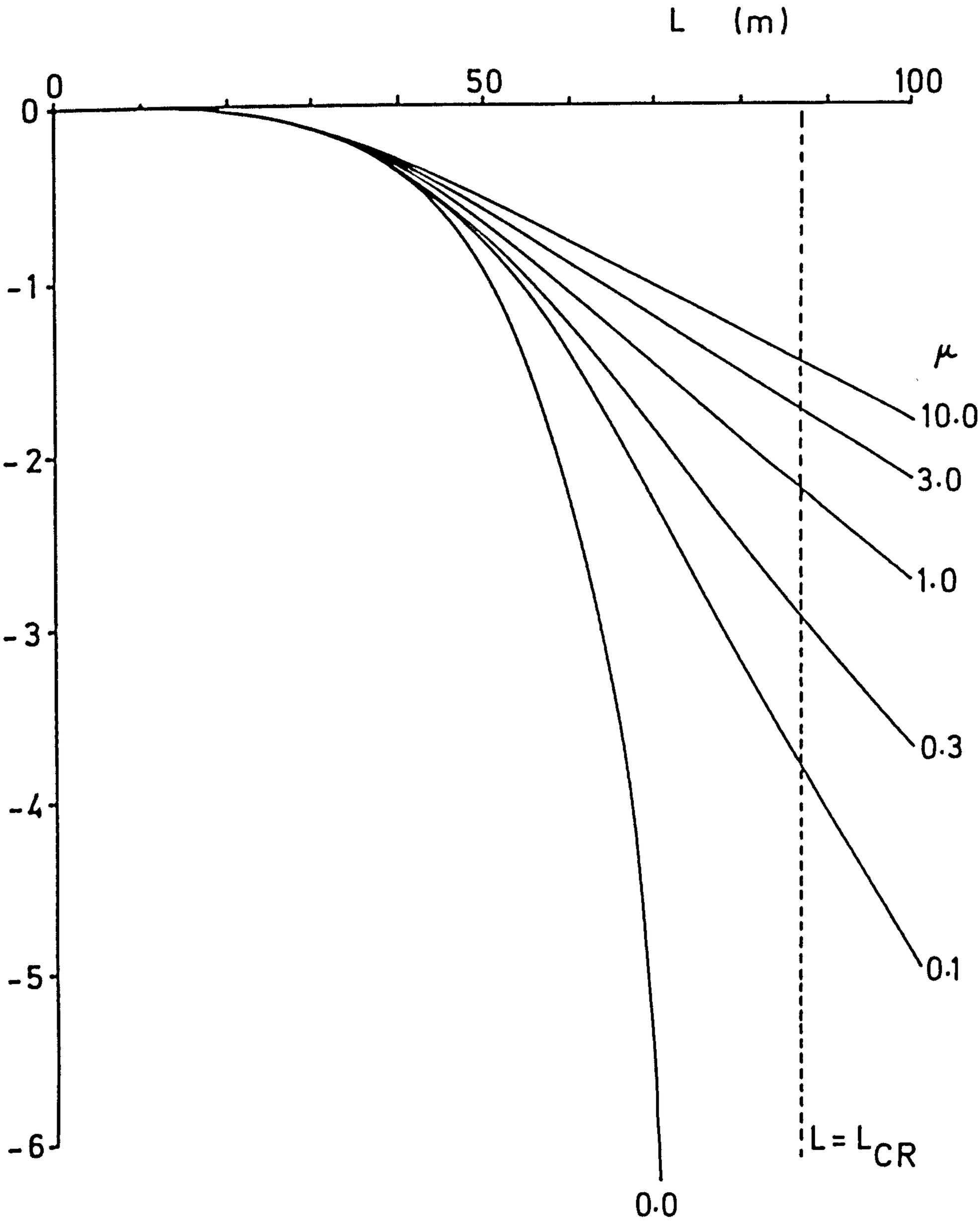

FIG 3.32 Pipe 2 Centre Deflection

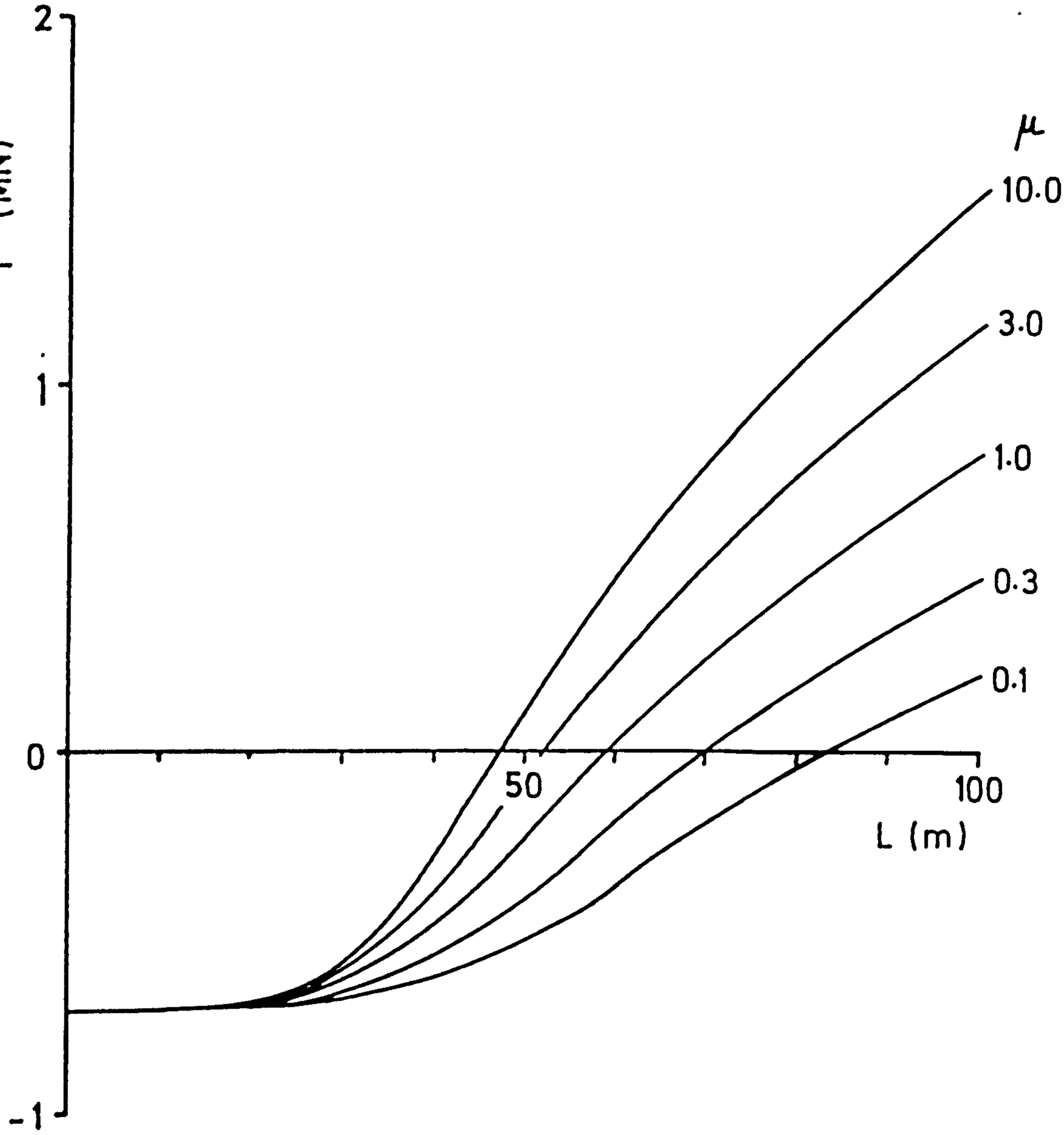

FIG 3.33 Pipe 2 Variable Effective Tension T^V

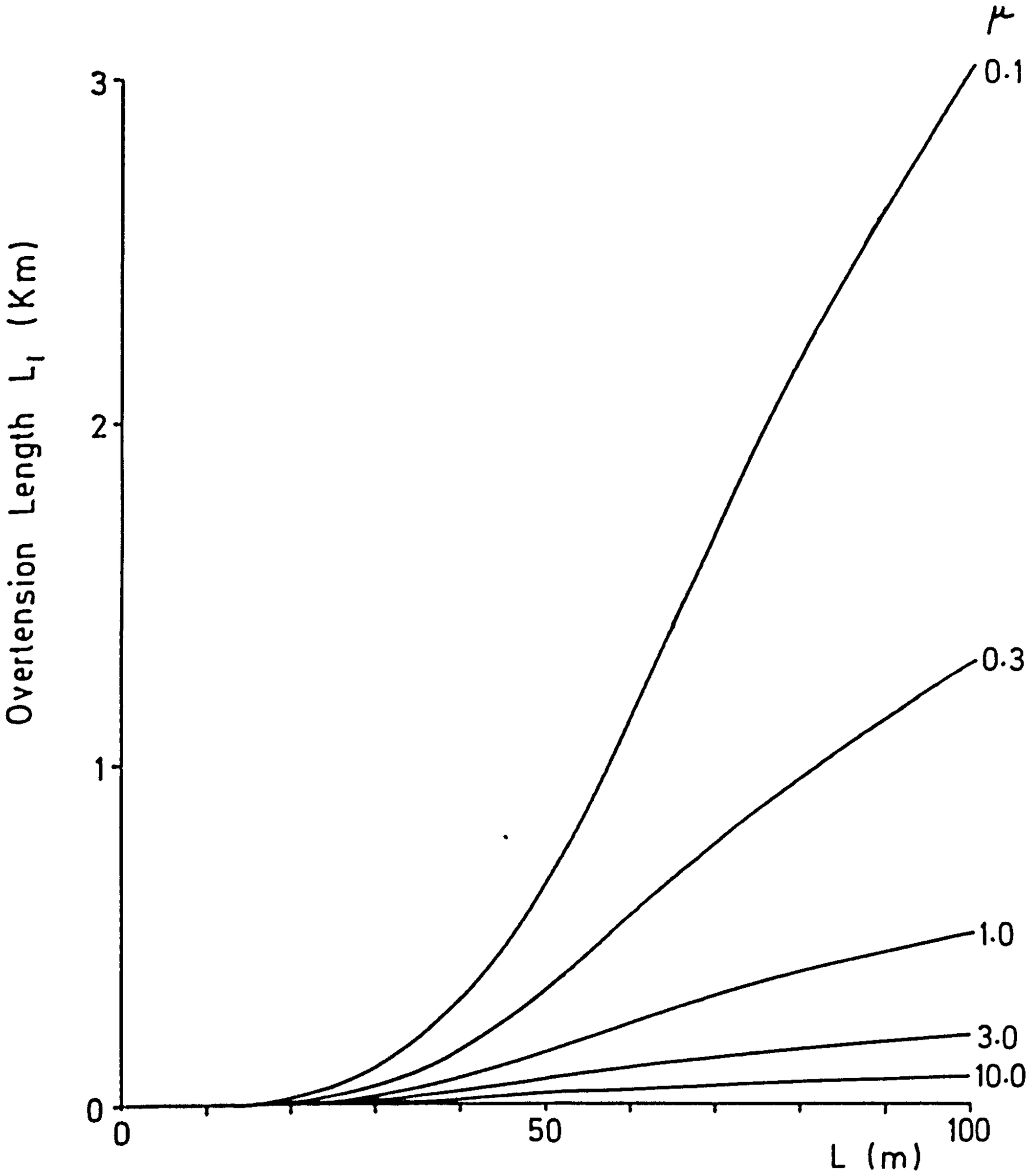

FIG 3.34 Pipe 2 Overtension Length L_1

(See Fig 3.9)

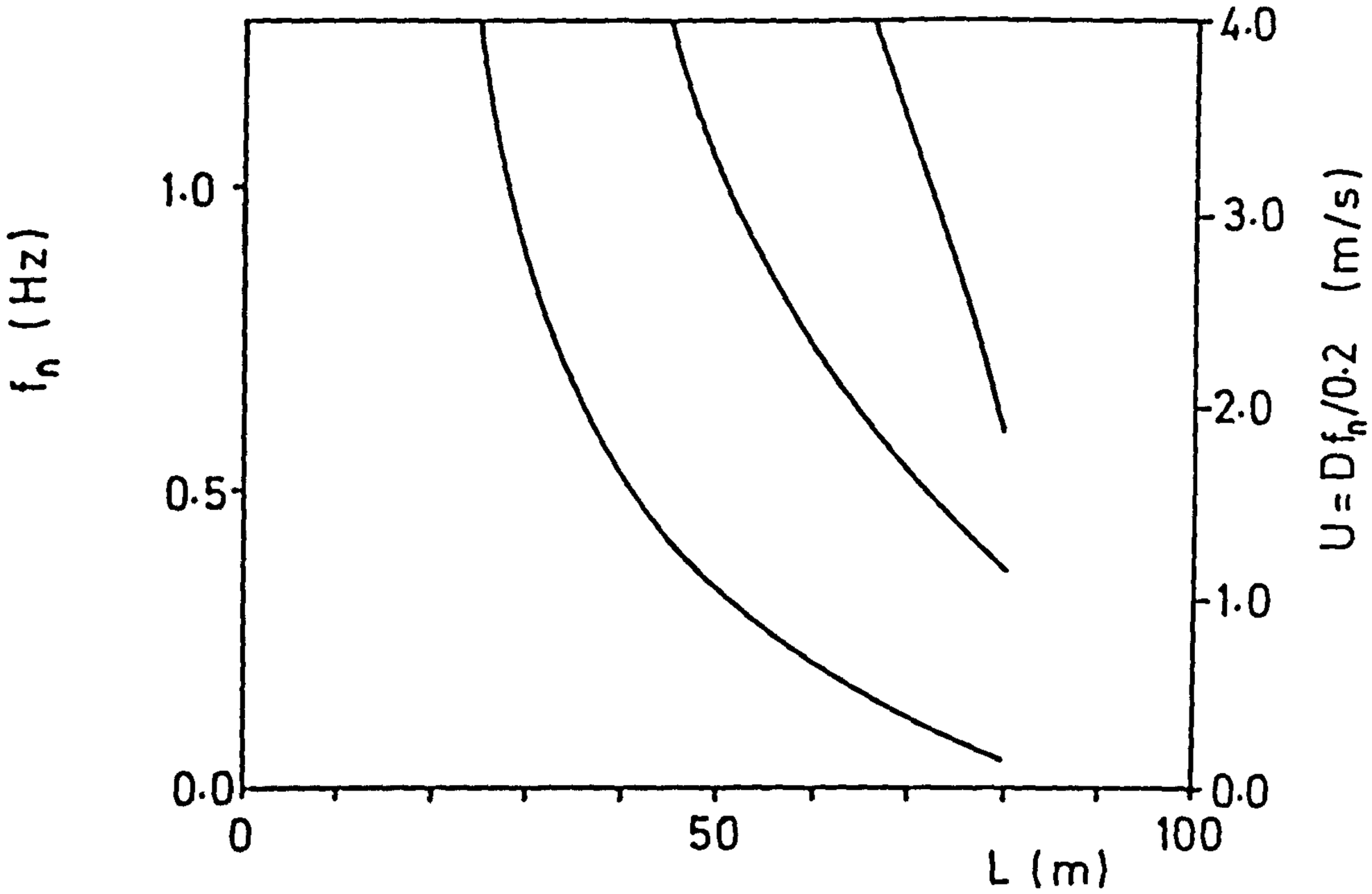

FIG 3.35 Pipe 2 Frequencies, μ = 0.0
(Ends Unconstrained)

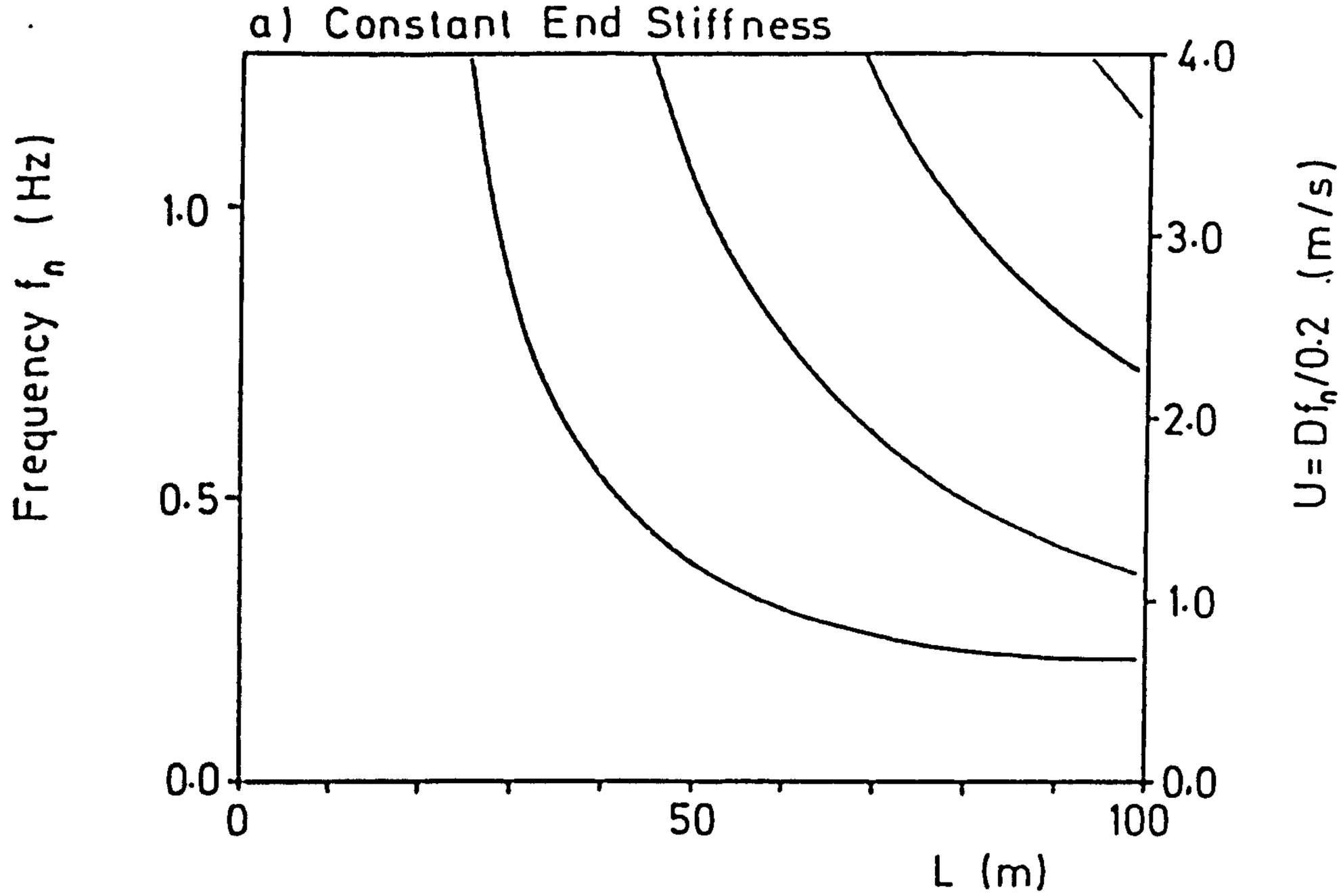

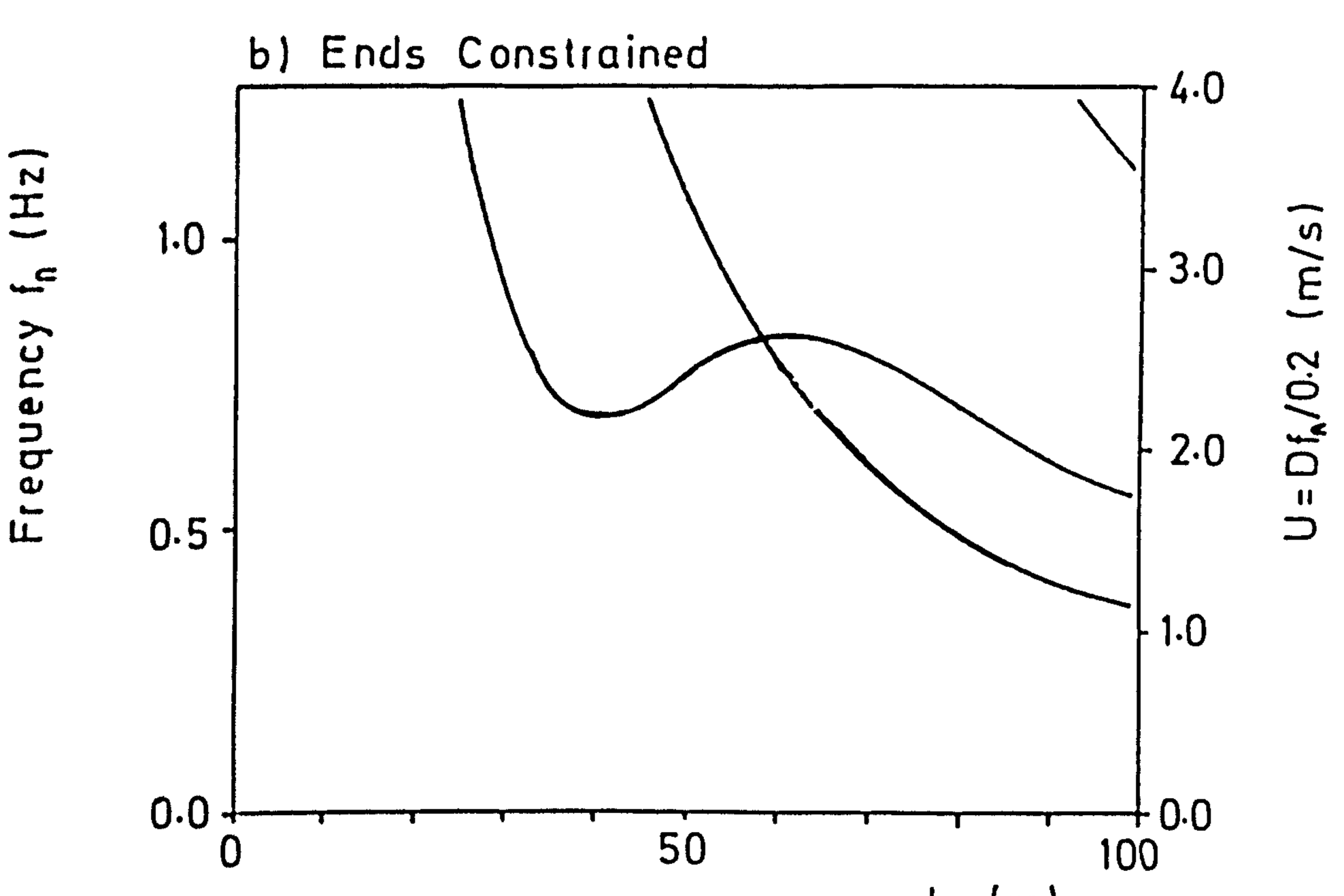

FIG 3.36 Pipe 2 Frequencies , $\mu = 0.1$

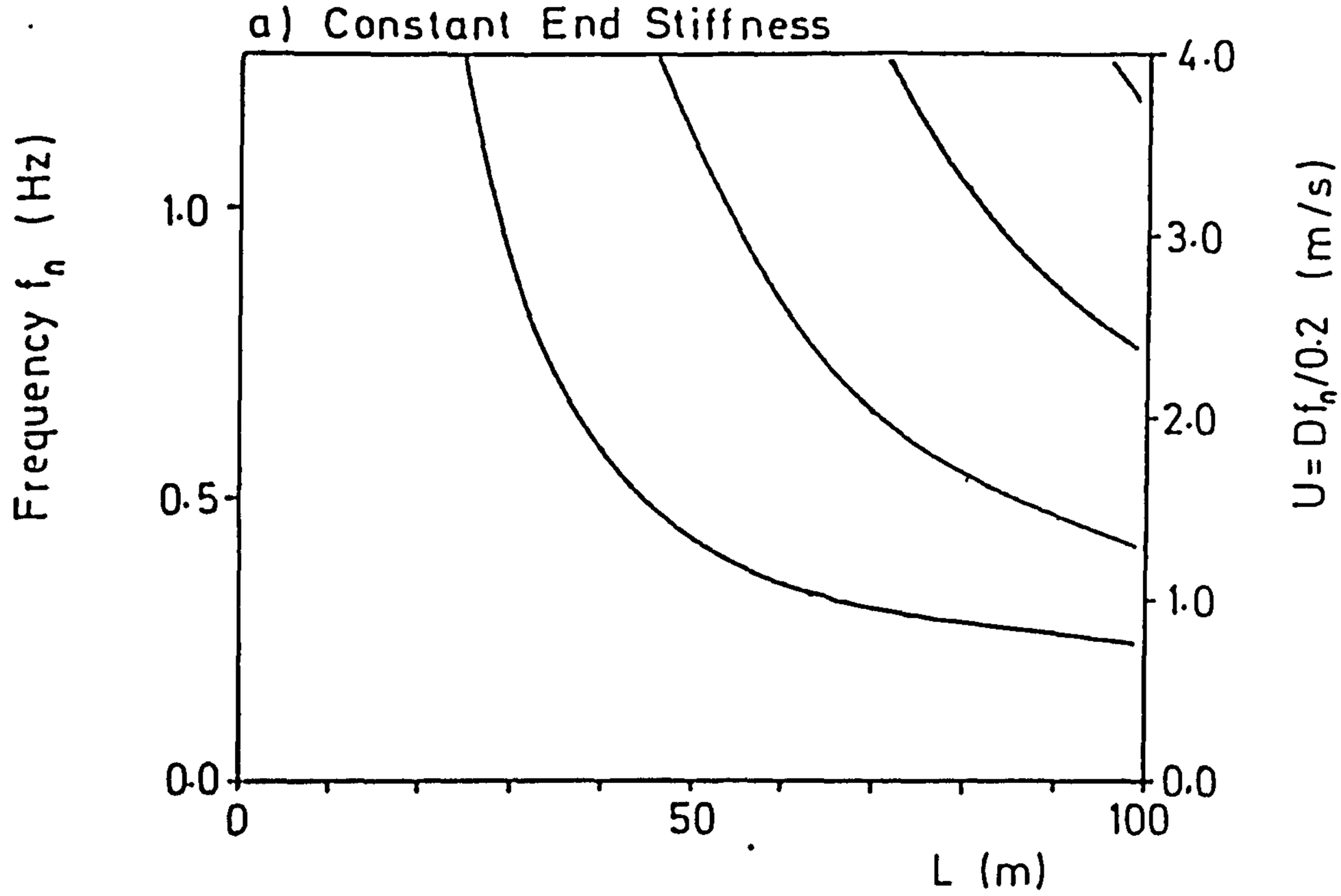

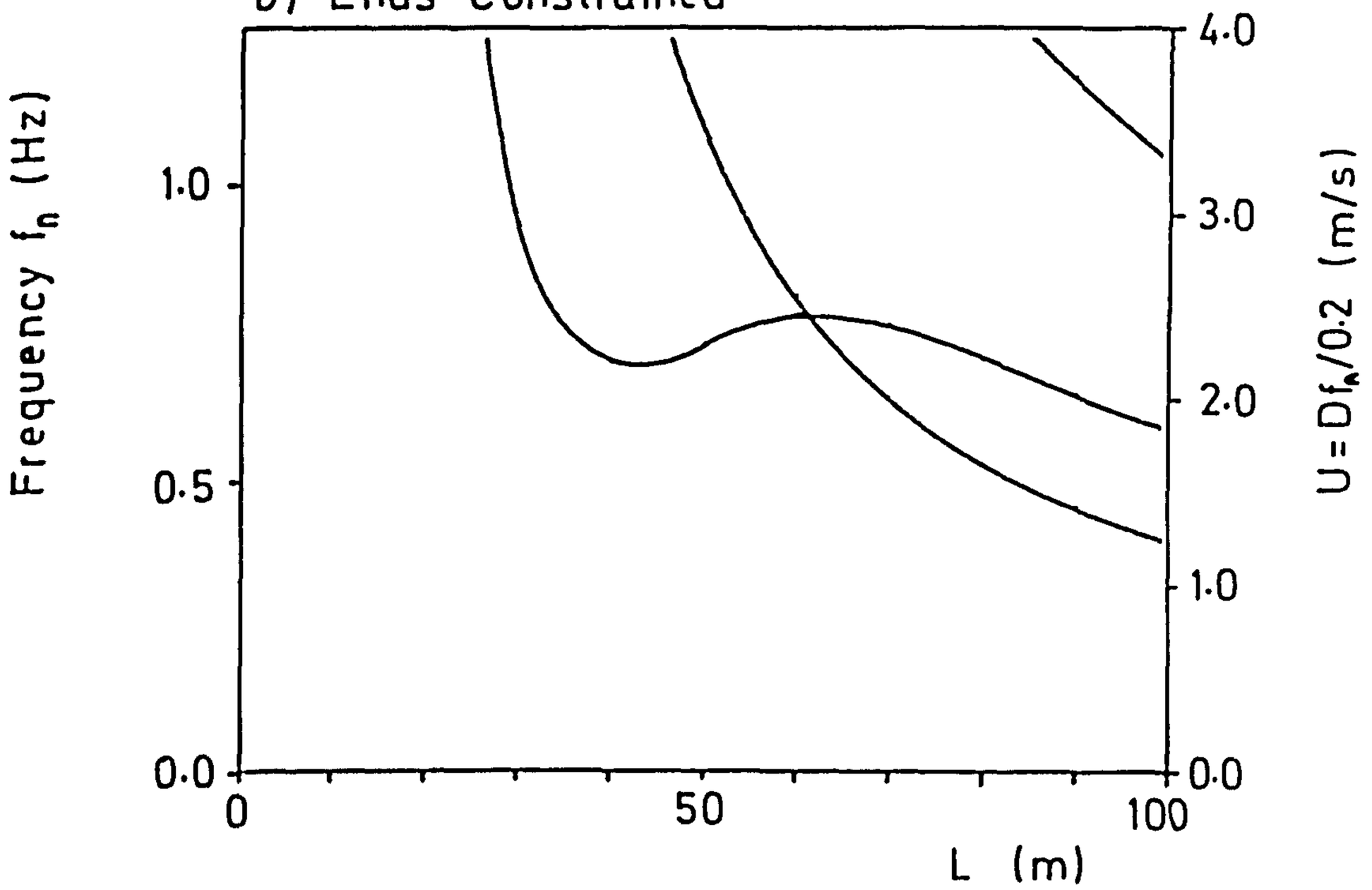

FIG 3.37 Pipe 2 Frequencies , $\mu = 0.3$

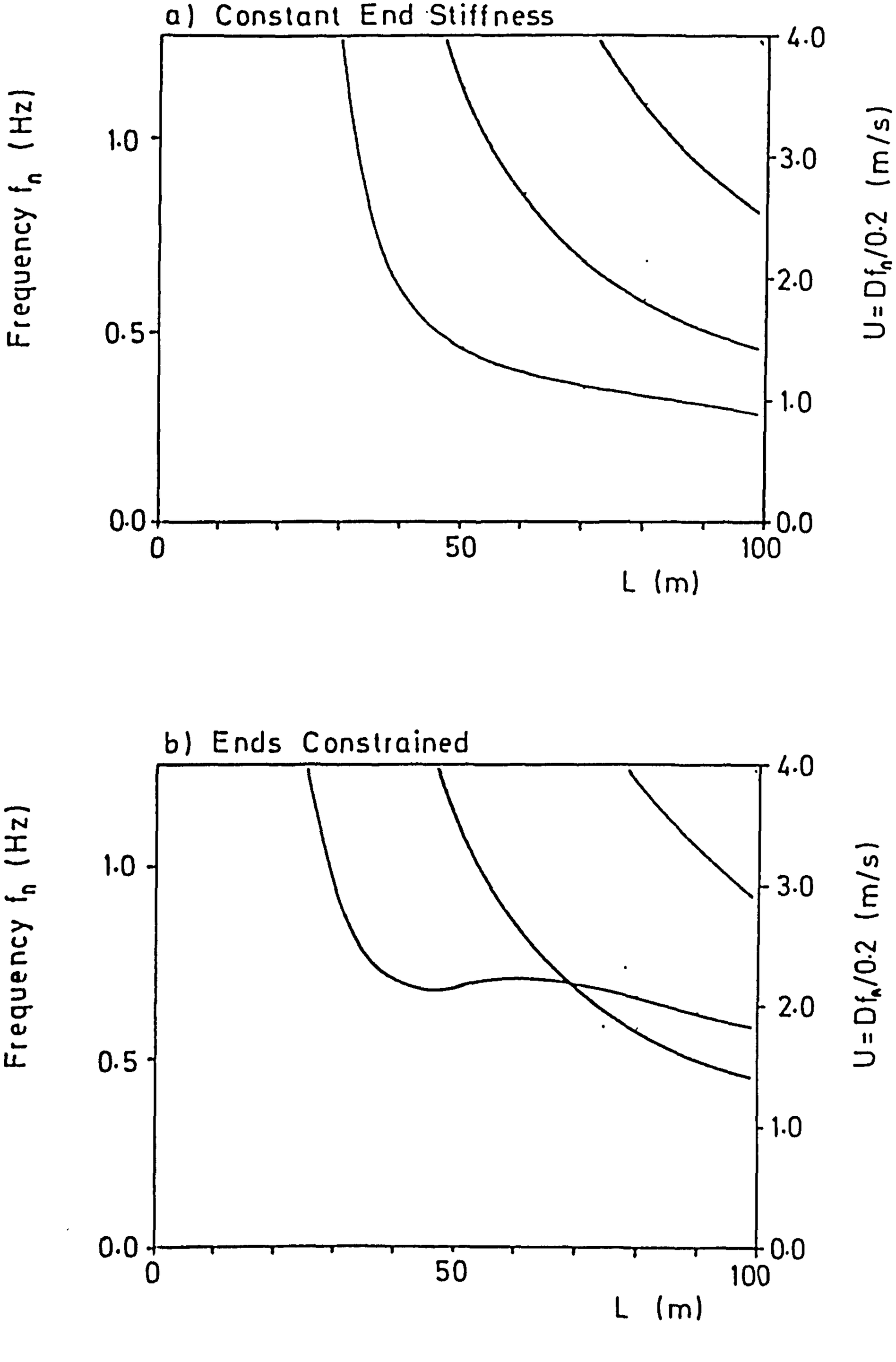

FIG 3.38 Pipe 2 Frequencies, $\mu = 1.0$

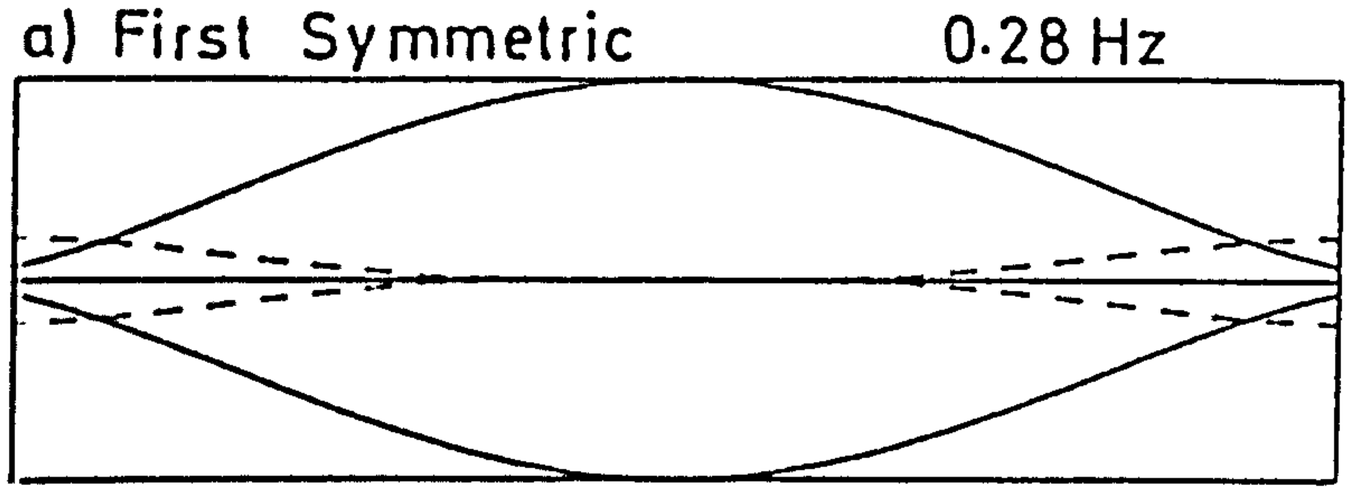

FIG 3.39a Pipe 2 Mode Shapes, L=100m, μ=1.0
Constant End Stiffness

a) First Antisymmetric 0.44 Hz

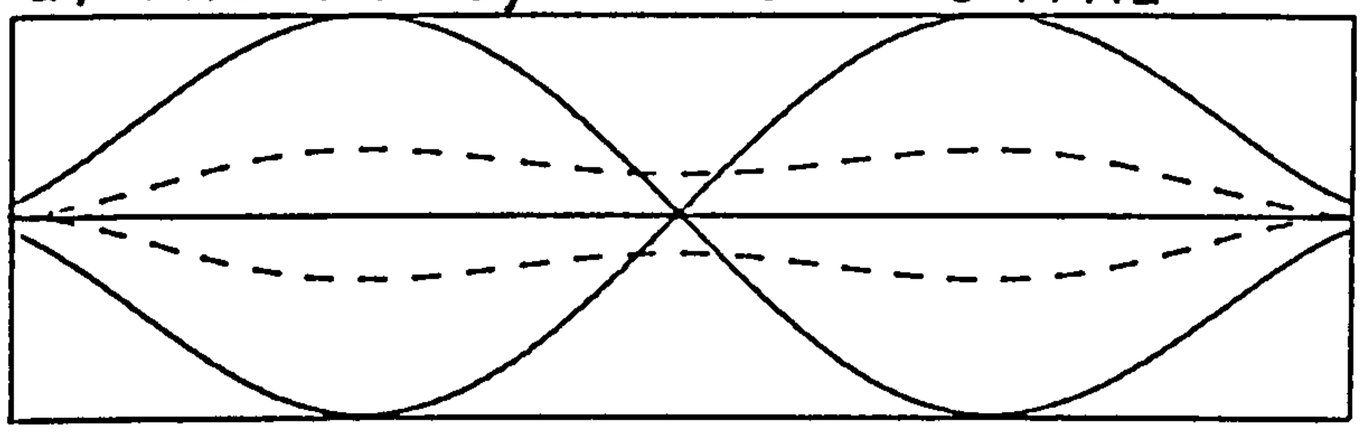

b) First Symmetric 0.58 Hz

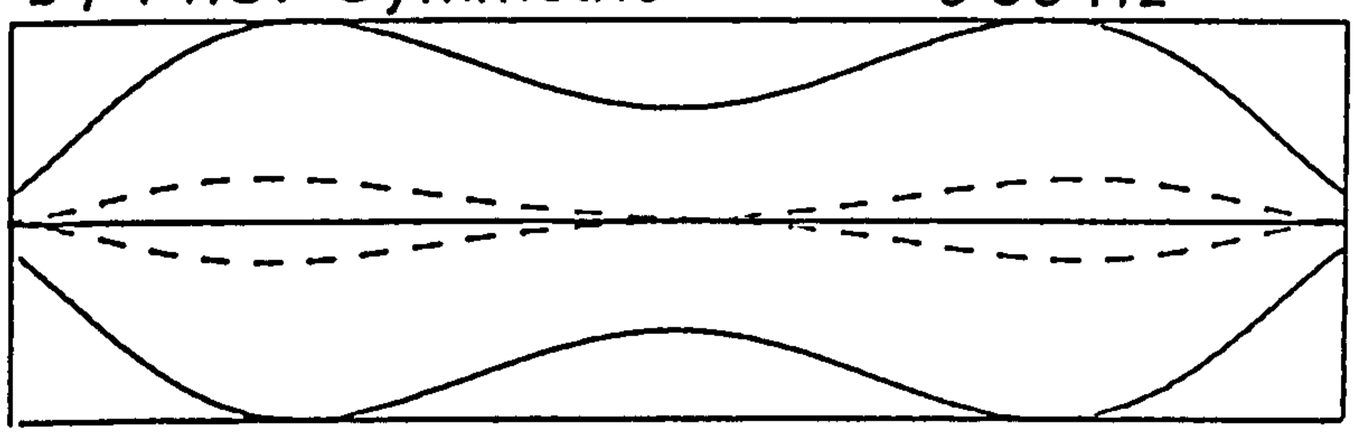

c) Second Symmetric 0.91 Hz

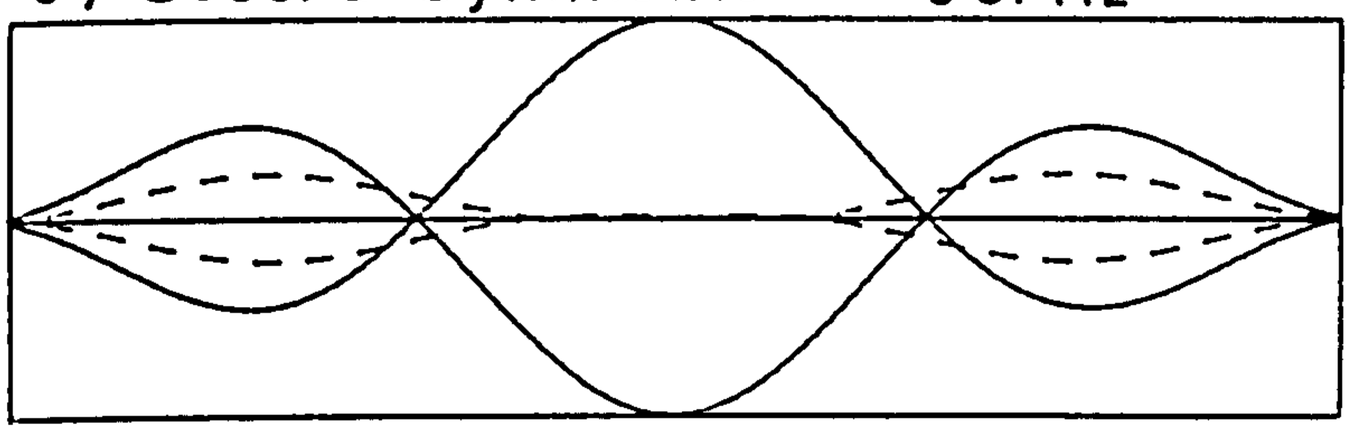

d) Second Antisymmetric 1.22 Hz

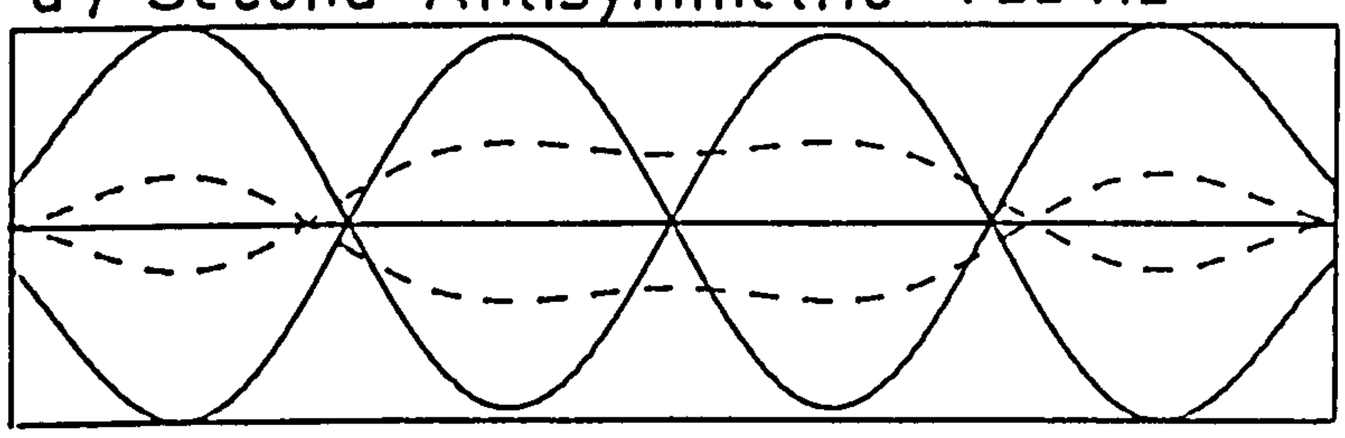

——— Vertical Disp.

--------- Horizontal Disp. (x5)

FIG 3.39b Pipe 2 Mode Shapes, L=100 m, μ =1.0
Ends Constrained

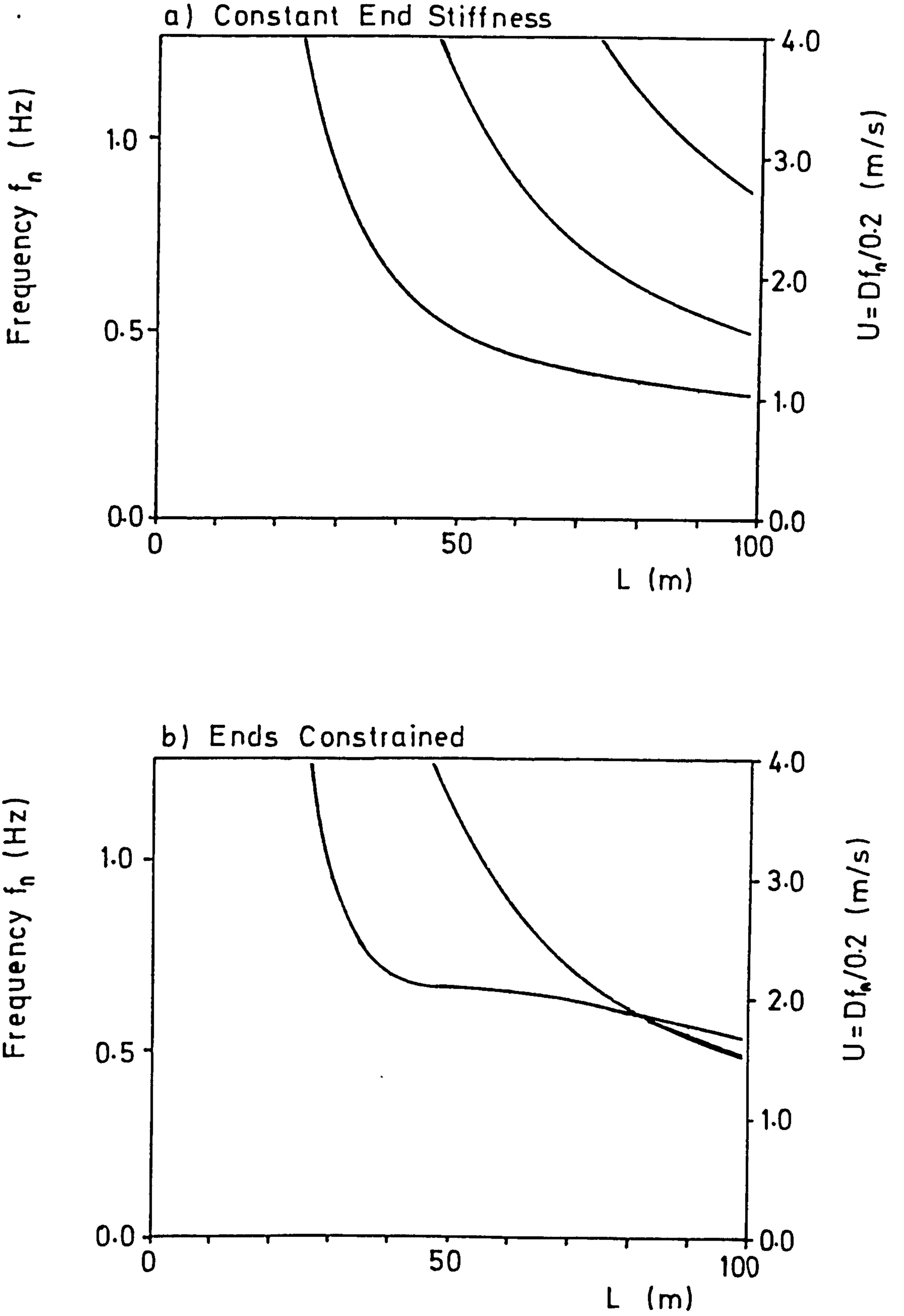

FIG 3.40 Pipe 2 Frequencies , $\mu = 3.0$

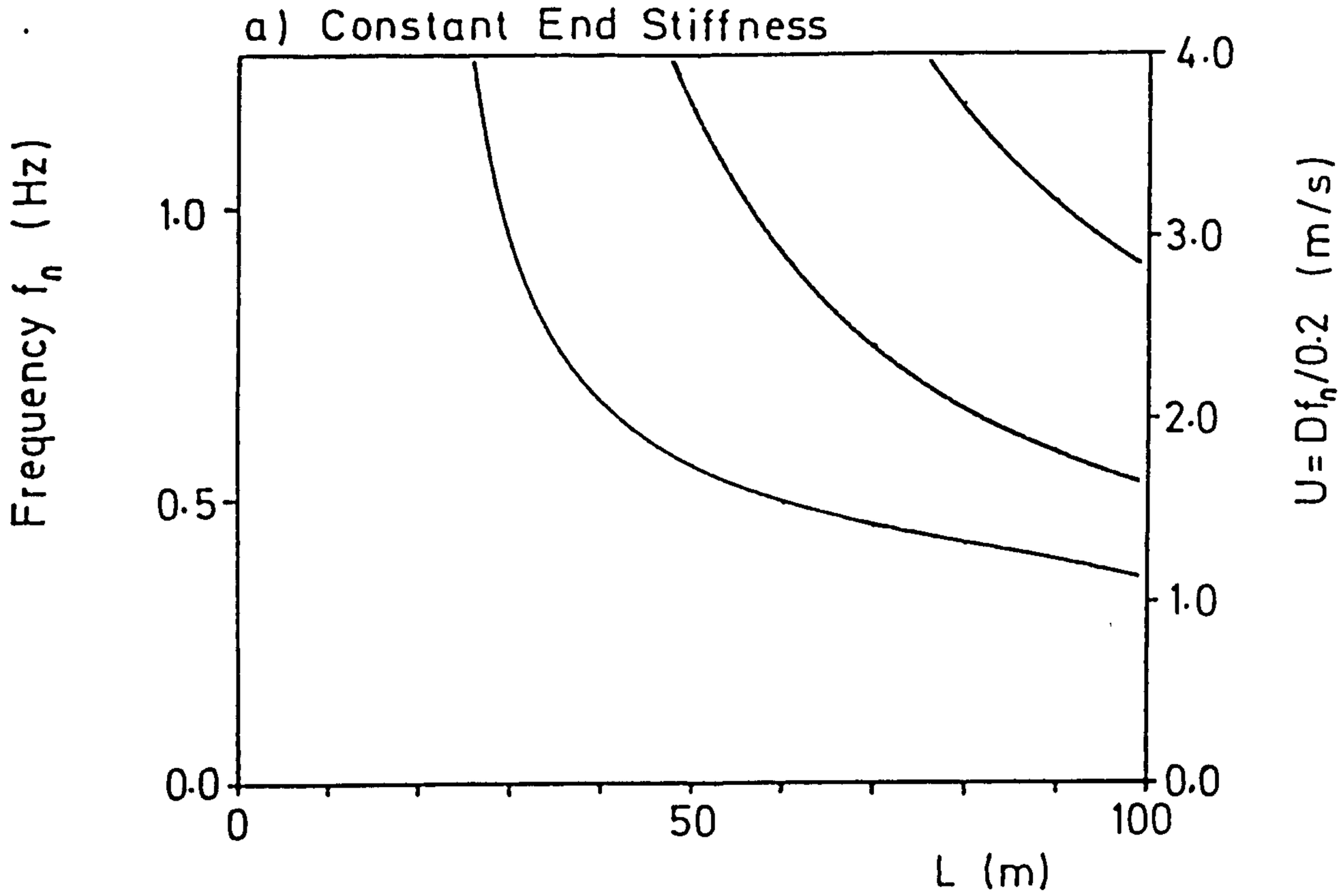

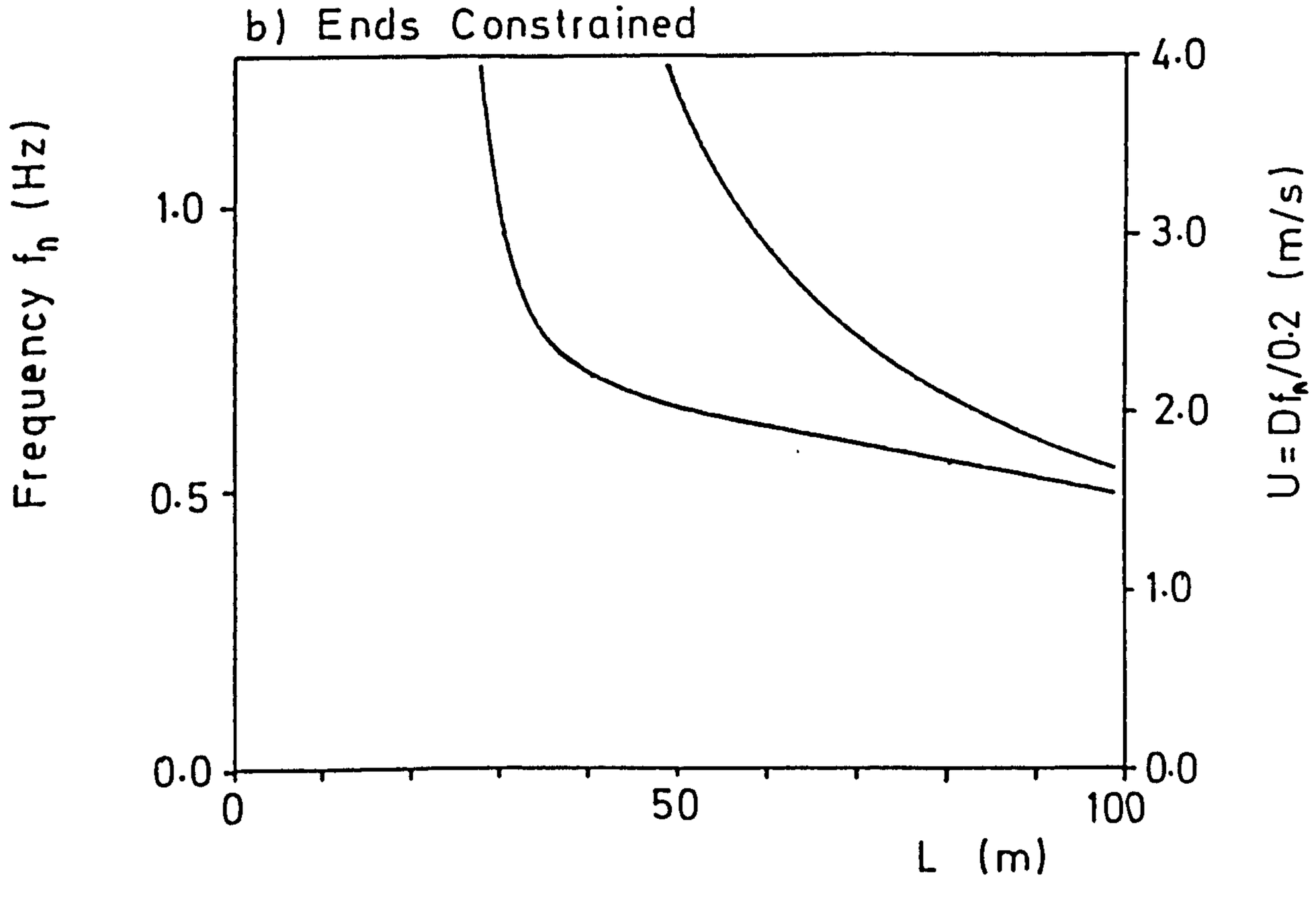

FIG 3.41 Pipe 2 Frequencies , $\mu = 10.0$

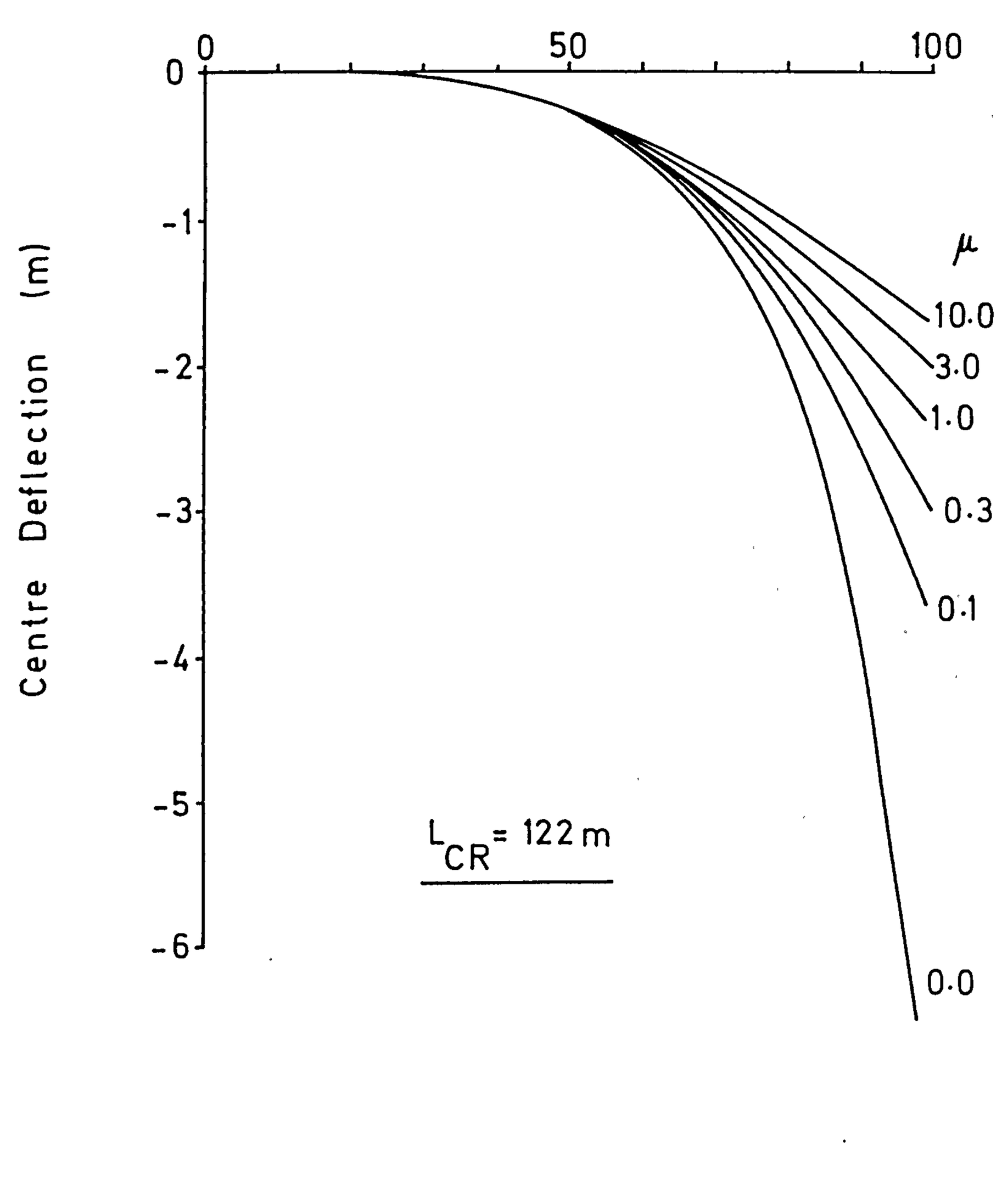

FIG 3.42 Pipe 3 Centre Deflection

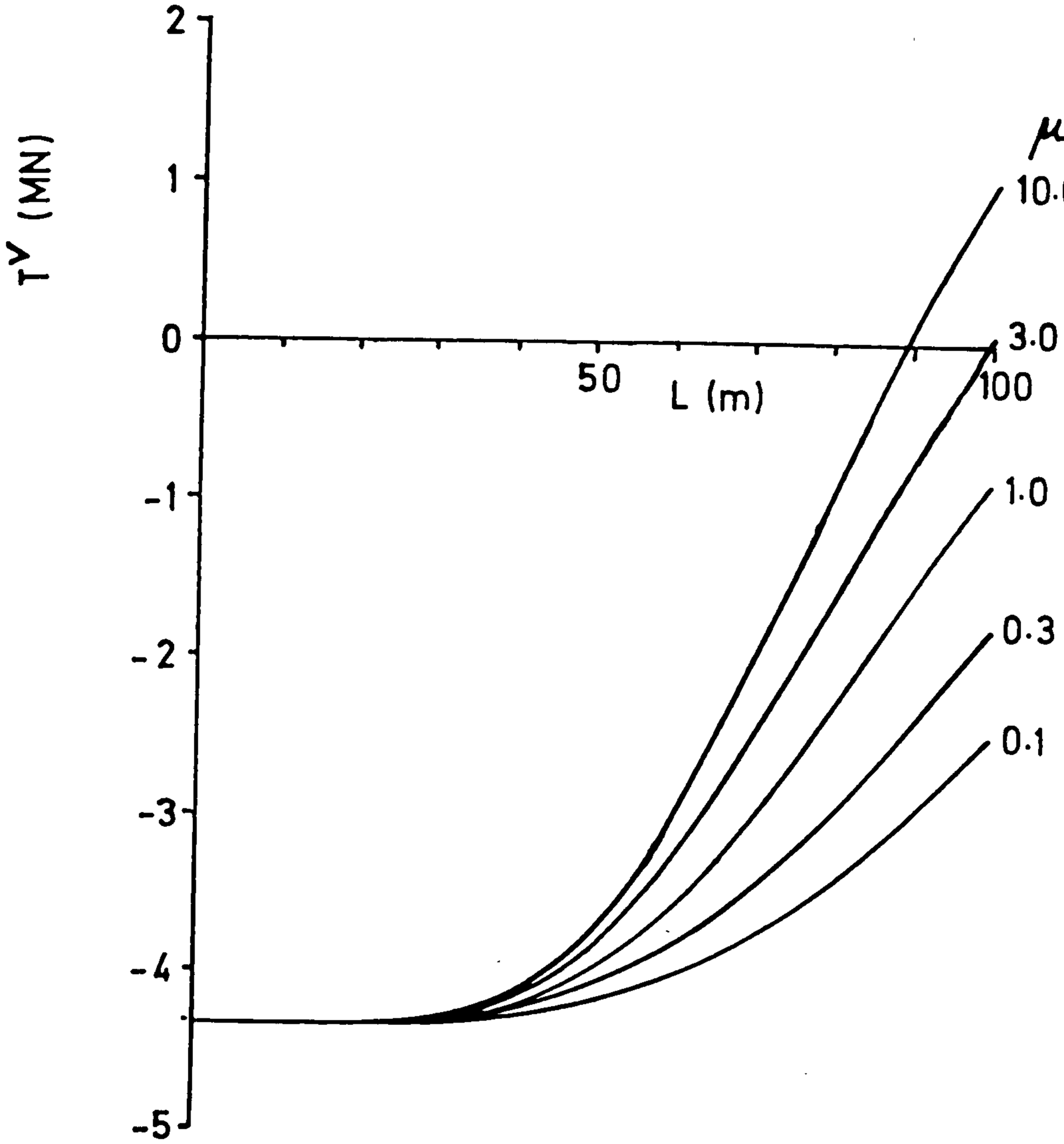

FIG 3.43 Pipe 3 Variable Effective Tension T^V

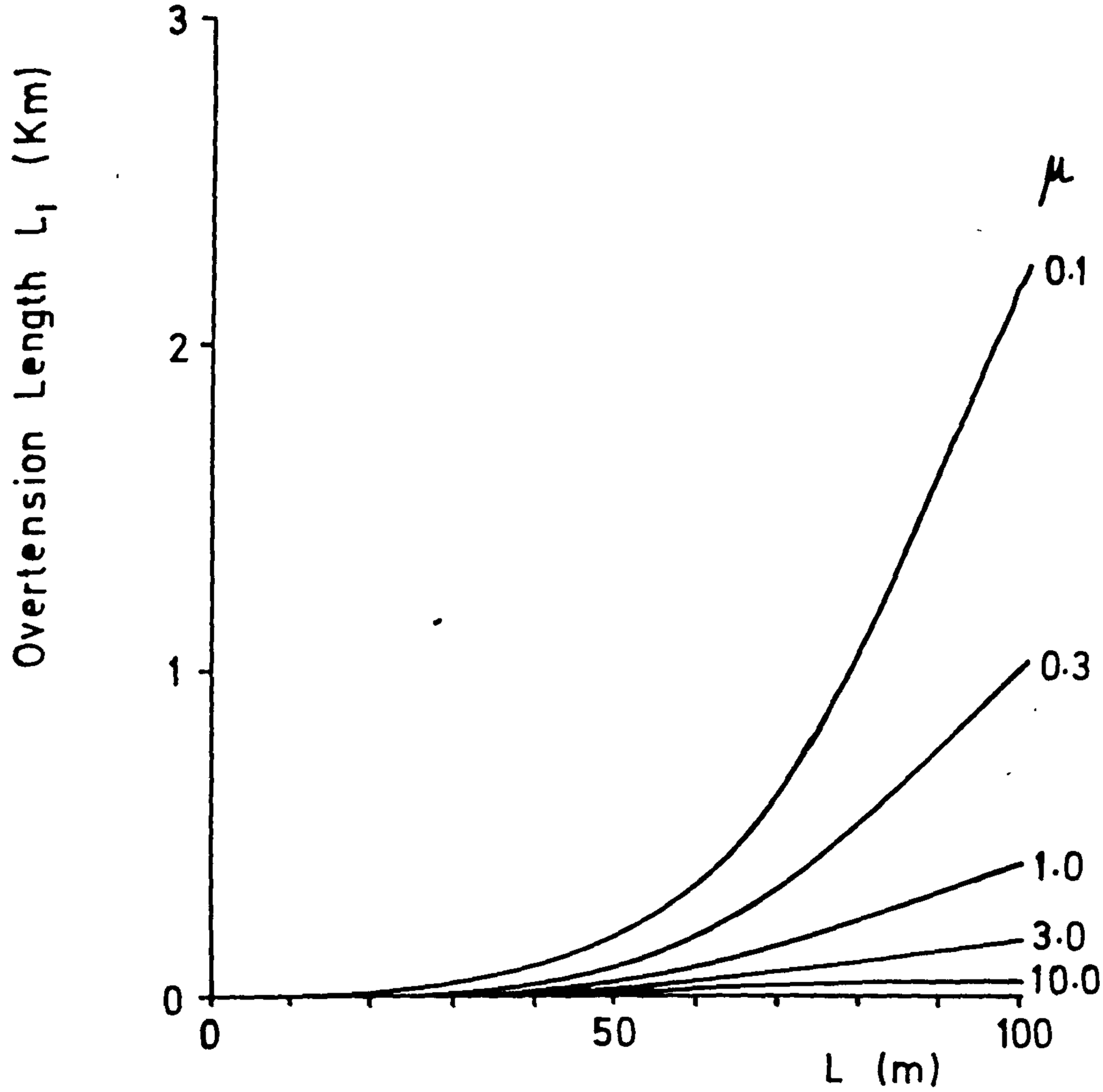

FIG 3.44 Pipe 3 Overtension Length L_1
(See FIG 3.9)

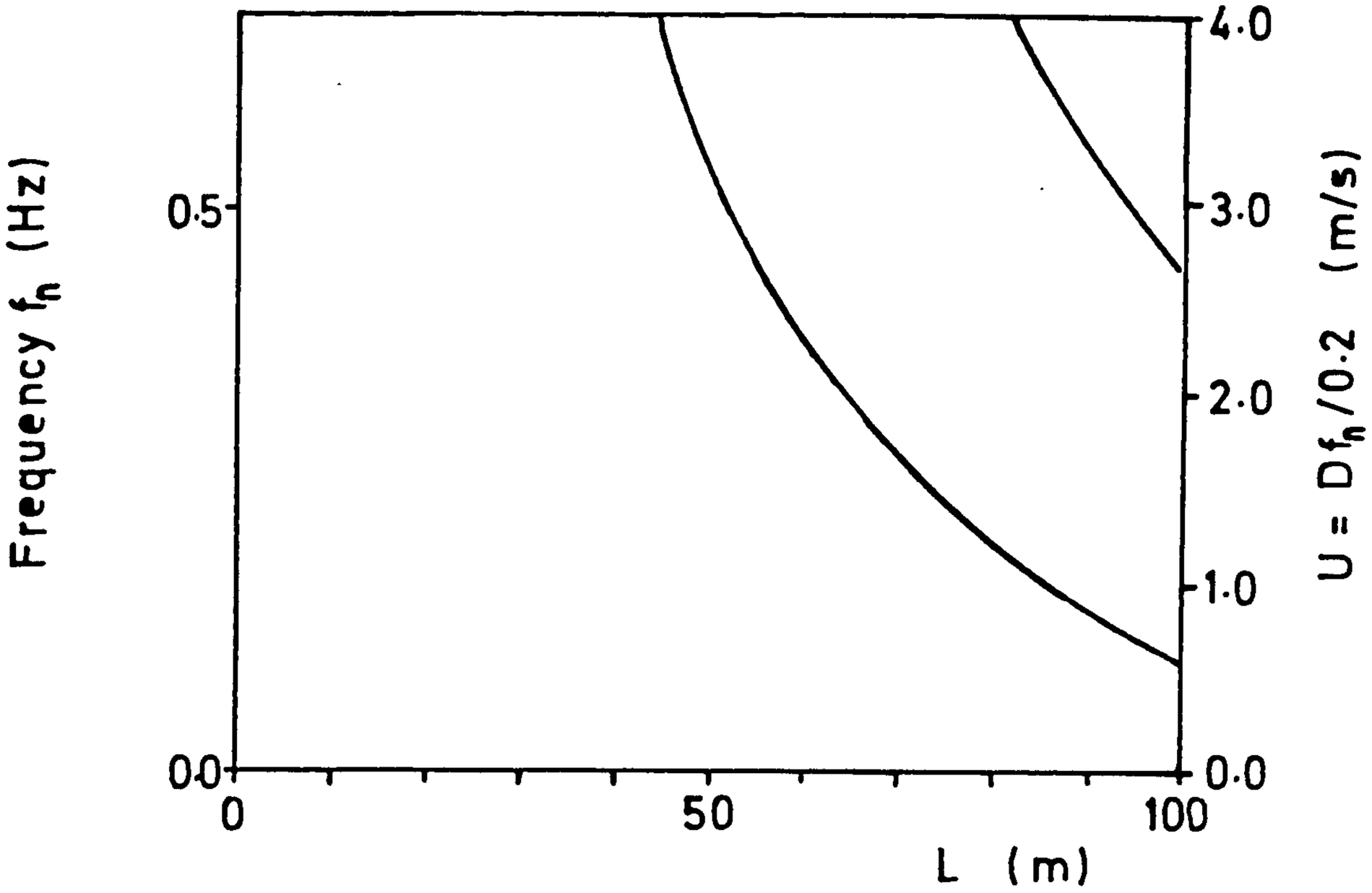

FIG 3.45 Pipe 3 Frequencies, $\mu = 0.0$
(Ends Unconstrained)

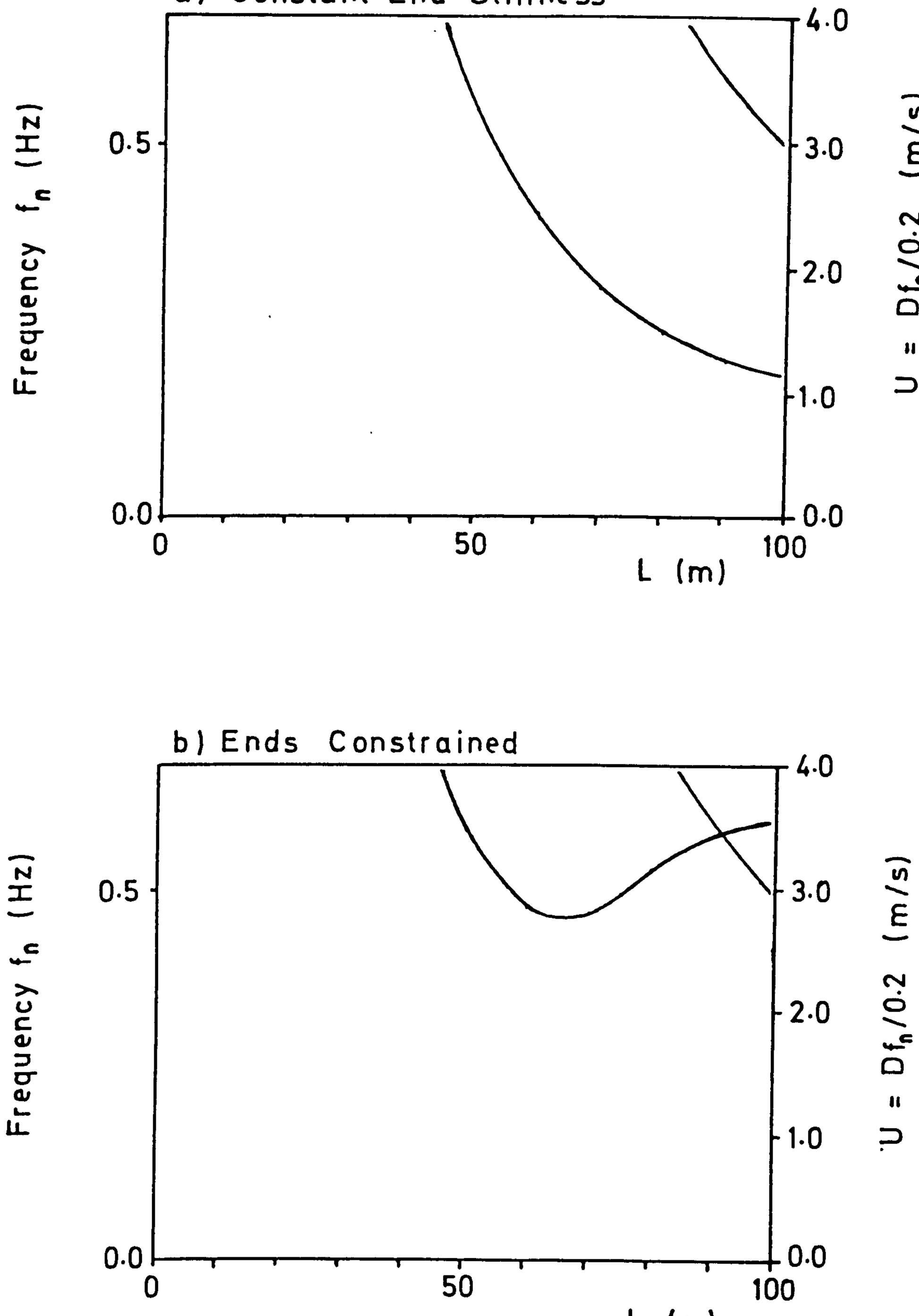

FIG 3.46 Pipe 3 Frequencies, $\mu = 0.1$

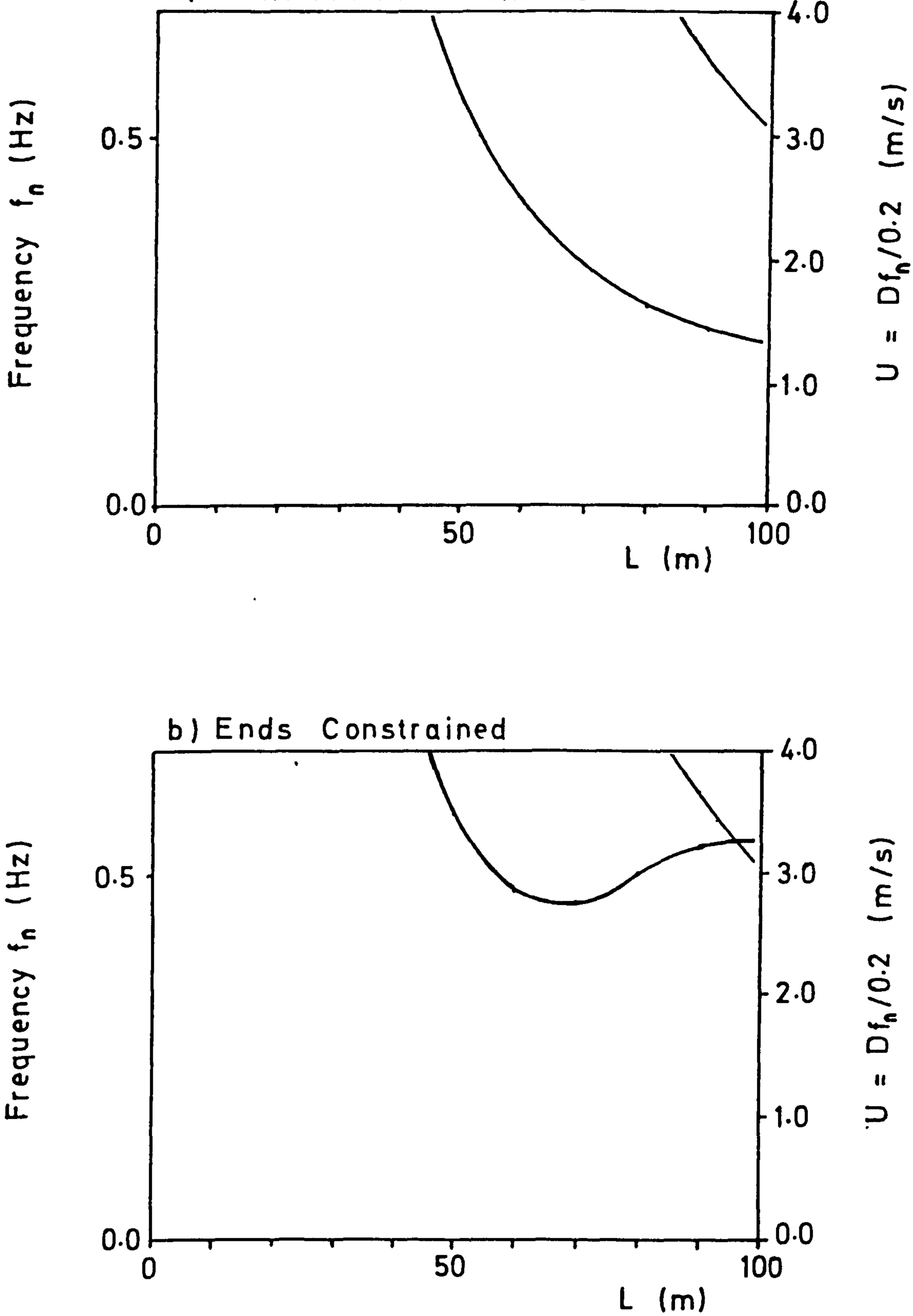

FIG 3.47 Pipe 3 Frequencies, $\mu = 0.3$

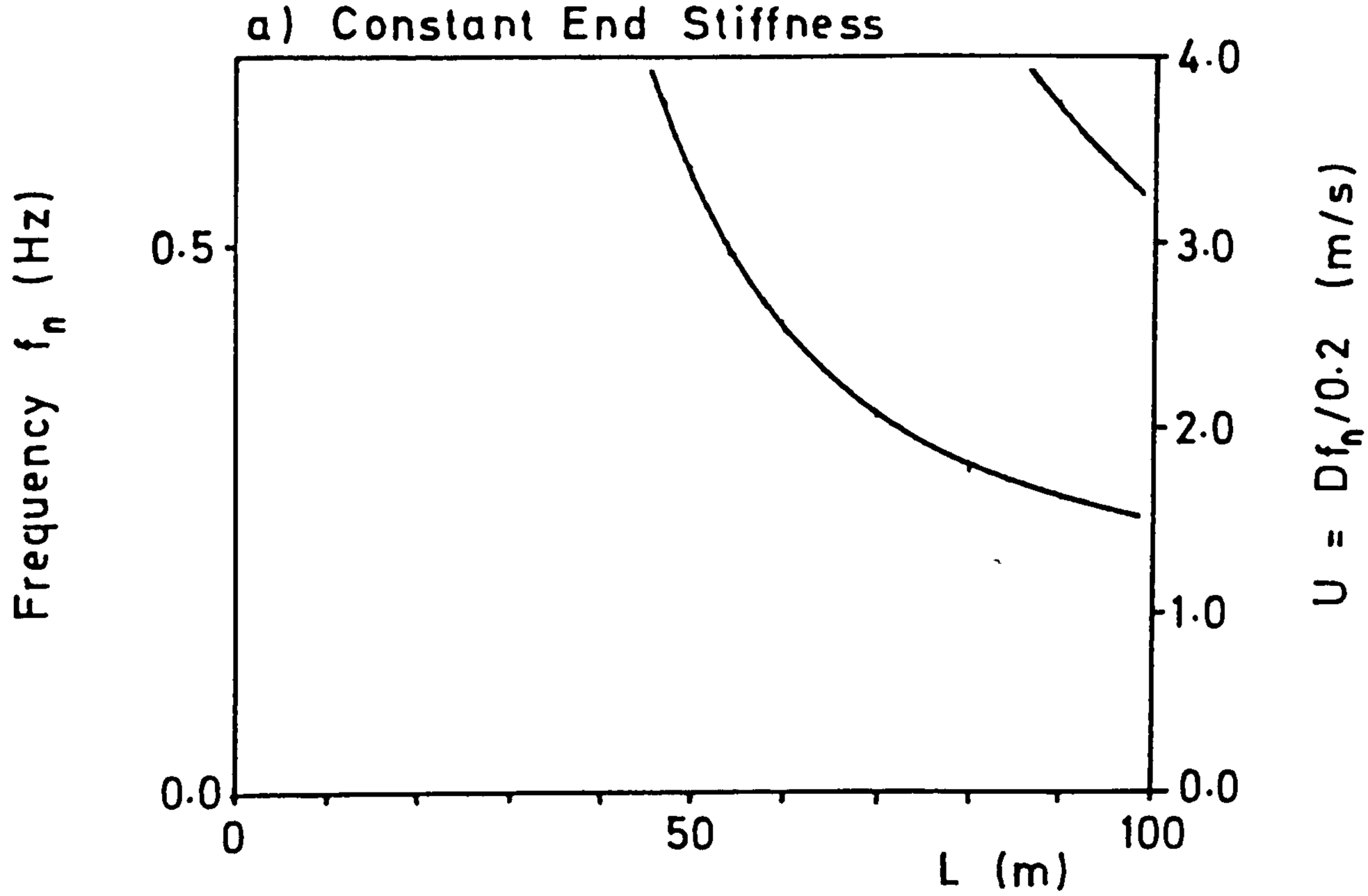

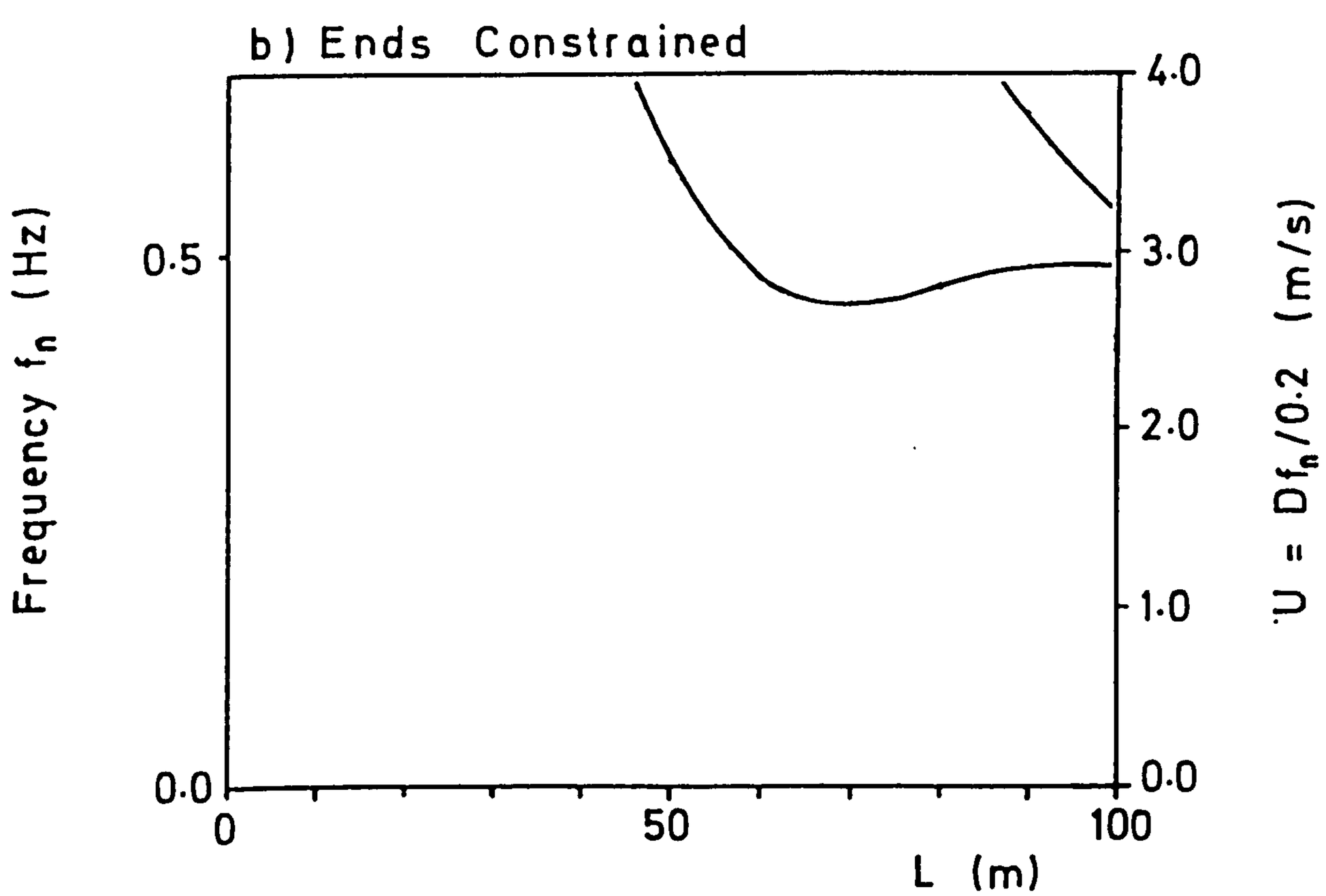

FIG 3.48 Pipe 3 Frequencies, $\mu = 1.0$

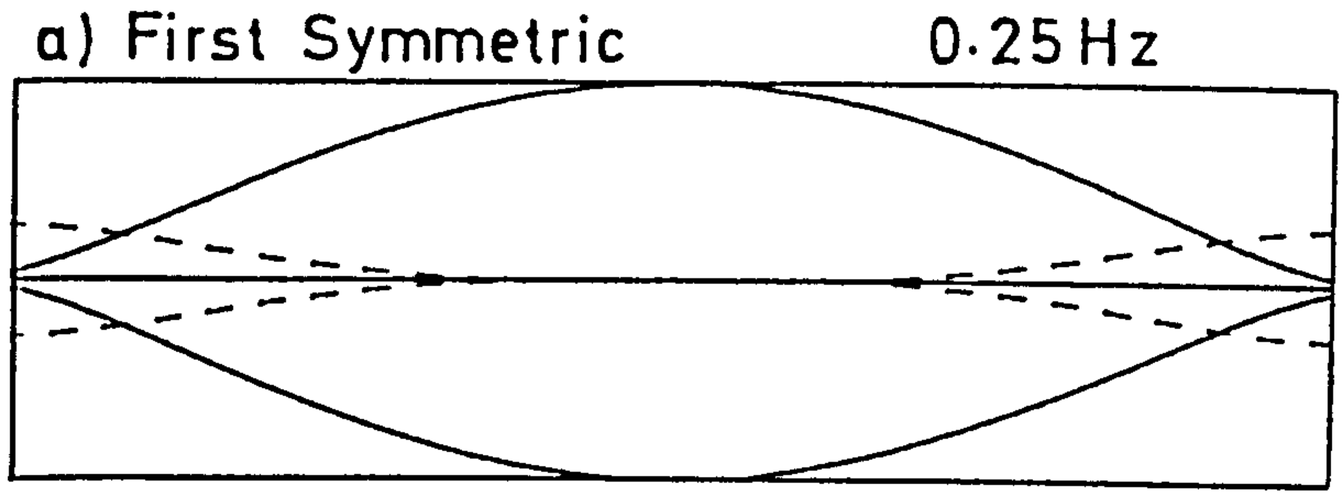

FIG 3·49a Pipe 3 Mode Shapes, L=100 m, μ = 1·0
Constant End Stiffness

a) First Symmetric 0.49 Hz

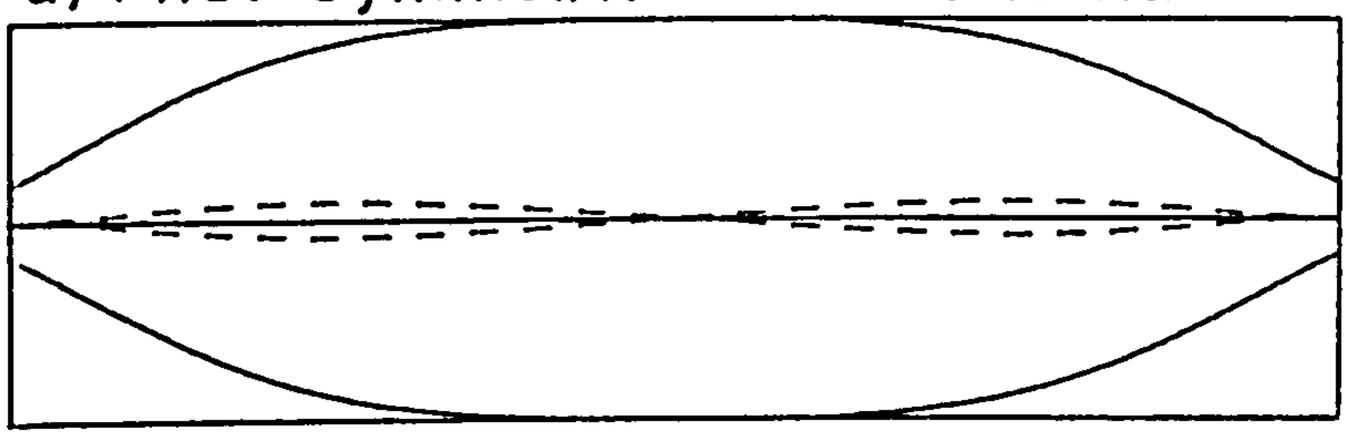

b) First Antisymmetric 0.54 Hz

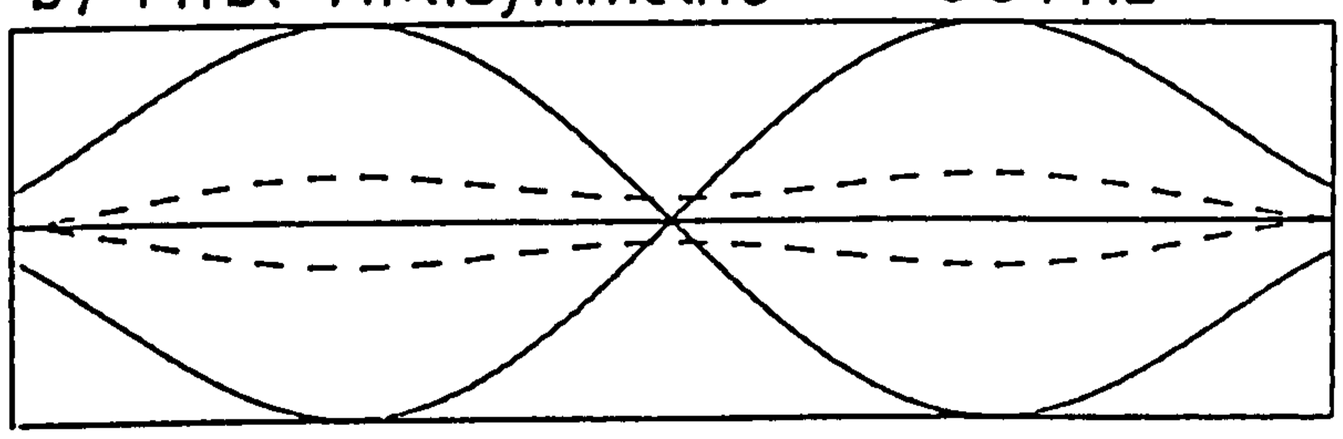

c) Second Symmetric 1.19 Hz

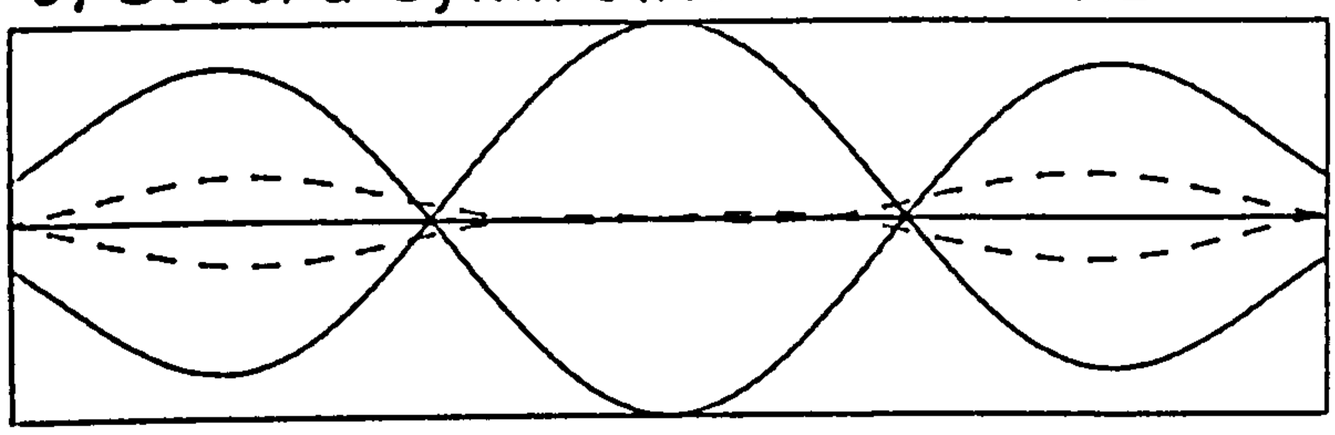

d) Second Antisymmetric 1.76 Hz

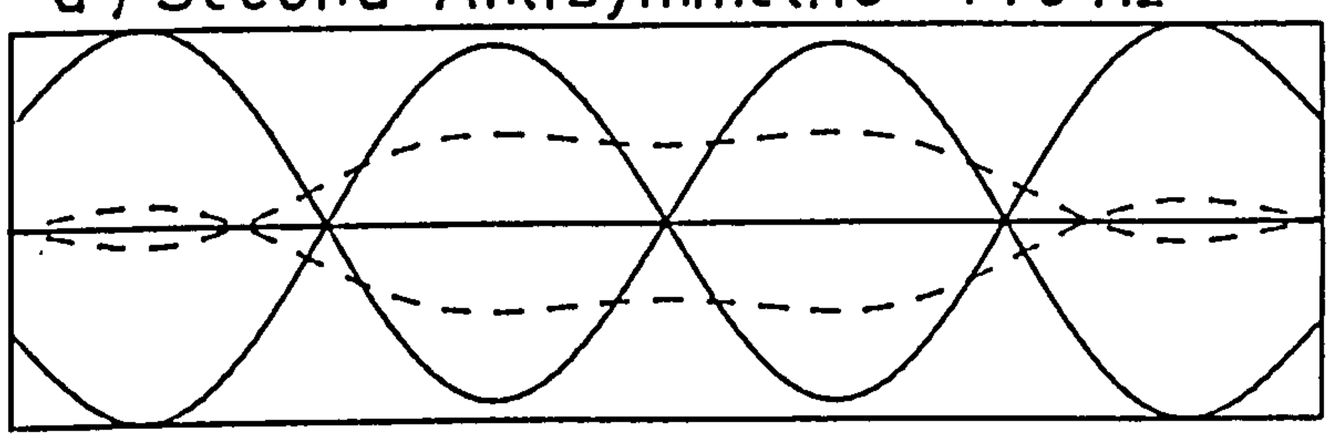

——— Vertical Disp.

- - - - - - - - Horizontal Disp. (x 5)

FIG 3.49b Pipe 3 Mode Shapes, L=100m, μ = 1.0
Ends Constrained

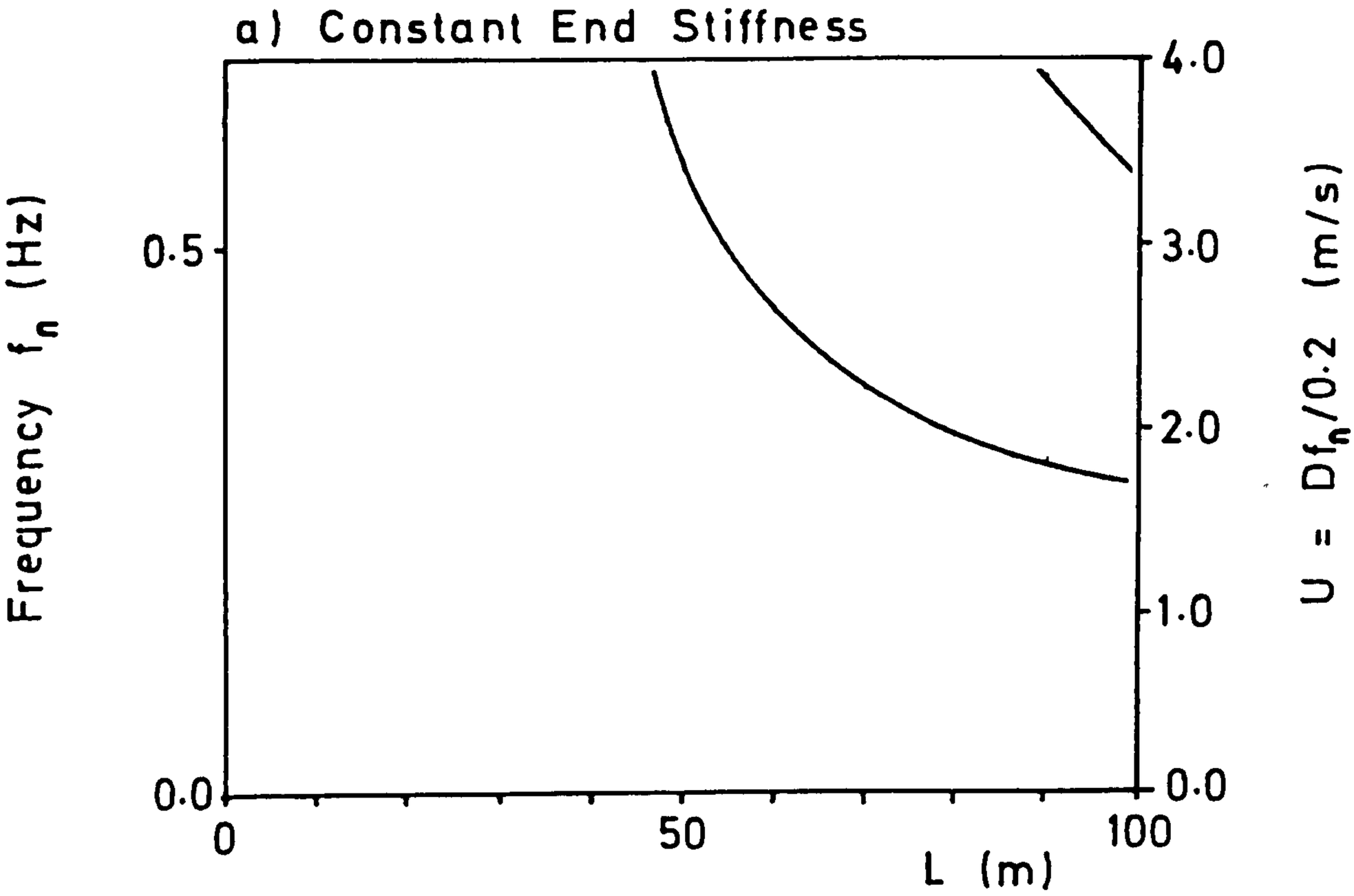

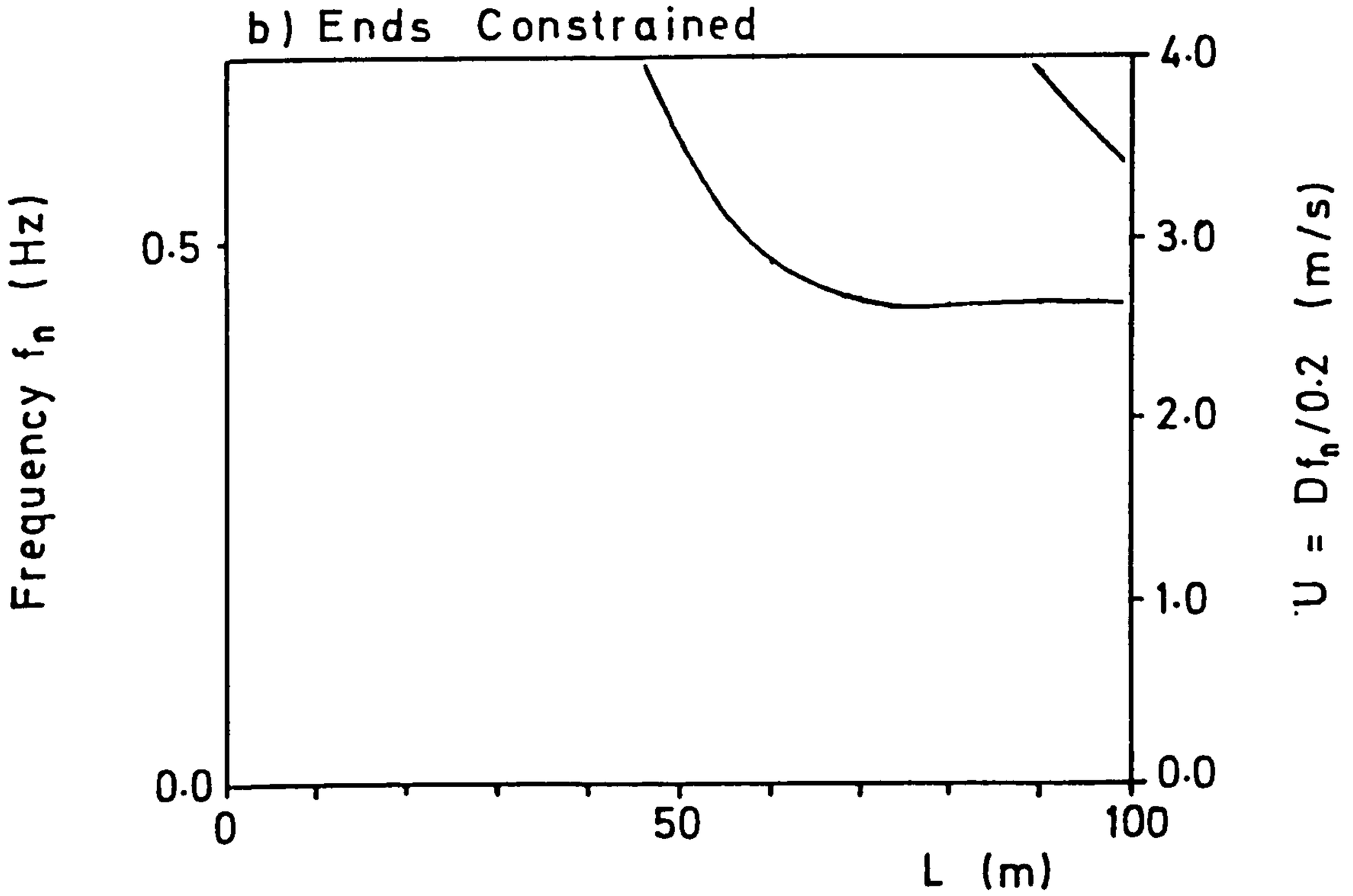

FIG 3.50 Pipe 3 Frequencies, $\mu = 3.0$

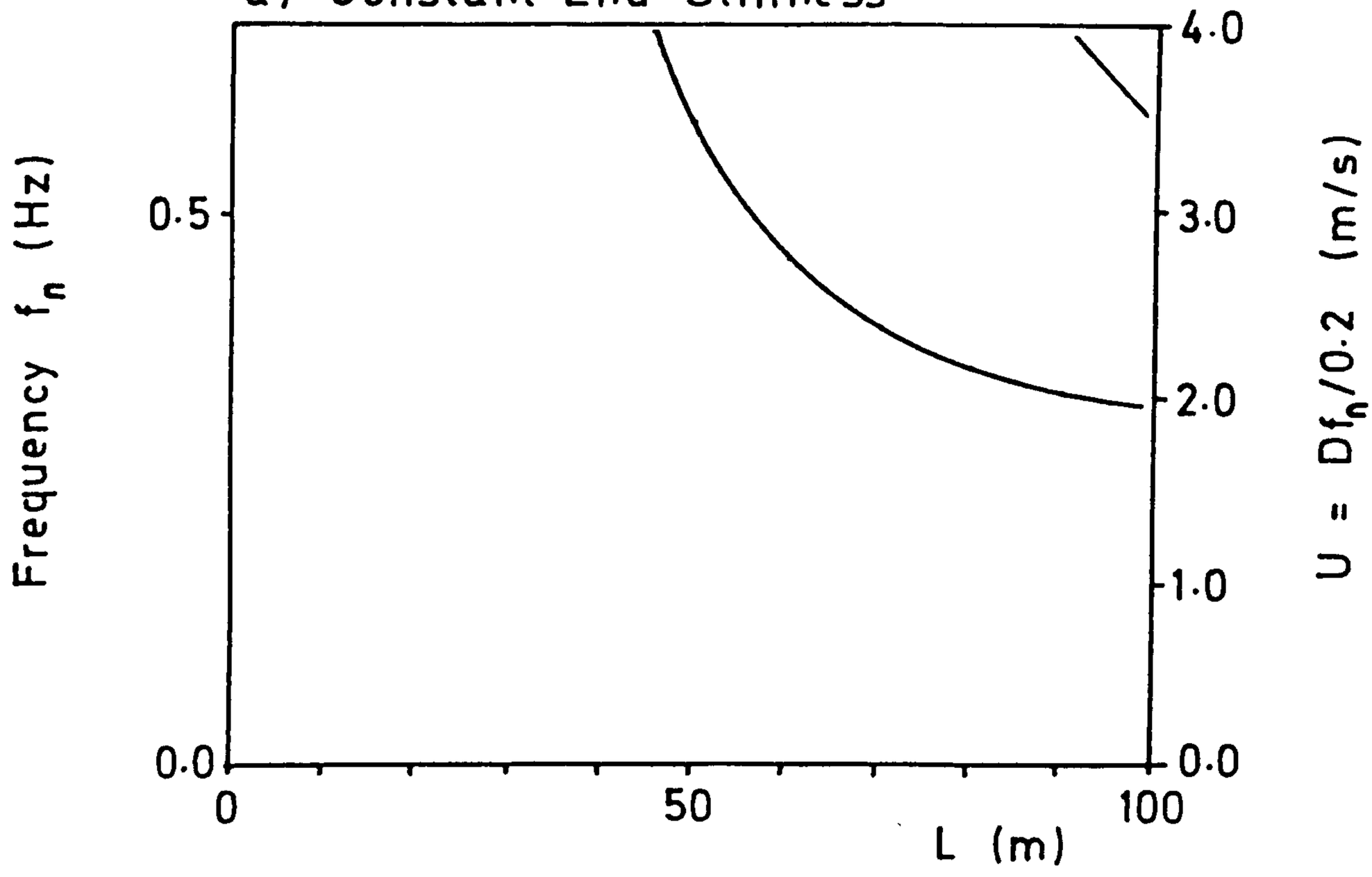

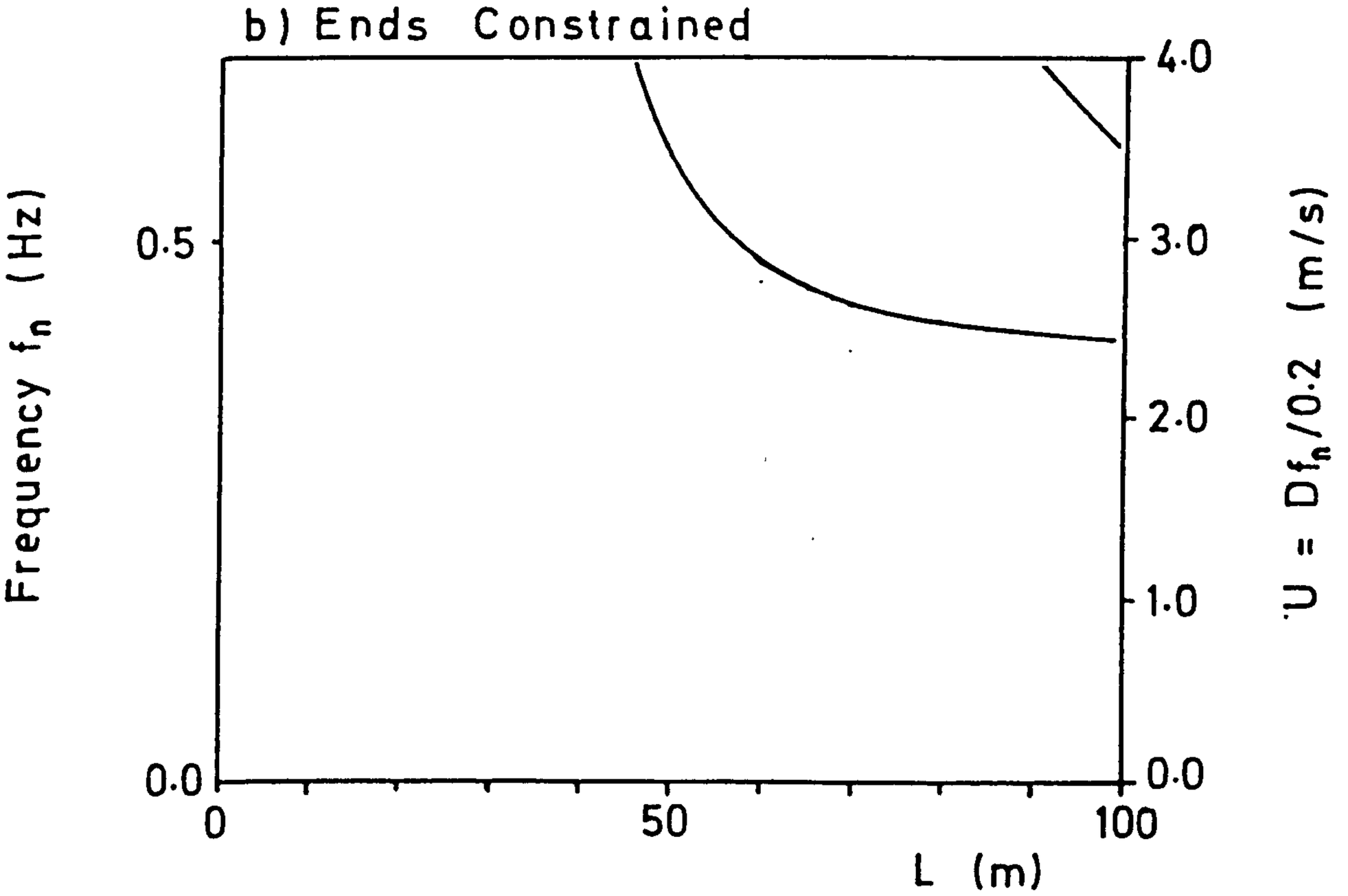

FIG 3.51 Pipe 3 Frequencies, $\mu = 10.0$

CHAPTER 4

EFFECT OF SEABED GEOMETRY

4.0 Introduction

The elastic foundation models developed in Chapters 2 and 3 have been based on an assumed initial geometry in which the supported sections of pipeline are straight, horizontal and on the same level, figure 3.1. In practice the initial seabed topography is often irregular with the result that more general geometries will occur, figure 2.1. These initial geometries will induce additional static stresses into the pipeline and will clearly affect the static equilibrium position taken up by any forming spans. Further, in view of the dependency of pipeline tangent stiffness on initial geometry and stress, such effects will also influence span frequencies and hence pipeline susceptibility to vortex induced vibrations. In this chapter these effects are included in the nonlinear Finite Element model developed in Chapter 3 and some typical cases investigated.

In describing the initial geometry of a local region of the seabed a large number of parametric representations are possible. As described in section 2.0.1 the parameters selected in this thesis are the end elevations δ_1 and δ_2 measured from some suitable datum plus the seabed slopes θ_1 and θ_2 (assumed constant) either side of the final span. The way in which these parameters are used to describe the seabed geometry is outlined in the following section.

4.1 Initial Seabed Geometry

Referring to figure 4.1 the initial seabed geometry is specified by the functions $S_i(x_i)$, $i = 1, 2, 3$, measured from the selected datum. Introducing local

coordinates (x_i, y_i) as shown and assuming that the support sections G_1G_2 and G_3G_4 are straight we find

$$G_1G_2 \quad : \qquad S_1(x_1) = \delta_1 + \theta_1 x_1 \tag{4.1a}$$

$$G_3G_4 \quad : \qquad S_3(x_3) = \delta_2 + \theta_2 x_3 \tag{4.1b}$$

The function $S_2(x_2)$ is now selected so that the complete seabed profile forms a smooth curve of suitable continuity. Here we specify displacement and slope compatibility at points G_2 and G_3 giving

$$S_2(x_2) = \delta_1 + \theta_1 x_2 + \gamma_2 x_2^2 + \gamma_3 x_2^3 \tag{4.2}$$

where the coefficients γ_i are defined in terms of the basic geometric parameters as

$$\gamma_2 = \frac{-2\theta_1 - \theta_2 + 3\theta_0}{L_4} \tag{4.3a}$$

$$\gamma_3 = \frac{\theta_1 + \theta_2 - 2\theta_0}{L_4^2} \tag{4.3b}$$

$$\theta_0 = \frac{\delta_2 - \delta_1}{L_4} \tag{4.3c}$$

and L_4 is the final span length, figure 4.1. As a result the functions $S_i(x_i)$ constitute a C_1 continuous curve for the seabed profile[1] while the function $S_2(x_2)$ represents the solution to the homogeneous beam equation (i.e. it is equivalent to equation (3.2)).

---

(1) The use of equation (4.2) is arbitrary since other possibilities can readily be obtained. For example requiring C_2 continuity we find

$$S_2(x_2) = \delta_1 + \theta_1 x_2 + \gamma_3 x_2^3 + \gamma_4 x_2^4 + \gamma_5 x_2^5$$

where the coefficients γ_3, γ_4 and γ_5 are now

$$\gamma_3 = (10\theta_0 - 6\theta_1 - 4\theta_2)/L_4^2$$

$$\gamma_4 = (8\theta_1 + 7\theta_2 - 15\theta_0)/L_4^3$$

$$\gamma_5 = (6\theta_0 - 3\theta_1 - 3\theta_2)/L_4^4$$

In addition it is noted that a completely different parametric representation of the seabed, using for example a Fourier series expansion, is equally valid.

4.2 Effective Displacement Load Vector

To evaluate the displacements occuring as a result of the initial seabed geometry $S(x)$ consider the elastic foundation model, figure 4.2. Connecting the pipe to the specified profile is an elastic foundation of stiffness R^S per unit length which, in common with previous models, is assumed to transmit forces in the vertical direction only. Now for a typical element of length L_e and transverse deflection $v(x)$, figure 3.4, the strain energy stored in the elastic foundation is

$$V^S = \frac{1}{2}\int_0^{Le} R^S\left(v(x) - S(x)\right)^2 dx \qquad (4.4)$$

Thus substituting for $v(x)$ using equation (3.2) and differentiating wrt a typical bending freedom a_i^B we find

$$\frac{\partial V^S}{\partial a_i^B} = \left(R^S\int_0^{Le} N_i^B N_j^B dx\right)a_j^B - \int_0^{Le} R^S S(x) N_i^B dx$$

$$= R^S R_{ij}^S a_j^B - q_i^B \qquad (4.5)$$

where, as normal, the repeated subscripts on the bending freedom a_j^B implies summation from 1 to 4. Comparing this to equation (3.5) indicates that the first term in the above is as previously used for the initial flat and level geometry while the second term may be used to form an equivalent element displacement load vector given by

$$\underset{\sim}{q}^B = \{q_i^B\} \qquad (4.6a)$$

$$q_i^B = \int_0^{Le} R^S S(x) N_i^B dx \qquad (4.6b)$$

It is noted that this load corresponds to a consistent load vector associated with a distributed pressure force of $R^S S(x)$ which, in the presence of the elastic foundation only, would produce a deflection given simply by $v(x) = S(x)$. To evaluate the terms (4.6b) $S(x)$ is in practice first approximated by

$$S(x) = (1-\xi)S_1 + \xi S_2 \qquad (4.7)$$

where $\xi = x/Le$ and S_1 and S_2 are respectively the specified ground profiles at ends 1 and 2 evaluated using equations (4.1) and (4.2) above. Now substituting for N_i^e using equation (3.3) and performing the integrations gives

$$q_1^e = \frac{R^S Le}{20}(7S_1 + 3S_2) \qquad (4.8a)$$

$$q_2^e = \frac{R^S Le^2}{60}(3S_1 + 2S_2) \qquad (4.8b)$$

$$q_3^e = \frac{R^S Le}{12}(3S_1 + 7S_2) \qquad (4.8c)$$

$$q_4^e = \frac{R^S Le^2}{60}(2S_1 + 3S_2) \qquad (4.8d)$$

The assembly of these element terms may now be written symbolically as

$$\underset{\sim}{Q} = \sum_{e_L, e_N} \underset{\sim}{q}^e \qquad (4.9)$$

so that the equilibrium condition equation (3.77) becomes

$$\underset{\sim}{F}(\underset{\sim}{\alpha}) = \underset{\sim}{P} + \underset{\sim}{Q} \qquad (4.10)$$

It is clear that for $S(x)=0$ the prescribed ground motion vector $\underset{\sim}{Q}$ is also null and equation (4.10) reverts to its original form equation (3.77).

4.3 Solution Procedure

To solve the equilibrium equation (4.10) a similar procedure to that developed in Chapter 3 may be used. Thus referring to figure 3.17 the first step is to evaluate the pipeline deflections prior to the span formation with all elements fully supported. To do this first consider the following points:

a) For the simple flat geometry of Chapter 3 this initial step yields a constant vertical deflection $v=-W/R^S$ with corresponding zero horizontal or axial motion. For more general geometries this simple state of affairs no longer applies since in general any rotations or slopes occurring in the nonlinear pipe elements will result in coupled horizontal motions.

b) At the end of this load step the pipe configuration may be considered applicable to either a recently installed surface resting pipeline or one buried at constant depth below the seabed. In both cases it is assumed that the effective tension T is constant along the pipeline.

It follows that it is necessary at this stage (i.e.Load Step 1) to deactivate the friction model by replacing the element equations (3.68) and (3.70) for each of the friction elements with

$$f^P = f_o^P \tag{4.11a}$$

$$k_T^P = 0 \tag{4.11b}$$

By this means the pipeline is maintained under constant tension with zero axial end restraint, a situation equivalent to the linear beam-column problem discussed in section 3.3.2.

Further points which should be noted here are

a) As a result of equation (4.11b) above the assembled tangent stiffness matrix k_T contains no elements connected to earth in the horizontal direction and is consequently singular. It follows that during the equilibrium iterations associated with load step 1 it is necessary to apply a horizontal constraint at some convenient point, taken here as the span centre.

b) The vertical contact force per length between pipe and elastic foundation is given by

$$p(x) = R^s(s(x) - v(x)) \tag{4.12}$$

Now for flat or almost flat initial geometries this contact force is positive at all points being equal or approximately equal to the pipe effective weight per length W. However for more uneven surfaces $p(x)$ becomes negative over certain lengths of pipe indicating a tensile stress system in the soil. For the case of a surface resting pipe this condition indicates the development of a noncontact region as the pipe lifts off the seabed.

Considering again figure 3.17 subsequent load steps are now invoked by removing the elastic foundation support from successive elements adjacent to the span centre, a process which in view of equations (4.8) and (4.9) now affects both the displacement load vector $\underset{\sim}{Q}$ as well as the element forces vector $\underset{\sim}{f}$. For the first of these steps the force occurring in a typical friction element is calculated using equation (3.68), repeated here for convenience as

$$a^p = a_0^p + \Delta a_1 \tag{4.13a}$$

$$f^p = f_0^p + \mathrm{sgn}(\Delta a_1) k_1 |\Delta a_1|^{1/2} \tag{4.13b}$$

Here defining the element displacement and force at the end of load step n as ${}^{n}a^{p}$ and ${}^{n}f^{p}$ respectively, the initial conditions are taken as (1)

$$a_0^p = {}^{1}a^{p} \tag{4.14a}$$

$$f_0^p = {}^{1}f^{p} \tag{4.14b}$$

During these subsequent load steps it was noted in Chapter 3 that for the case of an initially flat seabed the friction element displacements and forces increase monotonically with span length L . However for more complicated geometries this is no longer always the case. For example considering the initially arched pipeline, figure 4.6c, it is clear that as the span forms the pipe ends will initially push outwards leading to an increase in compression in the system. However as the span length continues to grow the sag deflections developed will eventually cause the span ends to pull back in so reversing the loading phase for the end friction elements. It follows that in order to incorporate these effects into the Finite Element Model it is necessary at each load step to determine the appropriate element

---

(1) It is noted that ${}^{n}a^{p}$, defined here as the displacement at the end of load step n , is distinct from a_i^p defined in section 3.4.4 as the displacement at the end of element loading phase i . This follows since solution load steps and friction element loading phases are in general not equal. In fact for the flat initial geometry used in Chapter 3 all load steps n corresponded to friction elements loading phase 1.

phase to use in the calculation of a typical friction element force f^{ρ}. To do this first define the element displacement increment occurring during load step n as

$$ {}^{n}\Delta a = {}^{n}a^{\rho} - {}^{n-1}a^{\rho} \tag{4.15} $$

Now for each load step $n \geq 3$ consider the inequality

$$ (a^{\rho} - {}^{n-1}a^{\rho})\,{}^{n-1}\Delta a > 0 \tag{4.16} $$

where a^{ρ} is the current element displacement. If this condition is true the current element loading phase i is given by

$$ i = i_{n-1} \tag{4.17} $$

where i_{n-1} represents the element phase associated with the previous load step $n-1$. If on the other hand equation (4.16) is false we have

$$ i = i_{n-1} + 1 \tag{4.18} $$

indicating a new loading phase. In this case the initial values associated with this new loading phase are taken here as

$$ a^{\rho}_{i-1} = a^{\rho}_{i_{n-1}} = {}^{n-1}a^{\rho} \tag{4.19a} $$

$$ f^{\rho}_{i-1} = f^{\rho}_{i_{n-1}} = {}^{n-1}f^{\rho} \tag{4.19b} $$

a process which assumes that the transition from element

loading phase i_{n-1} to $i_{n-1}+1$ occurs at a span length equal to the combined length of unsupported elements at the end of load step $n-1$ (1). Next a check is made to determine if previous maxima in the element load deflection history have been exceeded since, as noted in section 3.4.2, this causes the element to revert to an earlier loading phase. Thus considering the typical example, figure 4.3a, it is clear that if during element loading phase 5 the end displacement a^p is such that $a_3^p < a^p < a_1^p$ then fronts 3 and 5 coalesce and the element loading phase reverts to 3, figure 4.3b. Further if $a_1^p < a^p$ then all fronts except 1 disappear and the element reverts to its initial loading phase 1, figure 4.3c. Now in the general case the provisional phase i, calculated using equation (4.17) or (4.18) above is checked by considering the inequalities

$$\left| a^p - a_0^p \right| > \left| a_{i-2}^p - a_0^p \right|$$

$$\left| a^p - a_0^p \right| > \left| a_{i-4}^p - a_0^p \right|$$

$$\vdots$$

$$\left| a^p - a_0^p \right| > \left| a_1^p - a_0^p \right|$$

if i is odd or

$$\left| a^p - a_0^p \right| > \left| a_{i-2}^p - a_0^p \right|$$

$$\left| a^p - a_0^p \right| > \left| a_{i-4}^p - a_0^p \right|$$

$$\vdots$$

$$\left| a^p - a_0^p \right| > \left| a_2^p - a_0^p \right|$$

---

(1) This assumption may be progressively improved by incorporating more elements (and corresponding load steps) into the pipe section BC.

if i is even. Thus if a^p is such that

$$\left| a^p_{i-2j-2} - a^p_0 \right| > \left| a^p - a^p_0 \right| > \left| a^p_{i-2j} - a^p_0 \right| \qquad (4.20)$$

then the element phase is reset to $i-2j$. In addition if i now equals 2 and

$$\left| a^p - a^p_0 \right| > \left| a^p_1 - a^p_0 \right| \qquad (4.21)$$

the element reverts to its initial loading phase $i=1$ as indicated in figure 4.4. Now with the element phase i determined as above the element force f^p is calculated using equation (3.68) as

$$a^p = a^p_{i-1} + \Delta a_i \qquad (4.22a)$$

$$f^p = f^p_{i-1} + \mathrm{sgn}(\Delta a_i) k_i |\Delta a_i|^{1/2} \qquad (4.22b)$$

A flow chart summarising the above procedure together with a table summarising the main notation is given for convenience in figure 4.5. It is noted that this procedure must be executed for each friction element whenever a new element force vector $\underset{\sim}{F}$ is required. Thus with reference to figure 3.18 the above procedure is executed at each equilibrium iteration within each load step.

4.4 Classification of Geometries

The effect of seabed geometry on pipe span behaviour is investigated in this chapter by considering the 3 basic geometric configurations defined in figure 4.6. The parameters associated with these geometries are

a) Valley $\quad -\theta_1 = \theta_2 = \theta$

b) Valley Side $\quad \theta_1 = \theta_2 = \theta$

c) Hill $\quad \theta_1 = -\theta_2 = \theta$

where in all cases $\delta_1 = \delta_2 = 0$ and the final span length L_f is taken as 100m. It is noted that nonzero values for the end elevations δ_i cause a rigid body rotation

$$\theta_0 = \frac{\delta_2 - \delta_1}{L_f}$$

resulting in a tension variation in the free span, figure 4.7. In this thesis this effect is ignored and as stated above the end elevations δ_i are taken as zero. This implies that the more general case $\delta_i \neq 0$ may be effectively included here by considering the end slopes as being measured relative to the rigid body rotation θ_0, figure 4.7.

For all of these geometries the span is considered to grow evenly on either side of the centre point, figure 4.6.

4.5 FEM and Convergence

As indicated in figure 4.8 the pipeline finite element model is located centrally with respect to the above geometries with 40 elements used to model each of section AB, BC and CD. Following the initial load step for the enforced geometry, the free span formation is modelled using 20 separate steps, elastic foundation support being removed from 2 elements at a time. In practice this procedure leads to the convergence criteria, equation (3.85), being satisfied after 4 or 5 equilibrium iterations provided

the friction element loading phase is not changing during the current load step. For load steps where the friction element loading phase is changing convergence rates are slower with typically 8, but sometimes up to 30 iterations required. In exceptional cases, associated with the arched geometry figure 4.6c, no convergence is achieved as the friction element loading phase oscillates from one iteration to the next. These cases were rerun using

a) 80 elements in section BC together with 40 load steps for the span formation

b) Relaxation factor $R = 0.7$ in the displacement solution update $\underset{\sim}{\alpha} = \underset{\sim}{\alpha} + R\delta\underset{\sim}{\alpha}$

By this means satisfactory convergence was obtained for all cases although the introduction of the relaxation factor was found to considerably reduce convergence rates leading to increased run times. Finally once the total span length L has been achieved frequencies are calculated using fixed end conditions and the whole process repeated for the next required span length.

4.6 Results and Discussion

Pipe 2 behaviour for the case $\mu = 1.0$ is now summarised for each of the above initial geometries. Thus considering first the initial valley geometry $-\theta_1 = \theta_2 = \theta$ it is observed that:-

a) Centre deflection during span formation is reduced from almost 3m for the initially flat $\theta = 0^\circ$ case to just over 1m for the $\theta = 5^\circ$ case and 0.5m for the $\theta = 10^\circ$ case, figure 4.9.

b) Using figure 4.9 and taking end pull in as proportional to centre deflection squared, the end deflection during span formation may be estimated as

being proportional to

i) $\theta = 0^{o}$, $(2.75)^2 - (0.0)^2 = 7.56$

ii) $\theta = 5^{o}$, $(3.52)^2 - (2.17)^2 = 7.68$

iii) $\theta = 10^{o}$, $(5.0)^2 - (4.4)^2 = 5.64$

These figures suggest that the build up in effective tension will be similar for all three cases, a prediction confirmed by the actual results, figure 4.11.

c) The effective tension T includes the end pressure term

$$T_p = -\frac{\pi}{4}(p_i D_i^2 - p_o D_o^2)$$

which using the data given in section 3.7 is evaluated as T_p = -2351KN. Thus at T = -500KN the real tension is T_R = 1851KN with corresponding axial stress σ_R = 70N/mm^2 while at T = 500KN these values increase to T_R = 2851KN and σ_R = 107N/mm^2.

d) For the initially flat θ = 0^{o} case the maximum bending stress in the pipeline

$$\sigma_{B_{max}} = EI\, max(|v''|)$$

increases monotonically with span length reaching a value of 375N/mm^2 at L = 100m, figure 4.12. For $L >$ 30m this maxima occurs at the span ends where the soil support results in large hogging curvatures. For the θ = 5^{o} and 10^{o} cases the forming span encounters downward sloping pipeline with the result that maximum curvature occurs at the span centre, figure 4.9. These curvatures decrease at longer spans as a result of increased tension in the system, figure 4.12.

e) The increased curvature associated with this geometry causes a further upwards shift in the symmetric

mode frequencies, figure 4.13. In this figure the number of maxima occurring in the associated mode shapes (vertical component) are marked alongside the curves. Thus odd numbers indicate symmetric modes and even numbers antisymmetric modes. Comparing figures 3.38 and 4.13 it is seen that the antisymmetric modes are virtually unaffected by this geometry.

f) The contact force per length prior to span formation is positive at all points except for two local regions about points ζ_2 and ζ_3, figure 4.14. It is noted that this contact force distribution effectively constitutes two end couples at points ζ_2 and ζ_3 as required for the beam deformation profile $S_2(x_2)$.

Considering next the valley side geometry $\theta_1 = \theta_2 = \theta$ it is noted that

a) Both centre deflection, figure 4.15, and effective tension, figure 4.17, are little affected by this initial geometry being virtually identical to the flat $\theta = 0^o$ case up to $L = 70m$.

b) Maximum bending stresses, figure 4.18, are initially located near points ζ_2 and ζ_3 and so for small spans are unaffected by span length L. However at about $L = 20m$ these stress levels are overtaken by those occurring at the left hand support, figure 4.16. These stress levels continue to grow rapidly as a result of the adverse curvature encountered by the forming span.

c) The span fundamental frequency, figure 4.19, is reduced since the frequency shift observed in all previous cases no longer occurs. Instead the asymmetry of the pipeline static configuration, figure 4.16, results in a more general set of mode shapes, figure 4.20.

d) As a result of increased pipeline curvature contact

forces per length, figure 4.14, are substantially increased compared to those for the previous case. However despite this fact the contact force remains positive over the majority of the pipeline.

Finally considering the initially arched pipeline geometry $\theta_1 = -\theta_2 = \theta$ it is observed that

a) For the case $\theta = 5^o$ the centre deflection, figure 4.22, indicates that the pipeline initially supports itself via an arching effect with the result that the effective tension, figure 4.23, decreases. As a consequence the generalised stiffness of the span is reduced until at about $L = 50m$ the pipe experiences a rapid increase in deflection with further increase in span length L . In turn this deflection now causes the effective tension to increase so stabilising the system. This behaviour appears analogous to the snap through phenomena observed in many shallow arched structures.

b) In contrast to the above the results for the $\theta = 10^o$ case are virtually independent of span length with the large initial curvature enabling the pipe to support itself with minimal further deflection. This absence of deflection against increased span also appears in part to be due to the initial soil pipe contact force, figure 4.27. Here it is noted that for the case $\theta = 10^o$ the support offered to the pipeline section G_2G_3 is about 0.4KN/m, a value considerably less than the corresponding result for the valley geometry $-\theta_1 = \theta_2 = 10^o$ given in figure 4.14 as 5.6KN/m. As a result the effective load seen by the pipeline per metre increase in span length is much reduced with consequently lower deflection.

c) Maximum bending stress for the case $\theta = 5^o$ increases rapidly with span length, figure 4.25. These high stresses occur at the span ends where the

snapped through forming span is encountering upward sloping pipeline, figure 4.23. For the case $\phi = 10^{o}$ the maximum bending stress is virtually constant.

d) For the case $\phi = 5^{o}$ the fundamental mode frequency passes through a minimum at $L = 50m$, figure 4.26. This point corresponds closely to the minimum on the effective tension curve, figure 4.24, and marks the point at which the span is about to snap through. Further increase in span length now increases this frequency and at the same time causes a shift from first to second symmetric mode, figure 4.26.

e) For the case $\phi = 10^{o}$ the fundamental frequency occurs in the first antisymmetric mode for $L > 50m$. As the span length approaches 100m these frequencies reduce rapidly as the span appears to become increasingly unstable, figure 4.26.

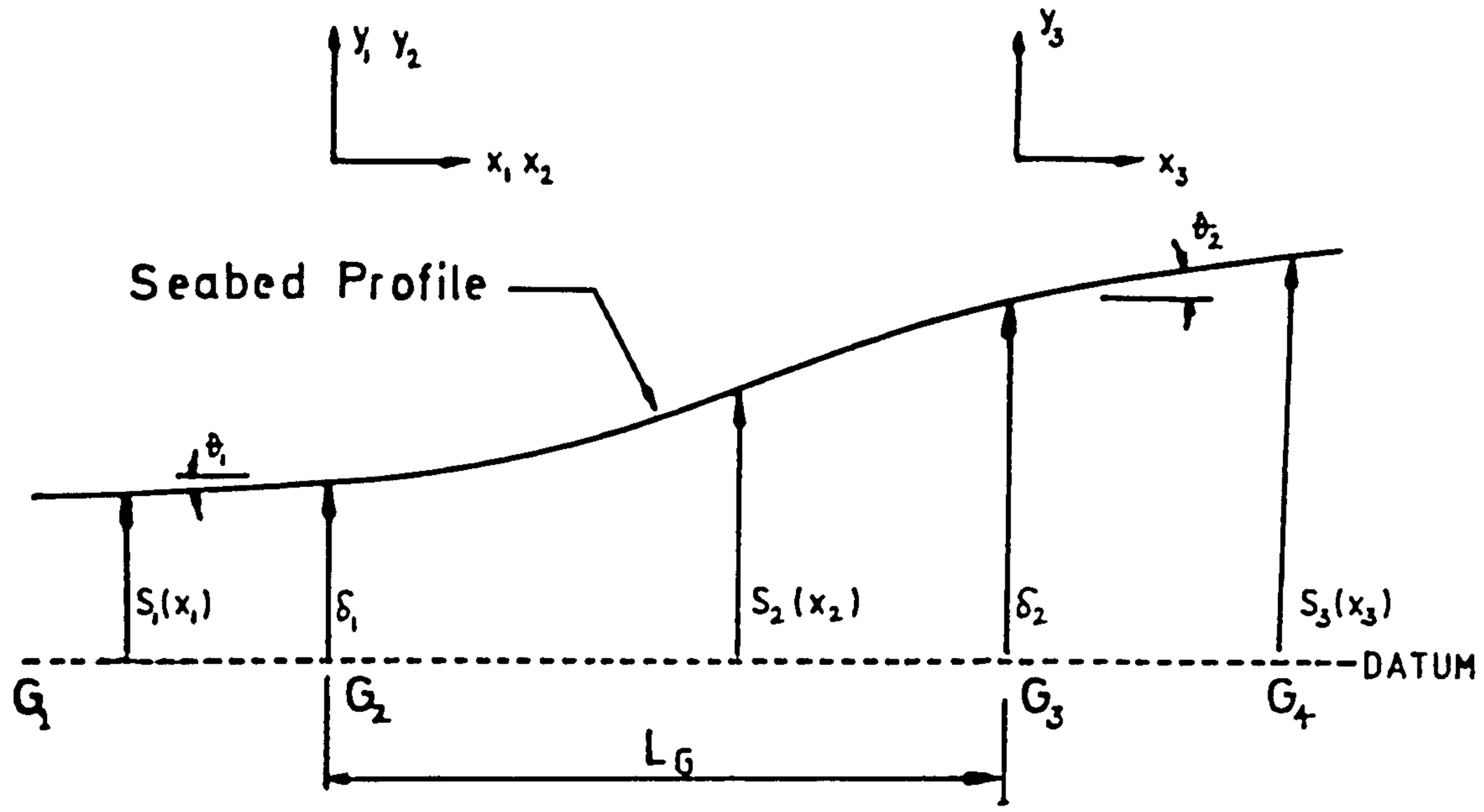

FIG 4.1 Initial Seabed Geometry

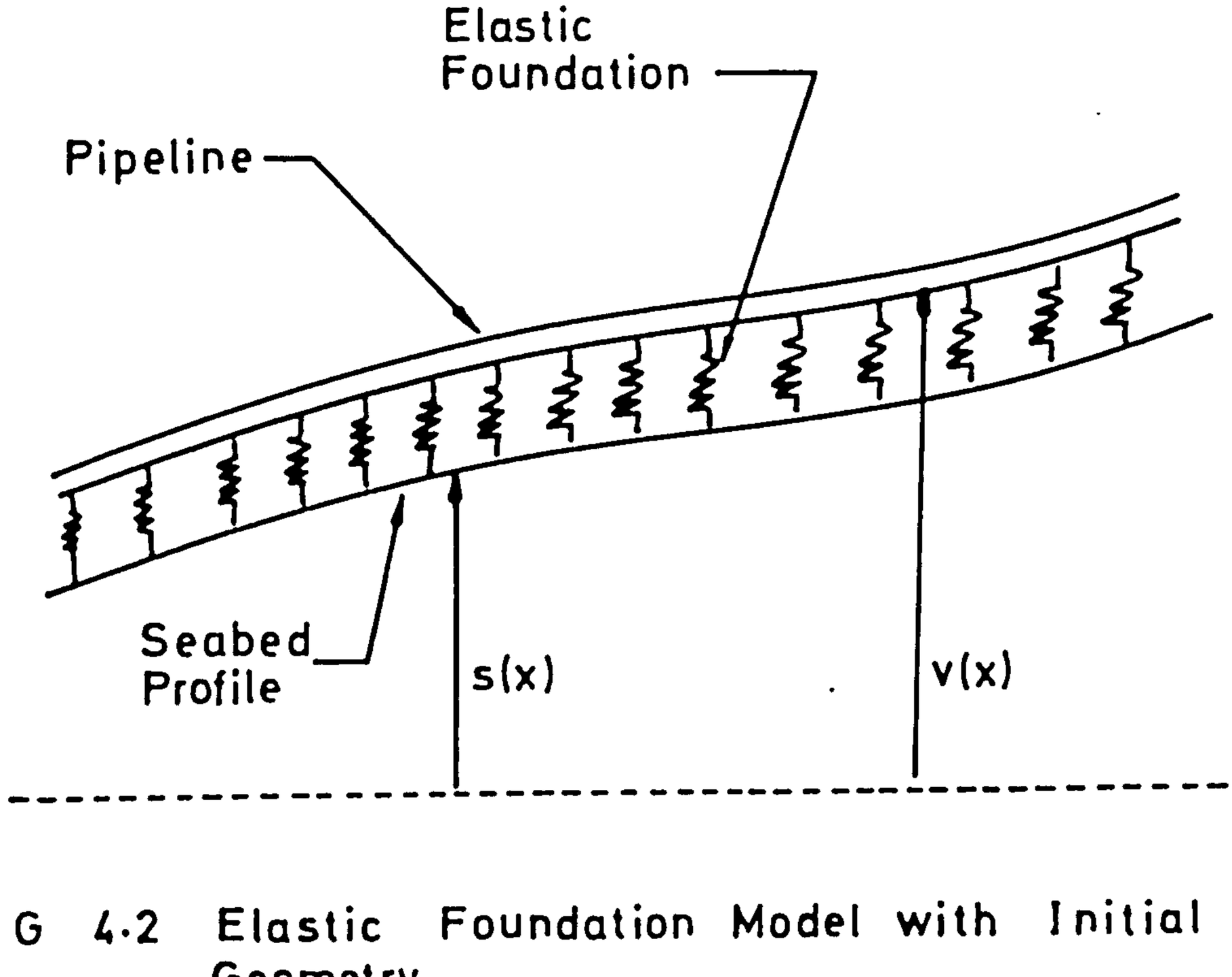

FIG 4.2 Elastic Foundation Model with Initial Geometry

a) Loading Phase 5

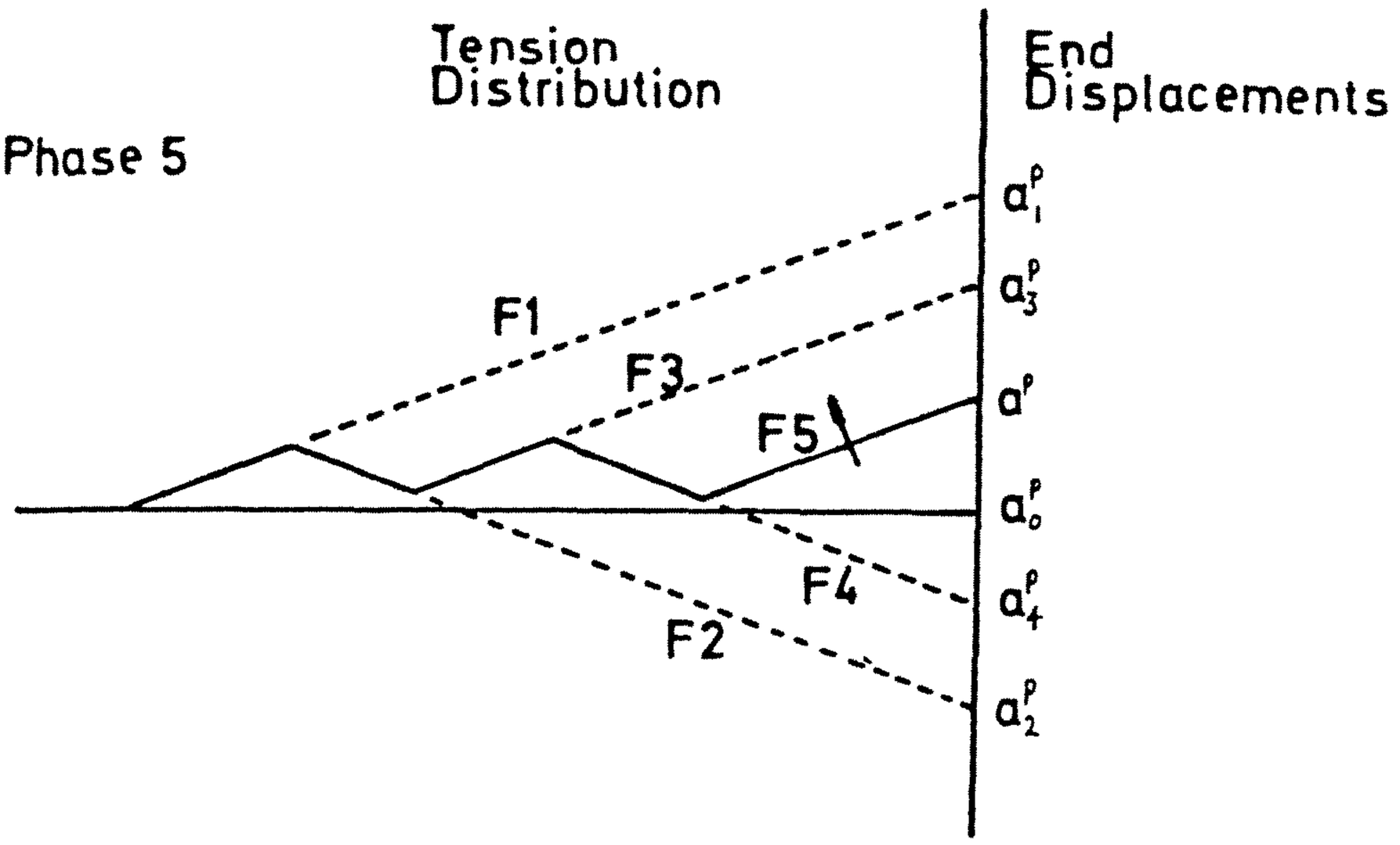

b) Loading Phase 3

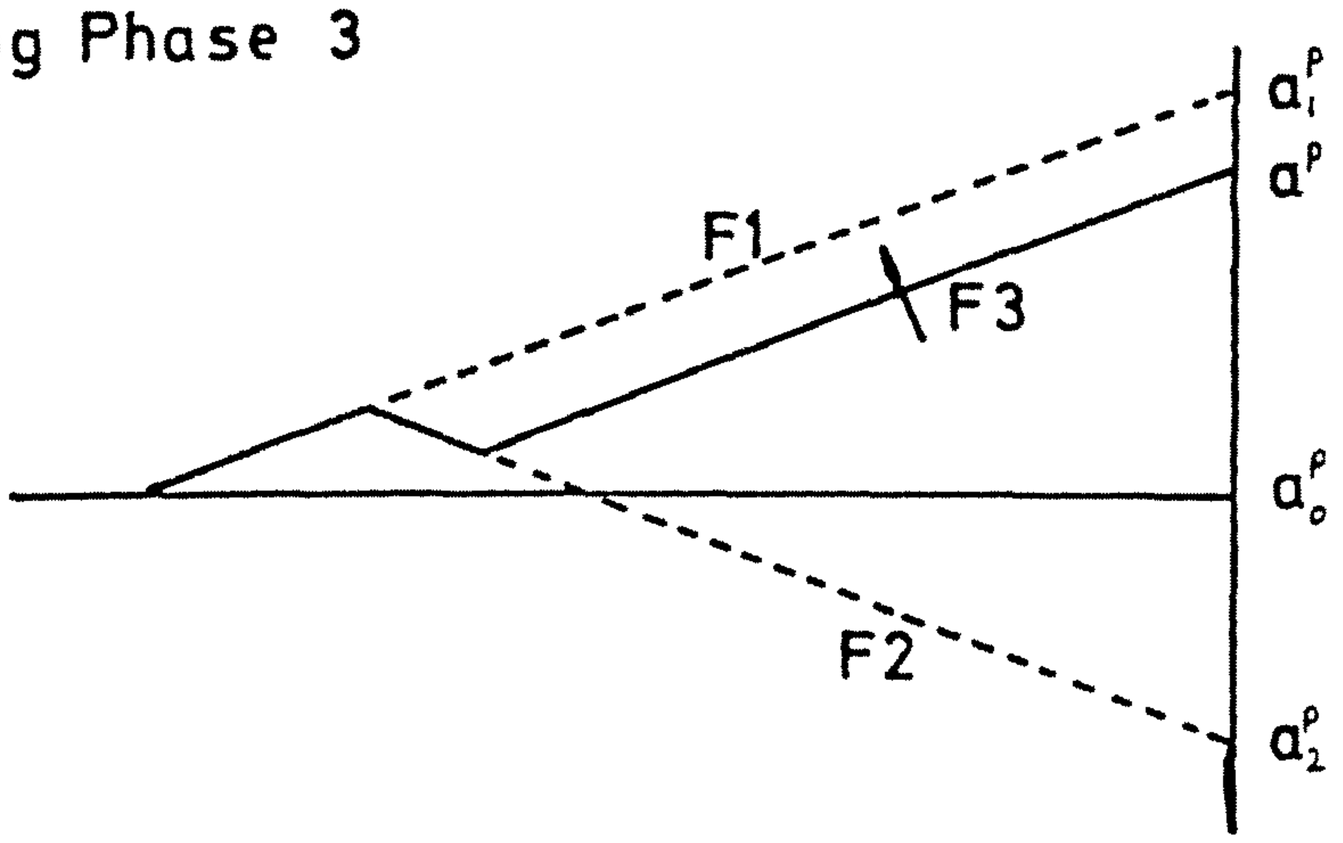

c) Loading Phase 1

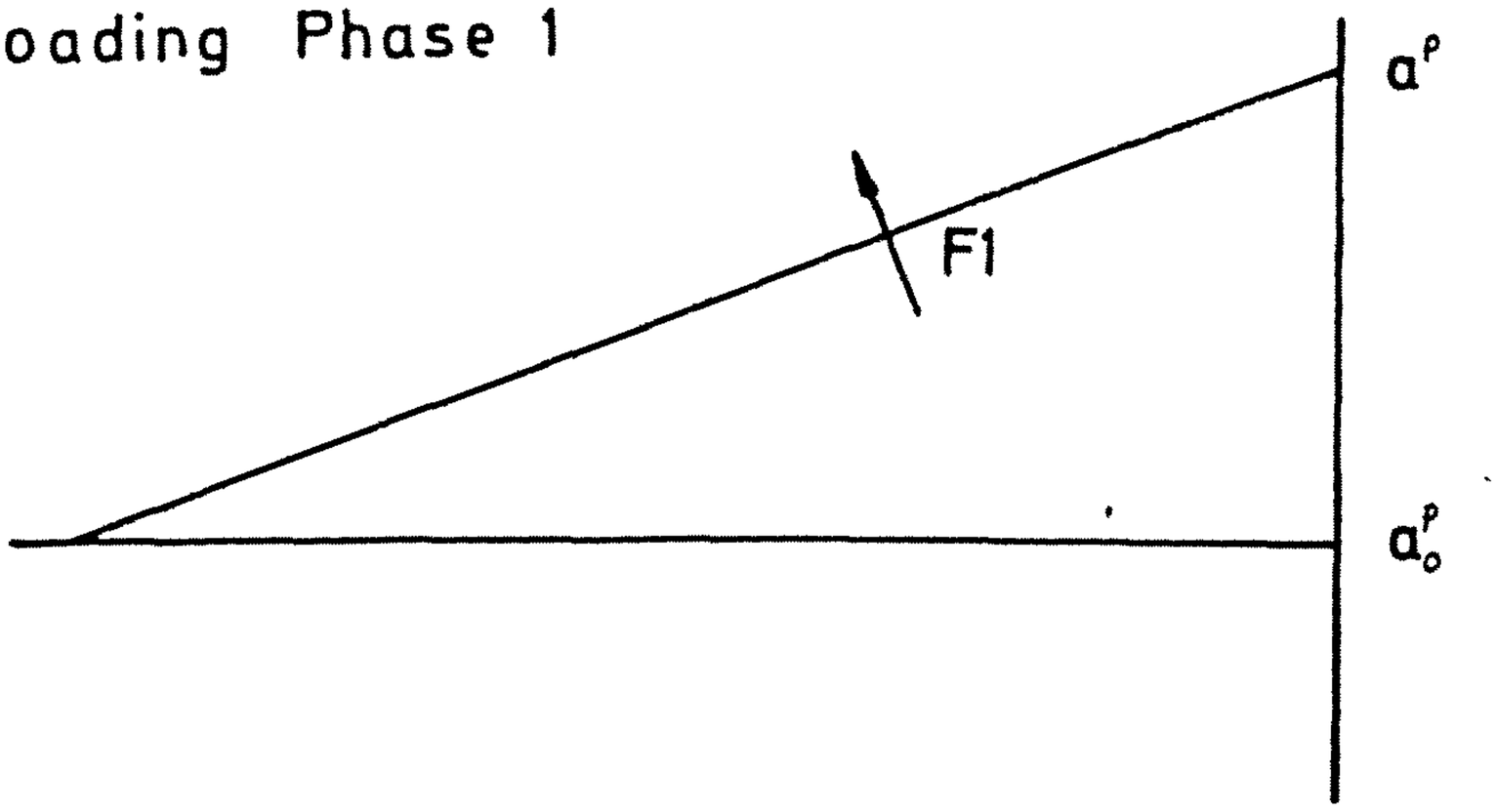

FIG 4.3 Typical Friction Element Loading Phases

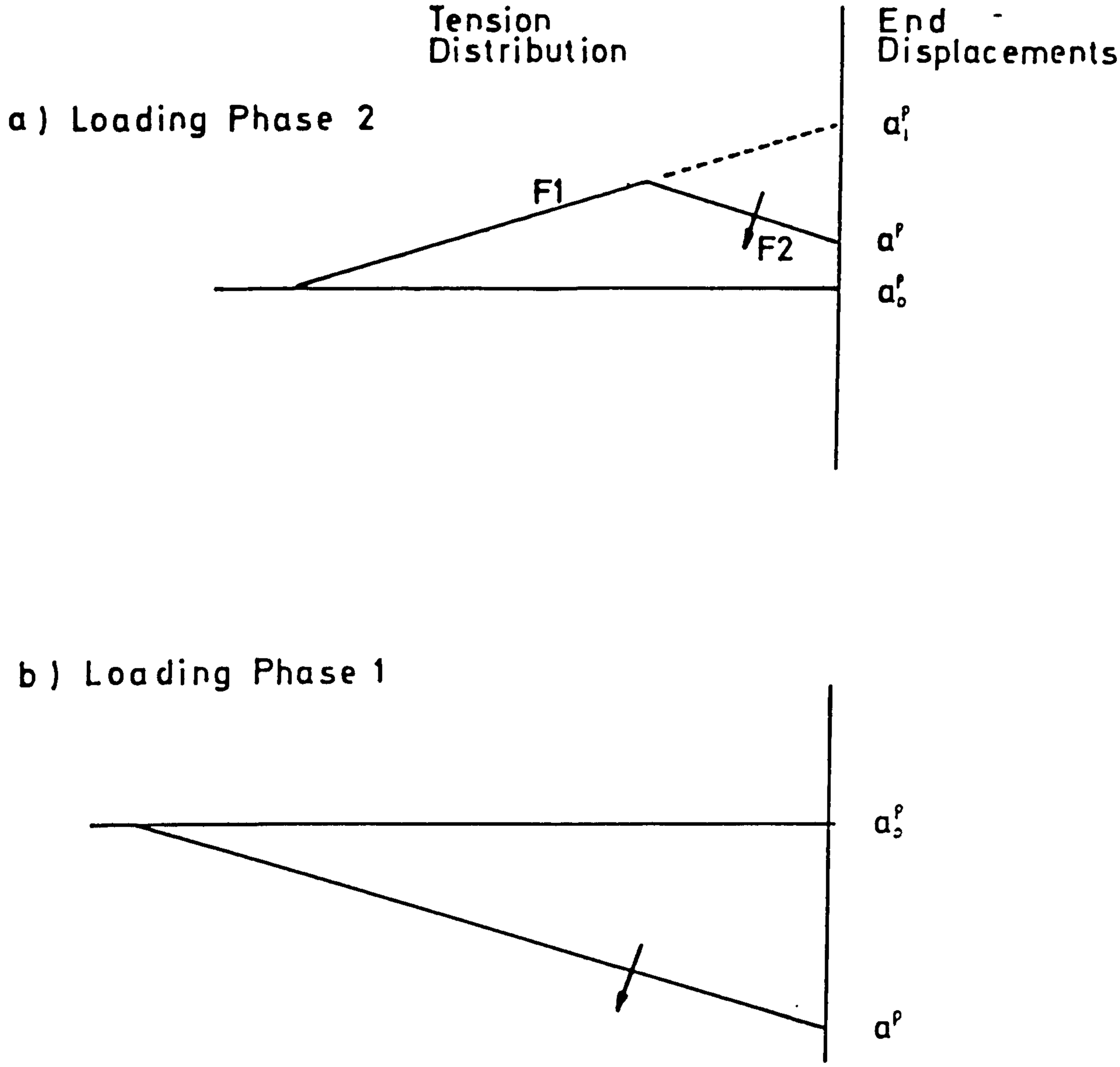

FIG 4.4 Conversion of Friction Element Loading Phase 2 to 1

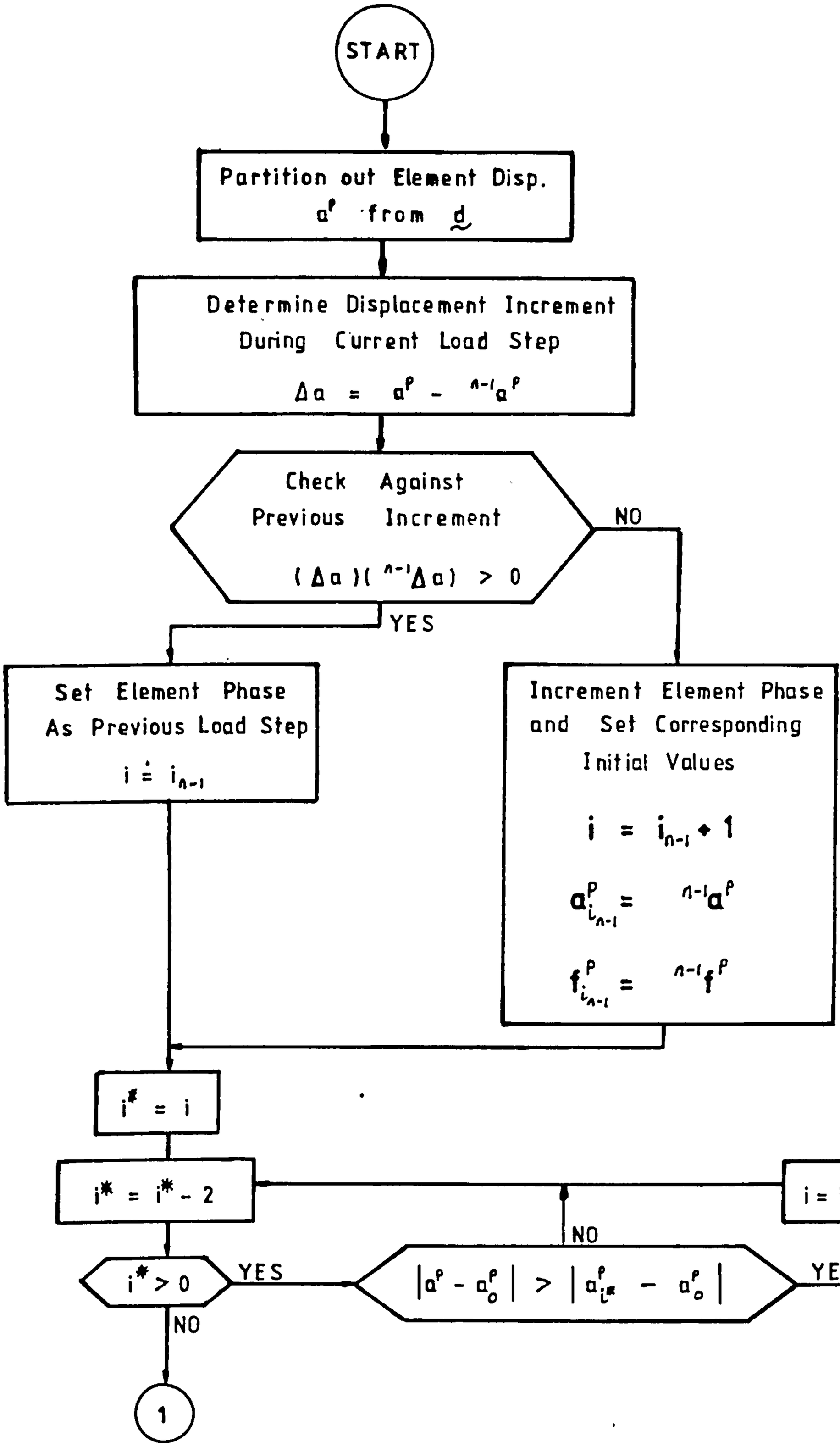
START
Partition out Element Disp.
a^p from $\underset{\sim}{d}$
Determine Displacement Increment
During Current Load Step
$\Delta a = a^p - {}^{n-1}a^p$
Check Against
Previous Increment
$(\Delta a)({}^{n-1}\Delta a) > 0$
NO
YES
Set Element Phase
As Previous Load Step
$i \doteq i_{n-1}$
Increment Element Phase
and Set Corresponding
Initial Values
$i = i_{n-1} + 1$
$a^p_{i_{n-1}} = {}^{n-1}a^p$
$f^p_{i_{n-1}} = {}^{n-1}f^p$
$i^* = i$
$i^* = i^* - 2$
$i^* > 0$
YES
NO
$\left|a^p - a^p_o\right| > \left|a^p_{i^*} - a^p_o\right|$
NO
YES
$i = i^*$
1

/....

/....

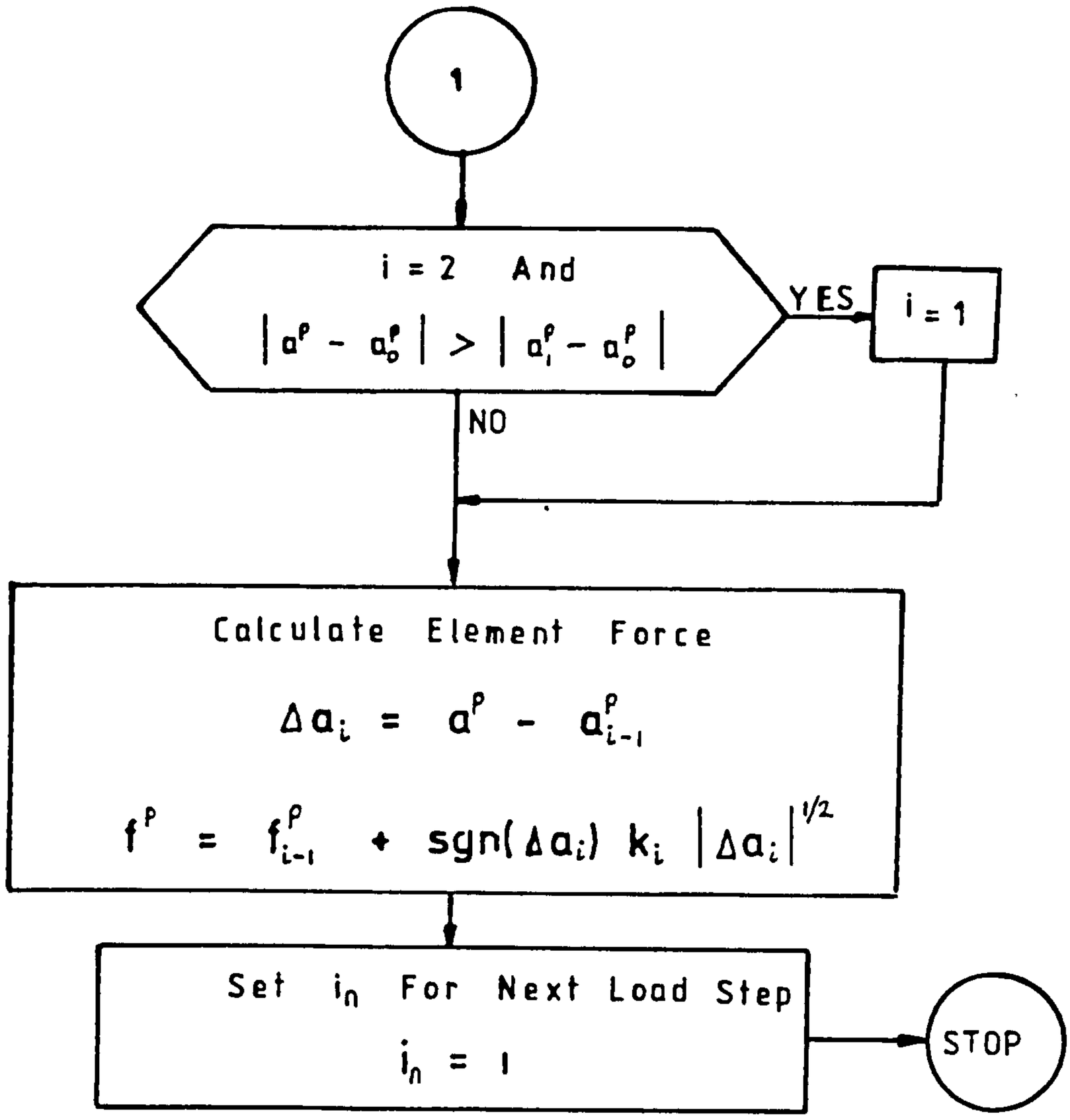

NOTATION

	Displacement	Force
Cutrent Value	a^p	f^p
Increment During Current Load Step	Δa^p	Δf^p
End of Load Step n	${}^n a^p$	${}^n f^p$
Increment During Load Step n	${}^n \Delta a^p$	${}^n \Delta f^p$
End of Elem. Loading Phase i	a_i^p	f_i^p
Increment During Loading Phase i	Δa_i^p	Δf_i^p

FIG 4.5 Friction Element Force Calculation

a) Valley $-\theta_1 = \theta_2 = \theta$

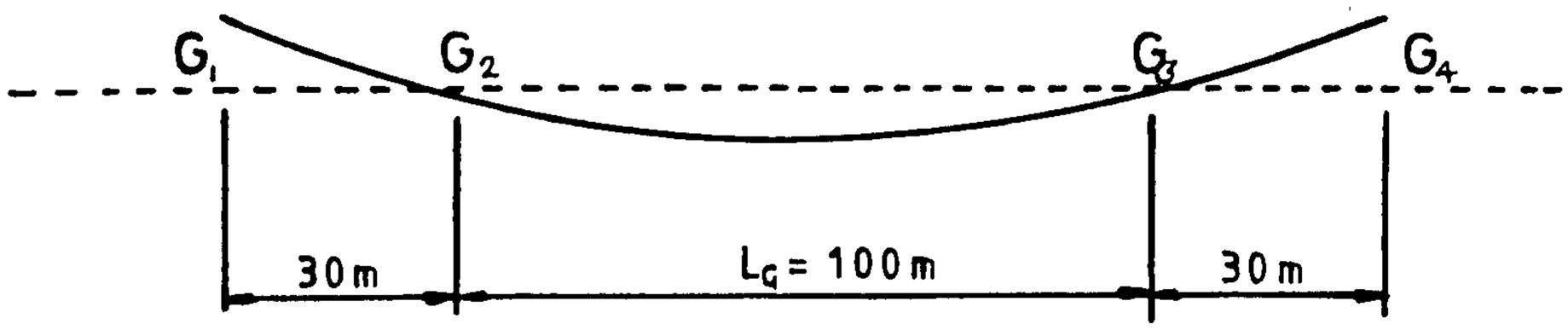

b) Valley Side $\theta_1 = \theta_2 = \theta$

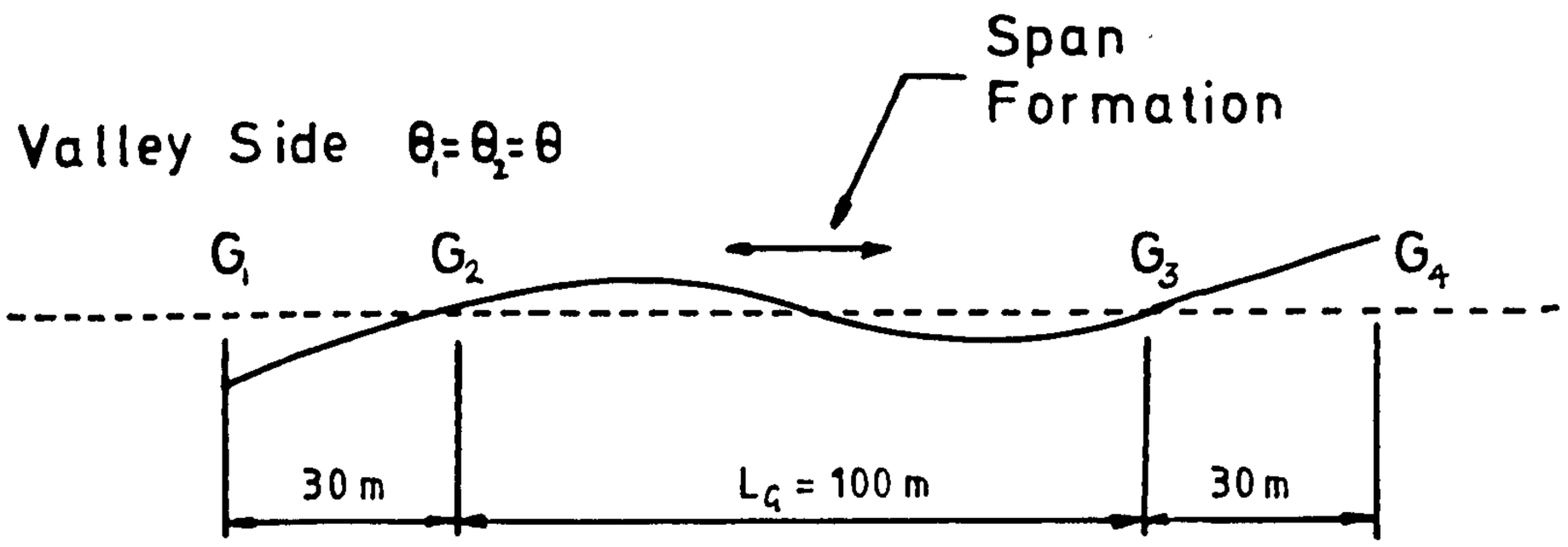

c) Hill $\theta_1 = -\theta_2 = \theta$

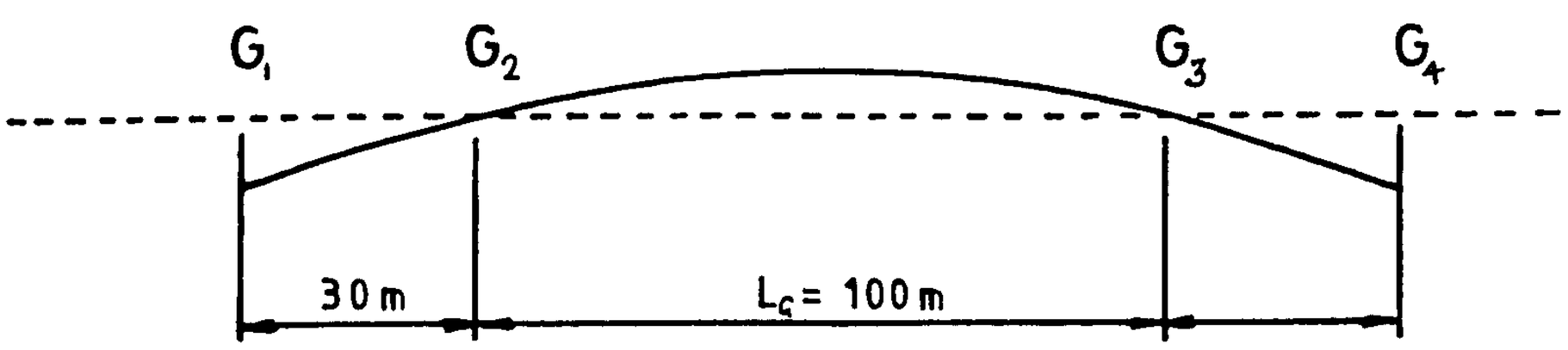

FIG 4.6 Basic Geometry Configurations

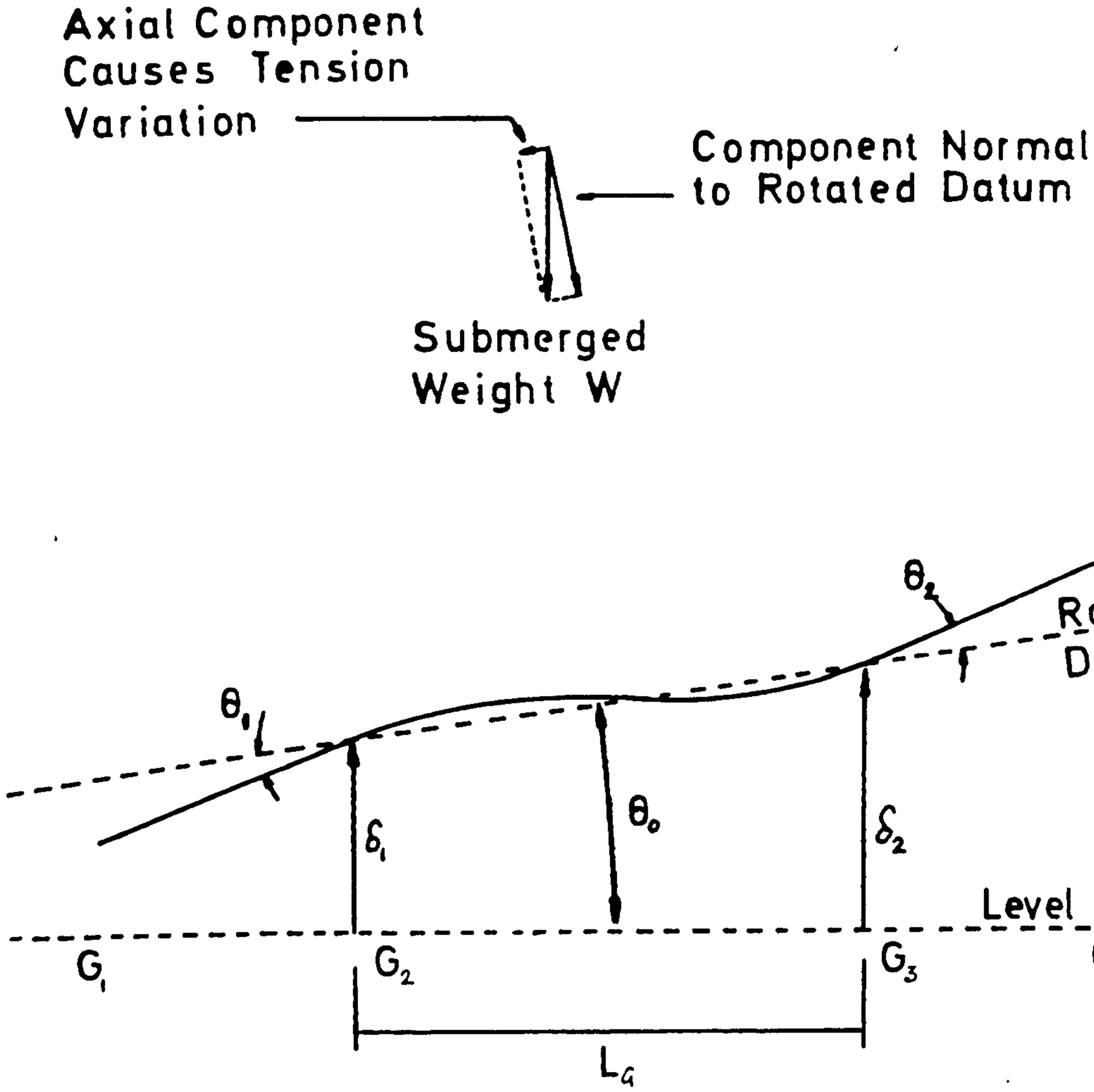

FIG 4.7 Rigid Body Rotation of Datum/Model

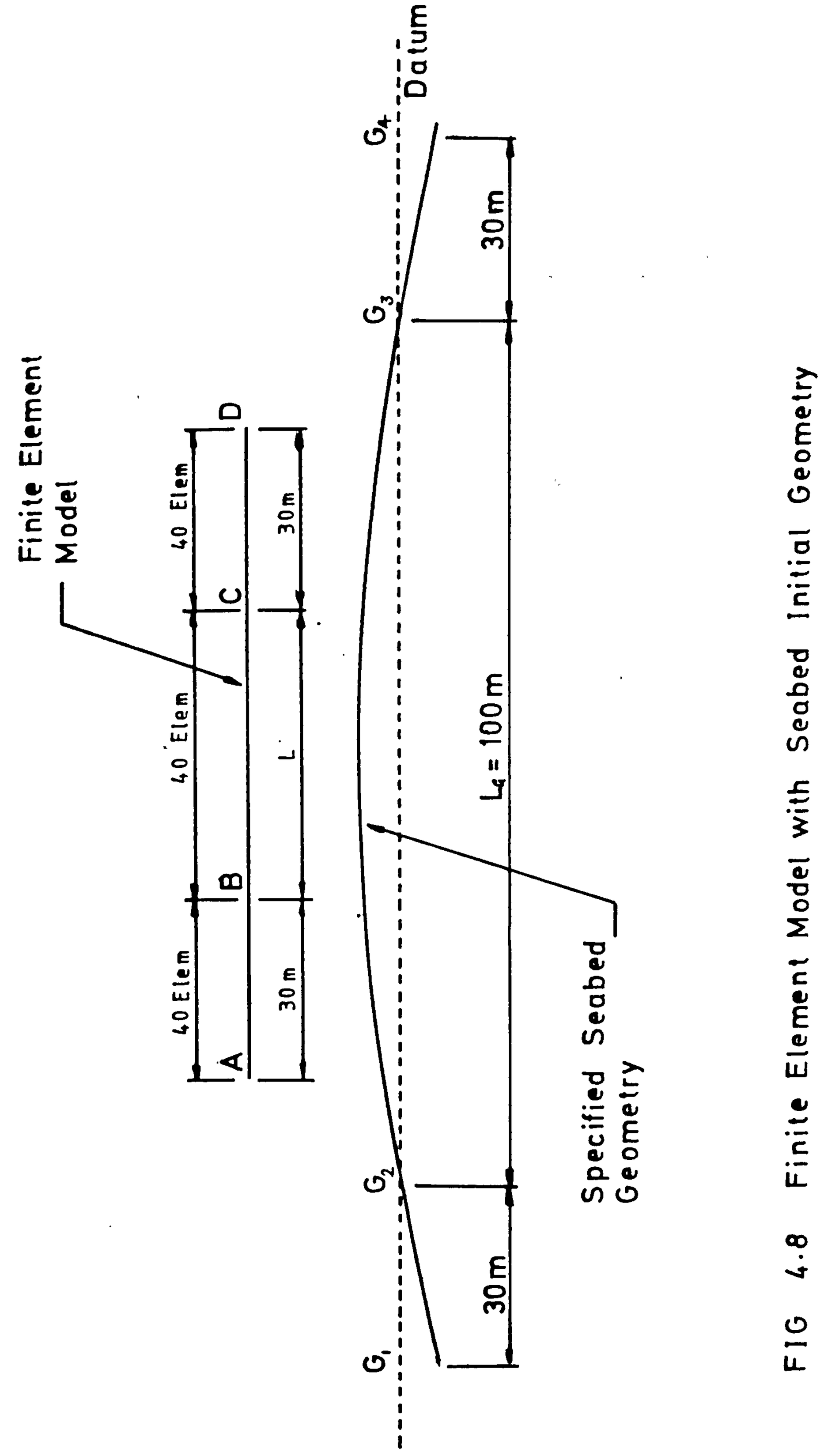

FIG 4.8 Finite Element Model with Seabed Initial Geometry

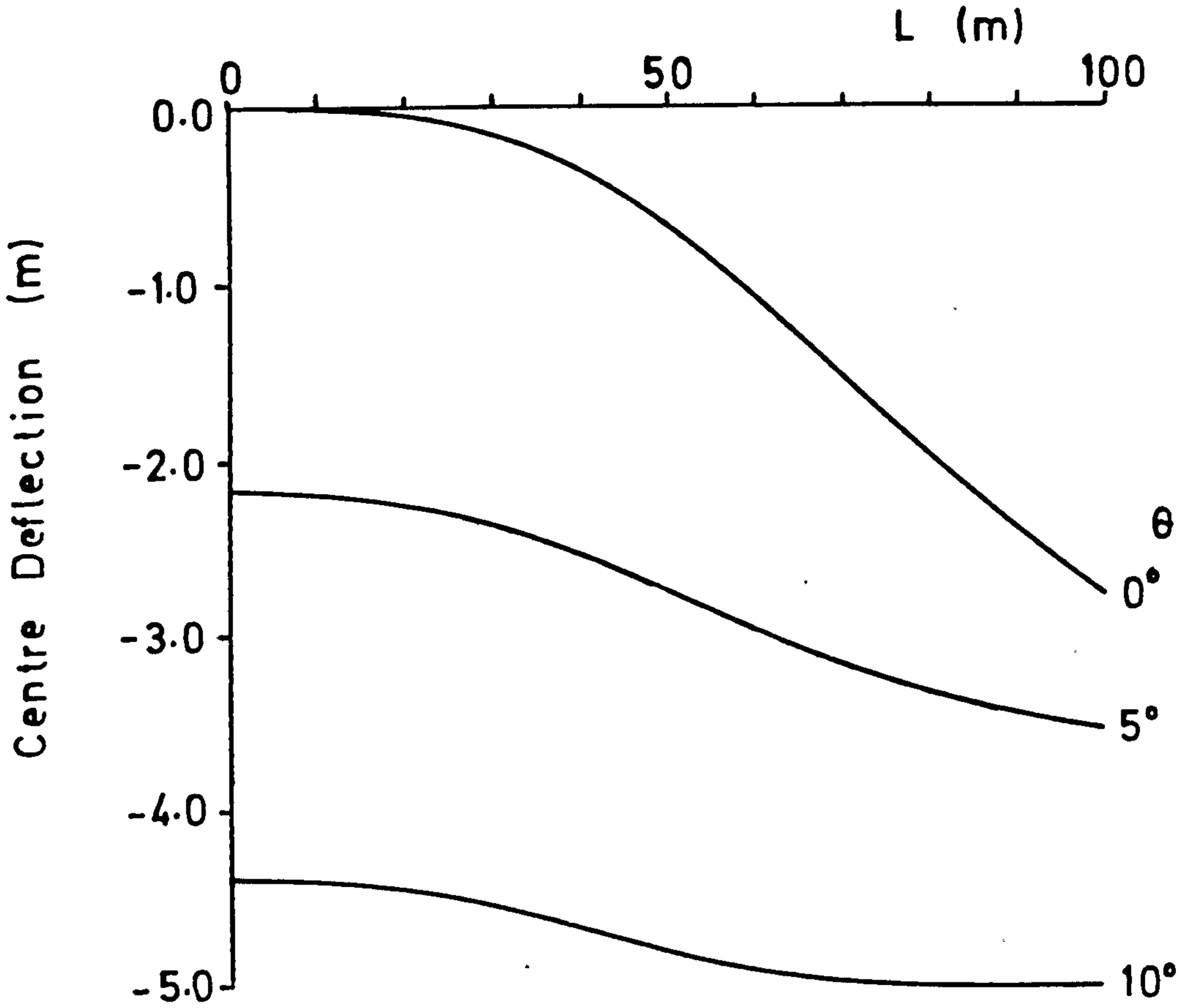

FIG 4.9 Pipe 2 Centre Deflection, $-\theta_1 = \theta_2 = \theta$

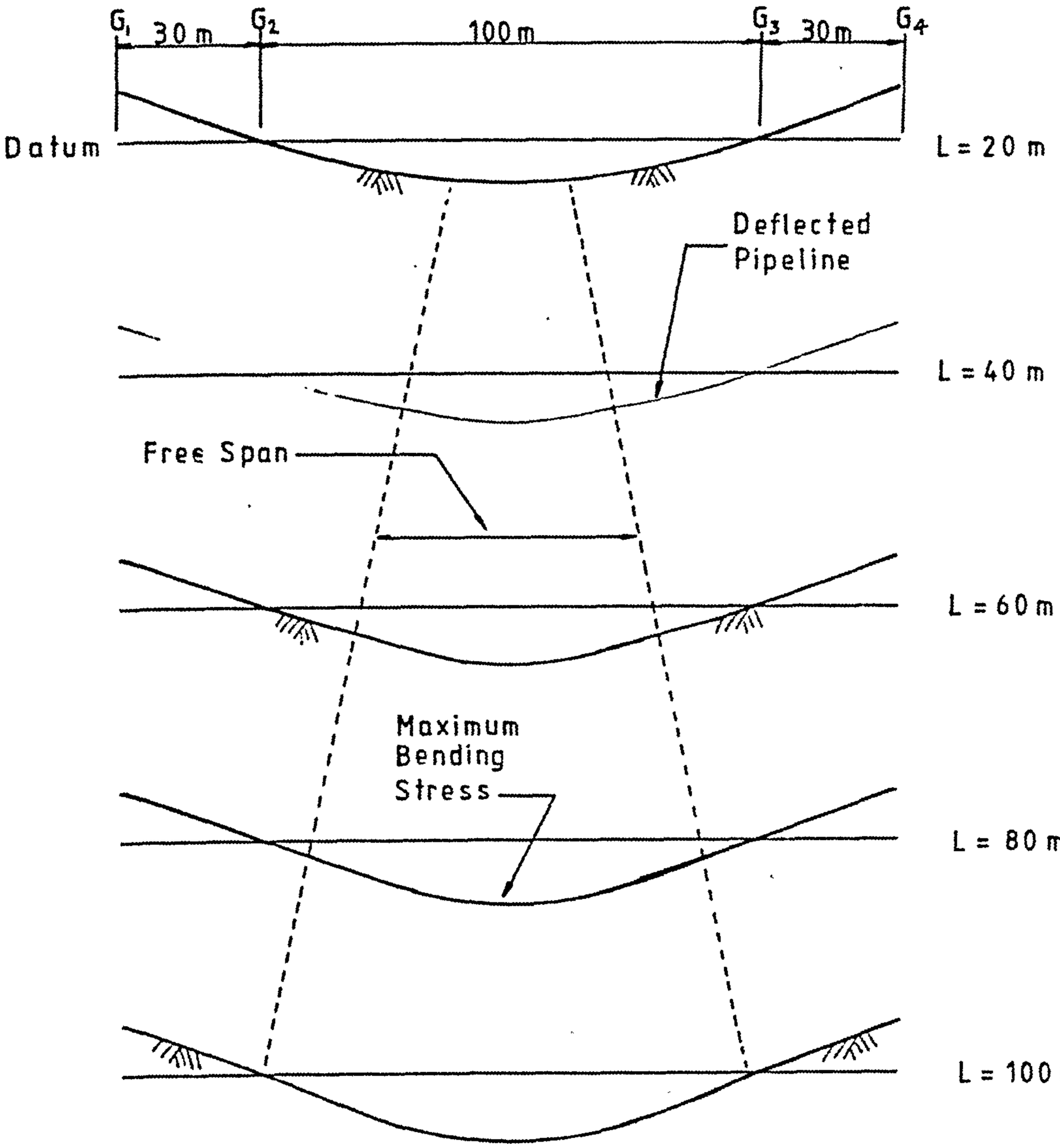

Note: Vertical Deflection x4

FIG 4.10 Pipe 2 Deflections , $-\theta_1 = \theta_2 = 5^\circ$

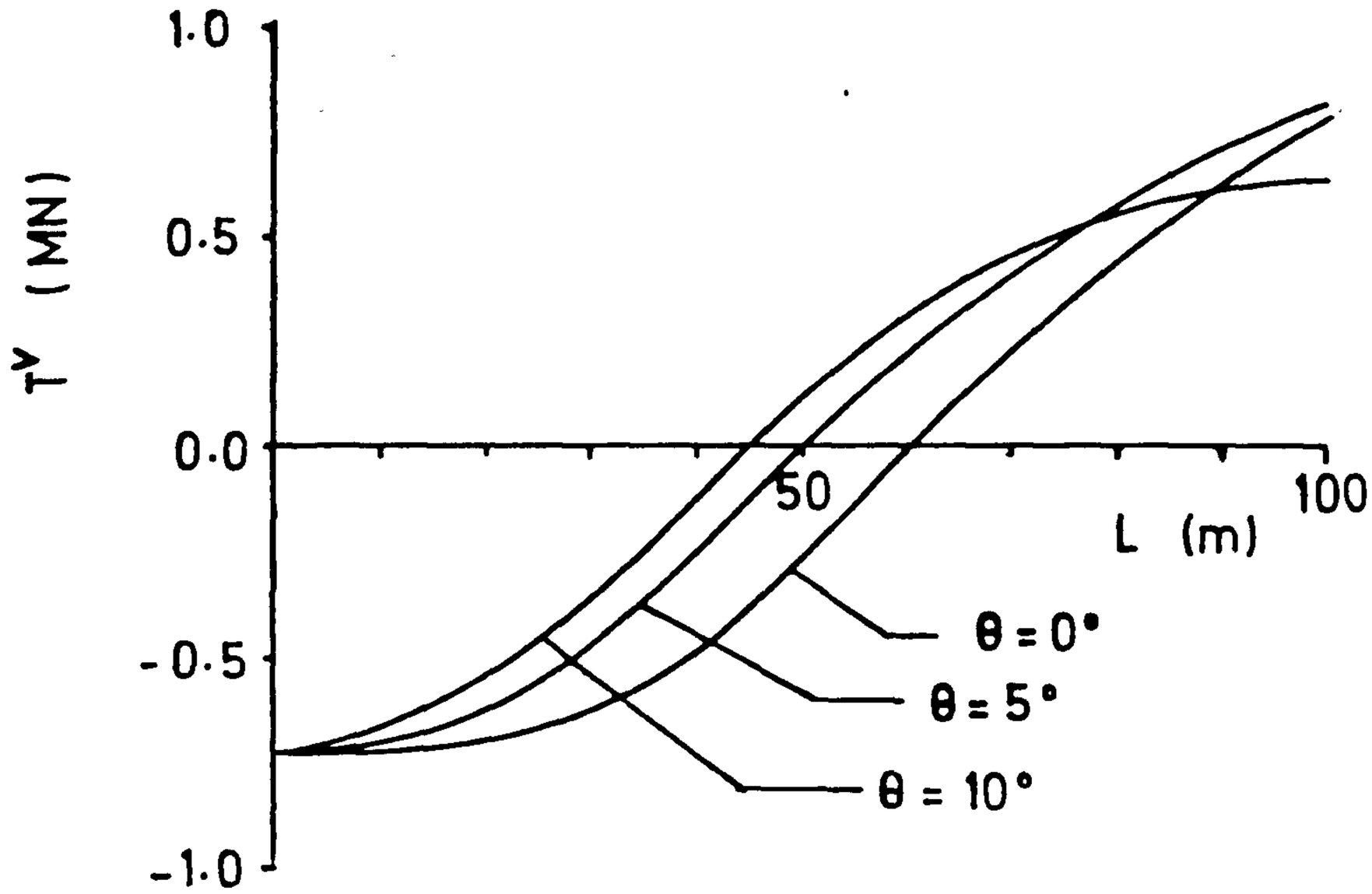

FIG 4.11 Pipe 2 Variable Effective Tension T^v, $-\theta_1 = \theta_2 = \theta$

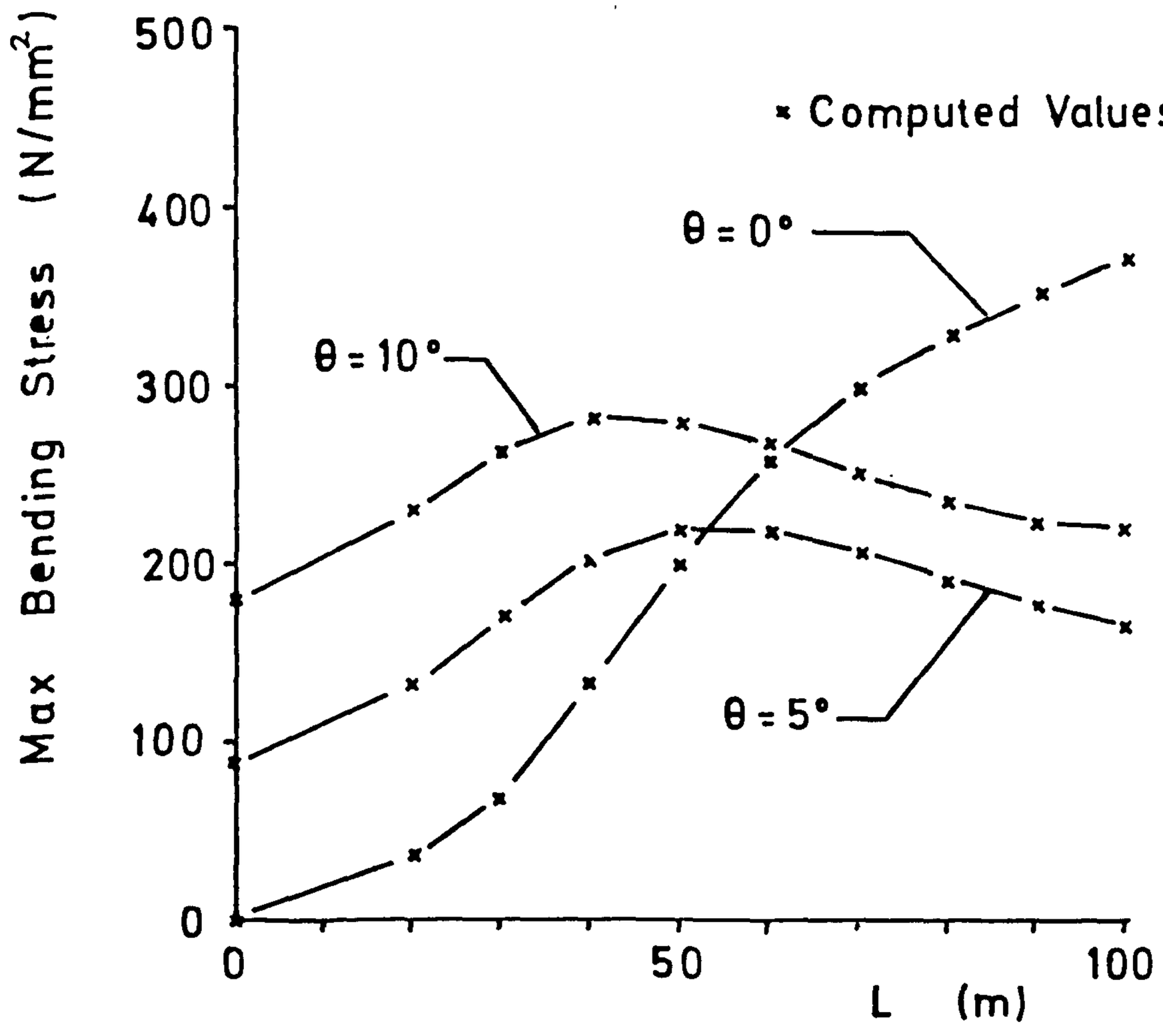

FIG 4.12 Maximum Bending Stress, $-\theta_1 = \theta_2 = \theta$

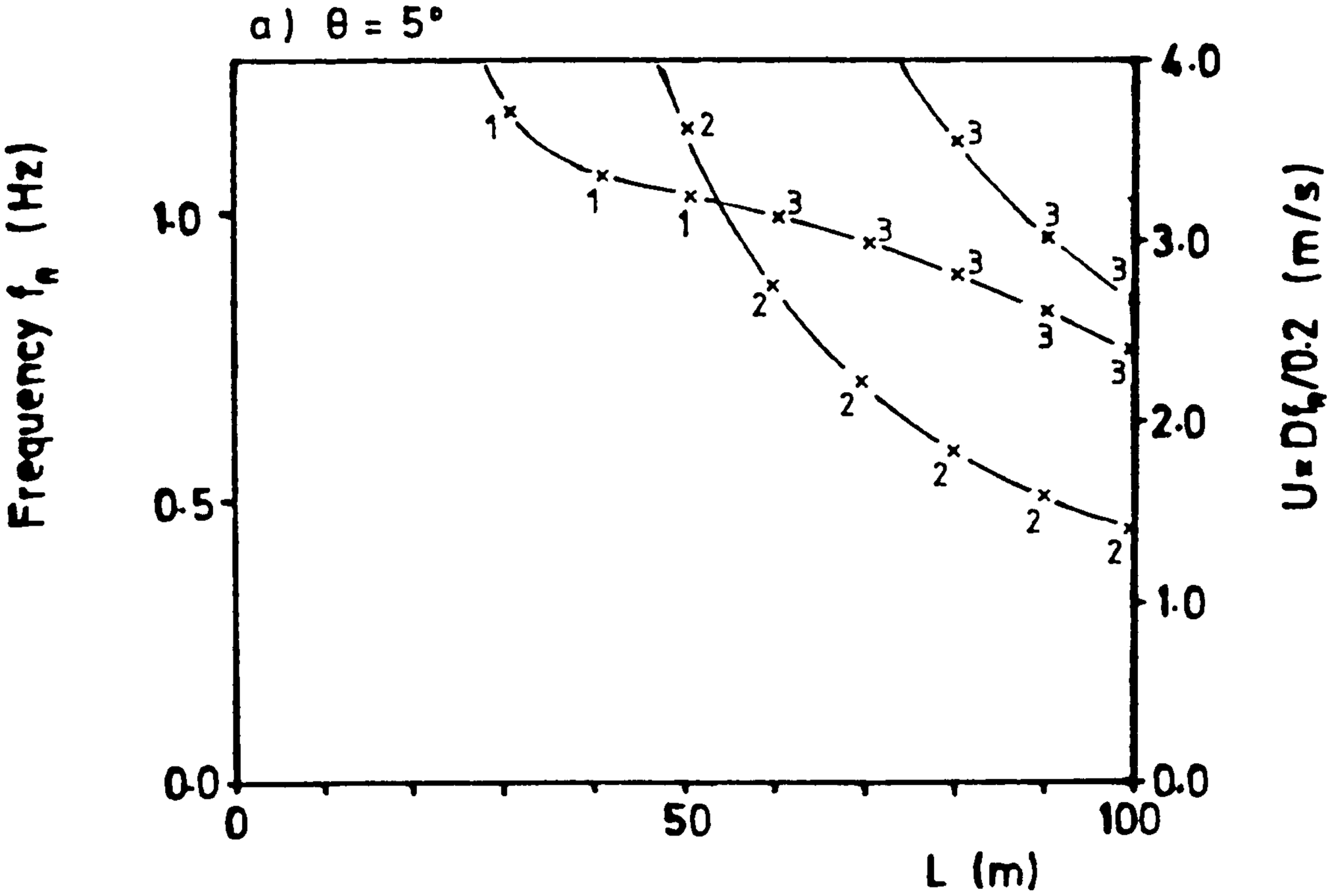

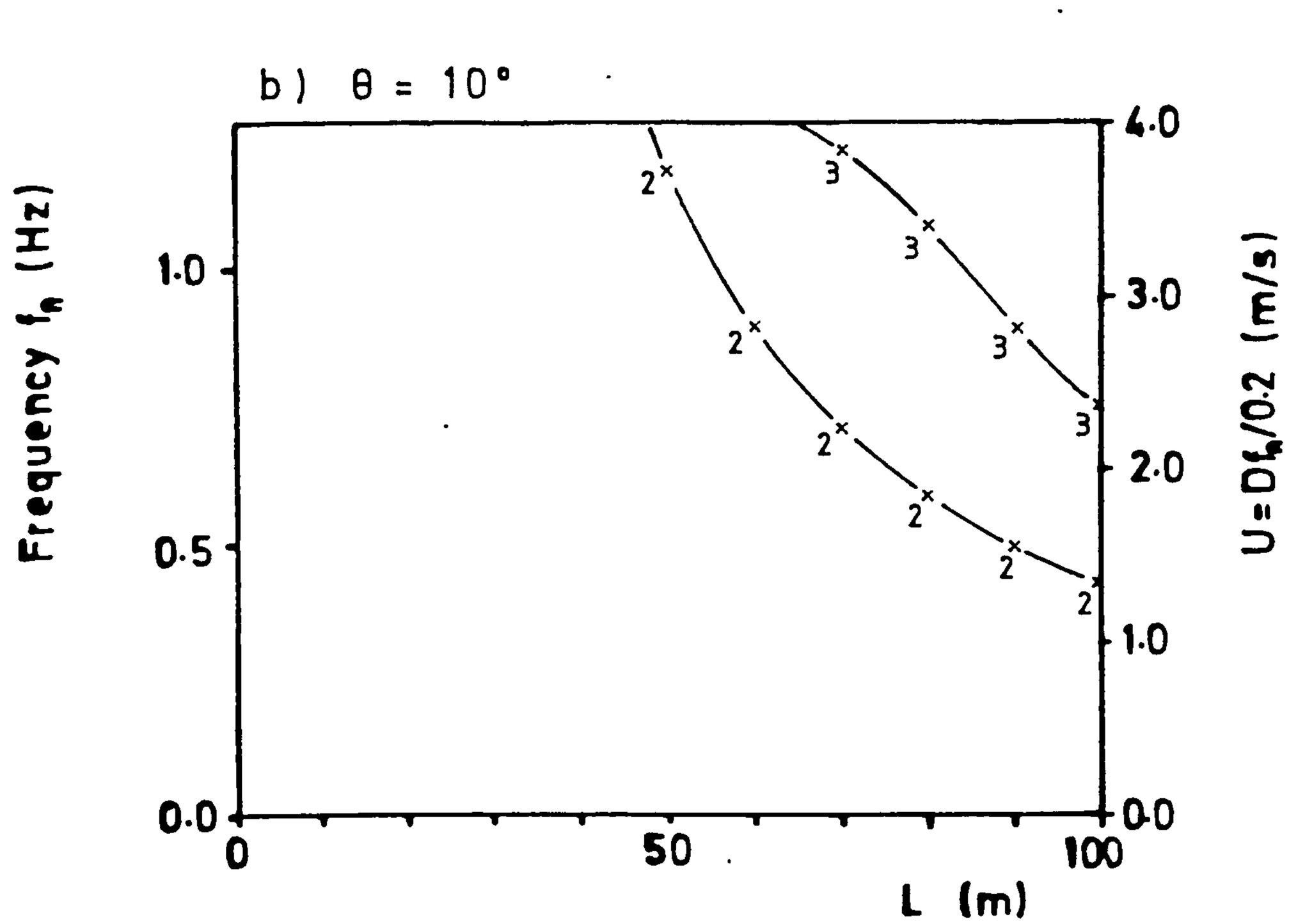

FIG 4.13 Pipe 2 Frequencies, $-\theta_1 = \theta_2 = \theta$

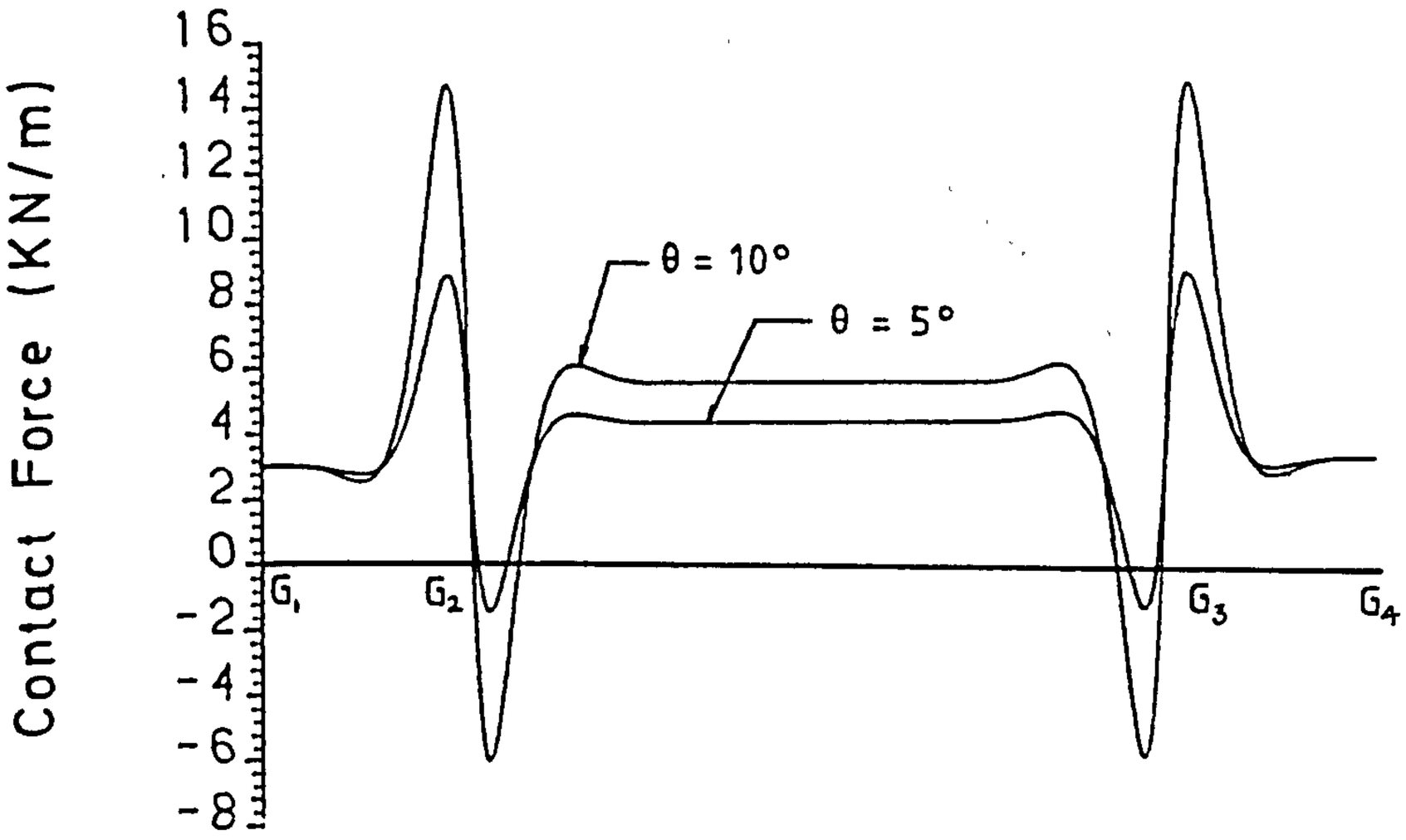

FIG 4.14 Pipe 2 Contact Force , $-\theta_1 = \theta_2 = \theta$

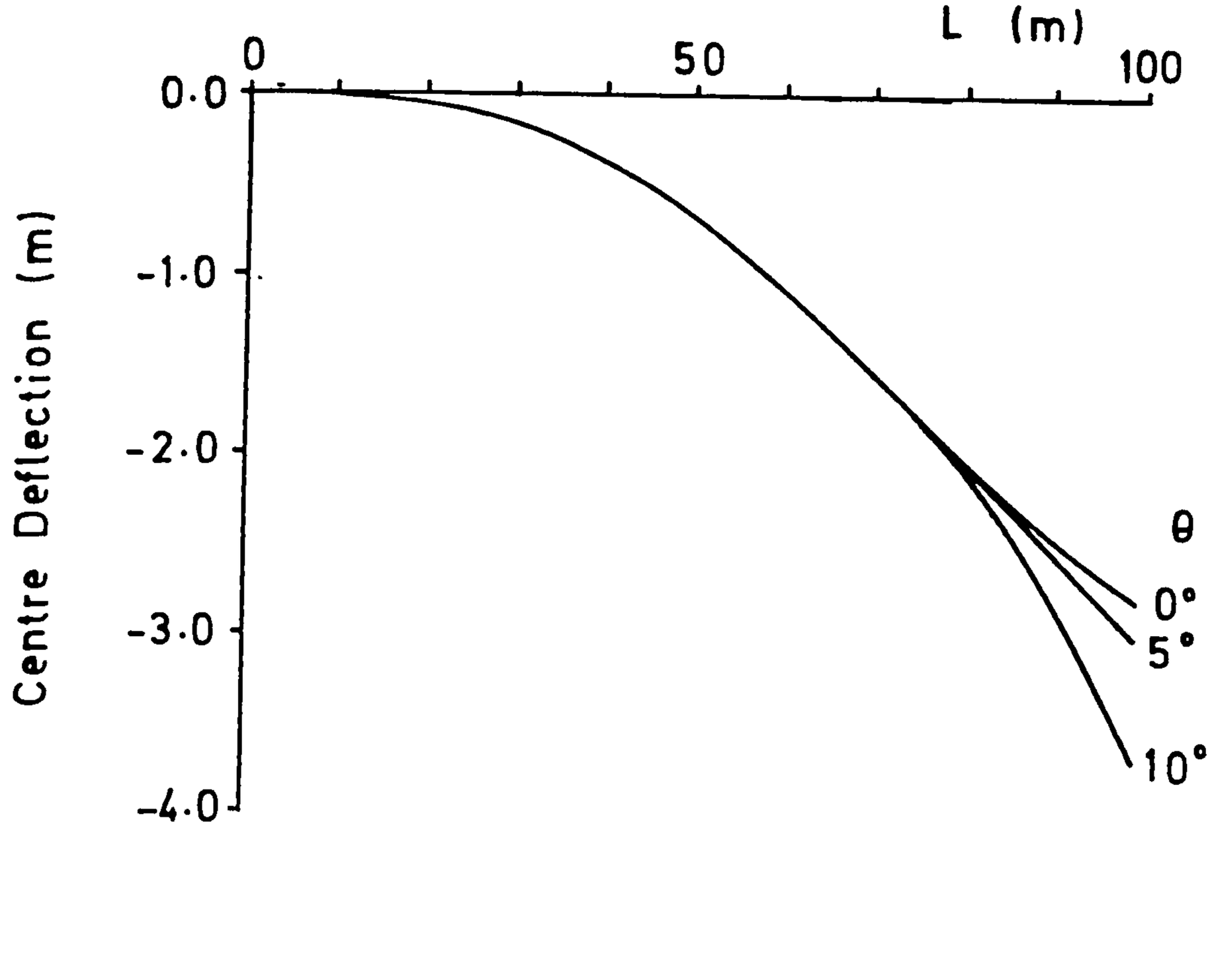

FIG 4.15 Pipe 2 Centre Deflection, $\theta_1 = \theta_2 = \theta$

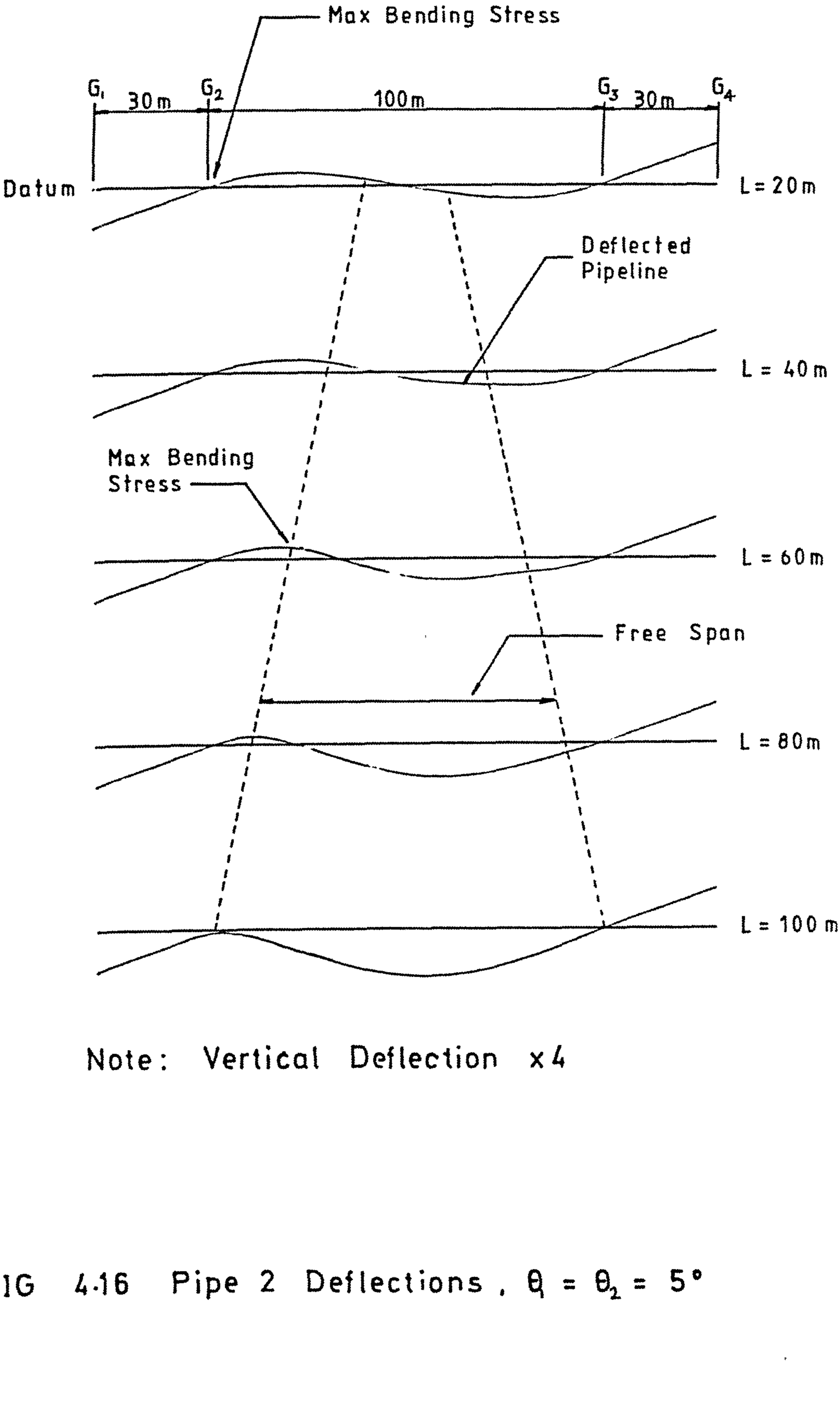

Note: Vertical Deflection x4

FIG 4.16 Pipe 2 Deflections, $\theta_1 = \theta_2 = 5°$

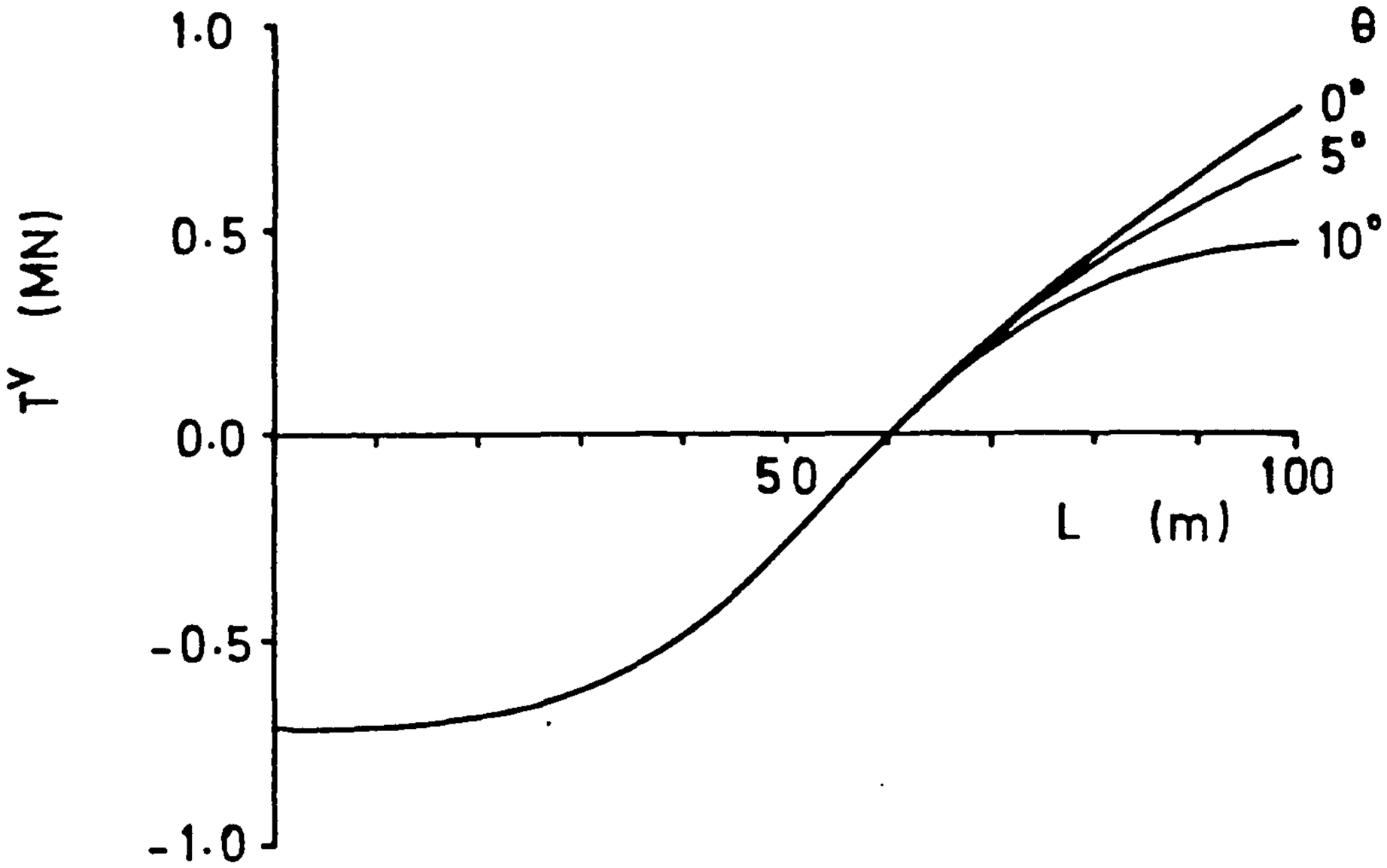

FIG 4.17 Pipe 2 Variable Effective Tension T^V, $\theta_1 = \theta_2 = \theta$

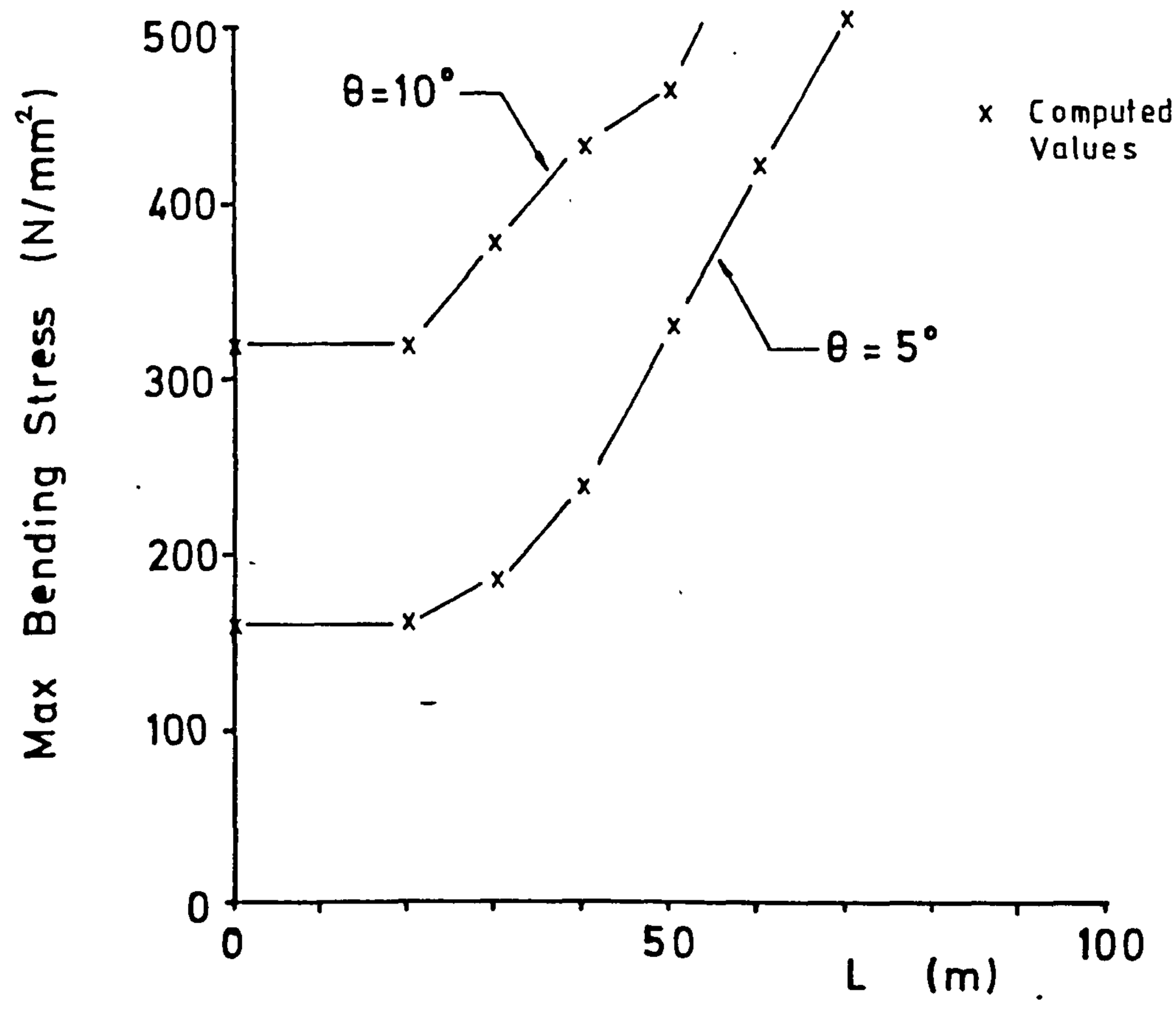

FIG 4.18 Maximum Bending Stress , $\theta_1 = \theta_2 = \theta$

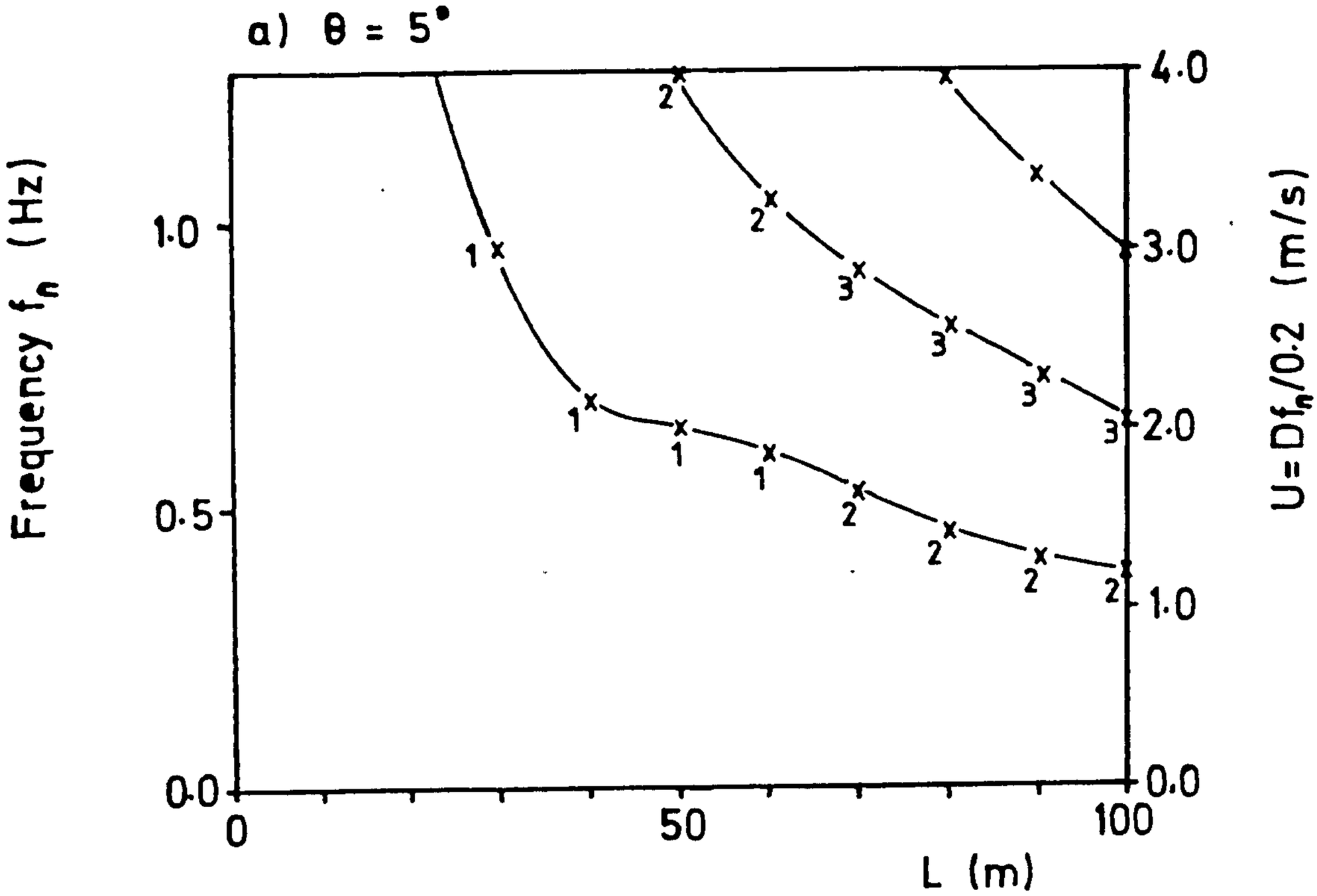

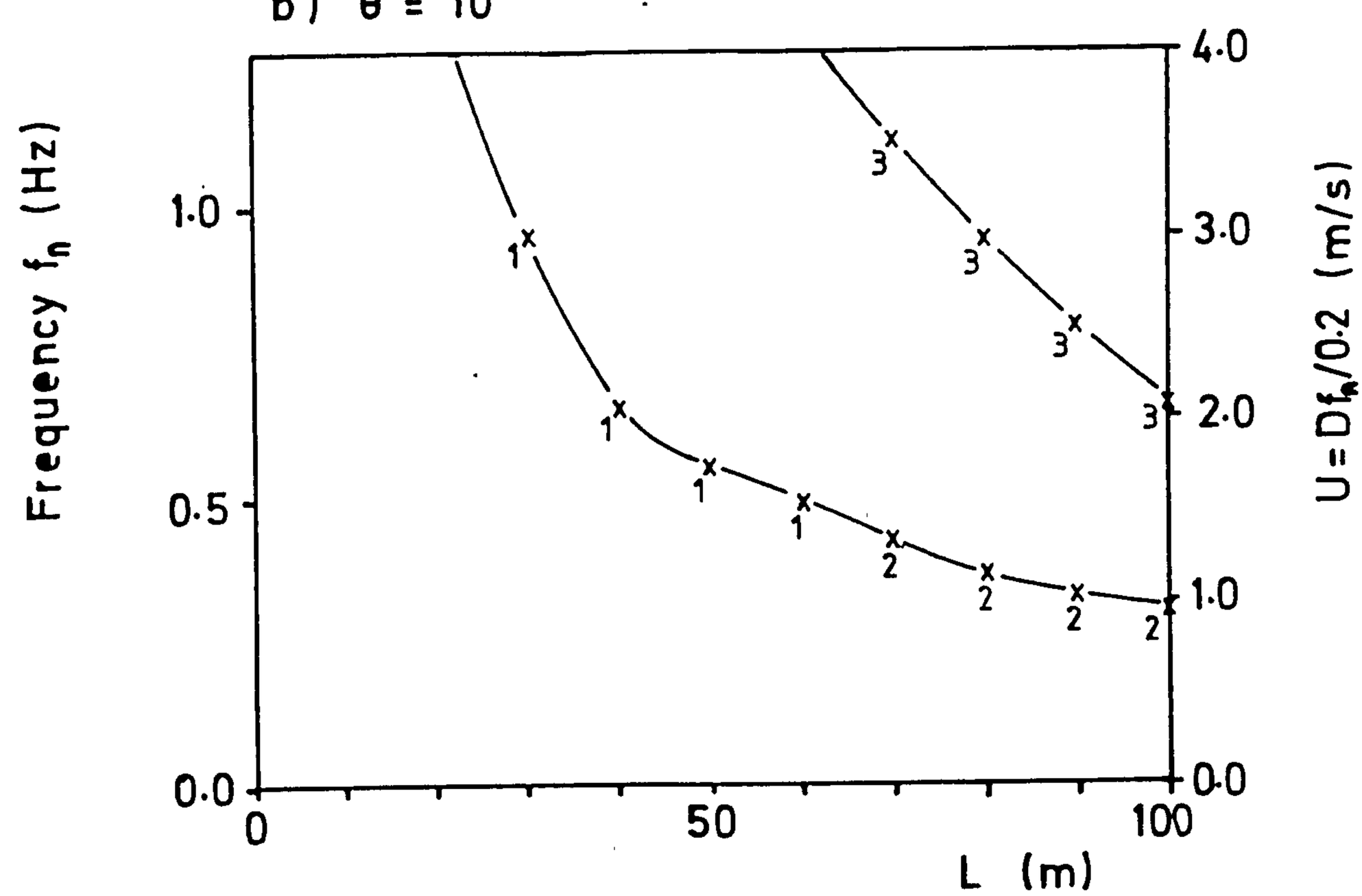

FIG 4.19 Pipe 2 Frequencies , $\theta_1 = \theta_2 = \theta$

a) L = 50 m

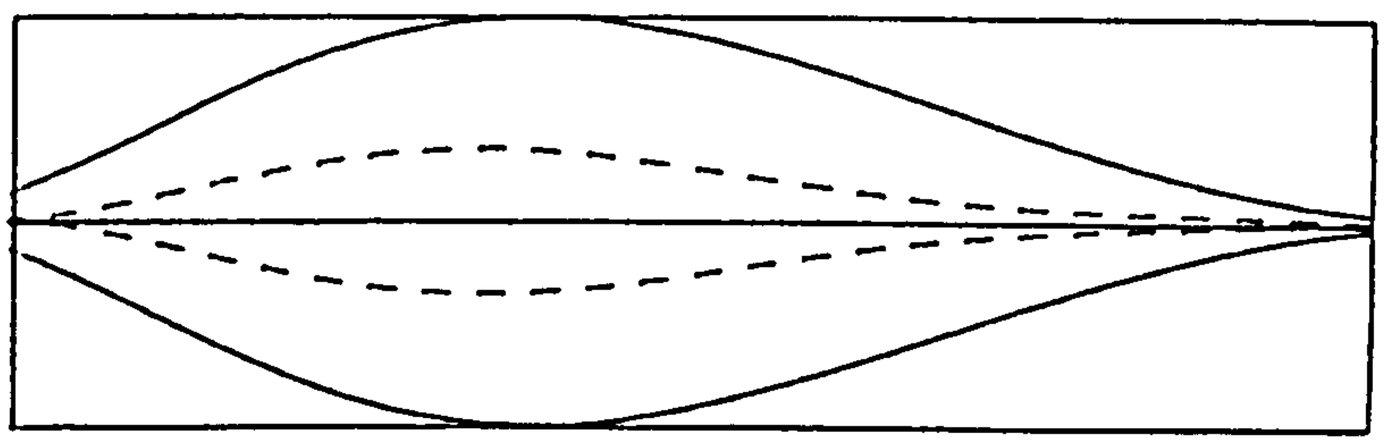

b) L = 60 m

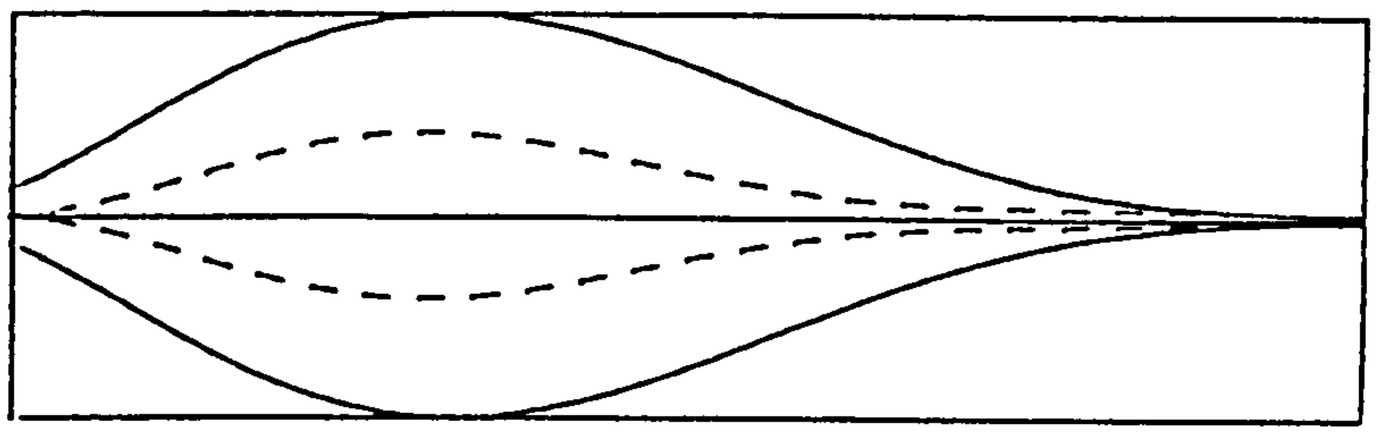

c) L = 70 m

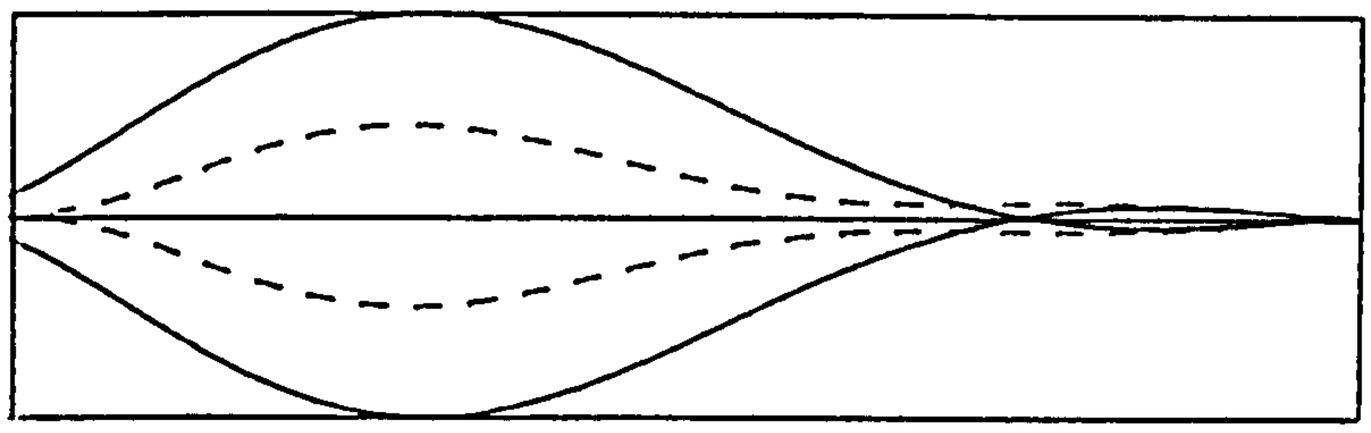

d) L = 80 m

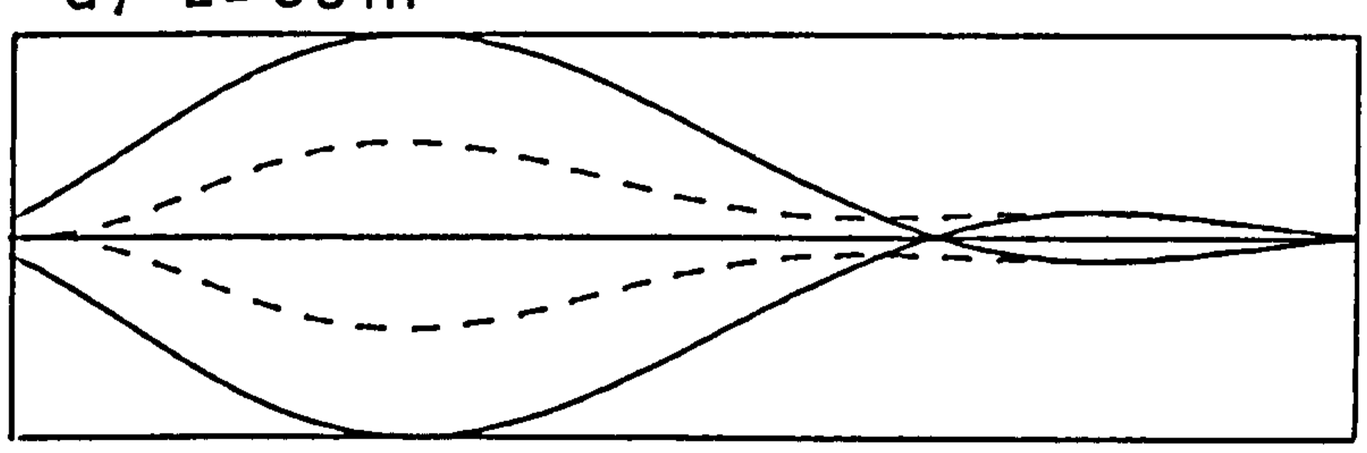

——— Vertical Disp.

------- Horizontal Disp. (x 5)

FIG 4.20 Pipe 2 Fundamental Mode Shape
$\theta_1 = \theta_2 = 5^\circ$

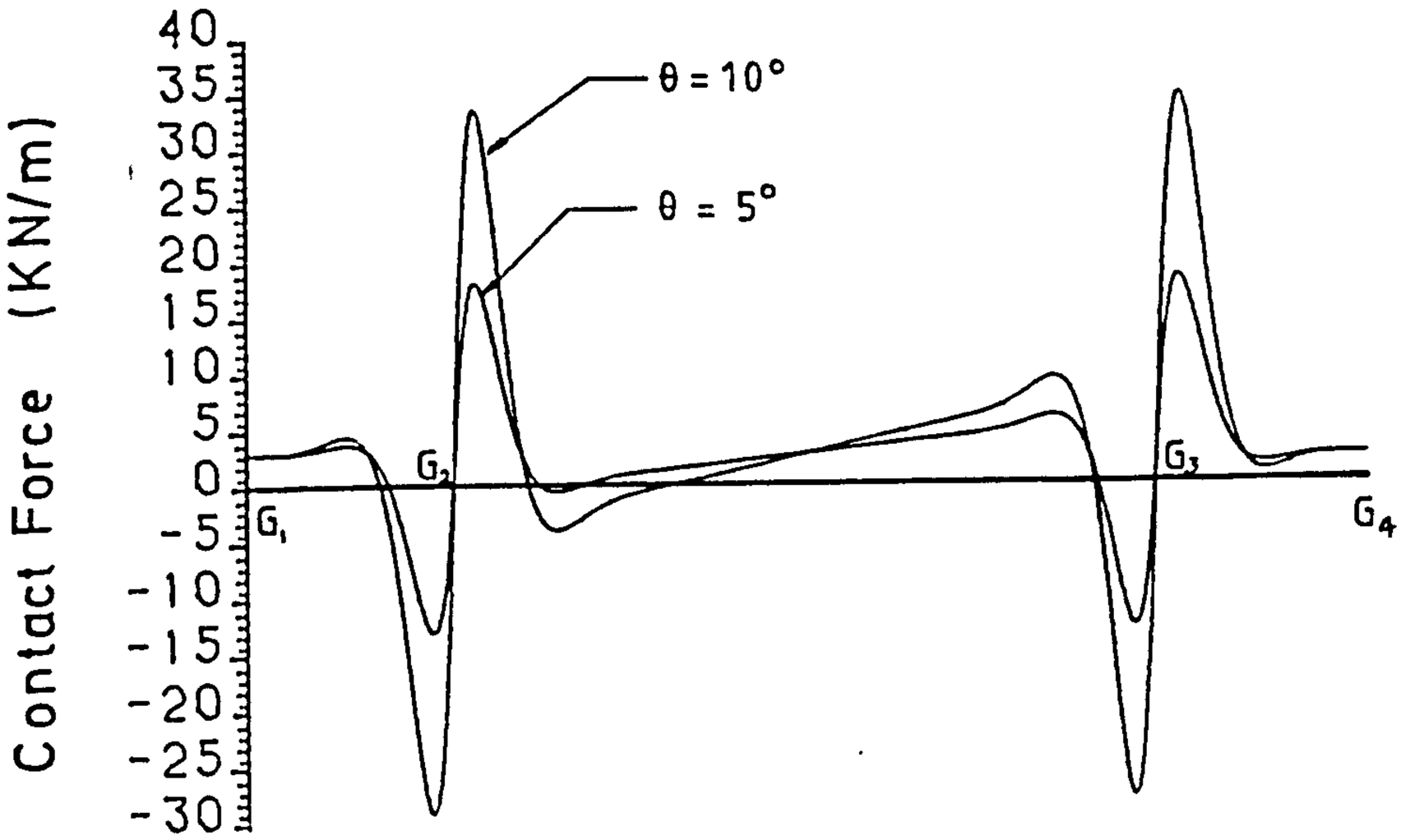

FIG 4.21 Pipe 2 Contact Force , $\theta_1 = \theta_2 = \theta$

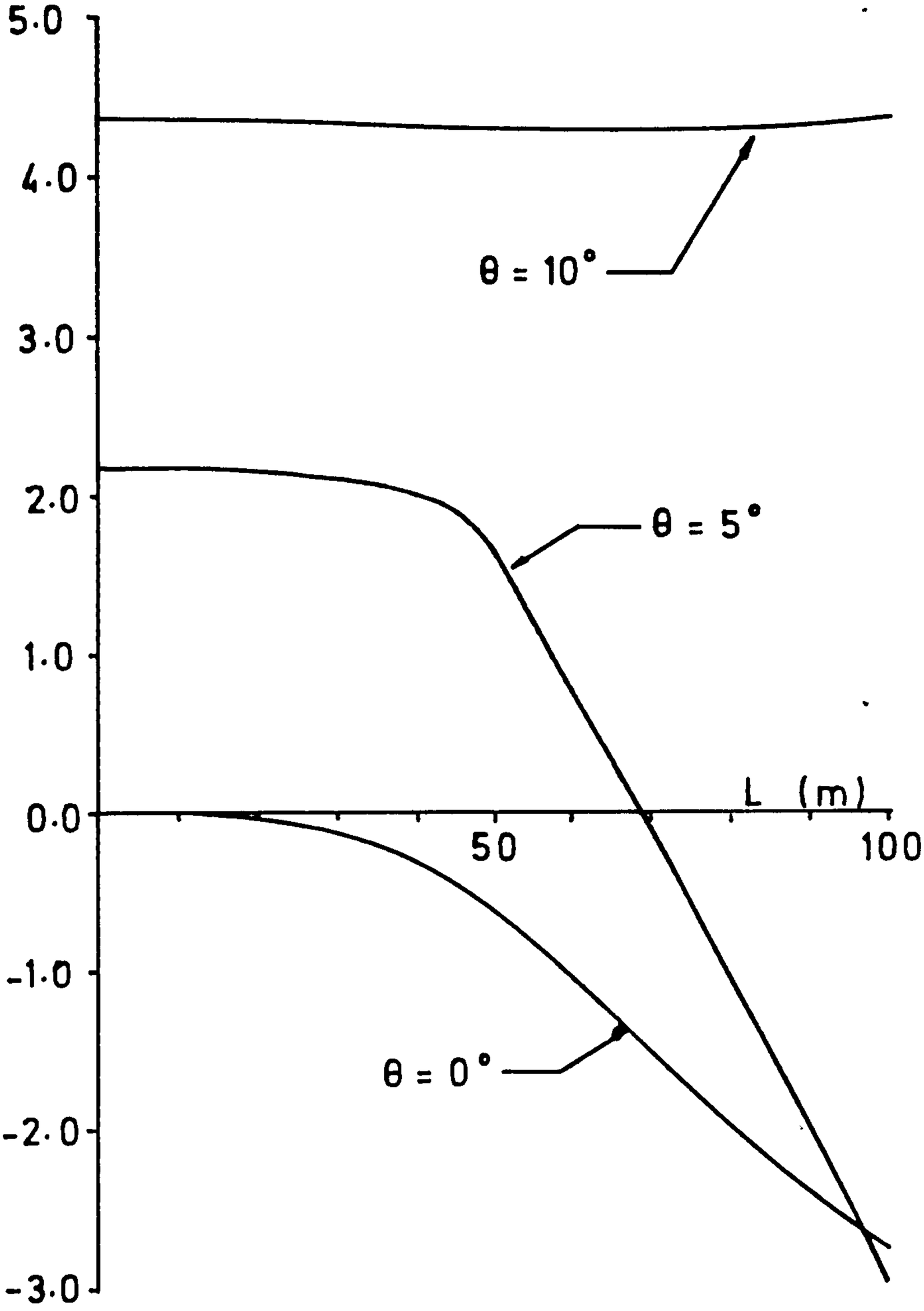

FIG 4.22 Pipe 2 Centre Deflection, $\theta_1 = -\theta_2 = \theta$

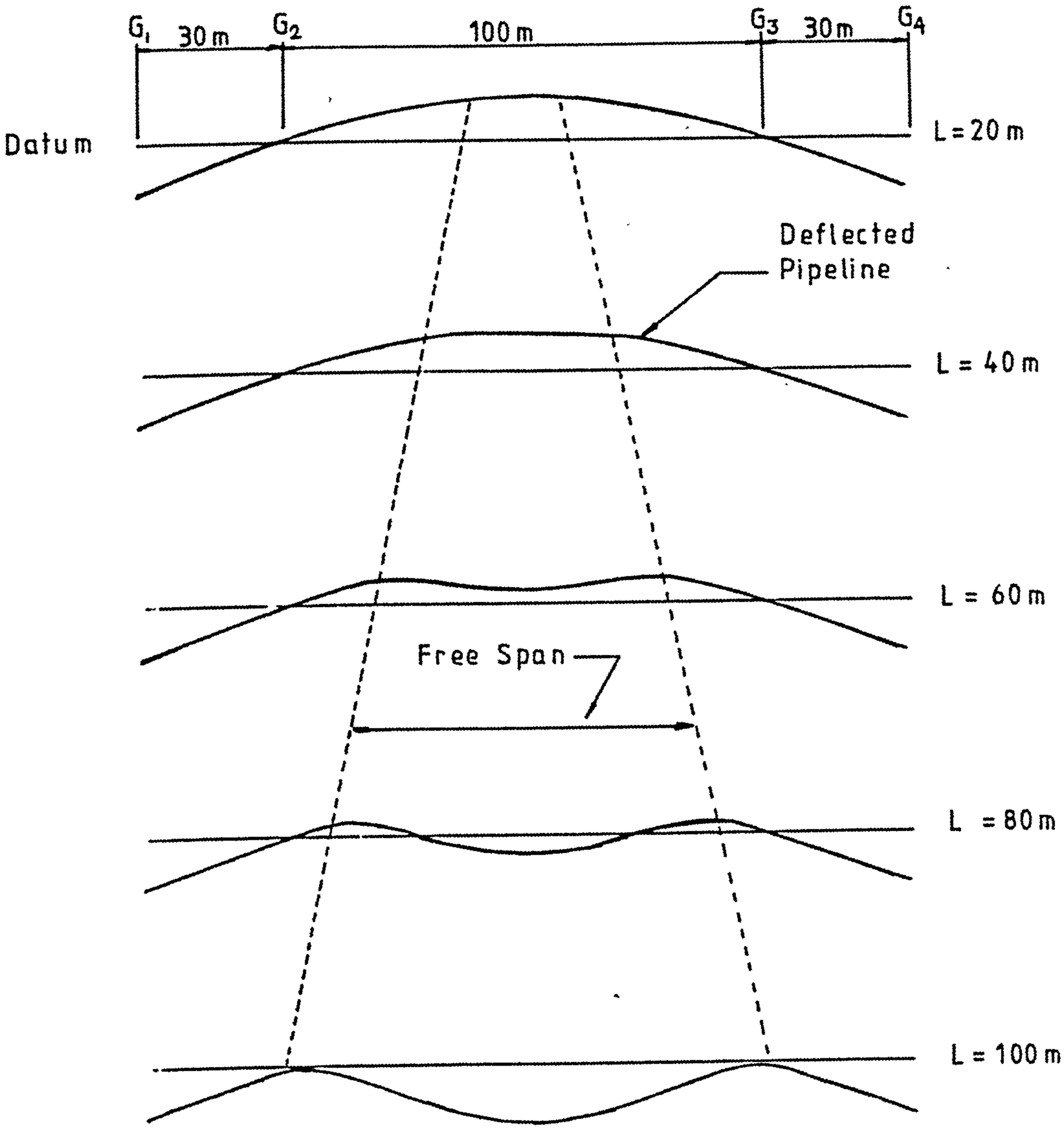

Note: Vertical Deflection x4

FIG 4.23 Pipe 2 Deflections, $\theta_1 = -\theta_2 = 5^\circ$

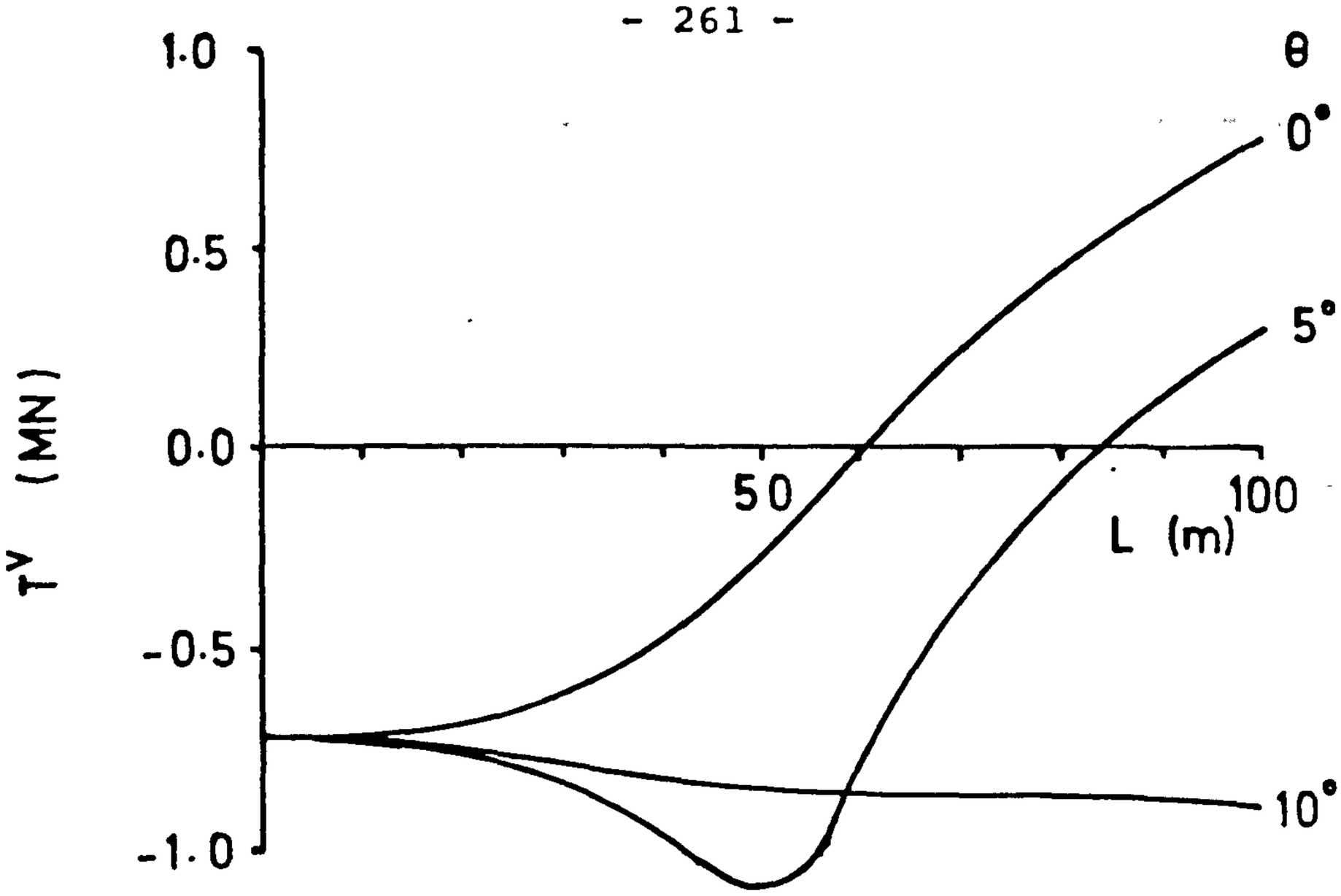

FIG 4.24 Pipe 2 Variable Effective Tension T^V, $\theta_1 = -\theta_2 = \theta$

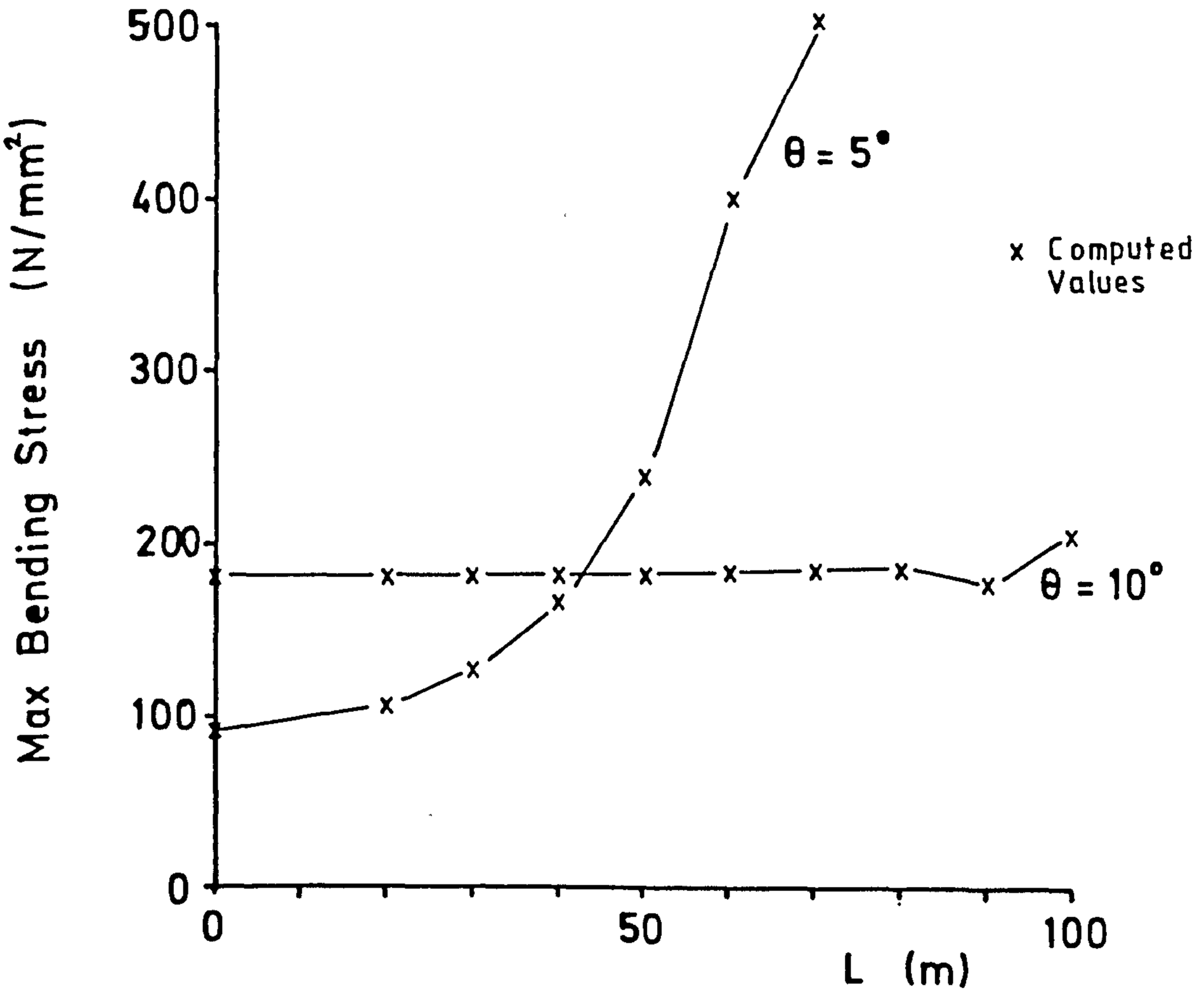

FIG 4.25 Maximum Bending Stress , $\theta_1 = -\theta_2 = \theta$

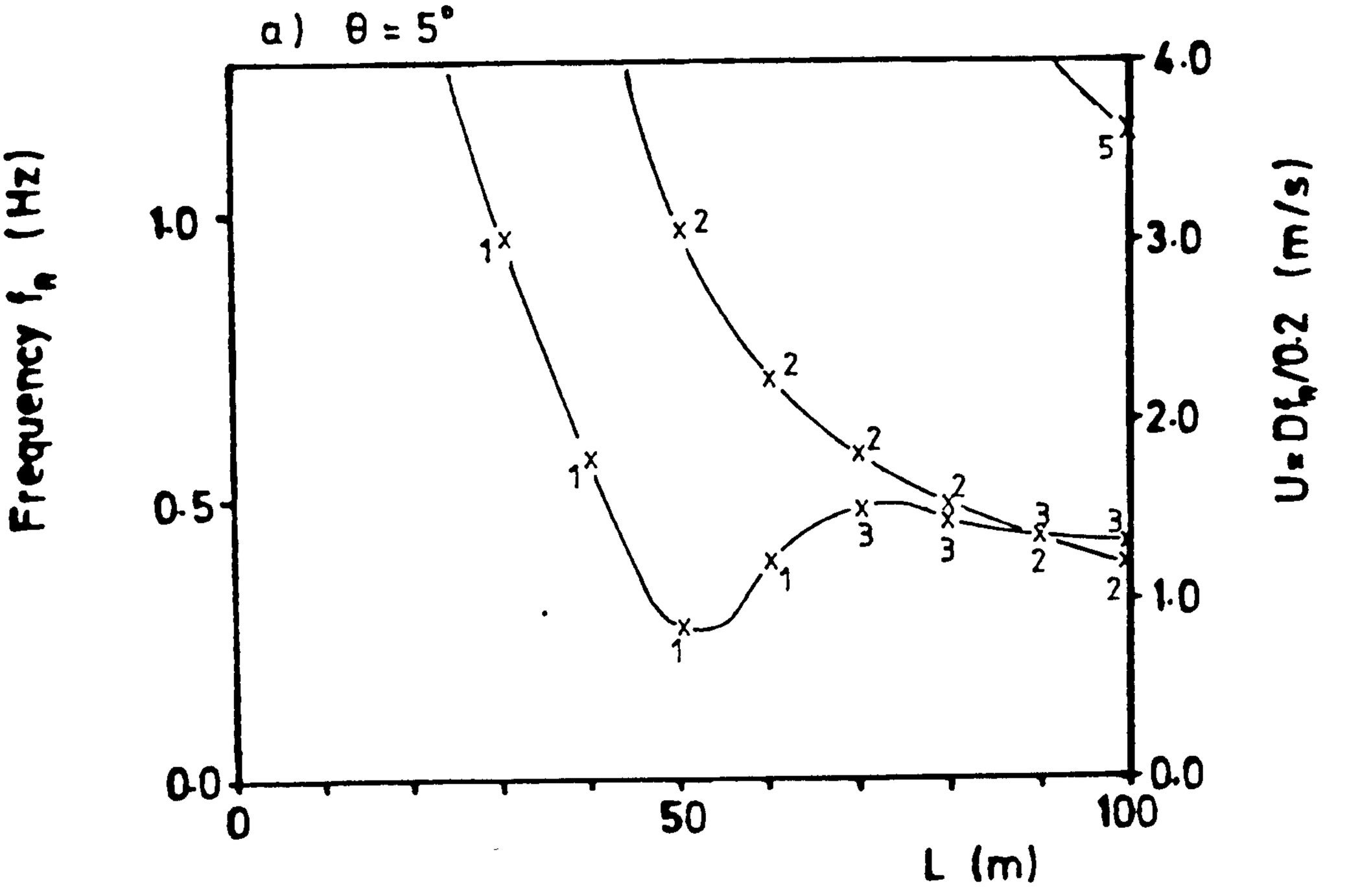

FIG 4.26 Pipe 2 Frequencies, $\theta_1 = -\theta_2 = \theta$

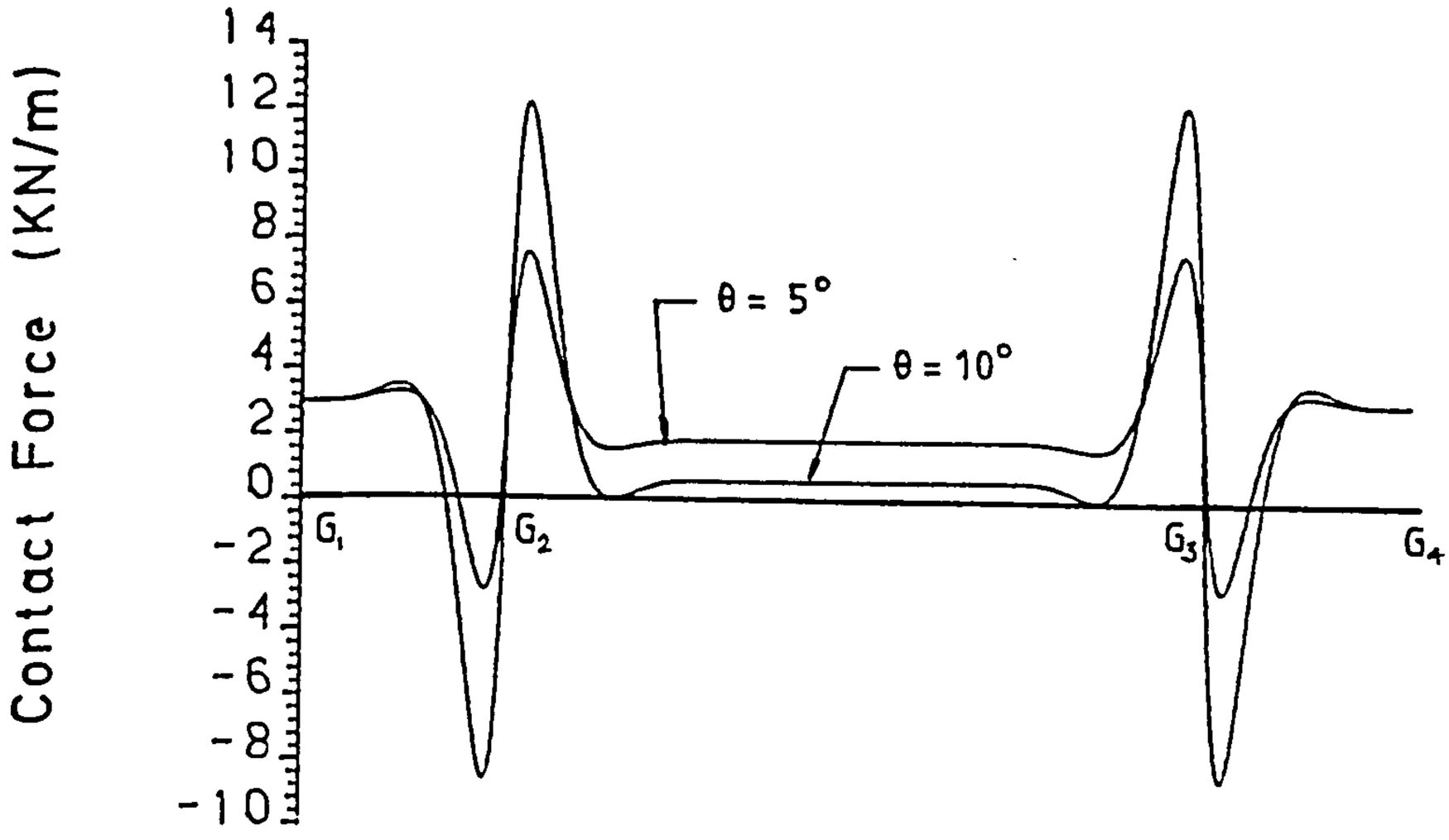

FIG 4.27 Pipe 2 Contact Force , $\theta_1 = -\theta_2 = \theta$

CHAPTER 5

EFFECT OF FINITE AMPLITUDE VIBRATIONS

5.0 Introduction

The calculation of span frequencies described in previous chapters utilised a standard eigenvalue algorithm involving the tangent stiffness matrix evaluated at the static equilibrium position. It follows that since this approach assumes a constant mass and stiffness, the results are valid for infinitesimally small amplitude motions only. In practice motions on the order of two diameters may be expected (Bruschi, 1982) with the result that significant structural and hydrodynamic nonlinearities may be brought into play. Under these conditions the concept of free vibration in a single mode is no longer valid (Clough, 1975) and instead the characteristics of the system must be investigated by (numerical) integration in the time domain. In this chapter an attempt is made to assess some of these effects and to initiate an understanding of their influence on free span dynamics.

5.1 Nonlinear Equations of Motion

Using the notation of chapters 3 and 4 the general equation of motion for nonlinear forced response of the pipline may be written in the form

$$[M]\ddot{\underset{\sim}{\alpha}} + \underset{\sim}{F}(\underset{\sim}{\alpha}) = \underset{\sim}{P} + \underset{\sim}{Q} + \underset{\sim}{H}(\underset{\sim}{\alpha}, \dot{\underset{\sim}{\alpha}}, \ddot{\underset{\sim}{\alpha}}, t) \qquad (5.1)$$

where the assembled mass matrix is here assumed constant and $\underset{\sim}{H}$ represents a vector of hydrodynamic loads. For a pipe undergoing vortex induced oscillations the development of a suitable model for these loads is extremely complicated and considered outside the scope

of this thesis. Instead attention is focused on the considerably simplified free vibration equation

$$[M]\ddot{\underset{\sim}{\alpha}} + \underset{\sim}{F}(\underset{\sim}{\alpha}) = \underset{\sim}{\ell} + \underset{\sim}{Q} \qquad (5.2)$$

in order to assess the influence of the basic structural nonlinearities on free span dynamics.(1) This equation may be integrated numerically by first discretizing the time axis using a point collocation method (Zienkiewicz, 1977). This approach relaxes the implied condition that equation (5.2) must be satisfied at all times, allowing instead the consideration of dynamic equilibrium at a finite number of discrete time points only. Thus at some time $t+\tau$ equation (5.2) may be written as

$$[M]\ddot{\underset{\sim}{\alpha}}_{t+\tau} + \underset{\sim}{F}(\underset{\sim}{\alpha}_{t+\tau}) = \underset{\sim}{R} \qquad (5.3)$$

where the subscripts indicate the time at which the associated quantity is to be evaluated and $\underset{\sim}{R} = \underset{\sim}{\ell} + \underset{\sim}{Q}$ is a constant vector of static loads. Now defining the displacement increment $\Delta\underset{\sim}{\alpha} = \underset{\sim}{\alpha}_{t+\tau} - \underset{\sim}{\alpha}_t$ the Taylor series expansion of $\underset{\sim}{F}(\underset{\sim}{\alpha}_{t+\tau})$ about $\underset{\sim}{\alpha}_t$ is

$$\underset{\sim}{F}(\underset{\sim}{\alpha}_{t+\tau}) = \underset{\sim}{F}(\underset{\sim}{\alpha}_t) + [k_T(\underset{\sim}{\alpha}_t)]\Delta\underset{\sim}{\alpha} \qquad (5.4)$$

where $k_T(\underset{\sim}{\alpha}_t)$ represents the tangent stiffness matrix evaluated at $\underset{\sim}{\alpha}_t$. Substituting this into equation (5.3) gives an incremental form of the equation of motion

---

(1) Equation (5.2) may be considered an extension of the eigenvalue equation in which the linear tangent stiffness is replaced by the full nonlinear element force vector .

$$[M]\ddot{\underset{\sim}{\alpha}}_{t+\tau} + [K_T(\underset{\sim}{\alpha}_t)]\Delta\underset{\sim}{\alpha} = \underset{\sim}{R} - \underset{\sim}{F}(\underset{\sim}{\alpha}_t) \qquad (5.5)$$

This equation is now integrated in the time domain using the well known Wilson-θ method (Wilson, 1973). The application of this algorithm to problems in nonlinear structural dynamics has been well documented (e.g. Owen, 1978) and requires little further explanation here. However, in addition to the geometric nonlinearities occuring in equation (5.3), the pipe span system also has a memory phenomena associated with the end friction elements. As discussed in section 5.2.2 this situation requires special consideration during the numerical integration in order to reasonably satisfy the basic assumptions inherent in the method. Thus as an introduction to this discussion a brief outline of the linear acceleration method and associated Wilson-θ scheme is first presented.

5.2 Linear Acceleration Method

In order to solve equation (5.5) for the displacement increment $\Delta\underset{\sim}{\alpha}$ it is first necessary to assume some functional form for the variation of acceleration $\ddot{\underset{\sim}{\alpha}}$ over the time interval $(t, t+\tau)$. In the linear acceleration method (Newmark, 1959) this variation is taken of the linear form

$$\ddot{\underset{\sim}{\alpha}}(s) = \ddot{\underset{\sim}{\alpha}}_t + \frac{s}{\tau}(\ddot{\underset{\sim}{\alpha}}_{t+\tau} - \ddot{\underset{\sim}{\alpha}}_t) \qquad (5.6)$$

where s is a local shifted time scale, figure 5.1. Integrating with respect to s

$$\dot{\underset{\sim}{\alpha}}(s) = \dot{\underset{\sim}{\alpha}}_t + s\ddot{\underset{\sim}{\alpha}}_t + \frac{s^2}{2\tau}(\ddot{\underset{\sim}{\alpha}}_{t+\tau} - \ddot{\underset{\sim}{\alpha}}_t) \qquad (5.7a)$$

$$\underset{\sim}{\alpha}(s) = \underset{\sim}{\alpha}_t + s\dot{\underset{\sim}{\alpha}}_t + \frac{s^2}{2}\ddot{\underset{\sim}{\alpha}}_t + \frac{s^3}{6\tau}(\ddot{\underset{\sim}{\alpha}}_{t+\tau} - \ddot{\underset{\sim}{\alpha}}_t) \qquad (5.7b)$$

indicating that the corresponding variations in velocity and displacement over the time interval $(t, t+\tau)$ are quadratic and cubic respectively. Now setting $s = \tau$ in equations (5.7) and solving for $\ddot{\underset{\sim}{\alpha}}_{t+\tau}$ and $\dot{\underset{\sim}{\alpha}}_{t+\tau}$ we find

$$\ddot{\underset{\sim}{\alpha}}_{t+\tau} = a_0 \Delta\underset{\sim}{\alpha} - a_2\dot{\underset{\sim}{\alpha}}_t - a_3\ddot{\underset{\sim}{\alpha}}_t \qquad (5.8a)$$

$$\dot{\underset{\sim}{\alpha}}_{t+\tau} = a_1 \Delta\underset{\sim}{\alpha} - a_4\dot{\underset{\sim}{\alpha}}_t - a_5\ddot{\underset{\sim}{\alpha}}_t \qquad (5.8b)$$

where the constants a_i are given by

$$a_0 = \frac{6}{\tau^2} \qquad a_2 = \frac{6}{\tau} \qquad a_3 = 2$$

$$a_1 = \frac{3}{\tau} \qquad a_4 = 2 \qquad a_5 = \frac{\tau}{2}$$

Substituting these expressions into equation (5.5) and rearranging

$$\left[a_0 M + K_T(\underset{\sim}{\alpha}_t)\right]\Delta\underset{\sim}{\alpha} = \left[M\right](a_2\dot{\underset{\sim}{\alpha}}_t + a_3\ddot{\underset{\sim}{\alpha}}_t) + \underset{\sim}{R} - \underset{\sim}{F}(\underset{\sim}{\alpha}_t) \qquad (5.9)$$

Thus assuming all quantities at time t as known we may solve for the displacement increment $\Delta\underset{\sim}{d}$ and hence, using equations (5.8), obtain the complete solution at time $t+\tau$. As with the incremental static analysis used in chapters 3 and 4, the accuracy of this solution may now be improved by applying a series of equilibrium iterations until some specified convergence is achieved. In fact, for the time integration of nonlinear dynamic problems this process is virtually mandatory (Bathe, 1982) in order to ensure reasonable engineering accuracy. Thus anticipating that the above solution is only approximate we first rewrite equation (5.9) in the form

$$\left[a_0 M + K_T(\underset{\sim}{d}_t)\right]\Delta\underset{\sim}{d}^{\circ} = [M](a_2\dot{\underset{\sim}{d}}_t + a_3\ddot{\underset{\sim}{d}}_t) + \underset{\sim}{R} - \underset{\sim}{F}(\underset{\sim}{d}_t) \qquad (5.10)$$

where the superscript on $\Delta\underset{\sim}{d}^{\circ}$ indicates that this is only an initial estimate. Solving equation (5.10) and using equation (5.8) gives the initial estimate solution

$$\ddot{\underset{\sim}{d}}^{\circ}_{t+\tau} = a_0\,\Delta\underset{\sim}{d}^{\circ} - a_2\dot{\underset{\sim}{d}}_t - a_3\ddot{\underset{\sim}{d}}_t \qquad (5.11a)$$

$$\dot{\underset{\sim}{d}}^{\circ}_{t+\tau} = a_1\,\Delta\underset{\sim}{d}^{\circ} - a_4\dot{\underset{\sim}{d}}_t - a_5\ddot{\underset{\sim}{d}}_t \qquad (5.11b)$$

$$\underset{\sim}{d}^{\circ}_{t+\tau} = \Delta\underset{\sim}{d}^{\circ} + \underset{\sim}{d}_t \qquad (5.11c)$$

which substituting into the equation of motion equation (5.3) gives the corresponding residual forces

$$\underset{\sim}{\Psi}(\underset{\sim}{d}^{\circ}_{t+\tau}) = [M]\ddot{\underset{\sim}{d}}^{\circ}_{t+\tau} + \underset{\sim}{F}(\underset{\sim}{d}^{\circ}_{t+\tau}) - \underset{\sim}{R} \qquad (5.12)$$

We now seek a correction $\delta\underset{\sim}{d}'$ to the displacement solution $\underset{\sim}{d}'^{o}_{t+\tau}$ such that

$$\underset{\sim}{d}'_{t+\tau} = \underset{\sim}{d}'^{o}_{t+\tau} + \delta\underset{\sim}{d}' \tag{5.13}$$

represents an improved solution. The corresponding residual forces are

$$\underset{\sim}{\Psi}(\underset{\sim}{d}'_{t+\tau}) = [M]\,\ddot{\underset{\sim}{d}}'_{t+\tau} + \underset{\sim}{F}(\underset{\sim}{d}'_{t+\tau}) - \underset{\sim}{R} \tag{5.14}$$

where using equation (5.8a) we may write

$$\begin{aligned}\ddot{\underset{\sim}{d}}'_{t+\tau} &= a_0(\Delta\underset{\sim}{d}'^{o} + \delta\underset{\sim}{d}') - a_2\dot{\underset{\sim}{d}}_t - \underset{\sim}{a}_3\ddot{\underset{\sim}{d}}_t \\ &= \ddot{\underset{\sim}{d}}'^{o}_{t+\tau} + a_0\delta\underset{\sim}{d}'\end{aligned} \tag{5.15}$$

Substituting this into equation (5.14) and expanding the internal force vector $\underset{\sim}{F}$ we may write

$$\begin{aligned}\underset{\sim}{\Psi}(\underset{\sim}{d}'_{t+\tau}) = [M](\ddot{\underset{\sim}{d}}'^{o}_{t+\tau} + a_0\delta\underset{\sim}{d}') + \underset{\sim}{F}(\underset{\sim}{d}'^{o}_{t+\tau}) \\ + [k_T(\underset{\sim}{d}'^{o}_{t+\tau})]\delta\underset{\sim}{d}' - \underset{\sim}{R}\end{aligned} \tag{5.16}$$

which using equation (5.12)

$$\underset{\sim}{\Psi}(\underset{\sim}{d}'_{t+\tau}) = \underset{\sim}{\Psi}(\underset{\sim}{d}'^{o}_{t+\tau}) + [a_0M + k_T(\underset{\sim}{d}'^{o}_{t+\tau})]\delta\underset{\sim}{d}' \tag{5.17}$$

Now requiring this to be zero for the improved solution $\underset{\sim}{a}'_{t+\tau}$ we obtain

$$\left[a_0 M + k_T(\underset{\sim}{a}^0_{t+\tau})\right]\delta\underset{\sim}{a}' = -\underset{\sim}{\psi}(\underset{\sim}{a}^0_{t+\tau})$$

$$= \underset{\sim}{R} - \underset{\sim}{F}(\underset{\sim}{a}^0_{t+\tau}) - [M]\,\ddot{\underset{\sim}{a}}^0_{t+\tau} \qquad (5.18)$$

which may be solved for the required displacement correction $\delta\underset{\sim}{a}'$. In practice a modified Newton procedure is often used in which equation (5.18) is replaced by

$$\left[a_0 M + k_T(\underset{\sim}{a}_t)\right]\delta\underset{\sim}{a}' = \underset{\sim}{R} - \underset{\sim}{F}(\underset{\sim}{a}^0_{t+\tau}) - [M]\,\ddot{\underset{\sim}{a}}^0_{t+\tau} \qquad (5.19)$$

The advantage of this approach is that the matrices on the left hand side of equations (5.10) and (5.19) are now identical so enabling a single assembly and decomposition at the start of each new load step. Generalising the above procedure we have for equilibrium iteration $i = 1, 2, \cdots$

$$\left[a_0 M + k_T(\underset{\sim}{a}_t)\right]\delta\underset{\sim}{a}^i = \underset{\sim}{R} - \underset{\sim}{F}(\underset{\sim}{a}^{i-1}_{t+\tau}) - [M]\,\ddot{\underset{\sim}{a}}^{i-1}_{t+\tau} \qquad (5.20)$$

with corresponding acceleration, velocity and displacement solutions

$$\ddot{\underset{\sim}{a}}^i_{t+\tau} = a_0\,\Delta\underset{\sim}{a}^i - a_2\,\dot{\underset{\sim}{a}}_t - a_3\,\ddot{\underset{\sim}{a}}_t \qquad (5.21a)$$

$$\dot{\underset{\sim}{a}}^i_{t+\tau} = a_1\,\Delta\underset{\sim}{a}^i - a_4\,\dot{\underset{\sim}{a}}_t - a_5\,\ddot{\underset{\sim}{a}}_t \qquad (5.21b)$$

$$\underset{\sim}{a}^i_{t+\tau} = \Delta\underset{\sim}{a}^i + \underset{\sim}{a}_t \qquad (5.21c)$$

$$\Delta\underset{\sim}{a}^i = \Delta\underset{\sim}{a}^{i-1} + \delta\underset{\sim}{a}^i \qquad (5.21d)$$

These iterations are continued until

$$\varepsilon > \frac{\|\delta \underset{\sim}{\alpha}^i\|}{\|\underset{\sim}{\alpha}^i_{t+\tau}\|} \qquad (5.22)$$

where ε is a small number taken here as 10^{-10}. In practice for the pipe span problem the use of the modified procedure equation (5.20) leads to rather slow convergence unless a small time step τ is used. On the other hand the use of the full Newton procedure equation (5.18) was also found to be computationally expensive due to the large number of matrix decompositions involved. After some experimentation these difficulties were minimised by using a compromise strategy in which the tangent matrix is updated at the start of every time step plus every N^{th} equilibrium iteration where typically $2 \leq N \leq 4$

5.2.1 Wilson-θ Algorithm

The linear acceleration method outlined above is only conditionally stable requiring the use of an excessively small time step (Clough, 1975). This difficulty is overcome in the Wilson-θ method by setting

$$\tau = \theta \Delta t \quad , \quad \theta > 1.37 \qquad (5.23)$$

where Δt is the time increment by which we seek to advance the solution. By this means the linear acceleration method is first applied to the computationally extended time step $\tau = \theta \Delta t$ after which the solution at time $t + \Delta t$ is obtained by interpolation, figure 5.2. Thus substituting $s = \Delta t$ into equations (5.6) and (5.7) we find

$$\ddot{\underset{\sim}{\alpha}}_{t+\Delta t} = \ddot{\underset{\sim}{\alpha}}_t + \frac{\Delta t}{\tau}\left(\ddot{\underset{\sim}{\alpha}}^{i}_{t+\tau} - \ddot{\underset{\sim}{\alpha}}_t\right) \tag{5.24a}$$

$$\dot{\underset{\sim}{\alpha}}_{t+\Delta t} = \dot{\underset{\sim}{\alpha}}_t + \Delta t\,\ddot{\underset{\sim}{\alpha}}_t + \frac{\Delta t^2}{2\tau}\left(\ddot{\underset{\sim}{\alpha}}^{i}_{t+\tau} - \ddot{\underset{\sim}{\alpha}}_t\right) \tag{5.24b}$$

$$\underset{\sim}{\alpha}_{t+\Delta t} = \underset{\sim}{\alpha}_t + \Delta t\,\dot{\underset{\sim}{\alpha}}_t + \frac{\Delta t^2}{2}\ddot{\underset{\sim}{\alpha}}_t + \frac{\Delta t^3}{6\tau}\left(\ddot{\underset{\sim}{\alpha}}^{i}_{t+\tau} - \ddot{\underset{\sim}{\alpha}}_t\right) \tag{5.24c}$$

which using equation (5.21a) may be rewritten in the compact form

$$\ddot{\underset{\sim}{\alpha}}_{t+\Delta t} = a_6 \Delta\underset{\sim}{\alpha}^{i} + a_7 \dot{\underset{\sim}{\alpha}}_t + a_8 \ddot{\underset{\sim}{\alpha}}_t \tag{5.25a}$$

$$\dot{\underset{\sim}{\alpha}}_{t+\Delta t} = \dot{\underset{\sim}{\alpha}}_t + \frac{\Delta t}{2}\left(\ddot{\underset{\sim}{\alpha}}_{t+\Delta t} + \ddot{\underset{\sim}{\alpha}}_t\right) \tag{5.25b}$$

$$\underset{\sim}{\alpha}_{t+\Delta t} = \underset{\sim}{\alpha}_t + \Delta t\,\dot{\underset{\sim}{\alpha}}_t + \frac{\Delta t^2}{6}\left(\ddot{\underset{\sim}{\alpha}}_{t+\Delta t} + 2\ddot{\underset{\sim}{\alpha}}_t\right) \tag{5.25c}$$

with constants a_6 to a_8 given by

$$a_6 = \frac{6}{\tau^3} \qquad a_7 = -\frac{6\Delta t}{\tau^2} \qquad a_8 = 1 - \frac{3\Delta t}{\tau}$$

It is ironic to note that although the converged solution at time $t+\theta\Delta t$ satisfies equilibrium this is in general not guaranteed for the interpolated solution at time $t+\Delta t$ as given by equations (5.25) above.

5.2.2 Friction Elements

In order to calculate the element force and tangent stiffness in a typical friction element it is necessary to first determine the appropriate element loading phase. For the incremental static analysis this was done by comparing the sign of the current element displacement increment to that used in the previous load step. On the other hand for a dynamic analysis this may now be done directly by incrementing the element loading phase whenever the element velocity passes through zero. Thus considering the element load deflection diagram, figure 5.3a, it is clear that the zero velocity point B marks the transition from element loading phase i to $i+1$. In passing through this transition point the discontinuity in the element tangent stiffness raises questions concerning the validity of the linear acceleration assumption used in the above outlined integration scheme. This difficulty is circumvented in this thesis by adopting the following strategy:

a) During any time step the element loading phase is held constant. This avoids any convergence problems as encountered in the static analysis and allows the element to initially unload along the same path as that used for the current loading phase i , figure 5.3b.

b) At the end of each time step a check is performed to determine if the element velocity has a zero during the time interval $(t, t+\Delta t)$. If so the computed solution is interpolated back to this point so that the element velocity at the start of the following time step is identically zero. For this following time step the element loading phase is taken as $i+1$. , figure 5.3b.

By this means the acceleration either side of point B is assumed linear with the physical discontinuity in the element behaviour forced to coincide with a natural discontinuity in the computed solution[1]. To perform the check described in (b) above consider equation (5.7a) for the assumed velocity variation

$$\underset{\sim}{\dot{a}}(s) = \underset{\sim}{\dot{a}}_t + s\,\underset{\sim}{\ddot{a}}_t + \frac{s^2}{2\tau}\left(\underset{\sim}{\ddot{a}}_{t+\tau} - \underset{\sim}{\ddot{a}}_t\right) \tag{5.26}$$

Partitioning out the appropriate equation for a typical friction element we may write

$$\dot{a}^{\rho}(s) = \dot{a}^{\rho}_t + s\,\ddot{a}^{\rho}_t + \frac{s^2}{2\tau}\left(\ddot{a}^{\rho}_{t+\tau} - \ddot{a}^{\rho}_t\right) \tag{5.27}$$

where here the superscript ρ indicates an inplane or axial freedom. Requiring this to be zero gives

$$\alpha s^2 + \beta s + \gamma = 0 \tag{5.28a}$$

$$\alpha = \frac{\ddot{a}^{\rho}_{t+\tau} - \ddot{a}^{\rho}_t}{2\tau} \tag{5.28b}$$

$$\beta = \ddot{a}^{\rho}_t \tag{5.28c}$$

$$\gamma = \dot{a}^{\rho}_t \tag{5.28d}$$

---

(1) The acceleration solution $\underset{\sim}{\ddot{a}}$ computed using the Wilson-θ method is C_0 continuous (with respect to time) since no attempt is made to match $\underset{\sim}{\dddot{a}}$ across adjacent time steps.

which solving for S gives

$$S_{1,2} = \frac{-\beta \pm (\beta^2 - 4\alpha\gamma)^{1/2}}{2\alpha} \tag{5.29}$$

Now if either (or both) of these roots are such that $0 < S_i \leq \Delta t$ the element velocity has passed through zero and a new element loading phase entered. Thus defining $S = \bar{\Delta t}$ as the minimum of any such roots and proceeding as section 5.2.1 we find

$$\ddot{\underset{\sim}{\alpha}}_{t+\bar{\Delta t}} = \bar{a}_6 \Delta\underset{\sim}{\alpha}^i + \bar{a}_7 \dot{\underset{\sim}{\alpha}}_t + \bar{a}_8 \ddot{\underset{\sim}{\alpha}}_t \tag{5.30a}$$

$$\dot{\underset{\sim}{\alpha}}_{t+\bar{\Delta t}} = \dot{\underset{\sim}{\alpha}}_t + \frac{\bar{\Delta t}}{2}(\ddot{\underset{\sim}{\alpha}}_{t+\bar{\Delta t}} + \ddot{\underset{\sim}{\alpha}}_t) \tag{5.30b}$$

$$\underset{\sim}{\alpha}_{t+\bar{\Delta t}} = \underset{\sim}{\alpha}_t + \bar{\Delta t}\dot{\underset{\sim}{\alpha}}_t + \frac{\bar{\Delta t}^2}{6}(\ddot{\underset{\sim}{\alpha}}_{t+\bar{\Delta t}} + 2\ddot{\underset{\sim}{\alpha}}_t) \tag{5.30c}$$

where the constants $\bar{a}_6$ to $\bar{a}_8$ are given by

$$\bar{a}_6 = \frac{6\bar{\Delta t}}{\tau^3} \qquad \bar{a}_7 = -\frac{6\bar{\Delta t}}{\tau^2} \qquad \bar{a}_8 = 1 - \frac{3\bar{\Delta t}}{\tau}$$

By this means the friction element velocity $\dot{a}^{\rho}_{t+\bar{\Delta t}}$ is identically zero as required. The corresponding element variables may now be initiated using

$$a_i^{\rho} = a^{\rho}_{t+\bar{\Delta t}} \tag{5.31a}$$

$$f_i^{\rho} = f^{\rho}_{t+\bar{\Delta t}} \tag{5.31b}$$

where i represents the element loading phase used during the current time step and $i+1$ is the phase to be used in the following step, figure 5.3b. This equation now completes the calculation for the current time step and the whole process may now be repeated until the required time interval has been integrated. A flow chart summarising this method is presented in figures 5.4 and 5.5.

5.3 Initial Conditions

The free vibration equation (5.2) may be used to integrate the response of the pipeline span by first displacing the pipeline from its initial static equilibrium position $\underset{\sim}{d}_S$. This is done here by performing a further static load step in which an additional load is applied to the pipeline. This process leads to a disturbed configuration $\underset{\sim}{d}_D$ such that

$$\underset{\sim}{F}(\underset{\sim}{d}_D) = \underset{\sim}{R} + \underset{\sim}{S} \tag{5.32}$$

where $\underset{\sim}{R}$ is the static load due to pipe weight plus specified seabed profile and $\underset{\sim}{S}$ is the additional disturbing load. The removal of this additional load now causes the pipeline to oscillate under the governing equation of motion (5.8) with initial conditions at time zero given by

$$\underset{\sim}{d}_0 = \underset{\sim}{d}_D \tag{5.33a}$$

$$\dot{\underset{\sim}{d}}_0 = 0 \tag{5.33b}$$

$$\ddot{\underset{\sim}{d}}_0 = [M]^{-1}(\underset{\sim}{R} - \underset{\sim}{F}(\underset{\sim}{d})) \tag{5.33c}$$

Now recalling the eigenvalue problem equation (3.76) the disturbing load $\underset{\sim}{S}$ is taken here as

$$\underset{\sim}{S} = q\, K_T^c(\underset{\sim}{\alpha}_s)\, \underset{\sim}{\phi}_i^c \qquad (5.34)$$

where constant q determines the intensity of load, $K_T^c(\underset{\sim}{\alpha}_s)$ is the constrained tangent stiffness corresponding to the initial equilibrium configuration $\underset{\sim}{\alpha}_s$, and $\underset{\sim}{\phi}_i^c$ the i^{th} mode shape normalised so that the largest translational component is unity. It follows that for sufficiently small q the resulting motion obtained by integration in the time domain will occur at frequency ω_i corresponding to the mode shape $\underset{\sim}{\phi}_i^c$ and have maximum amplitude q. For larger q the various nonlinearities included in the model will result in more general response.

5.4 Finite Element Time Domain Model

The FEM used for the time domain simulations, figure 5.6, comprises 32 beam elements plus 2 friction elements modelling pipe 2 on a flat elastic foundation. Two span lengths of 25m and 50m are considered for which the resulting response is obtained using time steps of 0.01sec and 0.05sec respectively. With these step lengths the convergence criteria (5.22) is typically satisfied after 3-4 equilibrium iterations although this increases to 9-10 iterations on each time step immediately following a friction element load phase increment. The corresponding CPU time for a typical 300 step simulation is 4 minutes using a VAX 782 enabling runs to be conveniently performed in either batch or time sharing modes.

Output is presented in the form of time history plots showing end axial displacement and velocity u_8 and $\dot{u}_8$ together with lateral deflections $v_{1/4}$ and $v_{1/2}$ at

quarter span and centre span respectively, figure 5.6. Stress output is presented for extreme fibre stresses at the top of the steel pipe calculated as

$$\sigma_T = T/A, \qquad \sigma_B = -EIv'', \qquad \sigma_c = \sigma_T + \sigma_B \tag{5.35}$$

where T is the effective tension. These stresses are evaluated at the left hand span support point B, figure 5.6.

5.5 Results and Discussion

Considering first a 25m span with initial disturbances characterised by q = 0.01, 0.1 and 0.5 the resulting time histories are shown in figures 5.7 to 5.9 and summarised in table 5.1.

SPAN (m)	$v_{1/2}$ STATIC (m)	f_1 (Hz) CONST.END STIF (3)	f_1 (Hz) ENDS CONSTRAINED (3)	q	f_1 (Hz) TIME DOMAIN (1)	$v_{1/2}$ DYNAMIC (m) (2)	σ_c (N/mm^2) PEAK TO PEAK (2)
25	.069	1.22	1.23	.01	1.23	.01	12
				.1	1.23	.1	120
				.5	1.24	.47	540
50	.661	.454	.692	.01	.648	.01	10
				.1	.522	.2	240
				.5	.440	1.3	750

Table 5.1 Pipe 2 fundamental mode ϕ_1^c with μ = 1.0

Considering these results it is observed that:

---

(1) Based on first two cycles

(2) Based on first half cycle

(3) Frequencies obtained using eigenvalue analysis of chapter 3.

a) As a result of friction element behaviour the end axial velocity $\dot{u}_B$ increases slowly after each zero so that the resulting response curve appears to repeat the initial conditions, figures 5.7a, 5.8a and 5.9a.

b) Following each zero in $\dot{u}_B$ the computed tension solution judders slightly, figure 5.7b. This (numerical) effect may be reduced by decreasing the time step: compare figure 5.7b with Δt = 0.01sec and figure 5.7c with Δt = 0.05sec.

c) For small amplitude vibration q = 0.01 the pipe span centre deflection $v_{1/2}$ is negative at all times so that u_B and $v_{1/2}$ oscillate at the same frequency, figure 5.7a. For increased amplitudes q = 0.1 and q = 0.5 the dynamic displacement exceeds the static sag with the result that u_B oscillates at twice the frequency of $v_{1/2}$, figures 5.8a and 5.9a.

d) The influence of amplitude on frequency is small, table 5.1.

e) The contribution of variable tension to the total dynamic stress at the end support point B is small, figures 5.7b, 5.8b and 5.9b.

f) The combined dynamic stress σ_c increases more or less linearily with amplitude, table 5.1.

For the 50m span the corresponding results are presented in figures 5.10 to 5.12 and again summarised in table 5.1. These results show similar characteristics to the 25m case except that:

a) A considreable shift in frequency is noted with increased amplitude. This frequency starts at the constrained eigenvalue figure for small amplitude and decreases to a value approximately equal to the constant end stiffness figure at increased amplitude, table 5.1.

b) The increase in dynamic stress with amplitude is no

longer linear.

c) The increased movement seen by the pipe end enables the pipe/soil friction forces to damp the response, figures 5.10a, 5.11a and 5.12a. Considering the amplitude decay occuring at the span centre for the case q = 0.1, figure 5.11a, the percentage of critical damping is estimated as 3-4%.

5.6 Conclusions from Elastic Foundation Models

In this section the main results and conclusions obtained using the elastic foundation models developed in Chapters 2 to 5 are summarised as follows:

a) Using linear (i.e. zero friction) buckling analysis the ND buckling load $\delta_{P_{CR}} = P_{CR} L^2/EI$ for a single span may be determined in terms of the ND soil stiffness $\gamma = kL^4/EI$, figure 2.7. For $\gamma > 10^7$ this load is within 10% of that for an equivalent built in beam.

b) Using linear frequency analysis the ND frequency ratios $\rho_i = \omega_i/\bar{\omega}$ may be determined in terms of γ plus ND tension/compression parameter $\delta = TL^2/EI$, figures 2.8 to 2.15. For $\gamma > 10^7$ frequencies are insensitive to γ being within 10% of those for an equivalent built in beam under equal tension. For small γ frequencies fall off rapidly to zero.

c) The damping length L_D for bending action either side of a free span is approximated by

$$L_D = 2\pi L/(2\gamma^{1/2})^{1/2}$$

where L is the span length. For most situations this length will be on the order of a few tens of metres and will lead to bending coupling between spans separated by less than this amount.

d) Pipe/soil friction forces combined with coupled axial/bending displacements in the pipeline generally cause local tension forces to develop so enabling long spans to form. An exception to this situation occurs in an initially arched pipeline prior to snap through where local compressive forces are initially generated.

e) The development of local tension forces enables tension coupling to occur between spans separated by several hundreds of metres.

f) For long span developing on a flat seated centre deflection appears insensitive to pipe size being on the order of 3m for a 100m span with μ = 1.0.

g) Static stress levels are considerably influenced by initial seabed geometry. In particular large bending stresses may develop where the forming span encounters upward sloping pipeline.

h) As a result of friction forces the pipe axial displacements at the span ends are effectively constrained for small amplitude oscillations. For an initially flat seabed this results in the symmetric modes experiencing a frequency shift where frequency may increase with span length. Antisymmetric modes are unaffected in this way.

i) For short span lengths the influence of amplitude on frequency is small. For longer spans frequencies start at the constrained eigenvalue figure for small amplitude and decrease to a value approximately equal to the constant end stiffness eigenvalue figure for increased amplitude.

j) The influence of initial seabed geometry on frequency is considerable.

k) As span lengths increase the initial wide spacing of mode frequencies is greatly reduced leading to the possibility of complicated mixed mode response.

l) The contribution of variable tension to dynamic stress

levels is small.

m) Friction damping on the order of 3-4% of critical was noted for a 50m span using pipe 2 (D_o = 500mm) and μ = 1.0.

5.7 Further Work

The elastic foundation models developed above have provided useful initial information concerning the development and behaviour of pipeline spans on an assumed elastic foundation. However by necessity these models are based on a number of simplifying assumptions and used to investigate a limited set of pipeline conditions. As a result the following relevant areas are included for further investigation:

a) In full scale experimental tests (Bruschi, 1982) significant 3D response is observed involving motion both inline and transverse to the incident current direction. These effects may be included in the finite element model by extending the 2D pipeline element developed in Chapter 3 into an equivalent 3D version in which the axial shortening due to bowing action arises from the transverse bending action in two orthogonal planes.

b) Further 3D effects may arise with an initially arched pipeline. In this case inline forces may cause the pipe to fall over rather than snap through leading to coupling between bending and torsion in the pipeline. In this situation torsion effects in the span will be resisted by circumferential friction forces on the supported sections leading to torsional friction elements analogous to the friction elements developed in Chapter 3 for axial effects.

c) In view of the large static and dynamic stresses occuring in the pipeline the inclusion of elasto-

plastic behaviour is indicated. Such effects have previously been included in the analysis of a non-linear pipeline unilaterally supported by a rigid uneven profile, (Maier et al, 1979).

d) Development of suitable theoretical/empirical hydrodynamic load model enabling forced response to be considered. Such models could be based on either existing wake oscillator models (Skop and Griffin, 1973) or correlation models (Blevins and Burton, 1976) and would ideally be accompanied by parallel experimental studies in which proper account is provided for pipe span end conditions and seabed proximity.

e) Development of improved fatigue life estimates. To date such estimates have assumed simply supported end conditions for the free span, (Tsahalis, 1983).

f) Many pipe spans are rectified by the use of weight mattresses. The finite element static analysis developed above could be developed to investigate the optimum weight and distribution of such devices and to estimate resulting pipeline stresses.

g) Investigation of effects of nonlinear soil properties on span behaviour.

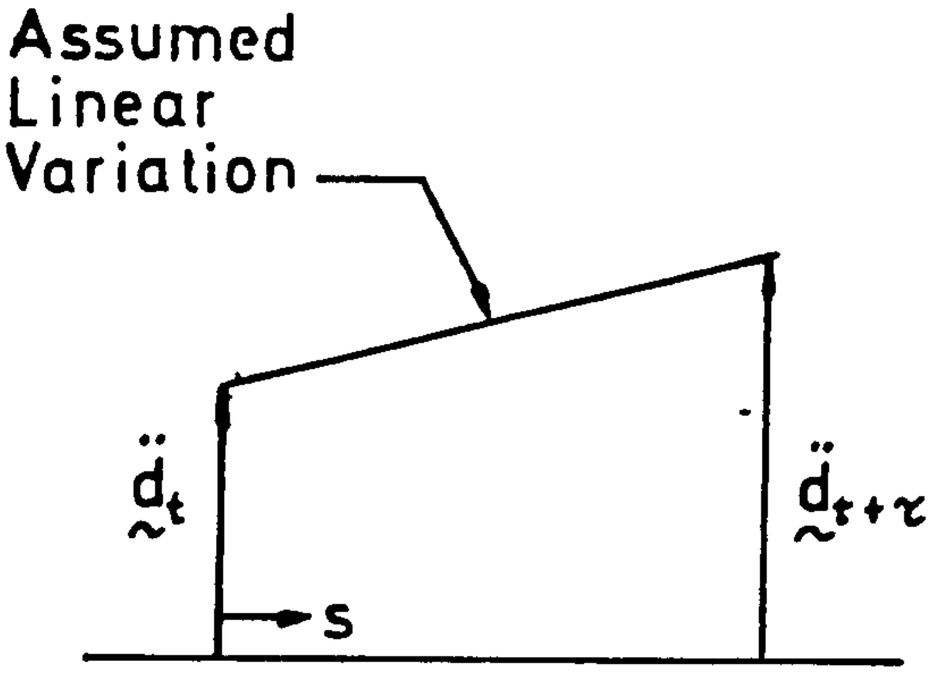

$$\ddot{\underset{\sim}{d}}(s) = \ddot{\underset{\sim}{d}}_t + \frac{s}{\tau}(\ddot{d}_{t+\tau} - \ddot{d}_t)$$

FIG 5.1 Linear Acceleration Over small time Step τ

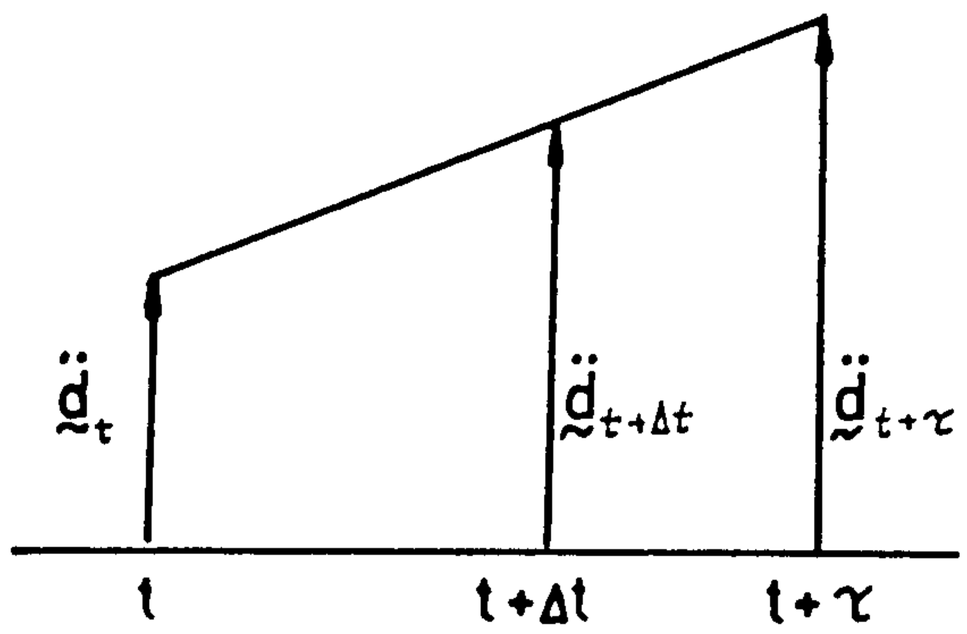

$$\underset{\sim}{d}_{t+\Delta t} = \underset{\sim}{d}_t + \frac{\Delta t}{\tau}(\underset{\sim}{d}_{t+\tau} - \underset{\sim}{d}_t)$$

FIG 5.2 Wilson - θ Method

a) Physical Process

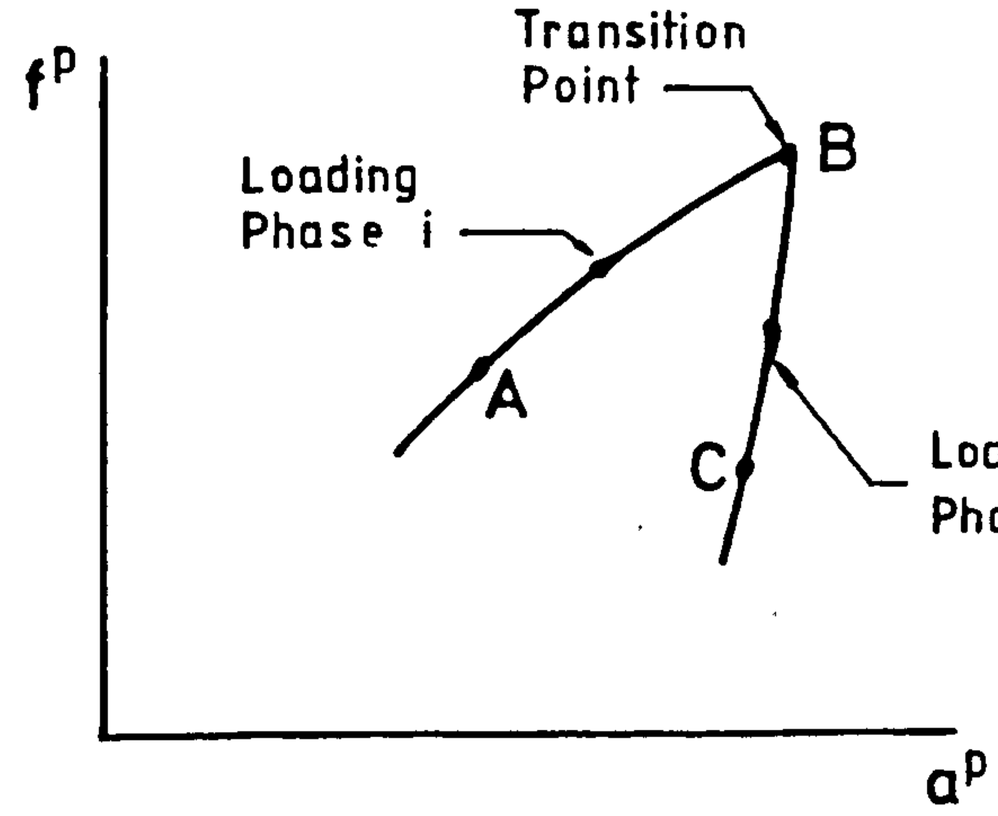

POINT	TIME	$\dot{a}^p$
A	t	>0
B	$t+\bar{\Delta t}$	0
C	$t+\Delta t$	<0

b) Numerical Simulation

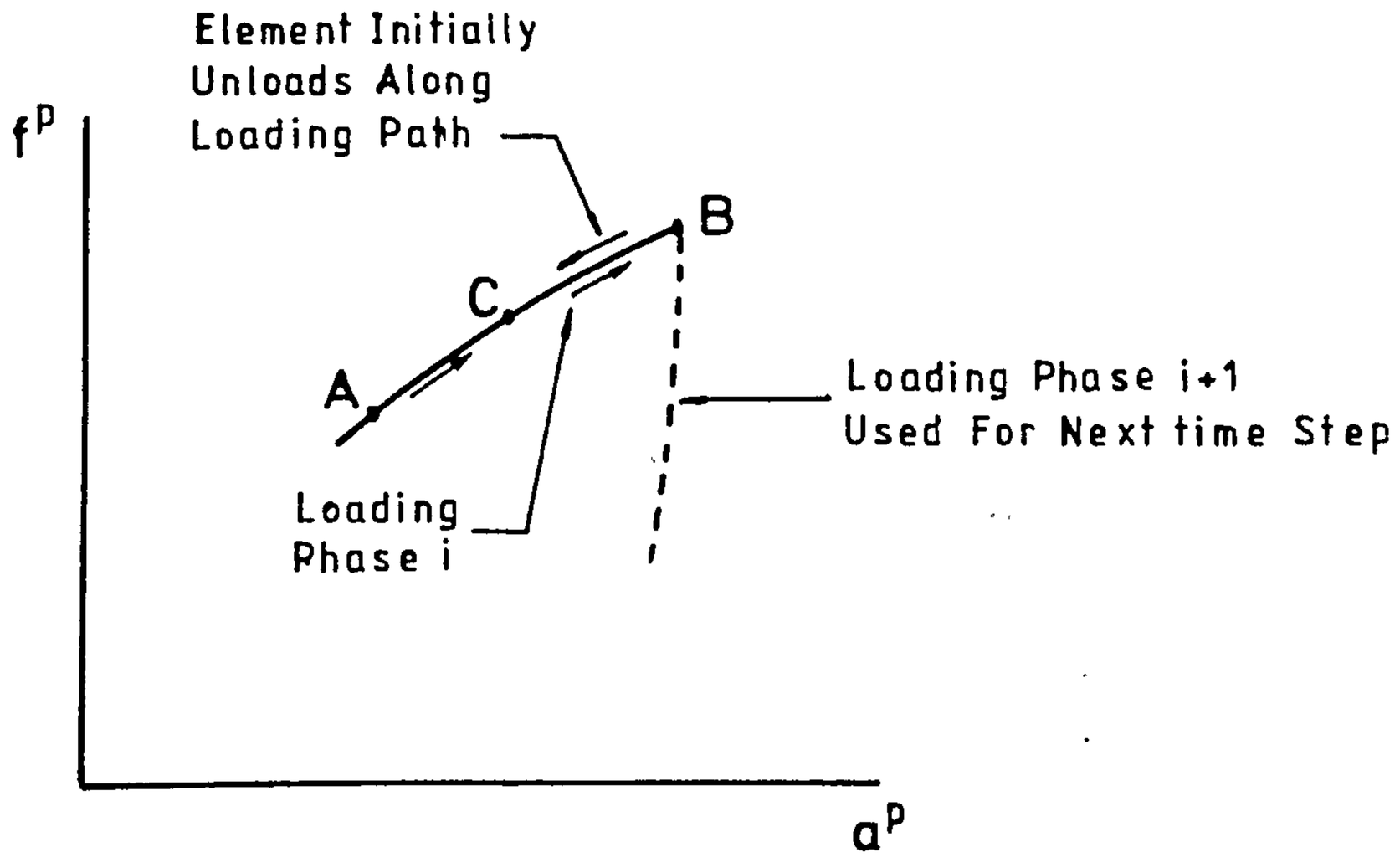

FIG 5.3 Friction Element Loading Phases During Time Step Integration

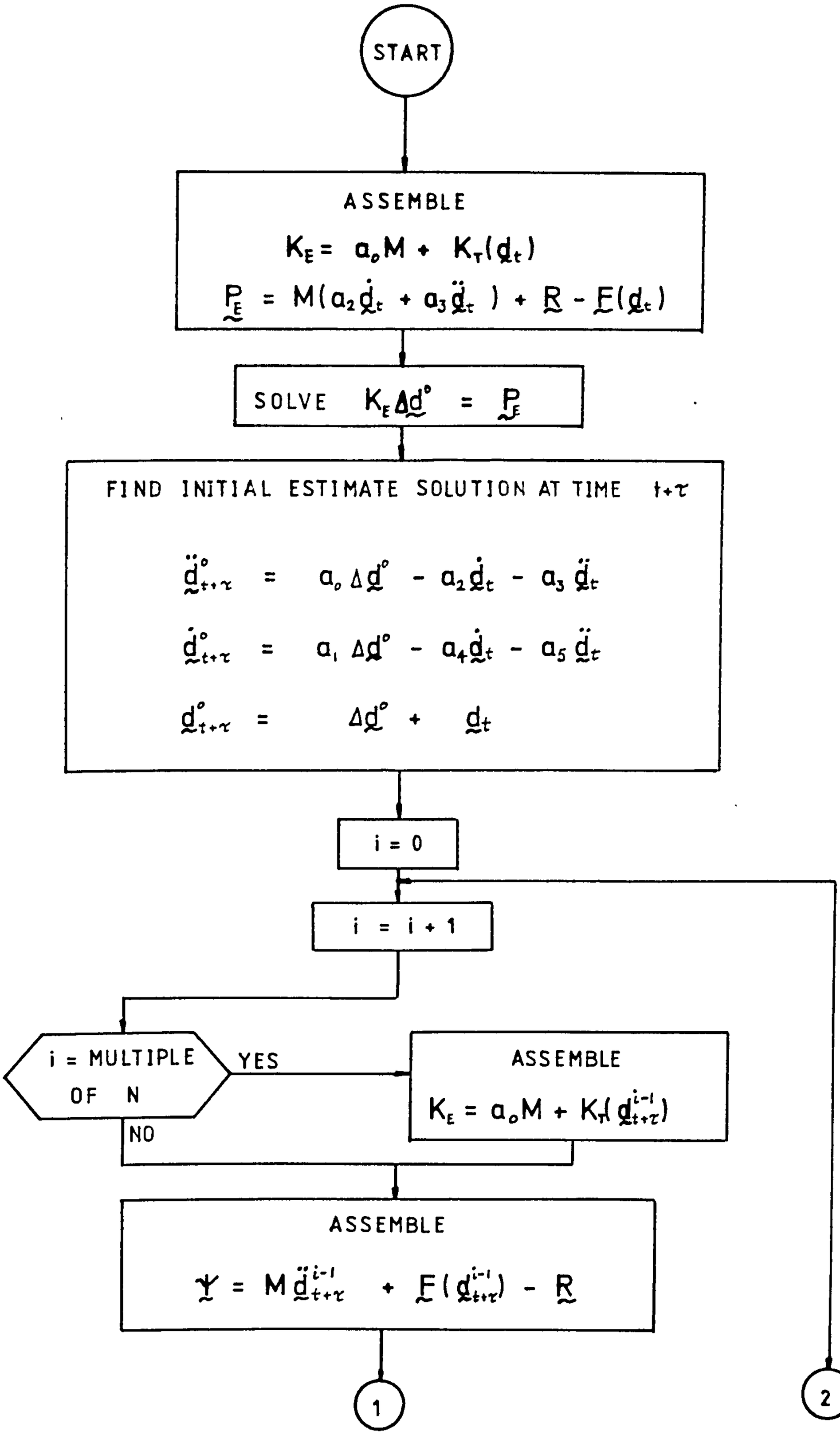
START
ASSEMBLE
$K_E = a_o M + K_T(q_t)$
$\underset{\sim}{P_E} = M(a_2 \dot{q}_t + a_3 \ddot{q}_t) + \underset{\sim}{R} - \underset{\sim}{F}(q_t)$
SOLVE $K_E \Delta q^o = P_E$
FIND INITIAL ESTIMATE SOLUTION AT TIME $t+\tau$
$\ddot{q}^o_{t+\tau} = a_o \Delta q^o - a_2 \dot{q}_t - a_3 \ddot{q}_t$
$\dot{q}^o_{t+\tau} = a_1 \Delta q^o - a_4 \dot{q}_t - a_5 \ddot{q}_t$
$q^o_{t+\tau} = \Delta q^o + q_t$
i = 0
i = i + 1
i = MULTIPLE OF N
YES
NO
ASSEMBLE
$K_E = a_o M + K_T(q^{i-1}_{t+\tau})$
ASSEMBLE
$\Psi = M \ddot{q}^{i-1}_{t+\tau} + F(q^{i-1}_{t+\tau}) - R$
1
2

/....

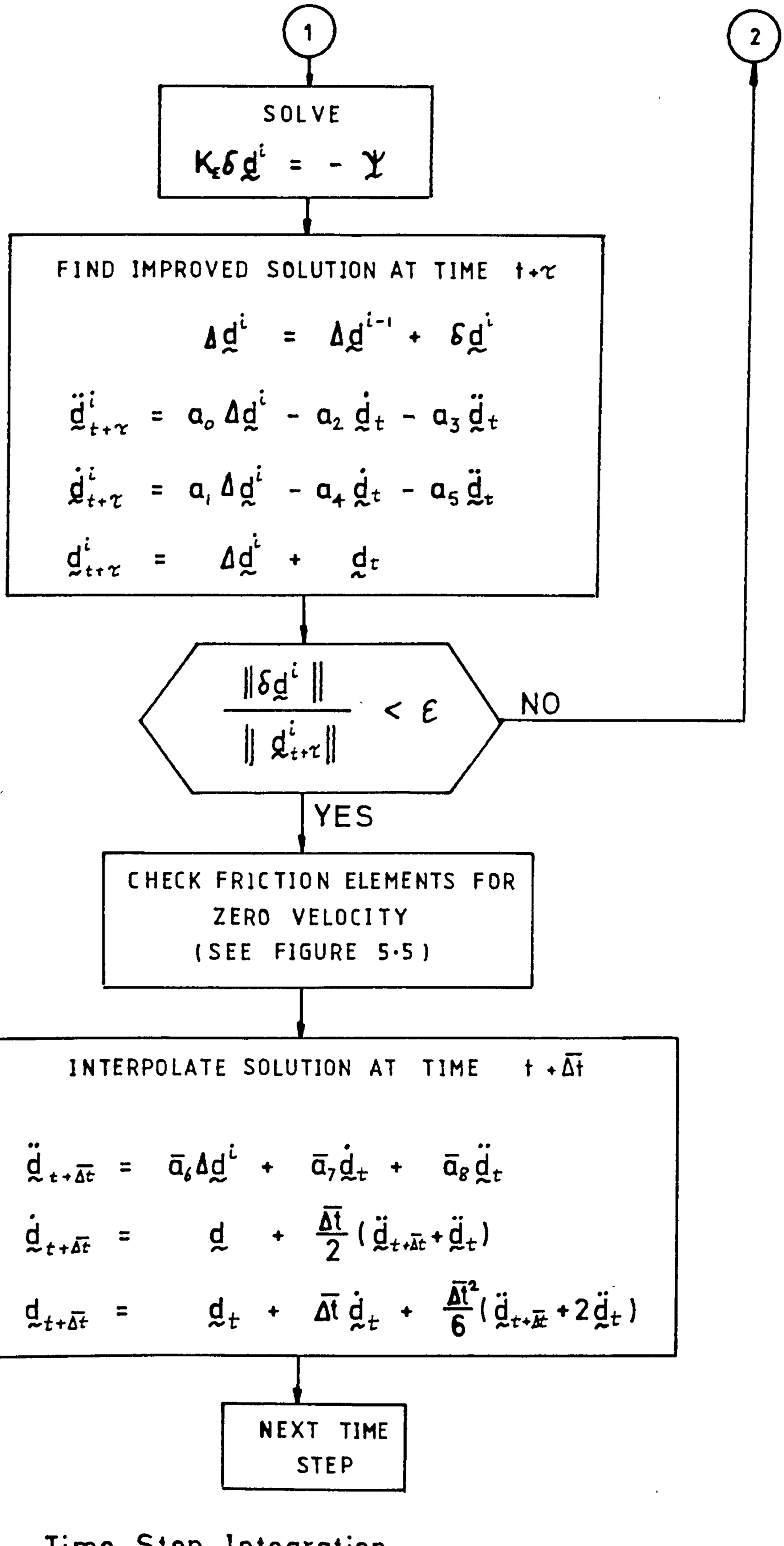

FIG 5.4 Time Step Integration

START

PARTITION OUT ELEMENT DISPLACEMENT $a^{\rho}_{t+\tau}$, VELOCITY $\dot{a}^{\rho}_{t+\tau}$ AND ACCELERATION $\ddot{a}^{\rho}_{t+\tau}$ FROM $\underset{\sim}{d}^{i}_{t+\tau}$, $\dot{\underset{\sim}{d}}^{i}_{t+\tau}$ AND $\ddot{\underset{\sim}{d}}^{i}_{t+\tau}$ RESPECTIVELY

FIND TIMES WHEN $\dot{a}^{\rho} = 0$

$$s_{1,2} = \frac{-\beta \pm (\beta^2 - 4\alpha\gamma)^{1/2}}{2\alpha}$$

$$\alpha = \frac{\ddot{\underset{\sim}{a}}^{\rho}_{t+\tau} - \ddot{\underset{\sim}{a}}^{\rho}_{t}}{2\tau}$$

$$\beta = \ddot{\underset{\sim}{a}}^{\rho}_{t} \qquad \gamma = \dot{\underset{\sim}{a}}^{\rho}_{t}$$

TWO ROOTS SUCH THAT $0 < s_i \leqslant \Delta t$ — YES → $\overline{\Delta t} = \text{Min}(s_1, s_2)$

NO

ONE ROOT SUCH THAT $0 < s_i \leqslant \Delta t$ — YES → $\overline{\Delta t} = s_i$

NO

$\overline{\Delta t} = \Delta t$

UPDATE ELEMENT VARIABLES

$$a^{\rho}_{i} = a^{\rho}_{t+\overline{\Delta t}}$$

$$f^{\rho}_{i} = f^{\rho}_{t+\overline{\Delta t}}$$

$$i = i + 1$$

STOP

FIG 5.5 Friction Element Check

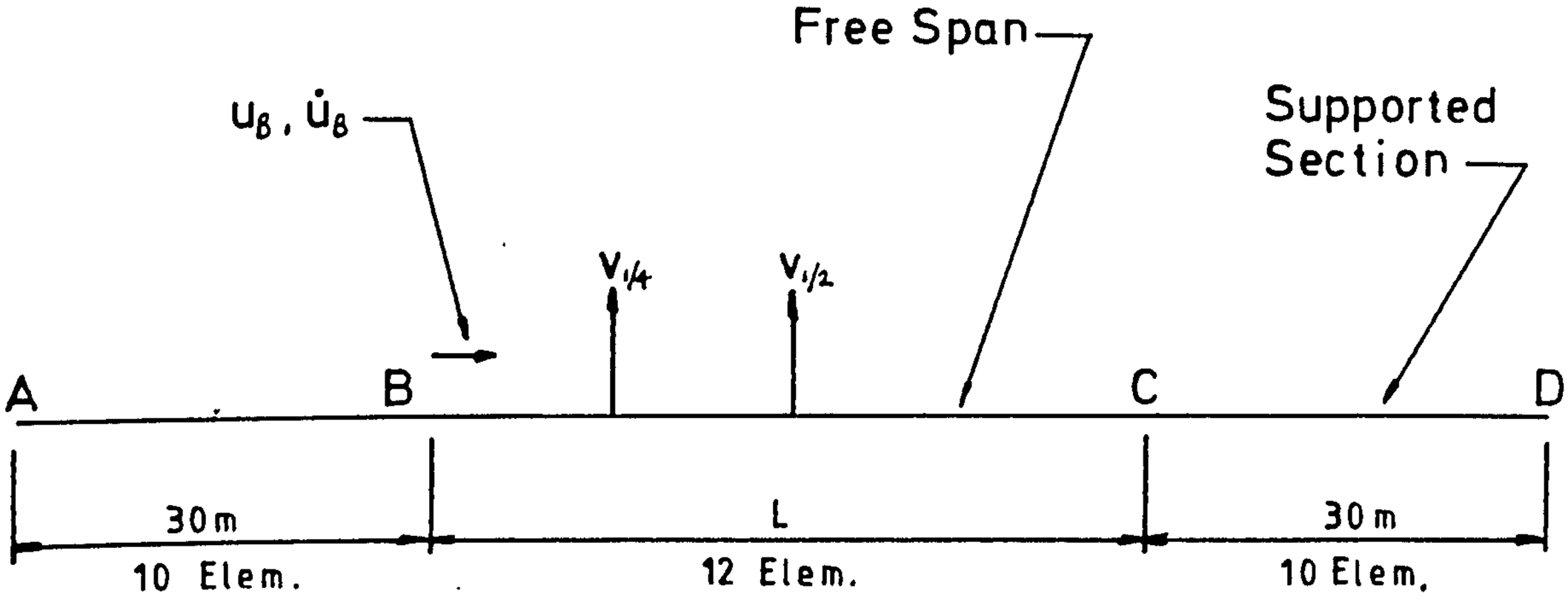

FIG 5.6 FEM For Time Domain Simulations

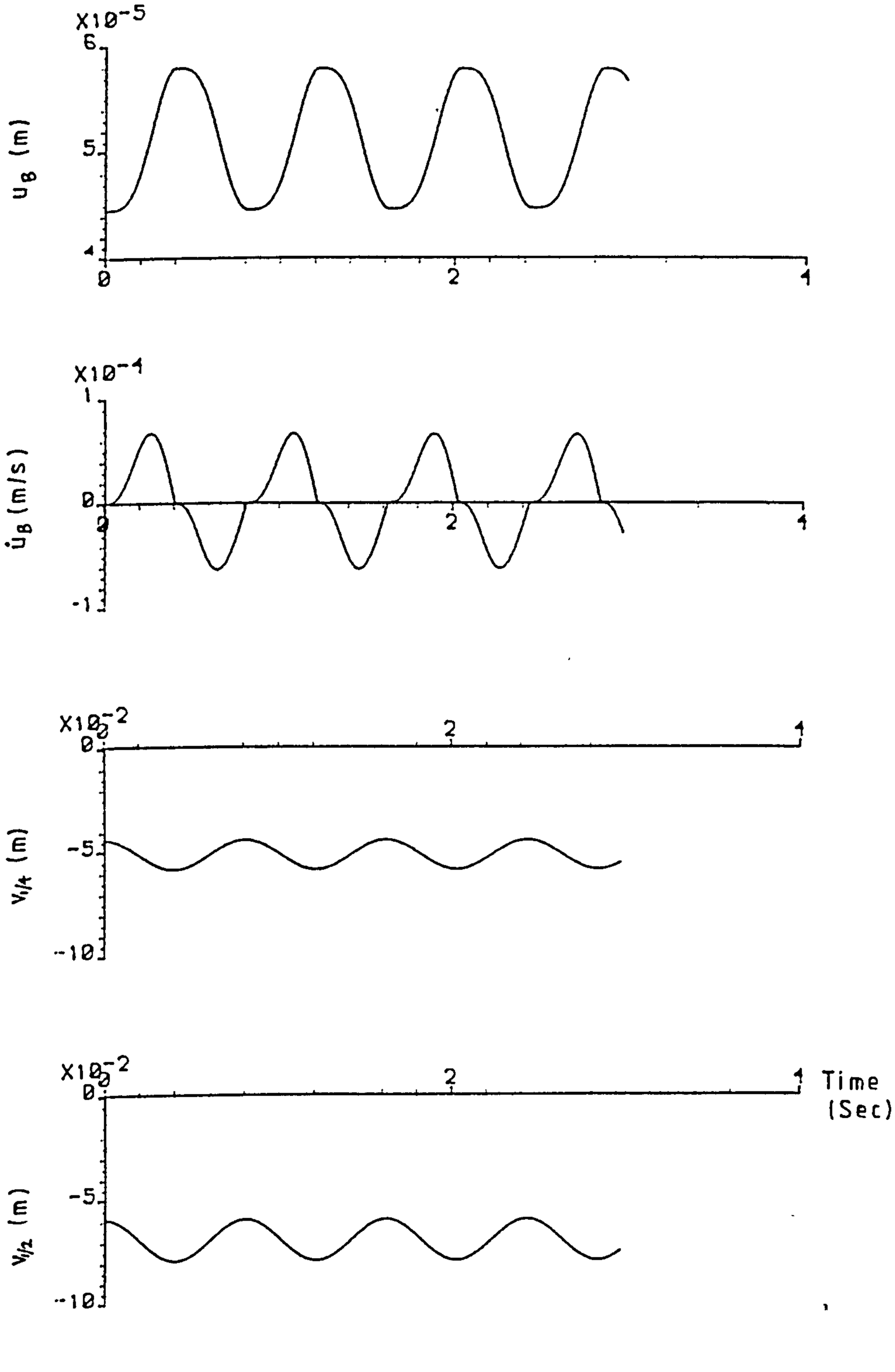

FIG 5.7a Pipe 2 Response , L=25m , q=0.01

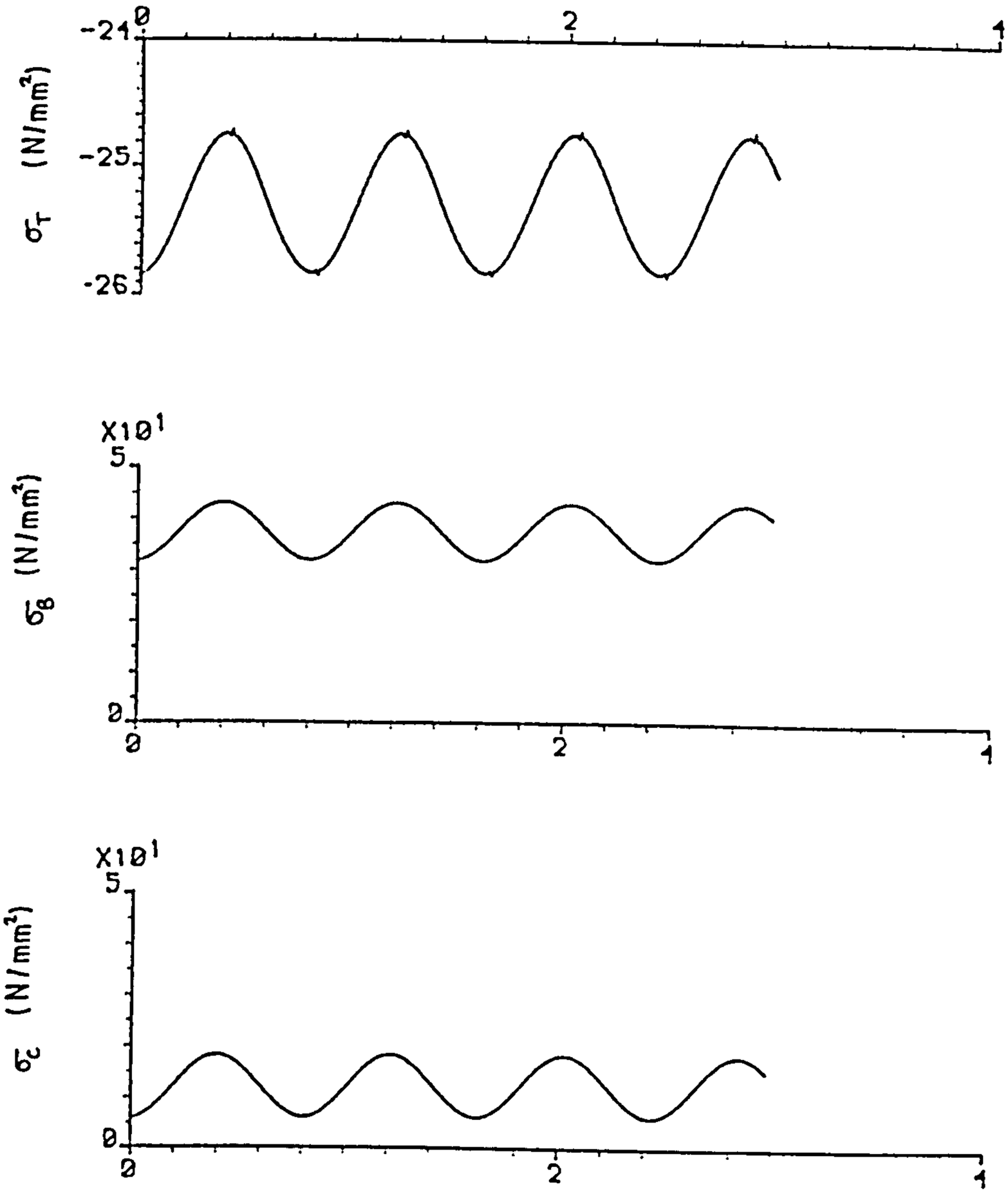

[$\Delta t = 0.01$ sec]

FIG 5.7b Pipe 2 Stress Time Histories , L=25 m, q = 0.01

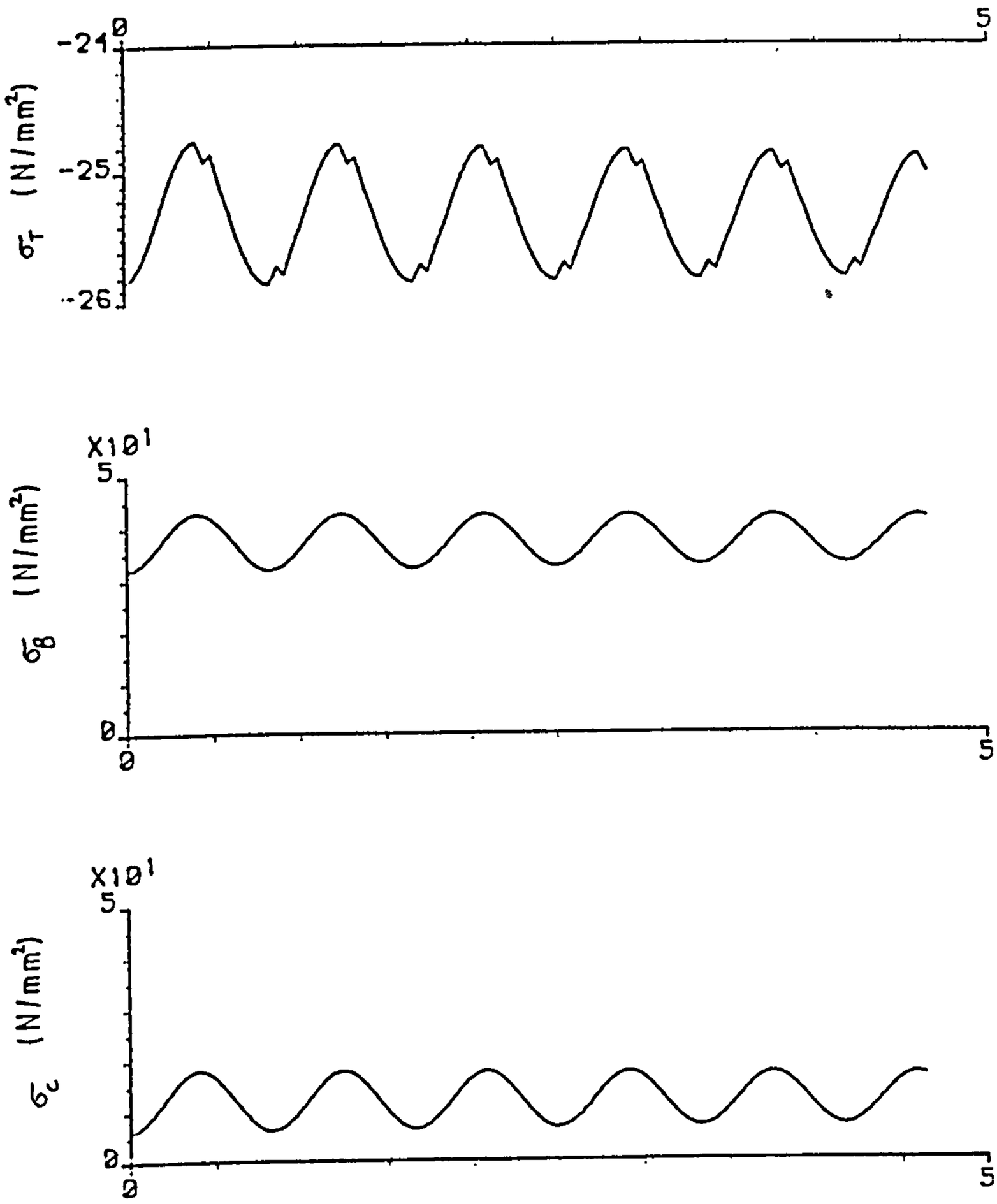

FIG 5.7c Pipe 2 Stress Time Histories , L = 25m,
q = 0.01 , Δt = 0.05 sec

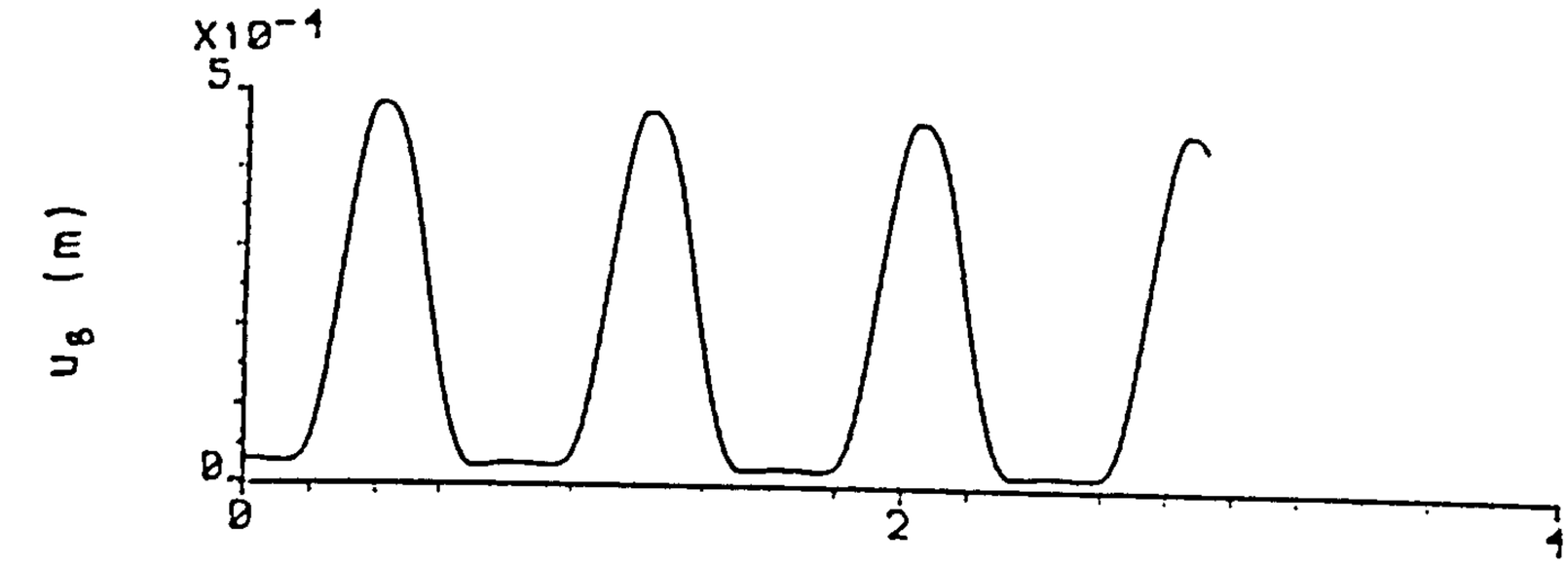

FIG 5.8a Pipe 2 Response , L= 25m , q= 0.1

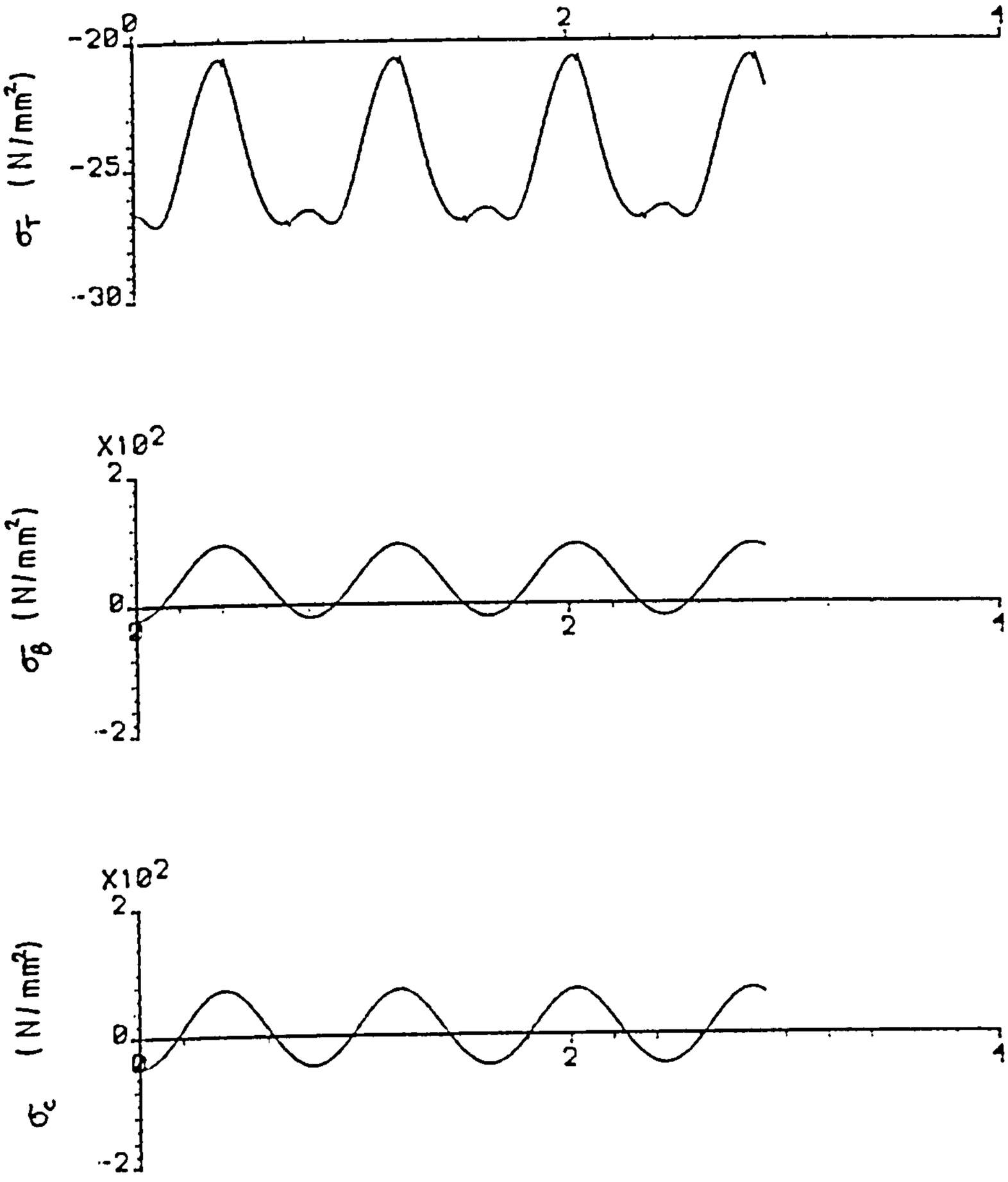

FIG 5.8b Pipe 2 Stress Time Histories , L = 25m ,
q = 0.1

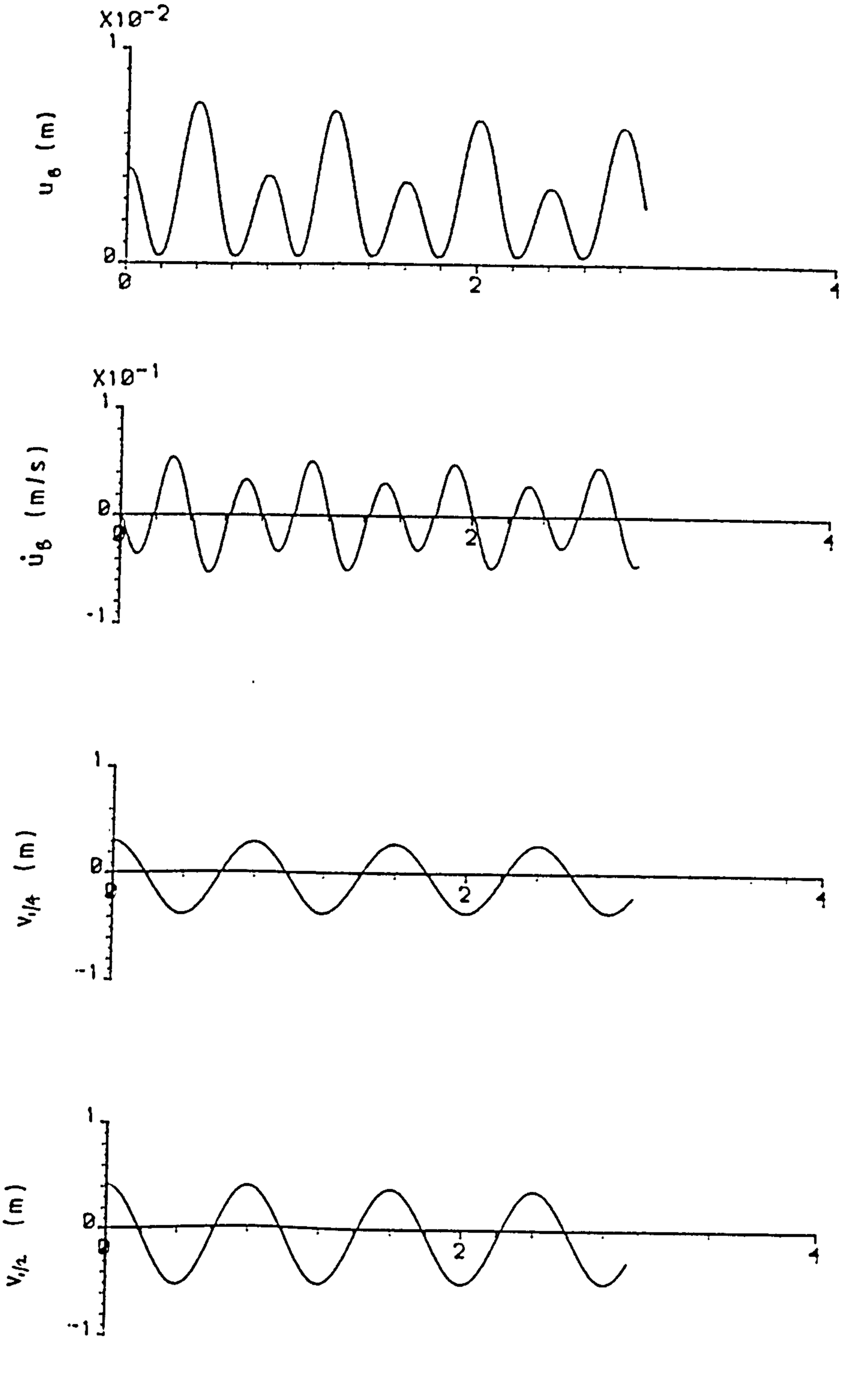

FIG 5.9a Pipe 2 Response , L=25m , q=0.5

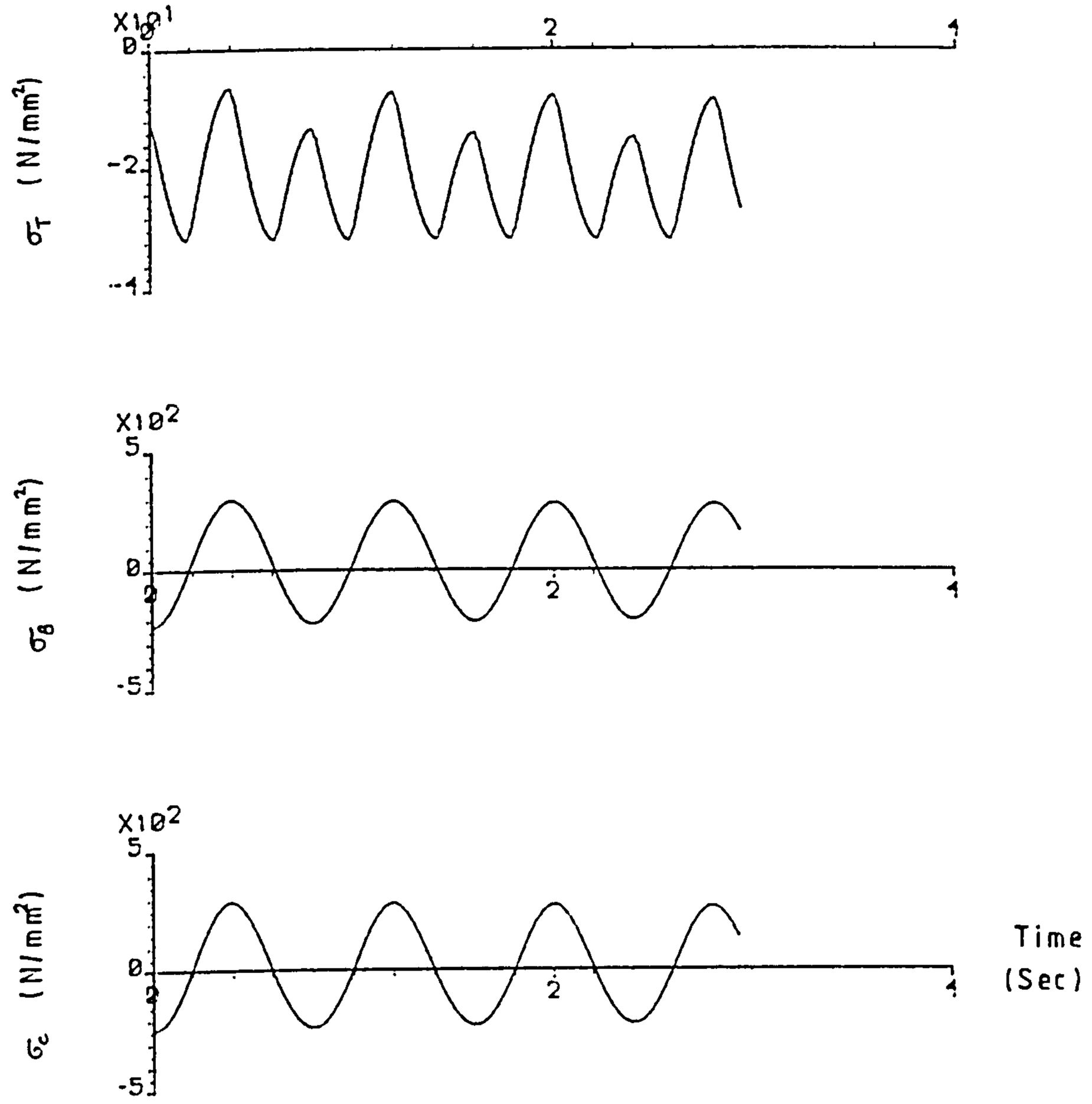

FIG 5.9b Pipe 2 Stress Time Histories , L = 25m, q = 0.5

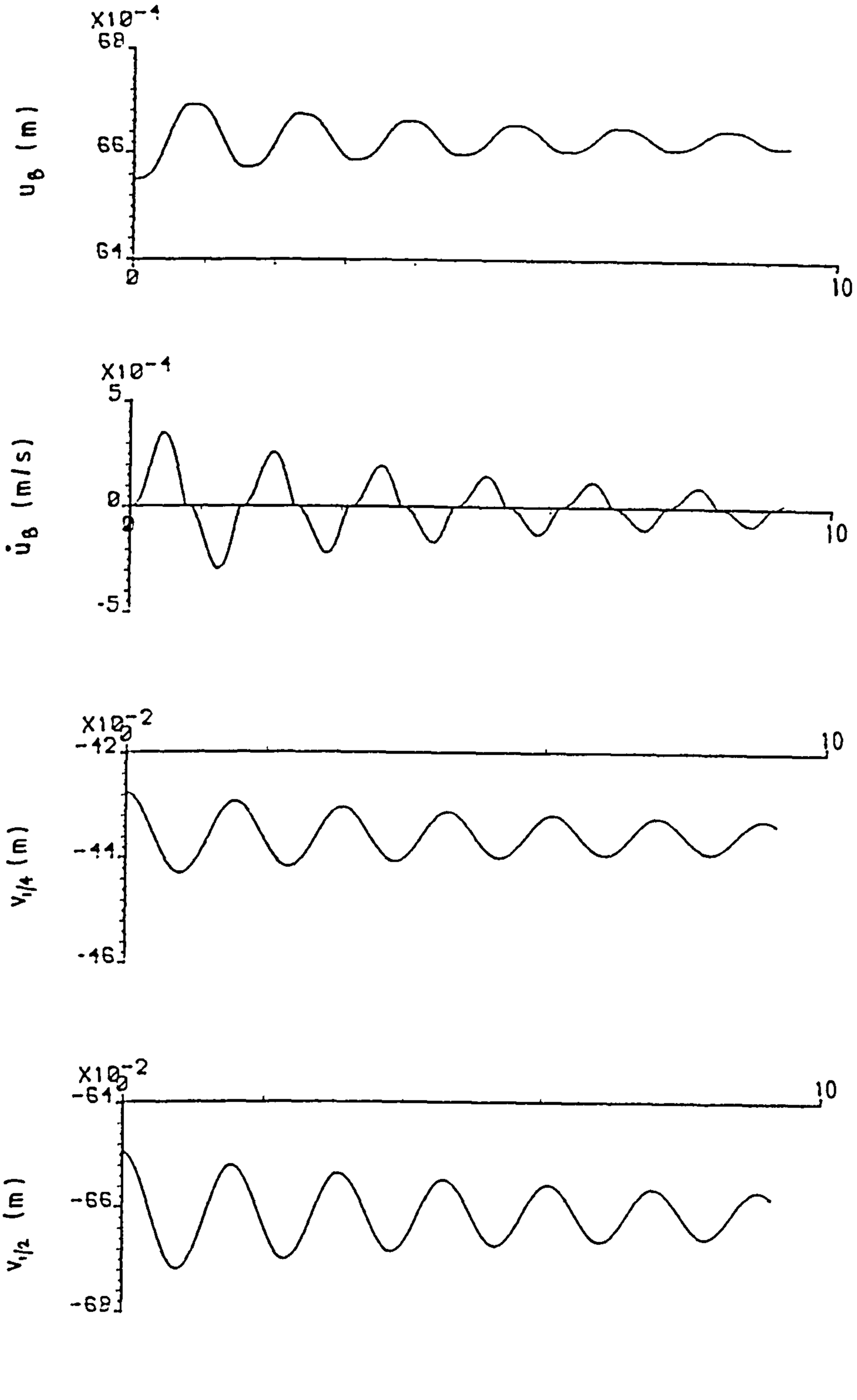

FIG 5.10a Pipe 2 Response, L = 50 m, q = 0.01

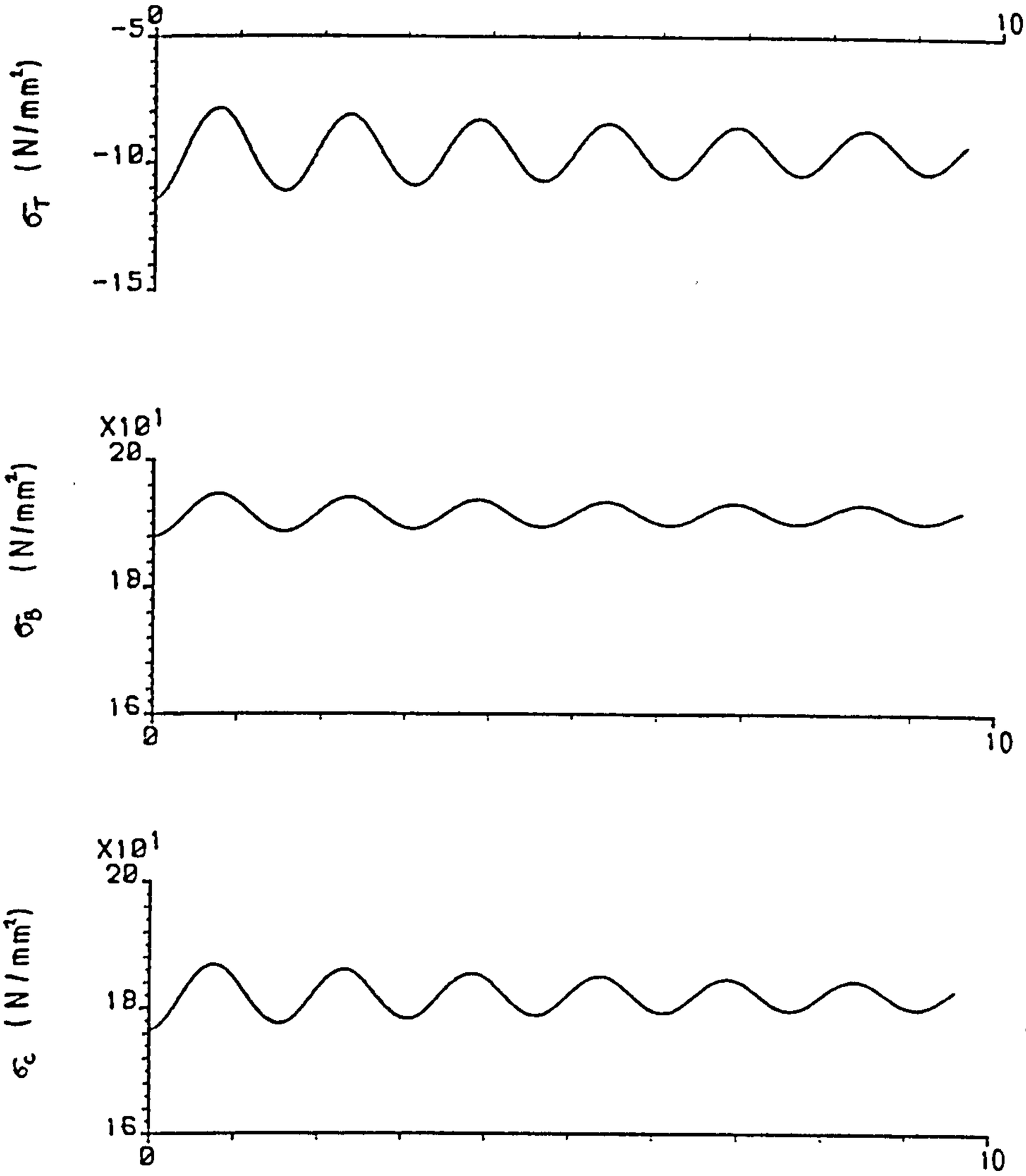

FIG 5.10b Pipe 2 Stress Time Histories, L = 50 m, q = 0.01

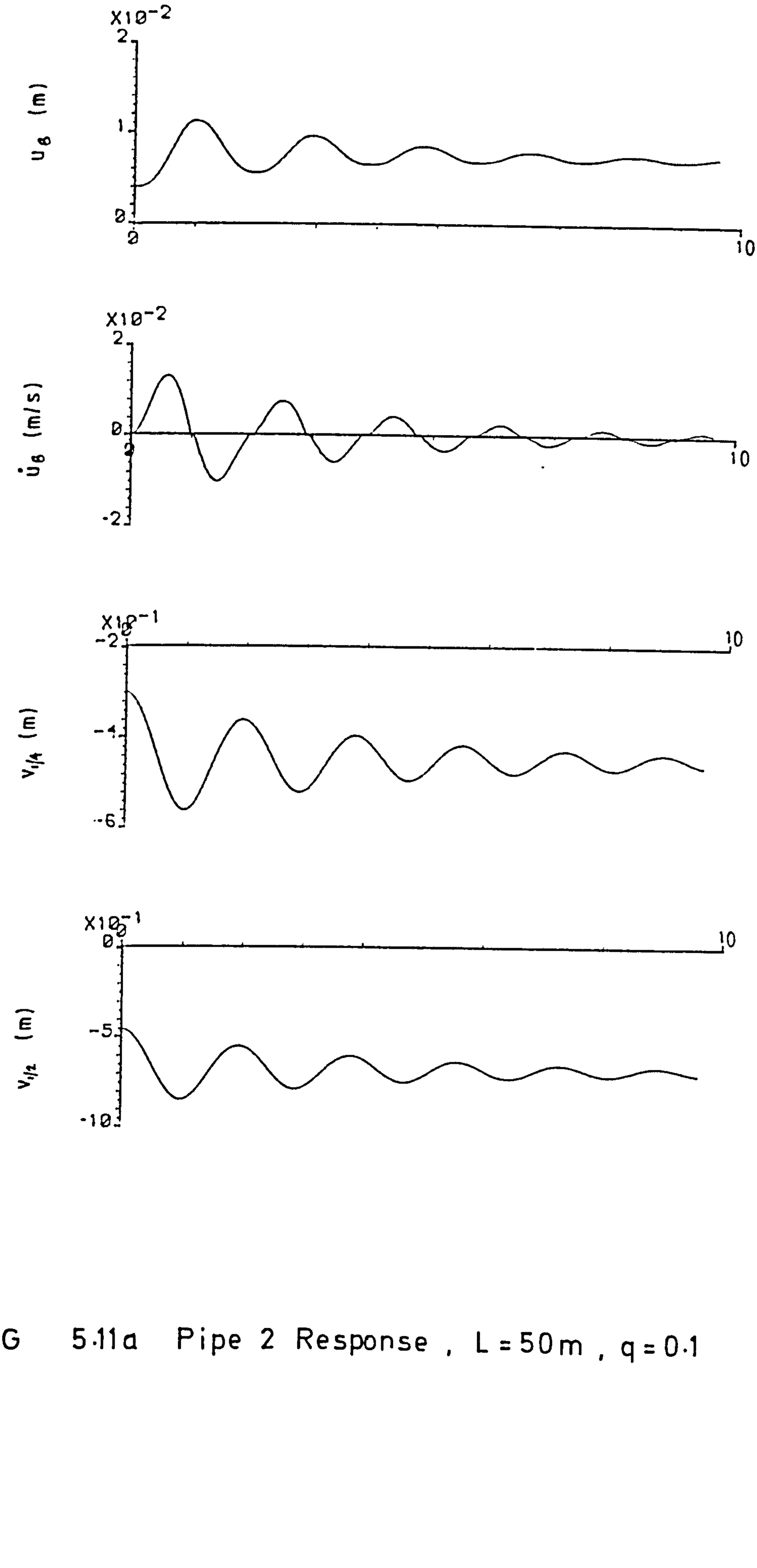

FIG 5.11a Pipe 2 Response , L = 50 m , q = 0.1

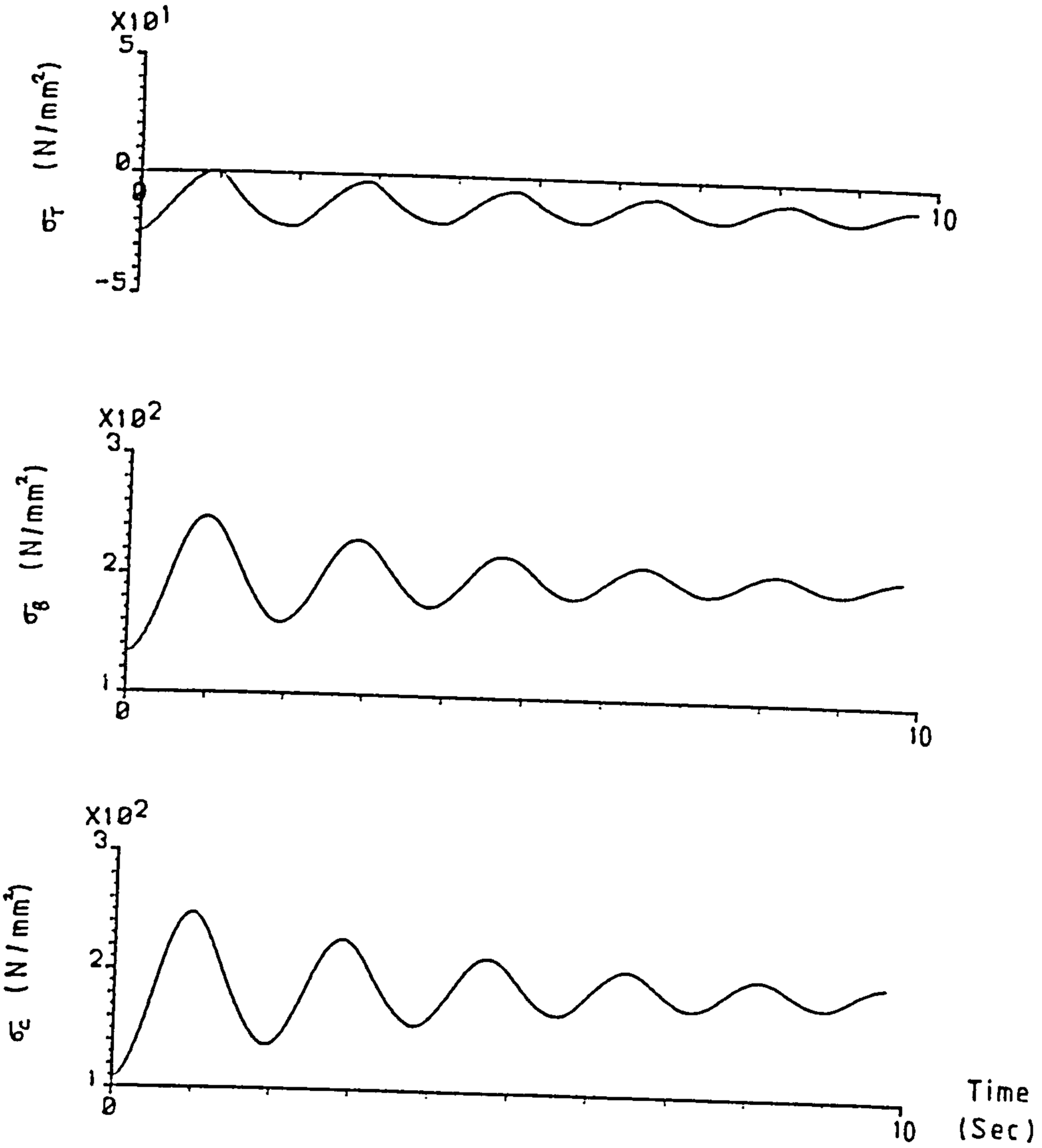

FIG 5.11b Pipe 2 Stress Time Histories , L = 50m, q = 0.1

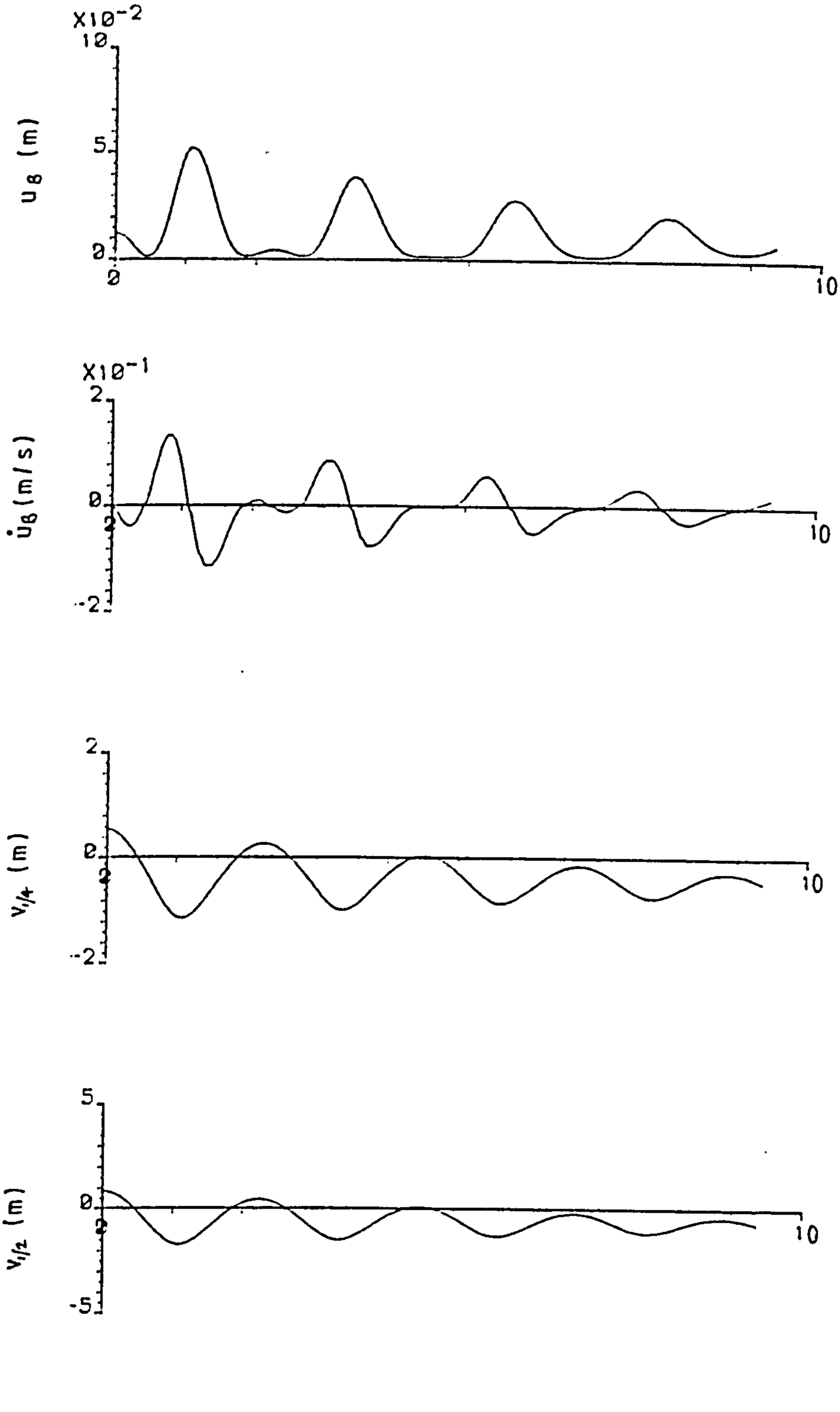

FIG 5·12a Pipe 2 Response, L = 50 m, q = 0·5

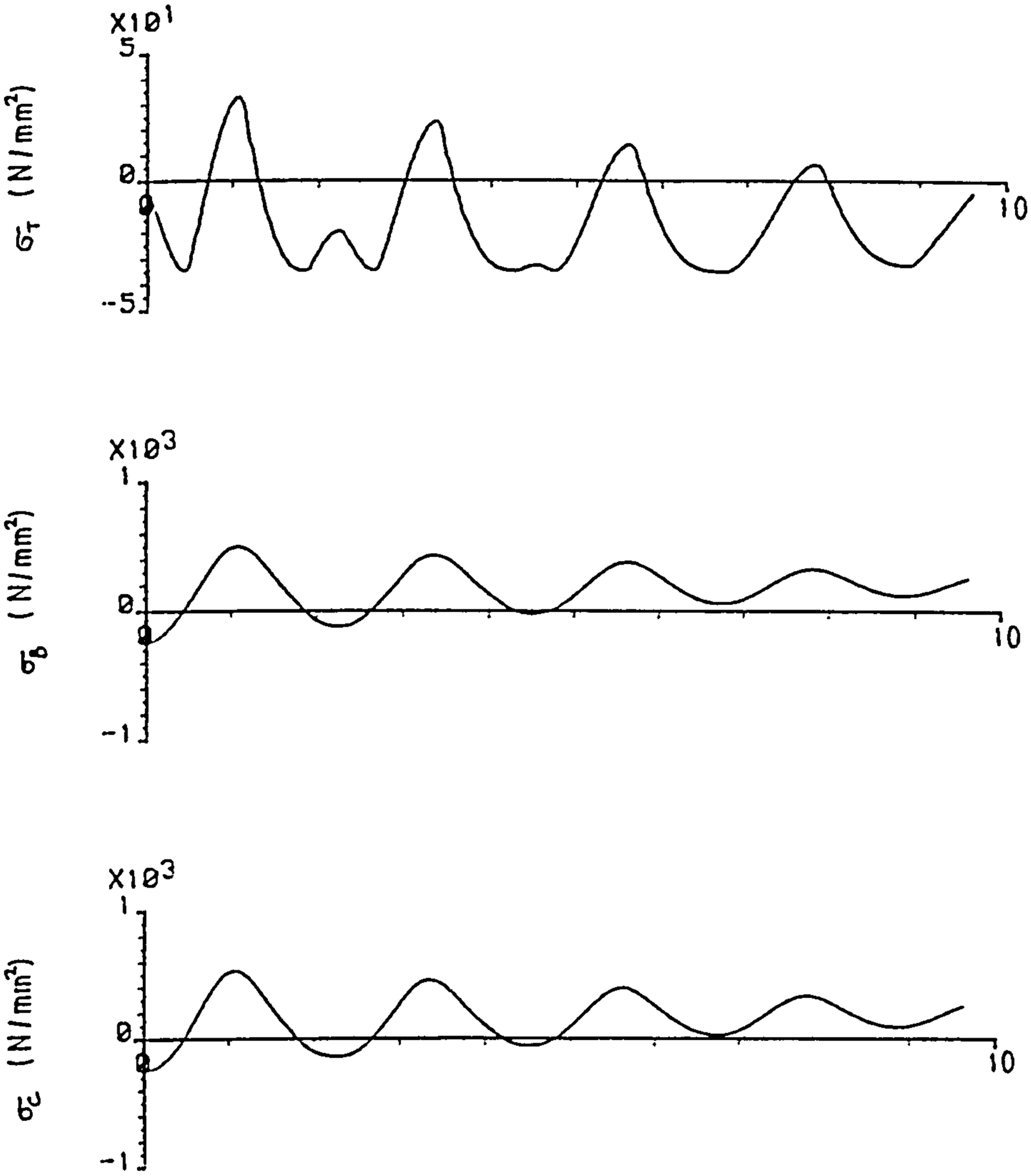

FIG 5.12b Pipe 2 Stress Time Histories, L = 50m, q = 0.5

CHAPTER 6

NONLINEAR PIPE CONTACT ELEMENT

6.0 Introduction

The analysis methods outlined in the preceding chapters have concerned the behaviour of free spans in an otherwise fully trenched pipeline. However pipe spans may also occur in untrenched pipelines, figure 6.1, as a result of

a) Design spans over uneven or rocky seabed. Such spans are formed when the line is installed and in most cases will remain for the complete service life of the system.

b) Soil erosion or movement under the pipeline resulting in unstable spans of time-varying length and form. In such cases pipe rotations at the main span ends may cause additional non-contact regions or spans to develop. The length of such side spans is now an initially unknown parameter involving the pipeline weight, line tension, bending stiffness and seabed geometry (Hoskins, 1982).

c) Pipeline tie-in, maintenance and repair operations involving pipe handling frames to lift the pipeline clear of the seabed.

From an analytical point of view a special difficulty associated with these problems is the unknown location of the pipeline seabed separation points. As a consequence the locations of these points must be treated as initially unknown with the result that an additional nonlinearity is introduced (Hobbs, 1984). In addition for dynamic problems the response of the pipeline causes these separation points to move rapidly along the line as the pipe comes into or looses contact with the seabed. Similar contact problems

arise during pipeline installation, figure 6.2, where the boundary condition at the seabed is often modelled using special contact elements (Nielson and Pendered, 1978). Such elements are intuitively simple relying on the insertion or removal of a spring stiffness depending on the current status of the element, figure 6.3. Unfortunately this method may cause numerical problems associated with slow or non-convergence of the solution as elements near to the separation point oscillate repeatedly between an open or closed status. An additional disadvantage of this method is the requirement to have a relatively fine mesh in the Finite Element Model along all points of the pipeline over which the separation point may travel. Because of these difficulties an attempt is made in this chapter to develop an alternative method in which the contact boundary condition is modelled directly using a variable length pipe contact element. This element is used to model the final section of the pipeline, figure 6.4, whose contact status with the seabed is unknown or, in the dynamic case, variable. Other sections of the pipeline, fully elevated at all times, are modelled using conventional beam elements as employed in preceding chapters.

6.1 Shape Functions

In this section the nonlinear equations of motion are derived for the pipe contact element shown in figure 6.5. The basic assumptions used in this analysis are

a) The support foundation is rigid, flat and frictionless
b) The deflections of the pipe are small
c) The tension force in the element is constant
d) The non-contact length ℓ is a function of time and is included in the element freedoms together with the end displacements v_1 and θ_1

Now considering the boundary condition of the separation point B we require

$$v(\ell) = v'(\ell) = v''(\ell) = 0 \qquad (6.1)$$

where v is the lateral deflection of the beam. Thus selecting polynomial functions to 4th order the shape functions associated with the end displacements v_1 and θ_1 are obtained as

$$N_1 = (1 - 6\xi^2 + 8\xi^3 - 3\xi^4) \qquad (6.2a)$$

$$N_2 = (\xi - 3\xi^2 + 3\xi^3 - \xi^4)\ell \qquad (6.2b)$$

where $\xi = x/\ell$, figure 6.5. As a result the lateral deflection v along the beam is

$$v(x,t) = v_1 N_1 + \theta_1 N_2 \qquad (6.3)$$

However, as indicated in section 6.5, although equation (6.3) ensures zero curvature at $x = \ell$ the associated generalised moment is in general non-zero. This fact follows directly from the approximation inherent in the use of the above (or any other) shape functions.

Consequently it is convenient at this stage to introduce a third shape function associated with the rotation θ_2 at the separation point B as given by

$$N_3 = (-3\xi^2 + 5\xi^3 - 2\xi^4)\ell \qquad (6.4)$$

The conditions satisfied by this function are for zero displacement and slope at A together with zero displacement, unit slope and zero curvature at B. The lateral deflection of the beam now becomes

$$v(x,t) = v_1 N_1 + \theta_1 N_2 + \theta_2 N_3 \qquad (6.5)$$

By this means the generalised moment at B, which corresponds in the virtual work sense to θ_2, may be calculated thus providing a measure on the accuracy of the solution. Following the calculation of the generalised forces the rotation θ_2 (together with its time derivatives) are set zero returning the solution to the original form equation (6.3).

6.2 Geometric Constraints

Using equations (6.2) and (6.3) the deflection of the pipe for the case $\theta_2 = 0$ may be written as

$$v = (1-\xi)^3 (v_1 + (3v_1 + \theta_1 \ell)\xi) \qquad (6.6)$$

Now due to the presence of the rigid foundation it is required that in the interval $0 \leq \xi < 1$ this displacement function is everywhere greater than zero. To ensure this it is first noted that the stipulated zero at $\xi = 1$ is in fact a triple root while the remaining fourth root occurs at

$$\xi = \frac{-v_1}{3v_1 + \theta_1 \ell} \qquad (6.7)$$

Now since $v_1 > 0$ the condition $3v_1 + \theta_1 \ell > 0$ ensures that this root occurs at $\xi < 0$. Thus for this acceptable situation we require

$$\theta_1 \ell > -3v_1 \tag{6.8}$$

An alternative is to ensure that

$$\frac{-v_1}{3v_1 + \theta_1 \ell} > 1 \tag{6.9}$$

This is clearly only possible if $3v_1 + \theta_1 \ell < 0$ ie $\theta_1 \ell < -3v_1$ so that equation (6.9) becomes

$$-v_1 < 3v_1 + \theta_1 \ell \quad \Rightarrow \quad -4v_1 < \theta_1 \ell$$

Thus equation (6.9) is satisfied provided $-4v_1 < \theta_1 \ell < -3v_1$ Finally since the condition $\theta_1 \ell = -3v_1$ is also acceptable (equation (6.6) becomes 3rd order with all three roots at $\xi = 1$) the required geometric constaint conditions may be written

$$v_1 > 0 \tag{6.10a}$$

$$\ell_1 > 0 \tag{6.10b}$$

$$A = 4v_1/\ell + \theta_1 > 0 \tag{6.10c}$$

Figure 6.6 shows for convenience the various acceptable and unacceptable deflection shapes for the pipe as given by equation (6.6).

6.3 Exact Static Solution

Before using the above shape functions to derive an approximate set of equations it is instructive to consider the exact static solution. For the case of zero tension this is conveniently obtained using the moment area theorems

$$\int_{x_1}^{x_2} \frac{M}{EI}\, dx = \theta_2 - \theta_1 \qquad (6.11a)$$

$$\int_{x_1}^{x_2} \frac{Mx}{EI}\, dx = (\theta_2 x_2 - \theta_1 x_1) - (v_2 - v_1) \qquad (6.11b)$$

where $(v_1\ \theta_1)$ and $(v_2\ \theta_2)$ are the pipe deflection and slopes at the two stations $x_1 = o$ and $x_2 = \ell$. Now defining the end shear force and moment corresponding to v_1 and θ_1 as F_{v_1} and F_{θ_1} respectively the moment at station x, figure 6.5, is

$$M(x) = F_{v_1} x - F_{\theta_1} - Wx^2/2 \qquad (6.12)$$

where W is the weight per length of pipe. Substituting this expression into equations (6.11) and setting $v_2 = \theta_2 = o$ gives

$$EI\theta_1 = F_{v_1} \ell^3/3 - F_{\theta_1} \ell^2/2 - W\ell^4/8 \qquad (6.13a)$$

$$EIv_1 = -F_{v_1} \ell^2/2 + F_{\theta_1} \ell + W\ell^3/6 \qquad (6.13b)$$

which solving for the generalised forces F_{v_1} and F_{θ_1} gives

$$F_{v_1} = \frac{12EI}{\ell^3} v_1 + \frac{6EI}{\ell^2} \theta_1 + \frac{W\ell}{2} \qquad (6.14a)$$

$$F_{\theta_1} = \frac{6EI}{\ell^2} v_1 + \frac{4EI}{\ell} \theta_1 + \frac{W\ell^2}{12} \qquad (6.14b)$$

The solution is now completed by ensuring zero moment at the separation point B. Thus using equations (6.12) and (6.14) we find

$$M(\ell) = F_{v_1}\ell - F_{\theta_1} + W\ell^2/2$$

$$= \frac{6EI}{\ell^2} v_1 + \frac{2EI}{\ell} \theta_1 - \frac{W\ell^2}{12}$$

which equating to zero and rearranging gives

$$3v_1 + \theta_1\ell = W\ell^4/24EI \qquad (6.15)$$

Now for any given end deflections (v_1 θ_1) this equation may be solved for the non-contact length ℓ and the result substituted into equations (6.14) above to determine the corresponding generalised forces. The resulting load deflection curves obtained for pipe 2 for the case $\theta_1 = 0$ (i.e. as might occur in lifting a continuous length of pipe using a single central sling) are shown in figure 6.7. It is noted that both the non-contact length ℓ and end shear F_{v_1} increase rapidly at the beginning of the lift and then increase more slowly after $v_1 = 0.2m$. Corresponding deflections in the pipe are obtained by setting $M = EIv''$ in equation (6.12) and integrating together with the end

conditions $v(0) = v_1$ and $v'(0) = \theta_1$ giving

$$v(x) = v_1(1 - 3\xi^2 + 2\xi^3) + \theta_1 \ell(\xi - 2\xi^2 + \xi^3)$$

$$+ \frac{W\ell^4}{24EI}(-\xi^2 + 2\xi^3 + \xi^4) \qquad (6.16)$$

Using equation (6.15) this may be rewritten as

$$v(x) = v_1(1 - 6\xi^2 + 8\xi^3 - 3\xi^4) + \theta_1 \ell(\xi - 3\xi^2 + 3\xi^3 - \xi^4) \qquad (6.17)$$

It is thus seen that the shape functions, equations (6.2), proposed for the approximate analysis correspond exactly to the static solution under zero tension. It is consequently anticipated that the approximate analysis will yield the exact generalised end forces and non-contact length ℓ for this special case.

For non-zero tension T in the pipeline the exact static solution is given in appendix F. In this case the non-contact length ℓ may be obtained by solving

$$\frac{\beta v_1 - \frac{W}{EI\beta^3}(1 + \beta^2\ell^2/2 - \cosh\beta\ell)}{\sinh\beta\ell - \beta\ell} = \frac{\theta_1 + \frac{W}{EI\beta^3}(\beta\ell - \sinh\beta\ell)}{1 - \cosh\beta\ell} \qquad (6.18)$$

where the tension parameter β is defined using $\beta^2 = T/EI$

6.4 Approximate Static Analysis

Assuming the deflection shape equation (6.5) the total strain/potential energy associated with the element is $V = V^B + V^\sigma$ where

$$V^B = \int_0^\ell \left(\frac{EI}{2}(v'')^2 + Wv \right) dx \qquad (6.19a)$$

$$V^\sigma = \int_0^\ell \frac{T}{2}(v')^2 dx \qquad (6.19b)$$

Using equation (6.5) these integrals are evaluated as

$$V^B = \frac{6EI}{5\ell^3}\left(8v_1^2 + 2\ell^2\theta_1^2 + 3\ell^2\theta_2^2 + 7\ell v_1\theta_1 + 9\ell v_1\theta_2 + 3\ell^2\theta_1\theta_2\right)$$

$$+ \frac{W\ell}{20}\left(8v_1 + \ell\theta_1 - 3\ell\theta_2\right) \qquad (6.20a)$$

$$V^\sigma = \frac{T}{35\ell}\left(24v_1^2 + \frac{3\ell^2}{2}\theta_1^2 + 6\ell^2\theta_2^2 + 2\ell v_1\theta_1 + 11\ell v_1\theta_2 - \ell^2\theta_1\theta_2\right) \qquad (6.20b)$$

Corresponding to the energy term V^B the following generalised forces for the condition $\theta_2 = 0$ can now be defined

$$F_{v_1} = \left.\frac{\partial V^B}{\partial v_1}\right|_{\theta_2=0} = \frac{6EI}{5\ell^3}\left(16v_1 + 7\ell\theta_1\right) + \frac{2W\ell}{5} \qquad (6.21a)$$

$$F_{\theta_1} = \left.\frac{\partial V^B}{\partial \theta_1}\right|_{\theta_2=0} = \frac{6EI}{5\ell^3}\left(7\ell v_1 + 4\ell^2\theta_1\right) + \frac{W\ell^2}{20} \qquad (6.21b)$$

$$F_{\theta_2} = \left.\frac{\partial V^B}{\partial \theta_2}\right|_{\theta_2=0} = \frac{6EI}{5\ell^3}\left(9\ell v_1 + 3\ell^2\theta_1\right) - \frac{3W\ell^2}{20} \qquad (6.21c)$$

In a similar manner for the term V^σ we have

$$G_{v_1} = \left.\frac{\partial V^\sigma}{\partial v_1}\right|_{\theta_2=0} = \frac{T}{35\ell}(48v_1 + 2\ell\theta_1) \qquad (6.22a)$$

$$G_{\theta_1} = \left.\frac{\partial V^\sigma}{\partial \theta_1}\right|_{\theta_2=0} = \frac{T}{35\ell}(2\ell v_1 + 3\ell^2\theta_1) \qquad (6.22b)$$

$$G_{\theta_2} = \left.\frac{\partial V^\sigma}{\partial \theta_2}\right|_{\theta_2=0} = \frac{T}{35\ell}(11\ell v_1 - \ell^2\theta_1) \qquad (6.22c)$$

In addition since the non-contact length ℓ is variable is also necessary to minimise the total potential with respect to this parameter. First we define

$$F_\ell = \left.\frac{\partial V^B}{\partial \ell}\right|_{\theta_2=0} = A\left\{\frac{W\ell}{10} - \frac{12EI}{5\ell^3}(3v_1 + \theta_1\ell)\right\} \qquad (6.23a)$$

$$G_\ell = \left.\frac{\partial V^\sigma}{\partial \ell}\right|_{\theta_2=0} = A\left\{\frac{3T}{70\ell}(\theta_1\ell - 4v_1)\right\} \qquad (6.23b)$$

where A is given by equation (6.10c). Thus we require

$$F_\ell + G_\ell = A\left\{\frac{W\ell}{10} - \frac{12EI}{5\ell^3}(3v_1 + \theta_1\ell) + \frac{3T}{70\ell}(\theta_1\ell - 4v_1)\right\}$$

$$= 0 \qquad \ldots . \qquad (6.24)$$

which since $A > 0$ requires

$$3v_1 + \theta_1\ell + \beta^2\left(\frac{v_1\ell^2}{14} - \frac{\theta_1\ell^3}{56}\right) = \frac{W\ell^4}{24EI} \qquad (6.25)$$

It is thus seen that the mathematical requirement of minimising the total potential wrt the non-contact length ℓ produces an equation which enables ℓ to be determined for any prescribed end displacements (v_1 , θ_1). For $T=0$ this equation reduces to

$$3v_1 + \theta_1 \ell = \frac{W\ell^4}{24\,EI}$$

which on substituting into equations (6.21) gives

$$F_{v_1} = \frac{2EI}{\ell^3} v_1 + \frac{6EI}{\ell^2} \theta_1 + \frac{W\ell}{2} \qquad (6.26a)$$

$$F_{\theta_1} = \frac{6EI}{\ell^2} v_1 + \frac{4EI}{\ell} \theta_1 + \frac{W\ell^2}{12} \qquad (6.26b)$$

$$F_{\theta_2} = 0 \qquad (6.26c)$$

Thus as anticipated in section 6.3 the approxiamte static analysis presented here yields the exact result for the zero tension case. For the non-zero tension case figure 6.8 shows a comparison of ℓ_{EXACT} , obtained by solving equation (6.18), against the approximate non-contact length ℓ obtained using equation (6.25) above. It is noted that negative values of θ_1 result in short non-contact lengths and reduced errors.

6.5 Generalised Inertia Forces

In the above section the generalised static forces have been calculated directly from the total strain/potential energy in the pipeline. In a similar manner for the dynamic case generalised inertia forces may be computed starting from the total kinetic energy. To do this the lateral velocity of the pipe is first obtained from equation (6.5) as

$$\dot{v} = \dot{v}_1 N_1 + \dot{\theta}_1 N_2 + \dot{\theta}_2 N_3 + \dot{\ell}(v_1 N_1' + \theta_1 N_2' + \theta_2 N_3') \qquad (6.27)$$

where dot indicates differentiation with respect to time and prime differentiation with respect to ℓ. Using equations (6.2) and (6.4) this may be written

$$\dot{v} = \dot{v}_1 N_1 + \dot{\theta}_1 N_2 + \dot{\theta}_2 N_3 + \dot{\ell} N_4 \qquad (6.28)$$

where the time dependent shape function N_4 is

$$N_4 = 3(4v_1/\ell + \theta_1 + \theta_2)\xi^2 - 2(12v_1/\ell + 3\theta_1 + 5\theta_2)\xi^3$$

$$+ 3(4v_1/\ell + \theta_1 + 2\theta_2)\xi^4 \qquad (6.29)$$

It is noted that setting $\xi = x/\ell$ equal to 0 and 1 gives N_4 equal to 0 and $-\theta_2$ respectively. Thus $\dot{v}(0) = \dot{v}_1$ as expected while $\dot{v}(\ell) = -\dot{\ell}\theta_2$. This later result may be justified by considering the limit process, figure 6.9. It is clear that as a result of the increase $\delta\ell = \dot{\ell}\delta t$ in the non-contact length ℓ the vertical displacement at $x = \ell(t)$ is given by

$$\delta v \Big|_{x=\ell(t)} = -\dot{\ell}\,\delta t\,(\theta_2 + \delta\theta_2) \tag{6.30}$$

Thus dividing by δt and taking the limit as $\delta t \to 0$ we find

$$v(\ell) = \lim_{\delta t \to 0} \frac{\delta v}{\delta t}\Big|_{x=\ell(t)} = -\dot{\ell}\theta_2 \tag{6.31}$$

It follows that since θ_2 is set zero during the analysis the vertical velocity at the point instantaneously coincident with the separation point B is zero. Now using equation (6.28) the kinetic energy may be written as

$$T_{KE} = \frac{m}{2}\int_0^{\ell} (\dot{v}_1 N_1 + \dot{\theta}_1 N_2 + \dot{\theta}_2 N_3 + \dot{\ell} N_4)^2 \, dx \tag{6.32}$$

where the mass per length m is assumed constant. Using equations (6.2), (6.4) and (6.29) this integral is evaluated as

$$T_{KE} = \sum_{i=1}^{4}\sum_{j=1}^{4} t_{ij}\,\dot{a}_i\,\dot{a}_j \tag{6.33a}$$

where $(a_1\ a_2\ a_3\ a_4) = (v_1\ \theta_1\ \theta_2\ \ell)$
and the coefficients $t_{ij} = t_{ji}$ are given by

$$t_{11} = \frac{m\ell}{7} \tag{6.33b}$$

$$t_{12} = \frac{5m\ell^2}{336} \tag{6.33c}$$

$$t_{13} = -\frac{37ml^2}{1680} \tag{6.33d}$$

$$t_{14} = \frac{ml}{280}(20v_1/l + 5\theta_1 - \theta_2) \tag{6.33e}$$

$$t_{22} = \frac{ml^3}{504} \tag{6.33f}$$

$$t_{23} = -\frac{19ml^3}{5040} \tag{6.33g}$$

$$t_{24} = \frac{ml^2}{1680}(20v_1/l + 5\theta_1 - 2\theta_2) \tag{6.33h}$$

$$t_{33} = \frac{19ml^3}{1260} \tag{6.33i}$$

$$t_{34} = \frac{ml^2}{1680}(68v_1/l + 17\theta_1 - 38\theta_2) \tag{6.33j}$$

$$t_{44} = \frac{ml}{140}\left(16\frac{v_1^2}{l^2} + \theta_1^2 + 16\theta_2^2 + \frac{8v_1\theta_1}{l} - \frac{12v_1\theta_2}{l} - 3\theta_1\theta_2\right) \tag{6.33k}$$

The corresponding generalised forces are defined as

$$H_{v_1} = \left(\frac{d}{dt}\frac{\partial T_{KE}}{\partial \dot{v}_1} - \frac{\partial T_{KE}}{\partial v}\right)\Bigg|_{\theta_2 = \dot{\theta}_2 = \ddot{\theta}_2 = 0} \tag{6.34a}$$

$$H_{\theta_1} = \left(\frac{d}{dt}\frac{\partial T_{KE}}{\partial \dot{\theta}_1} - \frac{\partial T_{KE}}{\partial \theta_1}\right)\Bigg|_{\theta_2 = \dot{\theta}_2 = \ddot{\theta}_2 = 0} \tag{6.34b}$$

$$H_{\theta_2} = \left(\frac{d}{dt}\frac{\partial T_{KE}}{\partial \dot{\theta}_2} - \frac{\partial T_{KE}}{\partial \theta_2}\right)\Bigg|_{\theta_2 = \dot{\theta}_2 = \ddot{\theta}_2 = 0} \tag{6.34c}$$

which using equations (6.33) are evaluated as

$$H_{v_1} = \frac{m\ell}{7}\left\{2\ddot{v}_1 + \frac{5\ell}{24}\ddot{\theta}_1 + \frac{A}{4}\ddot{\ell} + \frac{2}{\ell}\dot{\ell}\dot{v}_1 + \frac{1}{2}\dot{\ell}\dot{\theta}_1 - \frac{1}{20\ell}\left(32\frac{v_1}{\ell} + 3\theta_1\right)\dot{\ell}^2\right\} \qquad (6.35a)$$

$$H_{\theta_1} = \frac{m\ell}{7}\left\{\frac{5\ell}{24}\ddot{v}_1 + \frac{\ell^2}{36}\ddot{\theta}_1 + \frac{\ell A}{24}\ddot{\ell} + \frac{1}{3}\dot{\ell}\dot{v}_1 + \frac{\ell}{12}\dot{\ell}\dot{\theta}_1 - \frac{1}{60}\left(14\frac{v_1}{\ell} + \theta_1\right)\dot{\ell}^2\right\} \qquad (6.35b)$$

$$H_{\theta_2} = -\frac{m\ell}{7}\left\{\frac{37\ell}{120}\ddot{v}_1 + \frac{19\ell^2}{360}\ddot{\theta}_1 + \frac{\ell}{120}\left(68\frac{v_1}{\ell} + 17\theta_1\right)\ddot{\ell} + \frac{17}{15}\dot{\ell}\dot{v}_1 + \frac{17\ell}{60}\dot{\ell}\dot{\theta}_1 - \frac{1}{30}\left(\frac{v_1}{\ell} - 4\theta_1\right)\dot{\ell}^2\right\} \qquad (6.35c)$$

6.6 Equilibrium Check

As a check on the analysis to this stage it is shown that the system of Forces (F_{v_1} F_{θ_1} F_{θ_2}), (G_{v_1} G_{θ_1} G_{θ_2}) and (H_{v_1} H_{θ_1} H_{θ_2}) as given by equations (6.21), (6.22) and (6.35) respectively are in moment equilibrium with the pipe self weight W, the axial tension T and the distributed inertia forces due to vertical accelerations of the pipe. Thus considering the static forces(F_{v_1} F_{θ_1} F_{θ_2}) together with the self weight W, figure 6.10, equilibrium of moments about B requires

$$-F_{v_1}\ell + F_{\theta_1} + F_{\theta_2} + W\ell^2/2 = 0 \qquad (6.36)$$

In a similar manner considering the geometric or stress stiffening forces (G_{v_1} G_{θ_1} G_{θ_2}) together with the axial tension T , figure 6.11, we find

$$-G_{v_1} l + G_{\theta_1} + G_{\theta_2} + T v_1 = 0 \qquad (6.37)$$

By substituting for the various force terms using equations (6.21) and (6.22) these conditions are immediately verified. Next considering the generalised inertia forces (H_{v_1} H_{θ_1} H_{θ_2}) together with the distributed inertia force $m\ddot{v}$, figure 6.12, moments about B requires

$$-H_{v_1} l + H_{\theta_1} + H_{\theta_2} + \int_0^l (l-x) m \ddot{v}\, dx = 0 \qquad (6.38)$$

To evaluate the integral term in this expression first differentiate equation (6.3) with respect to time to obtain

$$\ddot{v} = \ddot{v}_1 N_1 + \ddot{\theta}_1 N_2 + \ddot{l}(v_1 N_1' + \theta_1 N_2') + (2N_1)\dot{l}\dot{v}_1$$

$$+ (2N_2')\dot{l}\dot{\theta}_1 + (v_1 N_1'' + \theta_1 N_2'')\dot{l}^2 \qquad (6.39)$$

where as in section 6.5 dash again indicates differentiation wrt l . Now using equations (6.2) we find

$$\int_0^l (l-x) m \ddot{v}\, dx = \frac{ml}{5}\left\{\frac{3l}{2}\ddot{v}_1 + \frac{l^2}{6}\ddot{\theta}_1 + \frac{1}{4}(4v_1 + \theta_1 l)\ddot{l}\right.$$

$$\left. + 2l\dot{l}\dot{v}_1 + \frac{l}{2}\dot{l}\dot{\theta}_1 - v_1\dot{l}^2\right\} \qquad (6.40)$$

With this result and using equations (6.35) it is now straight forward to confirm that the dynamic equilibrium condition given by equation (6.38) is satisfied.

6.7 Hydrodynamic Load Vector

In the static analysis outlined in section 6.4 the only external forces considered to act on the element are the axial tension T plus pipe self-weight in water W. For the dynamic case a distributed hydrodynamic force $f(x,t)$ must also be included. To calculate the generalised loads associated with this nonconservative force consider first a virtual displacement δv applied to the element which using equation (6.5) may be written as

$$\delta v = N_1 \delta v_1 + N_2 \delta \theta_1 + N_3 \delta \theta_2 + N_4 \delta \ell \qquad (6.41)$$

As a result the non-conservative virtual work done by $f(x,t)$ is

$$\delta W_{NC} = \int_0^L f(x,t)\, \delta v \, dx \qquad (6.42)$$

Now since the virtual displacements δv_1, $\delta \theta_1$, $\delta \theta_2$ and $\delta \ell$ are arbitrary this may be written

$$\delta W_{NC} = Q_{v_1} \delta v_1 + Q_{\theta_1} \delta \theta_1 + Q_{\theta_2} \delta \theta_2 + Q_\ell \delta \ell \qquad (6.43)$$

where the generalised loads are given by

$$Q_{v_1} = \int_0^\ell f(x,t) N_1 \, dx \qquad (6.44a)$$

$$Q_{\theta_1} = \int_0^{\ell} f(x,t)\, N_2\, dx \qquad (6.44b)$$

$$Q_{\theta_2} = \int_0^{\ell} f(x,t)\, N_3\, dx \qquad (6.44c)$$

$$Q_{\ell} = \int_0^{\ell} f(x,t)\, N_4\, dx \qquad (6.44d)$$

Using equations (6.2), (6.4), (6.29) and assuming a linear variation of force such that

$$f(x,t) = f_1(t)(1-\bar{x}) \qquad (6.45)$$

these forces are evaluated as

$$Q_{v_1} = 3f_1\ell/10 \qquad (6.46a)$$

$$Q_{\theta_1} = f_1\ell^2/30 \qquad (6.46b)$$

$$Q_{\theta_2} = -f_1\ell^2/15 \qquad (6.46c)$$

$$Q_{\ell} = \frac{f_1\ell}{20}(4v_1/\ell + \theta_1) \qquad (6.46d)$$

where in evaluating Q_ℓ the pipeline slope θ_2 has been set zero. It is noted that the forces Q_{v_1}, Q_{θ_1} and Q_{θ_2} produce the same net moment as the external load $f(x,t)$, figure 6.13.

6.8 Element Equations of Motion

The element equations of motion in terms of the end displacements (v_1, θ_1) are given by the Lagrange equations

$$\left(\frac{d}{dt}\frac{\partial T_{KE}}{\partial \dot{v}_1} - \frac{\partial T_{KE}}{\partial v_1} + \frac{\partial V}{\partial v_1}\right)\Big|_{\theta_2=\dot{\theta}_2=\ddot{\theta}_2=0} = H_{v_1} + F_{v_1} + G_{v_1} = Q_{v_1} \qquad (6.47a)$$

$$\left(\frac{d}{dt}\frac{\partial T_{KE}}{\partial \dot{\theta}_1} - \frac{\partial T_{KE}}{\partial \theta_1} + \frac{\partial V}{\partial \theta_1}\right)\Big|_{\theta_2=\dot{\theta}_2=\ddot{\theta}_2=0} = H_{\theta_1} + F_{\theta_1} + G_{\theta_1} = Q_{\theta_1} \qquad (6.47b)$$

In addition since these equations also contain the unknown non-contact length ℓ we also require

$$\left(\frac{d}{dt}\frac{\partial T_{KE}}{\partial \dot{\ell}} - \frac{\partial T_{KE}}{\partial \ell} + \frac{\partial V}{\partial \ell}\right)\Big|_{\theta_2=\dot{\theta}_2=\ddot{\theta}_2=0} = Q_\ell \qquad (6.48)$$

It is convenient to define

$$H_\ell = \left(\frac{d}{dt}\frac{\partial T_{KE}}{\partial \dot{\ell}} - \frac{\partial T_{KE}}{\partial \ell}\right)\Big|_{\theta_2=\dot{\theta}_2=\ddot{\theta}_2=0} \qquad (6.49)$$

which in view of equation (6.33) is evaluated as

$$H_\ell = \frac{m\ell A}{7}\left\{\frac{1}{4}\ddot{v}_1 + \frac{\ell}{24}\ddot{\theta}_1 + \frac{A}{10}\ddot{\ell} + \frac{4}{5\ell}\dot{v}_1\dot{\ell} + \frac{1}{5}\dot{\theta}_1\dot{\ell}\right.$$

$$\left. - \frac{1}{20\ell}(4v_1/\ell + \theta_1)\dot{\ell}^2\right\} \qquad (6.50)$$

Thus using equations (6.23) and (6.49) equation (6.48) above may be written compactly as

$$H_\ell + F_\ell + G_\ell = Q_\ell \tag{6.51}$$

In a similar manner to the static analysis this "ℓ" equation must be solved simultaneously with the (v_1, θ_1) equations as given by equations (6.47) above. Hence combining these equations in matrix form we may write the required element equations of motion as

$$[m^e]\ddot{\underset{\sim}{a}}^e + \dot{\ell} f_v^e(\dot{\underset{\sim}{a}}^e) + f_s^e(\underset{\sim}{a}^e) = \underset{\sim}{p}^e \tag{6.52a}$$

where using equations (6.21), (6.22), (6.23), (6.35), (6.46) and (6.50)

$$\underset{\sim}{a}^e = \begin{bmatrix} v_1 \\ \theta_1 \\ \ell \end{bmatrix} \tag{6.52b}$$

$$m^e = \frac{m\ell}{7}\begin{bmatrix} 2 & 5\ell/24 & (4v_1/\ell + \theta_1)/4 \\ & \ell^2/36 & (4v_1/\ell + \theta_1)\ell/24 \\ \text{Sym} & & (4v_1/\ell + \theta_1)^2/10 \end{bmatrix} \tag{6.52c}$$

$$f_v^e = \frac{M}{7}\begin{bmatrix} (2\dot{v}_1 + \ell\dot{\theta}_1/2 - (32v_1/\ell + 3\theta_1)\dot{\ell}/20) \\ (\ell\dot{v}_1/3 + \ell^2\dot{\theta}_1/12 - \ell(14v_1/\ell + \theta_1)\dot{\ell}/60) \\ (4\dot{v}_1/5 + \ell\dot{\theta}_1/5 - (4v_1/\ell + \theta_1)\dot{\ell}/20)(4v_1/\ell + \theta_1) \end{bmatrix} \tag{6.52d}$$

$$\underset{\sim}{f}_S^e = \frac{6EI}{5\ell^3}\begin{bmatrix} (16v_1 + 7\ell\theta_1) \\ (7\ell v_1 + 4\ell^2\theta_1) \\ -2(3v_1 + \theta_1\ell)(4v_1/\ell + \theta_1) \end{bmatrix} + \frac{T}{35\ell}\begin{bmatrix} (48v_1 + 2\ell\theta_1) \\ (2\ell v_1 + 3\ell^2\theta_1) \\ 3(\theta_1\ell - 4v_1)(4v_1/\ell + \theta_1)/2 \end{bmatrix}$$

.... (6.52e)

$$\underset{\sim}{p}^e = \frac{f_1(t)}{60}\begin{bmatrix} 18\ell \\ 2\ell^2 \\ 3\ell(4v_1/\ell + \theta_1) \end{bmatrix} - \frac{W}{5}\begin{bmatrix} 2\ell \\ \ell^2/4 \\ -\ell(4v_1/\ell + \theta_1)/2 \end{bmatrix}$$

.... (6.52f)

Further differentiating the static forces $\underset{\sim}{f}_S^e$ with respect to the displacements $\underset{\sim}{a}^e$ we may write

$$\delta\underset{\sim}{f}_S^e = \left[k_T^e\right]\delta\underset{\sim}{a}^e \qquad (6.53)$$

where the element tangent stiffness k_T^e is given by

$$k_T^e = \frac{6EI}{5\ell^3}\begin{bmatrix} 16 & 7\ell & -(48v_1/\ell + 14\theta_1) \\ & 4\ell^2 & -(14v_1/\ell + 4\theta_1)\ell \\ \text{Sym} & & (96v_1^2/\ell^2 + 42v_1\theta_1/\ell + 4\theta_1^2) \end{bmatrix} + \frac{T}{35\ell}\begin{bmatrix} 48 & 2\ell & -48v_1/\ell \\ & 3\ell^2 & 3\ell\theta_1 \\ \text{Sym} & & 48v_1^2/\ell^2 \end{bmatrix} \qquad (6.54)$$

It is noted that both matrices M^e and k_T^e although nonlinear are symmetric. Finally the θ_2 equation may be written as

$$H_{\theta_2} + F_{\theta_2} + G_{\theta_2} = Q_{\theta_2} + R_{\theta_2} \qquad (6.55)$$

where the generalised forces H_{θ_2}, F_{θ_2}, G_{θ_2} and Q_{θ_2} are given by equations (6.35c), (6.21c), (6.22c) and (6.46c) respectively and R_{θ_2} is the reaction force associated with the constraint $\theta_2 = 0$. For the static case with zero tension and using equation (6.26c) this reaction force is

$$R_{\theta_2} = F_{\theta_2} = 0 \qquad (6.56)$$

as required. For other cases the amount by which R_{θ_2} differs from zero may be considered as a measure on the error involved in modelling the boundary conditions at the moving separation point B.

6.9 Conclusions and Further Work

The contact element developed in this chapter may be used to investigate a variety of pipe installation and operating conditions where the location of the separation point is a function of time. Specific examples include design spans, spans formed by scouring and tie-in or maintenance operations. Further work required includes

a) Development of suitable models and solution methods in order to gain practical experience concerning the advantages/disadvantages of the proposed approach over more traditional methods.

b) Inclusion of further degrees of freedom into the contact element by introducing one or more internal nodes along the element length. This refinement should improve any errors encountered in modelling the contact boundary conditions.

c) Consideration of effects of pipe-surface friction.

a) Design Spans

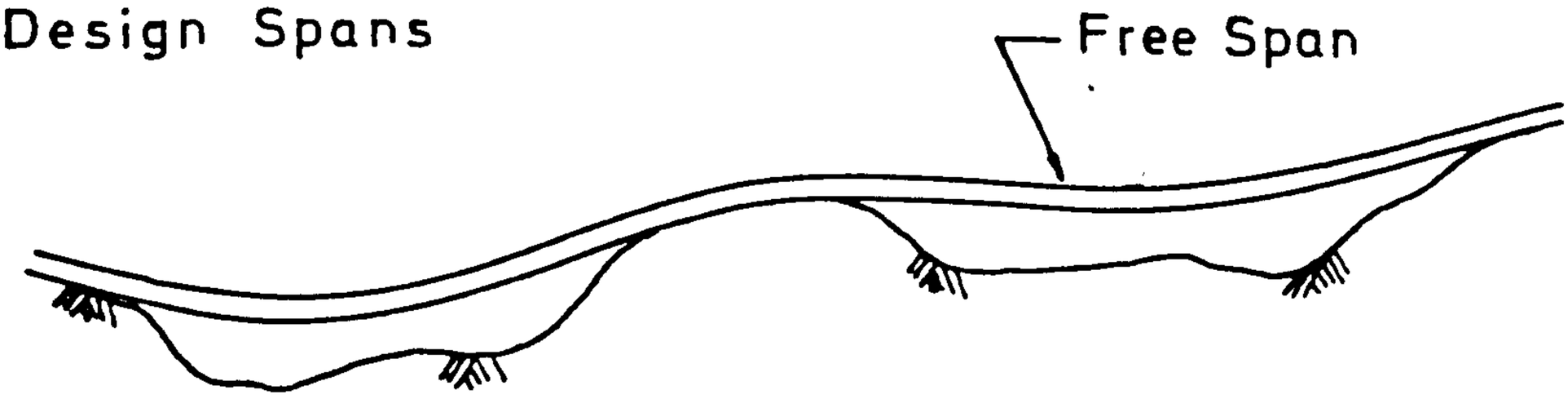

b) Soil Erosion

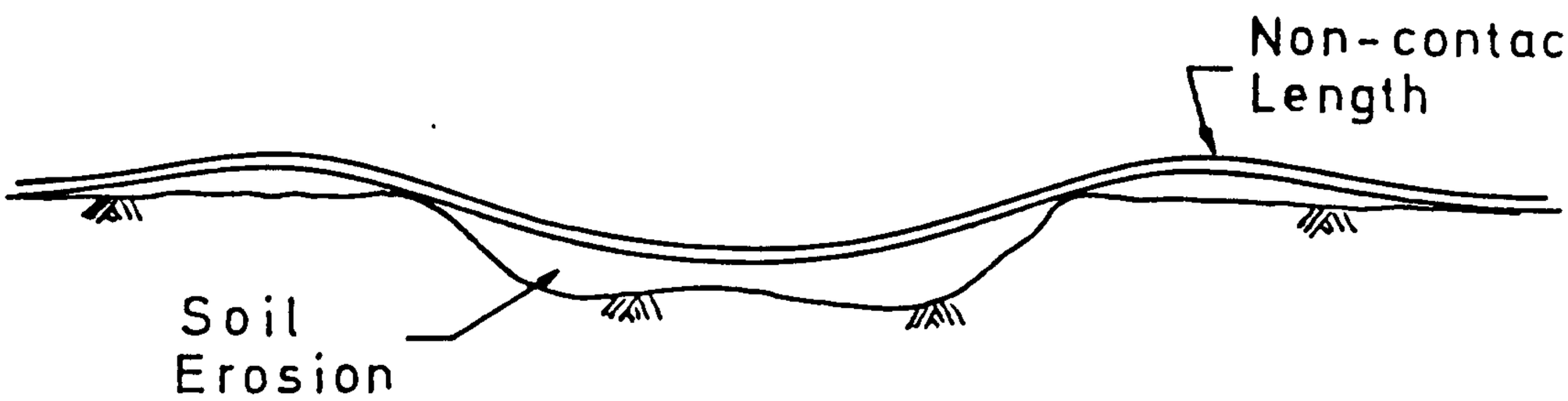

c) Maintenance / Tie-in

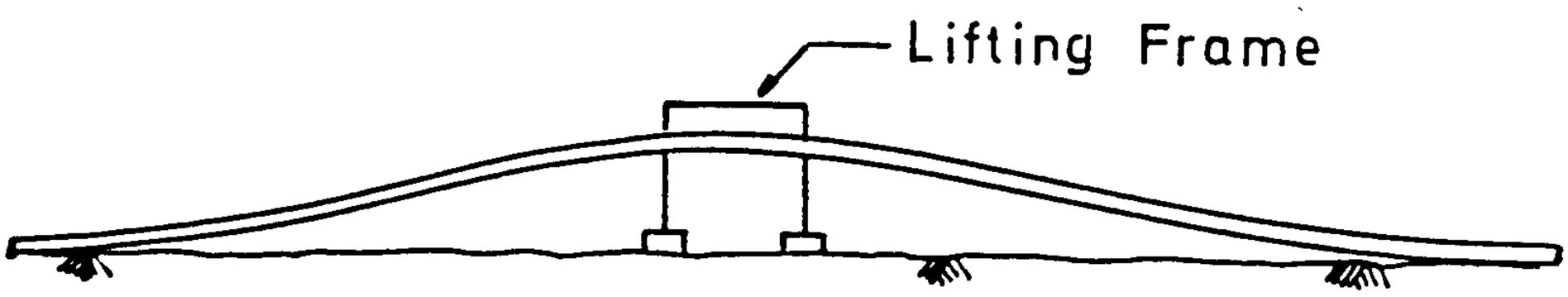

FIG 6.1 Pipe Spans in Untrenched Pipeline

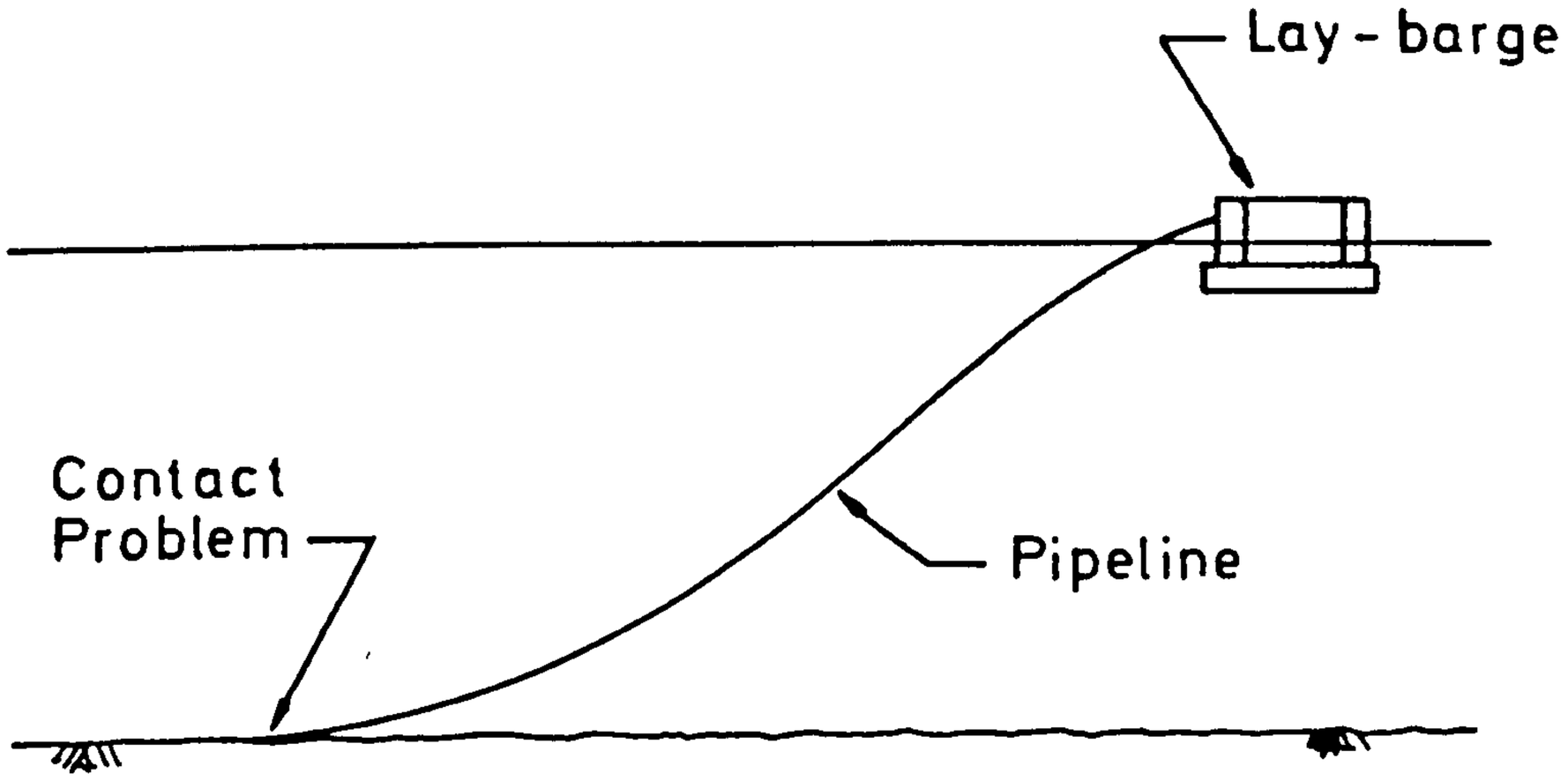

FIG 6.2 Pipeline Installation

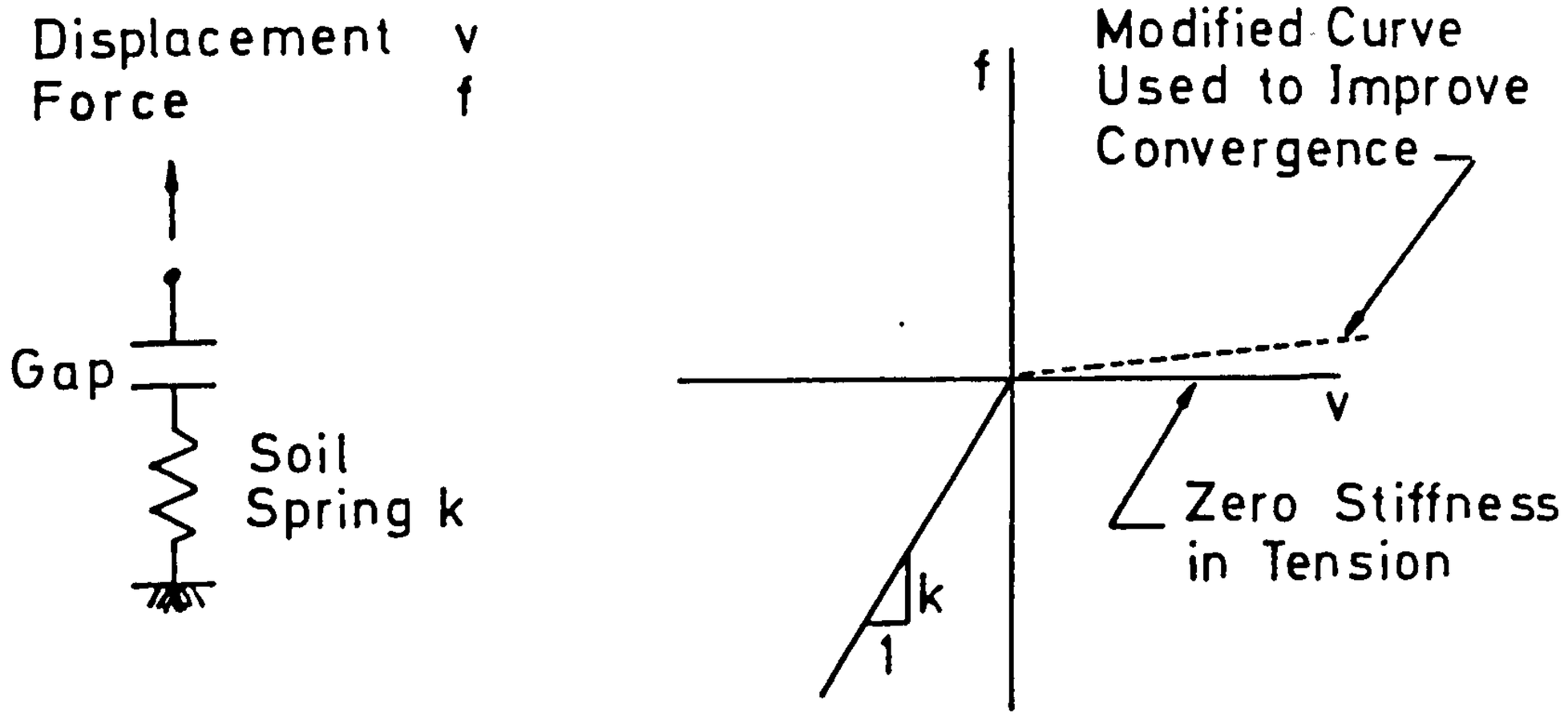

FIG 6.3 Simple Gap Element

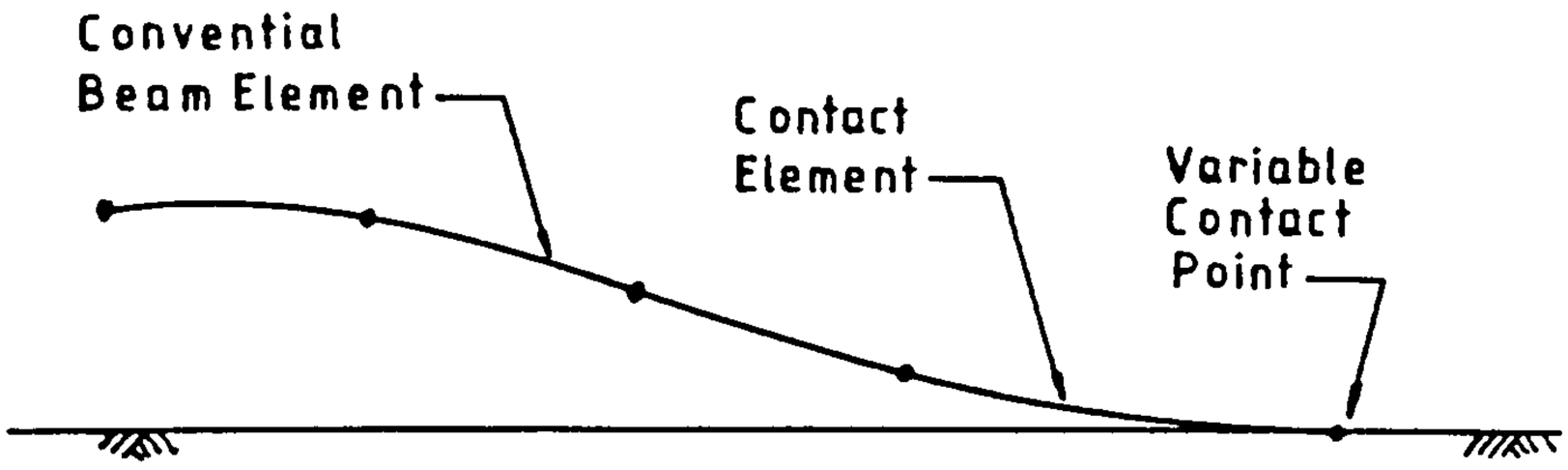

FIG 6.4 Typical Model with Contact Element

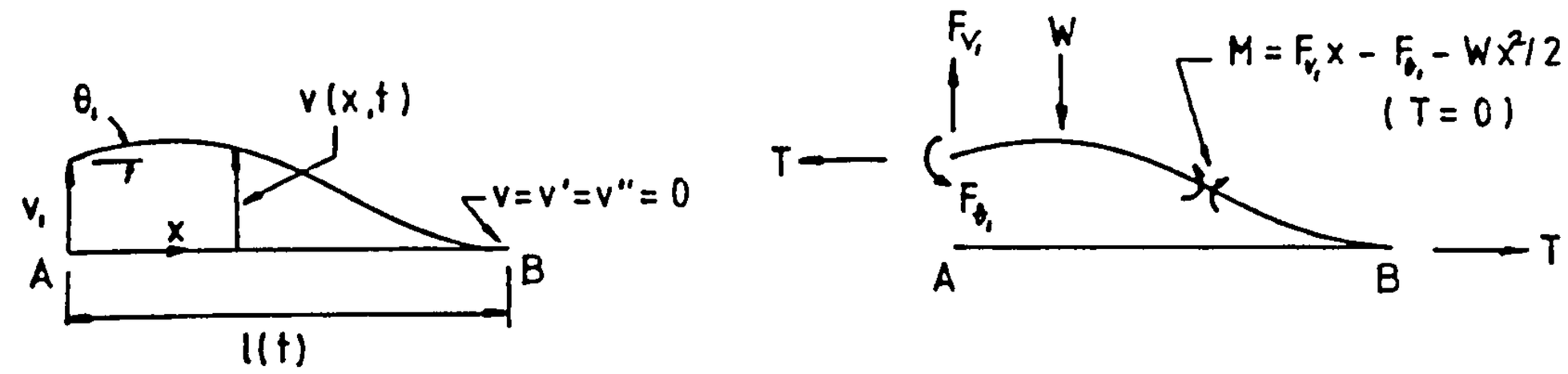

a) Deflections

b) Forces

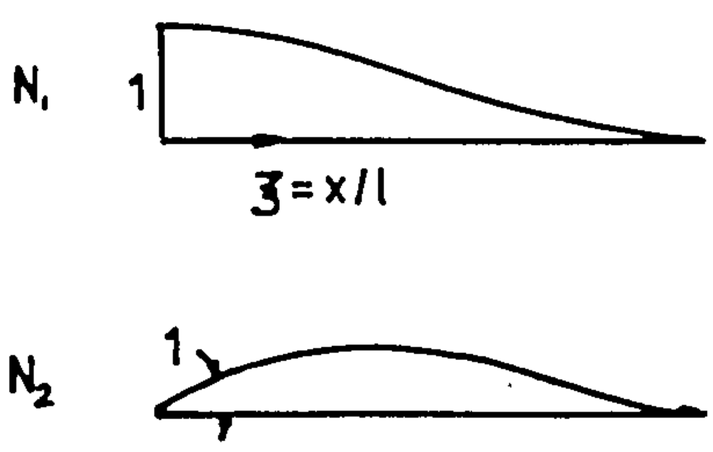

c) Shape Functions

FIG 6.5 Pipe/Rigid Foundation Contact Element

a) $0 \leq \theta_1 l$

b) $-3v_1 < \theta_1 l < 0$

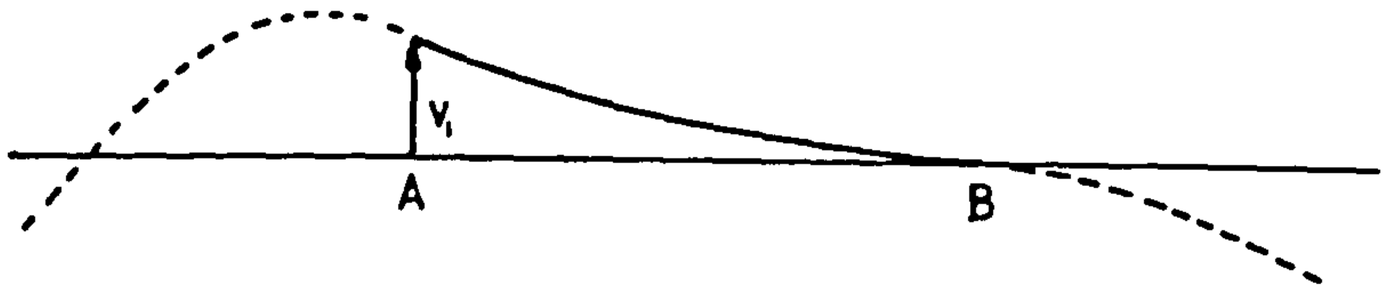

c) $-3v_1 = \theta_1 l$

d) $-4v_1 < \theta_1 l < -3v_1$

e) $-4v_1 = \theta_1 l$

f) $\theta_1 l < -4v_1$

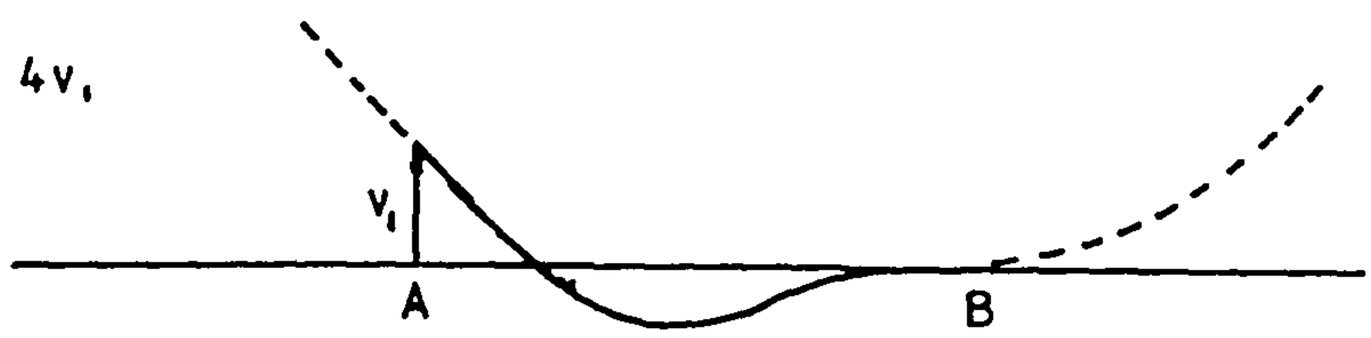

FIG 6.6 Possible Element Configurations

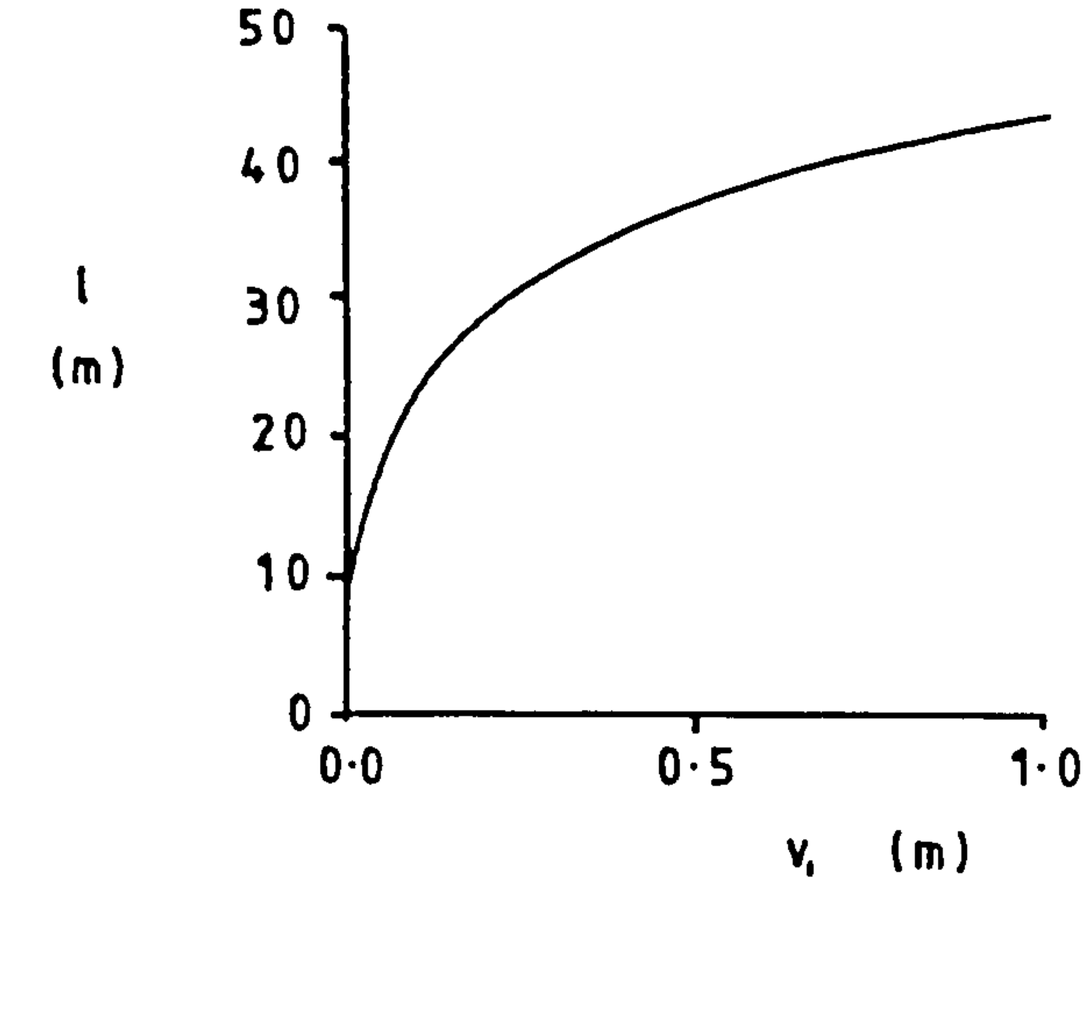

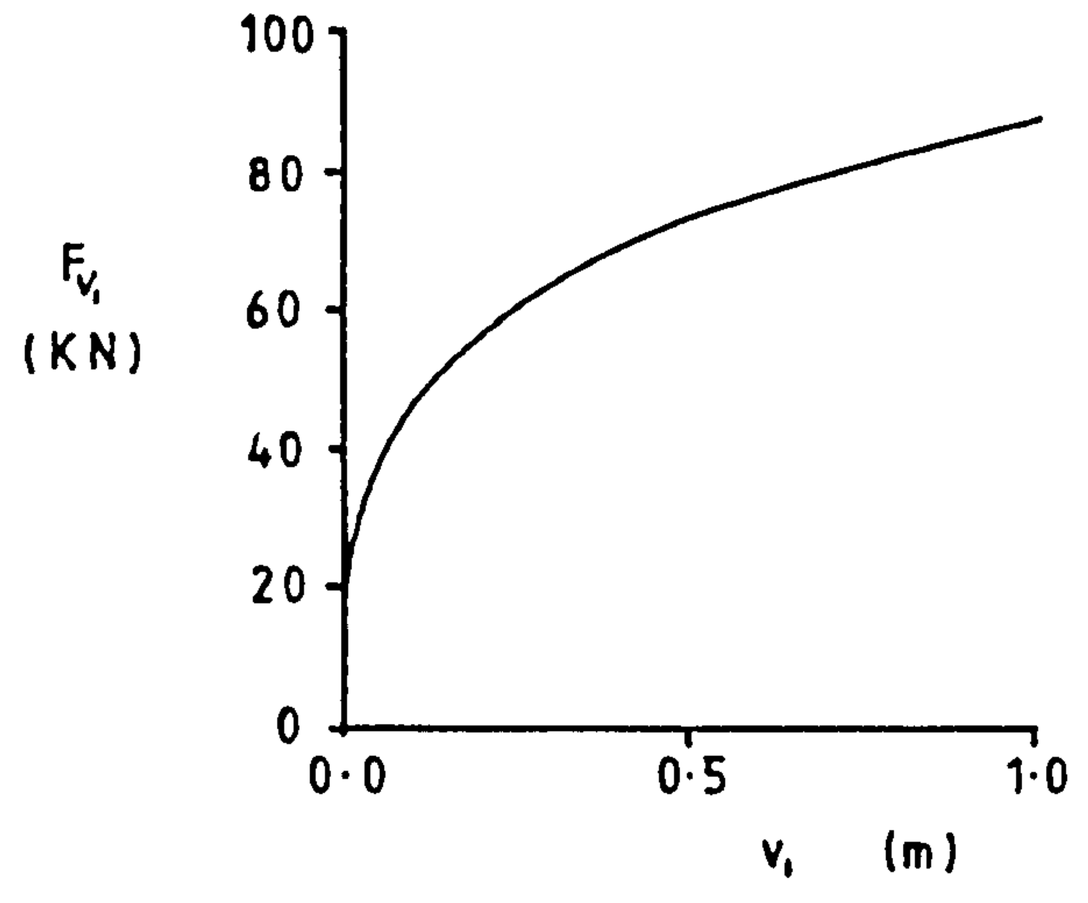

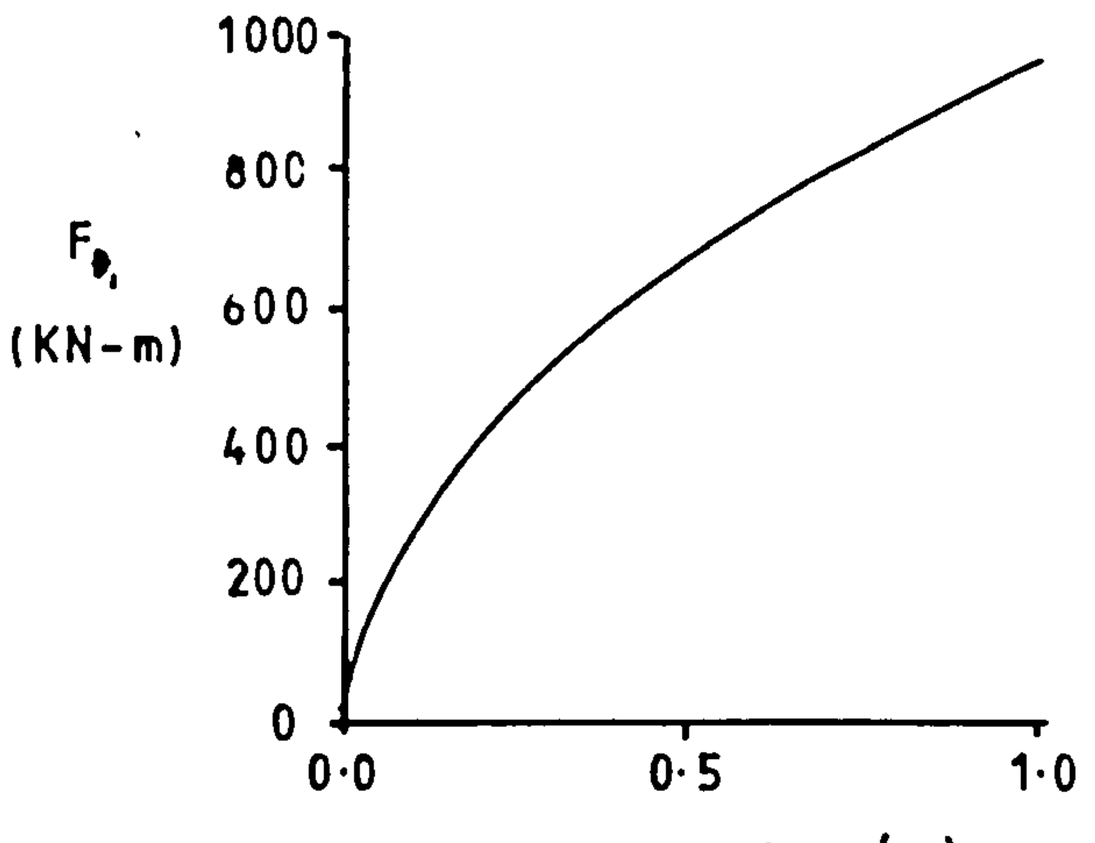

FIG 6.7 Pipe 2 Load Deflection Curves, $T=0$, $\theta_t=0$.

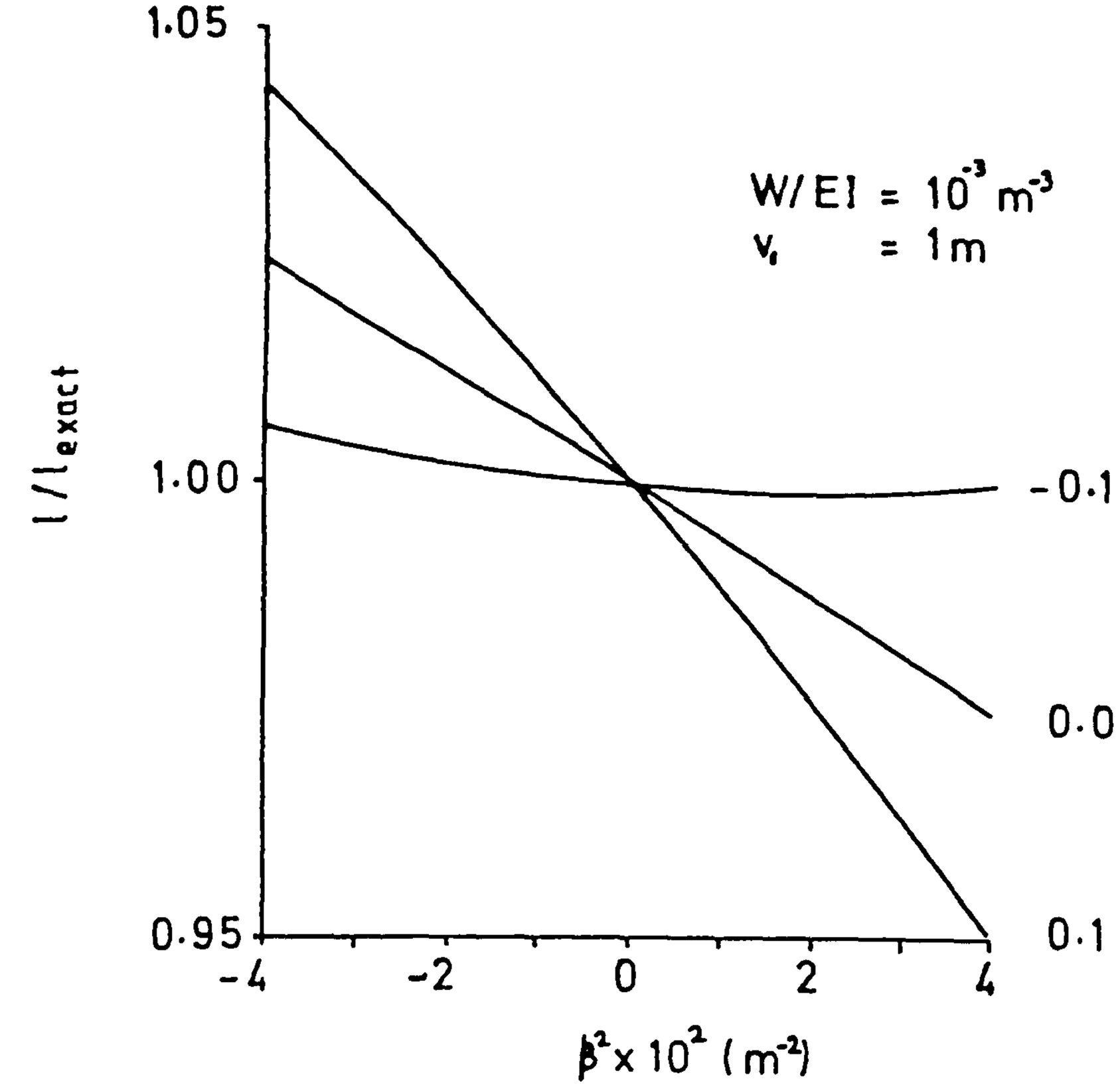

FIG 6.8 Comparison of l and l_{exact}

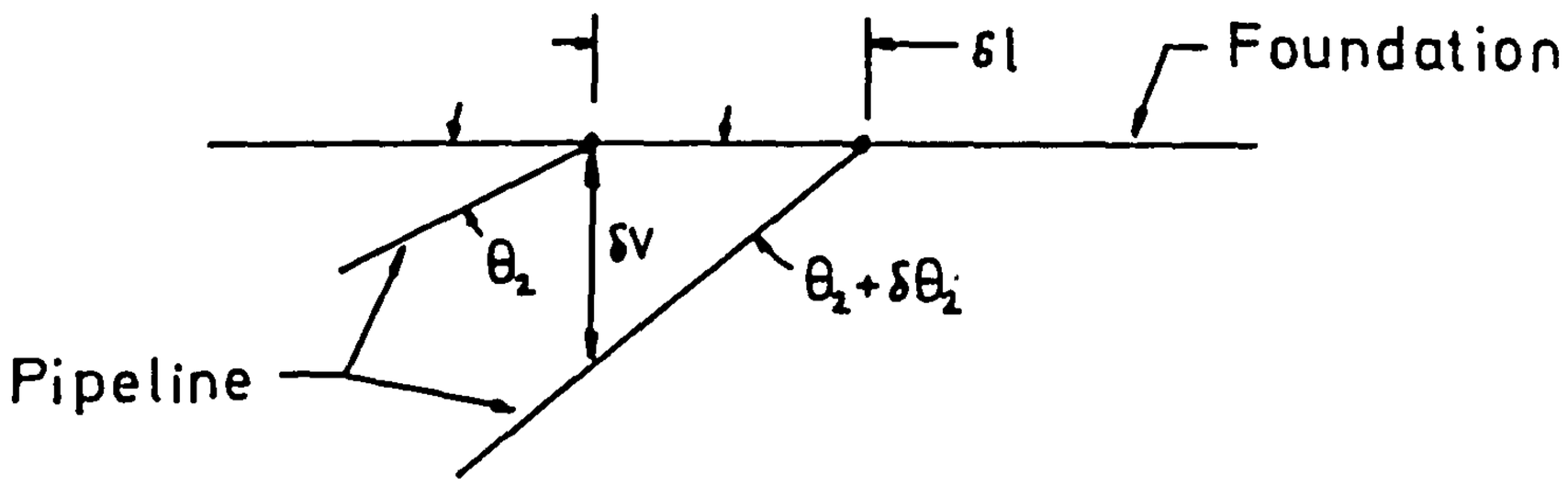

FIG 6.9 Moving Contact Point

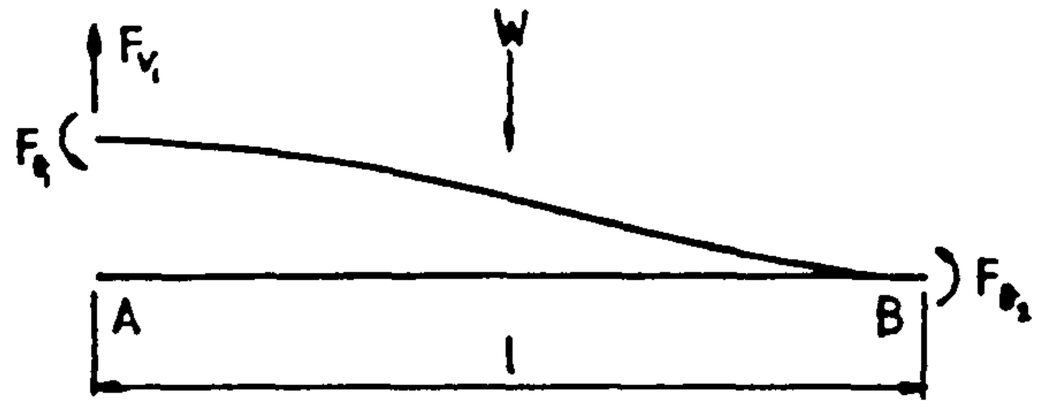

FIG 6.10 Generalised Elastic Forces

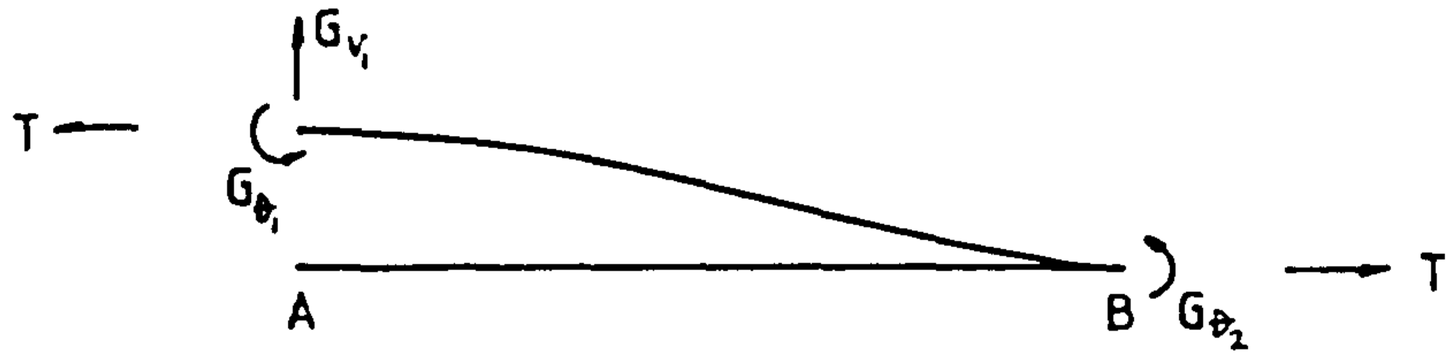

FIG 6.11 Generalised Stress Forces

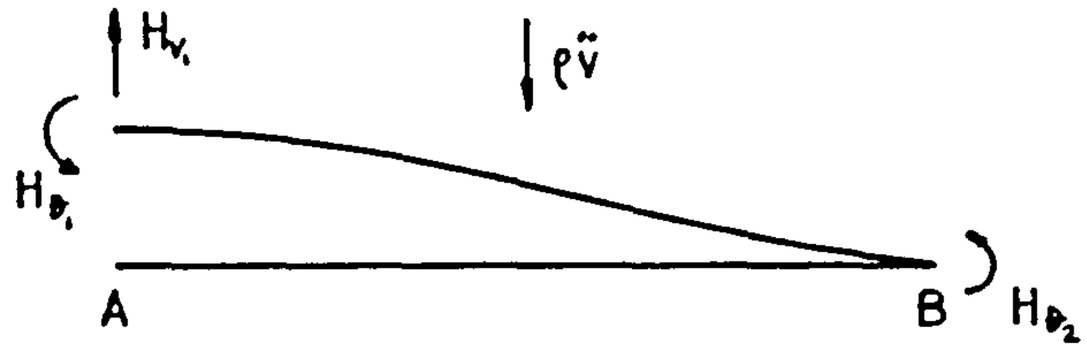

FIG 6.12 Generalised Inertia Forces

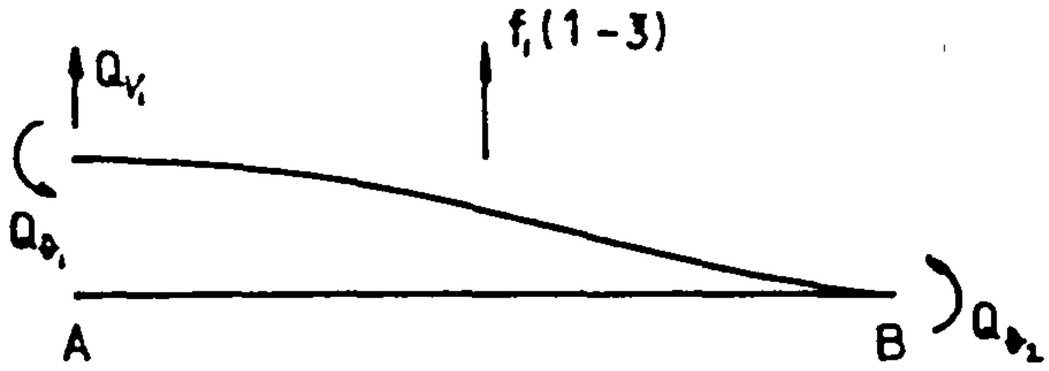

FIG 6.13 Generalised Loads

CHAPTER 7

RISER DYNAMICS

7.0 Introduction

A marine riser is essentially a slender conductor pipe connecting surface equipment to the wellhead on the seabed for the purpose of conveying fluids and hardware during drilling, operating and workover operations. As a result a failure of this system may result in severe environmental pollution and production shutdown with significant financial consequences. Thus a full understanding of the behaviour of the riser system under all installation, operating and survival conditions is required and over the last 10 years a considerable amount of literature has appeared addressed to such problems. From this work a large variety of solution methods have been developed including (Chakrabarti, 1982)

a) Analytical methods in which the riser differential equation is solved, normally by assuming a simple mathematical form for the deflection solution of the riser (Dareing and Huang, 1979, Kirk et al, 1979). Such methods are mathematically equivalent to the Galerkin method since global shape functions are normally selected and the required equation of motion obtained via a weighted residual method. The advantage of these methods is that only a relatively small number of freedoms are required for the dynamic analysis leading to light computing costs and making the approach highly attractive for initial design studies.

b) Direct numerical solution methods in which the riser differential equation is solved numerically by finite difference techniques (Sexton and Agbezuge, 1976) or direct integration (Burke, 1973). Such methods have the advantage that changes in geometry due to say

riser size or buoyancy modules are easily included but suffer from the disadvantage that often the boundary conditions must be handled in an iterative manner.

c) Finite Element methods in which the use of shape functions defined locally for each element in the model together with virtual work or energy considerations leads to an approximate set of coupled ordinary differential equations of motion in which the coefficient matrices are symmetric and banded (Gardner and Kotch, 1976). This method is well suited to complex geometries and in addition may be extended to include 3 dimensional problems and/or nonlinearities associated with large deformation or time variations in tension.

With the equations of motion formulated using one of the above methods the analysis approach may be classified according to the wave environment as (Kirk, 1984)

a) Deterministic or single wave in which the sea state is represented by a single wave of specified height and frequency. The resulting response of the riser, calculated in either frequency or time domains, is periodic enabling the distribution of maximum response and bending stress down the riser to be easily determined. Nonlinearities due to

i) Large displacement
ii) Time varying tension
iii) Change in wetted length
iv) Nonlinear hydrodynamic drag force

may all be included in the time domain analysis. In addition nonlinear wave theories such as Stokes III, Stokes V and Dean's Stream Function theory may also be used. For frequency domain analysis the above nonlinearities must either be neglected or linearised and wave forces calculated using linear wave theory.

b) Random analysis in which the sea state is

represented in the form of a continuous wave spectrum. This approach is more realistic than the single wave method in that the distribution of energy in the sea state is now represented. The resulting riser response may be calculated in the frequency domain using linearised spectral analysis leading to displacement and stress distributions in rms form. The main disadvantage of this method is that the nonlinear fluid drag force results in the probability distribution of these quantities being non-Gaussian with the result that expected peak values are not easily estimated. Alternatively a simulated random sea based on the wave spectrum may be used with linear wave theory to perform the analysis in the time domain. The nonlinearities outlined above may now be included and the resulting time histories of displacement and stress used directly to obtain peak values. The disadvantage of this approach is that reliable statistics for expected peak values can only be obtained by running a large number of simulations in which the coefficients appearing in the expression for the surface elevation are selected in a random manner (Tucker et al, 1984).

In addition to the wave environment the effects of tidal and wind generated current velocities may be added to those calculated using linear wave theory by

a) Assuming tidal and wave induced velocities are unidirectional leading in the absence of any lift forces to a 2D analysis. For a marine riser this approach is conservative since all the environmental forces are concentrated into a single direction or heading. In practice tank tests indicate that under such conditions considerable transverse response may occur as a result of vortex shedding along the length of the riser (Hartnup et al, 1982). Such effects are difficult to analyse exactly but approximate methods

have been presented for a regular wave (Rajabi et al, 1984).

b) Taking arbitrarily orientated current and wave headings leading to a full 3D analysis. For a regular wave this approach could be used in the time domain to investigate any coupling effects introduced by one or more of the above nonlinearities. For a random sea this method is mainly used with a spreading sea in which a spreading function is used to introduce an angular dependency into the normal unidirectional spectrum. In such seastates the recent Christchurch Bay Tower results indicate that transverse forces due to vortex shedding are not significant compared to the direct inline forces (Bishop, 1984).

In this chapter a linearised two dimensional frequency domain analysis under regular wave conditions is considered. The aim of this work is to synthesize the best aspects of the various analysis methods outlined above into a simple but flexible program. In order to enable consideration of a wide range of installation, operating and survival conditions, figure 7.1, the equations of motion are initially assembled using the Finite Element Method. The flexibility of this method is increased by the availability of simple linear and rotational spring and lumped mass elements together with the facility for moment releases at any point along the riser. Next in order to simplify the analysis a transformation is made to a mixed set of physical plus modal coordinates in a similar manner to that employed in component mode synthesis (Curnier, 1983). In addition to the reduced number of freedoms now involved in the dynamic analysis an important advantage of this approach is the increased physical insight accorded to the designer in interpreting the results of a modal analysis. To complete the analysis in the frequency domain an iterative solution is employed in which the nonlinear drag force is replaced at the start of each new

loop by an equivalent linear force calculated using the requirement of equal work per cycle. This is done using an improved version of the method originally proposed by Dareing and Huang (1979) in which the equivalent linear damping coefficient is calculated separately at each node in the original FE model. Finally the effect of the higher modes omitted in the truncated modal analysis is introduced as a static contribution to riser stresses using the modal acceleration method for data recovery.

7.1 Effective Tension

In resisting wave and current forces the tension distribution in the riser is of great importance and in most cases provides the majority of the overall stiffness. Now assuming the heave compensator on the surface vessel provides a constant top tension $T_t(0)$, figure 7.3, this tension distribution is obtained by resolving forces in the vertical direction as

$$T_t(X) = T_t(0) - \int_0^X W_t \, dX \qquad (7.1)$$

where W_t represents the weight/length of riser pipe in air and X is a global coordinate measured downwards from the top of the riser. In addition the effects of internal and external hydrostatic pressures acting on the pipe walls must be properly accounted for in the equations of motion (Sparks, 1984). In a similar manner to the linear pipespan analysis given in chapter 2 this is achieved most simply by utilising the concept of effective tension, figure 7.2. In this approach the internal and external fluid pressures acting on the pipe walls are first extended to act over the complete internal and external surfaces of the pipe element dX. These extended pressure fields may now be integrated directly using Archimedes' principle

and the resultant weight and buoyancy added into the pipe true weight in air W_t . Next balancing end pressure forces are introduced and added into the true tension so that the derived effective tension forces are completely equivalent to the original true forces. By this means the effective tension and weight are obtained as

$$T = T_t - p_i A_i + p_e A_e \tag{7.2}$$

$$W = W_t + g\rho_i A_i - g\rho_e A_e \tag{7.3}$$

where p_i, p_e = internal, external fluid pressure
A_i, A_e = internal, external pipe areas
ρ_i, ρ_e = internal, external fluid densities

Now resolving vertically for the effective forces the effective tension down the riser is given by

$$T(X) = T(0) - \int_0^X W\,dX \tag{7.4}$$

where the effective tension at $X = 0$ is given by

$$T(0) = T_t(0) - p_i(0)A_i(0) + p_e(0)A_e(0) \tag{7.5}$$

Equations (7.4) and (7.5) provide a convenient means of calculating the effective tension distribution in any given riser configuration.

7.2 Riser Finite Element Model

The riser Finite Element Model, figure 7.3, is obtained by dividing the riser pipe into a finite number of linear beam elements similar to those used in the pipeline model outlined in Chapter 3. Thus considering a typical element, figure 3.4, the riser lateral deflection is approximated by

$$v(x) = \left[N_1^\beta \; N_2^\beta \; N_3^\beta \; N_4^\beta \right] \underset{\sim}{a}^\beta = \left[N \right] \underset{\sim}{a}^\beta \qquad (7.6)$$

where here x is measured local to the element. For an element fully connected to its neighbours the shape functions N_i^β are given by equation (3.3) repeated here for convenience as

$$N_1^\beta = (1 - 3\xi^2 + 2\xi^3) \qquad (7.7a)$$

$$N_2^\beta = (\xi - 2\xi^2 + \xi^3) L_e \qquad (7.7b)$$

$$N_3^\beta = (3\xi^2 - 2\xi^3) \qquad (7.7c)$$

$$N_4^\beta = (\xi^3 - \xi^2) L_e \qquad (7.7d)$$

where $\xi = x/L_e$. For a moment release at end 1 these are modified to

$$N_1^\beta = (1 - \tfrac{3}{2}\xi + \tfrac{1}{2}\xi^3) \qquad (7.8a)$$

$$N_2^\beta = 0 \qquad (7.8b)$$

$$N_3^\beta = (\tfrac{3}{2}\xi - \tfrac{1}{2}\xi^3) \qquad (7.8c)$$

$$N_4^\beta = (-\tfrac{1}{2}\xi + \tfrac{1}{2}\xi^3) L_e \qquad (7.8d)$$

while for a moment release at end 2 we have

$$N_1^B = (1 - 3/2\,\xi^2 + 1/2\,\xi^3) \tag{7.9a}$$

$$N_2^B = (\xi - 3/2\,\xi^2 + 1/2\,\xi^3)L_e \tag{7.9b}$$

$$N_3^B = (3/2\,\xi^2 - 1/2\,\xi^3) \tag{7.9c}$$

$$N_4^B = 0 \tag{7.9d}$$

As noted in Chapter 3 for the set (7.7) these functions represent the deformations developed in an untensioned uniform beam subject to unit end displacements. The associated strain/potential energy in the element is

$$V = 1/2 \int_0^{L_e} \{ EI(v'')^2 + T(x)(v')^2 \}\, dx \tag{7.10}$$

where $T(x)$ is the effective tension distribution over the element. Now using equations (7.6) and (7.10) the linear element stiffness matrix may be evaluated using

$$k_{ij}^e = \frac{\partial^2 V}{\partial a_i^B\, \partial a_j^B} = \int_0^{L_e} \{ EI(N_i^B)''(N_j^B)'' + T(x)(N_i^B)'(N_j^B)' \}\, dx \tag{7.11}$$

To evaluate this integral it is now assumed that over the element the effective tension is given by [1]

(1) In view of equation (7.4) this assumption is equivalent to taking a constant effective weight along the element.

$$T(x) = T_0 + T_1 x \tag{7.12}$$

where T_0 and T_1 are constants. As a result equation (7.11) becomes

$$K_{ij}^e = EI K_{ij}^B + T_0 K_{ij}^\sigma + T_1 K_{ij}^x \tag{7.13}$$

where the subscripted quantities appearing on the RHS of this equation are evaluated using

$$K_{ij}^B = \int_0^{Le} (N_i^B)'' (N_j^B)'' \, dx \tag{7.14a}$$

$$K_{ij}^\sigma = \int_0^{Le} (N_i^B)' (N_j^B)' \, dx \tag{7.14b}$$

$$K_{ij}^x = \int_0^{Le} x (N_i^B)' (N_j^B)' \, dx \tag{7.14c}$$

Using these terms the element force-displacement transformation is given by the linear form

$$\underset{\sim}{f}^B = \left[EI k^B + T_0 k^\sigma + T_1 k^x \right] \underset{\sim}{a}^B \tag{7.15}$$

where the 4 x 4 matrices k^B, k^σ and k^x contain the coefficients (7.14) above. Next considering the element kinetic energy and proceeding as outlined in Chapter 3 the element mass matrix may be written as

$$m^e = \rho_B m^B = \rho_B \left[m_{ij}^B \right]$$

where ρ_B is the mass/length of riser pipe plus contents plus fluid added mass and

$$m_{ij}^B = \int_0^{Le} N_i^B N_j^B \, dx \tag{7.16}$$

In addition the element load vector arising from a distributed load $f(x,t)$ along the element is given by

$$\underset{\sim}{p}^e(t) = \{ p_i^e(t) \} \tag{7.17a}$$

where

$$p_i^e(t) = \int_0^{Le} f(x,t) N_i^B \, dx \tag{7.17b}$$

These element quantities may now be assembled to give the required global equation of motion as

$$M\ddot{\underset{\sim}{q}} + K\underset{\sim}{q} = \underset{\sim}{P}(t) \tag{7.18}$$

where symbolically

$$M = \sum_e^I m^e \tag{7.19a}$$

$$K = \sum_e^I k^e \tag{7.19b}$$

$$\underset{\sim}{P}(t) = \sum_e^I \underset{\sim}{p}^e(t) \tag{7.19c}$$

Here $\underset{\sim}{q}$ is an assembled vector of nodal displacements and rotations while $\sum_e^I$ represents a summation over elements. The element matrices k^B, k^σ, k^x and m^B required for this operation are tabulated for reference in appendix C

for the various end conditions considered above. In addition simple linear and rotational springs together with lumped mass elements may be included by simply adding the required spring rate/lumped masses into the appropriate diagonal locations of the assembled matrices K and M. The evaluation of the element load vector f^e is considered in the following section.

7.3 Fluid Loading Model

For a small diameter structure such as a marine riser the fluid-structure interaction cannot be modelled mathematically using incompressible potential flow theory since flow separation and vortex shedding introduces rotation into the flow. As a result the mathematical model must rely on a semi-empirical formulae, the most well known of which is Morison's equation (Morison et al, 1950). For a moving vertical cylinder this equation gives the hydrodynamic force/length as

$$f(x,t) = C_M \frac{\rho_e \pi D^2}{4} \dot{u}_w + \tfrac{1}{2} \rho_e C_D D (u_c + u_w - \dot{v}) |u_c + u_w - \dot{v}| \qquad (7.20)$$

where C_M and C_D are empirical inertia and drag coefficients, D is the hydrodynamic diameter of the riser, and u_c and u_w are the horizontal current and wave induced fluid particle velocities. Since the drag component of this load depends quadratically on the fluid-structure relative velocity $(u_c + u_w - \dot{v})$ an 'exact' response solution can only be obtained by numerically integrating equation (7.18) in the time domain. For the purpose of a linearised frequency domain solution the dynamic component in equation (7.20) is approximated by

$$f(x,t) = C_M \frac{\rho_e \pi D^2}{4} \dot{u}_w + C_E (u_w - \dot{v}) \qquad (7.21)$$

where as detailed in appendix E the equivalent coefficient C_E is calculated using the requirement of equal work/cycle. Substituting this into equation (7.17) and using equation (7.6) now gives

$$\underset{\sim}{F}^e = \underset{\sim}{F}_E^e - \left[b^e\right]\underset{\sim}{\dot{a}}^s \tag{7.22}$$

where the components of the equivalent element load vector $\underset{\sim}{F}_E^e$ and hydrodynamic damping matrix b^e are given by

$$(F_E^e)_i = \int_0^{Le} N_i^s f_E(x,t)\,dx \tag{7.23a}$$

$$b_{ij}^e = \int_0^{Le} C_E N_i^s N_j^s\,dx \tag{7.23b}$$

and the linearised hydrodynamic load acting on the element is

$$f_E(x,t) = C_M \frac{\rho_e \pi D^2}{4}\dot{u}_w + C_E u_w \tag{7.24}$$

Now using linear wave theory the horizontal fluid particle velocity at depth $X-h$, figure 7.3, due to a wave of height H and frequency ω may be written in complex form as

$$u_w(X,t) = \frac{\omega H}{2}\frac{\cosh k(d+h-X)}{\sinh kD}e^{i\omega t} = U_w(X)e^{i\omega t} \tag{7.25}$$

where the wave number k is given by the dispersion relation

$$k \tanh kd = \omega^2/g \qquad (7.26)$$

Thus substituting equation (7.25) into equation (7.24) we find

$$f_E(x,t) = \left(i\omega C_M \frac{\rho_e \pi D^2}{4} + C_E\right) U_w(X) e^{i\omega t} = F_E(X) e^{i\omega t} \qquad (7.27)$$

which for the purpose of evaluating (7.23a) is approximated to

$$f_E(x,t) = \left\{F_E(X_1)(x/he) + F_E(X_2)(1-x/he)\right\} e^{i\omega t} \qquad (7.28)$$

where X_1 and X_2 are the global coordinates at the element nodes 1 and 2. As a result the element load vector $\underset{\sim}{P}_E^e$ may be written as

$$\underset{\sim}{P}_E^e = \underset{\sim}{P}_E^e e^{i\omega t} \qquad (7.29)$$

where the components of the complex element load $\underset{\sim}{P}_E^e$ are given by

$$(P_E^e)_i = F_E(X_1)\int_0^{Le} N_i^B(x/Le)dx + F_E(X_2)\int_0^{Le} N_i^B(1-x/Le)\,dx \qquad (7.30)$$

These generalised loads are evaluated in terms of $F_e(X_1)$ and $F_E(X_2)$ in appendix C for the various element end

conditions considered above. In addition in evaluating equation (7.23b) it is assumed that

$$C_E = \tfrac{1}{2}(C_{E_1} + C_{E_2}) \tag{7.31}$$

where C_{E_1} and C_{E_2} are the equivalent damping coefficients evaluated at nodes 1 and 2. As a result we find

$$b_{ij}^{e} = C_E \int_0^{L_e} N_i^B N_j^B dx = C_E M_{ij}^B \tag{7.32}$$

Now with all terms in equation (7.22) evaluated the riser response equation (7.18) becomes

$$M\ddot{\underset{\sim}{a}} + B\dot{\underset{\sim}{a}} + K\underset{\sim}{a} = \underset{\sim}{P}_E e^{i\omega t} \tag{7.33}$$

where the assembled hydrodynamic damping matrix B and complex fluid loading vector $\underset{\sim}{P}_E$ are given symbolically by

$$B = \sum_{e}^{1} b^{e} \tag{7.34a}$$

$$\underset{\sim}{P}_E = \sum_{e}^{1} \underset{\sim}{P}_E^{e} \tag{7.34b}$$

It is noted that the element quantities b^e and P_E^e are only evaluated for fully submerged members (i.e. both ends below MWL).

7.4 Modal Solution

Even for a relatively simple structure such as a marine riser the equations of motion in physical coordinates, as represented by equation (7.33), may typically contain 100 - 200 dof in order to accurately model both structure and load. As a consequence the volume of output produced may be unhelpful in initially interpreting the response characteristics of a new design. For this reason a transformation is now made into modal coordinates in which 5 - 20 dof are typically retained in the dynamic analysis. As a preliminary to this transformation an eigenvalue analysis must be performed in order to determine the free vibration frequencies and mode shape of the structure. Once this has been done the response of the riser in each of these modes may be readily understood in terms of SDOF dynamics. For marine riser analysis one complication associated with this general procedure is that certain dof in the assembled displacement vector have prescribed time histories and so must consequently be retained in the analysis. One method for doing this is now outlined as follows. First the global displacement vector $\underset{\sim}{a}$ is partitioned into the following sets

$$\underset{\sim}{a} = \begin{bmatrix} \underset{\sim}{a}_R \\ \underset{\sim}{a}_P \\ \underset{\sim}{a}_Z \end{bmatrix} \tag{7.35}$$

where $\underset{\sim}{a}_Z$ represents freedoms having zero response, $\underset{\sim}{a}_P$ represent freedoms having non zero prescribed response and $\underset{\sim}{a}_R$ are the remaining unknown freedoms. Now considering the set $\underset{\sim}{a}_P$ as initially fixed the equation of motion for free undamped vibration is

$$M_{RR}\,\ddot{\underset{\sim}{a}}_R + K_{RR}\,\underset{\sim}{a}_R = 0 \tag{7.36}$$

where the matrices M_{RR} and K_{RR} are obtained from M and K respectively by deleting all rows and columns pertaining to the freedoms q_z and q_p . For vibration in a single mode we may set

$$q_R = \phi_R \sin \omega t \tag{7.37}$$

which on substituting into equation (7.36) yields the standard eigenvalue problem

$$(-\omega^2 M_{RR} + K_{RR})\phi_R = 0 \tag{7.38}$$

Solving this for the first N eigenpairs (ω_i, ϕ_{R_i}) enables the displacements q_R to be written as

$$q_R = \sum_{i=1}^{N} q_i(t)\phi_{R_i} = \left[\Phi_{RN}\right] q_N \tag{7.39}$$

where $q_i(t)$ are generalised modal displacements. Expanding this to the full displacement set q gives

$$q = \sum_{i=1}^{N} q_i(t)\phi_i = \left[\Phi_N\right] q_N \tag{7.40}$$

where each eigenvector ϕ_i is obtained from the corresponding vector ϕ_{R_i} by inserting zeroes at all locations corresponding to the freedoms q_z and q_p . The required nonzero motion at the freedoms q_p is now added in by rewriting this equation as

$$q = \left[\Phi_N\right] q_N + \left[\Phi_p\right] q_p = \left[\Phi\right] q \tag{7.41a}$$

where $$\left[\underset{\sim}{\Phi}\right] = \left[\underset{\sim}{\Phi}_N \quad \underset{\sim}{\Phi}_P\right] \tag{7.41b}$$

$$\underset{\sim}{q} = \begin{bmatrix} \underset{\sim}{q}_N \\ \underset{\sim}{q}_P \end{bmatrix} \tag{7.41c}$$

Here each column in the matrix $\underset{\sim}{\Phi}_P$ represents the static deflection of the riser associated with a unit deflection in the corresponding freedom$ $\underset{\sim}{q}_P$. Now substituting equation (7.41a) into equation (7.33) and considering virtual work the modal equation of motion in terms of the set $\underset{\sim}{q}$ is obtained as

$$m\ddot{\underset{\sim}{q}} + b\dot{\underset{\sim}{q}} + k\underset{\sim}{q} = \underset{\sim}{Q} e^{i\omega t} \tag{7.42}$$

where the reduced mass, damping, stiffness and load are given by

$$m = \underset{\sim}{\Phi}^T M \underset{\sim}{\Phi} \tag{7.43a}$$

$$b = \underset{\sim}{\Phi}^T B \underset{\sim}{\Phi} \tag{7.43b}$$

$$k = \underset{\sim}{\Phi}^T K \underset{\sim}{\Phi} \tag{7.43c}$$

$$\underset{\sim}{Q} = \underset{\sim}{\Phi}^T \underset{\sim}{Q}_E \tag{7.43d}$$

Next on setting $\underset{\sim}{q} = \underset{\sim}{Q} e^{i\omega t}$ this becomes

$$\left[D\right]\underset{\sim}{Q} = \left[-\omega^2 m + i\omega b + k\right]\underset{\sim}{Q} = \underset{\sim}{Q} \tag{7.44}$$

where D represents the dynamic stiffness matrix and $\underset{\sim}{Q}$ is a vector of complex unknown plus prescribed displacements. Partitioning this equation as equation (7.41c) gives

$$\begin{bmatrix} D_{NN} & D_{NP} \\ D_{PN} & D_{PP} \end{bmatrix} \begin{bmatrix} \underset{\sim}{Q}_N \\ \underset{\sim}{A}_P \end{bmatrix} = \begin{bmatrix} \underset{\sim}{P}_N \\ \underset{\sim}{P}_P + \underset{\sim}{R}_P \end{bmatrix} \tag{7.45}$$

where $\underset{\sim}{A}_P$ are the prescribed complex displacements and $\underset{\sim}{P}_P$ the associated reaction forces. Thus considering the first of these equations we may write

$$\begin{aligned} \left[D_{NN}\right] \underset{\sim}{Q}_N &= \left[-\omega^2 M_{NN} + i\omega b_{NN} + k_{NN}\right] \underset{\sim}{Q}_N \\ &= \underset{\sim}{P}_N - \left[D_{NP}\right] \underset{\sim}{A}_P \end{aligned} \tag{7.46}$$

which may be solved by the following direct iteration scheme

$$\underset{\sim}{Q}_N^{\,i} = \left[D_{NN}^{\,i-1}\right]^{-1} \left\{ \underset{\sim}{P}_N^{\,i-1} - \left[D_{NP}^{\,i-1}\right] \underset{\sim}{A}_P \right\} \tag{7.47}$$

Here the hydrodynamic damping and load terms evaluated using the riser response $\underset{\sim}{Q}_N^{\,i-1}$ at the end of iteration $i-1$ are represented by

$$\left[D_{NN}^{\,i-1}\right] = \left[D_{NN}\left(\underset{\sim}{Q}_N^{\,i-1}\right)\right] \tag{7.48a}$$

$$\left[D_{NP}^{\,i-1}\right] = \left[D_{NP}\left(\underset{\sim}{Q}_N^{\,i-1}\right)\right] \tag{7.48b}$$

$$\underset{\sim}{P}_N^{\,i-1} = \underset{\sim}{P}_N\left(\underset{\sim}{Q}_N^{\,i-1}\right) \tag{7.48c}$$

Hence the process is to first assemble these quantities based on some initial assumed response Q_N^0 and using equation (7.47) solve for an improved response Q_N' . This solution is then used to update the above quantities and the whole process continued until convergence is achieved. At each step in this process it is necessary to factorise the $N \times N$ matrix D_{NN} which in view of the b_{NN} term appearing in equation (7.46) is a full matrix. This may be avoided by utilising a modified scheme in which the damping matrix b_{NN} is first written as

$$b_{NN} = b_D + b_{OF} \tag{7.49}$$

where b_D and b_{OF} contain respectively the diagonal and off-diagonal terms in b_{NN} . As a result equation (7.46) becomes

$$\begin{aligned}\left[D_D\right] \underset{\sim}{Q}_N &= \left[-\omega^2 M_{NN} + i\omega b_D + k_{NN}\right] \underset{\sim}{Q}_N \\ &= \underset{\sim}{P}_N - \left[D_{NP}\right] \underset{\sim}{A}_P - \left[i\omega b_{OF}\right] \underset{\sim}{Q}_N \end{aligned} \tag{7.50}$$

which may be solved by the iterative scheme

$$\underset{\sim}{Q}_N^i = \left[D_D^{i-1}\right]^{-1} \left\{ \underset{\sim}{P}_N^{i-1} - \left[D_{NP}^{i-1}\right] \underset{\sim}{A}_P - \left[i\omega b_{OF}^{i-1}\right] \underset{\sim}{Q}_N^{i-1} \right\} \tag{7.51}$$

Here it is noted that

a) The matrix b_D is by definition diagonal while the matrices M_{NN} and k_{NN} are diagonal as a result of the orthogonality of normal modes. It follows that the combined matrix D_D is also diagonal and the numerical solution to equation (7.51) is trivial.

b) Practical experience with this scheme has shown that convergence rates can be significantly improved by introducing a relaxation factor R using

$$\underset{\sim}{Q}_N^i = R\underset{\sim}{Q}_N^i + (1-R)\underset{\sim}{Q}_N^{i-1} \qquad (7.52)$$

Here $\underset{\sim}{Q}_N^i$ appearing on the RHS is first found using equation (7.51) above while the value on the LHS is the relaxed value for use in the next iteration. Using this scheme R = 0.7 - 0.8 appears optimum with typically 7÷8 iterations being required to reduce the maximum percentage change in $\underset{\sim}{Q}_N$ (calculated on a component by component basis) between two successive iterations to less than 1%.

c) In practice it is often convenient to undertake the analysis in two steps. First a combined static and eigenvalue analysis is undertaken in Batch mode to determine the various columns in the matrix appearing in equation (7.41a). This is then followed by any number of response runs using the above modified iterative scheme. As a result of the highly efficient solution scheme such restart runs may conveniently be made in interactive mode even on relatively small machines.

7.5 Modal Acceleration Data Recovery

The truncated modal analysis outlined in the above section produces a displacement solution which converges rapidly as the number of modes included in the displacement series, equation (7.40), is increased. As a consequence the dynamic analysis may often be performed with as few as 5 dynamic modes, (Dareing and Huang, 1979). Unfortunately, for many structures, the convergence of the corresponding stress solution is less rapid indicating the requirement for an increased number of dof in the dynamic analysis. However since the response of such

truncated modes will be quasi-static or stiffness dominated this can be avoided by including the effect of all such modes in a static manner. To do this the final converged modal solution

$$\underset{\sim}{q} = \underset{\sim}{Q} e^{i\omega t} = \begin{bmatrix} \underset{\sim}{Q}_N \\ \underset{\sim}{A}_P \end{bmatrix} e^{i\omega t} \tag{7.53}$$

is substituted into equation (7.41a) to give the initial displacement solution

$$\underset{\sim}{a} = [\underset{\sim}{\Phi}]\,\underset{\sim}{q} = [\underset{\sim}{\Phi}]\,\underset{\sim}{Q}\, e^{i\omega t} = \underset{\sim}{A}\, e^{i\omega t} \tag{7.54}$$

The corresponding riser velocities and accelerations are

$$\dot{\underset{\sim}{a}} = i\omega \underset{\sim}{A}\, e^{i\omega t} \tag{7.55a}$$

$$\ddot{\underset{\sim}{a}} = -\omega^2 \underset{\sim}{A}\, e^{i\omega t} \tag{7.55b}$$

which on substituting into the untransformed equation of motion (7.33) and rearranging gives

$$[K]\underset{\sim}{a} = \left\{ \underset{\sim}{P}_E - [i\omega B]\,\underset{\sim}{A} + [\omega^2 M]\,\underset{\sim}{A} \right\} \tag{7.56}$$

Solving this equation for $\underset{\sim}{a}$ now provides an improved displacement solution in which the static effect of the truncated modes is now included. Element internal stress resultants may now be obtained from this solution by partitioning out the element displacements $\underset{\sim}{a}^{\beta}$ and using equation (7.15).

7.6 Results and Discussion

The modelling and analysis procedure proposed in the above sections is now illustrated by considering the following structures

a) Deep water Drilling Riser
b) Production Riser
c) Partially run Riser with guide wires
d) Articulated column

In each case an outline of the problem is first presented followed by a description of the corresponding Finite Element Model. By this means the engineering assumptions and modelling methods inherent in the problem formulation stage are described. This is then followed by a brief description of some typical results.

7.6.1 Deep Water Drilling Riser

In order to verify the basic accuracy of the program the first problem considered is the American Petroleum Institute test case 1500-20-1-D for which published results, obtained from a large number of programs, are available (API, 1977). This case consists of a 1520ft (465m) long 16 inch (.406m) diameter drilling riser attached at its upper and lower ends by frictionless pinned connections, figure 7.4. The riser is assumed to contain drill mud only and to carry two externally attached 4" control lines. Other basic data calculated from the API Bulletin is:-

Internal diameter of Riser Pipe	.3746m
Second moment of area of Riser Pipe	$3.714m^4$
Effective weight (i.e. total weight per length of 50ft joint plus contained drill mud in water)	2.77KN/m
Top Tension	1291KN

Here it is noted that the second moment of area (as used in the structural model) is calculated on the riser pipe section only while the total weight includes all accessories such as connection joints plus control lines. This configuration is now subjected to colinear wave and current action for which the following data is specified:-

Wave Period	9 secs
Wave Height	6.1m
Current Profile: Linear, 0.26 m/s	
at MWL, zero at Lower Ball joint	
Effective Hydrodynamic Diameter	0.66m
Drag coefficient,	0.7
Inertia coefficient,	1.5
Vessel Surge (peak-peak)	1.22m
Vessel phase (after wave crest)	15^{o}

The Finite Element model used for this problem, figure 7.4, consists of 5 elements above the MWL (these elements have zero hydrodynamic load), 40 elements in the first 100m of water depth and 55 elements in the final section to the lower ball joint. The corresponding nodes are numbered 1 (upper ball joint) through 101 (lower ball joint) so that the physical displacement set $\underset{\sim}{a}$, equation (7.35), contains 202 freedoms. The zero and prescribed sets are given by

$$\underset{\sim}{a}_z = \{ v_{101} \}$$

$$\underset{\sim}{a}_p = \{ v_1 \}$$

with the result that the static and dynamic modes (all normalised for 1m maximum displacement) are obtained as figure 7.5. Here it is noted that the high tension variation in the riser (1291KN at UBJ to zero at LBJ)

causes the static and dynamic shapes to bulge excessively near the LBJ. The effect of this on riser bending stress is shown in figure 7.6 where a maximum stress amplitude of 35N/mm^2 is observed at a location 40m above the LBJ. These values compare favourably with those given in the API Bulletin. This stress is reduced to less than 10N/mm^2 by increasing the top tension to 2225KN for which the effective tension at the LBJ is now 940KN. The effect on the static and dynamic deflection shapes is shown in figure 7.7.

7.6.2 Production Riser

Figure 7.8 shows an early design configuration for a production riser on Conoco's Hutton field Tension Leg Platform. The top of this riser is connected via a casing hanger to a Christmas Tree unit with fluid transfer to production equipment accomodated via a flexible "gooseneck" hose. The combined weight of this unit is 15,000 lbs. Immediately below this level a total tension of 110,000 lbs is provided via hydraulic cylinders so that the riser tension (real) at the upper analysis datum, figure 7.8, is 95,000 lbs. In addition the maximum internal operating pressure at this point is 500 psi which acting over the internal cross sectional area gives a maximum force of 200 lbs. Since this is small compared to the real tension the effective and real tensions at the upper analysis datum are assumed equal. At its lower end the riser is connected to the subsea tieback unit via a 50 ft taper joint in which the external diameter varies linearly from 9.625" to 16.77". This unit is provided to relieve the cantilever stresses occurring in the system as a result of the full connectivity to the subsea wellhead, figure 7.8. Other structural data used in the analysis is

Riser pipe internal diameter (includes taper joint)	8.681"
Riser pipe external diameter	9.625"
Effective weight of riser pipe (assumed constant over complete length)	67 lb/ft

while the environmental data is

Wave height	10 ft
Wave Period	7 sec
Current velocity	zero
Inertia coefficient,	2.0
TLP surge (peak-peak)	1 m
TLP phase (after wave crest)	50°

The FEM used, figure 7.8, is obtained by dividing the constant section length of the riser into 50 elements with a further 10 elements being used for the lower taper joint. Since these elements assume a constant section the properties of each element are calculated using the dimensions of the taper section occurring at the centre of each element. By this means the continuous increase in stiffness is modelled as 10 discreet steps. It is noted however that the mass and effective weight per length for these elements are taken in the model as equal to the values used for the rest of the riser pipe. The zero and prescribed motion sets are now

$$\underset{\sim}{a}_z = \{ v_{61} , \theta_{61} \}$$

$$\underset{\sim}{a}_p = \{ v_1 \}$$

with corresponding static and dynamic deflection shapes as shown in figure 7.9. The riser response in these modes

for the above 10 ft 7 second wave is summarised in the following table for a range of C_D values

Mode	ω/ω_n	C_D = 0.5		C_D = 1.0		C_D = 2.0	
		β %	Q ft	β %	Q ft	β %	Q ft
1	1.06	18.4	5.8	26.6	4.3	38.2	3.2
2	0.52	6.4	0.44	9.2	0.46	13.1	0.47
3	0.34	4.0	0.15	5.7	0.15	8.1	0.16

Here ω/ω_n is the wave to mode frequency ratio, β is the percentage of critical damping calculated using the damping coefficients occurring in the matrix b_D, equation (7.50), and Q is the amplitude of the generalised modal displacement. It is clear that the response is dominated by the first resonant mode with increased leading to increased damping and reduced response. The corresponding bending stress distributions are shown in figure 7.10 where it is noted that the maximum bending stress occurs at the top of the taper section and decreases rapidly thereafter due to the increased steel cross sectional area. These bending stress distributions are essentially the distributions associated with a combined deflection due to static plus first dynamic mode shapes and show a point of contraflexure close to that occurring in the first mode, figure 7.9.

7.6.3 Partially run Riser with Guide Wires

Figure 7.11 shows a partially run riser tensioned by means of a heavy guideframe attached to its lower end. In turn this guideframe passes over pretensioned guidelines which as well as ensuring accurate stabing at the wellhead also provide a horizontal stiffness to the system. Denoting the length and total combined tension in these

guidewires as L_G and T_G respectively and assuming small deflections the static force required to produce an out-of-line deflection v_G at the guideframe is

$$F_G = \frac{L_G T_G}{L_R(L_G - L_R)} u_G = K_G u_G \qquad (7.57)$$

where L_R is the length of run riser and K_G is the equivalent guidewire static stiffness, figure 7.12. This stiffness is noted to be infinite at the beginning and end of the running operation and to have a minimum at $L_R = L_G/2$. As a result of this arrangement the riser tension (real) immediately above the guideframe is

$$T_R(L_R) = W - p_e A_e + p_i A_i \qquad (7.58)$$

where W is the effective weight in water of the unconnected guideframe and $p_e A_e$ and $p_i A_i$ are pressure forces acting over the riser external/internal sections, figure 7.13. The corresponding effective tension is obtained using equation (7.2) as $T(L_R) = W$ with the result that the effective tension distribution over the run length of riser is

$$T(X) = W + w(L_R - X) \qquad (7.59)$$

where w is the effective weight per length of riser pipe. The FEM used for this problem is obtained by dividing the run section of riser into 50 beam elements connecting nodes 1 to 51, figure 7.11. Also connecting node 51 is a lumped mass element M_G representing the inertia effects of the guideframe together with a guidewire spring support K_G as calculated by equation (7.57)

above. The zero and prescribed displacement sets for this model are

$$\underset{\sim}{q}_z = \{ \theta_{52} \}$$

$$\underset{\sim}{q}_p = \{ v_1 \}$$

while in view of the guidewire geometry, figure 7.12, we also require the linear constraint condition

$$v_{52} = \frac{L_G - L_R}{L_G} v_1 \qquad (7.60)$$

Since v_1 is a prescribed displacement this condition is most simply accounted for by using equation (7.60) to obtain a prescribed input for v_{52} . The numerical data used with this model is

Riser external diameter	250mm
Riser internal diameter	225mm
Riser effective weight (assuming flooded)	0.7KN/m
Guideframe mass	10 tonne
Guideframe effective weight	100KN
Guidewire tension (all lines)	300KN
Guidewire length	160m
Water depth	150m

As a result the static and dynamic deflection shapes for a range of L_R are obtained as shown in figures 7.14 to 7.17. It is noted that for small L_R the static deflection shape corresponds closely to a horizontal rigid body translation of the riser. Figure 7.18 shows the corresponding variation in modal frequencies with mode 2 experiencing increased frequency between L_R = 120m

and L_R = 160m. This phenomena is associated with the rapidly increasing end stiffness seen by the riser during this final stage of running. Finally figure 7.19 shows the amplitude of dynamic response resulting from a 4m 9 sec wave. Such data may be used to ensure the riser does not sustain any damage during installation as a result of impacting other parts of the structure.

7.6.4 Articulated Column

Figure 7.20 shows an articulated loading column similar to that originally used in the UK Thistle Field. In common with other articulated loading platforms this structure is attached to the seabed by means of a universal joint enabling the lower riser section to oscillate in any vertical plane. However in view of the exposed location and water depth the design also provides for a second articulated connection between the riser and the upper buoy section at a depth 40m below the MWL. This upper buoy provides the necessary top tension for the riser system and also supports a small deck together with associated equipment. In addition, in certain designs, the buoy may also provide for oil storage so enabling continued production when weather conditions inhibit tanker loading. The basic structural data for this design as taken here is

Diameter of buoy	7.27m
Wall thickness	30mm
Weight in air	53KN/m
Effective weight (in water)	-365KN/m
Diameter of riser	3.5m
Riser wall thickness	25mm
Weight in air	21KN/m
Effective weight (in water)	-75KN/m

As a consequence the real and effective tension distributions down the column are computed as shown in figure 7.21.

It is noted that unlike the riser systems considered above the effective tension T is zero at $x=0$ and increases with depth as a result of buoyancy.

The FEM used for this structure, figure 7.20, is obtained by dividing the column into a total of 80 elements with the riser/buoy articulation accounted for by specifying a moment release on element 40 node 41. The zero displacement set for this model is

$$\underset{\sim}{q}_z = \{ v_{81} \}$$

while since no prescribed motion is specified the set $\underset{\sim}{q}_p$ is null. The associated dynamic mode shapes consist of two essentially rigid body motions with the first "elastic" mode (i.e. mode 3) corresponding closely to the fundamental mode of the simply supported riser, figure 7.22. Next figure 7.23 shows the horizontal shear force per unit wave height acting on the upper articulated joint. It is noted that

a) All curves peak at frequencies corresponding closely to the two rigid body modes.
b) Even for the relatively large diameter members used the effect of the nonlinear drag force is significant causing the unit response to decrease with increasing wave height at frequencies near to resonance. This behaviour may be understood by noting that at $\omega = 0.25$ rad/sec (i.e. resonant with lst mode) the percentages of critical damping observed for the first mode at H = 10, 20 and 30m are respectively 41%, 59% and 75%. Thus increasing H leads to increased damping and decreased unit response. Away from resonance damping ratios also increase with H but have little effect on response.

Figure 7.24 shows the effect of increasing C_D to 1.75 where it is noted that the response is now slightly flatter. Finally figure 7.25 shows the bending stress distribution in the steel plating for a 30 second 30 metre design wave.

7.7 Conclusions and Further Work

Based on the theory and example problems considered in the previous sections the following conclusions are made

a) The use of the finite element method to model the riser system provides considerable flexibility and enables a single program to handle a wide range of installation, operating and survival conditions.

b) The transformation from physical to generalised or modal coordinates involving a mixed set of static plus dynamic deflection shapes provides a major reduction in problem size leading to an efficient and easily understood solution.

c) The modified iterative scheme presented provides a simple means of effectively removing the drag coupling between modes and leads to a reliable and cost effective solution. The efficiency of this algorithm may be further improved by the use of a relaxation factor R such that $0.7 \leq R \leq 0.8$.

d) The calculation of an equivalent drag coefficient C_E at each node point in the FEM is straight forward and yields results in satisfactory agreement with those published in the API Bulletin (API, 1977). Since this method accurately represents the spacial variation in the drag force it is anticipated to be more accurate than the original "averaged" method (Dareing and Huang, 1977).

As a consequence the basic aim of synthesising from existing methods a flexible but simple programme has been achieved. Further development work which may be undertaken includes

a) Development of linearised spectral analysis in which the drag force is linearised across the whole wave spectrum (Langley, 1984). Here the advantage of the proposed solution algorithm will be even more marked since once the reduced equations have been formulated it is necessary to solve for a range of discreet frequencies across the spectrum. As a result the machine time required to perform the matrix operations required in the transformation to modal coordinates (a significant percentage of total time in the single wave analysis) becomes insignificant leading to an extremely efficient solution scheme.

b) Development of static analysis to determine the mean displacement and stress distributions associated with a linearised frequency domain solution. This calculation must follow the response analysis since, as a consequence of the nonlinear hydrodynamic drag force, the mean static load on the riser depends on its own dynamic motion.

c) Time domain simulation utilising the modal coordinates introduced in this chapter. This approach may be used to investigate the accuracy of the various drag force linearisation methods employed in the frequency domain as well as studying the effect of nonlinear loading due to

i) Change in wetted length

ii) Calculation of hydrodynamic forces at the displaced configuration.

As a result of the small number of degrees of freedom involved in this analysis the time step numerical integration may conveniently be performed using an

explicit scheme such as central difference or a Runge-Kutta method. Simulated seastates may be either single wave or random.

d) Time domain simulations utilising the original finite element displacement freedoms. This approach is completely general in that any structural or loading nonlinearities may now be considered.

Suitable applications include

i) Ribbon riser system, figure 7.26, in which the riser system is attached directly to the surface vessel with motion compensation and tension being provided by a weighted seabed boom (Shotbolt, 1983). As a result of vertical axial motions of this system significant tension variations may occur which may be accounted for by utilising the nonlinear element developed in Chapter 3.

ii) Flexible catenary riser or hose possibly supported at intermediate depths by an under-water buoy, figure 7.27. Such a system is subjected to complicated three-dimensional behaviour (Beynet and Frase, 1982) which due to the high level of compliancy in the system is likely to require a nonlinear finite displace-ment analysis.

a) Drilling Riser

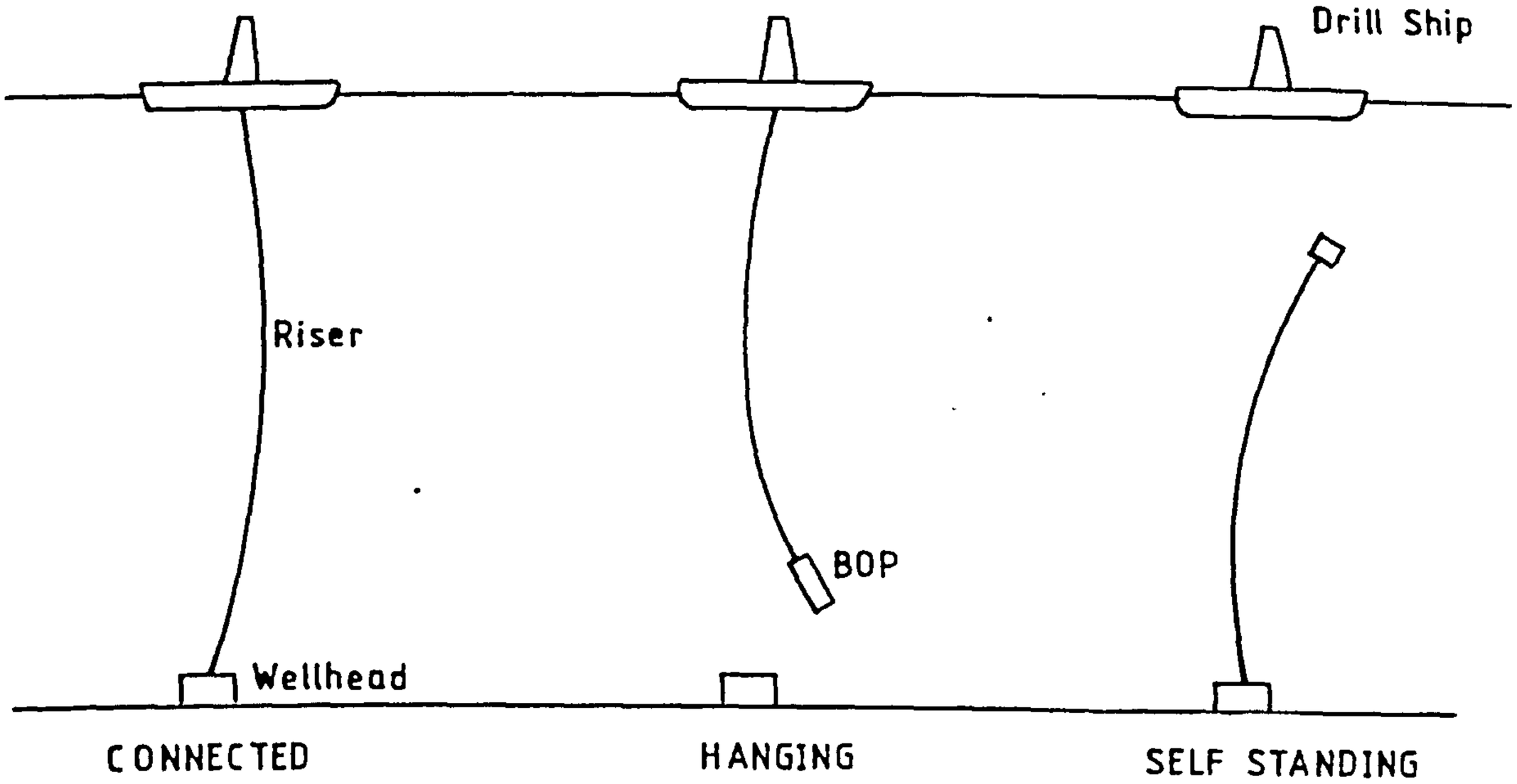

b) Floating Production System

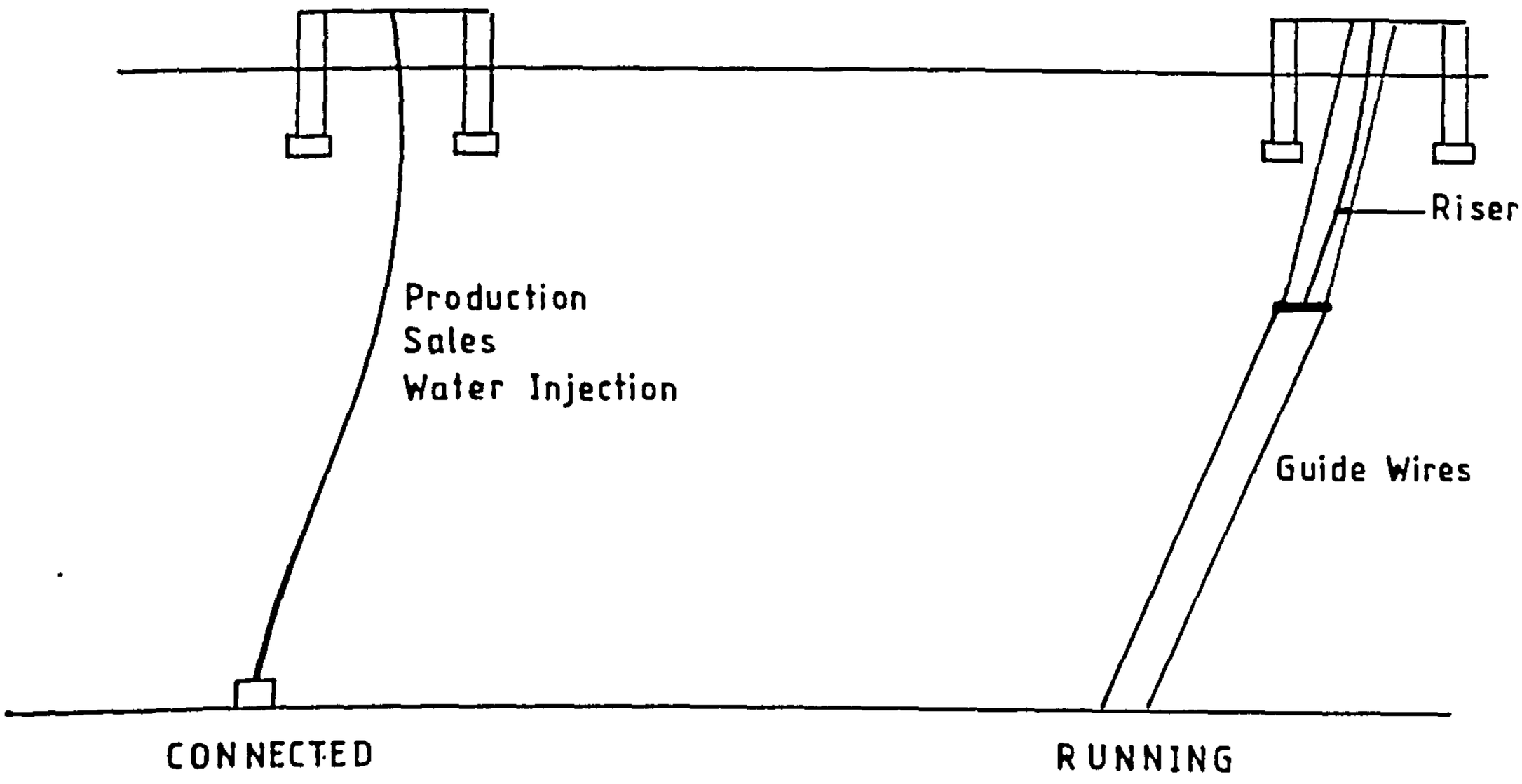

FIG 7.1 Typical Riser Configurations

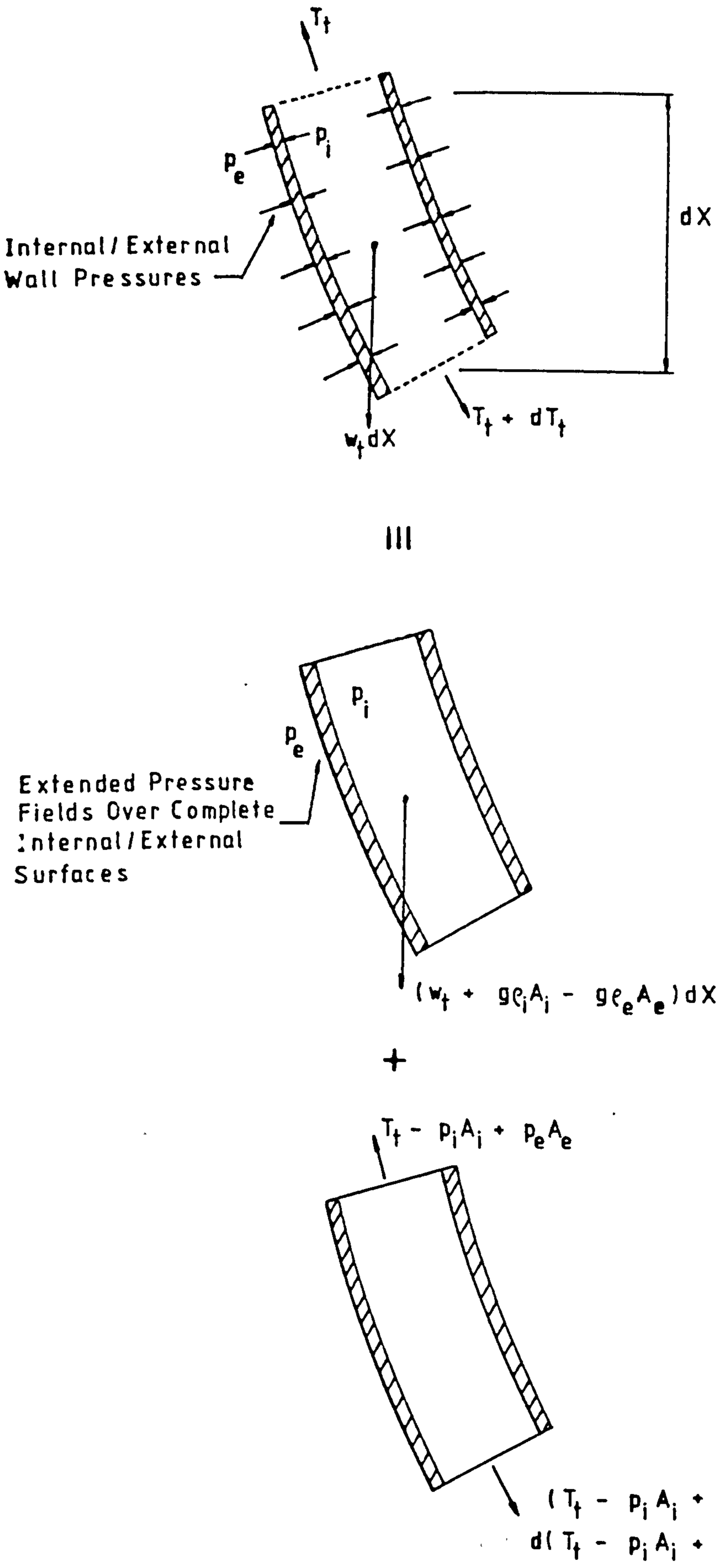

FIG 7.2 Riser Element Real and Effective Forces

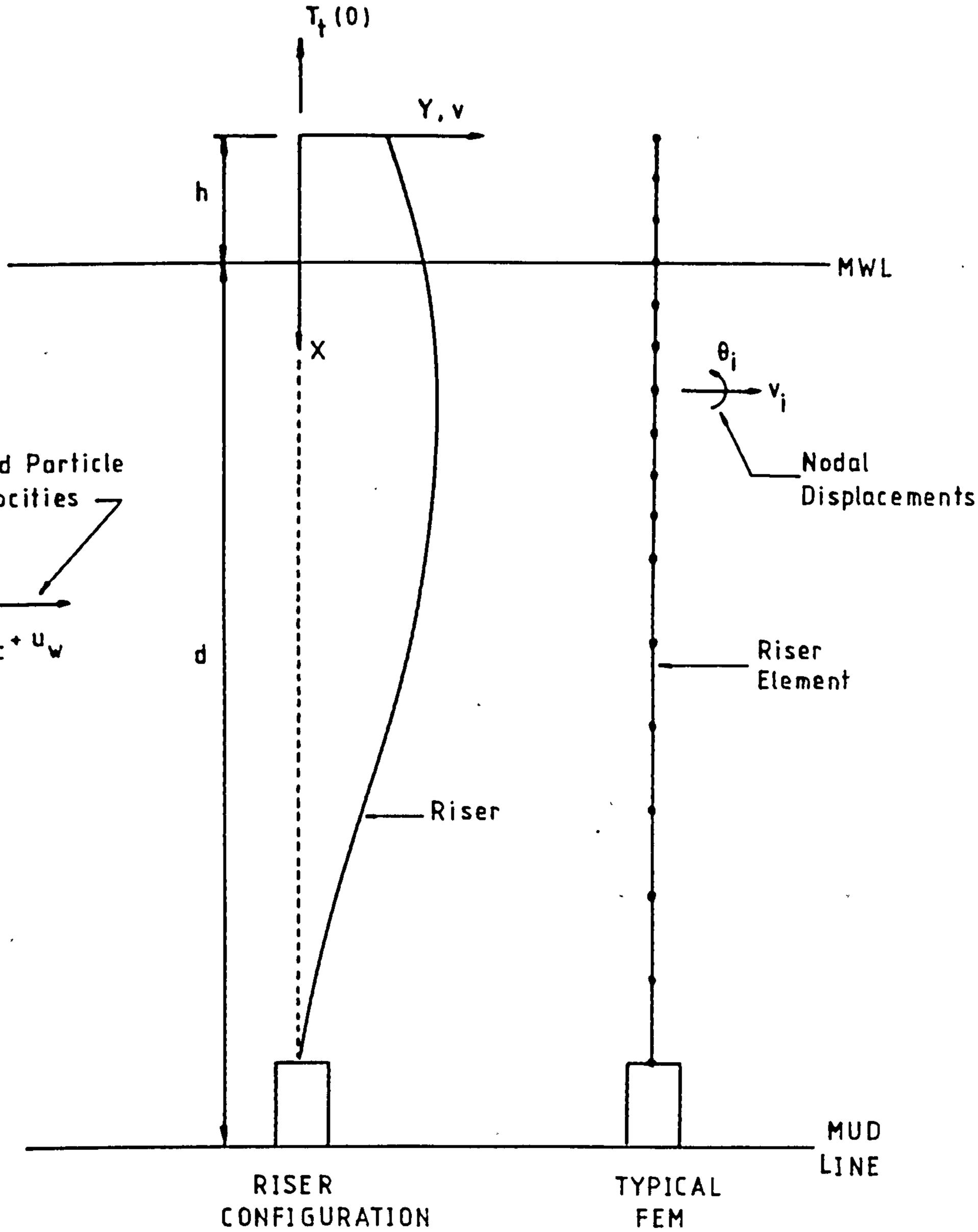

FIG 7.3 Riser Finite Element Model

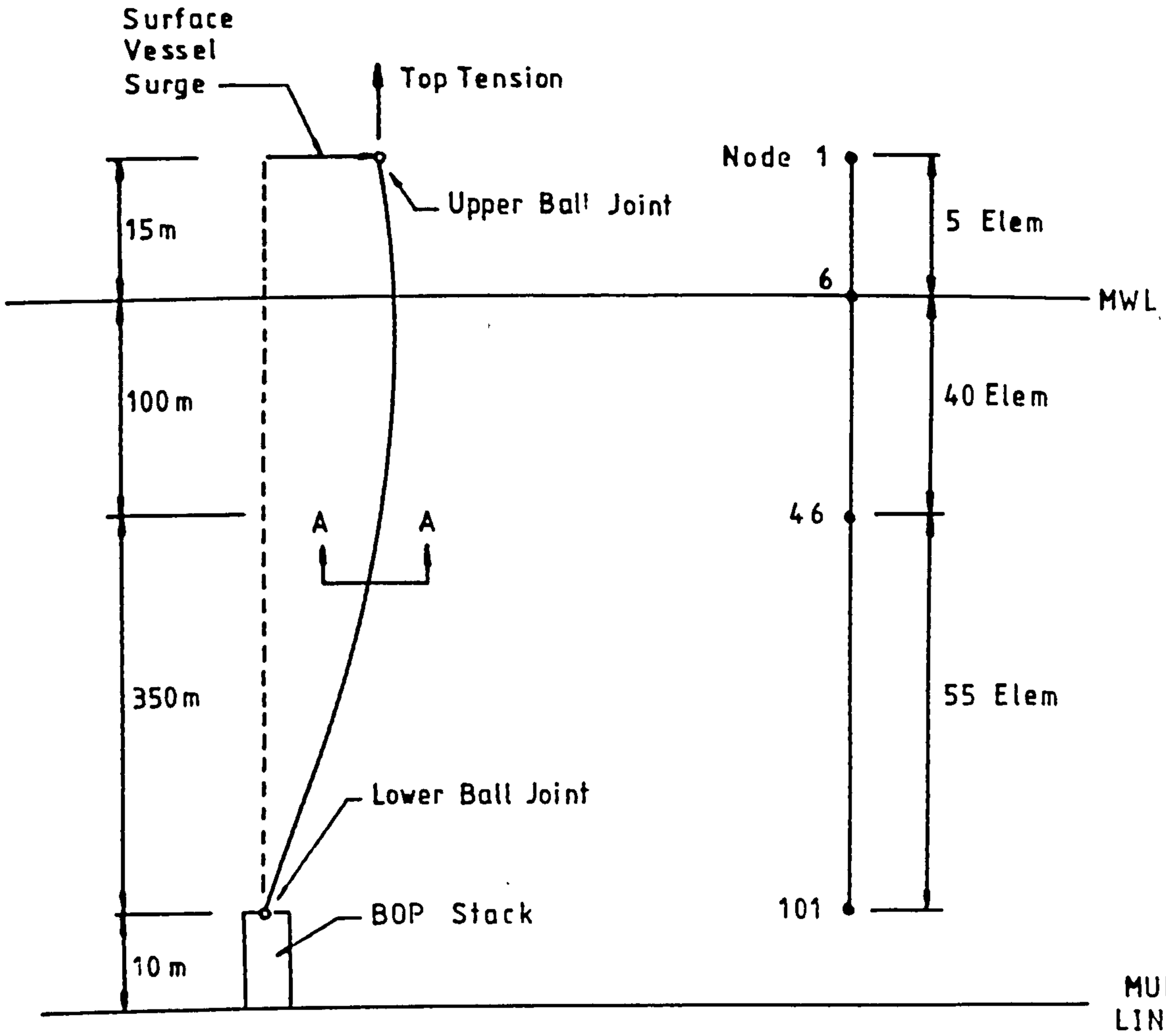

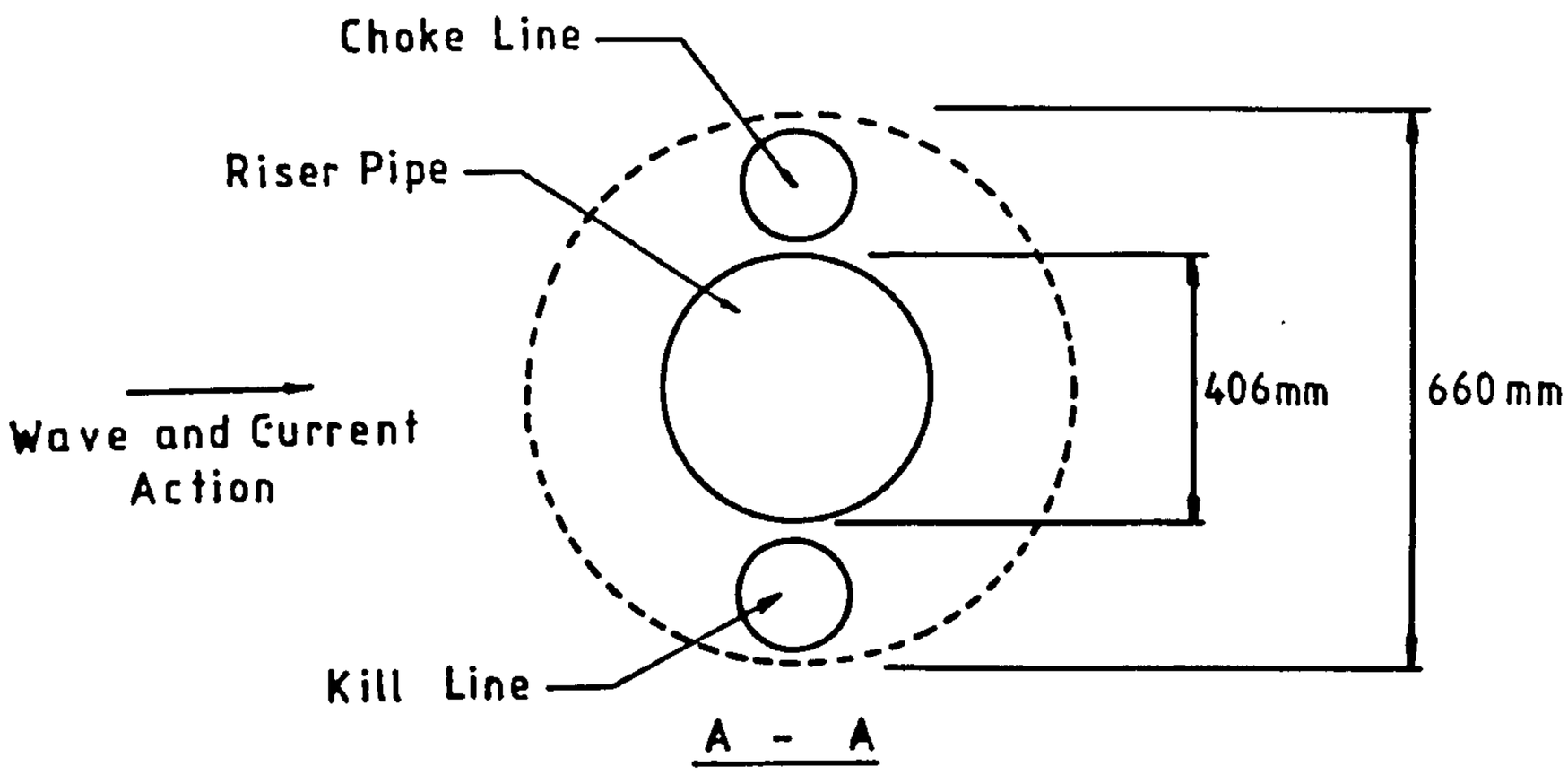

FIG 7.4 API Test Case 1500-20-1-D

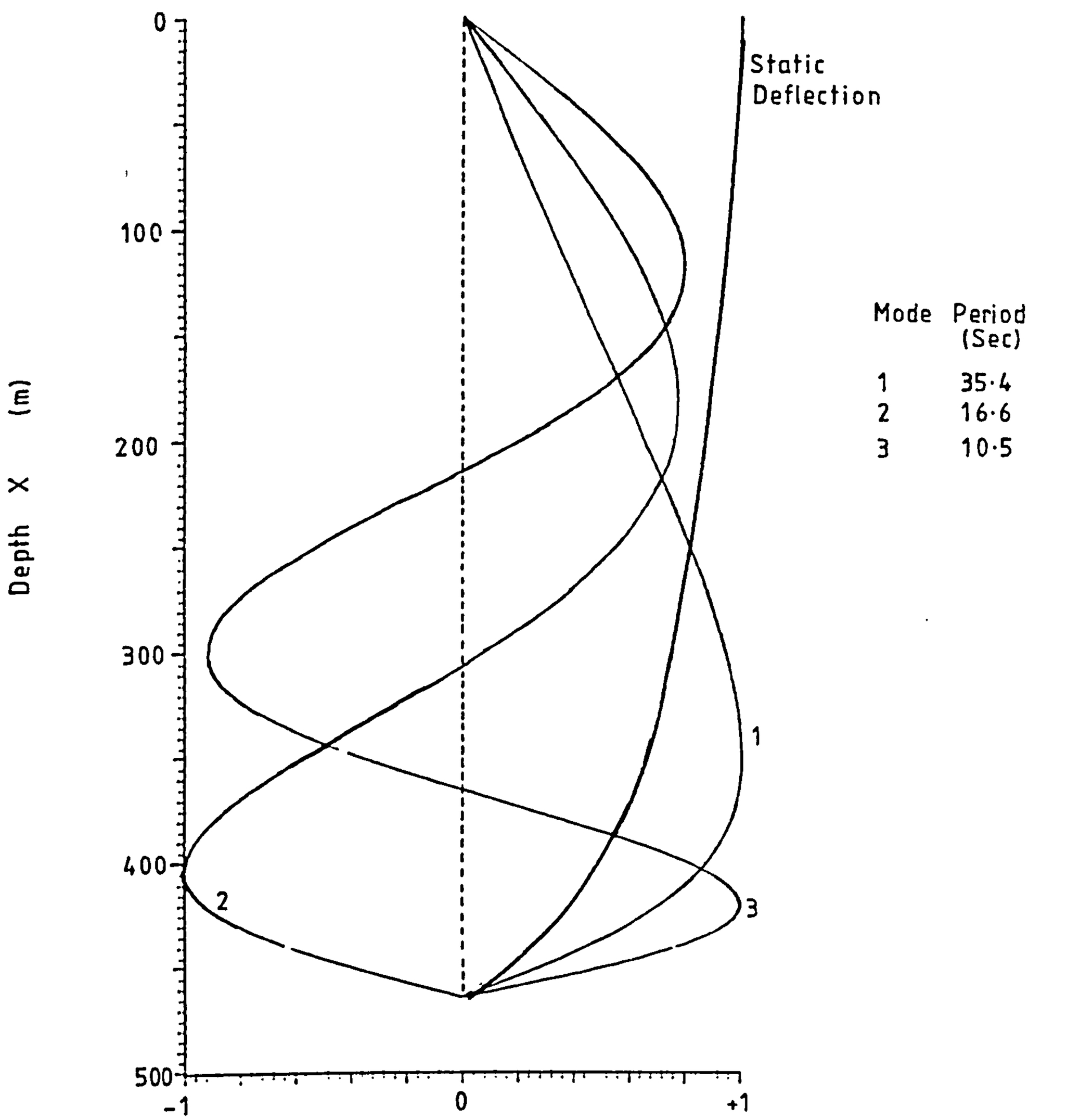

FIG 7.5 Riser Mode Shapes For T(0) = 1291 KN

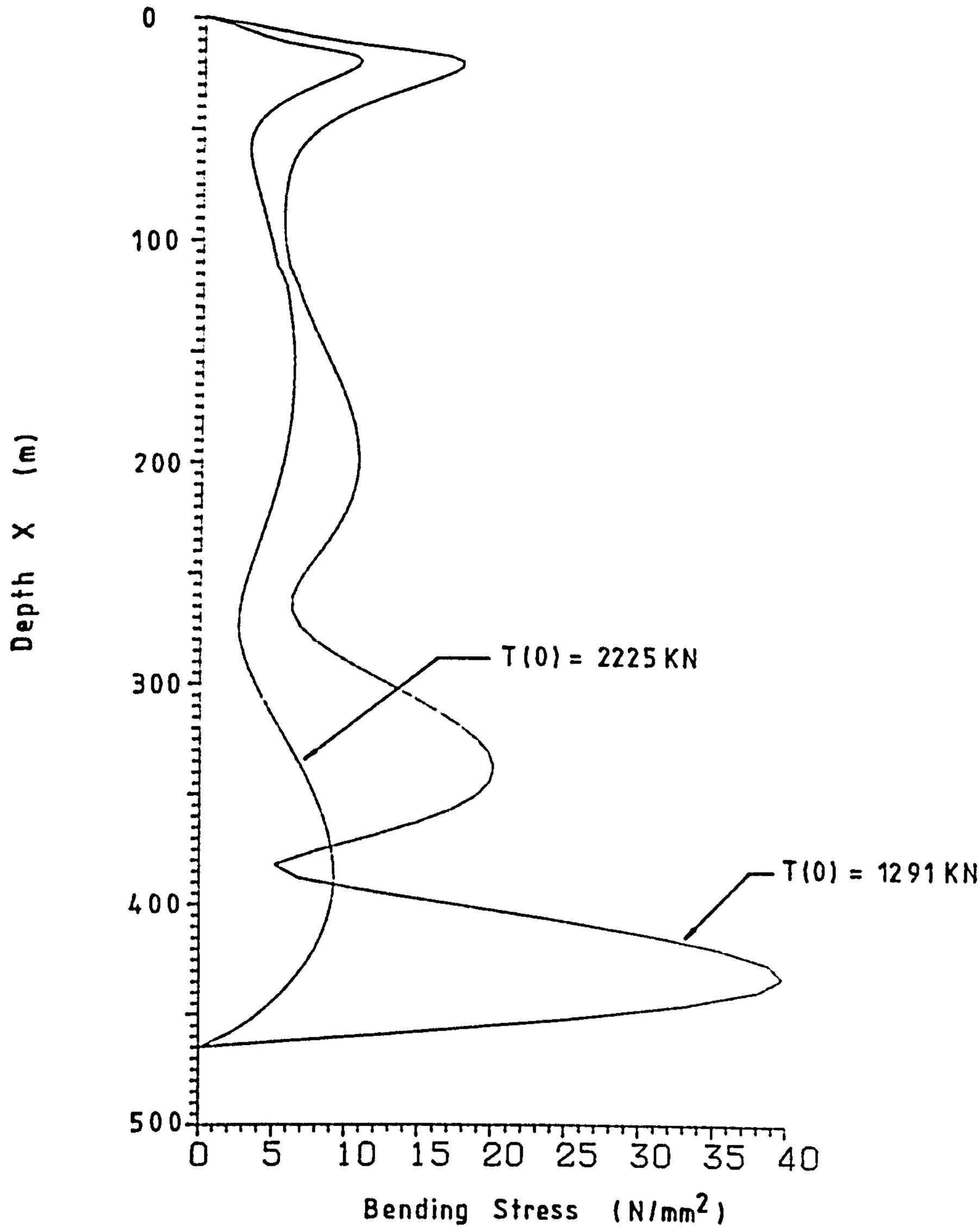

FIG 7.6 Riser Bending Stress Amplitude

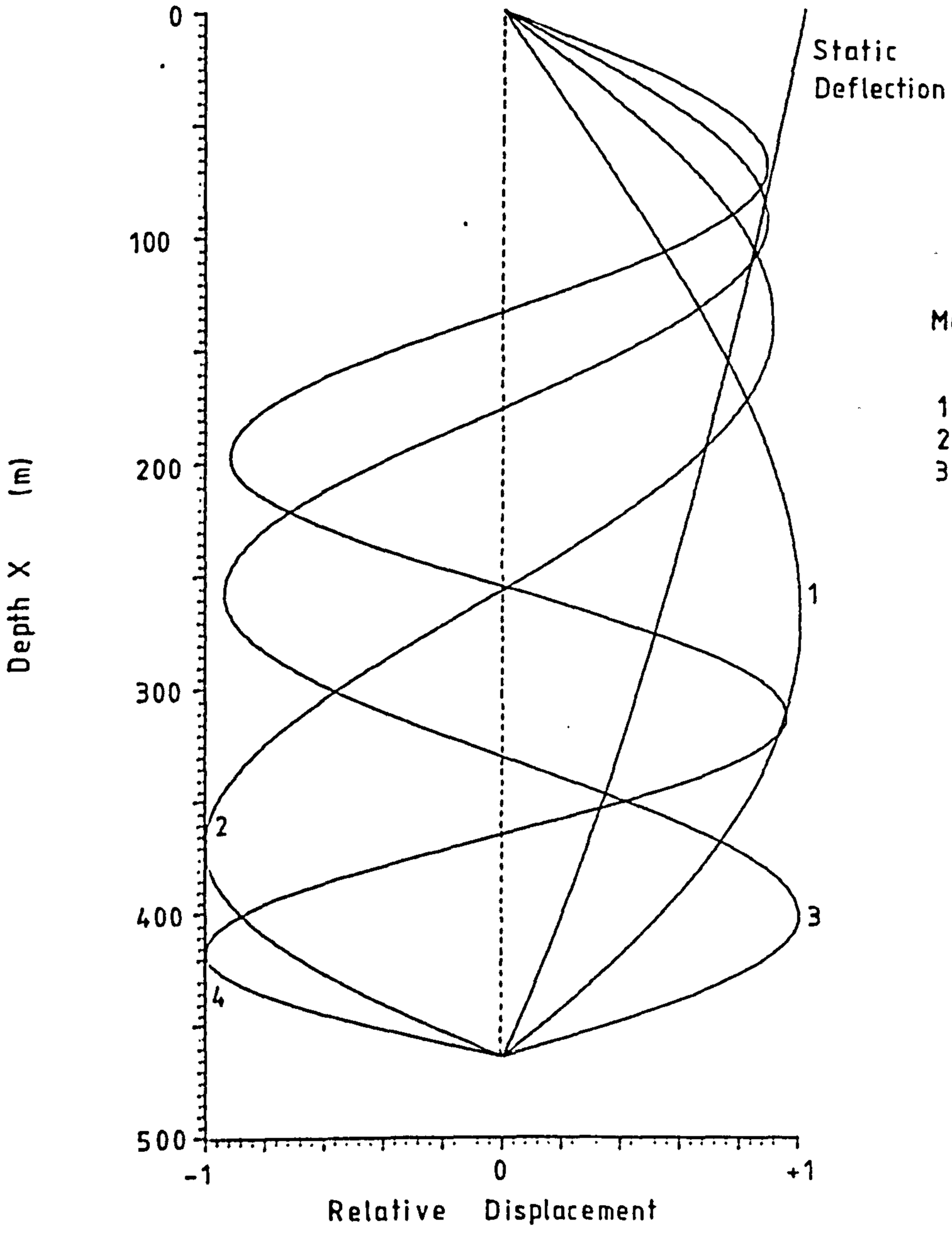

FIG 7.7 Riser Mode Shapes For T(0)= 2225 KN

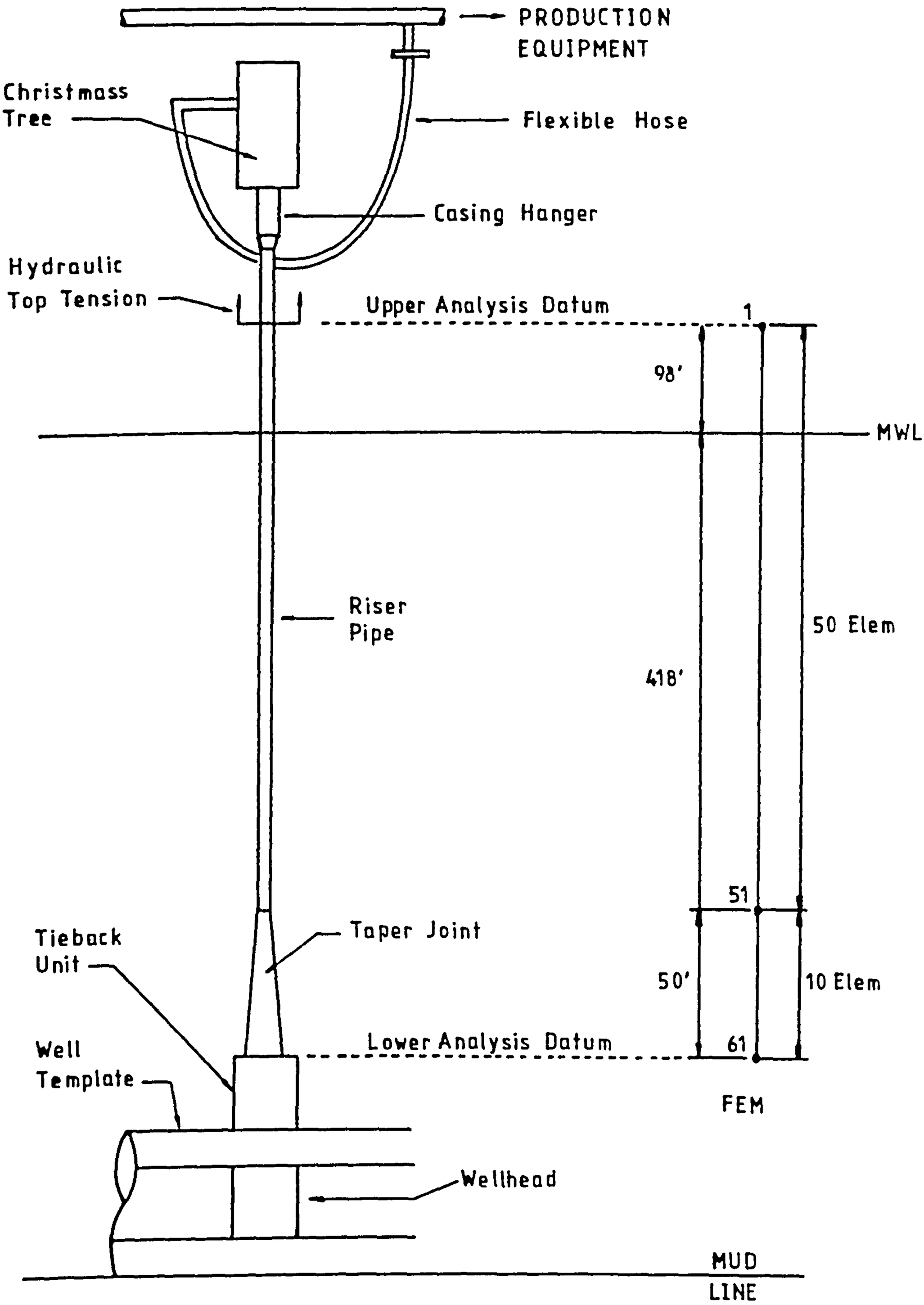

FIG 7.8 Production Riser

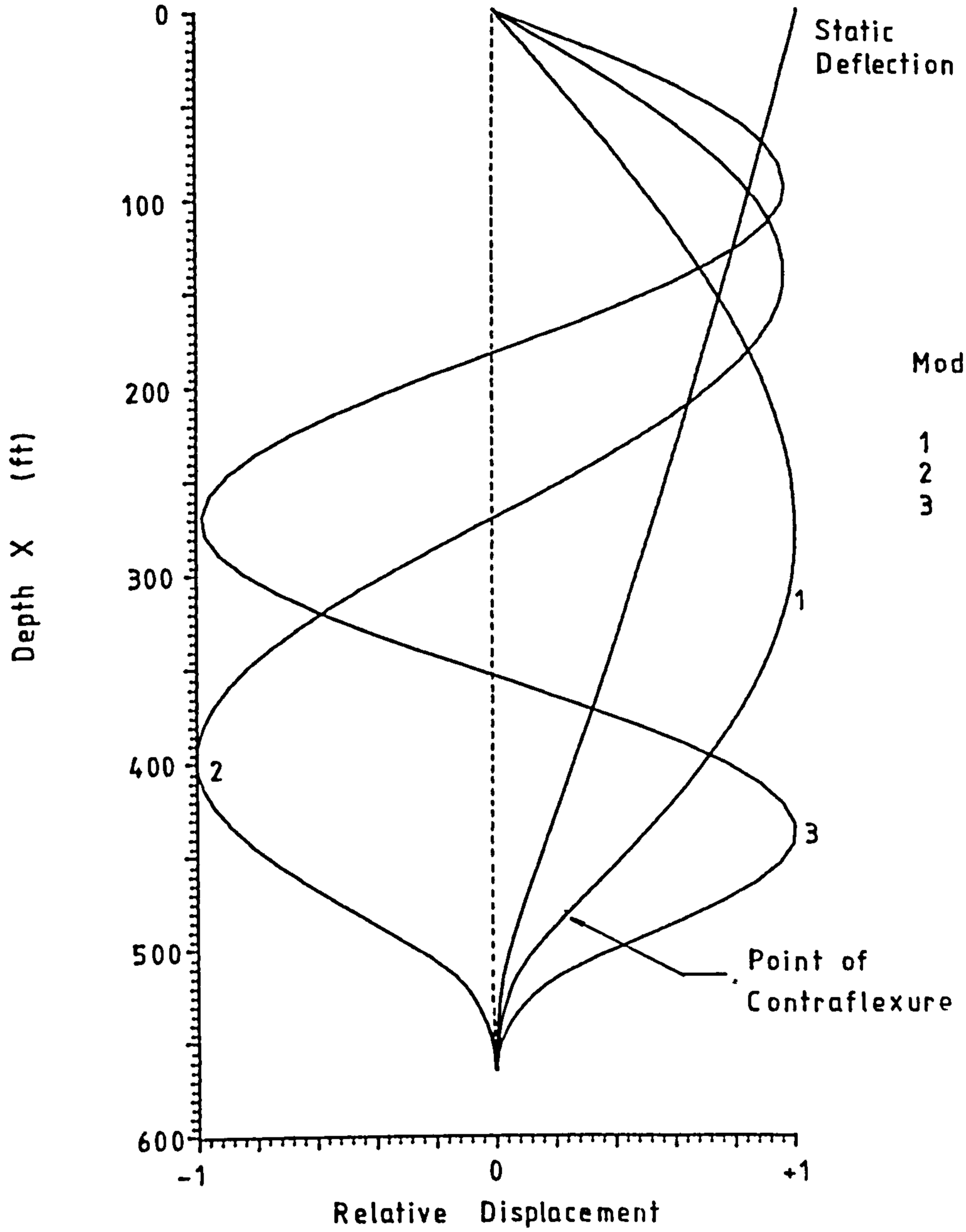

FIG 7.9 Production Riser Mode Shapes

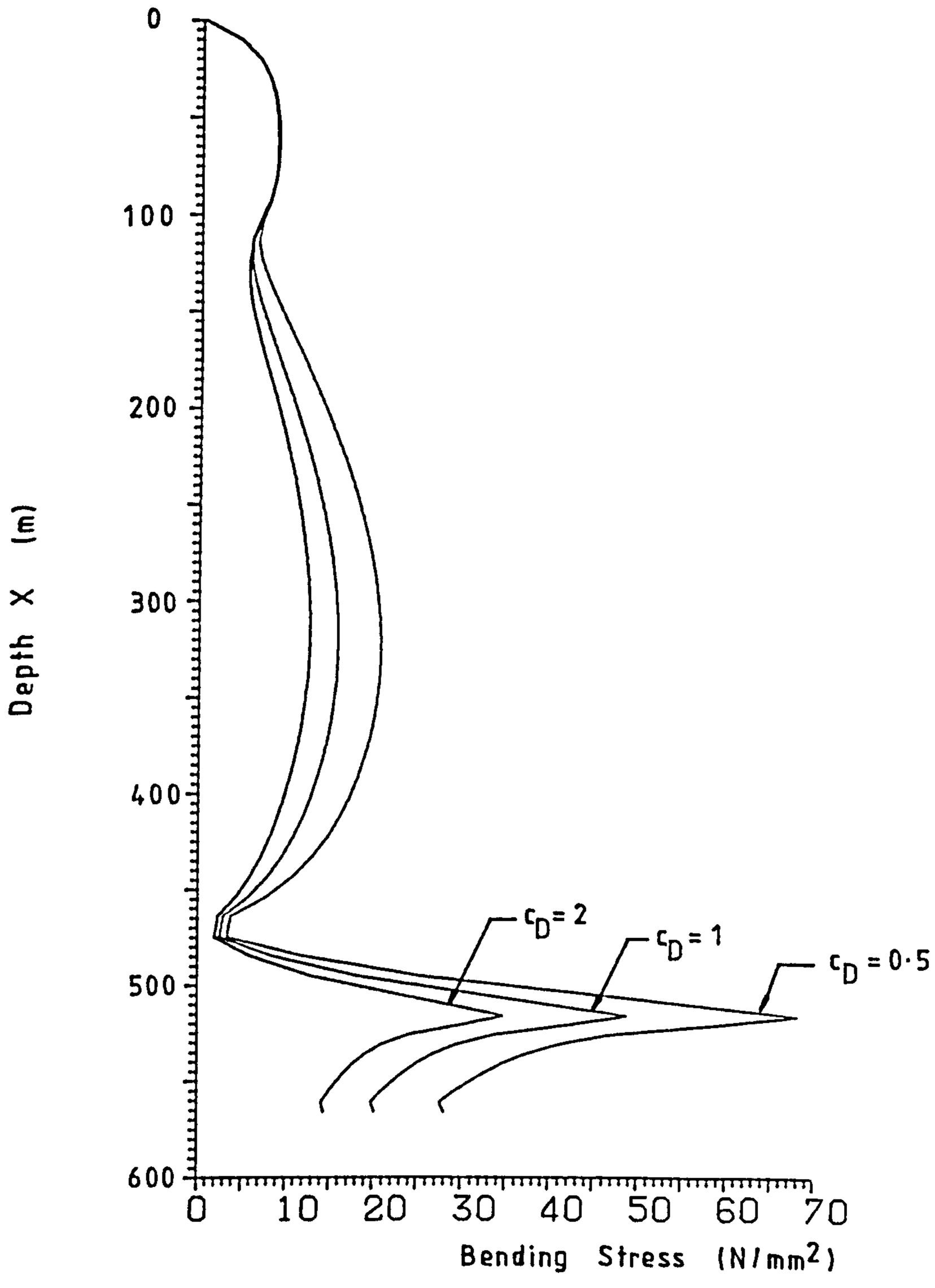

FIG 7.10 Riser Bending Stress Amplitude

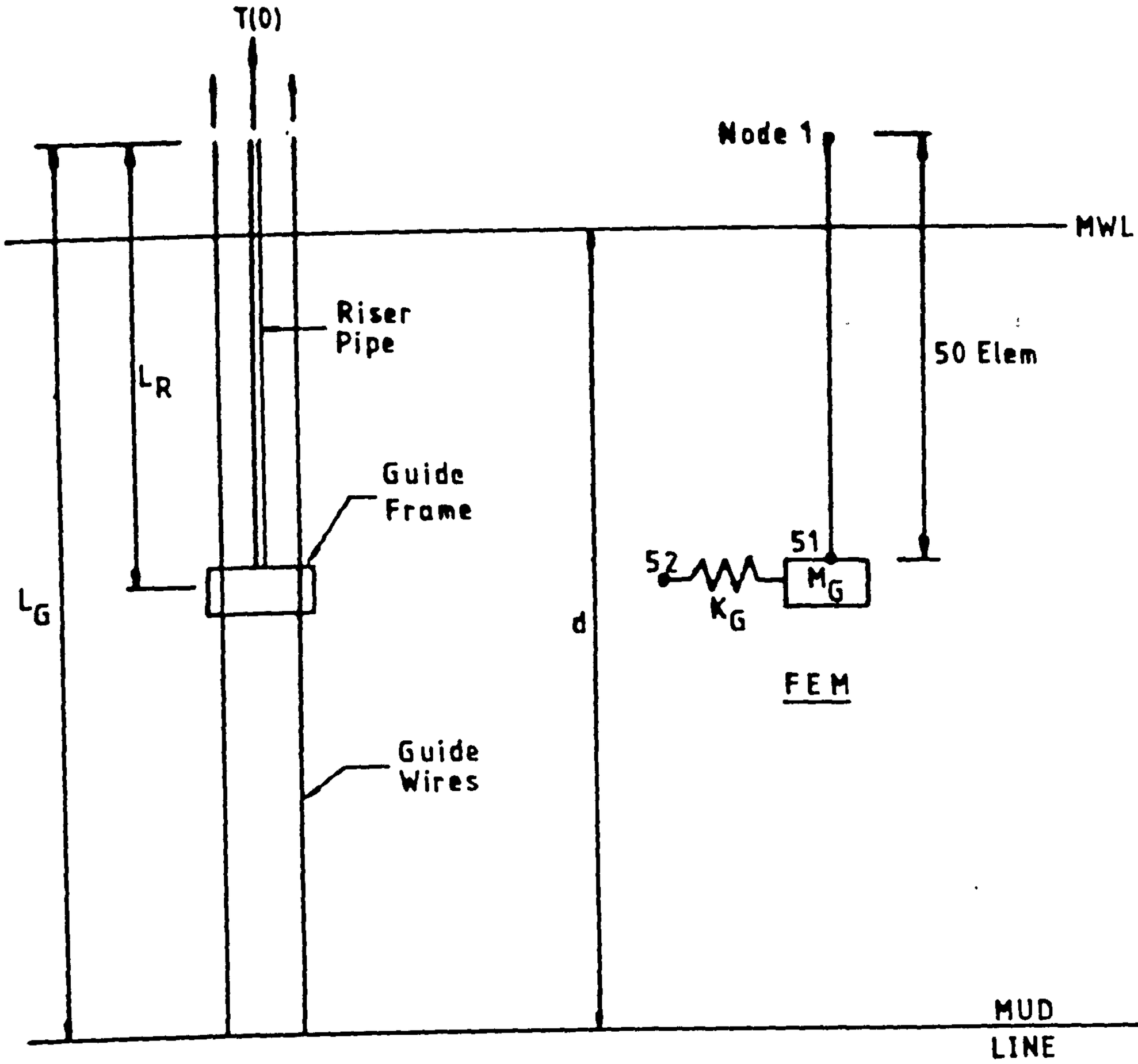

FIG 7.11 Riser Running Operation

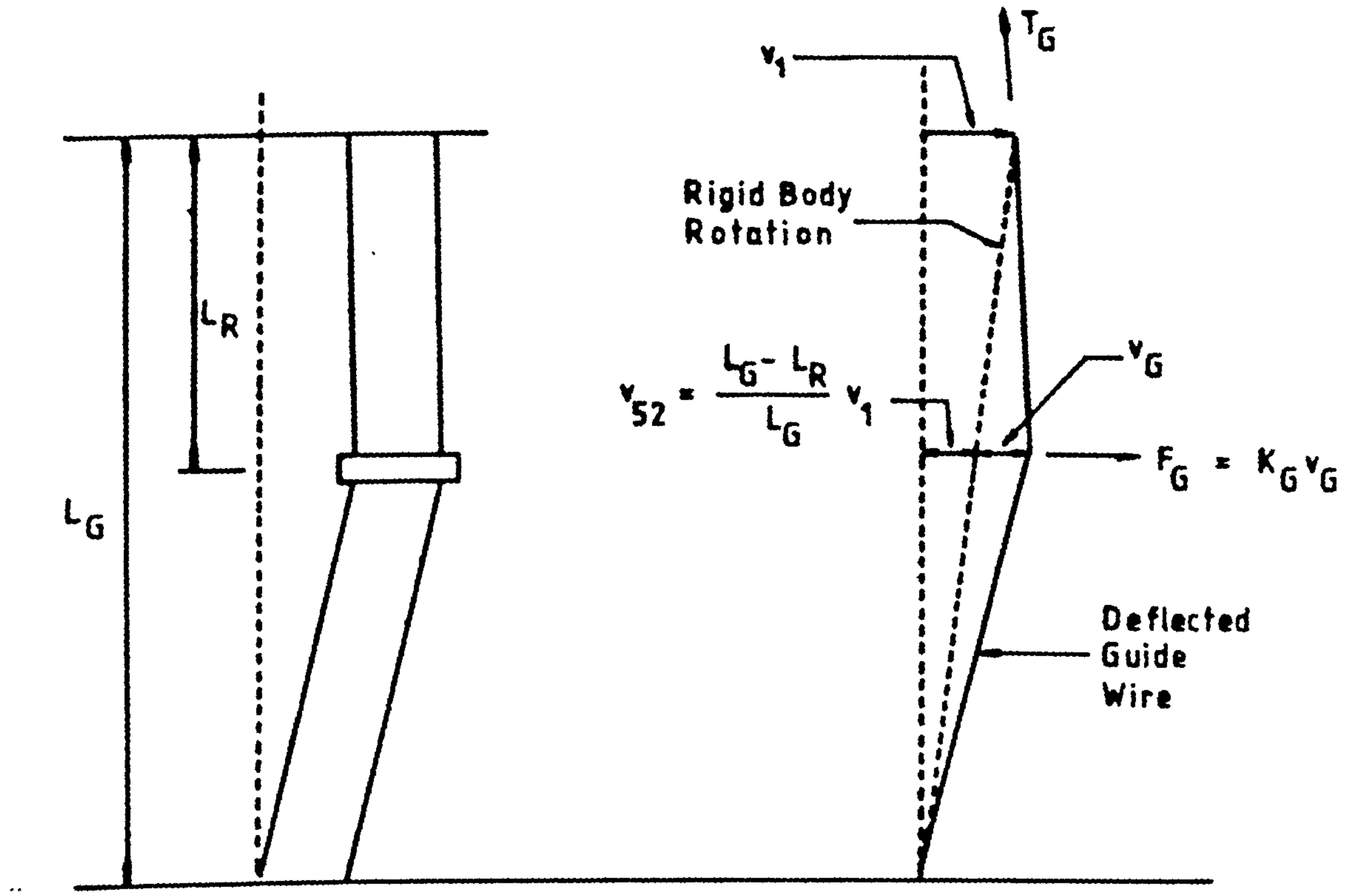

FIG 7.12 Guidewire Geometry

W_G = Guideframe Weight (in air)

B_G = Guideframe Buoyancy

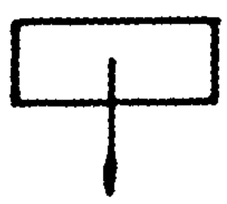

a) Unconnected Guideframe

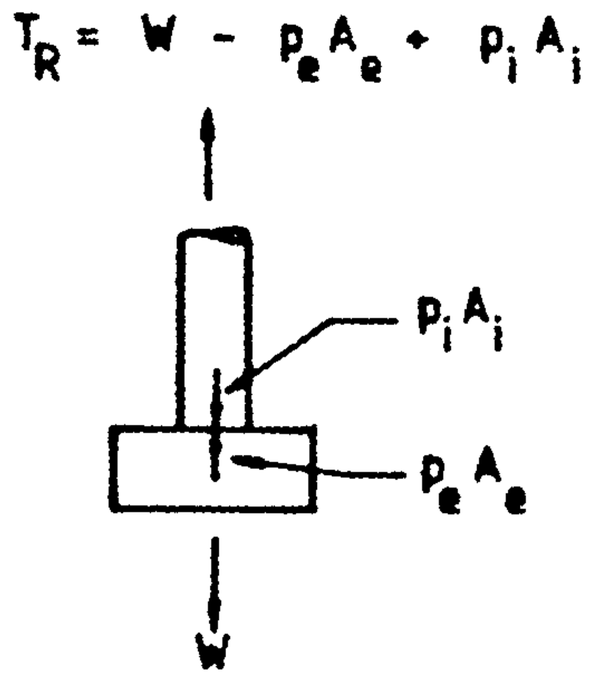

b) Connected Guideframe

FIG 7.13 Riser Tension at Guideframe Connection

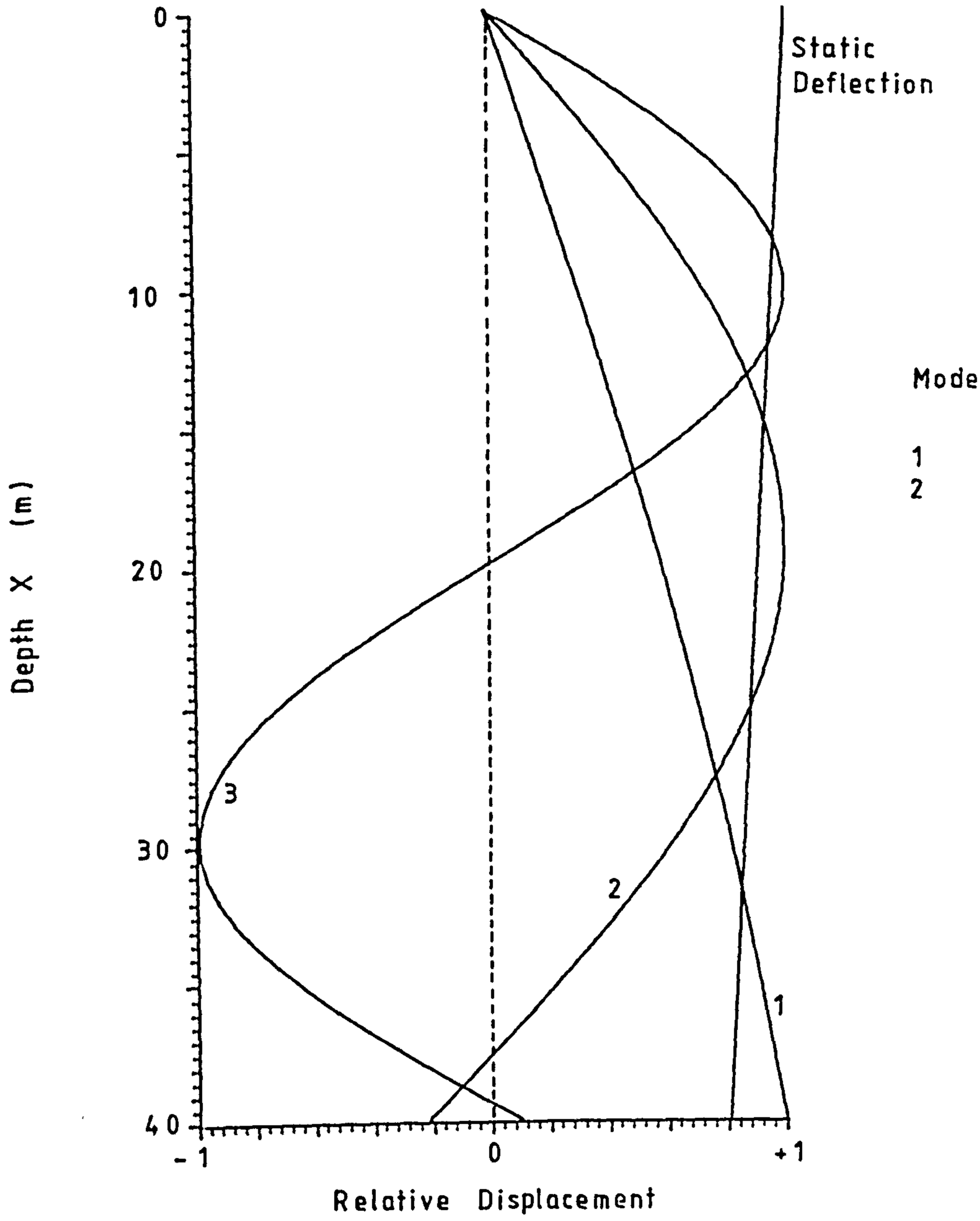

FIG 7.14 Riser Mode Shapes , $L_R = 40m$

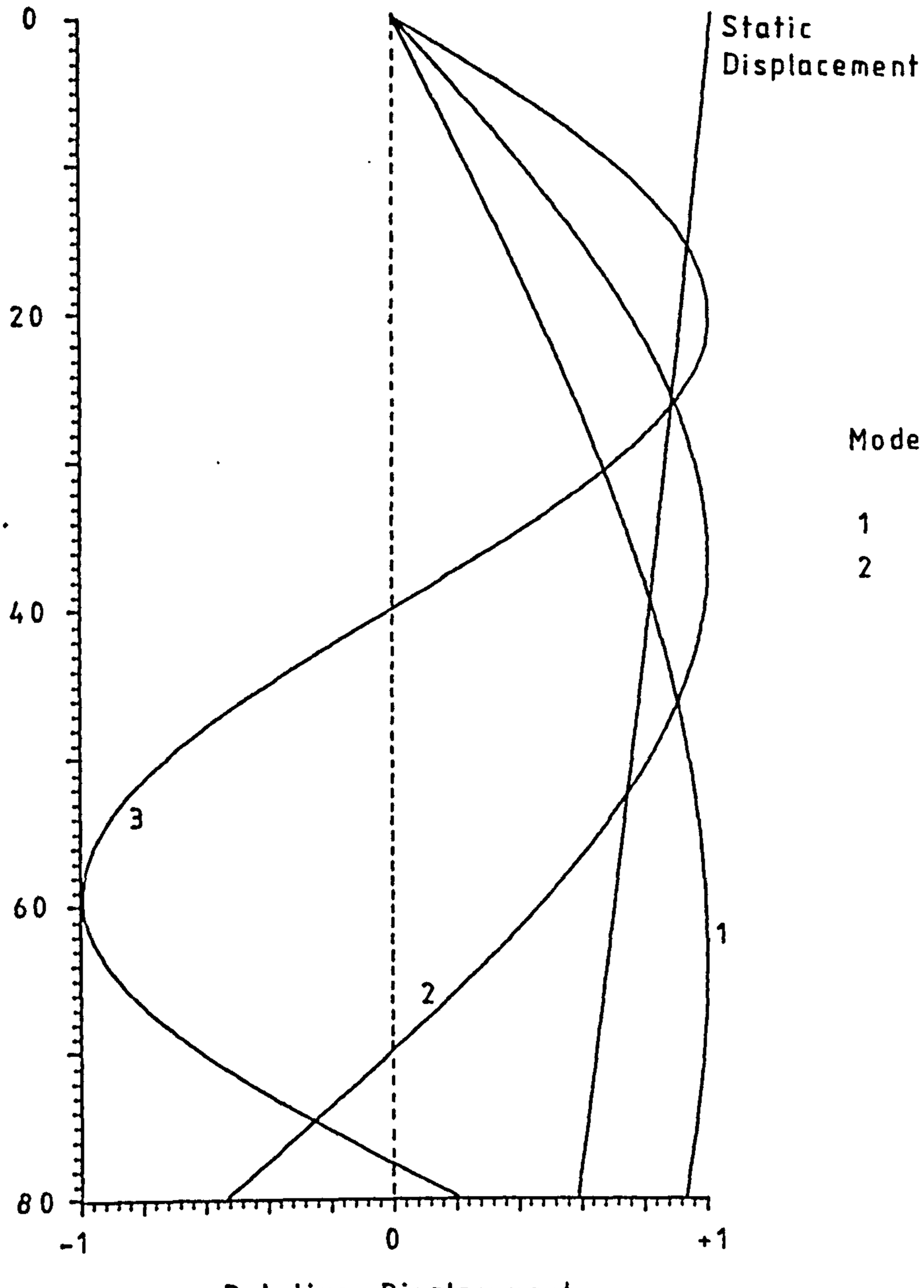

FIG 7.15 Riser Mode Shapes , L_R= 80m

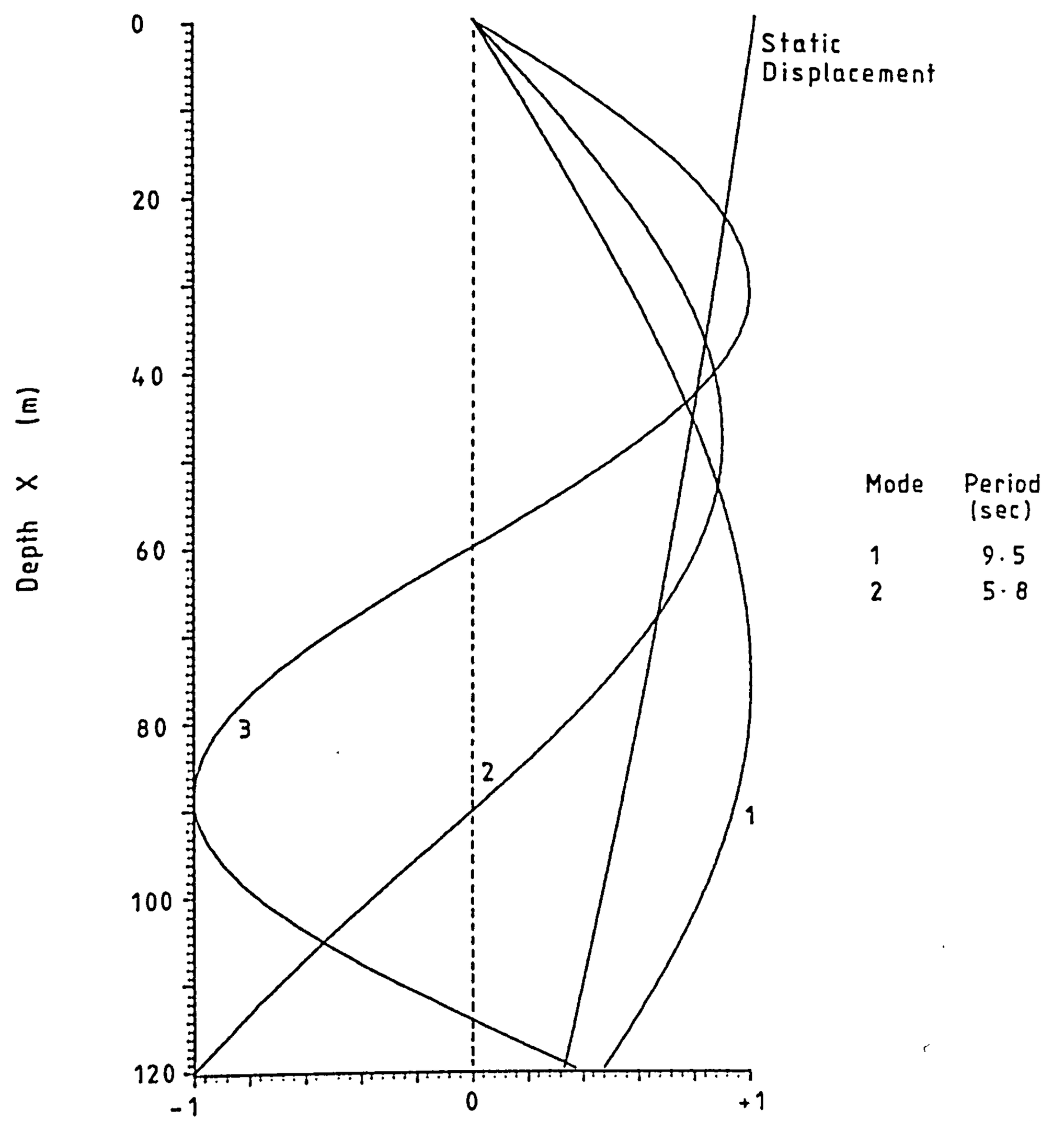

FIG 7.16 Riser Mode Shapes , L_R = 120 m

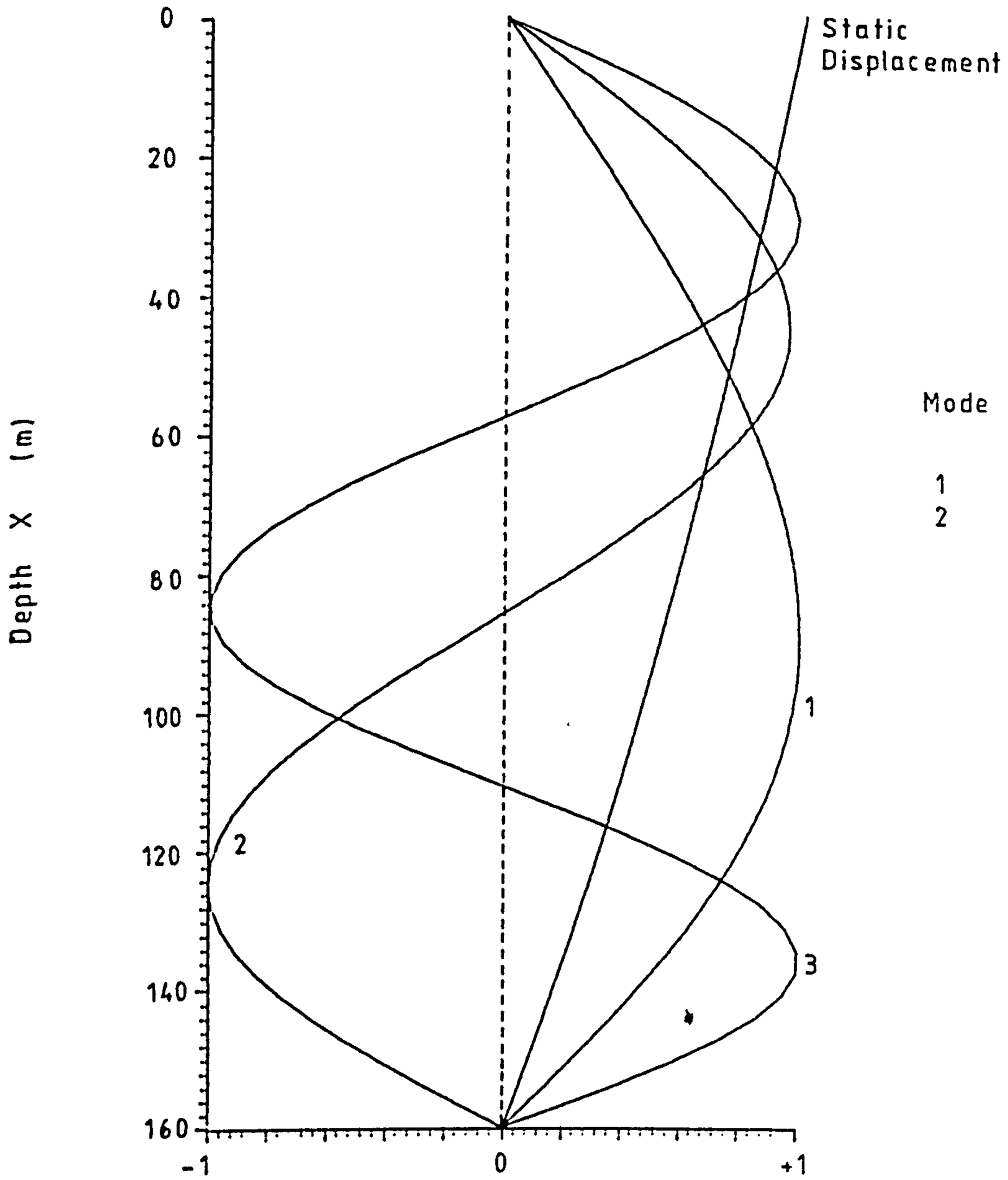

FIG 7.17 Riser Mode Shapes, L_R = 160m

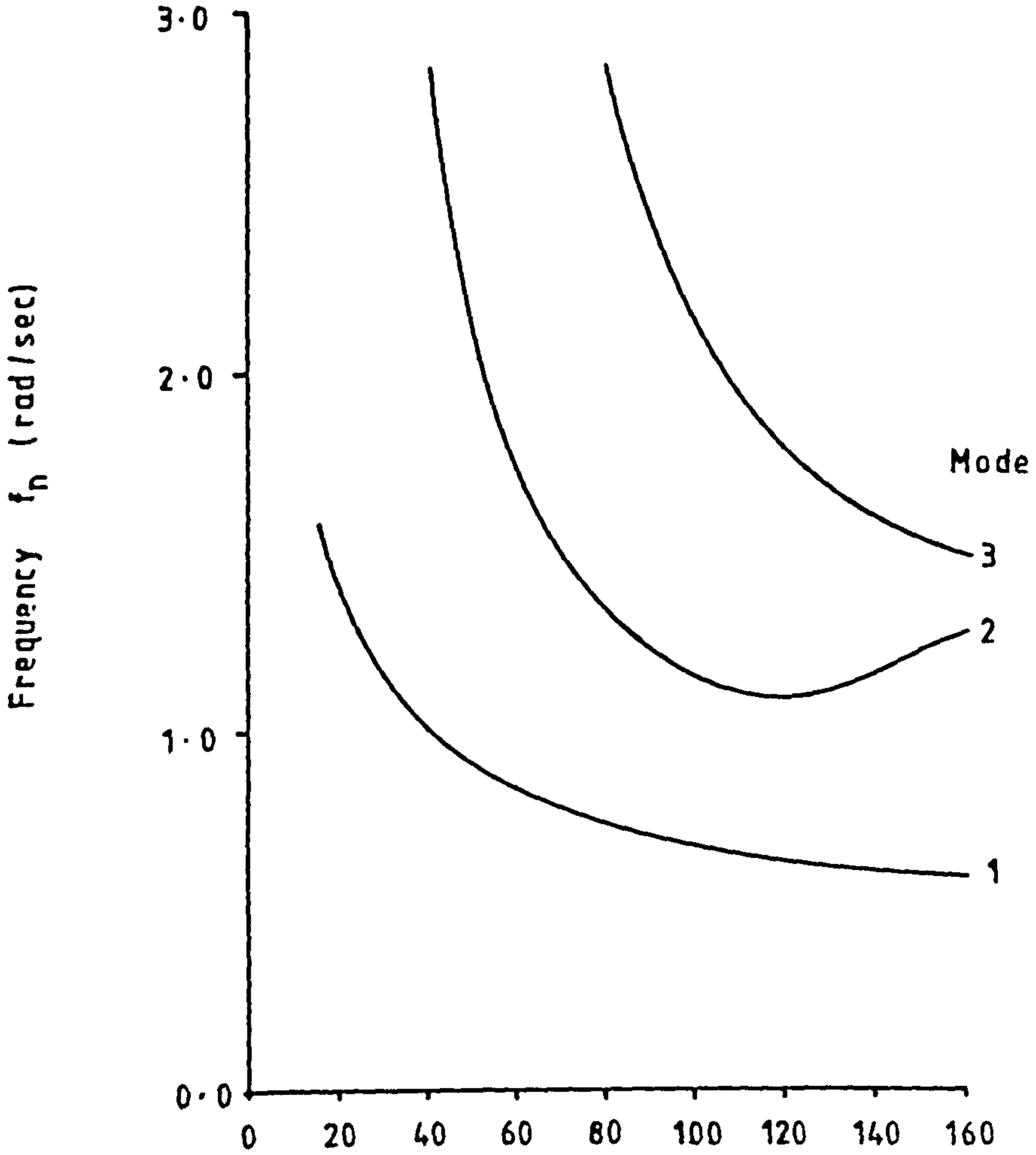

FIG 7.18 Riser Frequencies during Running

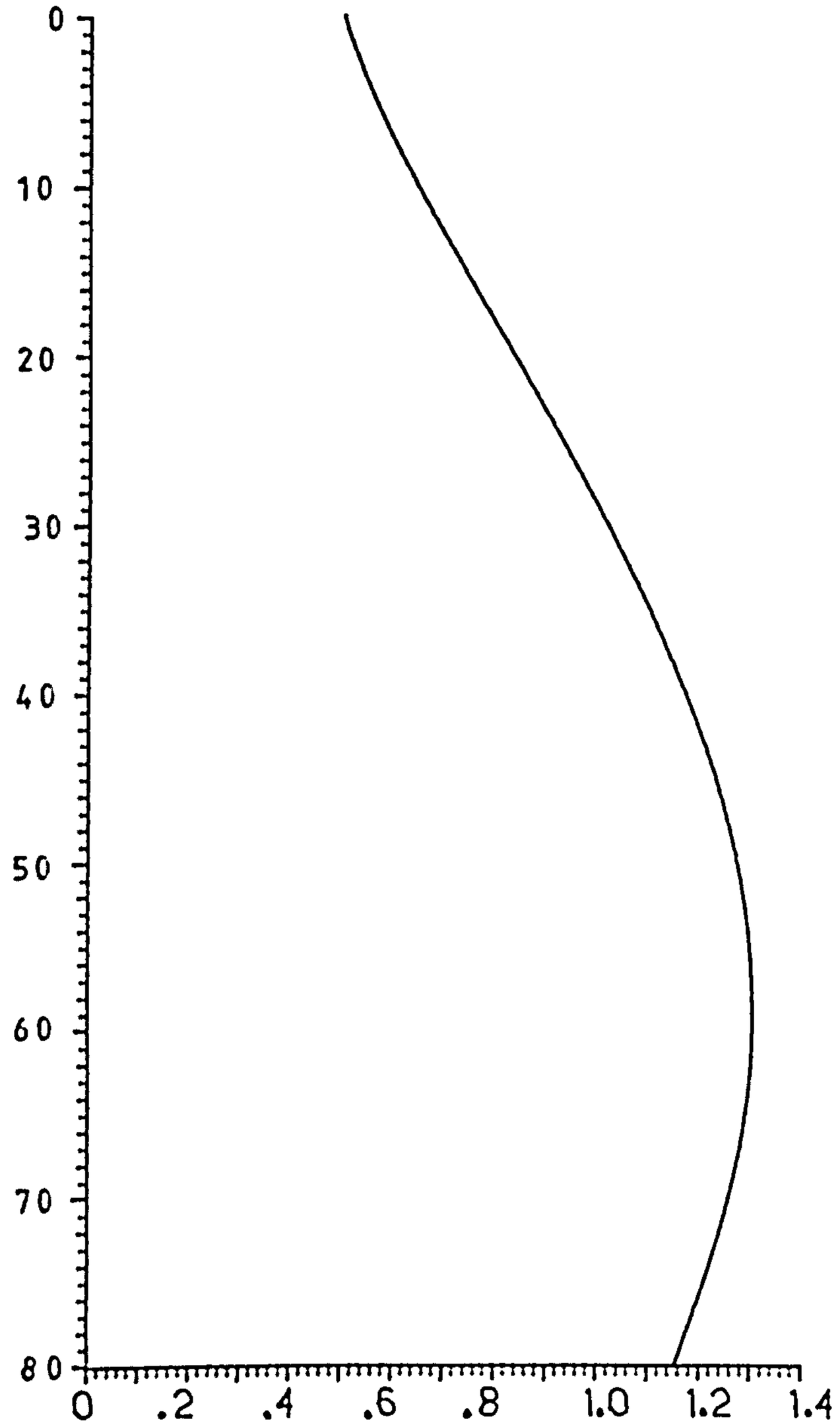

FIG 7.19 Riser Deflections , $L_R = 80m$

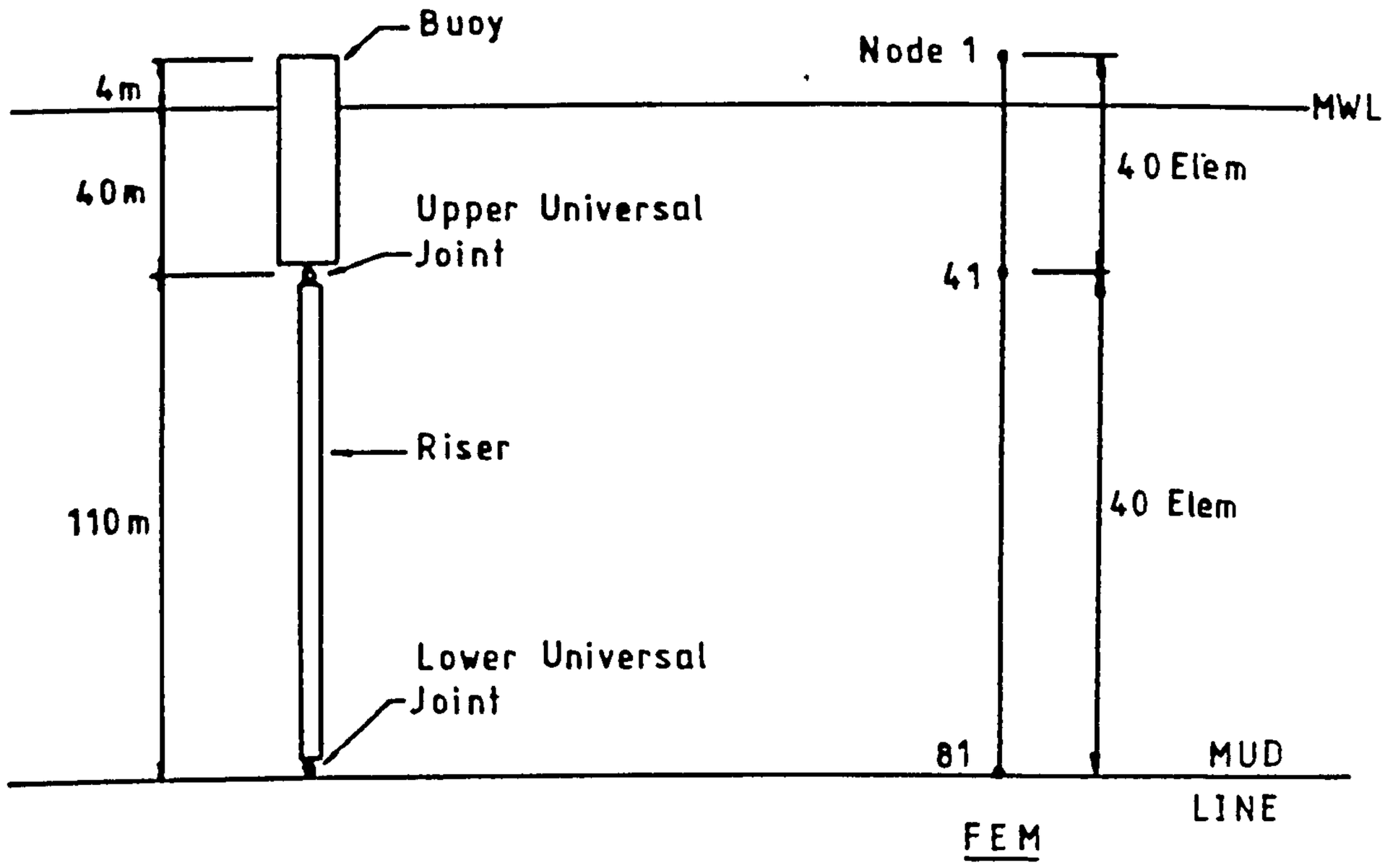

FIG 7.20 Articulated Column

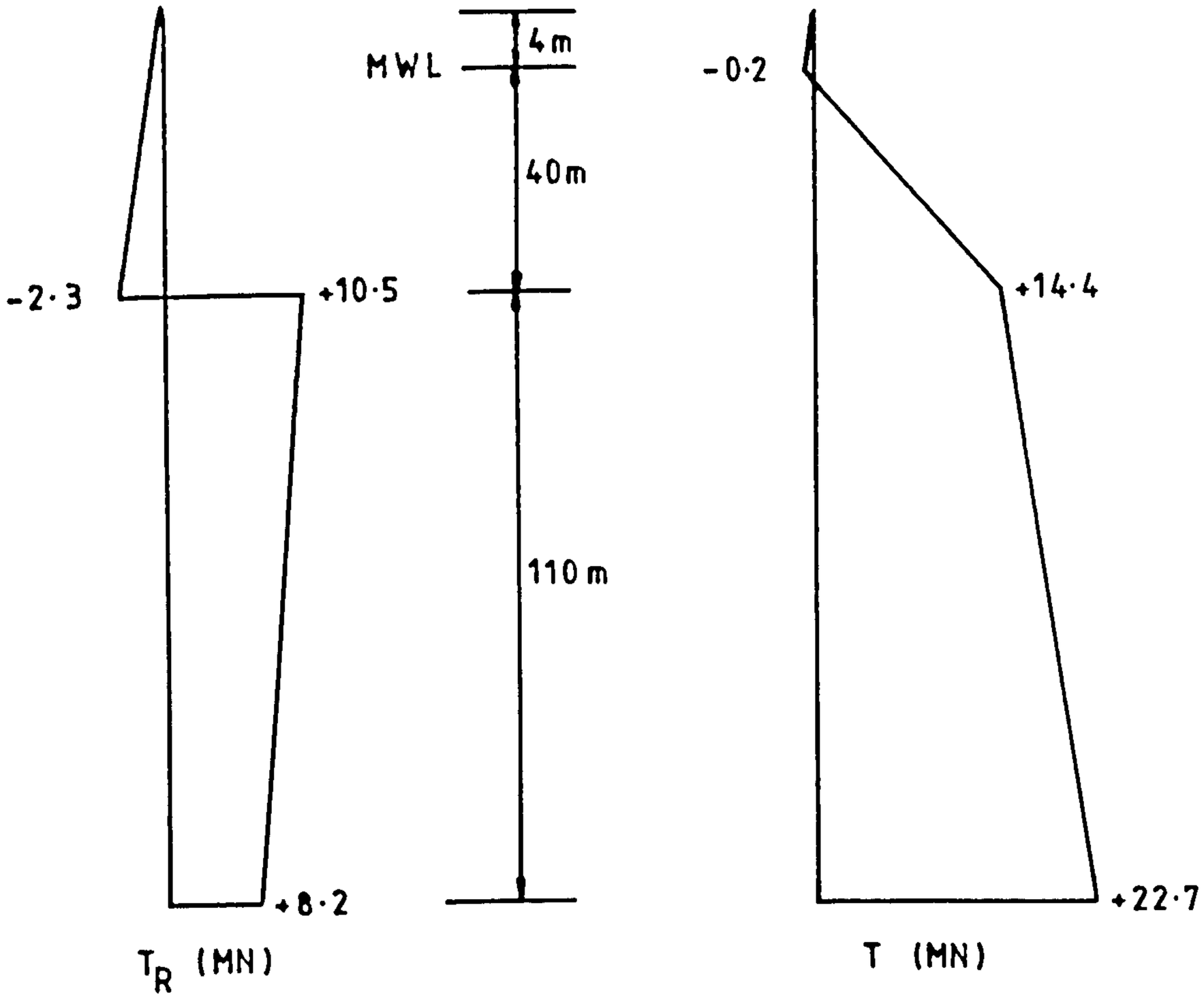

FIG 7.21 Real and Effective Tension Distributions

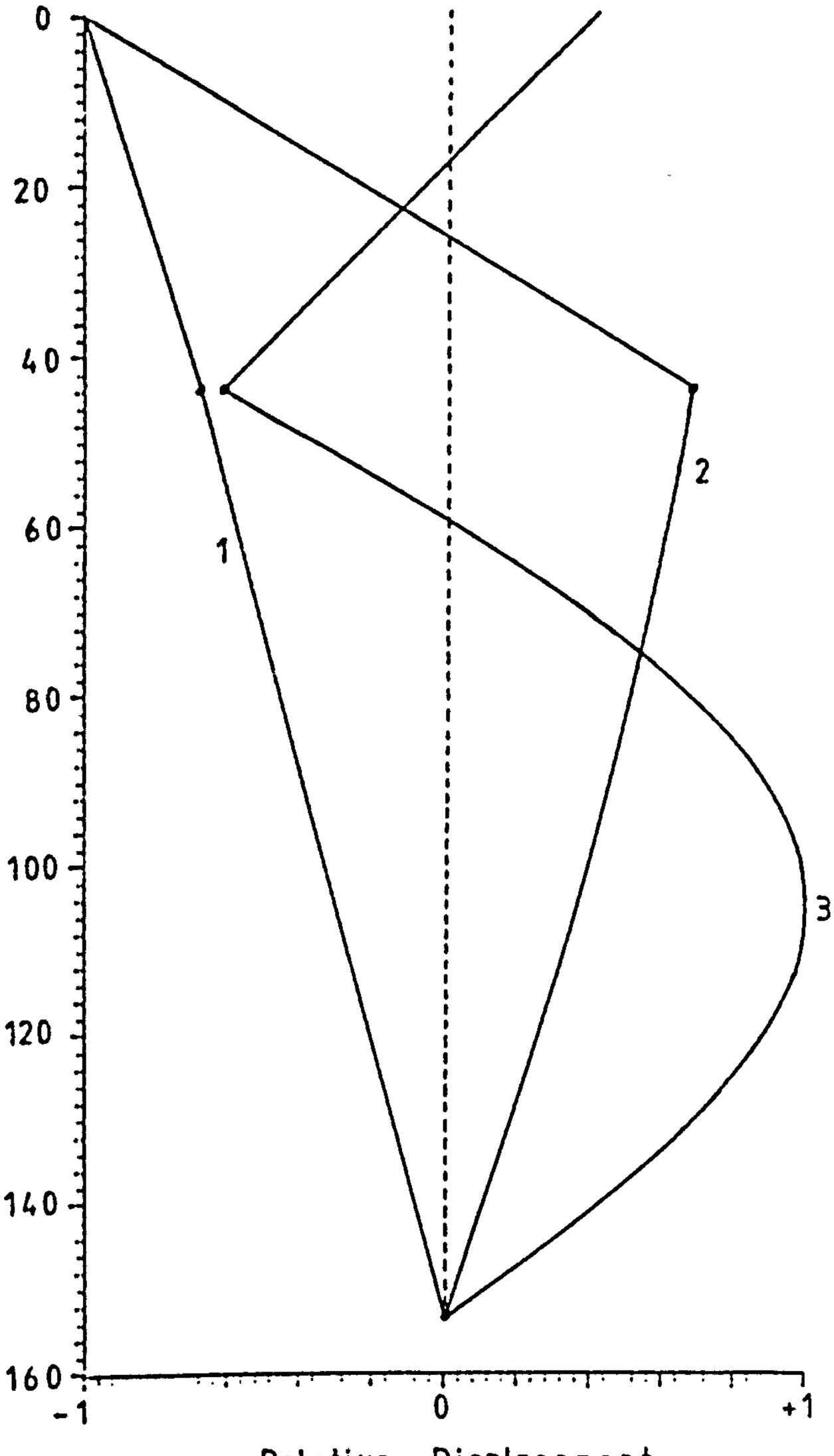

FIG 7.22 Articulated Column Mode Shapes

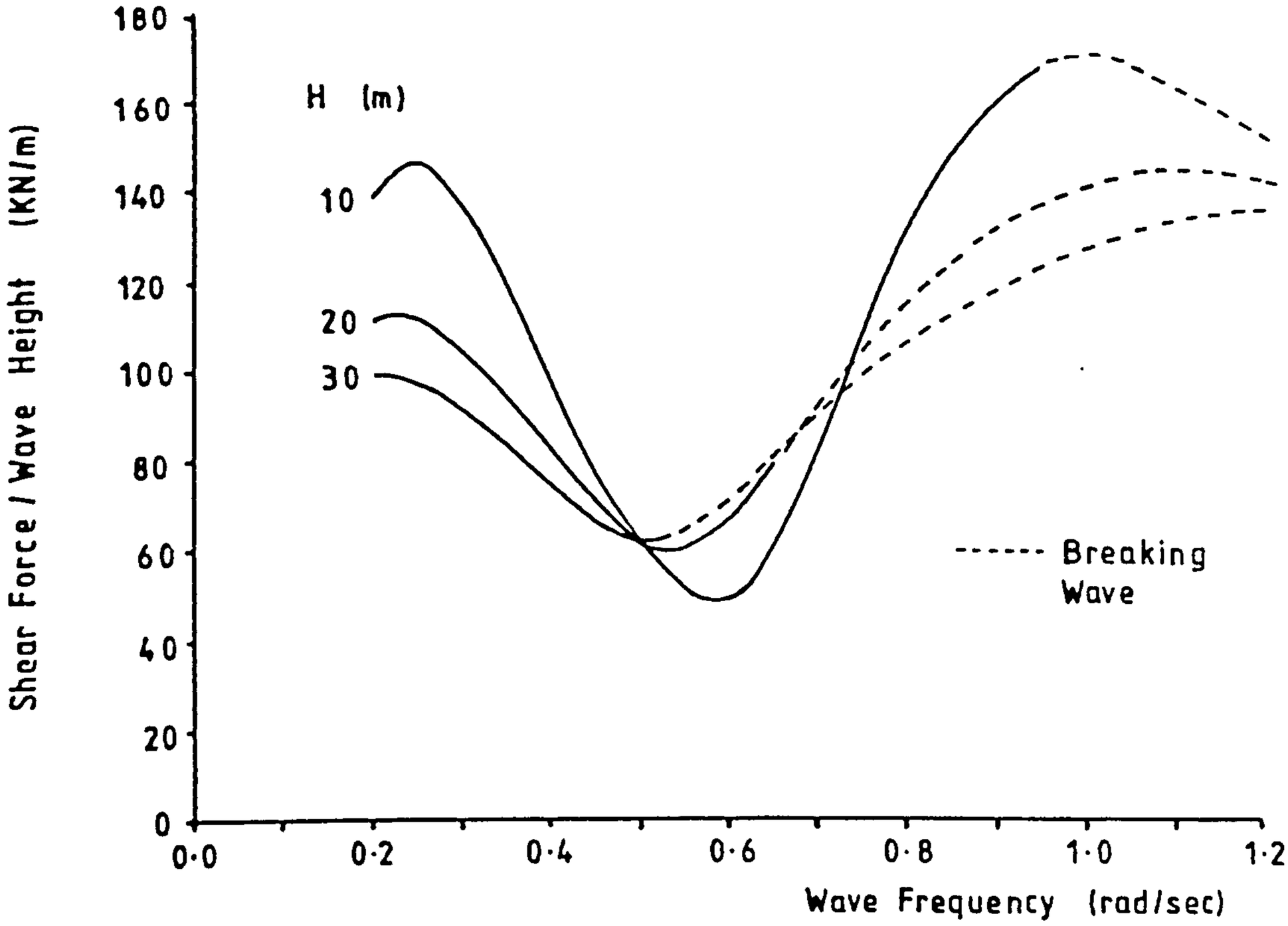

FIG 7.23 Upper Joint Horizontal Shear Force, $c_D = 1.1$

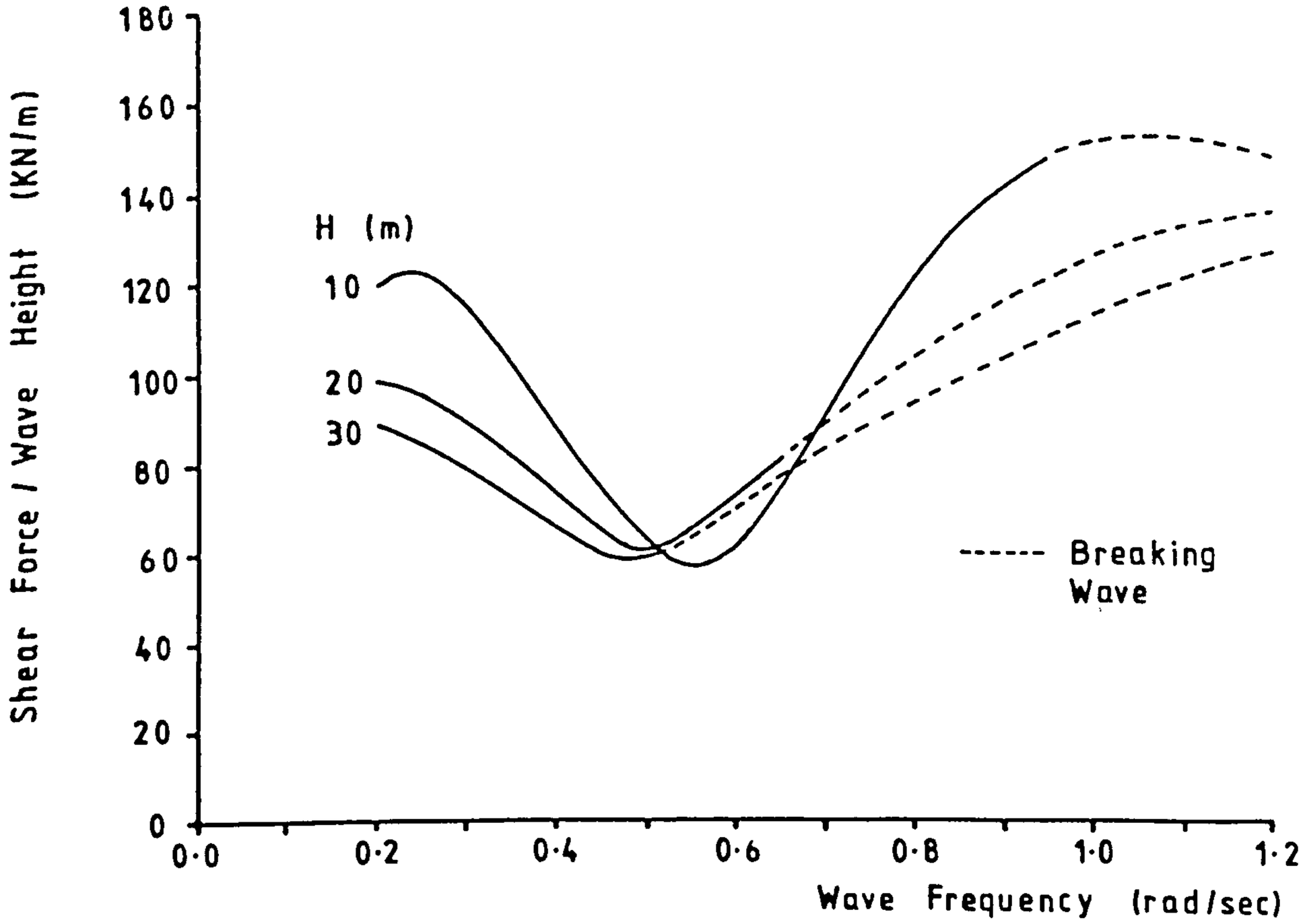

FIG 7.24 Upper Joint Horizontal Shear Force, $c_D = 1.75$

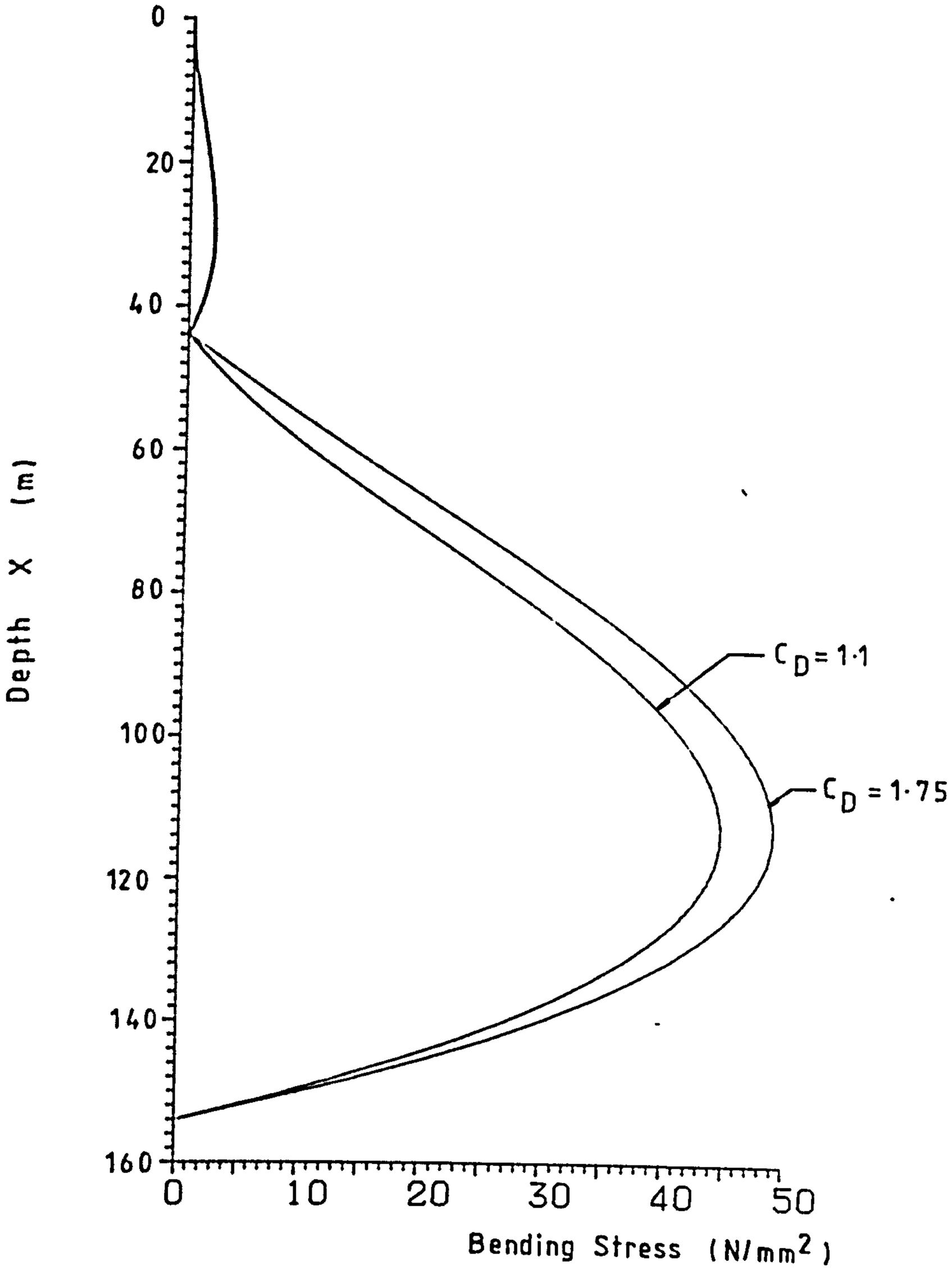

FIG 7.25 Articulated Column Bending Stress Amplitude

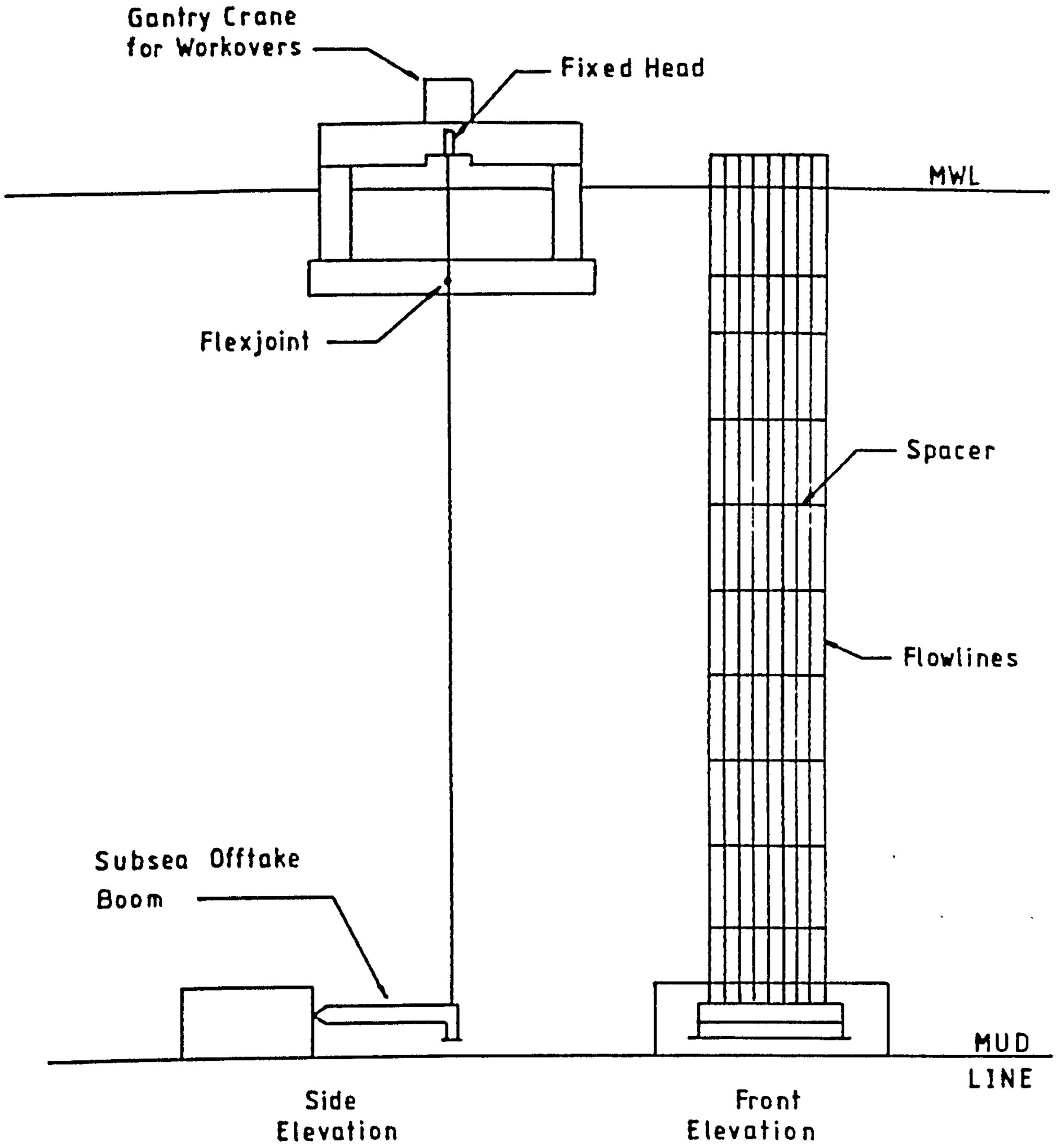

FIG 7.26 Ribbon Riser System

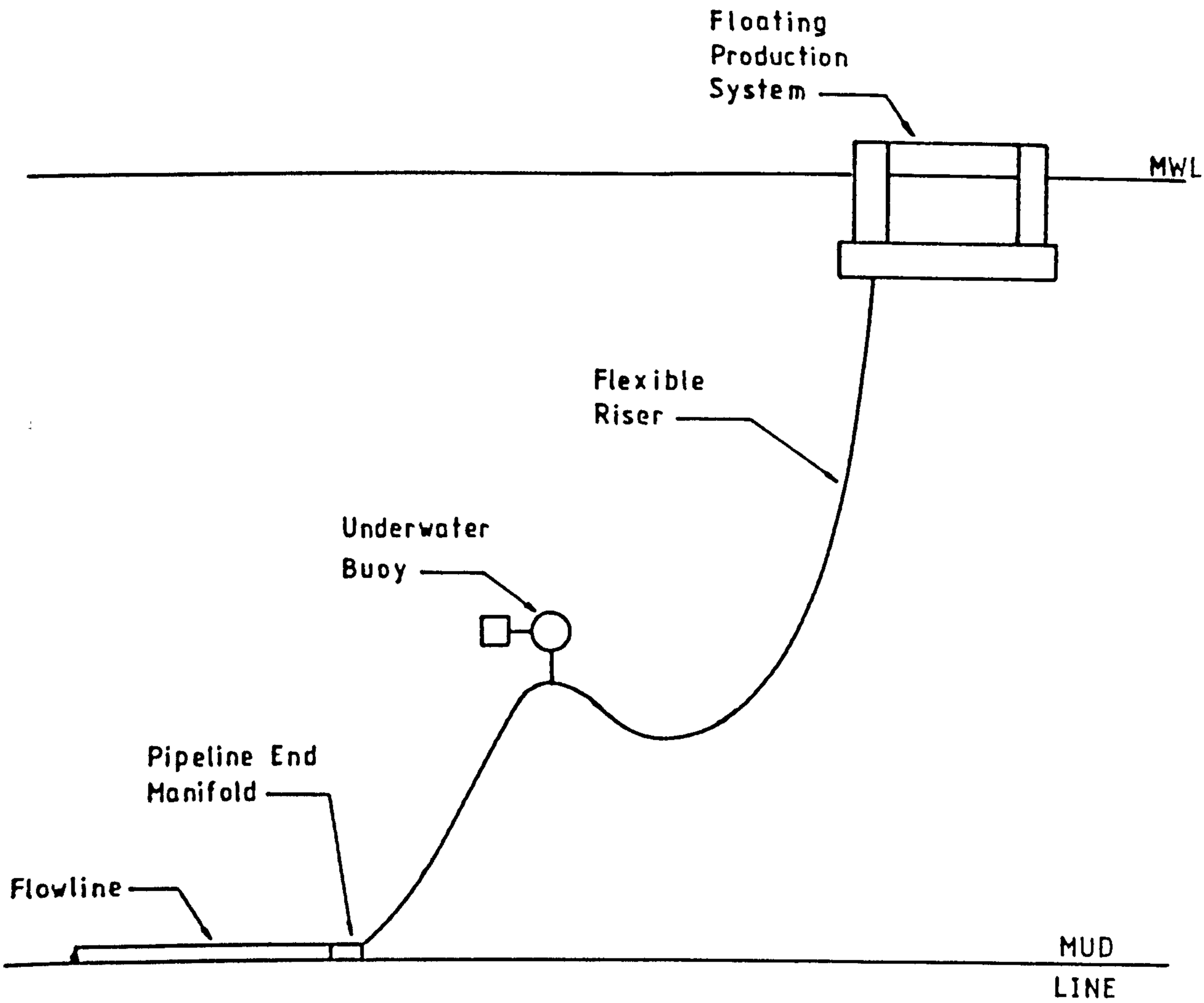

FIG 7.27 Flexible Riser System

REFERENCES

1. ANAND, S.
   AGARWAL, S.L.
   "Field and Laboratory Studies for Evaluating Submarine Pipeline Frictional Resistance"
   ASME J. Energy Res. Tech. 103, 205-254, 1981.

2. ANGRILLI, F.
   BERGAMASCHI, S.
   COSSALTER, V.
   "Investigation of Wall Induced Modifications to Vortex Shedding from a Circular Cylinder"
   ASME J. Fluids Eng. 104, 518-522,1982.

3. BATHE, K.J.
   "Finite Element Procedures in Engineering Analysis"
   Prentice-Hall Inc., 1982.

4. BAYNET, P.A.
   FRASE, J.R.
   "Flexible Riser for a Floating Storage and Offloading System"
   OTC Paper No. 4321, 1982.

5. BEARMAN, P.W.
   ZDRAVKOVICH, M.M.
   "Flow around a Circular Cylinder near a Plane Boundary"
   J. Fluid Mech. 89, 33-47, 1978.

6. BISHOP, J.R.
   TICKELL, R.G.
   GALLAGHER, K.A.
   "The UK Christchurch Bay Project; A Review of Results"
   OTC Paper No. 3796, 1980.

7. BISHOP, J.R.
   "Summary Report of Wave Force Results from the Second Christchurch Bay Tower"
   NMI Ltd. OT-O-82100, 1984.

8. BLEVINS, R.D.
   BURTON, T.E.
   "Fluid Forces Induced by Vortex Shedding"
   J.Fluid Eng. 95, 19-24, 1976.

9. BLEVINS, R.D. "Flow-Induced Vibrations"
Van Nostrand Reinhold Co., New York, 1977.

10. BLEVINS, R.D. "Flow-Induced Vibration of Nuclear Reactors: A Review"
Progress in Nuclear Energy 4, 25-49, 1979.

11. BRUSCHI, R.M.
BURESTI, G.
CASTOLDI, A.
MIGLIAVACCA, E. "Vortex Shedding Oscillations for Submarine Pipelines: Comparison between Full-Scale Experiments and Analytical Models"
OTC Paper No. 4232, 1982.

12. BURESTI, G.
LANCIOTTI, A. "Vortex Shedding from Smooth and Roughened Cylinders in a Cross Flow Near a Plane Surface"
Aeronautical Quarterly, 305-321, Feb. 1979.

13. BURKE, B.G. "An Analysis of Marine Risers for Deep Water"
OTC Paper No. 1771, 1973.

14. CHAKRABARTI, S.K.
FRAMPTON, R.E. "Review of Riser Analysis Techniques"
Applied Ocean Research 4/2, 73-90, 1982.

15. CHEN, S.S. "Flow-Induced Vibrations of Circular Cylindrical Structures, Part I: Stationary Fluids and Parallel Flow"
Shock Vib. Digest 9, 25-38, 1977.

16. CLOUGH, R.W.
PENZIEN, J. "Dynamics of Structures"
McGraw-Hill Kogakusha Ltd., 1975.

17. CURNIER, A. "On Three Modal Synthesis Variants" J. Sound Vib. 90/4, 1983.

18. DAREING, D.W.
HUANG, T. "Marine Riser Vibration Response Determined by Modal Analysis" J.Energy Resources Tech 101/159,1979.

19. FENG, C.C. "The Measurement of Vortex Induced Effects on Flow Past Stationary and Oscillating Circular and D-Section Cylinders" M.A.Sc. thesis, The University of British Columbia, 1968.

20. FUNG, Y.C. "Foundations of Solid Mechanics" Prentice Hall Int., 1965.

21. GARDNER, T.N.
KOTCH, M.A. "Dynamic Analysis of Risers and Caissons by the Element Method" OTC Paper No. 2651, 1976.

22. GEORGIOU "Static and Dynamic Analysis of Multiple Pipeline Spans" MSc Thesis, Cranfield Inst.Tech.,1983.

23. GOKTUN, S. "The Drag and Lift Characteristics of a Cylinder Placed near a Plane Surface" MSc Thesis, U.S. Naval Postgraduate School, Monterey, 1975.

24. GRASS, A.J.
RAVEN, P.W.J.
STUART, R.J.
BRAY, J.A. "The Influence of Boundary Layer Velocity Gradients and Bed Proximity of Vortex Shedding from Free Spanning Pipelines" ASME J.Energy Res. 106, 70-78, 1984.

25. GRIFFIN, O.M.
RAMBERG, S.E.
"The Effects of Synchronized Cylinder Vibrations on Vortex Formation and Strength, Velocity Fluctuations, and Mean Flow"
Paper E-3, Symposium on Flow Induced Structural Vibrations, Karlsruhe, Germany, 1972.

26. GRIFFIN, O.M.
RAMBERG, S.E.
"Some Recent Studies of Vortex Shedding with Application to Marine Tubulars and Risers"
ASME J.Energy Res. 104/1, 2-13,1982.

27. HAFFEN, B.
"Forces on a Transverse Circular Cylinder in a Steady Uniform Flow near a Plane Boundary"
MSc Thesis, Oregon State University, 1975.

28. HALL, J.E.
HEALEY, A.J.
"Dynamics of Suspended Marine Pipelines"
ASME J.Energy Res. Tech 102, 112-119, 1980.

29. HARTLEN, R.T.
"Vortex-excited Oscillations of a Circular Cylinder"
U.T.I.A.S. Report UTME-TP-6809, 1968.

30. HARTNUP, G.
AIREY, R.G.
WILKINSON, P.
"Hydrodynamic Tests on Marine Risers"
OTC Paper No. 4319, 1982.

31. HEALEY, A.J.
SEO, Y.G.T.
"Dynamic Motions of Marine Pipelines on the Ocean Bottom"
ASME J.Energy Res.Tech.106, 65-69, 1984.

32. HOBBS, R.E. "Soil Modulus and Longitudinal Pipeline Stresses" ASCE Transportation Engineering Journal 106/TE6, 775-786, 1980.

33. HOBBS, R.E. "Solutions for Pipeline Lifting Problems Arising in Tie-in and Repair Activities" Proc.2nd Int. Offshore Mechanics and Artic Eng. Symposium, ASME, New York, 538-552, 1983.

34. HOBBS, R.E. "Solutions for Small Slope Pipeline Lifting Problems" ASME J.Energy Res. Tech. 106, 63-64, 1984.

35. HOSKINS, E.C. "Sub-Sea Pipeline Free Span Vibration Analysis" Institute of Petroleum IP82-013,1982.

36. IRVINE, H.M. "Cable Structures" The MIT Press, 1981.

37. IWAN, W.D.
BLEVINS, R.D. "A Model for Vortex-Induced Oscillations of Structures" ASME J.Applied Mech. 96, 581-585,1974.

38. JACOBSEN,V.
BRYNDUM, M.B.
NIELSEN, R.
FINES, S. "Cross-Flow Vibration of a Pipe Close to a Rigid Boundary" ASME J.Energy REs. Tech. 106/4, 451-457, 1984.

39. JINSI, B.K. "Offshore Pipeline Design Parameters" Oil and Gas Journal, Feb. 1982.

40. KAN, W.C.
HEALEY, A.J.
"Finite Element Analysis with the State Variable Transfer Matrix and Geometric nonlinearity for Marine pipelines in Subsurface Tow"
ASME J.Energy Res.Tech.103/1, 26-31, 1981.

41. KING, R.
PROSSER, M.J.
JOHNS, D.J.
"On Vortex Excitation of Model Piles in Water"
J.Sound Vibration 29, 169-188, 1973.

42. KING, R.
"Vortex Excited Structural Oscillations of a Circular Cylinder in Flowing Water"
PhD Thesis, Loughborough University of Tech., 1974.

43. KING, R.
"Review of Vortex Shedding Research and its Applications"
Ocean Engineering 4, 141-172, 1977.

44. KIRK, C.L.
ETOK, E.V.
COOPER, M.T.
"Dynamic and Static Analysis of a Marine Riser"
Applied Ocean Research 1/3, 1979.

45. KIRK, C.L.
"Dynamic Response of Marine Risers by Single Wave and Spectral Analysis Methods"
Applied Ocean Research 7/1, 1985.

46. KIYA, M.
TAMURA, H.
ARIE, M.
"Vortex Shedding from a Circular Cylinder in Moderate Reynolds Number Shear Flow"
J.Fluid Mech. 141/4, 721-735, 1980.

47. KONUK, I. "Application of an Adaptive Numerical Technique to 3-D Pipeline Problems with Strong Nonlinearities" ASME J.Energy Res. Tech. 104/1, 58-62, 1982.

48. LANGLEY, R.S. "The Linearisation of Three Dimensional Drag Force in Random Seas with Current" Applied Ocean Research 6/3, 1984.

49. LIENHARD, J.H. "Synopsis of Lift, Drag and Vortex Frequency Data for Rigid Circular Cylinders" Washington State University, College of Engineering, Research Division Bulletin 300, 1966.

50. MAIER, G.
ANDREUZZI, F.
GIANNESSI, F.
JURINA, L.
TADDEI, F. "Unilateral Contact, Elastoplasticity and Complementarity with Reference to Offshore Pipeline Design" Computer Methods in Applied Mech. Eng. 17/18, 1979.

51. MAIR, W.A.
STANSBY, P.K. "Vortex Wakes of Bluff Cylinders in in Shear Flow" SIAM J.Appl. Math. 28, 1975.

52. McCROSKEY, W.J. "Some Current Research in Unsteady Fluid Dynamics" ASME J.Fluid Eng. 99, 8-39, 1977.

53. MORISON, J.R.
O'BRIEN, M.P.
JOHNSON, J.W.
SCHAAF, S.A. "The Forces Exerted by Surface Waves on Piles" Petroleum Transactions 189, TP2846, 149-154, 1950.

54. MOUSSELLI, A.H. "Offshore Pipeline Design, Analysis and Methods" PennWell Publishing Co., 1981.

55. NEWMARK, N.M. "A Method of Computation for Structural Dynamics" ASCE J.Eng. Mech. Div 85, 1959.

56. NIELSEN, R.
PENDERED, J.W. "Some Aspects of Marine Pipeline Analysis" Ch.17, Numerical Methods in Offshore Engineering, O.C. Zienkiewicz Ed., John Wiley and Sons, 1978.

57. NORDGREN, R.P. "Dynamic Analysis of Marine Risers with Vortex Excitation" ASME J. Energy Res. TEch. 104/1, 14-19, 1982.

58. ODORIZZI, S.
SCHREFLER, B.A. "A Three-Dimensional Geometrically Nonlinear Analysis of Pipelaying in an Ocean Environment" J.Pressure Vessel TEch., Trans ASME 103/2, 201-205, 1981.

59. ORAN, C. "Tangent Stiffness in Space Frames" ASCE J. Struct. Div., 1973.

60. ORAN, C.
KASSIMALI, A. "Large Deformation of Frame Structures Under Static and Dynamic Loads" Computers and Structures 6, 1976.

61. OWEN, D.R.J. "Implicit Finite Element Methods for the Dynamic Transient Analysis of Solids with Particular Reference to Nonlinear Situations"

61. continued — Ch.5, Advanced Structural Dynamics, Applied Science Publishers, 1978.

62. PARKINSON, G.V. — "Mathematical Models of Flow-Induced Vibrations of Bluff Bodies" Flow-Induced Structural Vibrations, ed. Nandascher, E., Springer-Verlag, Berlin, 1974.

63. PRZEMIENIECKI, J.S. — "Theory of Matrix Structural Analysis" McGraw-Hill Book Co., 1968.

64. RAJABI, F.; ZEDAN, M.F.; MANGIAVACCHI, A. — "Vortex Shedding Induced Dynamic Response of Marine Risers" ASME J.Energy Res. 106/1, 1984.

65. REGA, G.; VESTRONI, F.; BENEDETTINI, F. — "Parametric Analysis of Large Amplitude Free Vibrations of a Suspended Cable" Int. J.Solids Struct. 20/2, 1984.

66. ROSHKO, A. — "Experiments on the Flow Past a Cylinder at Very High Reynolds Number" J.Fluid Mech. 10, 345-356, 1961.

67. SARPKAYA, T. — "Vortex-Induced Oscillations - A Selective Review" ASME J.Applied Mech. 46, 241-258, 1979.

68. SARPKAYA, T. — "Mechanics of Wave Forces on Offshore Structures" Van Nostrand Reinhold Co., 1981.

69. SCRUTON, C. "On the Wind-Excited Oscillations of Stacks, Towers and Masts" Paper 16, Proc. Conf. on Wind Effects on Buildings and Structures, Teddington, U.K., 1963.

70. SEXTON, R.M.
AGBEZUGE, L.K. "Random Wave and Vessel Motion Effects on Drilling Riser Dynamics" OTC Paper No. 2650, 1976.

71. SHOTBOLT, K. "The Influence of Production Riser Design on the Configuration and Operation of Semi-Submersible Floating Production Systems" J.Soc. Underwater Tech., 1983.

72. SKOP, R.A.
GRIFFIN, O.M. " A Model for the Vortex Excited Resonant Vibrations of Bluff Bodies" J. Sound Vibration 27, 1973.

73. SPARKS, C.P. "The Influence of Tension Pressure and Weight on Pipe and Riser Deformations and Stresses" J.Energy Res. Tech. 106/1, 1984.

74. STRATING, J. "A Survey of Pipelines in the North Sea Incidents During Installation, Testing and Operation" OTC Paper No. 4069, 1981.

75. STROUHAL, V. "Uber eine besondere Art de Tonneregung" Ann. Physik (Leipzig), 1878.

76. TIMOSHENKO, S.P.
GERE, J.M. "Theory of Elastic Stability" McGraw-Hill, 2nd Edition, 1963.

77. TOEBES, G.H. "The Unsteady Flow and Wake Near an Oscillating Cylinder" J.Basic Eng. 91, 493, 1969.

78. TSAHALIS, D.T. JONES, W.T. "Vortex Induced Vibrations of a Flexible Cylinder near a Plane Boundary in Steady Flow" OTC Paper No. 3991, 1981.

79. TSAHALIS, D.T. JONES, W.T. "The Effect of the Sea-Bottom Proximity on the Fatigue Life of Suspended Spans of Offshore Pipelines Undergoing Vortex-Induced Vibrations" OTC Paper No. 4231, 1982.

80. TSAHALIS, D.T. "The Effect of Seabottom Proximity on the Vortex Induced Vibrations and FAtigue Life of Offshore Pipelines" J.Energy REsources Tech. 105, 1983.

81. TSAHALIS, D.T. "Vortex-Induced Vibrations of a Flexible Cylinder Near a Plane Boundary Exposed to Steady and Wave-Induced Currents" ASME J.Energy Res. 106/1, 206-213, 1984.

82. TUCKER, M.J. CHALLENOR, P.G. CARTER, D.J.T. "Numerical Simulation of a Random Sea: A Common error and its Effect upon Wave Group Statistics" Applied Ocean Research 6/2, 118-122, 1984.

83. VICKERY, B.J. WATKINS, "Flow-induced Vibrations of Cylindrical Structures" Proc. 1st Australiasian Conf., 213-241, 1962.

84. VICKERY, B.J.
CLARK, A.W.
"Lift or Across Wind Response of Tapered Stacks"
ASCE J.Struct. Div. 98, 1972.

85. WEN, K.
RAHIMZADEH, J.
"Nonlinear Elastic Frame Analysis by Finite Element"
J.Struct. Eng. 109/8, 1983.

86. WHITNEY, A.K.
CHUNG, J.S.
"Vibrations of Long Marine Pipes due to Vortex Shedding"
ASME J.Energy Res. Tech. 103/3, 231-236, 1981.

87. WHITNEY, A.K.
NIKKEL, K.G.
"Effects of Shear Flow on Vortex-Shedding-Induced Vibrations of Marine Risers"
OTC 4595, 1983.

88. WILSON, E.L.
FARHOOMAND, I.
BATHE, K.J.
"Nonlinear Dynamic Analysis of Complex Structures"
Int. J. Earthquake Eng. Struct. Dynamics 1, 1973.

89. WINTERKORN, H.F.
FANG, H.
"Foundation Engineering Handbook"
Van Nostrand Reinhold Co., 1975.

90. WOOTTON, L.R.
WARNER, M.H.
SAINSBURY, R.N.
COOPER, D.H.
"Oscillations of Piles in Marine Structures - A Description of the Full Scale Experiments at Immingham"
CIRIA Tech. Note 40, 1972.

91. ZIENKIEWICZ, O.C.
"The Finite Element Method"
McGraw-Hill Book Co. (UK) Ltd, 3rd Ed., 1977.

92. ANON "Comparison of Marine Drilling Riser Analyses"
API Bulletin 2J, 1st Edition, 1977.

93. ANON "Rules for Submarine Pipeline Systems"
Det Norske Veritas, 1981.

APPENDIX A

EQUATION OF MOTION FOR BEAM-COLUMN ON ELASTIC FOUNDATION

The equations of motion for the dynamic response of a beam-column resting on a continuous horizontal elastic foundation of stiffness k per length are derived by considering the beam shown in figure A1. The beam of mass ρ per length and flexural rigidity EI is subjected to a constant axial tension force T together with a distributed lateral load of intensity $f(x,t)$. An infinitesimal element of length dx between two cross sections taken normal to the original undeflected axis of the beam is shown in figure A2. The distributed forces acting along this element consists of the lateral force f , the foundation resisting force kv and the inertia relief force $\rho\ddot{v}$. Since dx is taken in the limit as tending to zero all of these forces may be assumed constant over the length of the element. The end forces on the element consist of the shear force S plus bending moment M and are taken positive as shown. Moment equilibrium taken in the limit as $dx \to 0$ now gives

$$S = T\frac{\partial v}{\partial x} - \frac{\partial M}{\partial x} \qquad \text{(A1)}$$

which setting $M = EIv''$ using simple beam theory gives

$$S = T\frac{\partial v}{\partial x} - EI\frac{\partial^3 v}{\partial x^3} \qquad \text{(A2)}$$

In a similar manner resolving forces in the vertical direction we find

$$\frac{\partial S}{\partial x} = \rho \ddot{v} + kv - f \qquad \text{(A3)}$$

Differentiating equation (A2) wrt x and substituting into equation (A3) now gives the required equation of motion as

$$\frac{\partial^2 v}{\partial t^2} + EI\frac{\partial^4 v}{\partial x^4} - T\frac{\partial^2 v}{\partial x^2} + kv = f(x,t) \qquad \text{(A4)}$$

If instead of a tensile force T the beam is subjected to a compression force ρ the equation of motion becomes

$$\frac{\partial^2 v}{\partial t^2} + EI\frac{\partial^4 v}{\partial x^4} + \rho\frac{\partial^2 v}{\partial x^2} + kv = f(x,t) \qquad \text{(A5)}$$

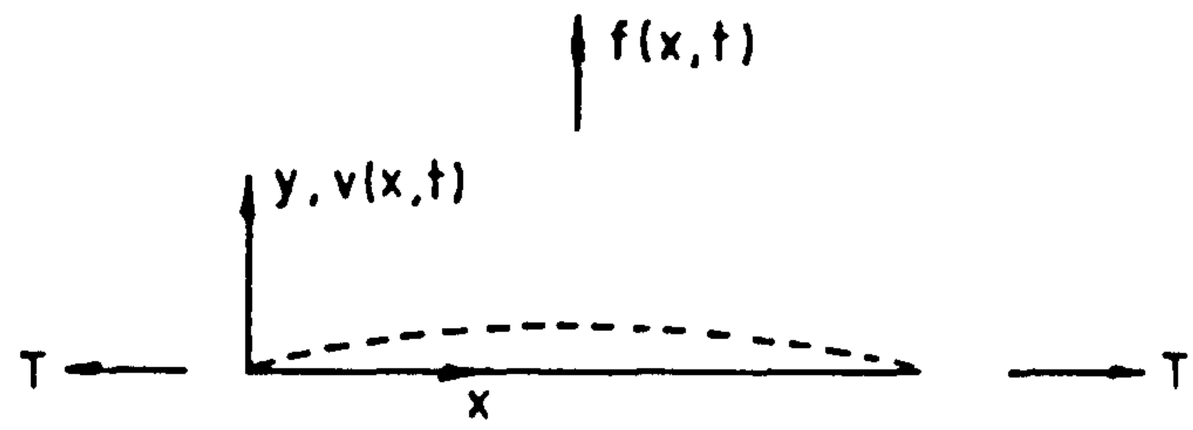

FIG A1

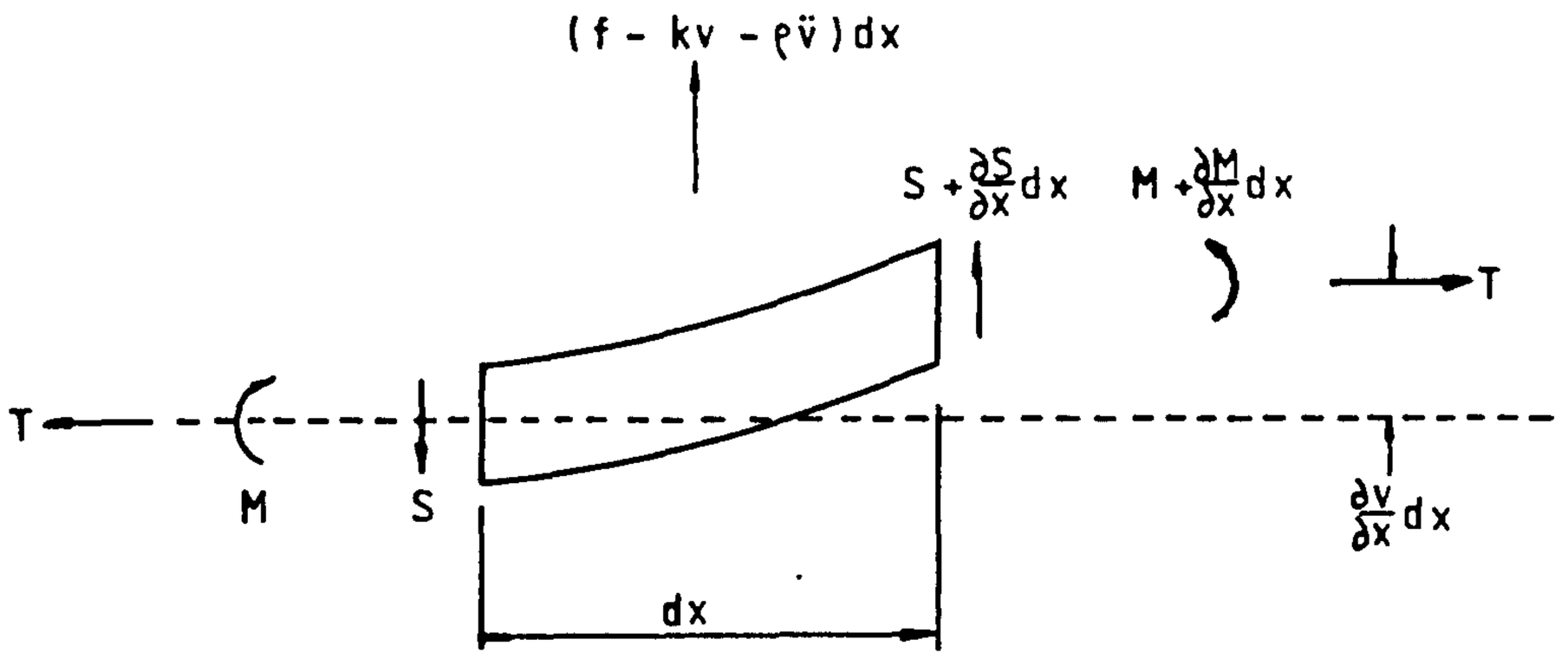

FIG A2

APPENDIX B

FREQUENCY EQUATIONS FOR PIPE SPAN

B.0 Notation

The following general notation defined in Chapter 2 is repeated here for convenience

$$\gamma^2 = T/4EI$$

$$\beta_1^4 = \rho\omega^2/4EI$$

$$\beta_2^4 = (k-\rho\omega^2)/4EI$$

$$\bar{\omega} = a\sqrt{EI/\rho L^4}$$

$$a = 22.37$$

$$R = \omega/\bar{\omega}$$

$$\gamma = RL^4/EI$$

$$\delta = TL^2/EI$$

$$\omega_c^2 = k/\rho - T^2/4EI\rho$$

$$\omega_{cb}^2 = k/\rho$$

$$R_c^2 = (\gamma - \delta^2/4)/a^2$$

$$R_{cb}^2 = \gamma/a^2$$

$$f_i = Det(F_i)$$

In the following sections mode shape solutions ϕ_1 and ϕ_2 together with the corresponding compatibility matrices F_i are tabulated for the six cases listed in table 2.2.

B.1 Symmetric Modes

The general solution for the free span section AB is given by

$$\phi_1 = A_1 \cos\lambda_1 x_1 + B_1 \cos\mu_1 x_1$$

$$\lambda_1 = (2\,[\gamma^4 + \beta_1^4]^{1/2} + 2\gamma^2)^{1/2}$$

$$\mu_1 = (2\,[\gamma^4 + \beta_1^4]^{1/2} - 2\gamma^2)^{1/2}$$

$$P_1 = \lambda_1 L/2 = \tfrac{1}{2}([a^2R^2 + \delta^2/4]^{1/2} + \delta/2)^{1/2}$$

$$Q_1 = \mu_1 L/2 = \tfrac{1}{2}([a^2R^2 + \delta^2/4]^{1/2} - \delta/2)^{1/2}$$

Solutions for the supported section $\beta\omega$ depend on frequency as follows

CASE 1 $R^2 < R_c^2 \quad (\omega^2 < \omega_c^2)$

$$\phi_2 = e^{-\lambda_2 x_2}(A_2 \cos\mu_2 x_2 + B_2 \sin\mu_2 x_2)$$

$$\lambda_2 = (\beta_2^2 + \gamma^2)^{1/2}$$

$$\mu_2 = (\beta_2^2 - \gamma^2)^{1/2}$$

$$P_2 = \lambda_2 L/2 = \tfrac{1}{2}(\tfrac{1}{2}[\sigma - a^2R^2]^{1/2} + \delta/4)^{1/2}$$

$$Q_2 = \mu_2 L/2 = \tfrac{1}{2}(\tfrac{1}{2}[\sigma - a^2R^2]^{1/2} - \delta/4)^{1/2}$$

$$F_1 = \begin{bmatrix} \cosh P_1 & \cos Q_1 & -1 & 0 \\ P_1 \sinh P_1 & -Q_1 \sin Q_1 & P_2 & -Q_2 \\ P_1^2 \cosh P_1 & -Q_1^2 \cos Q_1 & (Q_2^2 - P_2^2) & 2P_2Q_2 \\ P_1^3 \sinh P_1 & Q_1^3 \sin Q_1 & (P_2^3 - 3P_2Q_2^2) & (Q_2^3 - 3P_2^2Q_2) \end{bmatrix}$$

CASE 2 $\quad R^2 = R_c^2 \quad (\omega^2 = \omega_c^2)$

$$\phi_2 = e^{-\lambda_2 x_2}(A_2 + B_2 x_2/L)$$

$$\lambda_2 = \sqrt{2}\, \alpha$$

$$P_2 = \lambda_2 L/2 = \tfrac{1}{2}(\delta/2)^{1/2}$$

$$F_2 = \begin{bmatrix} \cosh P_1 & \cos Q_1 & -1 & -1 \\ P_1 \sinh P_1 & -Q_1 \sin Q_1 & P_2 & Q_2 \\ P_1^2 \cosh P_1 & -Q_1^2 \cos Q_1 & -P_2^2 & -Q_2^2 \\ P_1^3 \sinh P_1 & Q_1^3 \sin Q_1 & P_2^3 & Q_2^3 \end{bmatrix}$$

CASE 3 $\quad R_c^2 < R^2 < R_{RB}^2 \quad (\omega_c^2 < \omega^2 < \omega_{RB}^2)$

$$\phi_2 = A_2 e^{-\lambda_2 x_2} + B_2 e^{-\mu_2 x_2}$$

$$\lambda_2 = \left(2\alpha^2 + 2\left[\alpha^4 - \beta_2^4\right]^{1/2}\right)^{1/2}$$

$$\mu_2 = \left(2\alpha^2 - 2\left[\alpha^4 - \beta_2^4\right]^{1/2}\right)^{1/2}$$

$$P_2 = \lambda_2 L/2 = \tfrac{1}{2}\left(\delta/2 + \left[\delta^2/4 - \gamma + a^2R^2\right]^{1/2}\right)^{1/2}$$

$$Q_2 = \mu_2 L/2 = \tfrac{1}{2}\left(\delta/2 - \left[\delta^2/4 - \gamma + a^2R^2\right]^{1/2}\right)^{1/2}$$

$$F_5 = \begin{bmatrix} \cosh P_1 & \cos Q_1 & -1 & -1 \\ P_1 \sinh P_1 & -Q_1 \sin Q_1 & P_2 & Q_2 \\ P_1^2 \cosh P_1 & -Q_1^2 \cos Q_1 & -P_2^2 & -Q_2^2 \\ P_1^3 \sinh P_1 & Q_1^3 \sin Q_1 & P_2^3 & Q_2^3 \end{bmatrix}$$

B.2 Antisymmetric Modes

In this case the general solution for the free span AB becomes

$$\phi_1 = A_1 \sinh \lambda_1 x_1 + B_1 \sin \mu_1 x_1$$

where λ_1 and μ_1 (and hence P_1 and Q_1) are as defined in section B.1. For the supported section $B\infty$ the solution ϕ_2 depends on frequency in the same way as for the symmetric modes. The matrices F_4, F_5 and F_6 are therefore obtained from F_1, F_2 and F_3 respectively by replacing columns 1 and 2 with

$$\begin{bmatrix} \sinh P_1 & \sin Q_1 \\ P_1 \cosh P_1 & Q_1 \cos Q_1 \\ P_1^2 \sinh P_1 & -Q_1^2 \sin Q_1 \\ P_1^3 \cosh P_1 & -Q_1^3 \cos Q_1 \end{bmatrix}$$

B.3 Notes on Solution

By combining the above cases the complete non-dimensional frequency equations for symmetric and anti-symmetric modes may be written as

$$f_S(R, \gamma, \delta) = 0 \qquad \text{(B1)}$$

$$f_A(R, \gamma, \delta) = 0 \qquad \text{(B2)}$$

where

$$f_S = \begin{cases} f_1(R, \gamma, \delta) & , \quad R^2 < R_c^2 \\ f_2(R, \delta) & , \quad R^2 = R_c^2 \\ f_3(R, \gamma, \delta) & , \quad R_c^2 < R^2 < R_{RB}^2 \end{cases} \qquad \text{(B3)}$$

$$f_A = \begin{cases} f_4(R, \gamma, \delta) & , \quad R^2 < R_c^2 \\ f_5(R, \delta) & , \quad R^2 = R_c^2 \\ f_6(R, \gamma, \delta) & , \quad R_c^2 < R^2 < R_{RB}^2 \end{cases} \qquad \text{(B4)}$$

In solving these equations for the non-dimensional frequencies ℓ a certain amount of care is required. First for $\delta \leq 0$ (i.e. $\tau \leq 0$) only frequencies such that $\ell^2 < \ell_c^2$ should be sought since for higher frequencies the mode shapes have infinite extent along the section $\beta\infty$. Next considering equations (B3) and (B4) it is noted that the determinants f_2 and f_5 are independent of γ . Thus for any given $\delta > 0$ values of ℓ may be found which make these determinants zero and γ calculated using

$$\gamma = a^2\ell^2 + \delta^2/4$$

By this means a special set of roots is first determined for which the solution form β (see table 2.2) applies in section $\beta\infty$. These roots are indicated by a dotted line in figures 2.8, 2.10, 2.12 and 2.14. Next considering the matrix F_1 valid for $\ell^2 < \ell_c^2$ it is noted that as $\ell^2 \to \ell_c^2$ the non-dimensional term $Q_2 \to 0$. It follows that the 4th column in the matrix becomes arbitrarily small resulting in the determinant f_1 tending to zero. A similar situation applies to the matrix F_3 valid for $\ell^2 > \ell_c^2$ so that we may write

$$\lim_{\ell^2 \to \ell_c^2} f_1 = \lim_{\ell^2 \to \ell_c^2} f_3 = 0$$

However this situation does not imply that $\ell^2 = \ell_c^2$ is always a root of equation (B1) since for any given γ and δ the corresponding frequency ratio $\ell_c^2 = (\gamma - \delta^2/4)/a^2$ will not in general make f_2 zero. In fact the frequency equation $f_5 = 0$ has a discontinuity at $\ell^2 = \ell_c^2$ as indicated in figure B1.. To avoid any numerical problems

associated with this singularity the equation $f_S = 0$ should be solved by searching for zeroes separately in the domains $0 < R^2 \leq R_c^2 - \varepsilon$ and $R_c^2 + \varepsilon \leq R^2 < R_{RB}^2$ where ε is a small quantity taken here as 10^{-4}. Similar remarks apply to the antisymmetric case, equation (B2).

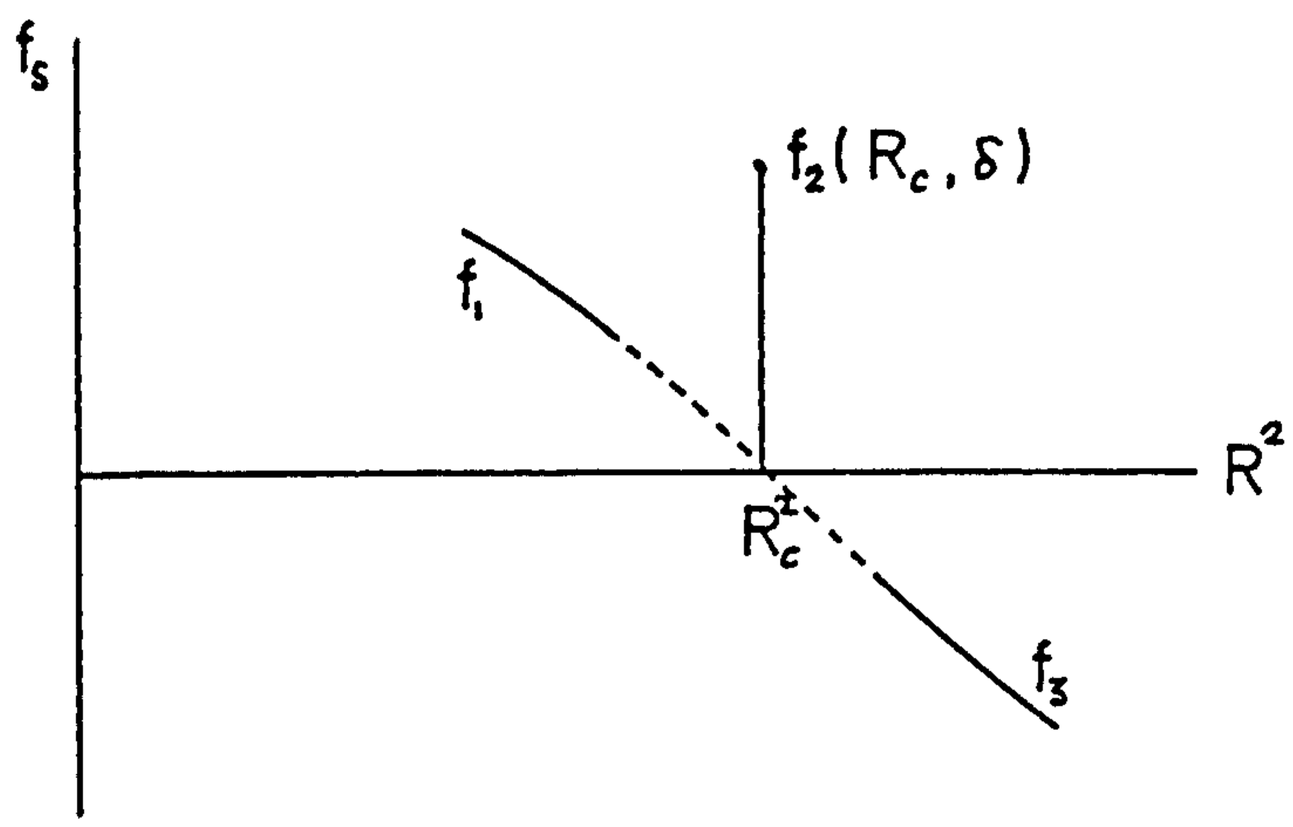

FIGURE B1

APPENDIX C

1. PIPELINE ELEMENT

$$k^B = \frac{1}{L_e^3}\begin{bmatrix} 12 & 6L_e & -12 & 6L_e \\ & 4L_e^2 & -6L_e & 2L_e^2 \\ & & 12 & -6L_e \\ \underline{Sym} & & & 4L_e^2 \end{bmatrix} \qquad \text{(C1)}$$

$$k^\sigma = \frac{1}{30L_e}\begin{bmatrix} 36 & 3L_e & -36 & 3L_e \\ & 4L_e^2 & -3L_e & -L_e^2 \\ & & 36 & -3L_e \\ \underline{Sym} & & & 4L_e^2 \end{bmatrix} \qquad \text{(C2)}$$

$$k^S = \frac{L_e}{420}\begin{bmatrix} 156 & 22L_e & 54 & -13L_e \\ & 4L_e^2 & 13L_e & -3L_e^2 \\ & & 156 & -22L_e \\ \underline{Sym} & & & 4L_e^2 \end{bmatrix} \qquad \text{(C3)}$$

$$\underset{\sim}{p}^{b} = -\frac{wLe}{12}\begin{bmatrix} 6 \\ Le \\ 6 \\ -Le \end{bmatrix} \qquad (C4)$$

$$m^{p} = \frac{Le}{6}\begin{bmatrix} 2 & 1 \\ 1 & 2 \end{bmatrix} \qquad (C5)$$

2. RISER ELEMENT

a) Fully Connected

k^{a} As equation (C1)

k^{σ} As equation (C2)

$$k^{x} = \frac{1}{60}\begin{bmatrix} 36 & 6Le & -36 & 0 \\ & 2Le^{2} & -6Le & -Le^{2} \\ & & 36 & 0 \\ & & & 6Le^{2} \end{bmatrix} \qquad (C6)$$

$$m^{a} = \frac{Le}{420}\begin{bmatrix} 156 & 22Le & 54 & -13Le \\ & 4Le^{2} & 13Le & -3Le^{2} \\ & & 156 & -22Le \\ & & & 4Le^{2} \end{bmatrix} \qquad (C7)$$

$$\underset{\sim}{P}_E^e = F_E(X_1)\frac{Le}{60}\begin{bmatrix} 21 \\ 3Le \\ 9 \\ -2Le \end{bmatrix} + F_E(X_2)\frac{Le}{60}\begin{bmatrix} 9 \\ 2Le \\ 21 \\ -3Le \end{bmatrix} \qquad \text{(C8)}$$

b) Moment Release at End 1

$$k^{\delta} = \frac{1}{Le^3}\begin{bmatrix} 3 & 0 & -3 & 3Le \\ & 0 & 0 & 0 \\ & & 3 & -3Le \\ \underline{Sym} & & & 3Le^2 \end{bmatrix} \qquad \text{(C9)}$$

$$k^{\sigma} = \frac{1}{5Le}\begin{bmatrix} 6 & 0 & -6 & Le \\ & 0 & 0 & 0 \\ & & 6 & -Le \\ \underline{Sym} & & & Le^2 \end{bmatrix} \qquad \text{(C10)}$$

$$k^{\chi} = \frac{1}{8}\begin{bmatrix} 3 & 0 & -3 & 0 \\ & 0 & 0 & 0 \\ & & 3 & 0 \\ \underline{Sym} & & & L_e^2 \end{bmatrix} \qquad \text{(C11)}$$

$$m^{e} = \frac{Le}{840}\begin{bmatrix} 198 & 0 & 117 & -33Le \\ & 0 & 0 & 0 \\ & & 408 & -72Le \\ \underline{Sym} & & & 16Le^2 \end{bmatrix} \qquad (C12)$$

$$\underset{\sim}{\rho}_E^{e} = F_E(X_1)\frac{Le}{120}\begin{bmatrix} 33 \\ 0 \\ 27 \\ -7Le \end{bmatrix} + F_E(X_2)\frac{Le}{120}\begin{bmatrix} 12 \\ 0 \\ 48 \\ -8Le \end{bmatrix} \qquad (C13)$$

c) Moment Release at End 2

$$k^{\beta} = \frac{1}{Le^3}\begin{bmatrix} 3 & 3Le & -3 & 0 \\ & 3Le^2 & -3Le & 0 \\ & & 3 & 0 \\ \underline{Sym} & & & 0 \end{bmatrix} \qquad (C14)$$

$$k^{\sigma} = \frac{1}{5Le}\begin{bmatrix} 6 & Le & -6 & 0 \\ & Le^2 & -Le & 0 \\ & & 6 & 0 \\ \underline{Sym} & & & 0 \end{bmatrix} \qquad (C15)$$

$$k^r = \frac{1}{40}\begin{bmatrix} 33 & 8Le & -33 & 0 \\ & 3Le^2 & -8Le & 0 \\ & & 33 & 0 \\ \underline{Sym} & & & 0 \end{bmatrix} \qquad \text{(C16)}$$

$$m^e = \frac{Le}{840}\begin{bmatrix} 408 & 72Le & 117 & 0 \\ & 16Le^2 & 33Le & 0 \\ & & 198 & 0 \\ \underline{Sym} & & & 0 \end{bmatrix} \qquad \text{(C17)}$$

$$\underset{\sim}{P}_E^e = F_E(X_1)\frac{Le}{120}\begin{bmatrix} 48 \\ 8Le \\ 12 \\ 0 \end{bmatrix} + F_E(X_2)\frac{Le}{120}\begin{bmatrix} 27 \\ 7Le \\ 33 \\ 0 \end{bmatrix} \qquad \text{(C18)}$$

APPENDIX D

ENERGY CHECK FOR FRICTION ELEMENT

Considering for simplicity the case $\Delta T_1 > 0$ and using equations (3.58) to (3.60) the force-displacement for the friction element during the initial loading phase may be written as

$$T^\rho = k_1 (a^\rho)^{1/2} \tag{D1}$$

where $k_1 = (2\mu N E A)^{1/2}$. Thus recalling that the total real end load on the pipe is $T_R + T^\rho$, figure D1, the work done by the end load during the initial loading phase is

$$W_e = T_R a^\rho + \int_0^{a^\rho} k_1 a^{1/2} da \tag{D2}$$

which using equation (D1) is evaluated as

$$W_e = T_R a^\rho + \frac{(T^\rho)^3}{3\mu N E A} \tag{D3}$$

Next considering the internal strain energy the increase in strain energy between stations x and $x + dx$ is given by

$$dV_i = \frac{1}{2EA}\left[(T_R + T^\rho(x))^2 - T_R^2\right] dx \tag{D4}$$

where $T^\rho(x)$ represents the overtension at station x , figure D1. Thus measuring x as shown we have

$$T^{\rho}(x) = \mu W x \tag{D5}$$

and equation (D4) is evaluated as

$$dV_i = \frac{1}{2EA}\left(2\mu W T_R x + \mu^2 W^2 x^2\right) dx \tag{D6}$$

The total increase in strain energy is therefore

$$V_i = \frac{1}{2EA}\int_0^{L_1}\left(2\mu W T_R x + \mu^2 W^2 x^2\right) dx \tag{D7}$$

which using $L_1 = T^{\rho}/\mu W$ is evaluated as

$$V_i = T_R a^{\rho} + \frac{(T^{\rho})^3}{6\mu W E A} \tag{D8}$$

Comparing this to equation (D3) it is clear that the first term represents the work done by the constant end load T_R, while the second term is one half of the work done by the variable overtension T^{ρ}.

Finally the work done by the nonconservative friction forces may be written as

$$W_{NC} = \int_0^{L}\mu W u(x)\, dx \tag{D9}$$

where the deflection $u(x)$ at station x is given by

$$u(x) = \int_0^x \varepsilon(x)\,dx = \int_0^x \frac{\mu W x}{EA}\,dx \qquad \text{(D10)}$$

Evaluating the integrals (D9) and (D10) gives

$$W_{Nc} = \frac{(T^p)^3}{6\mu W E A} \qquad \text{(D11)}$$

which equals the second half of the work done by the variable overtension T^p. Thus considering equations (D3), (D8) and (D11) we may write

$$W_e = V_i + W_{Nc} \qquad \text{(D12)}$$

indicating that the total work done by the external load is either stored in the pipe or lost against friction.

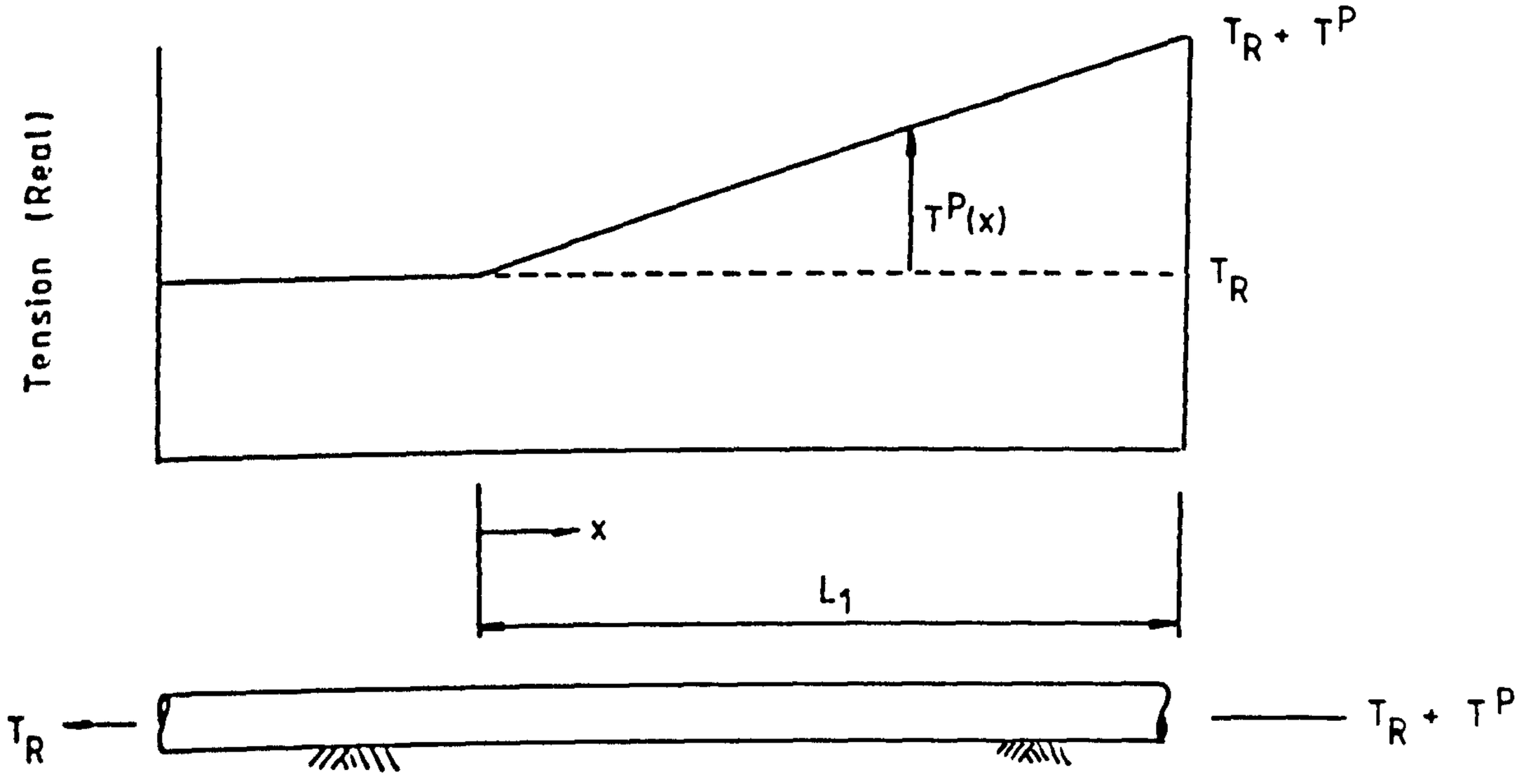

FIG D1 Real Tension Distribution in Friction Element

APPENDIX E

DRAG FORCE LINEARISATION USING EQUIVALENT WORK

Using Morison's equation the nonlinear drag force per length on a moving vertical cylinder of diameter D is

$$f_D = \tfrac{1}{2}\rho_e C_D D (u_c + u_w - \dot{v}) |u_c + u_w - \dot{v}| \qquad \text{(E1)}$$

where

ρ_e = External fluid density

C_D = Empirical drag coefficient

u_c = Current induced horizontal fluid velocity

u_w = Wave induced horizontal fluid velocity

$\dot{v}$ = Horizontal structural velocity of cylinder

For a linearised frequency domain analysis the dynamic component of this load is approximated by

$$f_E = C_E (u_c + u_w - \dot{v}) \qquad \text{(E2)}$$

where the coefficient C_E is to be determined such that both forces do equal work over one complete wave/response cycle. Thus considering first the work done by f_D we have

$$W_D = \int_0^T f_D \dot{v} \, dt$$

$$= \frac{1}{2}\rho_e C_D D \int_0^T (u_c + u_w - \dot{v}) |u_c + u_w - \dot{v}| \dot{v}\, dt \qquad \text{(E3)}$$

where $T = 2\pi/\omega$ represents the wave period. To evaluate this expression first write the dynamic component of the relative velocity as

$$r = u_w - \dot{v} \qquad \text{(E4)}$$

Now assuming u_w and $\dot{v}$ are both harmonic we may write

$$r = Re(Re^{i\omega t}) = Re(|R| e^{i(\theta_R + \omega t)})$$

$$= |R| \cos(\theta_R + \omega t) \qquad \text{(E5)}$$

where $R = |R| e^{i\theta_R}$ is the complex relative velocity. In a similar manner for the structural velocity

$$\dot{v} = Re(Ve^{i\omega t}) = Re(|V| e^{i(\theta_V + \omega t)})$$

$$= |V| \cos(\theta_V + \omega t) \qquad \text{(E6)}$$

so that equation (E3) becomes

$$W_D = \frac{1}{2}\rho_e C_D D \int_0^T (u_c + |R| \cos(\theta_R + \omega t)) |u_c + |R| \cos(\theta_R + \omega t)|$$

$$\times |V| \cos(\theta_V + \omega t)\, dt \qquad \text{(E7)}$$

Now setting $\theta_R + \omega t = \omega\tau$ and shifting the limits of integration (any complete cycle may be used)

$$\bar{W}_D = \frac{1}{2}\rho_e C_0 D |V| \int_0^T (u_c + |R|\cos\omega\tau)\left|u_c + |R|\cos\omega\tau\right| \cos(\theta_V - \theta_R + \omega\tau)\, d\tau$$

$$= \frac{1}{2}\rho_e C_0 D |V| \, I_D$$

(E8)

To evaluate the integral I_D consider first the indefinite integral

$$J_D = \int_0^T (u_c + |R|\cos\omega\tau)^2 \cos(\theta_V - \theta_R + \omega\tau)\, d\tau$$

$$= \cos(\theta_V - \theta_R) \int_0^T (u_c + |R|\cos\omega\tau)^2 \cos\omega\tau \, d\tau$$

$$- \sin(\theta_V - \theta_R) \int_0^T (u_c + |R|\cos\omega\tau)^2 \sin\omega\tau \, d\tau$$

(E9)

which on evaluation gives

$$J_D = \cos(\theta_V - \theta_R)\left\{ u_c^2 \frac{\sin\omega\tau}{\omega} + u_c|R| \frac{(2\omega\tau + \sin 2\omega\tau)}{2\omega} \right.$$

$$\left. + |R|^2 \frac{(3\sin\omega\tau - \sin^3\omega\tau)}{3\omega} \right\} + \sin(\theta_V - \theta_R) \frac{(u_c + |R|\cos\omega\tau)^3}{3\omega|R|}$$

Now on evaluating equation (E8) two cases apply

a) $\underline{u_c \geq |R|}$

$$I_D = J_0(\tau) - J_1(\theta) = \frac{2\pi}{\omega} u_c |R| \cos(\theta_v - \theta_R) \qquad \text{(E10)}$$

b) $\underline{u_c < |R|}$

$$I_D = J_0(\tau) - J_0(\theta) - 2\{J_0(\tau_2) - J_0(\tau_1)\}$$

$$= \frac{2\pi}{\omega} u_c |R| \cos(\theta_v - \theta_R) - 2\{J_0(\tau_2) - J_0(\tau_1)\} \qquad \text{(E11)}$$

Here τ_1 and τ_2 correspond to zero relative velocity, figure E1, and are given by

$$\omega\tau_1 = \cos^{-1}(-u_c/|R|)$$

$$\omega\tau_2 = 2\pi - \omega\tau_1$$

In a similar manner for the equivalent linearised force the work done is

$$W_E = \int_0^T f_E \dot{v}\, dt = C_E \int_0^T (u_c + u_w - \dot{v})\dot{v}\, dt$$

which using equations (E5) and (E6) becomes

$$W_E = C_E \int_0^T (u_c + |R|\cos(\theta_R + \omega t))|V|\cos(\theta_v + \omega t)\, dt$$

$$= C_E |V| \int_0^T (u_c + |R| \cos \omega\tau) \cos(\theta_V - \theta_R + \omega\tau) d\tau$$

$$= C_E |V| \, I_E \qquad \text{(E12)}$$

Here the integral I_E is evaluated as

$$I_E = \cos(\theta_V - \theta_R) \int_0^T (u_c + |R| \cos\omega\tau) \cos\omega\tau \, d\tau$$

$$- \sin(\theta_V - \theta_R) \int_0^T (u_c + |R| \cos\omega\tau) \sin\omega\tau \, d\tau$$

$$= \frac{\pi}{\omega} |R| \cos(\theta_V - \theta_R) \qquad \text{(E13)}$$

Thus equating W_D and W_E as given by equations (E8) and (E9) the equivalent damping coefficient C_E is given by

$$C_E = \frac{1}{2} \rho_e C_D D \frac{I_D}{I_E} \qquad \text{(E14)}$$

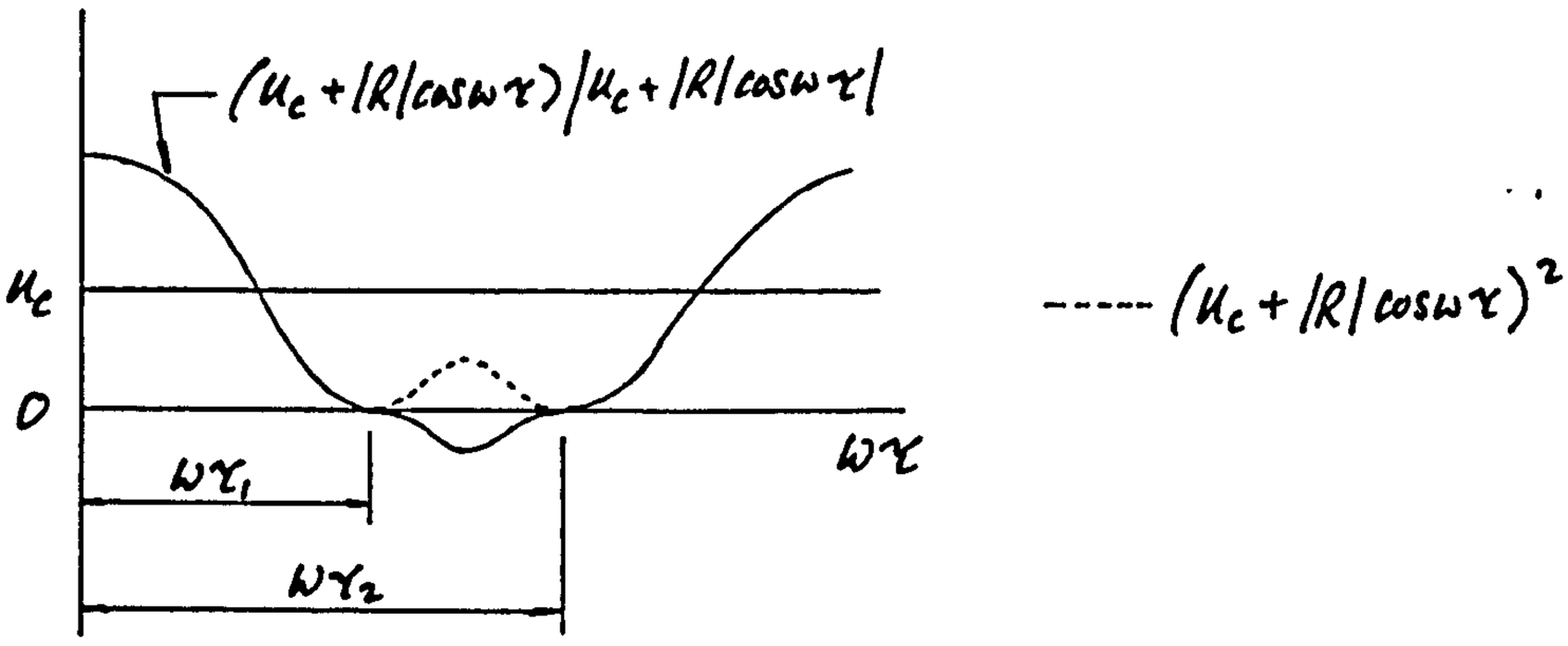

FIGURE E1

APPENDIX F

EXACT STATIC SOLUTION FOR PIPE CONTACT PROBLEM

In this section the exact static solution for the pipe-rigid foundation contact problem considered in Chapter 6 is derived for the non-zero tension case. To do this it proves convenient to introduce a second horizontal coordinate y measured from the pipe foundation separation point B, figure F1[1]. Thus with x measured from the end A the derivatives of the lateral deflection v with respect to x and y are related by

$$\frac{\partial^n v}{\partial x^n} = (-1)^n \frac{\partial^n v}{\partial y^n} \qquad \text{(F1)}$$

Now considering figure F2, and noting that the shear force and bending moment for $y<0$ are both zero, the moment at station $y \geq 0$ is

$$M(y) = Tv + R_B y - Wy^2/2 \qquad \text{(F2)}$$

where T is the tension in the pipeline, R_B is the vertical reaction at the separation point and W is the weight per length. Thus using $M = EI\partial^2 v/\partial x^2 = EI\partial^2 v/\partial y^2$ we find

$$EI\frac{d^2v}{dy^2} - Tv = R_B y - Wy^2/2 \qquad \text{(F3)}$$

---

(1) It is noted that the use of the coordinate y for the dynamic problem is ill-advised since in this case the origin of the coordinate system is moving.

with general solution

$$v(y) = A\cosh\beta y + B\sinh\beta y + \frac{WEI}{T^2} - \frac{R_B}{T}y + \frac{W}{2T}y^2 \qquad \text{(F4)}$$

Here the tension parameter β is defined by $\beta^2 = T/EI$ while A and B are arbitrary constants. Now using the geometric boundary conditions

$$v(y)\Big|_{y=0} = \frac{\partial v}{\partial y}\Big|_{y=0} = 0$$

equation (F4) becomes

$$v(y) = \frac{WEI}{T^2}\left(1+\beta^2y^2/2 - \cosh\beta y\right) + \frac{R_B}{\beta T}\left(\sinh\beta y - \beta y\right) \qquad \text{(F5)}$$

The solution is thus known once the reaction force is determined. To do this the prescribed motion $v(\ell) = v_1$ is substituted into equation (F5) giving

$$R_B = \frac{EI\beta^3 v_1 - \frac{W}{\beta}\left(1+\beta^2\ell^2/2 - \cosh\beta\ell\right)}{\sinh\beta\ell - \beta\ell} \qquad \text{(F6)}$$

In a similar manner substituting

$$\frac{\partial v}{\partial x}\Big|_{x=0} = -\frac{\partial v}{\partial y}\Big|_{y=\ell} = \theta_1$$

into equation (F5) we find

$$R_B = \frac{EI\beta^2\theta_1 + \frac{W}{\beta}(\beta\ell - \sinh\beta\ell)}{1 - \cosh\beta\ell} \qquad \text{(F7)}$$

Thus equating equations (F6) and (F7) we obtain

$$\frac{\beta v_1 - \frac{W}{EI\beta^3}(1 + \beta^2\ell^2/2 - \cosh\beta\ell)}{\sinh\beta\ell - \beta\ell} = \frac{\theta_1 + \frac{W}{EI\beta^3}(\beta\ell - \sinh\beta\ell)}{1 - \cosh\beta\ell} \qquad \text{.... (F8)}$$

Now for any prescribed (v_1, θ_1) this equation may be solved for the unknown contact length ℓ and the result substituted into either (F6) or (F7) to obtain R_B .

It is noted that substituting

$$\cosh\beta\ell = 1 + \beta^2\ell^2/2 + \beta^4\ell^4/24 + \ldots$$

$$\sinh\beta\ell = \beta\ell + \beta^3\ell^3/6 + \beta^5\ell^5/120 + \ldots$$

into equation (F8) and rearranging gives

$$3v_1 + \theta_1\ell + \beta^2\ell^2\left(\frac{v_1}{4} + \frac{\theta_1\ell}{20} - \frac{W\ell^4}{160}\right) = \frac{W\ell^4}{24EI} + O(\beta^4)$$

Thus for small β the solution for ℓ tends to the exact zero tension solution as given by equation (6.15). Finally substituting equation (F5) into equation (B2) the shear force distribution is obtained as

$$S = T\frac{\partial v}{\partial x} - EI\frac{\partial^3 v}{\partial x^3}$$

$$= -T\frac{\partial v}{\partial y} + EI\frac{\partial^3 v}{\partial y^3}$$

$$= R_B - Wy$$

(F9)

Thus at the contact point $y = 0$ the shear force is $S = R_B$ as expected.

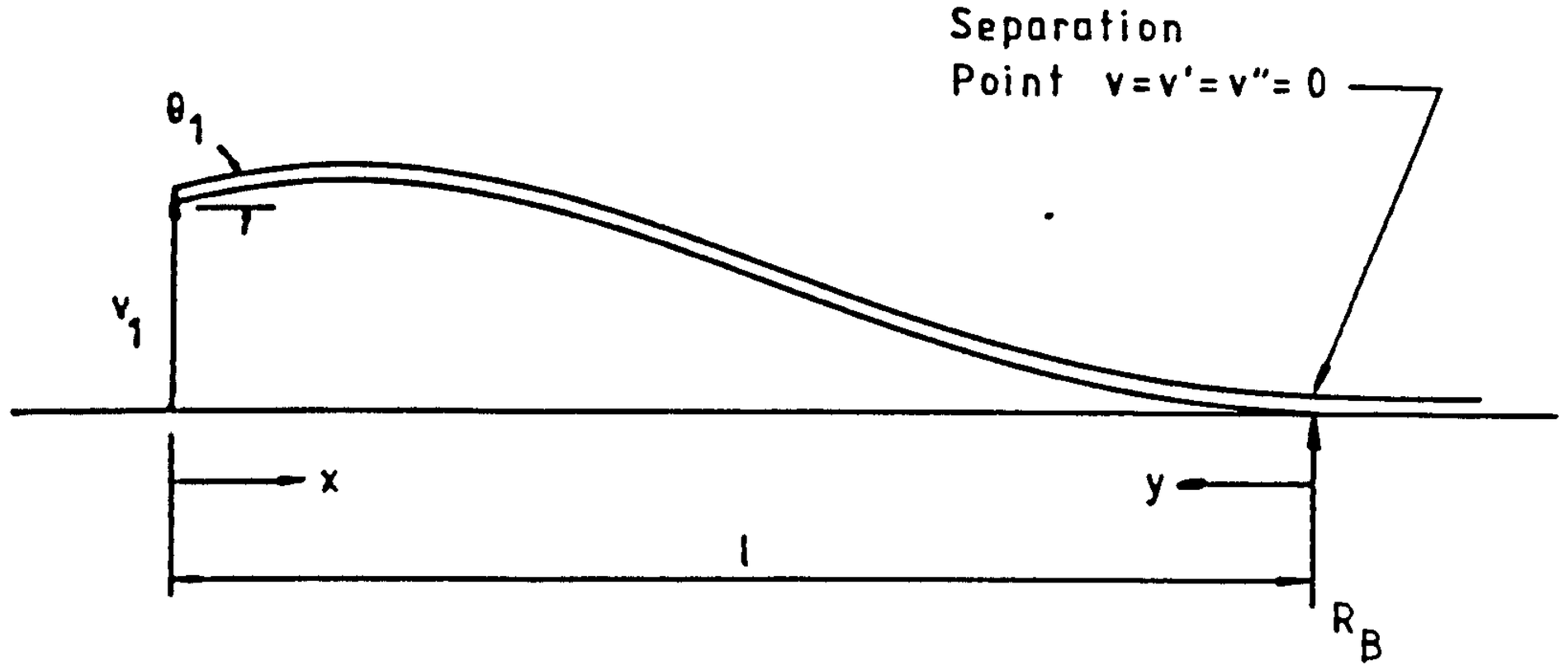

FIG F1

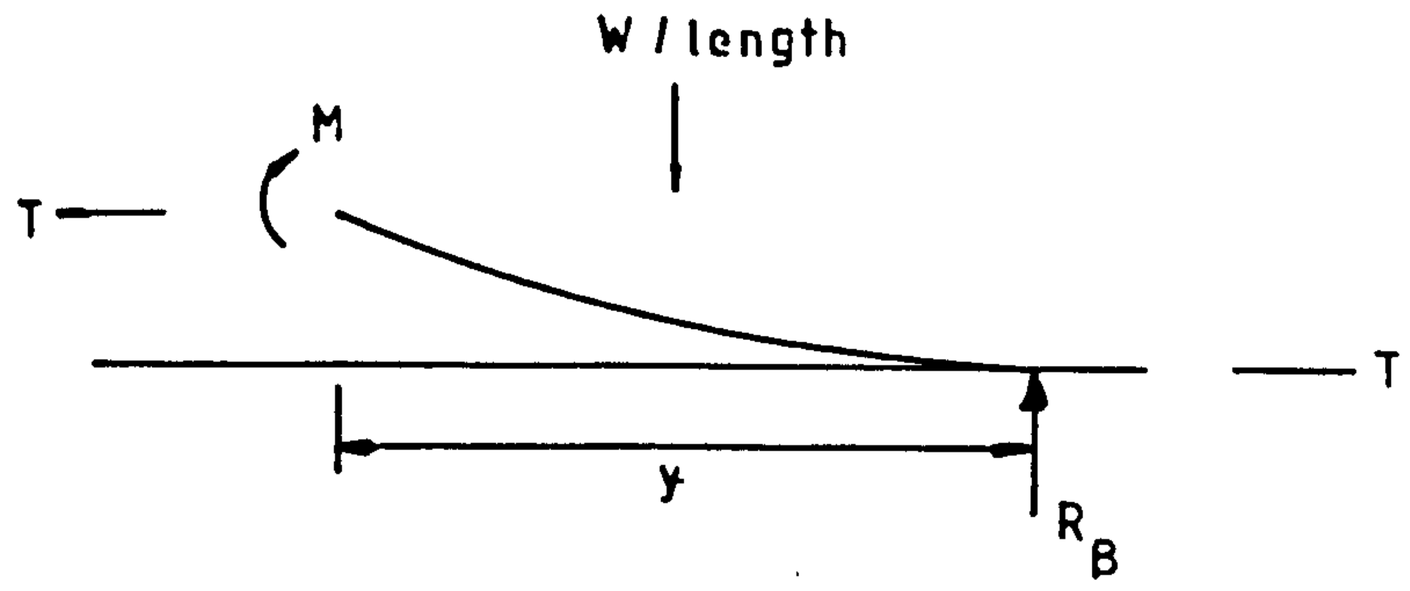

FIG F2